Spectroscopic And Computational Studies On Functionalized Nanohybrids For Potential Manifold Applications

THESIS

Submitted for the Degree of

DOCTOR OF PHILOSOPHY (SCIENCE)

In

NANOSCIENCE AND NANOTECHNOLOGY

By

TUHIN KUMAR MAJI

CENTRE FOR RESEARCH IN NANOSCIENCE AND NANOTECHNOLOGY

UNIVERSITY OF CALCUTTA

2020

To
Those who Kept Faith on Me

Acknowledgements

This gives me enormous pleasure and satisfaction to pay my admiration to those who have helped, motivated and contributed to accomplish my dissertation work. I would like to thank all of them for their kind support.

First and foremost, I owe my sincere and humble gratitude to my enthusiastic supervisor, Professor Samir Kumar Pal, and co-supervisor Dr. Debjani Karmakar for providing me the opportunity to work under their supervision. I am extremely fortunate to have such enthusiastic supervisors who sacrifice all their leisure for our academic success and are always available to answer our queries despite their busy schedules. I would like to thank Sir and Madam for believing in my capabilities and motivating me constantly. Sir's immense knowledge in the multidisciplinary field of science and technology, commitment to the highest scientific standards, unconditional support during crisis, makes him an exemplary mentor. I feel to be fortunate enough to learn from his instrumental expertise and detailed insight into various experimental problems. At the same time, it was the stern yet very valuable expert guidance, constant push, endless enthusiasm, prompt ideas from Madam that helped me a lot during my research work. I feel to be extremely lucky enough to learn the detail of computational calculation and different perspective to deal with the problem from her. It has been my privilege to work with such scientifically driven honourable figures like my supervisor and my co-supervisor. This work would not have been possible without their thoughtful guidance, warm encouragement, unconditional support, constructive criticism with simultaneous allocation to express my ideas to work independently and their inexhaustible help. Their positive vibes, everlasting energy, disciplined nature, great leadership quality and enduring willingness for learning motivates me substantially and thank you very much Sir for inspiring me to believe in my dreams.

I am grateful to get the opportunity to actively work with talented researchers from various national and international institutes. I would like to thank Prof. Peter Lemmens and Dr. Dirk Wulferding of TU Braunschweig, Germany, Prof. Saleh A. Ahmed of Umm Al-Qura University, KSA, Dr. KV Adarsh, IISER Bhopal, Dr. Kaushik Majumdar of IISc Bengalore, Dr. Ranjit Hawaldar of CMET Pune, Dr. Chinmoy Bhattacharya of IIEST, Shibpur India for fruitful collaborations.

I express my gratitude to all the faculty members and the office staffs of S. N. Bose National Centre for Basic Sciences for their assistance in my research career. A sincere appreciation goes to all other non-academic staff and gardeners of SNBNCBS who have actively maintained the magnificent ambiance of the centre. I would like to give special thanks to all technical cell members (Surajit Da, Shakti Da, Amit da, Samik Da, Urmi Di, Dipayan da, Joy Da) for their help during performing different experiments. I have bothered you a lot to get slots. I acknowledge the Department of Science and Technology (DST), India for providing me INSPIRE fellowship as financial assistance. I would like to thank SERB for funding me Florida (USA) conference and CSIR for funding me Sochi (Russia) conference.

I'd like to express my sincere gratitude to all my seniors and colleagues for providing an enriching work environment. I am especially thankful to Dr. Prasenjit Kar and Damayanti for mentoring me at the initial stage of my research work. I am grateful to Dr. Probir Kumar Sarkar for helping me out from many technical difficulties during my works. My sincere appreciation goes to all my seniors: Dr. Samim Sardar, Dr. Nabarun Polley, Dr. Susobhan Choudhury, Dr. Prasanna Kumar Mondal, Dr. Siddhi Choudhuri, Dr. Sreyashi Dutta, Dr. Gautam Chanda, Dr. Priya Singh, and earlier lab-member Mr. Ramesh Nandi. I acknowledge Dr. Tanushree Dutta for discussing with me on the topic of hybrid materials. My sincere admiration goes to all the present group members: Nur, Dipanjan, Arka, Arpan, Nivedita, Neha, Animesh da, Soumendra da, Dr. Jayita, Aniruddha, Susmita, Pritam, Dr. Tatini Rakshit, Dr. Soumendra Darbar, Lopamudra, Deep Shikha, Mahasweta, Amrita, Nairit, Ria, Sumana di, Manali, Aman, Alisha, Oiendrila for providing a homely and a cheerful environment, and also for assisting me during research work. I am grateful to Abhijit da and Sanjay Sir who have assisted me to solve all computers and cluster related problem. Special thanks to Nur, Dipanjan and Pritam for their assistance in formatting and proof-reading my thesis. Very special thanks to Probir da for standing behind me in my crisis times. I also thank Damayanti and Priya with whom I shared many joyful moments in the recent past.

I pay tribute to all my teachers throughout my life.Utilizing this scope I would like to thank my school teachers and particularly my school, BBNV itself, for I am what I am because of that place. It was them, who kept faith in me first. I would like to mention the names: Sarit Sir, Narayan Sir, Chandra Madam, Susmita Madam, Partha Sir, Avay Sir, Nikhil Sir, Ujjal Sir and many others. I would like to thank Pinaki Sir, low profile

yet most impactful physics teacher, for he was the person who got me interested in physics in the first place. The professors at my alma mater, Ramakrishna Mission Vidyamandira have been a fantastic inspiration and through their constant encouragement have pushed me to explore physics and go into research. It will be an injustice if I do not thank Vinay Maharaj, Debanjan Maharaj and Principal Maharaj (Tyagarupananada). They taught me many life lessons during my 3 year stay at RKMV. I would extend my thanks to the fantastic Physics group at RKMV, our group studies helped a lot to crack IIT-JAM.

My time at the S. N. Bose Centre would not have been so great without a few trusted persons that I had here. First, I must thank Shreya who is the best company always, with whom I shared many glorious moments. We spent several hours to resolve our PhD life problems and again started working with new enthusiasm. I have been fortunate enough to have a good friend circle, seniors and juniors at our institute. Due to their presence, the environment has always been very charming and joyful. I must mention the name of the Suraka, Khata, Anubhab, Samrat, Piya, Aritra, Sudip, Sourav, Sayani Di, Subhasish Da, Nirnay Da, Biplab Da, Sumanta Da, Rakesh Da, Aslam Da, Soumyadip Da, Shirshendu da, Basudeb da, Arpan Da, Hrisit Da, Debanjan Da, Ishita Di, Sankar da, Kallol Da, Kausik Chanda, Saniur, Swarnali, Abhik, Soham, Jayarshi, Biswajit, Sahoo, Arnab Da (my TT Partner) and many others. I have been quite active in the activities of "Muktangan" and I thank all my friends and companions who have been in these committees (especially Anupam) and made it really easy to work and make our centre a better and more productive place not only in science but in other aspects as well. The PhotoFest 2020 was one of the best memories of my SNB life. Subhodh and Utpal made my life easier at BARC.

I would like to pay regards to my family and all of my relatives for their love, affection, praise, and good wishes. I must thank my sister (Boni), who is really close to my heart and who supports me always. I would like to thank my parents to give me life and brought me up. Here I would like to mention that my maternal uncle (Mejo Mama) was the first to inspire me to get into Research work. I hereby acknowledge and thank all those who directly or indirectly supported me in this mesmerizing venture.

Finally, I would like to thank everybody who played an important role throughout my journey. I apologize if I missed anyone, who has helped me through these testing years.

Dated: 15/12/2020

Department of Chemical, Biological and Macromolecular Sciences,
S. N. Bose National Centre for Basic Sciences,
Salt Lake, Kolkata 700106, India

Tuhin Kumar Maji

(Tuhin Kumar Maji)

CONTENTS

Page

Thesis Title: Spectroscopic And Computational Studies On Functionalized Nanohybrids For Potential Manifold Applications

Abstract

Nanohybrid materials and heterostructures are constituted of different components, wherein, interactions at the molecular level provide an enhanced or novel characteristic compared to the pristine and unreacted constituents. To obtain an understanding of such systems, it is of prime importance to explore the modulation of the electronic properties at the interface of the hybrid after using a variety of spectroscopic tools including ultrafast technique. In addition, the first principles-based theoretical investigations provide an idea of the microscopic property of the heterostructure. The present thesis is composed of an in-depth study of the electronic properties of various types of nanohybrids and heterostructures with their enriched multifunctional applications using combined spectroscopic and computational investigations. The prime motivations of the thesis are; a) efficient harvesting of the full solar spectrum by using oxide-based nanohybrid systems, b) exploring the engineered electronic properties of Graphene analogous transition metal dichalcogenide (TMDC) based heterostructure after using theoretical as well as experimental tools, c) predicting effective nanohybrids and heterostructures for potential manifold applications, and d) developing nanohybrids for multipurpose applications including drug delivery after removing the toxic contaminants from food additives. The works include synthesis, structural characterization, optical studies, and computational analysis of various semiconductor nanohybrids and heterostructure towards improved performance.

In the present works, we have developed different oxide-based ($ZnO/TiO_2/Fe_2O_3$) semiconductor nanohybrids for full solar light harvesting. Electronic properties of 2D heterostructures ($MoSe_2$/GO and MoS_2/TiO_2) have been investigated for potential device application. We have designed nano-heterostructure of Drude metals (Au/Ag) and interfaces of Drude metal/Weyl semimetal systems having novel correlated attributes leading to intriguing electronic and optical properties. A new target-specific drug has been discovered using Fe_2O_3 and folate receptor for cancer treatment. We have developed a simple, efficient, and field-deployable technique to remove toxic heavy metals like Mercury from essential food additive Curcumin.

In summary, the results obtained in this thesis for the designing and development of hybrid materials, from synthesis to optical and theoretical investigation for improvement of their multifunctional activity, could be useful in designing smart materials having potential applications in various field including optics, optoelectronics, light-harvesting, drug-delivery, food-technology and so on.

Tuhin Kumar Maji

Chapter 1

Introduction

1.1. Background:

Hybrid materials represent emerging material classes in the contemporary scientific arena [1-6]. Nanohybrid (NH) is a special class of hybrid material having a dimension in the nanoscale region [6]. Many of the well-established traditional materials cannot accomplish all modern age technological necessities for the numerous new generation applications. Thus the development of hybrid material is of utmost importance to fulfill the current demand of society. The massive technological advancement in the last two decades demands multifunctional hybrid material that can fulfill the requirement in different fields. Accomplishing nanostructured hybrid material includes cross-cutting synthetic strategies where all the wings of chemistry (organic, inorganic, physical, polymer, solid-state, material, and biological), and material science, soft matter, and processing are synergistically interconnected.

Due to the growing population and lavish lifestyle, the energy demand is increasing day by day [7]. As fossil fuel is very limited, it imperative to utilize renewable energy as an alternative to it [8]. Solar energy is one of the most abundant and inexpensive renewable energy resources on the earth. Sunlight can be converted into electrical energy, chemical energy, and thermal energy. The amount of energy humans consume annually, about 4.6×10^{20} joules, is supplied to Earth by the Sun in roughly one hr. So, the efficient harvesting of solar energy can solve the present energy crisis. Therefore, the invention of smart hybrid materials is essential which can harvest solar light efficiently and convert the

energy to use in different fields including artificial photosynthesis to clean up the environment.

Beyond solar light harvesting, other optoelectronic material also gains a lot of attention in the modern age scientific field due to the rapid development of the semiconductor industry [9-11]. Consequently, the demand for high quality, efficient, ultra-compact optoelectronic nanoscale devices has emerged in recent days. The two-dimensional (2D) material based device can be used as a promising replacement of Si in the optoelectronic device field as it has several advantages [11, 12]. 2D material can be grown or transferred to any substrate without considering a lattice mismatch. Moreover, it has excellent optoelectronic properties, high carrier mobility which can be very advantageous for high-performance optoelectronic devices. Moreover, the tunability of the device made from 2D material is also an issue of researchers' concerns. Heterostructure made of 2D material can be beneficial to 'tune' many fundamental properties of the system [13]. Therefore, the development of 2D-hybrid material to fabricate next-generation controllable optoelectronic devices is one of the prime challenges in the optoelectronic device development field.

Furthermore, enhanced activity in hybrid material gains lots of attention in various other fields including developing a new medicine, drug delivery, detection and decontamination of heavy metals from essential food elements, development of an efficient device, superconductor, supercapacitor, etc. [14-19] Predicting the engineered hybrid system using computational calculation is an impactful new-age research topic in material science. Besides exploring the underlying microscopic property of the interface of the hybrid systems for their anomalous behavior is also crucial for efficient engineering of the NH material.

1.2. Nanohybrid Materials- A Brief Overview:

A hybrid material is a composite of two different moieties that interact at the molecular level [20]. The interactions of the two constituent at the molecular level raise completely new properties compare to pristine components. The field of hybrid material is relatively new but already it has an immense impact on material science; they are anticipated to provide a strong impact in the field of design and development of new materials. A reduction of the constituent dimensions of the hybrid system down to the molecular scale makes it possible to tune the material properties preciously. In addition to that, if one of the constituents of the hybrid system is in a defined size range of 1–100 nm then the hybrid system can be termed as nanohybrid. As the nanoparticle (NP) has a very high surface to volume ratio the 'active surface area' can interact with other moieties. The molecular-level interaction at the surface/interface between the two constituents can produce novel properties of the hybrid material and thus can improve their activities compared to their pristine equivalent [21]. In most of the cases, NH materials result in producing novel properties produced by the synergistic effect between the components, and thus often mentioned as a new type of functional materials [22, 23].

Depending on molecular interaction and parent constituent NH can be categorized into different categories. In terms of the possible interaction connecting two species, a hybrid system can be classified into two categories: *Class I* hybrid materials are those that show weak non-covalent interactions between the two phases, such as van der Waals (vdW), hydrogen bonding, or weak electrostatic interactions. On the contrary, *Class II* materials are those which show strong covalent interactions between two constituents [24]. The properties of the hybrid system are highly dependent on the strength of the interaction between the two constituents.

On the other hand, apart from bond strength depending upon the nature of two-parent counterparts of hybrid materials, it can be classified into many types: a) organic/inorganic, b) inorganic/inorganic, c) organic/organic, d) metal/metal, e) metal/semimetal, etc. However, among all, the most common type of hybrid material is the inorganic/organic hybrid system which consists of one inorganic and another organic component assembled at the nanoscale level [25]. Organic/inorganic hybrid materials have a wide diversity of potentialities to introduce novel structural design in material sciences [26-28]. Besides, two inorganic materials interacting at the molecular level can impart alteration in the property of the individuals. The hybridization of two different inorganic materials makes a novel material which can overcome the shortcomings of individual identities and raise some new enhanced properties to individual components [29, 30]. Sometimes, one organic material interacts with another organic moiety alters the characteristics of each entity. In summary, hybrid material consists of two different entities, which after molecular interaction can heighten up many new properties compare to the pristine one.

1.3. Heterostructure Materials- A Brief Overview:

In recent years, considerable efforts have been employed on the design and fabrication of heterostructures for better application purposes. Heterostructure (HS) has been defined as an interface that occurs between two layers or regions of dissimilar systems (metal, semimetal, or semiconductor). Overall, the HS can be classified as five types, including: (1) the semiconductor–semiconductor (abbreviated as S–S) HS; (2) the semiconductor-metal (abbreviated as S-M) HS; (3) the metal-semimetal (M-S) HS; (4) the semiconductor–carbon group (abbreviated as S–C) heterojunction (carbon group: activated carbon, carbon nanotubes (CNTs) and Graphene); and (5) the multicomponent heterojunction. In the present thesis, we have worked on three types of HS material including S-S HS, M-M HS, and M-S HS.

In general, the S–S heterojunction systems can be divided into two different types: *p–n* semiconductor heterojunction and non-*p–n* heterojunction systems. The usefulness of S-S heterostructures is that they offer precise control over the states and motions of charge carriers in the semiconductors. The *p–n* junction semiconductor HS is an effective structural design for the highly efficient charge collection and separation in the HS. In general, when the *p*- and *n*-type semiconductors are in contact, they form a *p–n* junction with depletion charge region at the interfaces due to the diffusion of electrons and holes, and thus create a built-in electrical potential that can direct the electrons and holes to travel in the opposite direction [31]. The *p-n* junction S-S HS has several advantages i.e. (a) efficient charge separation, (b) fast transfer rate, (c) longer lifetime of the charge carrier, endow the system for better application purposes. There are several ways to form S-S heterostructure including wet-chemical synthesis, mechanical compressing, deposition process, etc [31].

Recently, M-M HS systems became a fascinating topic in the field of material science after the discovery of different interesting properties including room temperature superconductivity [32-35]. Electronic interaction at the interface of two metals can introduce completely new properties to its individual units [32, 33]. Many new optical, electronic, and thermoelectric properties can be generated in the M-M HS systems. In addition to conventional semiconductor and metal materials, Dirac/Weyl semimetals are emerging as capable functional quantum materials for optoelectronic and photonic applications [36, 37]. In the same way, metal contacts with semimetal can introduce various new properties. The orbital overlap and electronic cross-talking between metal and semimetal at the interface can enhance many properties in the hybrid.

1.4. Nanohybrid and Heterostructure Materials for Manifold Applications:

As there are enormous numbers of combinations to make hybrid material using two or more different constituents, it is possible to design many hybrid materials depending upon the requirement. Hybrid materials represent a fundamentally interdisciplinary field of research and development connecting a variety of groups of material sciences such as hybrid interfaces, organometallics, colloids, soft matter, coordination polymers including MOFs, sol-gel, catalysis, and surfaces, clays and lamellar compounds, nanocomposites, nanoporous and mesoporous materials. Hybrid material can be used in different fields in optoelectronics, sensing, biomedicine, biomaterials, biochemistry, and engineering. NH and HS are contributing as emergent material in different important fields including energy harvesting, healthcare and drug delivery, environment remedy, electronics, supercapacitor, superconductor, sensing, optoelectronics, etc. [14-19] Another important aspect of hybrid material is the multifunctionality due to the synergistic effect of its two components. In the hybrid system, one may get the properties of both pristine systems as well as some new properties. By tailoring the pristine systems or the molecular level attachment between systems, it is possible to tune the different properties of the NHs. HS are the building blocks of many of the most advanced semiconductor devices presently being developed and produced. HS system can be used for high-performance IR detection process, providing new thinking for next-generation commercial photodetectors [32]. One of the main challenges in the current century is energy storage. HS materials with proper band alignments are showing the pathways to harvest energy efficiently [33, 34]. Apart from that, semiconductor HS has been used in laser technology also. In 1963 Herbert Kroemer, proposed that population inversion [35] could be greatly enhanced by HS, which is the

fundamental technology of laser. In summary, depending on our requirement hybrid material can be developed towards its application in various fields.

1.5. Scope of the Spectroscopic Investigation on Hybrid Materials for Manifold Applications:

The most evident benefit of hybrid material is that there is a possibility of combining two materials having completely different properties and it results in "*best of both*" properties. Most of the time shortcomings of pristine material have been solved by the hybrid system. Since there is a possibility of numerous combinations between different constituents, this research field is very much innovative, as it offers the prospect to invent an almost indefinite set of novel materials with enhanced multifunctional properties. Research on the transformed physicochemical properties of hybrid material has gained a lot of attention from the scientific community as they have an extensive range of applications including solar light harvesting, multi-sensor, high-temperature superconductivity, novel drug design, and higher device performance. Moreover, NH has an additional benefit of higher active surface area which escalates its functionality. So, there is an enormous scope to investigate and develop new NH for enhanced multifunctional activity in various fields.

One of the most important applications of NH is to harvest the full solar spectrum and convert the solar photons into electricity and chemical energy efficiently using suitable semiconductor NH [36, 37]. Increasing environmental pollution and limited resource of fossil fuels demand to work on clean and renewable energy resources [38-40]. Solar light is undoubtedly the most convenient and widely available sustainable energy source. Photocatalysis using solar light has attracted universal attention as a potentially efficient, environmentally friendly, and low-cost method to purify contaminated water as well as for renewable hydrogen production [41, 42]. For the last few decades,

oxide-based wide bandgap semiconductor NP such as TiO_2, ZnO have been widely used as a photocatalytic material to harvest solar light [43-48]. However, ZnO has some intrinsic surface defects [49] which limit its activity as a photocatalyst. Defect induced recombination of photoinduced electron-hole pair in the semiconductors for their photocatalytic activities are very much disadvantageous. Surface modification of inorganic NP using different ions is a familiar strategy to induce substantial modulation in the functionality of the NP. In one of our works, we report surface modification of ZnO NP by halide ions using a simple precipitation method and demonstrate that proximity of various halide ions to the NP modifies their various electronic properties. The attachment of halide ion on the surface defect state of ZnO has been confirmed via various spectroscopic tools. It is found that defect state healing by a particular halide ion can heighten up the photocatalytic activity of ZnO NP.

Although defect state healing of wide bandgap semiconductor can increase its photocatalytic activity, the main problem of those systems is that they can harvest only the ultraviolet portion of solar spectra which is ~4% of the full solar spectrum due to their large bandgap (TiO_2 (~3.2 eV) or ZnO (~3.37eV)). Thus, a new approach is required to overcome this difficulty. A key strategy to proficient solar energy conversion is the development of novel high-performance NH materials with an absorption band similar to the solar spectrum and an efficient photoexcited charge carrier separation property to arrest fast electron-hole recombination rate. A rationalized design of NH material can give a better performance towards harvesting the visible part of solar light efficiently. The development of organic-inorganic NH light-harvesting materials satisfies the above-mentioned conditions where the organic ligand is used as a sensitizer to harvest the visible light. Although, the functionality of the hybrid material highly relies on the charge transfer dynamics across the interface of NPs associated with the constituents [50].

NIR part of solar light contains almost 50% of the solar spectra. So to harvest full solar light, it is highly required to design a nanomaterial that can harvest the NIR part of solar light. However, the main disadvantage of low bandgap NIR harvesting semiconductors is its very high recombination rate which limits its activity as a photocatalyst. So, developments of hybrid systems that can harvest the NIR light efficiently to use it for photocatalysis are of utmost importance. A combination of low bandgap semiconductor and wide bandgap semiconductor with proper band alignment can resolve this problem.

Another significant motivation of the thesis is to develop new-age optoelectronic devices using 2D materials. With the rapid development of technologies, the community demands high-performance optoelectronic devices. Compared to bulk semiconductor, the 2D material based optoelectronic device shows extraordinary performance due to higher carrier mobility, fast photoresponse, high performance, etc. [12, 51, 52] In one of our work, we developed a heterostructure based on 2D material MoS_2 and wide bandgap semiconductor TiO_2 using different deposition techniques. The formation of HS has been verified by Raman spectroscopy. Furthermore, the X-Ray Photoelectron spectroscopy (XPS) reveals the *p*-type doping nature of the HS system. This 2D HS system has been tested for potential photo-transistor application purposes.

Furthermore, one more major objective of this thesis is to study the photoinduced dynamical processes at the heterogeneous interface present in NH materials which are important from both fundamental and application perspectives. This investigation is very much crucial to develop high-performance photocatalysts, photoelectrochemical materials as well as photo-medicines. Light-harvesting materials used in photocatalysis and photovoltaic, optoelectronics, or photo-medicine field are associated with ultrafast excited-state charge transfer across the interfaces [53, 54]. Thus to understand the excited-state charge transfer between the two constituents of the NH is very much essential to understand the

detailed microscopic mechanism related to higher photocatalysis, photo-electrochemistry, or enhance the activity of photomedicine. Spectroscopy is a crucial tool to understand the dynamical process in the interface of the hybrid systems. In one of our studies, we have sensitized magnetic NP Fe_2O_3 with a low-cost dye phthalocyanine to form NH for application in photocatalytic devices and photoelectrochemical field. This study reveals the role of phthalocyanine ligand in excited state electron transfer processes and its implications in the photocatalytic activity and enhances the photocurrent response of the NH. In another study, we have investigated the impact of the central metal ion in protoporphyrin IX (PPIX) functionalized TiO_2 NP. The study reveals the role of copper ion in the PPIX and the excited state charge delocalization mechanism from PPIX to TiO_2. Moreover, the manifestation of higher charge transfer in NH has been manifested in the enhanced photocatalytic property. The enhanced charge transfer route for which the catalytic activity is increasing is established by various spectroscopic tools including picosecond measurement. In another work, near-infrared (NIR) light induce charge separation processes at the semiconductor-semiconductor (CuS-ZnO) interface are explored for efficient NIR light harvesting. The formation of hybrid material has been established using Ultrafast Spectroscopy and Raman Spectroscopy. The synergistic combination of low bandgap semiconductor (CuS) and wide bandgap semiconductor (ZnO) gives higher electron delocalization of CuS upon excitation using NIR light, which manifests higher photocatalytic activity. In another work, we have investigated the target-specific drug delivery using folic acid (FA) mediated water-soluble iron oxide NPs (FA-Fe_2O_3). Here, folic acid targets the cancer cells by using its folate receptor. Photoinduced charge separation at the semiconductor-drug (FA-Fe_2O_3) interface through Förster resonance energy transfer (FRET) enhances the reactive oxygen species (ROS) generation of FA-Fe_2O_3 with respect to Fe_2O_3. This newly synthesized NH can be used as an MRI contrast agent for diagnosis. Furthermore, the generation of the midgap state and trap states can affect the electronic structure of the hybrid

system heavily [55]. We have used transient absorption spectroscopy of the MoS_2/TiO_2 heterostructure to investigate the trap states in the hybrid system and time-resolved two-photon spectroscopy to probe the midgap states within the system.

The experimental tools used for studying the dynamical processes involve picosecond-resolved carrier relaxation dynamics, such as photoinduced electron transfer (PET) [56] and FRET [57, 58]. Transient Absorption (TA), Two-photon spectroscopy has been utilized to probe the mid-gap state within the bandgap. *Z*-scan measurement was utilized for studying the non-linear dynamics. The different experimental techniques employed for the structural and functional characterization of the hybrid materials include steady-state UV-Vis absorption and fluorescence, thermo-gravimetric analysis (TGA), Fourier transform infrared spectroscopy (FTIR), Raman scattering, dynamic light scattering (DLS), powder X-ray diffraction (XRD), cyclic voltammetry (CV), X-ray photoelectron spectroscopy (XPS), field emission scanning electron microscopy (FESEM) and high-resolution transmission electron microscopy (HRTEM).

1.6. Scope of the Computational Investigation on Hybrid Materials for Manifold Applications:

Computational modeling of hybrid materials is a powerful tool being used in the development of advanced materials and their device applications [59]. The unique benefit of computational modeling lies in the possibility to calculate macroscopic properties of materials based on calculations of microscopic quantities. In the last few decades, many experimental phenomena including photochemical reaction pathway, radiative and nonradiative decay processes have drawn substantial attention of the computational chemists to offer the explanations of several unanswered queries in photophysics and photochemistry. Using computational calculation it is possible to investigate the comprehensive

mechanisms of unexplored complicated chemical reactions, ground state, and excited state charge delocalization pathway, excitonic feature, and device transport characteristics of the systems.

Another important motivation of the thesis is the prediction of highly efficient NH using the computational calculation for high-performance activity in the different field i.e. solar light harvesting, development of nanomedicine, toxic metal decontamination pathway, the device performance of the hybrid system, investigation of unexpected behavior in metal/metal, metal/semimetal hybrid system, etc. In this thesis, we have carried out computational investigations on different NH to understand the fascinating intrinsic property at the interfaces. In one of our works, we have calculated the efficient charge separation from phthalocyanine to Fe_2O_3 NP in the NH system which supports the experimental ligand to metal charge transfer mechanism. The reason behind the increment of the magnetic moment is also investigated. In another work, we have investigated the role of trap state generation and removal and its effect in photocatalysis in ZnO NP. Time-resolved fluorescence spectroscopy shows an electron migration pathway in both Mn-doped ZnO NP and Cl-ZnO NP (at the surface). However, Density Functional Theory (DFT) calculations show that for Mn-doped ZnO electron has been confined in the trap state generated by the dopant and became unavailable. But Cl-ZnO shows the removal of the trap state and in this case, excited state electron has been migrated to the system and became available which results in higher catalytic activity. In another work, we have used computational calculation to predict that Cu-ion can replace the toxic Hg from contaminated Hg-Curcumin complex which has been later verified experimentally. Our first-principles DFT study shows that the formation of Hg-Curcumin is energetically unstable whereas the formation of Cu-Curcumin is energetically stable. In another case, we have predicted the formation of HS using two semiconductors CuS and ZnO. We found the formation of CuS-ZnO HS is energetically stable, and due to

the favorable band alignment, there is a possibility of higher charge separation from CuS to ZnO. This hybrid system gives better photocatalytic activity due to the higher carrier separation. In a different study, we have shown the possibility of modulation the doping property of Graphene Oxide/$MoSe_2$ HS by varying the ligand type and concentration. Moreover, the device performance of the HS is also predicted using quantum transport calculation. We have also investigated the electronic properties of MoS_2/TiO_2 HS. It is found that heterostructure shows *p*-type doping which validates experimental findings. The experimental finding of the midgap state in the hybrid structure is verified by band-structure analysis. Moreover, it has been observed that surface termination of the TiO_2 layer plays a key role to modulate the electronic structure of the HS. Recently, researchers have shown that a combination of two Drude metal (Au and Ag) can enhance the room temperature transport properties heavily. The electronic property of the Au/Ag interface needs to be investigated to understand the anomalous behavior of the combined hybrid system. In another study, we probed the first principles electronic structure analysis of the different combination of Au/Ag hybrid systems (large area interface and nanostructure) to understand the fascinating properties of the hybrid. It is found that, in the hybrid system highly hybridized flat bands are generated near Fermi level which is the reason behind the new anomalous properties in the Au/Ag hybrid. Moreover, the nano Au/Ag hybrid shows epsilon near zero behavior and phonon instability. Furthermore, a combination of metal/semimetal HS with different geometric orientations has been investigated. In one of our studies, we have shown that plasmonic metal (Au and Ag) attachment on Weyl semimetal TaAs shows many new properties. Furthermore, single interface (Metal/TaAs) and stacked interface (Metal/TaAs/Metal/TaAs…) can show completely different phenomena in the HS.

The computational tools used for studying the electronic interaction include DFT as implemented in Vienna Ab initio Simulation Package (VASP) [60, 61] with norm-conserving projector augmented wave (PAW) pseudopotentials and generalized gradient approximated (GGA) Perdew-Burke-Ernzerhof (PBE) exchange-correlation functionals [62] with the incorporation of spin-orbit coupling. vdW corrections are incorporated by following the semi-empirical Grimme DFT-D2 method [63]. Monkhorst-Pack *k*-points grid [64] has been used and ionic relaxations are performed by using the conjugate gradient algorithm [65] with the cutoff for the Hellmann-Feynman force as 0.01 eV/Å. For the DFT-coupled quantum transport, we have used the Atomistic Toolkit 15.1 packages [66], with the GGA-PBE exchange-correlation and double-zeta plus polarization basis set. The time-dependent optical properties are calculated by using the all-electron full-potential linearized augmented plane wave approach including local orbitals (FP-LAPW + lo) within the framework of DFT as implemented in the ELK 4.3.6 code [50]. We have treated the exchange-correlation potentials with local density approximation (LDA) with Perdew-Wang/Ceperley Alder functional.

1.7. Objective:

The prime objective of the present thesis can be categorized into four main sections: a) application of the NH system towards harvesting full solar spectra; b) development of 2D HS for future device application; c) prediction and development of new engineered hybrid material for improved application in various fields; and d) development of NH for advanced medicinal activity and food adulterate purification.

The use of hybrid materials for its beneficial applications in the energy harvesting field has gained enormous attention in recent times to address the global energy crisis challenges. Among all, semiconductor materials such as TiO_2, ZnO have been extensively used in the field of photocatalysis and photovoltaic

applications as they have very high photo-conversion efficiency. However, these systems can absorb only the UV part of the solar light. So it is imperative to develop efficient hybrid materials using those semiconductors which have a broader absorption band, high charge separation ability, and better photo-conversion rate. One of the prime objectives of this thesis is to develop light-harvesting material by investigating the ultrafast dynamical processes and electron delocalization pathway across the interface of the newly developed NH to enhance the solar light-harvesting efficiency. However, the correlation between the spectroscopic studies and computational studies on hybrid systems for their application in the light-harvesting field is sparse in the literature. In the thesis, we have established a bridge between spectroscopic studies and computational findings.

The intrinsic surface defect on wide bandgap semiconductors (TiO_2/ZnO) limits its photocatalytic activity. Two of our studies focus on the engineering of surface defects of wide bandgap semiconductor ZnO to enhance photocatalytic activity. We have attached different halide ions on the surface of ZnO NP to reduced defect-related trap states which enhances the photocatalytic activity. However, pristine ZnO or TiO_2 can only absorb UV light. One of the common ways to utilize those wide bandgap semiconductors for visible light photocatalysis is to sensitize them with visible light-absorbing dyes. A substantial amount of research has been carried out in this direction to make cost-effective and environment-friendly dye-sensitized NHs [67, 68]. In this context, low-cost and biocompatible porphyrin and phthalocyanine based NHs are gaining lots of attention from the researchers [69-74]. Two of our studies in this direction are aimed to investigate the role of phthalocyanine or porphyrin sensitization on oxide-based semiconductor NH and its implications in solar light harvesting. A combined experimental and computational approach reveals that there is charge transfer from the dye to the metal of the semiconductor (LMCT) [75]. However,

apart from UV and visible light, the NIR part of solar spectra contains half of the spectra. As NIR light produces a lot of heat, NIR absorbing dye-sensitized semiconductor is not a good choice for NIR light-driven photocatalysis. So, for harvesting the NIR part of the solar light, besides organic dye sensitization, we have carried out another approach; which is to combine two suitable semiconductors of different bandgaps [31, 42]. The development of a semiconductor heterojunction has gained a lot of attention due to its higher efficiency in improving photocatalytic activity. Combining a low bandgap semiconductor and a wide bandgap semiconductor with proper band alignment can harvest a bigger portion of the solar spectrum [76]. Recently, Shang *et al.* show visible light-induced photocatalysis using Bi_2WO_6/TiO_2 hybrid system [77]. This hybrid system shows a type II HS. In this direction, we have explored the formation of semiconductor-semiconductor (CuS/ZnO) NH with a proper band alignment which facilitates higher charge separation. The CuS/ZnO NH leads to efficient photocatalytic properties using NIR lights. The formation of NH has been confirmed via spectroscopic studies whereas the increment of catalytic activity has been explained using proper band alignment as predicted by DFT calculations. In summary, we have used several suitable approaches to modulate the band gap of semiconductors to harvest the complete solar spectra.

Recently, 2D material vdW HS systems gain a lot of attention due to its prospect in various fields of applications. A revolutionary development is to flexibly construct many different kinds of HS with a diversity of 2D materials. The combined hybrid structures reveal unique properties that individual systems do not possess, which forecast promising future applications in different fields [78-80]. Therefore, a detailed understanding of the structural, electronic, and optical properties of the hybrid system is very crucial to the effective design and construction of new electronic devices or understands new physical properties of the hybrids. In one of our works, we have investigated the tunable doping

property and device performance of GO/$MoSe_2$ HS by rational modification of the ligand type and concentration of the GO. An increment of oxygen concentration leads to the alteration of the doping property of the hybrid from *n*-type to *p*-type. Our investigation reveals a device constructed from this heterostructure with vertical contact can sustain the tunable doping property.

Rational, data-driven hybrid materials discovery would be an enormous benefit for research and development [81]. Predicting the band alignment in the HS system can give information about the charge transfer pathways. On the other hand, designing hybrid material and investigating its property by modulating the parameter of the hybrid is of extreme importance to improve the performance of the hybrid system. One of the motivations of the thesis is to design new engineered hybrid systems or interface and investigate the microscopic properties at the surface of the hybrid system. Higher superconducting critical temperature and large-area epsilon-near-zero systems are two long-standing goals of the scientific community. Motivated by the recent experimentally observed strongly correlated phenomena in nanostructures of simple bimetallic systems, we have attempted to investigate the physics behind the unusual properties of the bimetallic combinations using first-principles DFT calculations. We have chosen different potential bimetallic FCC combinations starting from a large-area interface to embed and doped 2D nanostructures, having similarities with the experimentally studied systems. We have investigated the microscopic property of the interface of the metal/metal system namely Au/Ag. The engineered hybrid system shows interface morphology induced localized bands near Fermi level which leads to epsilon near zero behavior in the ultra-violet to visible (UV-vis) optical range. Phonon-dispersion of the nanostructured interface systems has also been investigated to understand the unusual properties. The presence of soft phonons is found in the bimetallic interface system which indicates the dynamical instabilities. Investigation of Metal/TaAs interface reveals the occurrence of

phonon-mediated correlated phenomena in the presence of Noble metal. Quantum transport calculations on different device geometries show the role of contact geometry for spin-transport in TaAs devices.

Nowadays, the use of hybrid materials for its potential application in medical science and food processing has attracted enormous attention to address healthcare challenges and food safety technology worldwide [82, 83]. Organic-inorganic NHs are becoming popular for their potential biological applications including diagnosis and treatment of cancerous cells. The current trend in research in the medicinal field focuses on the use of NH material in diverse fields including drug delivery [84], new medicinal-discovery [85], cancer treatments [85, 86], etc. NH material consists of inorganic semiconductor and organic drug or receptor has numerous potential in the medicinal field for targeted drug delivery. The interfacial properties of the hybrid system need to be investigated for advancement in the medicinal activity. One of the objectives of this thesis is to fabricate the medicinally active hybrid system and understand the ultrafast dynamical processes across the interface of heterostructure to improve the medicinal efficacy of the hybrid. The present research includes the synthesis of a novel NH for the diagnosis and therapy of colorectal cancer. Herein, we have synthesized a novel cost-effective magnetic NP based hybrid system using folic acid and Fe_2O_3 using the hydrothermal method for the theranostics application. The excited state interaction between Fe_2O_3 and FA are thoroughly characterized using ultrafast spectroscopic tools. The NH (FA-Fe_2O_3) is a combination of two nontoxic ingredients FA and Fe_2O_3, which shows remarkable photodynamic therapy (PDT) activity in human colorectal carcinoma cell lines (HCT 116) via generation of intracellular ROS.

Moreover, at the same time, decontaminating toxic things from food additives is also a big challenge nowadays. Due to the increment of soil pollution producing from industrial waste, toxic metals can be adsorbed by plants during

cultivation. Curcumin (known as 'Haldi') is a very common food additive that can chelate with toxic heavy metal Hg. It is very difficult to differentiate Hg-Curcumin and pure Curcumin by the naked eye. A new strategy has been developed where toxic Hg has been replaced by non-toxic Cu ion in Curcumin via a simple transmetalation technique. The transformation of Hg-Curcumin to Cu-Curcumin in presence of Cu is duly verified by different spectroscopic techniques. Surface Plasmon Resonance (SPR) of Ag-NP has been employed to detect free Hg which has been expelled from Curcumin. The excited state decay of Cu-treated Hg-Curcumin resembles Cu-Curcumin which indicates that Hg-Curcumin transforms to Cu-Curcumin. The real mechanism of metal exchange has been investigated using density functional calculation. This transmetalation technique can be very efficient to remove toxic metal from other food additives also.

The results acquired from all these studies of NH heterojunction systems using combined spectroscopic and computational study could be very promising in designing new-age materials for benefit in different practical fields including energy harvesting, device fabrication, high-temperature superconductivity, development of medicine, sensing application, etc.

1.8. Summary of the Work Done:

1.8.1. Spectroscopic and Computational Studies on the Role of Surface Defects of UV Light Harvesting Nanomaterials:

1.8.1.1. Enhanced Charge Separation through Modulation of Defect-state in Wide Band-gap Semiconductor for Potential Photocatalysis Application: Ultrafast Spectroscopy and Computational Studies [87]: Structural defects of wide bandgap semiconductors play important role in their functionality. Defect mediated recombination of photoinduced electron-hole pair in the semiconductors for their photocatalytic activities, is detrimental. The present work indicates that

for metal oxides semiconductor, the use of anionic attachment like chloride ion as surface defect healer proves to be more useful for photocatalytic application than bulk doping using cationic dopant like Mn. ZnO NPs of different sizes (5 nm and 30 nm) are synthesized via precipitation method and allowed to interact with chloride ions in an aqueous solution. A variety of electron microscopy and picosecond resolved spectroscopic techniques have been employed to study the role of chloride ions for the enhanced photoinduced charge separation in aqueous environments. Our first-principles DFT calculations for ZnO nanoclusters with surface oxygen vacancy indicate that the introduction of trap states within the bandgap of the nanocluster can effectively confine the photoinduced electrons. However, upon chloride ion attachment to the defect states, the energy of the trap states was found to be healed, recovering the efficacy of reactive oxygen species (ROS) generation in the aqueous solution. The DFT calculation on the Mn^{2+} ion impregnated ZnO lattice reveals more defect states compare to that of a pristine lattice. The rate of electron recombination is found to be much faster through the non-radiative pathway, leading to a decrease in photocatalytic activity in the case of Mn-doped ZnO. Attachment of chloride ion to the Mn-doped ZnO partially recovers the ROS generation.

1.8.1.2. Halide Modulated Functionality of Wide Bandgap Zinc Oxide Semiconductor Nanoparticle [88]: Surface modification of inorganic nanomaterials using different ions is well-known to induce significant modulation in the functionality of the NP which improves tuning their relevant properties for suitable applications in the field of nanotechnology. In this work, we demonstrate synthesis and surface modification of a model inorganic wide bandgap semiconductor ZnO NP by halide ions using simple precipitation method and exhibit that proximity of various halide ions to the NP modifies their electronic properties. It is interesting to note that such surface modulation has little impact on its morphology, while significantly influencing their applications in

photocatalytic activity or magnetism. Indeed, the halide attached ZnO NP displays a large reduction of defect state emission. Various microscopic and spectroscopic tools (including the picosecond resolved technique) were used to characterize and understand the key role of the halide ions to modulate the light-induced charge separation in ZnO NP. Picosecond resolved fluorescence spectra unveil a significant quenching, implying an electronic cross-talking between the NP and the attached halide ions. Magnetic measurements indicate that the attachment of a suitable halide ion introduces room temperature ferromagnetism in this system. Finally, the photocatalytic activity of the ZnO NP for the photodegradation of a model pollutant, methyl orange was evaluated under UV light irradiation. Halide ZnO is anticipated to be a very promising photocatalytic agent; hence it can be used to clean up environmental pollution. First principles analysis has been performed to understand the modulation of electronic properties like photocatalysis and magnetism in halide attached nanosystem. The experimental finding resembles with theoretical results.

1.8.2. Spectroscopic and Ab Initio Studies on Organic-Inorganic Nanohybrid for Visible Light Harvesting:

1.8.2.1. Development of a Photo-Catalytic Converter for Potential Use in the Detoxification of Cr(VI) Metal in Water from Natural Resources [89]: Porphyrin dye-sensitized NHs for applications in photocatalysis are advantageous due to their additional absorption band in the visible region. Here we have impregnated protoporphyrin IX with copper (II) ion and sensitized a porous microsphere TiO_2 (~1.5 μm diameter) to synthesize a novel NH for visible light photocatalysis application. Various spectroscopic tools have been employed to confirm nanohybrid formation. The hexavalent chromium a known carcinogen is commonly found in the aquatic environment as a heavy metal pollutant, whereas Cr(III) is non-toxic and considered to be an essential nutrient for living organisms.

We have applied the NH for an efficient reduction of a toxic metal ion Cr(VI) to non-toxic Cr(III) in water under visible light illumination. The advantage of the Cu ion impregnation in the sensitizing protoporphyrin dye has been justified by the intact efficacy in the photocatalytic reduction in presence of water dissolved metal ions (Cr^{3+} and Fe^{3+}) is confirmed from our study. On the other hand, the NH without the Cu (II) suffers interference from the other dissolved metal ions during the photocatalytic reduction process. Picosecond resolved fluorescence studies on the sensitizing metal-protoporphyrin molecules reveal the mechanism of higher photocatalytic activity in Cu-protoporphyrin-TiO_2 NH. For a prototype application, we have developed an active filter by depositing the NH on an extended surface of a stainless-steel metal mesh (size 2 cm × 2 cm, pore size 150 µm × 200 µm). The prototype active filter exhibits significant potential for chemical filtering of toxic Cr(VI) ions (photoreduction to Cr(III)) along with physical cleaning of suspended particulates present in water.

1.8.2.2. Development of a Magnetic Nanohybrid for Multifunctional Application: From Immobile Photocatalysis to Efficient Photoelectrochemical Water Splitting: A Combined Experimental and Computational Study [90]: Engineering of highly efficient magnetic nanomaterials with enhanced visible-light photocatalytic activity and photoelectrochemical (PEC) activity for hydrogen production is the ultimate goal in the ongoing research in the field of solar light harvesting. Hematite (α-Fe_2O_3) is a promising material that offers both enhanced photocatalytic activity and PEC activity due to its electronic band structure, high chemical stability, great abundance, and low cost. Despite these promising properties, the application of this system is limited due to its very fast electron-hole recombination rate and low carrier mobility. Here we report the design and synthesis of a newly developed NH based on Fe_2O_3 and phthalocyanine. The formation of the NH is established using a picosecond resolved optical technique as well as by Raman Spectroscopy. Ab initio study on a similar modeled system

has been performed to investigate the insight of various physical properties. While the photocatalytic activity of the NH increased 1.5 times with respect to the pristine system, the Photoelectrochemical activity almost doubles in the hybrid system. Time-resolved spectroscopy reveals there is charge transfer from phthalocyanine to Fe_2O_3 in the presence of light, which is the reason for the enhancement of activity. DFT + U calculation results show there is a possibility of higher charge separation from phthalocyanine to Fe_2O_3, which is the reason for the higher activity in the hybrid systems. To test real-world applications our developed NH has been deposited on an extended surface of a stainless-steel metal. Such a prototype active filter containing an immobilized photocatalyst shows significant chemical filtration of methylene blue (by a degradation process) along with a physical filtration by separating the suspended particulates from the water.

1.8.3. Experimental and Computational Studies on Inorganic-Inorganic Nanohybrid for Efficient NIR Light Harvesting:

1.8.3.1. A Combined Experimental and Computational Study on a Nanohybrid Material for Potential Application in NIR Photocatalysis [91]: Complete utilization of solar light in the photocatalytic reaction is of paramount importance for efficient conversion of solar light. Although NIR constitutes almost 50% of the solar energy, there are very few efforts towards its effective utilization in photocatalysis. The difficulty of NIR usage is its associated low energetic photons, which can lead to exciton generation only for low bandgap semiconductor system, which is sometimes not enough to initiate the photocatalytic process. Moreover, these types of systems have a very fast charge recombination process. Assembling one low bandgap semiconductor with a wide bandgap semiconductor to form an NH heterojunction could be an efficient NIR harvesting photocatalyst. Herein, we report a novel CuS-ZnO NH, bound by a cysteine ligand, to exhibit efficient

photocatalytic performance using the NIR fraction of the solar light spectrum. Raman spectroscopy and picosecond resolved studies have been carried out to confirm the electronic coupling of the NH. An improved photocatalytic activity towards the degradation of methyl orange was observed by the NH compared to its individual counterparts (ZnO and CuS) under NIR light illumination. First-principles investigations had guided us in obtaining an insight into the photocatalytic process. Computationally predicted band alignment implies that the NH forms a type-II heterojunction. An increment of significant charge separation from the conduction bands of CuS to those of ZnO is the key mechanism behind the enhanced photocatalysis.

1.8.4. Computational Studies on the Interlayer Modulation of Graphene Analogous Heterostructure:

1.8.4.1. Intricate Modulation of Interlayer Coupling at Graphene Oxide (GO)/$MoSe_2$ Interface: Application in Time-dependent Optics and Device Transport [92]: In GO/$MoSe_2$ semiconductor HS, we have demonstrated a subtle control on the doping dynamics by modulating interlayer coupling through the combination of strain-reducing relative rotation of the constituting layers and variation of ligand type as well as concentration. By first-principles DFT calculations incorporating spin-orbit coupling, we have investigated the impact of variable interlayer coupling in introducing non-collinear magnetic behavior in the heterostructure. The outcome of varying carrier types and their respective concentrations are investigated by static as well as time-dependent density functional calculations, which indicate the presence of optical anisotropy and time-dependent optical phenomena like exciton quenching and band-gap renormalization. The performance of such heterostructures as a channel material in devices with top and edge metal contacts is analyzed. Our self-consistent quantum transport calculations have evinced that the interface-induced variation in doping pattern is extrapolated only for devices with top contacts. The edge

contact, although exhibits a better transmission, is inefficient in sensing the ligand-induced doping modulation introduced via vertical inter-layer charge transfer.

1.8.5. Computational and Optical Studies on the Interface of MoS_2 and High *k* Dielectric Oxides for Potential Device Application:

1.8.5.1. Combinatorial Large-area MoS_2/Anatase-TiO_2 Interface: A Pathway to Emergent Optical and Optoelectronic Functionalities [93]:

A suitable combination of transition metal dichalcogenide (TMDC) and high-*k* dielectric transition metal oxides (TMO) can reduce the contact resistance and confine the Fermi-level pinning. In this work, we have fabricated a large area interface of MoS_2 and TiO_2 HS using different deposition techniques (PLD and ALD). Different characterization technique including XPS, Raman Spectroscopy, and time-resolved transient absorbance and two-photon technique has been employed to confirm the HS formation and understand the electronic properties at the interface of the HS. First-principles DFT study has been done on the HS system to understand the experimental findings. DFT result predicts *p*-type doping in the hybrid system which is consistent with the experimental result found from the XPS study. The presence of intermediate states within the bandgap of HS has been validated by both the two-photon absorption experiment and computational calculation. This kind of intermediate state can highly affect the properties of the hybrid systems. Furthermore, MoS_2/TiO_2 (PLD) interface shows a better photo-transport. We found that MoS_2/TiO_2 (PLD) interface shows better photo-transport behavior. A potential application of MoS_2/TiO_2 (PLD) is demonstrated by the fabrication of a *p*-type photo-transistor with the ionic-gel top gate. This study demonstrates the prospective of large-area interfaces in the field of optics and optoelectronics.

1.8.6. First Principles Studies on Bimetallic, Metal/Weyl Semimetal Heterostructure, and Topological Material:

1.8.6.1. Intriguing Electronic and Optical Prospects of FCC Bimetallic Two-dimensional Heterostructures: Epsilon Near-zero Behaviour in UV-vis Range [94]: Higher superconducting critical temperature and large-area epsilon-near-zero systems are two important fields of research to the scientific community. Motivated by the recent experimentally observed strongly correlated phenomena in nanostructures of simple Drude systems, we have theoretically investigated some potential bimetallic FCC combinations starting from a large-area interface to embedded and doped 2D nanostructures, having resemblance with the experimentally studied systems. Using different first-principles techniques, encompassing DFT, TDDFT, phonon and DFT-coupled quantum transport, we propose the following strongly correlated prospects of potential bimetallic nanostructures like Au/Ag and Pt/Pd: 1) For 2D doped and embedded nanostructures of these systems, DFT-calculated non-trivial band-structure and Fermi-surface topology may be emblematic to the presence of instabilities like charge density waves; 2) the optical attributes extracted from the TDDFT calculations for these systems indicate interfacial morphology induced band-localization leading to near-zero behavior of both real and imaginary parts of the dynamical dielectric response in the ultra-violet to visible (UV-Vis) optical range; 3) low-energy intra-band plasmonic oscillations, are completely suppressed for embedded and doped nanostructures manifesting the sole importance of inter-band transitions, as observed from the TDDFT-derived electron-energy loss spectra; 4) phonon-dispersion of the nanostructured systems indicate the presence of soft phonons and dynamical instabilities; 5) quantum transport calculations on a simplest possible device made out of these bimetallic systems reveal the generation of highly transmitting pockets over the cross-sectional area for some selected device geometry. We envisage that, if scrutinized experimentally, such

systems may unveil many fascinating aspects of orbital chemistry, physics, and optics promoting relevant applications in diverse fields.

1.8.6.2. Broken Inversion Symmetry and Related Interface-induced Effects at Weyl-system TaAs in Proximity of Noble Metals [95, 96]: Weyl semimetal TaAs, a congenial host to the massless Weyl fermions, spontaneously lacks the inversion symmetry and thus effectuates topologically stable Weyl nodes, resembling magnetic monopoles in momentum space. An earlier experimental analysis, reveals that the near-zero spin-polarization of bulk TaAs experiences a boost in the proximity of point-contacts of non-magnetic metals along with the associated tip-induced superconductivity, provides the impetus to study the large-area stacked interfaces of TaAs with noble metals like Au and Ag. The primary outcomes of the present work can be listed as follows: 1) first-principles calculations on the interfacial systems have manifested an increment of the interface-induced spin-polarization and contact-induced transport spin-polarization of TaAs in the proximity of noble metals; 2) in contrast to the single interface, for vertically stacked cases, the broken inversion symmetry of the system introduces a z-directional band-dispersion, resulting in an energetically separated series of Weyl cones; 3) quantum transport calculations on different device geometries reveal the importance of contact geometry for spin-transport in TaAs devices. Lateral contacts are found to be more effective to obtain a uniform and effective spin transport; 4)the phonon dispersion behavior of TaAs displays a closure of band-gap with the associated increase of phonon-density of states for the acoustic modes in the proximity of noble metals (lateral contact), indicating the occurrence of phonon-mediated correlated phenomena.

1.8.6.3. Doping Induced Carrier and Band-gap Modulation in Bulk Versus Nano for Topological Insulators: A Test Case of Stibnite [97]: We aim at comparing the electronic properties of topological insulator Sb_2S_3 in bulk and Nanorod using the density-functional scheme and investigating the effects of Se-doping at chalcogen-site. While going from bulk to nano, there is a drastic change in the bandgap due

to surface-induced strain. However, the trend of bandgap modulation with increased Se doping is more prominent in bulk. Interestingly, Se-doping introduces different types of carriers in bulk and nano.

1.8.7. Combined Experimental and Computational Studies on Organic-Inorganic Nanohybrid Heterostructure for their Manifold Applications:

1.8.7.1. A Combined Spectroscopic and Ab Initio Study on Transmetalation of a Polyphenol for Potential Purification Strategy of Food Additive [98]: Metal-organic complexes (MOCs) are a class of organic-inorganic hybrid substances composed of metal linked with organic moiety. Recently metal exchange (transmetalation) techniques have become popular in the post-synthesis modification of MOCs. Here, we have explored the possibilities of toxic metal ions (mercury (Hg)) exchange from a model polyphenol, Curcumin, which is an important food additive, by using a much less toxic counterpart (copper). The attachment of different metals on the polyphenol is confirmed by the picosecond resolved fluorescence technique. Surface plasmon resonance (SPR) band of Ag NP is employed as a tool to detect uncoupled Hg ions in the aqueous medium. Further, the microscopic understanding of the experimental observation is achieved through DFT-based theoretical studies. The presence of Cu ion in the vicinity of Hg-Curcumin, upon ground state optimization, is observed to extrude most of the Hg from the Curcumin complex and replaces its position. The study may find relevance in the development of a purification strategy of heavily toxic metal-contaminated food additives.

1.8.7.2. A Novel Nanohybrid for Cancer Theranostics: Folate Sensitized Fe_2O_3 Nanoparticle for Colorectal Cancer Diagnosis and Photodynamic Therapy [99]: Organic-inorganic NHs are becoming popular for their potential biological applications including diagnosis and treatment of cancerous cells. The motive of

this study is to synthesize an NH for the diagnosis and therapy of colorectal cancer. Here we have developed a facile and cost-effective synthesis of folic acid (FA) templated water-soluble Fe_2O_3 nanoparticles using the hydrothermal method for the theranostics application. The attachment of FA to Fe_2O_3 was confirmed using various spectroscopic techniques including FTIR and picoseconds resolved fluorescence studies. The NH (FA-Fe_2O_3) is a combination of two nontoxic ingredients FA and Fe_2O_3, showing remarkable photodynamic therapy (PDT) activity in human colorectal carcinoma cell lines (HCT 116) via the generation of intracellular ROS. The light-induced enhanced ROS activity of the NH causes significant nuclear DNA damage which was confirmed from comet assay. Assessment of p53, Bax, Bcl2, cytochrome c (cyt c) protein expression, and caspase 9/3 activity provides vivid evidence of cell death via an apoptotic pathway. *In vitro* magnetic resonance imaging (MRI) experiment in folate receptor overexpressed cancer cells (HCT 116) and FR deficient human embryonic kidney cells (HEK 293) reveal a target specificity of the NH towards cancer cell, thus asserting its MRI contrasting agent for the diagnosis of colorectal cancer.

1.9. Plan of the Thesis:

The plan of the thesis is as follows:

Chapter 1: This chapter includes a concise introduction to the scope and motivation of the entire thesis work. A summary of the work done is also presented in this chapter.

Chapter 2: This chapter provides an overview of the steady-state and dynamical tools, the structural aspects of dyes, and fluorescent probes used in the experiments.

Chapter 3: This chapter includes the details of instrumentation, data analysis, and experimental procedures that have been used during the entire thesis work. A

summary of the working principle of the instruments and synthesis procedure of materials has been described here.

Chapter 4: This chapter contains the detail of the theoretical methodology of our computational calculation. This section includes density functional theory, applying the same, how in practice one can solve a many-electron Hamiltonian. Furthermore, we discuss the time dependent density functional theory and its application towards investigating the excitonic dynamics of the system. A brief introduction of phonon calculation and electron-phonon coupling is also provided. In addition, model device application using non-equilibrium Green's Function (NEGF) has been discussed.

Chapter 5: The role of defect state in the application of wide bandgap semiconductor ZnO has been thoroughly investigated in this chapter. A brief investigation of different trap states and their role in the activity of ZnO is also explored. The role of different halide ion to 'heal' the surface defect and heighten different properties of ZnO has been described in this chapter. The mechanism behind the change of properties due to doping of Mn-ion within the ZnO NP and surface modification by halide ion on ZnO NP has been compared.

Chapter 6: In this chapter, inorganic-organic NH and its role in the field of visible light harvesting has been investigated. The role of metallated porphyrin dye sensitization in TiO_2 NP is explored considering the enhancement of its visible-light photocatalytic activity. Finally, oxide-based magnetic NP (hematite) has been synthesized and functionalized using phthalocyanine dye and its enhanced photocatalytic and photoelectrochemical activity has been investigated.

Chapter 7: To harvest near-infrared (NIR) light efficiently a new inorganic-inorganic HS consisting of low bandgap semiconductor (CuS) and wide bandgap semiconductor (ZnO) has been proposed. The band alignment of the CuS-ZnO hybrid has been predicted using DFT calculation. The modulated band structure of the hybrid system gives higher charge separation which results in better light harvesting.

Chapter 8: In this chapter, we have discussed the properties of 2D HS and their applications. The electronic and excited state dynamical property of a 2D inorganic HS consisting of $MoSe_2$ and Graphene oxide has been investigated in this chapter. Time-dependent excited state dynamics of the hybrid system has been studied. The model device application of the system is also explored.

Chapter 9: In this chapter, we further investigated the electronic and optical properties of a large area interface of MoS_2/TiO_2 HS. Several excited state dynamics have been performed to understand the nature of the hybrid system. The device performance of the HS is also explored in the presence of light.

Chapter 10: In this chapter, we have discussed computation studies on different metal/metal, metal/semimetal, and topological insulators for their applications in different fields. Some interesting behavior on Au/Ag HS has been investigated here. The role of metal contact on Weyl semimetal like TaAs has been explored. The modulation of the electronic property with respect to an increment of surface in a model topological insulator (stibnite) has been discussed in this chapter.

Chapter 11: Detoxification of heavy metal from essential food additive Curcumin, and detection of decoupled free heavy metal using surface plasmon resonance (SPR) band of Ag NP has been explored in this chapter. The mechanism of metal-exchange in the Curcumin has been investigated using first principles DFT calculation. Moreover, folate capped Fe_2O_3 NH and their potential biological applications including diagnosis and treatment of cancerous cells have been investigated.

References

[1] M. Faustini, L. Nicole, E. Ruiz-Hitzky, C. Sanchez, History of organic–inorganic hybrid materials: Prehistory, art, science, and advanced applications, *Adv. Func. Mater.* 28 (2018) 1704158.

[2] M. S. Saveleva, K. Eftekhari, A. Abalymov, T. E. L. Douglas, D. Volodkin, B. V. Parakhonskiy, A. G. Skirtach, Hierarchy of hybrid materials—The place of inorganics-in-organics in it, their composition and applications, *Front. Chem.* 7 (2019) 1.

[3] R. Mobin, T. A. Rangreez, H. T. N. Chisti, Inamuddin, M. Rezakazemi, Organic-inorganic hybrid materials and their applications in M.A. Jafar Mazumder, H. Sheardown, A. Al-Ahmed, Functional Polymers, *Springer International Publishing*, Cham, Switzerland, 2019.

[4] S. H. Mir, L. A. Nagahara, T. Thundat, P. Mokarian-Tabari, H. Furukawa, A. Khosla, Review—Organic-inorganic hybrid functional materials: An integrated platform for applied technologies, *J. Electrochem. Soc.* 165 (2018) B3137.

[5] N. Zhao, L. Yan, X. Zhao, X. Chen, A. Li, D. Zheng, X. Zhou, X. Dai, F. J. Xu, Versatile types of organic/inorganic nanohybrids: From strategic design to biomedical applications, *Chem. Rev.* 119 (2019) 1666.

[6] L. H. Liu, R. Métivier, S. Wang, H. Wang, Advanced nanohybrid materials: Surface modification and applications, *J. Nanomater.* 2012 (2011) 1.

[7] L. Suganthi, A. A. Samuel, Energy models for demand forecasting—A review, *Renew. Sust. Energ. Rev.* 16 (2012) 1223.

[8] P. A. Owusu, S. Asumadu-Sarkodie, A review of renewable energy sources, sustainability issues and climate change mitigation, *Cogent Eng.* 3 (2016) 1167990.

[9] X. Wang, Y. Cui, T. Li, M. Lei, J. Li, Z. Wei, Recent advances in the functional 2D photonic and optoelectronic devices, *Adv. Optics. Mater.* 7 (2019) 1801274.

[10] S. J. Sweeney, J. Mukherjee, Optoelectronic devices and materials in S. Kasap, P. Capper, Springer handbook of electronic and photonic materials, *Springer International Publishing*, New York, USA, 2017.

[11] X. Wang, Y. Cui, T. Li, M. Lei, J. Li, Z. Wei, Recent advances in the functional 2D photonic and optoelectronic Devices, *Adv. Optical Mater.* 7 (2019) 1801274.

[12] C. Lan, Z. Shi, R. Cao, C. Li, H. Zhang, 2D materials beyond graphene toward Si integrated infrared optoelectronic devices, *Nanoscale* 12 (2020) 11784.

[13] T. Musso, P. V. Kumar, A. S. Foster, J. C. Grossman, Graphene oxide as a promising hole injection layer for MoS_2-based electronic devices, *ACS Nano* 8 (2014) 11432.

[14] X. Liu, J. Iocozzia, Y. Wang, X. Cui, Y. Chen, S. Zhao, Z. Li, Z. Lin, Noble metal–metal oxide nanohybrids with tailored nanostructures for efficient solar energy conversion, photocatalysis and environmental remediation, *Energy Environ. Sci.* 10 (2017) 402.

[15] S. Prakash, M. Malhotra, W. Shao, C. Tomaro-Duchesneau, S. Abbasi, Polymeric nanohybrids and functionalized carbon nanotubes as drug delivery carriers for cancer therapy, *Adv. Drug Delivery Rev.* 63 (2011) 1340.

[16] S. Chang, X. Wu, Y. Li, D. Niu, Z. Ma, W. Zhao, J. Gu, W. Dong, F. Ding, W. Zhu, A hydrophobic dye-encapsulated nano-hybrid as an efficient fluorescent probe for living cell imaging, *Adv. Healthc. Mater.* 1 (2012) 475.

[17] S. J. Kwon, J. H. Choy, D. Jung, P. V. Huong, Heterostructured high-T_c superconducting nanohybrid: $(Me_3S)_2HgI_4{-}Bi_2Sr_2CaCu_2O_y$, *Phys. Rev. B* 66 (2002) 224510.

[18] D. H. Kim, H. S. Lee, H. J. Shin, Y. S. Bae, K. H. Lee, S. W. Kim, D. Choi, J. Y. Choi, Graphene surface induced specific self-assembly of poly (3-hexylthiophene) for nanohybrid optoelectronics: From first-principles calculation to experimental characterizations, *Soft Matter* 9 (2013) 5355.

[19] S. G. Chatterjee, S. Chatterjee, A. K. Ray, A. K. Chakraborty, Graphene–metal oxide nanohybrids for toxic gas sensor: A review, *Sensors Actuat. B: Chem.* 221 (2015) 1170.

[20] C. Kagan, D. Mitzi, C. Dimitrakopoulos, Organic-inorganic hybrid materials as semiconducting channels in thin-film field-effect transistors, *Science* 286 (1999) 945.

[21] P. Gómez-Romero, C. Sanchez, Functional hybrid materials, *John Wiley & Sons*, New Jersey, USA, 2006.

[22] A. E. Nel, L. Mädler, D. Velegol, T. Xia, E. M. Hoek, P. Somasundaran, F. Klaessig, V. Castranova, M. Thompson, Understanding biophysicochemical interactions at the nano–bio interface, *Nat. Mater.* 8 (2009) 543.

[23] J. E. Gagner, S. Shrivastava, X. Qian, J. S. Dordick, R. W. Siegel, Engineering nanomaterials for biomedical applications requires understanding the nano-bio interface: A perspective, *J. Phys. Chem. Lett.* 3 (2012) 3149.

[24] H. Ishii, K. Sugiyama, E. Ito, K. Seki, Energy level alignment and interfacial electronic structures at organic/metal and organic/organic interfaces, *Adv. Mater.* 11 (1999) 605.

[25] P. J. Hagrman, D. Hagrman, J. Zubieta, Organic–inorganic hybrid materials: From "simple" coordination polymers to organodiamine-templated molybdenum oxides, *Angew. Chem.* 38 (1999) 2638.

[26] R. Vendamme, S. Y. Onoue, A. Nakao, T. Kunitake, Robust free-standing nanomembranes of organic/inorganic interpenetrating networks, *Nat. Mater.* 5 (2006) 494.

[27] Y. Otsuka, Y. Okamoto, H. Y. Akiyama, K. Umekita, Y. Tachibana, S. Kuwabata, Photoinduced formation of polythiophene/TiO_2 nanohybrid heterojunction films for solar cell applications, *J. Phys. Chem. C* 112 (2008) 4767.

[28] K. Vallé, P. Belleville, F. Pereira, C. Sanchez, Hierarchically structured transparent hybrid membranes by in situ growth of mesostructured organosilica in host polymer, *Nat. Mater.* 5 (2006) 107.

[29] J. Y. Kwak, J. Hwang, B. Calderon, H. Alsalman, N. Munoz, B. Schutter, M. G. Spencer, Electrical characteristics of multilayer MoS_2 FET's with MoS_2/graphene heterojunction contacts, *Nano Lett.* 14 (2014) 4511.

[30] H. Liu, X. Chen, L. Deng, X. Su, K. Guo, Z. Zhu, Preparation of ultrathin 2D MoS_2/graphene heterostructure assembled foam-like structure with enhanced electrochemical performance for lithium-ion batteries, *Electrochim. Acta* 206 (2016) 184.

[31] H. Wang, L. Zhang, Z. Chen, J. Hu, S. Li, Z. Wang, J. Liu, X. Wang, Semiconductor heterojunction photocatalysts: Design, construction, and photocatalytic performances, *Chem. Soc. Rev.* 43 (2014) 5234.

[32] W. Hu, H. Cong, W. Huang, Y. Huang, L. Chen, A. Pan, C. Xue, Germanium/perovskite heterostructure for high-performance and broadband photodetector from visible to infrared telecommunication band, *Light: Sci. Appl.* 8 (2019) 106.

[33] H. Zhong, J. Xia, F. Wang, H. Chen, H. Wu, S. Lin, Graphene-piezoelectric material heterostructure for harvesting energy from water flow, *Adv. Func. Mater.* 27 (2017) 1604226.

[34] A. Rawat, R. Ahammed, Dimple, N. Jena, M. K. Mohanta, A. De Sarkar, Solar energy harvesting in type II van der Waals heterostructures of semiconducting group III monochalcogenide monolayers, *J. Phys. Chem. C* 123 (2019) 12666.

[35] H. Kroemer, A proposed class of hetero-junction injection lasers, *Proceed. IEEE* 51 (1963) 1782.

[36] Y. Li, S. Witharana, H. Cao, M. Lasfargues, Y. Huang, Y. Ding, Wide spectrum solar energy harvesting through an integrated photovoltaic and thermoelectric system, *Particuology* 15 (2014) 39.

[37] M. P. Lumb, S. Mack, K. J. Schmieder, M. González, M. F. Bennett, D. Scheiman, M. Meitl, B. Fisher, S. Burroughs, K. T. Lee, J. A. Rogers, R. J. Walters, GaSb-based solar cells for full solar spectrum energy harvesting, *Adv. Energy Mater.* 7 (2017) 1700345.

[38] S. Chu, A. Majumdar, Opportunities and challenges for a sustainable energy future, *Nature* 488 (2012) 294.

[39] C. Wang, D. Astruc, Nanogold plasmonic photocatalysis for organic synthesis and clean energy conversion, *Chem. Soc. Rev.* 43 (2014) 7188.

[40] G. Liu, N. Hoivik, K. Wang, H. Jakobsen, Engineering TiO_2 nanomaterials for CO_2 conversion/solar fuels, *Sol. Energy Mater. Sol. Cells* 105 (2012) 53.

[41] A. A. Ismail, D. W. Bahnemann, Photochemical splitting of water for hydrogen production by photocatalysis: A review, *Sol. Energy Mater. Sol. Cells* 128 (2014) 85.

[42] Y. Wang, Q. Wang, X. Zhan, F. Wang, M. Safdar, J. He, Visible light driven type II heterostructures and their enhanced photocatalysis properties: A review, *Nanoscale* 5 (2013) 8326.

[43] A. Fujishima, K. Honda, Electrochemical photolysis of water at a semiconductor electrode, *Nature* 238 (1972) 37.

[44] B. O'Regan, M. Gratzel, A low-cost, high-efficiency solar cell based on dye-sensitized colloidal TiO_2 films, *Nature* 353 (1991) 737.

[45] N. Serpone, A. V. Emeline, Semiconductor photocatalysis — Past, present, and future outlook, *J. Phys. Chem. Lett.* 3 (2012) 673.

[46] O. Legrini, E. Oliveros, A.M. Braun, Photochemical processes for water treatment, *Chem. Rev.* 93 (1993) 671.

[47] M. A. Fox, M. T. Dulay, Heterogeneous photocatalysis, *Chem. Rev.* 93 (1993) 341.

[48] M. R. Hoffmann, S. T. Martin, W. Choi, D. W. Bahnemann, Environmental applications of semiconductor photocatalysis, *Chem. Rev.* 95 (1995) 69.

[49] L. Schmidt-Mende, J. L. MacManus-Driscoll, ZnO–nanostructures, defects, and devices, *Mater. Today* 10 (2007) 40.

[50] P. V. Kamat, Manipulation of charge transfer across semiconductor interface. A criterion that cannot be ignored in photocatalyst design, *J. Phys. Chem. Lett.* 3 (2012) 663.

[51] C. R. Dean, A. F. Young, I. Meric, C. Lee, L. Wang, S. Sorgenfrei, K. Watanabe, T. Taniguchi, P. Kim, K. L. Shepard, Boron nitride substrates for high-quality graphene electronics, *Nat. Nanotech.* 5 (2010) 722.

[52] P. Ma, Y. Salamin, B. Baeuerle, A. Josten, W. Heni, A. Emboras, J. Leuthold, Plasmonically enhanced graphene photodetector featuring 100 Gbit/s data reception, high responsivity, and compact size, *ACS Photonics* 6 (2018) 154.

[53] S. G. Kumar, L. G. Devi, Review on modified TiO_2 photocatalysis under UV/Visible light: Selected results and related mechanisms on interfacial charge carrier transfer dynamics, *J. Phys. Chem. A* 115 (2011) 13211.

[54] J. Nieto-Pescador, B. Abraham, L. Gundlach, Photoinduced ultrafast heterogeneous electron transfer at molecule-semiconductor interfaces, *J. Phys. Chem. Lett.* 5 (2014) 3498.

[55] K. Konstantinou, F. C. Mocanu, T. H. Lee, S. R. Elliott, Revealing the intrinsic nature of the mid-gap defects in amorphous $Ge_2Sb_2Te_5$, *Nat. Commun.* 10 (2019) 1.

[56] G. J. Kavarnos, Fundamentals of photoinduced electron transfer, *Weinheim/VCH Publishers,* New York, USA, 1993.

[57] J. R. Lakowicz, Principles of fluorescence spectroscopy, *Springer*, New York, USA, 2006.

[58] A. Periasamy, Fluorescence resonance energy transfer microscopy: A mini review, *J. Biomed. Opt.* 6 (2001) 287.

[59] Y. Liu, T. Zhao, W. Ju, S. Shi, Materials discovery and design using machine learning, *J. Materiomics* 3 (2017) 159.

[60] G. Kresse, J. Furthmüller, Efficient iterative schemes for ab initio total-energy calculations using a plane-wave basis set, *Phys. Rev. B* 54 (1996) 11169.

[61] G. Kresse, D. Joubert, From ultrasoft pseudopotentials to the projector augmented-wave method, *Phys. Rev. B* 59 (1999) 1758.

[62] M. Ernzerhof, G. E. Scuseria, Assessment of the Perdew–Burke–Ernzerhof exchange-correlation functional, *J. Chem. Phys.* 110 (1999) 5029.

[63] S. Grimme, J. Antony, S. Ehrlich, H. Krieg, A consistent and accurate ab initio parametrization of density functional dispersion correction (DFT-D) for the 94 elements H-Pu, *J. Chem. Phys.* 132 (2010) 154104.

[64] H. J. Monkhorst, J. D. Pack, Special points for Brillouin-zone integrations, *Phys. Rev. B* 13 (1976) 5188.

[65] J. R. Shewchuk, An introduction to the conjugate gradient method without the agonizing pain (Technical Report No. CMU-CS-94-125, School of Computer Science, Carnegie Mellon University), Pittsburgh, USA, 1994.

[66] S. Smidstrup, T. Markussen, P. Vancraeyveld, J. Wellendorff, J. Schneider, T. Gunst, B. Verstichel, D. Stradi, P. A. Khomyakov, U. G. Vej-Hansen, QuantumATK: An integrated platform of electronic and atomic-scale modelling tools, *J. Phys. Cond. Mat.* 32 (2019) 015901.

[67] H. Zhou, T. Fan, D. Zhang, Biotemplated materials for sustainable energy and environment: Current status and challenges, *ChemSusChem* 4 (2011) 1344.

[68] Y. Sun, Q. Wu, G. Shi, Graphene based new energy materials, *Energy Environ. Sci.* 4 (2011) 1113.

[69] N. Robertson, Optimizing dyes for dye-sensitized solar cells, *Angew. Chem. Int. Ed.* 45 (2006) 2338.

[70] H. Hayashi, I. V. Lightcap, M. Tsujimoto, M. Takano, T. Umeyama, P. V. Kamat, H. Imahori, Electron transfer cascade by organic/inorganic ternary composites of porphyrin, zinc oxide nanoparticles, and reduced graphene oxide on a tin oxide electrode that exhibits efficient photocurrent generation, *J. Am. Chem. Soc.* 133 (2011) 7684.

[71] A. Yella, H. W. Lee, H. N. Tsao, C. Yi, A. K. Chandiran, M. K. Nazeeruddin, E. W. G. Diau, C. Y. Yeh, S. M. Zakeeruddin, M. Grätzel, Porphyrin-sensitized solar cells with cobalt (II/III)–based redox electrolyte exceed 12 percent efficiency, *Science* 334 (2011) 629.

[72] L. L. Li, E. W. G. Diau, Porphyrin-sensitized solar cells, *Chem. Soc. Rev.* 42 (2013) 291.

[73] M. Y. Duan, J. Li, G. Mele, C. Wang, X. F. Lü, G. Vasapollo, F. X. Zhang, Photocatalytic activity of novel tin porphyrin/TiO_2 based composites, *J. Phys. Chem. C* 114 (2010) 7857.

[74] S. D. Oosterhout, M. M. Wienk, S. S. van Bavel, R. Thiedmann, L. Jan Anton Koster, J. Gilot, J. Loos, V. Schmidt, R. A. J. Janssen, The effect of three-dimensional morphology on the efficiency of hybrid polymer solar cells, *Nat. Mater.* 8 (2009) 818.

[75] G. Zhang, G. Kim, W. Choi, Visible light driven photocatalysis mediated via ligand-to-metal charge transfer (LMCT): An alternative approach to solar activation of titania, *Energy Environ. Sci.* 7 (2014) 954.

[76] P. V. Kamat, Quantum dot solar cells. Semiconductor nanocrystals as light harvesters, *J. Phys. Chem. C* 112 (2008) 18737.

[77] M. Shang, W. Wang, L. Zhang, S. Sun, L. Wang, L. Zhou, 3D Bi_2WO_6/TiO_2 hierarchical heterostructure: Controllable synthesis and enhanced visible photocatalytic degradation performances, *J. Phys. Chem. C* 113 (2009) 14727.

[78] S. Li, M. Sun, J. P. Chou, J. Wei, H. Xing, A. Hu, First-principles calculations of the electronic properties of SiC-based bilayer and trilayer heterostructures, *Phys. Chem. Chem. Phys.* 20 (2018) 24726.

[79] S. Wang, C. Ren, H. Tian, J. Yu, M. Sun, MoS_2/ZnO van der Waals heterostructure as a high-efficiency water splitting photocatalyst: A first-principles study, *Phys. Chem. Chem. Phys.* 20 (2018) 13394.

[80] M. Sun, J. P. Chou, Q. Ren, Y. Zhao, J. Yu, W. Tang, Tunable Schottky barrier in van der Waals heterostructures of graphene and g-GaN, *App. Phys. Lett.* 110 (2017) 173105.

[81] B. Meredig, A. Agrawal, S. Kirklin, J. E. Saal, J. W. Doak, A. Thompson, K. Zhang, A. Choudhary, C. Wolverton, Combinatorial screening for new materials in unconstrained composition space with machine learning, *Phys. Rev. B* 89 (2014) 094104.

[82] X. He, H. Deng, H. M. Hwang, The current application of nanotechnology in food and agriculture, *J. Food Drug Anal.* 27 (2019) 1.

[83] D. C. Manatunga, V. U. Godakanda, R. M. de Silva, K. M. N. de Silva, Recent developments in the use of organic–inorganic nanohybrids for drug delivery, *WIREs Nanomed. Nanobiotechnol.* 12 (2020) e1605.

[84] G. F. Paciotti, L. Myer, D. Weinreich, D. Goia, N. Pavel, R. E. McLaughlin, L. Tamarkin, Colloidal gold: A novel nanoparticle vector for tumor directed drug delivery, *Drug Deliv.* 11 (2004) 169.

[85] X. Wu, H. Liu, J. Liu, K. N. Haley, J. A. Treadway, J. P. Larson, N. Ge, F. Peale, M. P. Bruchez, Immunofluorescent labeling of cancer marker Her2 and other cellular targets with semiconductor quantum dots, *Nat. Biotech.* 21 (2002) 41.

[86] L. R. Hirsch, R. J. Stafford, J. A. Bankson, S. R. Sershen, B. Rivera, R. E. Rrice, J. D. Hazle, N. J. Halas, J. L. West, Nanoshell-mediated near-infrared thermal therapy of tumors under magnetic resonance guidance, *Proc. Natl. Acad. Sci. USA* 100 (2011) 13549.

[87] T. K. Maji, D. Bagchi, P. Kar, D. Karmakar, S. K. Pal, Enhanced charge separation through modulation of defect-state in wide band-gap semiconductor for potential photocatalysis application: Ultrafast spectroscopy and computational studies, *J. Photochem. Photobiol. A: Chem.* 332 (2017) 391.

[88] T. K. Maji, P. Kar, H. Mandal, C. Bhattacharya, D. Karmakar, S. K. Pal, Halide-modulated functionality of wide band gap zinc oxide semiconductor nanoparticle, *ChemistrySelect* 3 (2018) 6382.

[89] P. Kar, T. K. Maji, P. K. Sarkar, P. Lemmens, S. K. Pal, Development of a photo-catalytic converter for potential use in the detoxification of Cr (VI) metal in water from natural resources, *J. Mater. Chem. A* 6 (2018) 3674.

[90] T. K. Maji, M. N. Hasan, S. Ghosh, D. Wulferding, C. Bhattacharya, P. Lemmens, D. Karmakar, S. K. Pal, Development of a magnetic nanohybrid for multifunctional application: From immobile photocatalysis to efficient

photoelectrochemical water splitting: A combined experimental and computational study, *J. Photochem. Photobiol. A: Chem.* 397 (2020) 112575.

[91] T. K. Maji, P. K. Sarkar, P. Kar, B. Liu, P. Lemmens, D. Karmakar, S. K. Pal, A combined experimental and computational study on a nanohybrid material for potential application in NIR photocatalysis, *Appl. Catal. A: Gen.* 583 (2019) 117124.

[92] T. K. Maji, K. Vaibhav, S. K. Pal, K. Majumdar, K. V. Adarsh, D. Karmakar, Intricate modulation of interlayer coupling at the graphene oxide/$MoSe_2$ interface: Application in time-dependent optics and device transport, *Phys. Rev. B* 99 (2019) 115309.

[93] T. K. Maji, J. R. Aswin, S. Mukherjee, R. Alexander, A. Mondal, S. Das, R. K. Sharma, N. K. Chakraborty, K. Dasgupta, A. M. R. Sharma, R. Hawalder, M. Pandey, A. Naik, K. Majumdar, S. K. Pal, K. V. Adarsh, S. K. Ray, D. Karmakar, Combinatorial large-area MoS_2/anatase-TiO_2 interface: A pathway to emergent optical and opto-electronic functionalities, *ACS Appl. Mater. Interfaces* 12 (2020) 44345.

[94] T. K. Maji, K. Vaibhav, R. Hawaldar, K. Adarsh, S. K. Pal, D. Karmakar, Intriguing electronic and optical prospects of FCC bimetallic two-dimensional heterostructures: Epsilon near-zero behavior in UV-Vis range, *Phys. Chem. Chem. Phys.* 22 (2020) 16314.

[95] T. K. Maji, S. K. Pal, D. Karmakar, Hole-doping and contact induced spin-polarization in Weyl semimetal TaAs, *AIP Conf. Proceed.* 1942 (2018) 130053.

[96] T. K. Maji, K. Vaibhav, S. K. Pal, D. Karmakar, Broken inversion symmetry and interface-induced spin-polarization for metal-Weyl semimetal stacked interfaces, *Sci. Rep.* 10 (2020) 14438.

[97] T. K. Maji, S. K. Pal, D. Karmakar, Doping induced carrier and band-gap modulation in bulk versus nano for topological insulators: A test case of stibnite, *AIP Conf. Proceed.* 1942 (2018) 090029.

[98] T. K. Maji, D. Bagchi, N. Pan, A. Sayqal, M. Morad, S.A. Ahmed, D. Karmakar, S. K. Pal, A combined spectroscopic and ab initio study of the transmetalation of a

polyphenol as a potential purification strategy for food additives, *RSC Adv.* 10 (2020) 5636.

[99] R. Nandi, S. Mishra, T. K. Maji, K. Manna, P. Kar, S. Banerjee, S. Dutta, S. K. Sharma, P. Lemmens, K. D. Saha, S. K. Pal, A novel nanohybrid for cancer theranostics: Folate sensitized Fe_2O_3 nanoparticles for colorectal cancer diagnosis and photodynamic therapy, *J. Mater. Chem. B* 5 (2017) 3927.

Chapter 2

An Overview of Experimental Techniques and Systems

To investigate the dynamical processes involved in the synthesis of hybrid materials, different steady-state and dynamical tools have been employed. These include the photoinduced electron transfer (PET), Förster resonance energy transfer (FRET), Langmuir−Hinshelwood (L−H) model for surface catalysis, etc. In this chapter, we have included a brief discussion about the above-mentioned tools. Concise overviews of the various systems, probes, and dyes used in the studies have also been provided.

2.1. Steady-state and Dynamical Tools:

2.1.1. Photoinduced Electron Transfer (PET): PET can be described as the movement of an electron caused by the absorption of light from an electron-rich species (D) to an electron-deficient species (A), as shown in Eq. (2.1).

$$D + A \rightarrow D^{+} + A^{-} \tag{2.1}$$

The first law of photochemistry tells us that a photo-induced process must be initiated by the absorption of light. In PET, the absorbing species can either be a donor, the acceptor, or a ground-state complex between the donor and acceptor, often referred to as a charge transfer complex. These possibilities are shown in Eq. (2.2−2.4).

$$D \xrightarrow{h\upsilon} D^{*} + A \longrightarrow D^{+} + A^{-} \tag{2.2}$$

$$A \xrightarrow{h\upsilon} A^{*} + D \longrightarrow D^{+} + A^{-} \tag{2.3}$$

$$(D \cdots A) \xrightarrow{h\upsilon} (D \cdots A)^{*} \longrightarrow D^{+} + A^{-} \tag{2.4}$$

Transport of charges or excitons is commonly seen as fundamental processes in many optoelectronic devices as well as biological systems. The creation, diffusion, and annihilation of excitons and the mobility of charges are some of the key processes in many devices that interconvert electric and light energies [1, 2]. PET is an important process in many biochemical systems, such as those in respiration and photosynthesis [3, 4]. To gain a deep understanding of these systems, it is important to describe the rates of these processes with a few empirically derived parameters [5, 6]. Therefore, it has become increasingly important to develop computational techniques that allow us to calculate the rate of charge or energy transport. In our systems, the apparent rate constants, k_{nr}, were determined for the nonradiative processes by comparing the lifetimes of the donor in the absence (τ_0) and the presence (τ) of an acceptor, using Eq. (2.5) [7].

$$k_{nr} = 1/\langle \tau \rangle - 1/\langle \tau_0 \rangle \tag{2.5}$$

The direction of electron transfer in the excited state is determined by the oxidation and reduction potential of the ground and excited states. Upon excitation the electron donor transfers an electron to the acceptor with a rate k_{nr}, forming the charge transfer complex. This complex may emit as an exciplex ($h\nu_E$) or be quenched and return to the ground state. The important part of this process is the decrease in the total energy of the charge transfer complex. The energy decreases because the ability to donate or accept electrons changes when a fluorophore is in the excited state. Excitation provides the energy to drive charge separation. D and A do not form a complex when both are in the ground state because this is energetically unfavorable. The energy released by electron transfer can also change if the ions become solvated and/or separated in a solvent with a high dielectric constant. Upon excitation the electron donor transfers an electron to the acceptor with a rate k_P, forming the charge transfer complex $[D^+A^-]^*$ (Figure

2.1). This complex may emit as an exciplex ($h\nu_E$) or be quenched and return to the ground state.

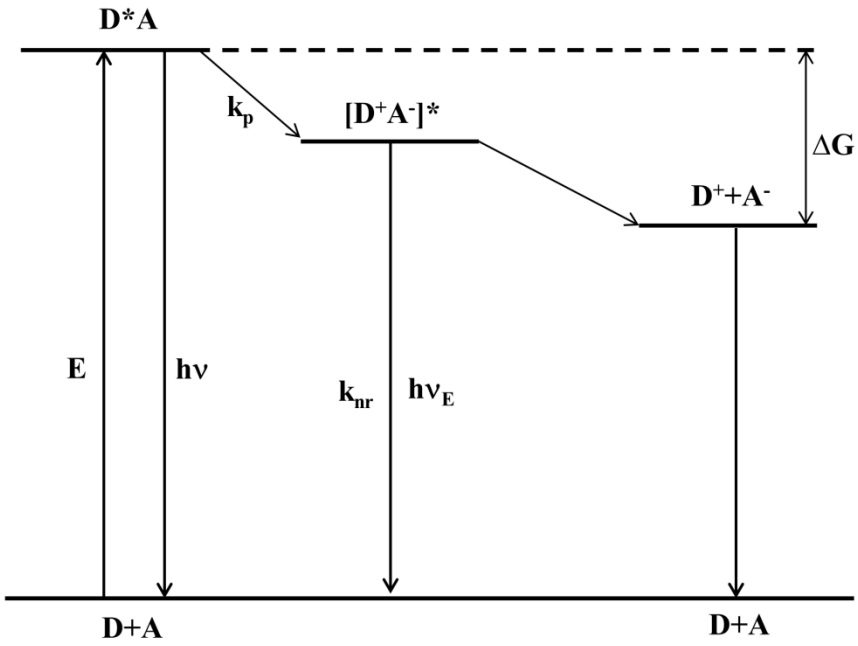

Figure 2.1: *Energy diagram for photoinduced electron transfer (PET). The excited molecule is assumed to be the electron donor.* ν *and* ν_E *are emission frequencies from the fluorophore and exciplex, respectively.*

This thesis demonstrates several PET processes, particularly in light-harvesting materials, and discusses the consequences of various interfacial electron transfer processes. In heterogeneous photocatalysis, the photoinduced charge separation in the photocatalyst is necessary, and several strategies have been employed to facilitate the charge separation. In heterostructure/dye-sensitized semiconductor nanohybrid a series of charge transfer processes had to occur cooperatively so that the solar light can be harnessed efficiently. These include (i) electron injection from excited dye into the conduction band of the semiconductor, (ii) electron transport from one semiconductor to another semiconductor in the semiconductor nanohybrid, (iii) electron shuttling pathway from the conduction band of the semiconductor. The matching of the band energies of the two semiconductors facilitates desired functionality either to

induce electron−hole recombination (e.g., light-emitting diodes) or to improve charge separation by driving electrons and holes in two different nanoparticles (e.g., photocatalysis in semiconductor heterostructure). In each instance where semiconductor nanocrystals are implemented into a practical device, PET reactions are intimately involved, and they dictate the overall functionality. This thesis focuses on the recent progress made in understanding the kinetics and mechanistic aspects of various PET processes at the semiconductor interface and their role in the direction of efficient solar light harvesting.

2.1.2. Förster Resonance Energy Transfer (FRET): FRET is an electrodynamic phenomenon involving the nonradiative transfer of the excited state energy from the donor dipole (D) to an acceptor dipole (A) in the ground state (Figure 2.2a). FRET is of two types: (i) homo-molecular FRET and (ii) hetero-molecular FRET. In the former case, the same fluorophore acts both as an energy donor and acceptor, while in the latter case two different molecules act as donor and acceptor.

Each donor-acceptor (D-A) pair participating in FRET is characterized by a distance known as Förster distance (R_0) i.e., the D-A separation at which energy transfer is 50% efficient. The rate of resonance energy transfer (k_T) from donor to an acceptor is given by [8]:

$$k_T = \frac{1}{\tau_D}\left(\frac{R_0}{r}\right)^6 \tag{2.6}$$

where τ_D is the lifetime of the donor in the absence of acceptor and r is the donor to acceptor (D-A) distance. The rate of transfer of donor energy depends upon the extent of overlap of the emission spectrum of the donor with the absorption spectrum of the acceptor ($J(\lambda)$), the quantum yield of the donor (Q_D), the relative orientation of the donor and acceptor transition dipoles (κ^2) and the distance between the donor and acceptor molecules (r) (Figure 2.2b). The methodology to

estimate the FRET efficiency of the donor and distances between donor-acceptor pairs is described below:

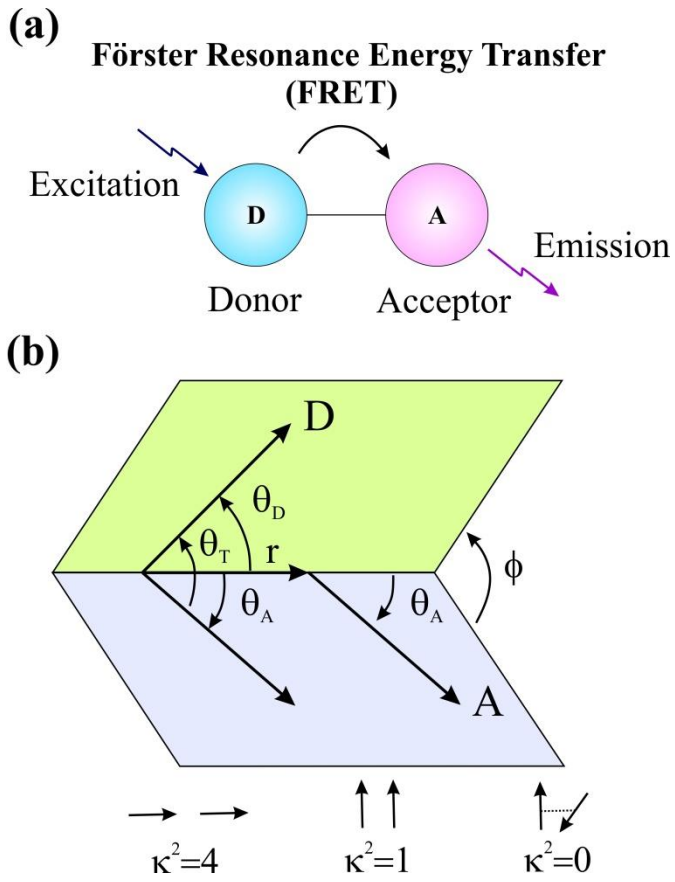

Figure 2.2: *a) Schematic illustration of the FRET process. b) Dependence of the orientation factor κ^2 on the directions of the emission and absorption dipoles of the donor and acceptor, respectively.*

The Förster distance (R_0) is given by [8]:

$$R_0 = 0.211\left[\kappa^2 n^{-4} Q_D J(\lambda)\right]^{1/6} \text{ (in Å)} \tag{2.7}$$

where n is the refractive index of the medium, Q_D is the quantum yield of the donor, and $J(\lambda)$ is the overlap integral. κ^2 is defined as:

$$\kappa^2 = \left(\cos\theta_T - 3\cos\theta_D \cos\theta_A\right)^2 = \left(\sin\theta_D \sin\theta_A \cos\varphi - 2\cos\theta_D \cos\theta_A\right)^2 \tag{2.8}$$

where θ_T is the angle between the emission transition dipole of the donor and the absorption transition dipole of the acceptor, θ_D and θ_A are the angles between these dipoles and the vector joining the donor and acceptor, and φ is the angle

between the planes of the donor and acceptor (Figure 2.2b). κ^2 value can vary from 0 to 4. For collinear and parallel transition dipoles, $\kappa^2 = 4$; for parallel dipoles, $\kappa^2 = 1$; and for perpendicularly oriented dipoles, $\kappa^2 = 0$. For donors and acceptors that randomize by rotational diffusion before energy transfer, the magnitude of κ^2 is assumed to be 2/3. However, in systems where there is a definite site of attachment of the donor and acceptor molecules, to get physically relevant results, the value of κ^2 has to be estimated from the angle between the donor emission and acceptor absorption dipoles [9]. $J(\lambda)$, the overlap integral, which expresses the degree of spectral overlap between the donor emission and the acceptor absorption, is given by:

$$J(\lambda) = \frac{\int_0^\infty F_D(\lambda)\varepsilon_A(\lambda)\lambda^4 d\lambda}{\int_0^\infty F_D(\lambda)d\lambda} \tag{2.9}$$

where $F_D(\lambda)$ is the fluorescence intensity of the donor in the wavelength range of λ to $\lambda+d\lambda$ and is dimensionless. $\varepsilon_A(\lambda)$ is the extinction coefficient (in $M^{-1} cm^{-1}$) of the acceptor λ. If λ is in nm, then $J(\lambda)$ is in units of $M^{-1} cm^{-1} nm^4$. Once the value of R_0 is known, the efficiency of energy transfer can be calculated. The efficiency of energy transfer (E) is the fraction of photons absorbed by the donor which are transferred to the acceptor and is defined as:

$$E = \frac{k_T(r)}{\tau_D^{-1} + k_T(r)} \tag{2.10}$$

$$\text{Or, } E = \frac{R_0^6}{r^6 + R_0^6} \tag{2.11}$$

For D-A systems decaying with multiexponential lifetimes, E is calculated from the amplitude weighted lifetimes $\langle\tau\rangle = \sum_i \alpha_i \tau_i$ of the donor in the absence (τ_D) and presence (τ_{DA}) of the acceptor as:

$$E = 1 - \frac{\tau_{DA}}{\tau_D} \tag{2.12}$$

The D-A distances can be measured using Eq. (2.11) and (2.12).

2.1.3. Data Analysis of Time-Resolved Fluorescence Transients: Curve fitting of the time-resolved fluorescence transients was carried out using a nonlinear least square fitting procedure to a function Eq. (2.13) comprised of convolution of the IRF:

$$(X(t) = \int_0^t E(t')R(t-t')dt') \tag{2.13}$$

(E(t)) with a sum of exponentials (Eq. 2.14) with pre-exponential factors (B_i),

$$(R(t) = A + \sum_{i=1}^{N} B_i e^{-t/\tau_i}) \tag{2.14}$$

characteristic lifetimes (τ_i) and a background (A). Relative concentration in a multiexponential decay is expressed as Eq. (2.15).

$$c_n = \frac{B_n}{\sum_{i=1}^{N} B_i} \times 100 \tag{2.15}$$

The average lifetime (amplitude-weighted) of a multiexponential decay is expressed as:

$$\tau_{av} = \sum_{i=1}^{N} c_i \tau_i \tag{2.16}$$

2.1.4. Langmuir−Hinshelwood (L−H) Model: In the Langmuir−Hinshelwood (L−H) model [10, 11] of heterogeneous surface reactions, the rate of the photochemical degradation can be expressed in general terms for both the oxidant (e.g., O_2) and the reductant (e.g., $CHCl_3$) as follows:

$$-\frac{d[\mathrm{Re}\,d]}{dt} = -\frac{d[Ox]}{dt} = k_d \theta_{\mathrm{Re}\,d} \theta_{Ox} \tag{2.17}$$

where k_d is the photo-degradation rate constant, θ_{Red} represents the fraction of the electron-donating reductant (e.g., chloroform) adsorbed to the surface, and θ_{Ox} represents the corresponding fraction of the electron-accepting oxidant (e.g., oxygen) adsorbed to the surface. This treatment is subjected to the assumption that sorption of both the oxidant and the reductant is a rapid equilibrium process in both the forward and reverse directions, and that the rate-determining step of the reaction involves both species present in a monolayer at the solid-liquid interface. The Langmuir adsorption coefficient, K, for adsorption of each reactant is assumed to be readily determined from a classical Langmuir adsorption isotherm. In this case, the surface concentration of the reactants is related to their corresponding activities or concentrations in the bulk aqueous phase as follows:

$$R_0 = \frac{dC_0}{dt} = \frac{k_{L-H} K C_0}{1 + K C_0} \tag{2.18}$$

where C_0 is the initial concentration of reactants, k_{L-H} is the Langmuir–Hinshelwood (L–H) rate constant, and R_0 is the rate of reaction. If the initial concentration of the reactant solution is sufficiently low ($KC_0 << 1$), then Eq. (2.18) can be simplified to an apparent first-order equation:

$$R_0 = k_{L-H} K C_0 = k_{app} C_0 \tag{2.19}$$

where k_{app} is the apparent first-order rate constant. If the initial concentration of the solution (containing pollutants) is sufficiently high ($KC_0 >> 1$), then Eq. (2.18) can be simplified to a zero-order rate equation:

$$R_0 = k_{L-H} \tag{2.20}$$

The L−H model appears to be a promising tool that has several applications in semiconductor photocatalysis such as dye degradation, air purification, hazardous waste remediation, and water purification. Also, the basic research that underlies the application of this potential tool is forging a better understanding of the complex heterogeneous photochemistry of metal oxide systems in multiphasic environments.

2.2. Systems:

2.2.1. Molecular Probes: In this section, we will discuss the different probe molecules that have been used in the course of the study.

2.2.1.1. Methylene Blue (MB): MB is a heterocyclic aromatic chemical compound with molecular formula: $C_{16}H_{18}ClN_3S$. It has many uses in a range of different fields. At room-temperature it appears as a solid, odorless, and dark green powder, which yields a blue solution when dissolved in water. They are widely used as model water contaminants [12]. Its structure is given in Figure 2.3a. When dissolved in water, the UV-visible spectrum of MB showed three absorption maxima. The first band was observed at 246 nm and then 291 nm and more intensely at 663 nm [13]. The absorption maxima wavelength of MB (λ_{max} = 663 nm) was used for the analysis during the decolorization of MB dye.

2.2.1.2. Methyl Orange (MO): MO is an azo compound with molecular formula: $C_{14}H_{14}N_3NaO_3S$. It is a model dye which belongs to the class of synthetic organic compounds and is widely used in the textile industry. The removal of these non-biodegradable organic chemicals from the environment is a crucial ecological problem [14]. At room-temperature it appears as a solid, odorless, orange-yellow powder. MO shows orange color in acidic medium and yellow color in basic medium. Its structure is given in Figure 2.3b. MO has a strong absorption at λ_{max} = 461 nm [15] which was used for the analysis during decolorization of MO dye.

2.2.1.3. 3,7,12,17-Tetramethyl-8,13-divinyl-2,18-porphinedipropionic Acid (Protoporphyrin IX, PP): Protoporphyrin IX (PPIX) is an important organic compound, which plays an important role in living organisms as a precursor to other critical compounds like hemoglobin and chlorophyll. Protoporphyrin IX belongs to the porphyrin family, which is a class of tetrapyrroles. Its structure is given in Figure 2.3c. PPIX exhibits an intense Soret band absorption at 406 nm (S_0-S_2 transition), together with four weaker Q-bands at (506, 542, 577, and 630 nm (S0-S1 transition) [16, 17]. PPIX is a well-known photosensitizer (PS) for photodynamic therapy, visible light-harvesting applications [18, 19]. The efficiency of visible light harvesting depends on the PS loading on the active semiconductor photocatalysts.

2.2.1.4. Phthalocyanine (PC): PC is very well-known for its widespread applications in the field of optical recording, photodynamic therapy, and solar energy harvesting applications [20-22]. Its structure is given in Figure 2.3d. In visible light photocatalysis, sensitizers with extended absorption in the near IR region of the sun emission spectra are paramount, and phthalocyanines are perfectly suited for their integration in light energy conversion systems. They exhibit very high extinction coefficients around 680 nm for efficient photon harvesting [23], as well as reversible redox properties and excellent photoconductivity.

2.2.1.5. L-Cysteine (Cys): L-Cysteine is one of the sulfur-containing proteinogenic amino acids incorporated into proteins as directed by the genetic code. Its structure is given in Figure 2.3e. Cysteine is a semi-essential proteinogenic amino acid with the formula $HO_2CCH(NH_2)CH_2SH$. At room-temperature it appears as a solid and is odorless white powder [24]. It contains sulfur in the form of a thiol group (-SH) at the end of its side chain, another side of the chain contains a carboxyl group (-COOH). As Cys has two attaching groups, it can be used as a

linker between two molecules. We have used Cys as a linker to attach two semiconductors to make a heterostructure.

2.2.1.6. 2,2-Diphenyl-1-picrylhydrazyl (DPPH): DPPH is a well-known radical and a trap ("scavenger") for other radicals. Therefore, the reduction rate of a chemical reaction upon the addition of DPPH is used as an indicator of the radical nature of that reaction [25]. Because of a strong absorption band centered at about 520 nm, the DPPH radical has a deep violet color in solution, and it becomes colorless or pale yellow when neutralized. This property allows visual monitoring of the reaction, and the number of initial radicals can be counted from the change in the optical absorption at 520 nm. Its structure is given in Figure 2.3f.

2.2.1.7. Dichlorofluorescin (DCFH): Dichlorofluorescin (DCFH) is a probe that is trapped within cells and is easily oxidized to fluorescent dichlorofluorescein (DCF) [26]. DCFH is non-fluorescent which converts to fluorescent DCF upon oxidation through reacting with reactive oxygen species (ROS). This quantifies the amount of ROS as well as cellular oxidative stress. Its structure is given in Figure 2.3g.

2.2.1.8. 3-(4,5-dimethylthiazol-2-yl)-2,5-diphenyltetrazolium Bromide (MTT): Tetrazolium dye MTT converted into its insoluble formazan through NAD(P)H-dependent cellular oxidoreductase enzymes under defined conditions that reflect the number of viable cells present [27]. Tetrazolium dye reduction is generally assumed to be dependent on NAD(P)H-dependent oxidoreductase enzymes largely in the cytosolic compartment of the cell. Therefore, the reduction of MTT depends on cellular metabolic activity due to NAD(P)H flux [28]. Cells with a low metabolism such as thymocytes and splenocytes reduce very little MTT. In contrast, rapidly dividing cells exhibit high rates of MTT reduction. It is important to keep in mind that assay conditions can alter metabolic activity and thus

tetrazolium dye reduction without affecting cell viability. Its structure is given in Figure 2.3h.

2.2.1.9. Ethidium Bromide (EtBr): EtBr is a well-known fluorescent probe (Figure 2.3) for DNA, which readily intercalates into the DNA double helix [29]. Compared to bulk water, the emission intensity and lifetime of EtBr increases significantly when EtBr intercalates into the double helix of DNA [30]. This remarkable fluorescence enhancement of EtBr is utilized to study the motion of DNA segments, and the interaction of DNA with surfactants and drugs. Absorption maxima of EtBr in aqueous solution are at 285 nm and 480 nm, after excitation EtBr emits orange light with wavelength maxima at 620 nm [31]. Its structure is given in Figure 2.3i.

2.2.1.10. 4',6-Diamidino-2-phenylindole (DAPI): The dye DAPI (Figure 2.3j) is a commercially available fluorescent cytological stain for DNA [32]. Studies on the DAPI-DNA complexes show that the probe exhibits a wide variety of interactions of different strength and specificity with DNA [33]. The dye exhibits intramolecular proton transfer as an important mode of excited state relaxation at physiological pH [34], which takes place from the amidino to the indole moiety.

2.2.1.11. Acridine Orange (AO): AO is an organic dye with molecular formula $C_{17}H_{19}N_3$. AO is widely used as a nucleic acid-selective fluorescent cationic dye which is commonly used to determine cell cycle [35]. AO has strong absorption at λ_{max} = ~480 nm [36]. As AO is cell-permeable, it interacts with DNA and RNA by intercalation or electrostatic attractions respectively. When bound to DNA, it is very similar spectrally to fluorescein, with an excitation maximum at 502 nm and an emission maximum at 525 nm (green) [35]. In association with RNA, the excitation maximum of AO shifts to 460 nm (blue), and the emission maximum shifts to 650 nm (red). AO can be used in conjunction with ethidium bromide or propidium iodide to differentiate between viable, apoptotic, and necrotic cells.

Additionally, AO may be used to detect nuclear damage or chromatin condensation aiding in clinical diagnosis [37]. Its structure is given in Figure 2.3k.

2.2.1.12. Folic Acid (FA): Folic Acid is a water-soluble B vitamin that is naturally present in some foods, and available as a dietary supplement [38]. Its structure is given in Figure 2.3k. Folic acid (FA) is a stable and cheap ligand that can target cancer cells via a Folate receptor (FR) [39]. Folate is also known as vitamin B_9 and folacin. Folate, in the form of folic acid, is used to treat anemia caused by folate deficiency. Folic acid is also taken as a supplement by women during pregnancy to reduce the risk of neural tube defects (NTDs) in the baby. Taking advantage of FRs targeting cancer cells is a well-known strategy to implement targeted drug delivery.

2.2.1.13. Curcumin (Cur): Curcumin is a natural yellowish-orange diarylheptanoid derived from the rhizomes of *Curcuma longa L.* popularly known as turmeric, a member of the ginger family [40]. The diverse pharmacological applications of curcumin towards various diseases include Alzheimer's disease, breast cancer, pancreatic cancer, colon cancer, arthritis, and oxidative stress-induced pathogenesis [41, 42]. Furthermore, its promising antioxidant activity anticipates its possible use as a novel drug also for other lethal diseases. Curcumin is a linear polyphenol consisting of two o-methoxy phenolic groups that are connected by a seven-carbon linker consisting of an α, β-unsaturated β-diketo moiety (Figure 2.3m). The diketo group exhibits keto-enol tautomerism and can exist in different types of conformers depending on the nature of the solvent [43]. The diketo group exhibits keto-enol tautomerism and can exist in different types of conformers depending on the nature of the solvent. Due to the presence of β-diketone linkers in the seven-carbon chain, curcumin tends to chelate with metal. Sometimes, this metal chelating property can be detrimental, as it can attach to toxic metals like mercury or lead.

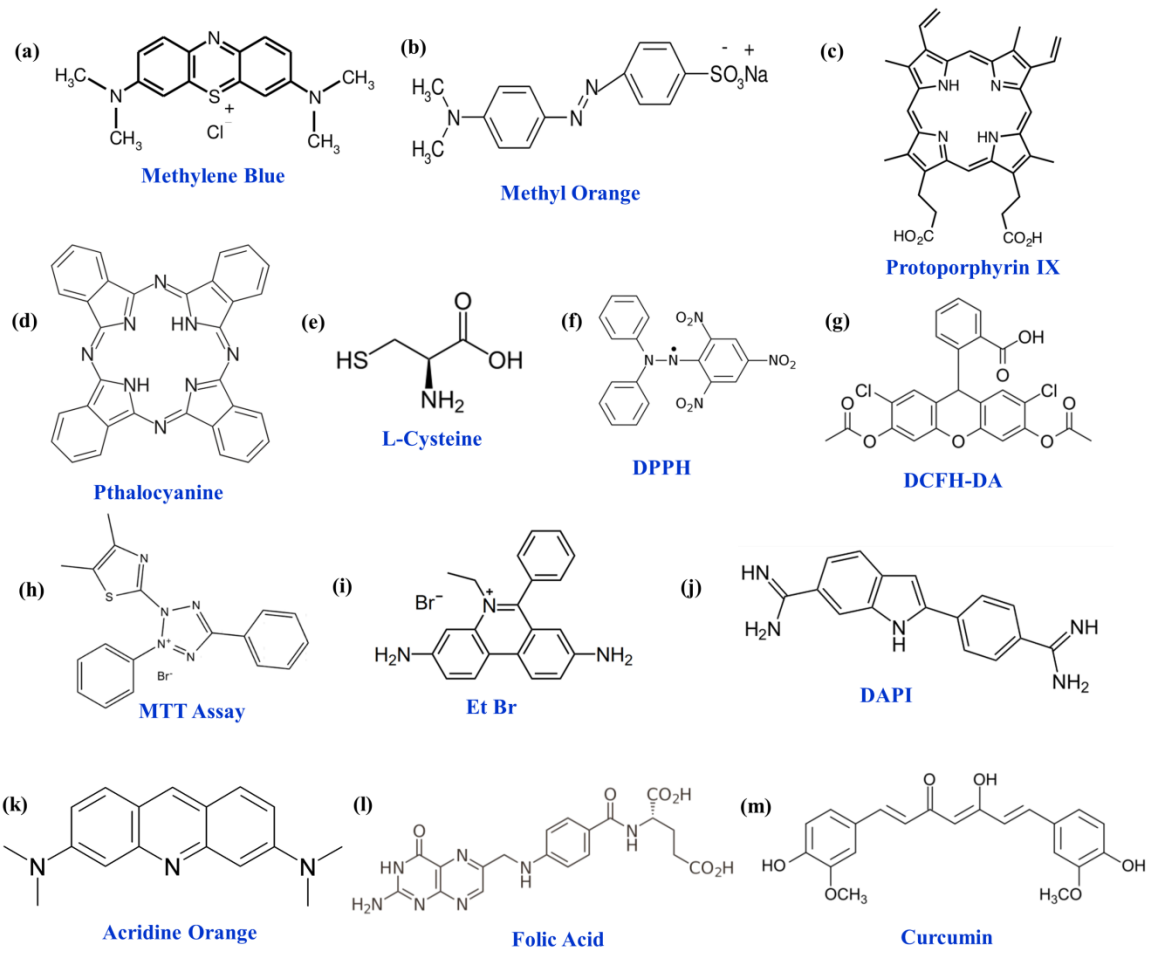

Figure 2.3: *Schematic representation of the fluorescent probes used in the course of study.*

References

[1] H. Spanggaard, F. C. Krebs, A brief history of the development of organic and polymeric photovoltaics, *Sol. Energy Mater. Sol. Cells* 83 (2004) 125.

[2] Y. Shirota, H. Kageyama, Charge carrier transporting molecular materials and their applications in devices, *Chem. Rev.* 107 (2007) 953.

[3] H. B. Gray, J. R. Winkler, Electron tunneling through proteins, *Q. Rev. Biophys.* 36 (2003) 341.

[4] G. McLendon, R. Hake, Interprotein electron transfer, *Chem. Rev.* 92 (1992) 481.

[5] H. Bassler, Charge transport in disordered organic photoconductors: A Monte Carlo simulation study, *Phys. Status Solidi B* 175 (1993) 15.

[6] V. M. Kenkre, J. D. Andersen, D. H. Dunlap, C. B. Duke, Unified theory of the mobilities of photoinjected electrons in naphthalene, *Phys. Rev. Lett.* 62 (1989) 1165.

[7] J. H. Bang, P. V. Kamat, Quantum dot sensitized solar cells. A tale of two semiconductor nanocrystals: CdSe and CdTe, *ACS Nano* 3 (2009) 1467.

[8] J. R. Lakowicz, Principles of fluorescence spectroscopy, *Springer*, New York, USA, 2006.

[9] D. Banerjee, S. K. Pal, Simultaneous binding of minor groove binder and intercalator to dodecamer DNA: Importance of relative orientation of donor and acceptor in FRET, *J. Phys. Chem. B* 111 (2007) 5047.

[10] B. Ohtani, Photocatalysis by inorganic solid materials: Revisiting its definition, concepts, and experimental procedures, *Adv. Inorg. Chem.* 63 (2011) 395.

[11] K. J. Laidler, J. H. Meiser, Physical chemistry, *Benjamin/Cummings Pub. Co.*, California, USA, 1982.

[12] N. Xu, Z. Shi, Y. Fan, J. Dong, J. Shi, M. Z. C. Hu, Effects of particle size of TiO_2 on photocatalytic degradation of methylene blue in aqueous suspensions, *Ind. Eng. Chem. Res.* 38 (1999) 373.

[13] D. Melgoza, A. Hernández-Ramírez, J. M. Peralta-Hernández, Comparative efficiencies of the decolourisation of methylene blue using Fenton's and photo-Fenton's reactions, *Photochem. Photobiol. Sci.* 8 (2009) 596.

[14] Y. Li, X. Li, J. Li, J. Yin, Photocatalytic degradation of methyl orange by TiO_2-coated activated carbon and kinetic study, *Wat. Res.* 40 (2006) 1119.

[15] A. Zyoud, A. Zu'bi, M. H. Helal, D. Park, G. Campet, H. S. Hilal, Optimizing photo-mineralization of aqueous methyl orange by nano-ZnO catalyst under simulated natural conditions, *J. Environ. Health Sci. Eng.* 13 (2015) 46.

[16] Y. Tokuoka, A. Niitsu, N. Watabe, T. N. Murakami, N. Kawashima, ESR spectroscopy of singlet oxygen generated by protoporphyrin IX in aqueous surfactant solutions, *J. Oleo Sci.* 52 (2003) 135.

[17] R. M. Valentine, S. H. Ibbotson, K. Wood, C. T. A. Brown, H. Moseley, Modelling fluorescence in clinical photodynamic therapy, *Photochem. Photobiol. Sci.* 12 (2013) 203.

[18] W. E. Grant, A. MacRobert, S. G. Bown, C. Hopper, P. M. Speight, Photodynamic therapy of oral cancer: Photosensitisation with systemic aminolaevulinic acid, *Lancet* 342 (1993) 147.

[19] E. Zahavy, I. Willner, Photoinduced electron transfer in Eosin-modified Co (II)-protoporphyrin IX reconstituted myoglobin and α-or β-hemoglobin subunits: Photocatalytic transformations by the reconstituted photoenzymes, *J. Am. Chem. Soc.* 118 (1996) 12499.

[20] A. L. Thomas, Phthalocyanine research and applications, *CRC Press*, Florida, USA, 1990.

[21] D. Gu, Q. Chen, X. Tang, F. Gan, S. Shen, K. Liu, H. Xu, Application of phthalocyanine thin films in optical recording, *Opt. Comm.* 121 (1995) 125.

[22] M. A. Loi, P. Denk, H. Hoppe, H. Neugebauer, C. Winder, D. Meissner, C. Brabec, N. S. Sariciftci, A. Gouloumis, P. Vázquez, Long-lived photoinduced charge separation for solar cell applications in phthalocyanine–fulleropyrrolidine dyad thin films, *J. Mater. Chem.* 13 (2003) 700.

[23] D. M. Krichevsky, A. V. Zasedatelev, A. Y. Tolbin, S. Y. Luchkin, A. B. Karpo, V. I. Krasovskii, L. G. Tomilova, Highly transparent low-symmetry zinc phthalocyanine-based monolayers for NO_2 gas detection, *Thin Solid Films* 642 (2017) 295.

[24] S. Kaçar, V. Şahintürk, B. Can, A. Musmul, L-Cysteine partially protects against acrylamide-induced testicular toxicity, *Bal. Med. J.* 35 (2018) 311.

[25] M. Szabo, D. Radu, S. Gavrilas, D. Chambre, C. Iditoiu, Antioxidant and antimicrobial properties of selected spice extracts, *Int. J. Food Prop.* 13 (2010) 535.

[26] S. Sardar, S. Chaudhuri, P. Kar, S. Sarkar, P. Lemmens, S. K. Pal, Direct observation of key photoinduced dynamics in a potential nano-delivery vehicle of cancer drugs, *Phys. Chem. Chem. Phys.* 17 (2015) 166.

[27] J. Van Meerloo, G. J. Kaspers, J. Cloos, Cell sensitivity assays: The MTT assay in I.A. Cree, Cancer cell culture, *Humana Press*, New Jersy, USA, 2011.

[28] D. Gerlier, N. Thomasset, Use of MTT colorimetric assay to measure cell activation, *J. Immunol. Methods* 94 (1986) 57.

[29] D. Millar, R. Robbins, A. Zewail, Torsion and bending of nucleic acids studied by subnanosecond time-resolved fluorescence depolarization of intercalated dyes, *J. Chem. Phys.* 76 (1982) 2080.

[30] J. Olmsted, D. R. Kearns, Mechanism of ethidium bromide fluorescence enhancement on binding to nucleic acids, *Biochem.* 16 (1977) 3647.

[31] S. K. Pal, D. Mandal, K. Bhattacharyya, Photophysical processes of ethidium bromide in micelles and reverse micelles, *J. Phys. Chem. B* 102 (1998) 11017.

[32] J. Kapuscinski, DAPI: A DNA-specific fluorescent probe, *Biotech. Histochem.* 70 (1995) 220.

[33] W. D. Wilson, F. A. Tanious, H. J. Barton, R. L. Jones, K. Fox, R. L. Wydra, L. Strekowski, DNA sequence dependent binding modes of 4', 6-diamidino-2-phenylindole (DAPI), *Biochemistry* 29 (1990) 8452.

[34] M. Barcellona, E. Gratton, A molecular approach to 4′, 6-diamidine-2-phenylindole (DAPI) photophysical behaviour at different pH values, *Biophys. Chem.* 40 (1991) 223.

[35] N. Atale, S. Gupta, U. Yadav, V. Rani, Cell-death assessment by fluorescent and nonfluorescent cytosolic and nuclear staining techniques, *J. Microscopy* 255 (2014) 7.

[36] A. Pitchaimani, A. Renganathan, S. Cinthaikinian, K. Premkumar, Photochemotherapeutic effects of UV-C on acridine orange in human breast cancer cells: Potential application in anticancer therapy, *RSC Adv.* 4 (2014) 22123.

[37] E. E. M. Mohammed, E. Mosad, A. M. Zahran, D. A. Hameed, E. A. Taha, M. A. Mohamed, Acridine orange and flow cytometry: Which is better to measure the effect of varicocele on sperm DNA integrity?, *Adv. Urology* 814150 (2015) 1.

[38] D. O. Kennedy, B vitamins and the brain: Mechanisms, dose and efficacy—A review, *Nutrients* 8 (2016) 68.

[39] D. Lee, R. Lockey, S. Mohapatra, Folate receptor-mediated cancer cell specific gene delivery using folic acid-conjugated oligochitosans, *J. Nanosci. Nanotech.* 6 (2006) 2860.

[40] K. M. Nelson, J. L. Dahlin, J. Bisson, J. Graham, G. F. Pauli, M. A. Walters, The essential medicinal chemistry of curcumin: Miniperspective, *J. Med. Chem.* 60 (2017) 1620.

[41] D. Perrone, F. Ardito, G. Giannatempo, M. Dioguardi, G. Troiano, L. Lo Russo, A. De Lillo, L. Laino, L. Lo Muzio, Biological and therapeutic activities, and anticancer properties of curcumin, *Exp. Ther. Med.* 10 (2015) 1615.

[42] S. Wanninger, V. Lorenz, A. Subhan, F. T. Edelmann, Metal complexes of curcumin–synthetic strategies, structures and medicinal applications, *Chem. Soc. Rev.* 44 (2015) 4986.

[43] M. Pröhl, U. S. Schubert, W. Weigand, M. Gottschaldt, Metal complexes of curcumin and curcumin derivatives for molecular imaging and anticancer therapy, *Coord. Chem. Rev.* 307 (2016) 32.

Chapter 3

Instrumentation and Sample Preparation

In this chapter, the details of instrumental setup and sample preparation techniques used in the thesis work have been described thoroughly.

3.1. Instrumental Setups:

3.1.1. Steady-state UV-Vis Absorption and Emission Measurement: Steady-state UV-Vis absorption and emission spectra were measured with Shimadzu UV-2600 spectrophotometer and Horiba Fluorolog, respectively. Schematic ray diagrams of these two instruments are shown in Figures 3.1 and 3.2 respectively.

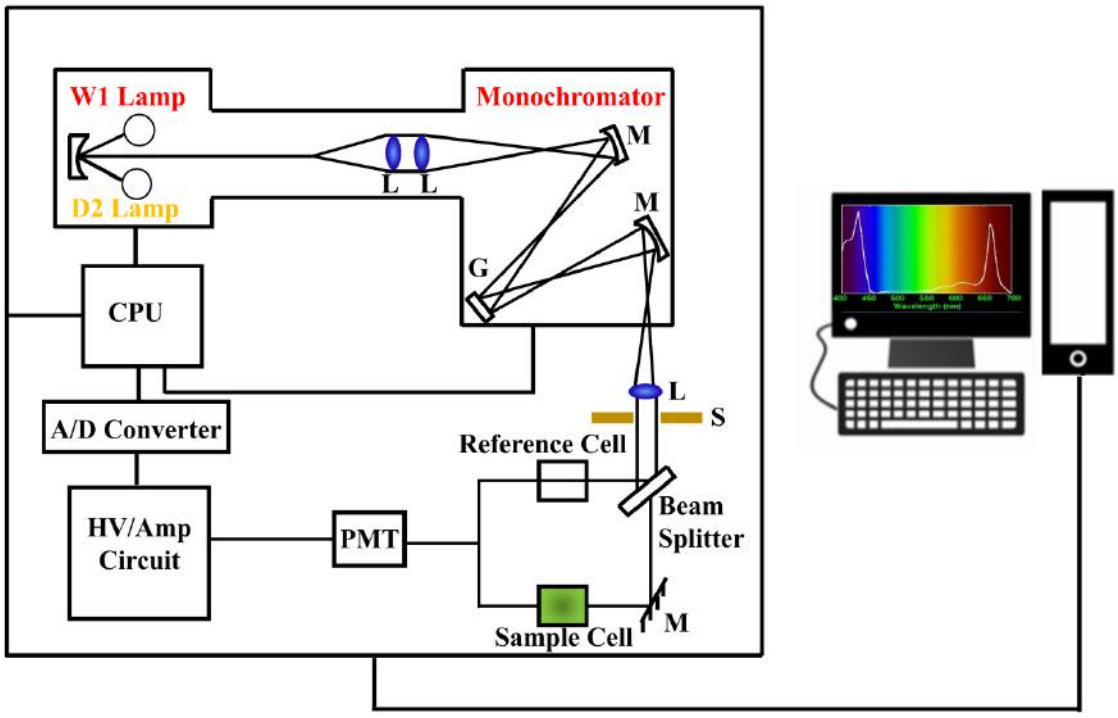

Figure 3.1: *Schematic ray diagram of an absorption spectrophotometer. Tungsten halogen (W1) and deuterium lamps (D2) are used as light sources in the visible and UV regions, respectively. M, G, L, S, PMT designate mirror, grating, lens, shutter, and photomultiplier tube, respectively. CPU, A/D converter, and HV/amp indicate central processing unit, analog to digital converter, and high-voltage/amplifier circuit, respectively.*

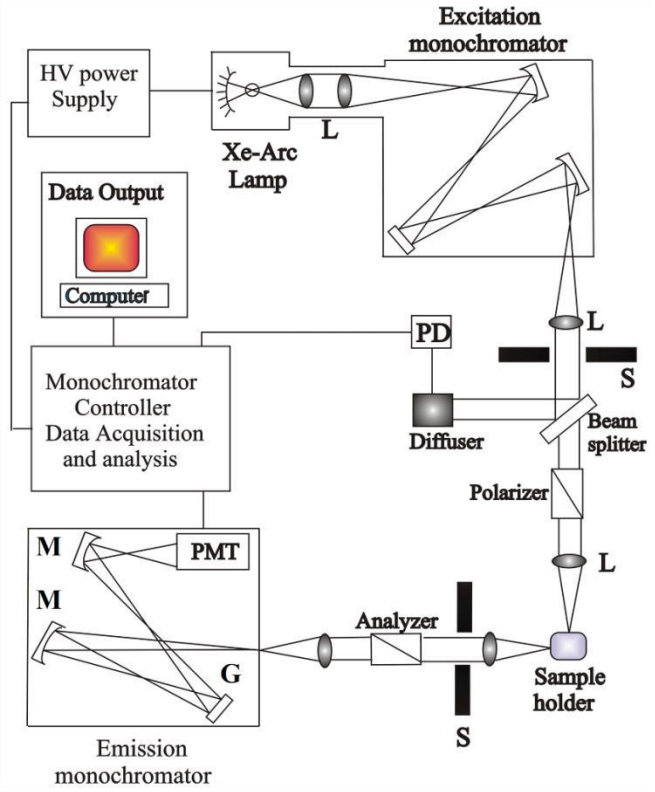

Figure 3.2: *Schematic ray diagram of an emission spectrofluorometer. M, G, L, S, PMT, and PD represent mirror, grating, lens, shutter, and photomultiplier tube and reference photodiode, respectively.*

3.1.2. Time-correlated Single Photon Counting (TCSPC) Technique: All the picosecond-resolved fluorescence decays were collected using the TCSPC technique. The schematic block diagram of a TCSPC system is shown in Figure 3.3. A commercial TCSPC setup from Edinburgh instruments (U.K.) was used during fluorescence decay acquisitions. The instrument response functions (IRFs) of the laser sources at different excitation wavelengths varied between 70 ps to 90 ps. The fluorescence from the sample was detected by a photomultiplier after dispersion through a grating monochromator [1].

For all excited state lifetime measurement experiments, the polarizer in the emission side was adjusted to be at 54.7° (magic angle) to the polarization axis of the excitation beam.

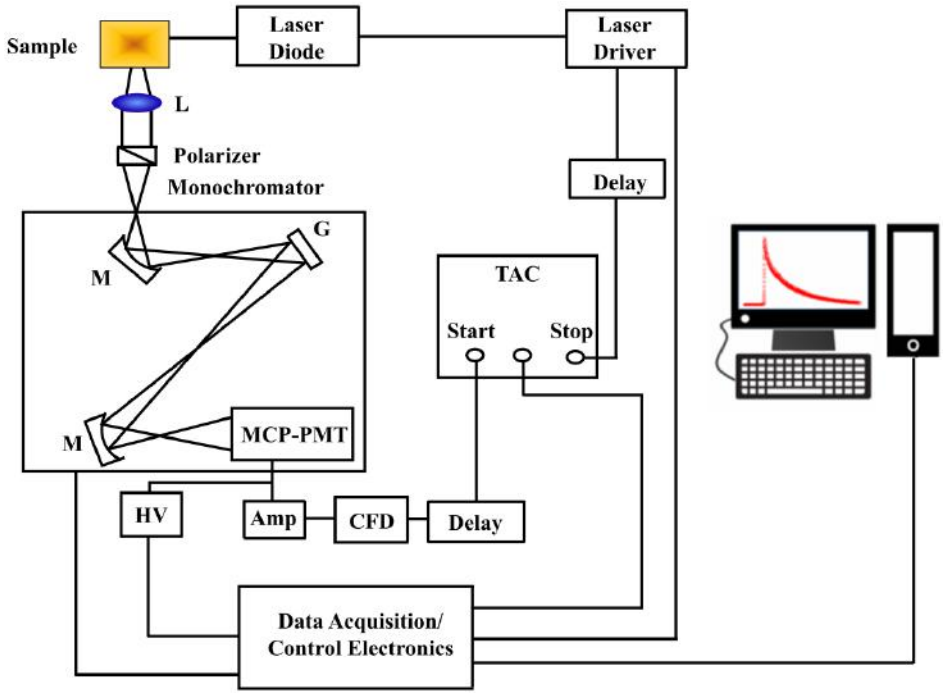

Figure 3.3: *Schematic ray diagram of time-correlated single photon counting (TCSPC) spectrophotometer. A signal from a microchannel plate photomultiplier tube (MCP-PMT) is amplified (Amp) and connected to the start channel of time to amplitude converter (TAC) through constant fraction discriminator (CFD) and delay. The stop channel of the TAC is connected to the laser driver via a delay line. L, M, G and HV represent lens, mirror, grating, and a high voltage source, respectively.*

3.1.3. Femtosecond Resolved Fluorescence Upconversion Technique: The femtosecond resolved fluorescence spectroscopy was carried out using a femtosecond upconversion setup (FOG 100, CDP, Figure 3.4) in which the sample was excited at 400 nm, using the second harmonic of a mode-locked Ti-sapphire laser with 80 MHz repetition rate (Tsunami, Spectra Physics), pumped by 10 W Millennia (Spectra Physics). The fundamental beam was passed through a periscopic arrangement (P) (Figure 3.4) before getting frequency-doubled in a nonlinear crystal, NC1 (1 mm BBO (β-barium borate), $\theta = 25°$, $\phi = 90°$). This beam was then sent into a rotating circular cell of 1 mm thickness containing the sample via a dichroic mirror (DM), a polarizer, and a mirror (M6). The resulting fluorescence emission was collected, refocused with a pair of lenses (L4 and L5)

and mixed with the fundamental beam (770 nm) coming through a delay line to yield an upconverted photon signal in a nonlinear crystal, NC2 (0.5 mm BBO, θ = 10°, ϕ = 90°). The upconverted light was dispersed in a double monochromator and detected using photon counting electronics. A cross-correlation function obtained using the Raman scattering from water displayed a full width at half maximum (FWHM) of 195 fs. The femtosecond fluorescence decays were fitted using a Gaussian shape for the exciting pulse.

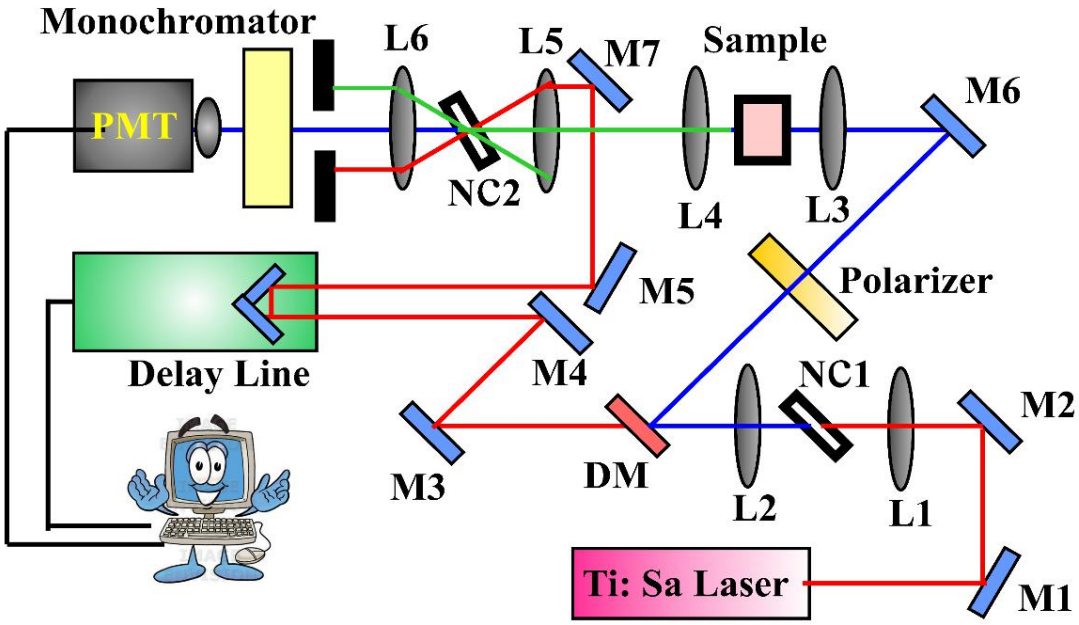

Figure 3.4: *Schematic diagram of a femtosecond fluorescence upconversion experimental setup. A BBO crystal (NC1) is used for the second harmonic generation, which provides a pump beam in the UV region. Another BBO crystal (NC2) generates the upconversion signal of the pump and probe beams. L and M indicate lenses and mirrors, respectively. M1, M2, M3, M4, M5, and M7 are IR mirrors whereas M6 is a UV mirror. DM is a dichroic mirror, and P is the periscope.*

3.1.4. Transmission Electron Microscopy (TEM): A FEI TecnaiTF-20 field-emission high-resolution TEM (Figure 3.5) equipped with energy dispersive X-ray (EDAX) spectrometer was used to characterize the microscopic structures of samples and to analyze their elemental composition.

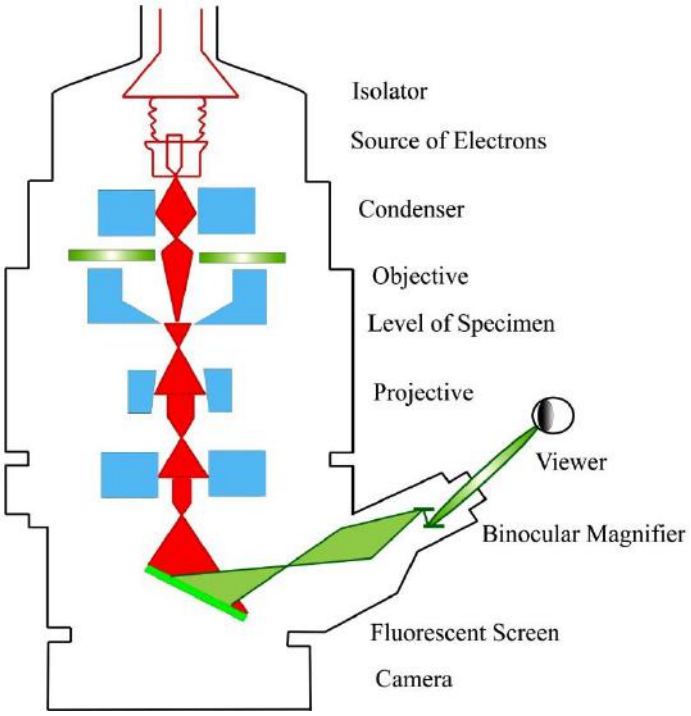

Figure 3.5: *Schematic diagram of a typical transmission electron microscope (TEM). After the transmission of the electron beam through a specimen, the magnified image is formed either in the fluorescent screen or can be detected by a charge-coupled device (CCD) camera.*

The sizes of the nanostructures were determined from the TEM images obtained at 200 kV acceleration voltage of the microscope. Samples for TEM were prepared by placing a drop of the colloidal solution on a carbon-coated copper grid and allowing the film to evaporate overnight at room temperature.

3.1.5. Scanning Electron Microscopy (SEM): Surface characterization of nanomaterials was done by scanning electron microscope FE (field emission)-SEM; JEOL. Ltd., JSM-6500F. An electron-gun is attached to SEM and the electrons from filament are triggered by 0 kV to 30 kV voltages. Electrons first go through a condenser lens and then through an objective lens, after that through an aperture, and finally, reach the specimen. The high energy electrons across the sample give rise to secondary electrons. The signal from secondary electrons is detected by the detector and amplified. The ray diagram of the SEM setup is shown in Figure 3.6.

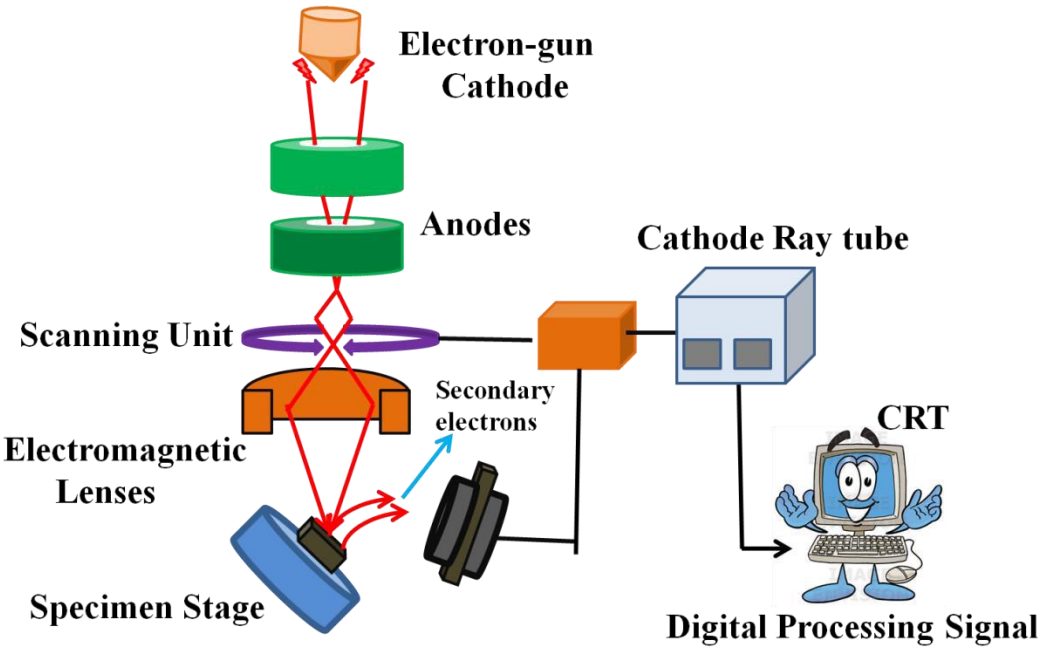

Figure 3.6: *Schematic diagram of a typical scanning electron microscope.*

3.1.6. Dynamic Light Scattering (DLS): Dynamic light scattering (DLS), also known as Photon Correlation Spectroscopy (PCS) or Quasi-Elastic Light Scattering (QELS), is one of the most popular techniques used to determine the hydrodynamic size of the particle. DLS measurements were performed on a Nano S Malvern instruments (U.K.), employing a 4 mW He-Ne laser (λ = 632.8 nm) and equipped with a thermostatic sample chamber. The instrument allows DLS measurements in which all the scattered photons are collected at a 173° scattering angle (Figure 3.7). The instrument measures the time-dependent fluctuation in intensity of light scattered from the particles in solution at a fixed scattering angle. The ray diagram of the DLS setup is shown in Figure 3.7.

It has been seen that particles in dispersion are in a random Brownian motion and this causes the intensity of scattered light to fluctuate as a function of time. The correlator used in a DLS instrument constructs the intensity autocorrelation function G(τ) of the scattered intensity, where τ is the time difference (the sample time) of the correlator. For a large number of monodisperse

particles in Brownian motion, the correlation function (G) is an exponential decay function of the correlator time delay τ:

$$G(\tau) = A[1 + Be^{-2\Gamma\tau}] \tag{3.2}$$

where A is the baseline of the correlation function, B is the intercept of the correlation function. Γ is the first cumulant which is related to the translational diffusion coefficient as, $\Gamma = Dq^2$, where q is the scattering vector and its magnitude is defined as:

$$q = \left(\frac{4\pi n}{\lambda_0}\right) \sin\left(\frac{\theta}{2}\right) \tag{3.3}$$

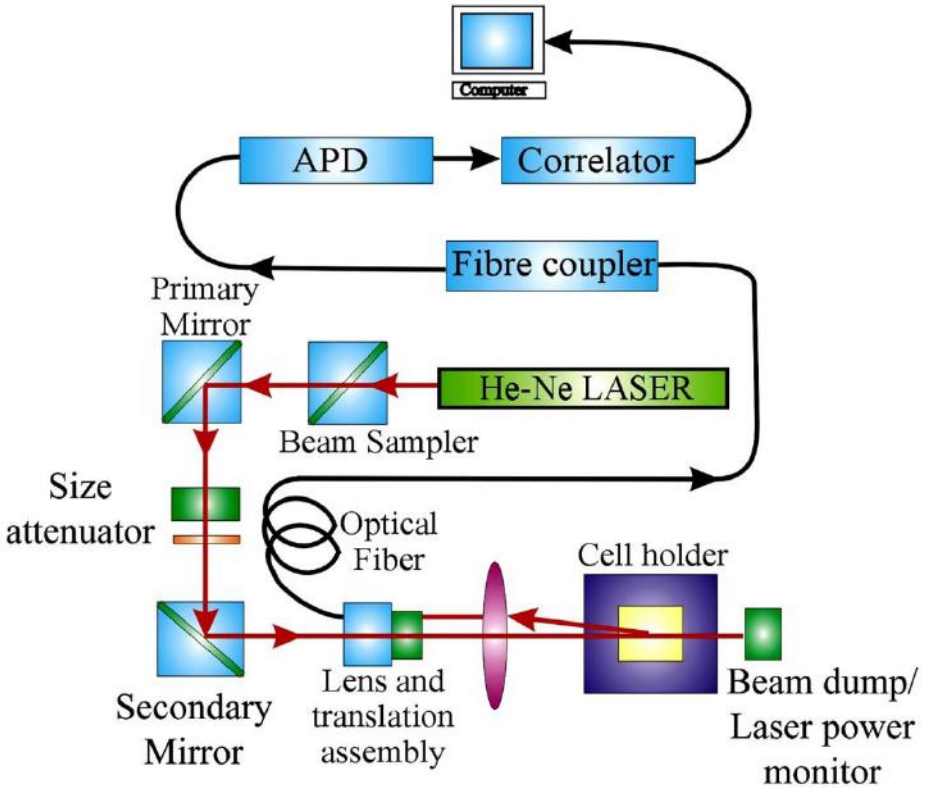

Figure 3.7: *Schematic ray diagram of dynamic light scattering (DLS) instrument. The avalanche photodiode (APD) is connected to the preamplifier/amplifier assembly and finally to the correlator. It has to be noted that lens and translational assembly, laser power monitor, size attenuator, and laser are controlled by the computer.*

where n is the refractive index of dispersant, λ_0 is the wavelength of the laser, and θ is the scattering angle. For polydisperse samples, the equation can be written as:

$$G(\tau) = A\left[1 + B\left|g^{(1)}(\tau)\right|^2\right] \tag{3.4}$$

where the correlation function $g^{(1)}(\tau)$ is no longer a single exponential decay and can be written as the Laplace transform of a continuous distribution G(Γ) of decay times:

$$g^{(1)}(\tau) = \int_0^\infty G(\tau)e^{-\Gamma\tau}d\Gamma \tag{3.5}$$

The scattering intensity data in DLS are processed using the instrumental software to obtain the hydrodynamic diameter (d_H) and the size distribution of the scatterer in each sample. In a typical size distribution graph from the DLS measurement, X-axis shows a distribution of size classes in nm, while the Y-axis shows the relative intensity of the scattered light. The diffusion coefficient (D) can be calculated using the d_H of the particle from the Stoke-Einstein relation:

$$D = \frac{k_B T}{3\pi\eta d_H} \tag{3.6}$$

where k_B, T, d_H, η are Boltzmann constant, the temperature in Kelvin, hydrodynamic diameter and viscosity, respectively.

3.1.7. X-ray Diffraction (XRD) Measurement: XRD is a popular and powerful technique for determining the crystal structure of crystalline materials. By examining the diffraction pattern, one can identify the crystalline phase of the material. Small-angle scattering is useful for evaluating the average interparticle distance while wide-angle diffraction is useful for refining the atomic structure of nanoclusters. The widths of the diffraction lines are closely related to strain and defect size and distribution in nanocrystals. As the size of the nanocrystals decreases, the line width is broadened due to the loss of long-range order relative

to the bulk. This XRD line-width can be used to estimate the size of the particle by using the Debye-Scherrer formula:

$$D = \frac{0.9\lambda}{\beta \cos\theta} \tag{3.7}$$

where, D is the nanocrystal diameter, λ is the wavelength of light, β is the full-width half-maximum (FWHM) of the peak in radians, and θ is the Bragg angle.

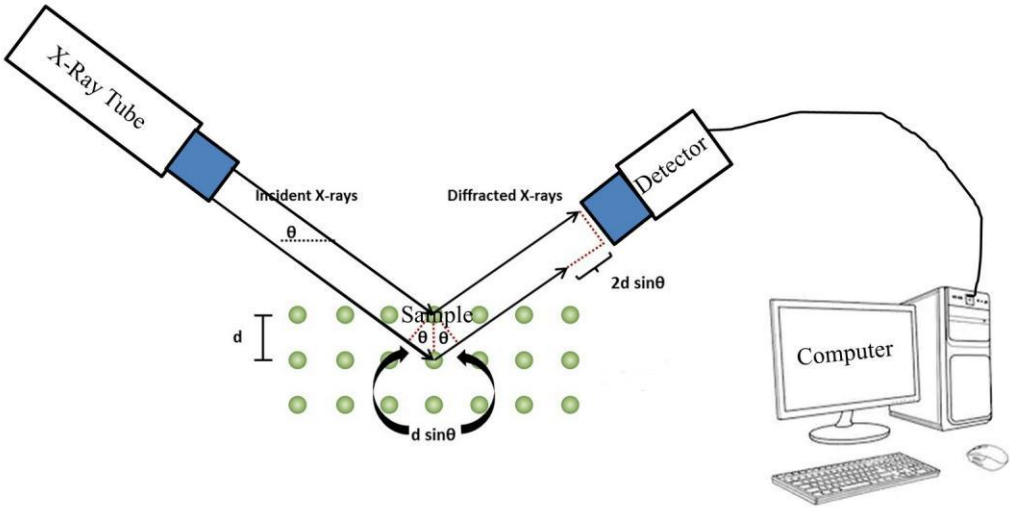

Figure 3.8: *Schematic diagram of an X-ray Diffraction (XRD) instrument. By varying the angle θ, the Bragg's Law conditions, nλ = 2dsinθ are satisfied by different d-spacings in polycrystalline materials. Plotting the angular positions and intensities of the resultant diffracted peaks of radiation produces a pattern, which is characteristic of the sample.*

XRD measurements were performed on a PANalytical XPERT-PRO diffractometer (Figure 3.8) equipped with CuK_α radiation (λ = 1.5418 Å at 40 mA, 40 kV). XRD patterns were obtained by employing a scanning rate of 0.02° s^{-1} in the 2θ range from 10° to 80°.

3.1.8. Thermogravimetric Differential Thermal Analyzer (TG-DTA) Setup: The thermogravimetric (TG) analysis was carried out using Diamond TG-differential thermal analyzer (DTA) from Perkin Elmer. The TG determines the weight change of a sample whereas the DTA measures the change in temperature between a

sample and the reference as a function of temperature and/or time. The schematic representation of the TG-DTA setup is shown in Figure 3.9. When a weight change occurs on the sample side, the beam holding the platinum pans are displaced. This movement is detected optically and the driving coil current is changed to return the displacement to zero. The detected driving coil current change is proportional to the sample weight change and the output is the TG signal. The DTA detects the temperature difference between the sample holder and the reference holder using the electromotive force of thermocouples, which are attached to the holders. This difference is measured as the DTA signal.

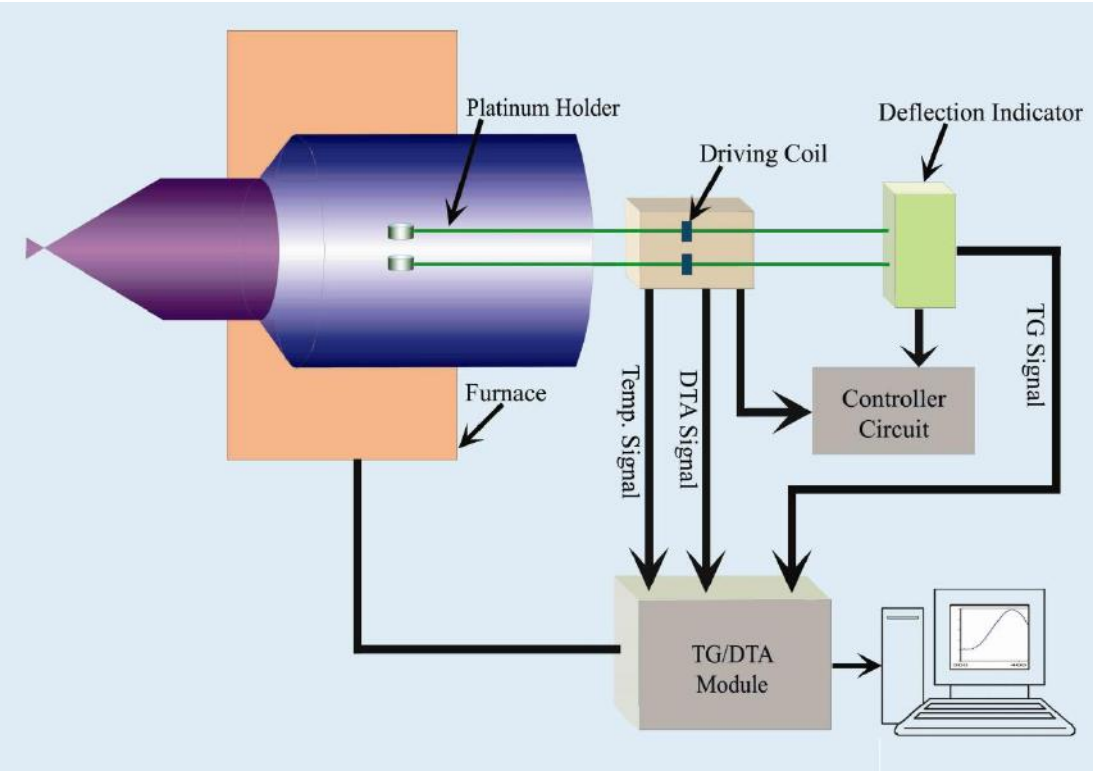

Figure 3.9: *The schematic representation of the TG-DTA setup.*

3.1.9. Fourier Transform Infrared (FTIR) Measurement: FTIR spectroscopy is a technique that can provide very useful information about functional groups in a sample. An infrared spectrum represents the fingerprint of a sample with absorption peaks which correspond to the frequencies of vibrations between the bonds of the atoms making up the material. Because each different material is a

unique combination of atoms, no two compounds produce the same infrared spectrum. Therefore, infrared spectroscopy can result in an identification (qualitative analysis) of different kinds of material. Also, the size of the peaks in the spectrum is a direct indication of the amount of material present. The two-beam Michelson interferometer is at the heart of the FTIR spectrometer.

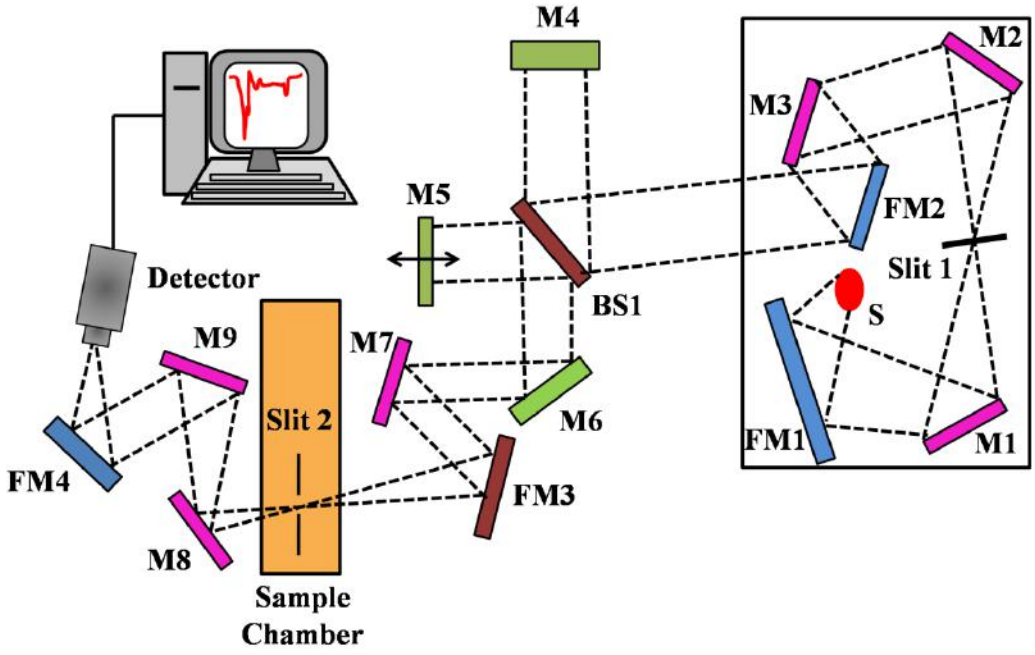

Figure 3.10: *Schematic representation of a Fourier Transform Infrared (FTIR) spectrometer. It is a Michelson interferometer in which one of the two fully-reflecting mirrors is movable, allowing a variable delay (in the travel-time of the light) to be included in one of the beams. M, FM, and BS1 represent the mirror, focusing mirror and beam splitter, respectively. M5 is a moving mirror.*

It consists of a fixed mirror (M4), a moving mirror (M5), and a beam-splitter (BS1), as illustrated in Figure 3.10. The beam-splitter is a laminate material that reflects and transmits light equally. The collimated IR beam from the source is partially transmitted to the moving mirror and partially reflected in the fixed mirror by the beam-splitter. The two IR beams are then reflected in the beam-splitter by the mirrors. The detector then sees the transmitted beam from the fixed mirror and reflected beam from the moving mirror, simultaneously. The two combined beams interfere constructively or destructively depending on the wavelength of the light (or frequency in wavenumbers) and the optical path difference introduced by the

moving mirror. The resulting signal is called an interferogram which has the unique property that every data point (a function of the moving mirror position) which makes up the signal has information about every infrared frequency which comes from the source. Because the analyst requires a frequency spectrum (a plot of the intensity at each frequency) to make an identification, the measured interferogram signal cannot be interpreted directly. A means of "decoding" the individual frequencies is required, which can be accomplished via a well-known mathematical technique called the Fourier transformation. This transformation is performed by the computer which then presents the user with the desired spectral information for analysis. FTIR measurements were performed on a JASCO FTIR-6300 spectrometer (transmission mode). For the FTIR measurements, powdered samples were mixed with KBr powder and pelletized. The background correction was made using a reference blank KBr pellet.

3.1.10. Laser Raman Spectroscopy: Raman spectroscopy is a useful technique for the identification of a wide range of substances- solids, liquids, and gases. It is a straightforward, non-destructive technique requiring no sample preparation. Raman spectroscopy involves illuminating a sample with monochromatic light and using a spectrometer to examine light scattered by the sample.

At the molecular level photons can interact with matter by absorption or scattering processes. Scattering may occur either elastically, or inelastically. The elastic process is termed Rayleigh scattering, whilst the inelastic process is termed Raman scattering. The electric field component of the scattering photon perturbs the electron cloud of the molecule and may be regarded as exciting the system to a 'virtual' state. Raman scattering occurs when the system exchanges energy with the photon and the system subsequently decays to vibrational energy levels above or below that of the initial state. The frequency shift corresponding to the energy difference between the incident and scattered photon is termed the Raman shift. Depending on whether the system has lost or gained vibrational energy, the

Raman shift occurs either as an up or down-shift of the scattered photon frequency relative to that of the incident photon. The down-shifted and up-shifted components are respectively called the Stokes and anti-Stokes lines. A plot of the detected number of photons versus Raman shift from the incident laser energy gives Raman spectrum. Different materials have different vibrational modes, and therefore characteristic Raman spectra. This makes Raman spectroscopy a useful technique for material identification. There is one important distinction to make between the Raman spectra of gases and liquids, and those taken from solids− in particular, crystals. For gases and liquids, it is meaningful to speak of the vibrational energy levels of the individual molecules which make up the material. Crystals do not behave as if composed of molecules with specific vibrational energy levels; instead, the crystal lattice undergoes vibration. These macroscopic vibrational modes are called phonons.

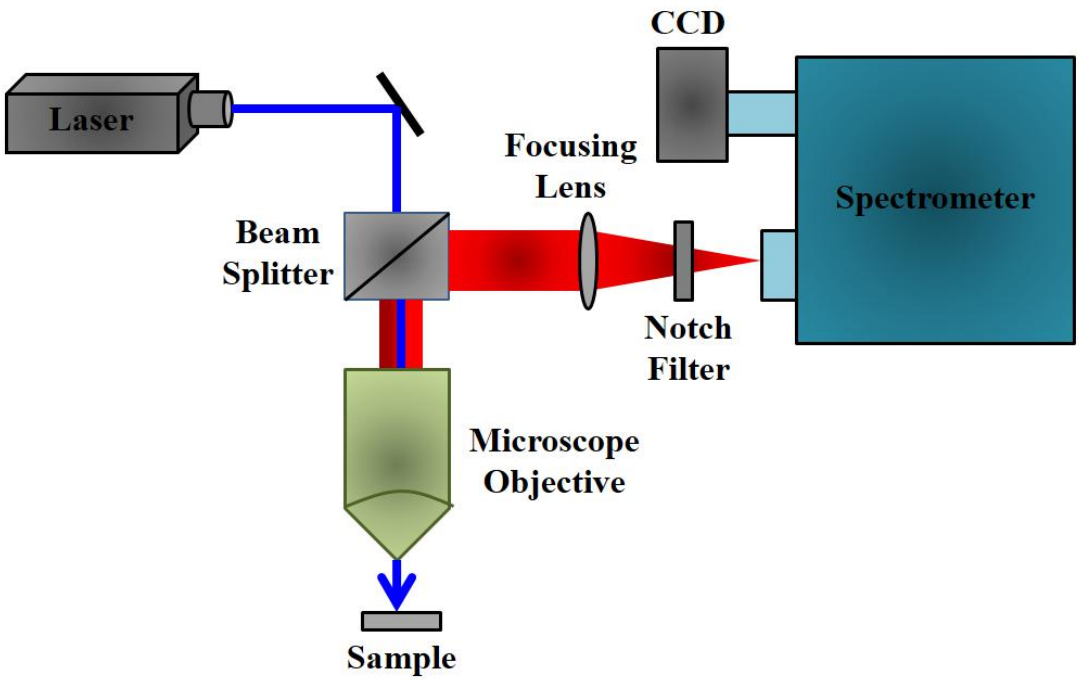

Figure 3.11: *A schematic diagram of a Raman spectrometer.*

In modern Raman spectrometers (Horiba LabRAM set up), lasers are used as a photon source due to their highly monochromatic nature, and high beam

fluxes (Figure 3.11). This is necessary as the Raman effect is weak, typically the Stokes lines are ~10^5 times weaker than the Rayleigh scattered component. In the visible spectral range, Raman spectrometers use notch filters to cut out the signal from a very narrow range centered on the frequency corresponding to the laser radiation. Most Raman spectrometers for material characterization use a microscope to focus the laser beam to a small spot (<1−100 μm diameter). Light from the sample passes back through the microscope optics into the spectrometer. Raman shifted radiation is detected with a CCD detector and a computer is used for data acquisition and curve fitting. These factors have helped Raman spectroscopy to become a very sensitive and accurate technique.

3.1.11. Surface Area Analysis using Brunauer, Emmett, and Teller (BET) Technique: The Brunauer, Emmett, and Teller (BET) technique [2] is the most common method for determining the surface area of powders and porous materials (Figure 3.12). The BET theory applies to systems of multi-layer

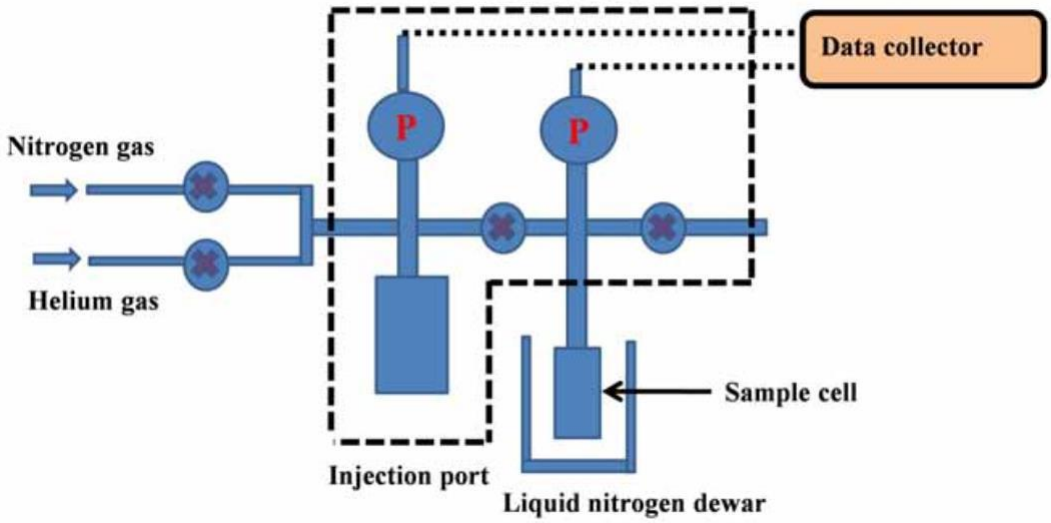

Figure 3.12: *Schematic diagram of a BET surface analyzer setup. P corresponds to the pressure gauge.*

adsorption and usually utilizes probing gases that do not chemically react with material surfaces as adsorbates to quantify specific surface area. Nitrogen gas is

generally employed as the probe molecule and is exposed to a solid under investigation at liquid nitrogen conditions (i.e. 77 K). Specific surface area is a scale-dependent property, with no single true value of specific surface area definable, and thus quantities of the specific surface area determined through BET theory may depend on the adsorbate molecule utilized and its adsorption cross-section.

3.1.12. Electrochemical Impedance Spectroscopy (EIS): Electrochemical Impedance Spectroscopy (EIS) is a powerful technique to investigate the electronic and ionic processes in photovoltaic devices. The electrochemical impedance is usually measured by applying an AC potential to an electrochemical cell and then measuring the current through the cell. An important advantage of EIS over other techniques is the possibility of using tiny AC voltage amplitudes exerting a very small perturbation on the system. A Nyquist plot can be made by plotting the real part of the transfer function on the X-axis and the imaginary part on the Y-axis. The Nyquist diagram features typically three semicircles that in the order of increasing frequency are attributed to the Nernst diffusion within the electrolyte, the electron transfer at the oxide/electrolyte interface, and the redox reaction at the platinum counter electrode. From applying appropriate equivalent circuits, the transport rate and lifetime of the electron in the mesoscopic film are derived.

EIS was performed on an electrochemical workstation CHI650E (CH instrument) with a frequency range from 100 kHz to 0.1 Hz in the open circuit condition. The schematic presentation of the EIS set up is shown in Figure 3.13. All impedance measurements were carried out under a bias illumination of 100mW/cm^2. The obtained spectra were fitted using the CHI650E software in terms of appropriate equivalent circuits. The system containing thin films were used as a working electrode with a 0.27 cm^2 geometric area exposed to the electrolyte solution under light irradiation. The experiments were performed in a conventional three-electrode cell using Ag/AgCl (3.5 M KCl) used as a reference

electrode, Pt-foil as counter electrode and the sample coated film as the working electrode. The photo-electrochemical measurement was executed in 0.1 M Na_2SO_3 with 0.1 M Na_2SO_4 solution for SO_3^{2-} (sacrificial) oxidation reaction within the potential range from 0.1 to 0.6 V using a CHI650E potentiostat (CH Instrument,

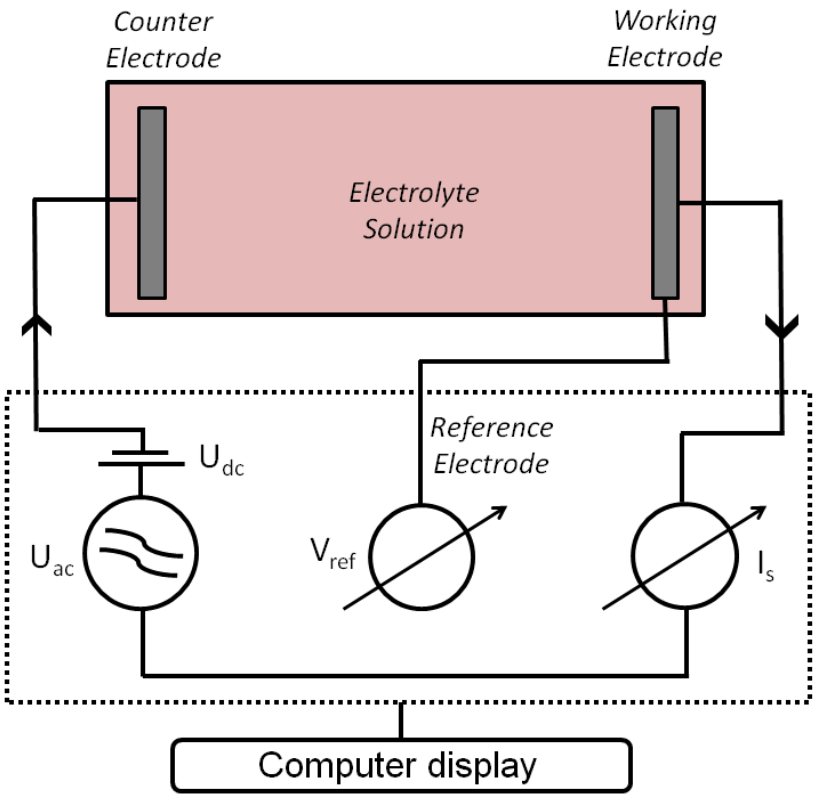

Figure 3.13: *Schematic diagram of a simplified measurement circuit for performing Electrochemical Impedance Spectroscopy (EIS).*

Austin, TX) at a scan rate of 10 mV/s. The water oxidation reaction was carried out in 0.1 M Na_2SO_4 solution in PBS (pH 7) using a similar experimental set up within the range from 0.0 to 1.0 V [3]. The EIS measurements were performed using a similar experimental setup with 0.1 M Na_2SO_4 (in pH 7 PBS) solution employing Autolab 302N PG-stat with a frequency response analyzer (FRA). In the Nyquist plot, the variation of real and imaginary parts of the impedance at different frequencies within the range of 100 kHz to 20 MHz was obtained under UV-visible illumination at an applied potential of 0.8 V. The stability of the system

undergoing a water oxidation reaction was examined through chronoamperometry using the same reaction condition under constant illumination of 100 W/cm^2 at an applied potential of 0.8 V for 30 min [3].

The classical definition of external quantum efficiency (EQE) is the ratio between the numbers of molecules degraded by the number of incident photons involved in the catalysis process [4-6]. The EQE is denoted by the below equation:

$$EQE = \frac{\langle reaction\ rate(mol/sec)\rangle}{\langle photon\ rate(einstein/sec)\rangle} \times 100\% \tag{3.8}$$

EQE of the semiconductor is also calculated from the photo-induced current measurement process. Incident Photon to Charge Carrier Efficiency (IPCE) was calculated by determining the power of the incidental beam of light at a specified wavelength, using the following equation:

$$IPCE(\%) = (\frac{1240}{\lambda}) \times \left(\frac{I_{Ph}}{P_{in}}\right) \times 100\% \tag{3.9}$$

where λ is the wavelength of the incident light, I_{Ph} is the measured photocurrent of the system (in mA/cm^2) and P_{in} is the power of incident beam (in mW/cm^2) [7].

3.1.12.1. Electrode Preparation for Photocurrent Measurement: 100 mg of nanoparticles (NPs) were suspended in 5 ml EG and the mixtures were kept in an ultra-sonication bath for ~1 hr. Then 400 µl of the mixture was dropped cast onto a clean ITO coated rectangular size glass plate of dimension 1.5 × 1.5 cm^2 to prepare thin films of samples. The NP coated thin films were annealed in air at ~350°C for 6 hr. with a ramping rate of 1°C per min. followed by soaking for 3 hr. to obtain a uniform, well-adhered thin films.

3.1.13. X-Ray Photoelectron Spectroscopy (XPS): The fundamental basis of X-ray photo-electron spectroscopy is based on the photoemission process of the material. If the material is bombarded with high energy X-ray photon, an electron can be ejected from it. The kinetic energy (KE) of the electron depends upon the photon

energy (hν) and the binding energy (BE) of the electron. The equation governing the process is KE = hν – BE. The spectrum from the emitted electron is used to calculate the binding energy of the core electrons in the material, providing elemental information and valence configuration of the exposed surface. The X-ray

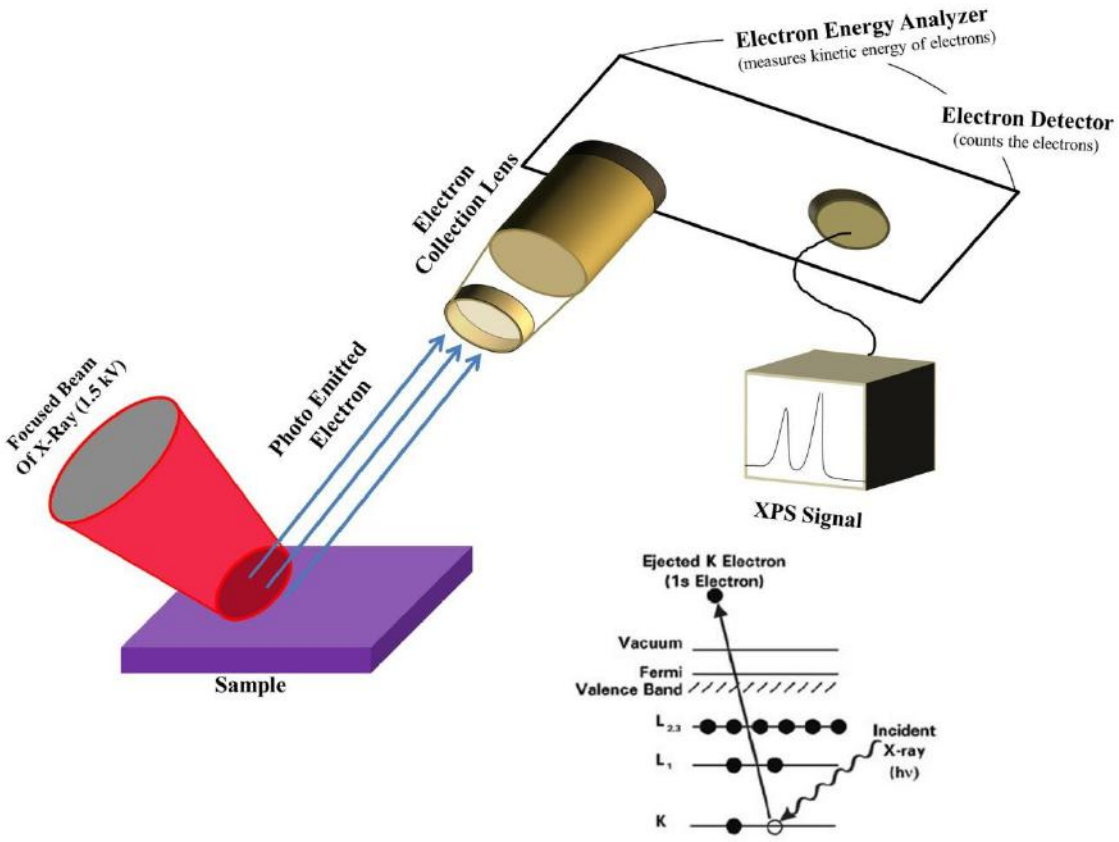

Figure 3.14: *Schematic diagram of the XPS system. The inset shows the photoemission process.*

photoelectron spectroscopic measurements were done at BL-14 beamline, which is used for high-resolution photoelectron spectroscopy of solids at hard X-ray energy-range (2-15 keV). High energy XPS can provide information at larger depths. The synchrotron source provides high-intensity X-rays over a wide range of energies and XPS at different energies is expected to provide chemical information as a function of depth. The beamline consists of a Pt-coated toroidal mirror for focusing the X-ray beam, a double crystal monochromator for wide

tunable X-Ray energy range up to 15 keV, water-cooled X-ray slits for defining beam opening, and a high-resolution hemispherical analyzer based experimental station for acquiring the XPS data.

3.1.14. Hydrothermal Technique: The hydrothermal technique has been the most popular one, gathering interest from scientists and technologists of different disciplines, for the synthesis of different nanomaterials. The hydrothermal reaction is defined as any heterogeneous chemical reaction in the presence of a solvent (whether aqueous or non-aqueous) above room temperature and a pressure greater than 1 atm in a closed system. Crystal growth under hydrothermal conditions requires a reaction vessel called an autoclave. The autoclave must be

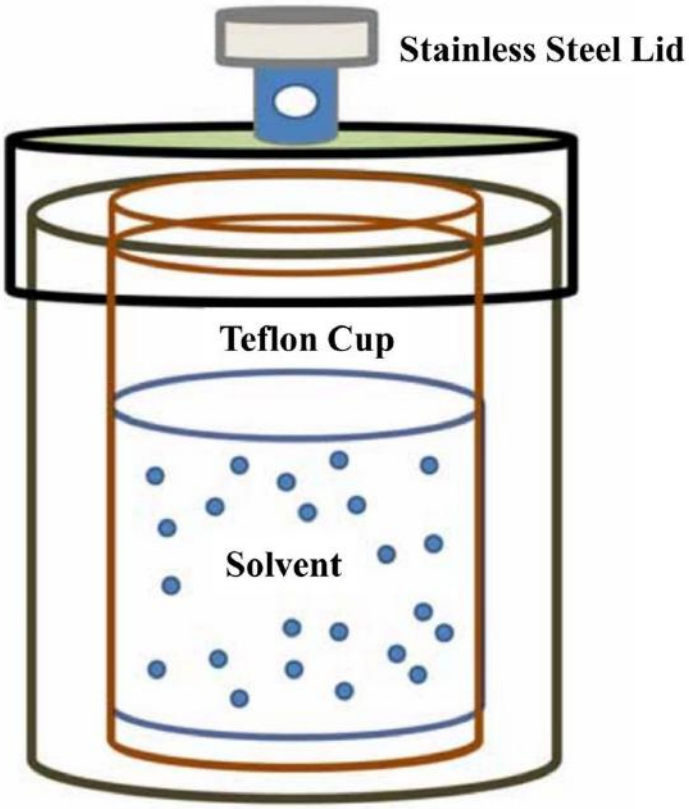

Figure 3.15: *Schematic representation of a lined stainless steel autoclave.*

capable of sustaining highly corrosive salt, which is used to synthesize inorganic materials at high temperatures and pressure for a longer duration of time. For

selecting a suitable autoclave, the first and foremost parameter is the experimental temperature and pressure conditions, and the corrosion resistance in that pressure-temperature range in a given solvent or hydrothermal fluid. To avoid corrosion of autoclave material it should be coated with non-reactive material called Teflon from inside. Due to the larger coefficient of thermal expansion of Teflon versus metal, the Teflon will expand and contract much more upon heating and cooling cycles than its enclosure material. For the synthesis of nanomaterials, we have used the Teflon-lined stainless steel autoclave of 30 mL capacity (Figure 3.15). The autoclave was rested at the desired temperature under autogenous pressure for the desired time.

3.1.15. Pulsed Laser Deposition (PLD) Technique: Pulsed laser deposition (PLD) is a physical vapor deposition technique where a high power pulsed laser beam is focused to strike a target material that is to be deposited. The whole process is done inside a vacuum chamber with an ultra-high vacuum (~10^{-7} Torr). In presence of an intense laser beam, the target material became vaporized (in a plasma plume form) which is deposited as a thin film on a substrate (such as a silicon wafer facing the target). PLD technique depends on the photon interaction to produce an emitted plume of material from any target which forms due to the fast explosion of the target surface as a result of heavy heating. When the laser pulse is absorbed by the target material, energy is first converted to electronic excitation and then into thermal, chemical, and mechanical energy resulting in evaporation, ablation, plasma formation, and even exfoliation. Complete PLD technique can be divided into 4 steps; a) Laser absorption at the surface of the target material, b) generation of plasma plume, c) deposition of the ablation material on the substrate, and d) nucleation and growth of the film on the substrate surface. A schematic diagram of the PLD is depicted in Figure 3.16.

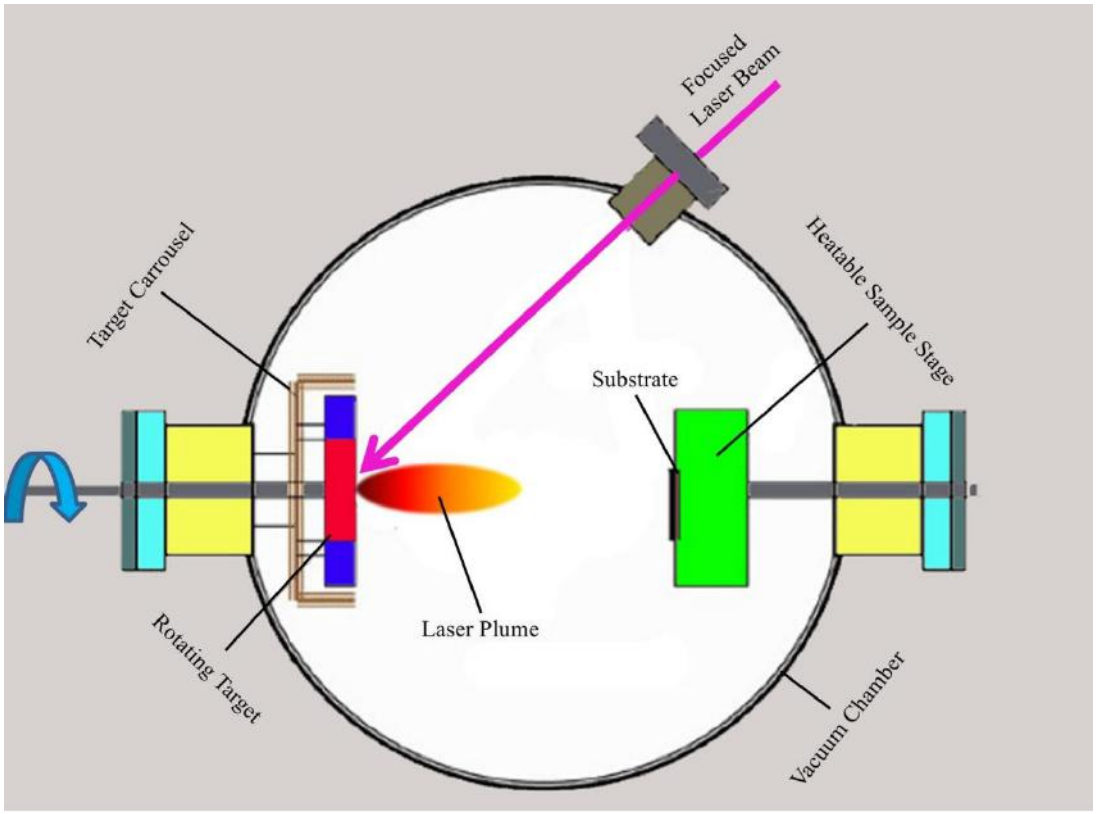

Figure 3.16: *Schematic representation of a pulsed laser deposition (PLD) setup.*

The vacuum chamber was evacuated by using the combination of a turbo molecular and rotary pump. The pressure of the chamber goes down up to ~1.33 × 10^{-6} mbar. Clean Quartz substrates of size 10mm × 10mm × 1mm were mounted on the sample holder. In our case, a KrF excimer laser with a wavelength of 248 nm has been used for pulsed deposition. The substrate annealing temperature is kept at 650°C.

3.1.16. Atomic Layer Deposition (ALD) Technique: Atomic Layer deposition is a sub-class of chemical vapor deposition where reactants (precursors) in the gaseous phase are brought together into the reaction chamber to form the desired material by using chemical surface reactions. In this process, the precursors are pulsed alternately and separated by inert gas purging to avoid gas-phase reactions. The main advantage of ALD offers is precise thickness control at the Å resolution and tunable film composition. The successive, self-terminated surface reaction of the

reactants allows precisely controlled growth of the desired material. Within our experimental framework, we deposited TiO_2 thin film. A schematic of the ALD deposition technique is depicted in Figure 3.17.

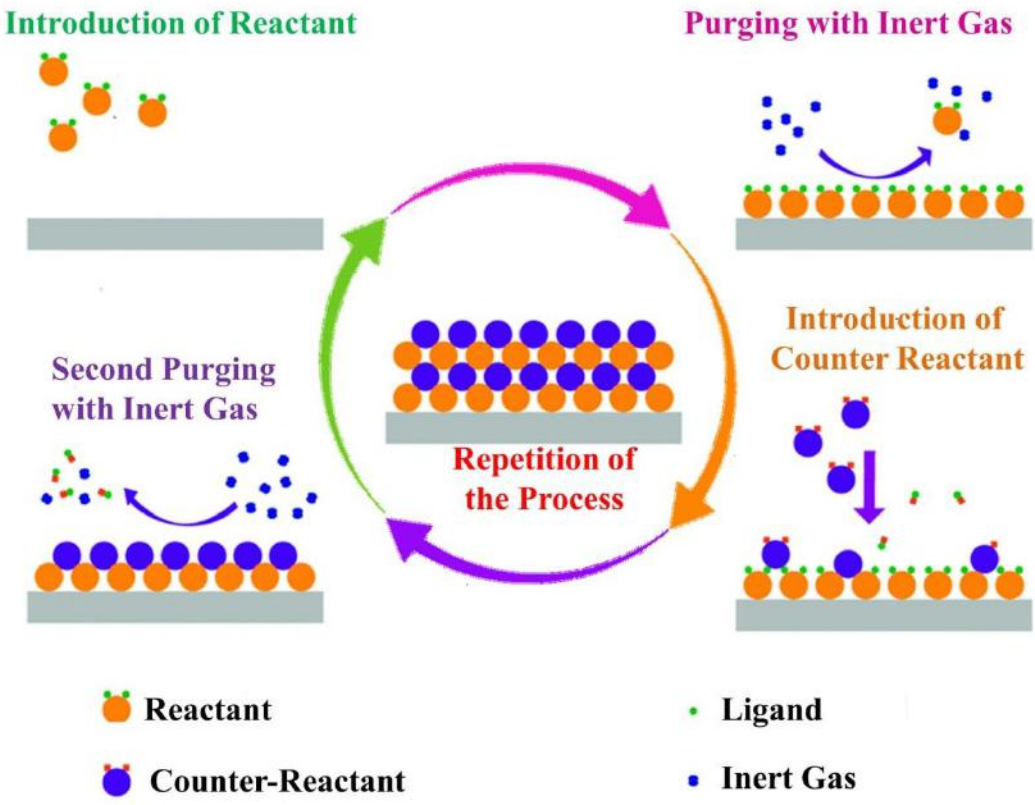

Figure 3.17: *Schematic representation of atomic layer deposition (ALD).*

3.1.17. Light Sources Used for Irradiation: For UV light-mediated experiment a homemade UV light source of 360 nm – 500 nm was used to irradiate samples under UV-blue range. For visible light-driven experiments a readymade light source (λ = ~400 nm to 560 nm and power = 3 mW/cm^2) has been used. For NIR light source a tungsten-halogen light source with a 650 nm high-pass filter has been used. A 300 W Xe-lamp source (Excelitas USA) with 100 mW/cm^2 illumination was maintained as the light source for the photo-electrochemical measurements.

3.1.18. Photocatalytic Measurements: The photocatalytic measurements of the systems have been carried out using photocatalytic degradation of textile dye (TD) at ambient temperature. The sample was taken in a quartz cuvette (1 mg in 2 ml aqueous medium) and TD was added to it to get an absorption peak height of 0.6 a.u. The total suspension was then exposed to a light source and absorbance data were collected at 10 min. irradiation intervals. The percentage degradation (%DE) of TD was determined using the following equation:

$$\%DE = \frac{I_0 - I(t)}{I_0} \times 100 \tag{3.10}$$

For photocatalysis using stainless steel mesh (SSM), a 1cm × 1cm mesh has been taken for the experiment. Initially, the sample has been decorated on the mesh using the hydrothermal method described above. The NP attached mesh is placed into a beaker containing 5 mL of water. The whole system is exposed to light for 4 hr. and data has been collected at 20-min. interval.

3.1.19. Preparation of DCFH for Extracellular ROS Generation Study: DCFH was prepared by the de-esterification reaction of DCFH-DA at room temperature [8]. 0.5 ml of 1.0 mM DCFH-DA in methanol was mixed with 2.0 ml of 0.01 N NaOH at room temperature for 30 min. Then the mixture was neutralized with 10 ml of 25 mM NaH_2PO_4 at pH 7.4. The resultant solution was kept at 4 ˚C in dark until use.

3.1.20. Cell Culture and Cytotoxicity Assay: HCT 116 cells were cultured in Dulbecco's Modified Eagle Medium (DMEM) supplemented with 10% fetal bovine serum (FBS) and 1% antibiotic (PSN) at 37°C in a humidified atmosphere under 5% CO_2. After 75-80% confluency, cells were harvested with 0.25% trypsin and 0.52 mM Ethylenediaminetetraacetic acid (EDTA) in phosphate-buffered saline (PBS) and seeded at a required density to allow them to re-equilibrate for a day before starting the experiment. 3-(4,5- dimethylthiazol-2-yl)-2,5-diphenyltetrazolium bromide (MTT) assay was conducted to evaluate the cell

viability. For the initial screening experimentation, the HCT 116 cells (4×10^3 cells per well) were seeded in 96 well plates and kept in an incubator followed by the treatment with different concentrations of FA, Fe_2O_3, and FA-Fe_2O_3 (0.01-100 µg/ml) for 24 hr. The rest of our cellular study was done after treatment with the requisite amount of drug followed by 24 hr. incubation unless mentioned otherwise. After 24 hr. of incubation, cells were rinsed with PBS then the MTT solution was added to each well and kept it in an incubator for 4 hr. to form formazan salt. The formazan salt was then solubilized using DMSO and the absorbance was monitored at 595 nm using an ELISA reader (Emax, Molecular device, USA) [9]. Cell proliferation was determined from the absorption intensity. Cell viability was determined using the following equations:

$$\text{Cell Viability (\%)} = \frac{OD_{control} - OD_{sample}}{OD_{control}} \times 100 \quad (3.11)$$

Absorbance values of treated cells and untreated cells are denoted as OD_{sample} and $OD_{control}$, respectively.

3.1.21. *In Vitro* Photodynamic Therapy (PDT): Based on the preliminary screening experimentation on HCT 116 cells, 0.1 µg/ml concentration of nanohybrid (NH) (herein FA-Fe_2O_3) was chosen for further experimentation whether it exhibits any photosensitizing effect within the cells. Thus, 0.1 µg/ml of FA-Fe_2O_3 treated HCT 116 cells were exposed to blue light in a time-dependent manner (5, 10, 15, 30, and 45 min.) following the MTT assay to determine the effectivity of photodynamic therapy.

3.1.22. Measurement of Intracellular ROS Generation Using Spectrofluorometry: Intracellular ROS accumulation was monitored using DCFH which is a well-known ROS marker. Briefly, the treated cells were incubated with 10 µM of DCFH at 37°C for 25 min. and then the cells were analyzed using a spectrofluorometer (JascoFP920, Hachioji, Tokyo, Japan) [10]. Fluorescence intensity was monitored at 522 nm upon excitation at 488 nm.

3.1.23. Measurement of Intracellular Hydroxyl Radical (ȮH) Accumulation Using Flow Cytometry: Intracellular hydroxyl radical (ȮH) accumulation was measured using hydroxyphenyl fluorescein (HPF), a specific indicator which reacts specifically with hydroxyl radical. HPF exhibit bright green fluorescence (excitation/emission maxima 490/515 nm) upon oxidation. Treated cells (2×10^6 cells) were incubated with HPF for 30 min. in dark followed by the acquisition using a flow cytometer (BD LSRFortessaTM San Jose, CA, USA). The acquired data were analyzed using Flow Jo (Version 10.0) software [11].

3.1.24. Quantification of Apoptosis Using Flow Cytometry: Apoptotic and necrotic cell death was determined using Annexin-V FITC/4',6-diamidino-2-phenylindole dihydrochloride (DAPI) apoptosis detection kit (Calbiochem, CA, USA). Briefly, HCT 116 cells were pretreated with 0.1 µg/ml of FA-Fe_2O_3 followed by different blue light exposure with different time duration (5, 10, and 15 min). Soon after the light exposure, the cells were washed and stained with DAPI as well as Annexin-V-FITC, following the manufacturer's instructions. The percentages of living, apoptotic (early and late), and necrotic cells were analyzed by flow cytometer (BD LSRFortessa TM San Jose, CA, USA). The acquired data were analyzed using Flow Jo (Version 10.0) software [12].

3.1.25. Quantification of Nuclear DNA in Different Phases of Cell Cycle: HCT 116 cells were pretreated with FA-Fe_2O_3 (0.1 µg/ml) followed by blue light exposure of differential time duration (5, 10, and 15 min). After the treatment, the harvested cells were fixed overnight in 70% ethanol at 4°C followed by centrifugation, resuspension in phosphate buffer saline (PBS) containing 25 µg/ml RNase and incubation for 1 hr. at 37°C. Cells were then stained with propidium iodide (PI) (50 µg/ml) for 15 min. at 4°C. The stained nuclear DNA was analyzed using a flow cytometer (BD LSRFortessa™, San Jose, CA, USA) [12].

3.1.26. Assessment of Nuclear DNA Damage Using Single Cell Gel Electrophoresis Assay: The oxidative DNA damage was assessed by performing a

comet assay. Treated cells were mixed with 100 ml of 0.5% low melting agar (LMA) at 39°C and then spread on a fully frosted microscopic slide pre-coated with 200 ml of 1% LMA. After agarose solidification, the slide was covered with 75 ml of 0.5% LMA and immersed in lysis solution (2.5 M NaCl, 100 mM Na-EDTA, 10 mM Tris, 1% TrionX-100 and 10% DMSO, pH 10) for 1 hr. at 4°C. The slides were placed in gel-electrophoresis apparatus containing 300 mM NaOH and 10 mM Na-EDTA (pH 13) for 40 min. to allow DNA unwinding and the expression of alkali labile damage. An electrical field was applied (300 mA, 25 V) for 20 min. at 4°C to draw negatively charged DNA towards an anode. After electrophoresis, the slides were washed three times for 5 min. at 4°C in a neutralizing buffer (0.4 M Tris pH 7.5) and then stained with a 75 ml ethidium bromide (EtBr) solution (20 mg/ml). The slides were photographed using a fluorescence microscope and the images were analyzed by Comet Score software (v1.5) [10].

3.1.27. Analysis of Protein Expression by Flow Cytometry: Briefly, the treated cells were fixed with 4% paraformaldehyde in PBS (pH 7.4) for 20 min. at room temperature. Then the cells were permeabilized with 0.1% Triton X-100 in PBS along with 0.1% FBS for 5 min. The permeabilized cells were incubated with primary antibody (p-p53^{Ser46}, Bax, Bcl2, and Cytochrome c) for 2 hr. at 4°C. The cells were then incubated with FITC-conjugated goat anti-rabbit IgG as a secondary antibody for 30 min. at room temperature and washed in PBS before performing flow cytometry. The mean fluorescence intensities (MFI) were calculated using Flow Jo (Version 10.0) software [13].

3.1.28. Measurement of Caspase 3 and Caspase 9 Activity: Caspase 3/9 activities were quantified according to the manufacture's instruction with commercially available caspase 3 and caspase 9 colorimetric assay kits (BioVision Research Products, Mountain View, CA) respectively. Caspase activities were determined at 405 nm by ELISA reader [14].

3.1.29. Determination of Nuclear Condensation and Fragmentation Using Fluorescence Microscopy: To detect nuclear damage or chromatin condensation, control cells with or without treatment of FA-Fe_2O_3 (0.1 µg/ml) along with light exposure (15 min) were stained with acridine orange (50 µg/ml) and EtBr (50 µg/ml) for 10 min. The images were acquired with an inverted phase-contrast microscope (OLYMPUS IX 70, Olympus Optical Co. Ltd., Sibuya-ku, Tokyo, Japan) and the photographs were analyzed using ImageJ software. The emission was collected at 525 nm and 605 nm upon excitation at 488 nm [15].

3.1.30. *In Vitro* Cellular MR Imaging Studies of FA-Fe_2O_3: For cellular MR imaging ~6×10^3 numbers of HEK 293 and HCT 116 cells were incubated in a 96 well plate. Cells were treated with FA-Fe_2O_3 NH of concentrations 0.01-0.08 ng/ml and kept for 8 hr. Then cells were washed with PBS three times and fixed using paraformaldehyde. To avoid air susceptibility 100 µL of 2% low melting agarose was added to each well. The plate was kept at 4˚C to solidify cell suspensions. MRI was performed keeping the samples under a 3T clinical MRI scanner (Siemens MAGNETOM Verio) using a pre-fabricated sample holder. MR phantom images were obtained by applying a spin-echo multi-section pulse sequence. To determine the transverse relaxation (T2) for the sample, coronal images were taken by variable echo times (TE) of 13.2–212.8 ms with a repetition time (TR) of 1770 ms, and acquisition matrix of 209 mm × 256 mm, the field of view of 208 mm × 230 mm and section thickness of 3 mm. The MRI signal intensity (SI) and visualization of the phantom images were analyzed using the standard software provided by the manufacturer.

3.1.31. Statistical Analysis: The data were presented as mean ± SEM. Statistical significance and differences among the groups were assessed by one-way analysis of variance (ANOVA) using OriginPro 8.0 software (San Diego, CA, USA). $p<0.05$ value was considered as significant.

3.2. Sample Preparation: In this section, the different sample preparation methods have been discussed.

3.2.1. Chemicals Used: The chemicals and spectroscopic probes were procured from the following sources. Analytical-grade chemicals were used for synthesis without further purification. Deionized (DI) water, obtained from Millipore, was used to prepare all aqueous solutions. Different solvents including Methanol, Ethanol, DMSO, and Ethylene Glycol were purchased from Sigma Aldrich. Polyethylene glycol PEG (M_w = 1000) was brought from Fluka. The probes methylene blue (Carlo Erba), methyl orange (Sigma Aldrich), DPPH (Sigma Aldrich), and the dyes protoporphyrin IX (Sigma Aldrich), curcumin (Sigma Aldrich), phthalocyanine (Sigma Aldrich) were used without any further purification. KCl, KBr, and KI were purchased from Sigma Aldrich. L-Cysteine and Folic Acid were purchased from Sigma Aldrich. HCT 116 (Human colorectal carcinoma) cell line and HEK 293 (Human embryonic kidney) cell lines were obtained from NCCS, Pune, India. DMEM, Penicillin/streptomycin/neomycin (PSN) antibiotic, FBS, trypsin, and EDTA were obtained from Gibco-Life Technologies (Grand Island, NY, USA). Tissue culture plastic wares were purchased from NUNC (Roskilde, Denmark) from Fermentas, EU. MTT, DAPI and Acridine orange were procured from SRL, (India), Invitrogen (California), Sigma-Aldrich (U.S), respectively. Antibodies were bought from Santa Cruz Biotechnology, Inc. USA and eBioscience, Inc. San Diego, USA. Millipore water was used as an aqueous solvent.

3.2.2. Synthesis of Fe_2O_3 Nanoparticles (NPs): Fe_2O_3 NPs were prepared following a method described in reference [16]. Typically 203 mg $FeCl_3$ was dissolved in 5 ml ethylene glycol by vigorous stirring. After 30 min. of stirring 15 ml, 0.25M NaOH was added drop-wise to the solution. Then the solution is vigorously mixed for 2 hr. after which the brown-colored precipitation was transferred into a Teflon lined stainless-steel autoclave. The sealed device is kept

at a constant temperature of 150°C for 18 hr. Under the solvothermal conditions, the complete nucleation process takes place.

3.2.3. Synthesis of TiO_2 Microspheres: In a typical synthesis of TiO_2 microspheres, 1mL of titanium isopropoxide was mixed with 15mL of anhydrous acetone and then stirred for 15 min [17, 18]. Then the solution was transferred into a 20 mL Teflon lined stainless-steel autoclave and heated at 180°C for 12 hr. without shaking. The system was then cooled to ambient temperature naturally. The final product was collected and washed with acetone and absolute alcohol several times. Then as-prepared samples were further annealed at 400°C for 5 hr. in the air to improve the crystallinity.

3.2.4. Synthesis of Hg-Curcumin Complex: Hg-Curcumin complex was prepared following our earlier reports [19]. 50 mL 2 mM Curcumin was dissolved in methanol by stirring and heating at 60°C. 2 mM $Hg(NO_3)$. $2H_2O$ was dissolved in 100 mL methanol. This solution was added to the Curcumin. An immediate reddish yellow color precipitation was visible upon addition which confirmed the complexation reaction. The reaction mixture was refluxed for 2 hr. The product was filtered and washed several times to remove the residue reactants.

3.2.5. Synthesis of Cu(II)–Curcumin complex from Hg(II)–Curcumin Complex: The as-prepared Hg-Curcumin complex was taken in methanol and a methanolic 2mM solution of $CuCl_2$:$2H_2O$ was added to the collected supernatant solution and cyclomixed for 2 hr. A fade-brown solution was generated. This solution contains a mixture of Cu-Curcumin and Hg-Curcumin with some free Hg^{2+} ions.

3.2.6. Synthesis of Silver Nanoparticles (NPs): Citrate functionalized Ag-NP was synthesized at ~0°C temperature in an aqueous solution (pH = 6.5) by following the synthesis technique described below [20]. In a typical synthesis process, 1 mL 5 mM aqueous solution of $AgNO_3$ was added to 16 mL 1mM aqueous solution of sodium citrate. The solution was then put under continuous stirring conditions in

an ice-bath at 0°C for 2 hr. 150 mL 5mM aqueous $NaBH_4$ solution was added to that solution dropwise. The color of the solution turned yellow. As-synthesized NP was kept at 0°C temperature until further use.

3.2.7. Synthesis of CuS Nanoparticles (NPs): Cysteine capped CuS (Cys-Cus) NPs were prepared using a simple one-step wet chemical technique [21]. Usually, 0.12 mmol of L-cysteine was dissolved in 50 mL of deionized water, 10 mmol $(CH_3COO)_2Cu$ was dissolved in 50 mL water-ethanol mixture (1:1 v/v). This solution is then added to the above solution dropwise under constant stirring. After complete mixing these two solutions, it is kept under vigorous stirring conditions for the next 30 min. After that, pH is adjusted to 3.0, adding HNO_3 drop by drop in the solution. Then 50 mL 10 mmol Na_2S was added to it. The complete solution was then stirred vigorously using a magnetic stirrer, and the temperature is maintained at 80°C for 2 hr. After that, the NPs were separated by centrifugation and washed several times with deionized water.

3.2.8. Synthesis of ZnO Nanoparticles (NPs): ZnO NPs of size ~5 nm were prepared in the ethanolic medium following the method as described in reference [22]. 20 mL 4mM zinc acetate dihydrate, $(CH_3COO)_2Zn$, $2H_2O$ was heated at 60°C around 30 min. 20 mL 4mM sodium hydroxide solution in ethanol was added with it. The mixture was vigorously stirred for 2 hr. at 60°C. The resulting solution was cooled at room temperature and stored at 4°C until further use. ZnO NPs of size ~30 nm were synthesized by the precipitation method [23]. Firstly, PEG (10% V/V) was taken in a three naked flux. Next, 0.05M zinc acetate and 0.1M Na_2CO_3 were added simultaneously into the PEG solution. The system was stirred vigorously for 2 hr. Then the precipitate was washed with double distilled water, ammonia solution (pH = 9), and ethanol. It was dried at room temperature. The precipitate was calcined in a muffle furnace at 450°C for 3 hr. Finally, ZnO NP of size ~25 - 30 nm was prepared.

3.2.9. Deposition of MoS_2 Thin Film: Commercially available MoS_2 powder was finely ground by mortar and pestle to make a fine powder. The obtained powder was then compressed to form a pellet of one-inch diameter and ~5 mm thickness at a pressure of 2 Mpa in a uni-axial press. The pellet is then sealed in a quartz cylinder in a vacuum. The cylinders containing MoS_2 was then sintered at 800°C for 5 hr. After that, the pallet was mounted on the target holders of the PLD chamber. For MoS_2 deposition, the frequency of PLD was set to 5 Hz and with an annealing time of 5 min.

3.2.10. Deposition of TiO_2 Thin Film: Anatase TiO_2 (99.9%) powders, brought from Sigma Aldrich was ground to make fine powder as mentioned previously, which was compressed to make TiO_2 pellet. The sintering process was also similar to the previous case. However, in the case of TiO_2, the sintering temperature was set to 1000°C. This pallet was then mounted on the target holder of the PLD. TiO_2 was deposited on the top of MoS_2, with a pulse recurrence rate of 10 Hz with the same annealing time. To get a continuous thin film growth, 3600 pulses were used. Moreover, we have also grown TiO_2 using the ALD technique. In this process, TiO_2 was deposited at 250 ^oC using titanium (IV) isopropoxide (TTIP) and H_2O as Ti and O precursors, respectively. To maintain sufficient vapor for the TiO_2 ALD process, the TTIP was heated to 250°C and the water was kept at room temperature. The pressure of the ALD chamber was maintained at 50 kPa, and a steady flow of N_2 carrier gas was set at 50 sccm (standard cubic centimeters per min.) for the ALD process. Here, we have used highly purified Nitrogen gas (99.99%) for both purging purpose and carrier gas for both precursors. The precursor pulse rates for TTIP and H_2O were set at 0.20 second and 0.15 second respectively with the ALD cycles sequence $H_2O/N_2/TTIP/N_2$. A blanket deposition of 2 nm thickness was performed with a growth per cycle of 0.04 Å/second.

3.2.11. Synthesis of Fe_2O_3-PC Nanohybrids (NHs): The NHs were prepared using a mechanical attachment process. 30 mg Fe_2O_3 NPs were taken in a 30 mL DMSO-water mixture. The pH of the system is slightly adjusted to basic by adding two drops of 0.25M NaOH. Then 0.2 mM PC solution was added and mixed at room temperature and shaken for 24 hr. to obtain PC attached Fe_2O_3 NH. The system is then washed several times using Millipore water to remove unattached PC. Finally, synthesized NH was dried in an oven and put in the dark until further use.

3.2.12. Sensitization of TiO_2 Microspheres with PP, Fe(III)PP, Cr(III)PP and Cu(II)PP: A 0.5 mM PP ($C_{34}H_{36}N_4O_5$) solution was prepared in a mixture of DMSO and deionized water (1:1, v/v) under constant stirring for 1 hr. Sensitization of PP with TiO_2 microspheres was done by the addition of TiO_2 microspheres into PP followed by overnight stirring. Next, the NH was filtered out and washed several times with DMSO-water to remove unbound PP. Finally, as synthesized NH was dried in an oven and put in the dark until further use. For the synthesis of Cr(III)PP, Fe(III)PP and Cu(II)PP was carried by addition of 1:1 PP (0.5 mM) and chromium chloride hexahydrate ($CrCl_3.6H_2O$), ferric chloride ($FeCl_3$), copper sulfate pentahydrate ($CuSO_4.5H_2O$) followed by overnight stirring.

3.2.13. Synthesis of Folic Acid Templated Fe_2O_3 (FA-Fe_2O_3): Anhydrous $FeCl_3$ (203 mg) was dissolved in 5 ml ethylene glycol with constant stirring for 30 min. followed by 5 ml of 0.25 M NaOH which was added dropwise, the resultant solution was stirred for 30 min (denoted as solution A). Meanwhile, FA (27.6 mg) was dissolved in 5 ml of Millipore water and pH was adjusted ~7.4 using 0.1 M NaOH solution (denoted as solution B). Then solution B was added to solution A dropwise with constant stirring. The resultant mixture was stirred for 30 min. and the pH was adjusted to ~7.4 using 0.25M NaOH. Then the solution was transferred into a Teflon-lined stainless-steel autoclave. The sealed autoclave was kept at 150°C for 18 hr. throughout the hydrothermal reaction period. After

completion of the reaction, the system was allowed to cool to ambient temperature naturally. The product is separated via the centrifugation process, washed three times with millipore water and ethanol, respectively to remove excess unattached folic acids. The final product was dried on a water bath and kept in a dry place until further use.

3.2.14. Preparation of CuS-ZnO Nanohybrids (NHs): The as-synthesized ZnO NPs were taken in a glass beaker and dispersed in water, and then the dispersed solution was sonicated for 20 min. to obtain a homogeneous ZnO solution in water. Briefly, 3 mmol Cys-CuS was dispersed in 10 mL deionized water by continuous stirring. The pH of the solution was adjusted to slight basic upon dropwise addition of NaOH solution in it. 3 mM ZnO is also dispersed in 10 mL of water in a separate beaker. This solution is added dropwise in the Cys-CuS solution and stirred vigorously for 24 hr. After that, the whole solution was centrifuged to remove the unconjugated NPs. The supernatant was removed and the precipitate was washed several times with distilled water and ethanol. Then the sample was dried in an oven at normal air, after that the dried product was kept in an air-tight container till further use.

3.2.15. Preparation of Halide-attached ZnO and Mn-doped ZnO: 5 mg ZnO NP (size ~30 nm) was taken in 10 mL distilled water. 1mL 0.1M KX (X = Cl, F, I) solution was mixed in the solution at room temperature and magnetically stirred for 12 hr. to obtain chloride attached ZnO NP. It is then dried and dispersed in water for further studies. For Mn-doped ZnO, 5 mM $MnCl_2$ solution was added to the reaction mixture containing zinc acetate following the same procedure of synthesis as 30 nm NP (Section 3.2.8).

References

[1] D. V. O'Conner, D. Philips, Time correlated single photon counting, *Academic Press*, London, UK, 1984.

[2] S. Brunauer, P. H. Emmett, E. Teller, Adsorption of gases in multimolecular layers, *J. Am. Chem. Soc.* 60 (1938) 309.

[3] H. Mandal, S. Shyamal, P. Hajra, B. Samanta, P. Fageria, S. Pande, C. Bhattacharya, Improved photoelectrochemical water oxidation using wurtzite ZnO semiconductors synthesized through simple chemical bath reaction, *Electrochim. Acta* 141 (2014) 294.

[4] N. Serpone, Relative photonic efficiencies and quantum yields in heterogeneous photocatalysis, *J. Photochem. Photobiol. A: Chem.* 104 (1997) 1.

[5] N. Serpone, A. Salinaro, Terminology, relative photonic efficiencies and quantum yields in heterogeneous photocatalysis. Part I: Suggested protocol, *Pure Appl. Chem*. 71 (1999) 303.

[6] M. J. Muñoz-Batista, A. Kubacka, A. B. Hungría, M. Fernández-García, Heterogeneous photocatalysis: Light-matter interaction and chemical effects in quantum efficiency calculations, *J. Catal.* 330 (2015) 154.

[7] S. Cho, J. W. Jang, S. H. Lim, H. J. Kang, S. W. Rhee, J. S. Lee, K. H. Lee, Solution-based fabrication of ZnO/ZnSe heterostructure nanowire arrays for solar energy conversion, *J. Mater. Chem.* 21 (2011) 17816.

[8] D. Bagchi, S. Chaudhuri, S. Sardar, S. Choudhury, N. Polley, P. Lemmens, S. K. Pal, Modulation of stability and functionality of a phyto-antioxidant by weakly interacting metal ions: Curcumin in aqueous solution, *RSC Adv.* 5 (2015) 102516.

[9] M. Price, J. J. Reiners, A. M. Santiago, D. Kessel, Monitoring singlet oxygen and hydroxyl radical formation with fluorescent probes during photodynamic therapy, *Photochem. Photobiol.* 85 (2009) 1177.

[10] I. Vermes, C. Haanen, H. Steffens-Nakken, C. Reutellingsperger, A novel assay for apoptosis flow cytometric detection of phosphatidylserine expression on

early apoptotic cells using fluorescein labelled annexin V, *J. Immun. Method.* 184 (1995) 39.

[11] D. J. Dwyer, M. A. Kohanski, B. Hayete, J. J. Collins, Gyrase inhibitors induce an oxidative damage cellular death pathway in Escherichia coli, *Mol. Syst. Biol.* 3 (2007) 91.

[12] A. Nandy, S. K. Dey, S. Das, R. N. Munda, J. Dinda, K. D. Saha, Gold (I) N-heterocyclic carbene complex inhibits mouse melanoma growth by p53 upregulation, *Mol. Cancer* 13 (2014) 1.

[13] K. Manna, U. Das, D. Das, S. Kesh, A. Khan, A. Chakraborty, S. Dey, Naringin inhibits gamma radiation-induced oxidative DNA damage and inflammation, by modulating p53 and NF-κB signaling pathways in murine splenocytes, *Free Rad. Res.* 49 (2015) 422.

[14] K. Manna, A. Khan, S. Biswas, U. Das, A. Sengupta, D. Mukherjee, A. Chakraborty, S. Dey, Naringin ameliorates radiation-induced hepatic damage through modulation of Nrf2 and NF-κB pathways, *RSC Adv.* 6 (2016) 23058.

[15] J. C. Kern, J. P. Kehrer, Acrolein-induced cell death: A caspase-influenced decision between apoptosis and oncosis/necrosis, *Chem. Biol. Interact.* 139 (2002) 79.

[16] R. Nandi, S. Mishra, T. K. Maji, K. Manna, P. Kar, S. Banerjee, S. Dutta, S. Sharma, P. Lemmens, K. D. Saha, A novel nanohybrid for cancer theranostics: Folate sensitized Fe_2O_3 nanoparticles for colorectal cancer diagnosis and photodynamic therapy, *J. Mater. Chem. B* 5 (2017) 3927.

[17] Z. Q. Li, Y. P. Que, L. E. Mo, W. C. Chen, Y. Ding, Y. M. Ma, L. Jiang, L. H. Hu, S. Y. Dai, One-pot synthesis of mesoporous TiO_2 micropheres and its application for high-efficiency dye-sensitized solar cells, *ACS Appl. Mater. Interfaces* 7 (2015) 10928.

[18] B. Liu, L. M. Liu, X. F. Lang, H. Y. Wang, X. W. Lou, E. S. Aydil, Doping high-surface-area mesoporous TiO_2 microspheres with carbonate for visible light hydrogen production, *Energy Environ. Sci.* 7 (2014) 2592.

[19] D. Bagchi, T. K. Maji, S. Sardar, P. Lemmens, C. Bhattacharya, D. Karmakar, S. K. Pal, Sensitized ZnO nanorod assemblies to detect heavy metal contaminated phytomedicines: Spectroscopic and simulation studies, *Phys. Chem. Chem. Phys.* 19 (2017) 2503.

[20] D. Paramelle, A. Sadovoy, S. Gorelik, P. Free, J. Hobley, D. G. Fernig, A rapid method to estimate the concentration of citrate capped silver nanoparticles from UV-visible light spectra, *Analyst* 139 (2014) 4855.

[21] X. Liu, B. Li, F. Fu, K. Xu, R. Zou, Q. Wang, B. Zhang, Z. Chen, J. Hu, Facile synthesis of biocompatible cysteine-coated CuS nanoparticles with high photothermal conversion efficiency for cancer therapy, *Dalton Trans.* 43 (2014) 11709.

[22] S. Sardar, P. Kar, S. Sarkar, P. Lemmens, S. K. Pal, Interfacial carrier dynamics in PbS-ZnO light harvesting assemblies and their potential implication in photovoltaic/photocatalysis application, *Sol. Energ. Mat. Sol. Cells* 134 (2015) 400.

[23] R. Hong, J. Li, L. Chen, D. Liu, H. Li, Y. Zheng, J. Ding, Synthesis, surface modification and photocatalytic property of ZnO nanoparticles, *Powder Technol.* 189 (2009) 426.

Chapter 4

An Overview of Computational Techniques and Methods

In order to investigate the microscopic properties (including electronic properties, charge transfer mechanism) involved in the hybrid materials, the first principles computational calculation has been employed. These include ground state electronic structure calculation using density functional theory (DFT), excited state optical properties calculation using time dependent density functional theory, transport analysis using non-equilibrium Green's function theorem. In this chapter, we have included a brief discussion on different methods and techniques used in our investigation of the electronic, magnetic, and optical properties of our systems. Depending upon the physical property of the system under study, we have chosen either the ab initio DFT method or the time dependent density functional theory (TDDFT). Non-equilibrium Green's function has been used to calculate the device property of the systems. Although the approach of various methods is different, the main objective of those methods is to solve the many-body Hamiltonian which is the fundamental Hamiltonian describing atoms, molecules, clusters, and bulk systems.

4.1. Density Functional Theory (DFT):

4.1.1. The Many Body Hamiltonian: Materials of different forms are made up of interacting atoms. The properties of matter are a combined result of different interactions between atoms. So, the microscopic properties of the matter are a complex problem. However, the regular periodicity of the atom leads to simplification to investigate the properties of the materials. According to quantum mechanical theory, the microscopic behavior of a collection of the interacting atom can be represented by an ensemble of electrons and nuclei, the fundamental

element of an atom, interacting through electrostatic (Coulombic) forces. In principle, the energy may be computed by the solution of the Schrödinger equation which, in the time-independent, nonrelativistic, Born-Oppenheimer approximation is:

$$\boldsymbol{H}\psi\,(R,r) = E\psi\,(R,r) \tag{4.1}$$

The exact Hamiltonian for many body systems can be written in a generalized form as:

$$H = -\sum_{I=1}^{P}\frac{\hbar^2}{2M_1}\nabla_I^2 - \sum_{i=1}^{N}\frac{\hbar^2}{2m_i}\nabla_i^2 + \frac{e^2}{2}\sum_{I=1}^{P}\sum_{J\neq 1}^{P}\frac{Z_I Z_J}{|\boldsymbol{R_I}-\boldsymbol{R_I}|} + \frac{e^2}{2}\sum_{i=1}^{N}\sum_{j\neq 1}^{N}\frac{1}{|\boldsymbol{r_i}-\boldsymbol{r_j}|} - \frac{e^2}{2}\sum_{I=1}^{P}\sum_{i=1}^{N}\frac{Z_I}{|\boldsymbol{R_I}-\boldsymbol{r_j}|} \tag{4.2}$$

where $\mathbf{R} = \{\mathbf{R}_I\}$, I = 1, …P, are the set of P nuclear coordinate and $\mathbf{r} = \{\mathbf{r}_i\}$, i = 1,….N, are the set of N electronic coordinates. Z_I and M_I are the P nuclear charges and masses respectively. m_i is the N electronic masses each of charge e. The first two terms in the right-hand side of the equation describe the kinetic energies of the nuclei and electron respectively. The last three terms denote the Coulomb interaction between nucleus-nucleus, different electrons, and nucleus-electron respectively. Despite its simplicity, the exact solution of Schrödinger's equation is very challenging as it contains a coupled electron-electron Coulomb interaction term. In practice, to solve Schrödinger's equation either in the analytical method or numerical method requires a 3N + 3P number of degrees of freedom which makes the equation very difficult to solve beyond the hydrogen atom.

One of the crucial works of computational material science is to solve the many body Hamiltonian equations with sufficient accuracy and provide a reliable result that can explain the diverse physical property of the broad range of materials. Thus usually one resorts to some sensible approximations. In this

matter, there are two most commonly known approximations are a) Born-Oppenheimer approximation and b) Classical Nuclei approximation.

4.1.2. The Born-Oppenheimer Approximation: The Born-Oppenheimer approximation [1] is the first successful approximation method attempted to solve the many body Hamiltonian problems. The simplest approximation one can make is to neglect the kinetic energy of the nuclei. The nuclear mass is much higher than the electronic mass (~1837 times), which implies that the velocity of the nucleus is negligible to that of the electron. Thus one can assume the nuclei to be stationary to electrons which move around it. This allows us to decouple the electron and nuclear degrees of freedom. Thus a possibility of factorizing the full wave functions hence solving the nuclear part and electronic part independently arises. So, the many body Hamiltonian can be written as:

$$\Psi(\boldsymbol{R}, \boldsymbol{r}, t) = \theta_m(\boldsymbol{R}, t)\varphi(\boldsymbol{R}, \boldsymbol{r}) \tag{4.3}$$

$$\boldsymbol{H} = \boldsymbol{H}_{electron} + \boldsymbol{H}_{nuclei} \tag{4.4}$$

$$= [\boldsymbol{T}_e + \boldsymbol{V}_{ee} + \boldsymbol{V}_{ne}] + [\boldsymbol{T}_{nn} + \boldsymbol{V}_{nn}] \tag{4.5}$$

where $\mathbf{T}_{nn}$ and $\mathbf{V}_{nn}$ are the nuclear kinetic and potential operator respectively, $\mathbf{T}_e$ and $\mathbf{V}_{ee}$ are the same for the electronic case, and $\mathbf{V}_{ne}$ is the potential energy operator for the electronic and nuclear interaction. As the nuclei are assumed to be fixed, the $\mathbf{T}_{nn}$ term can be ignored, while the $\mathbf{V}_{nn}$ term can be assumed to be constant, this constant nuclear potential energy is called Madelung energy and can be calculated classically.

Thus, by solving the electronic part of the Schrödinger equation it is possible to obtain electron energy $E_{electron}$ and electron wavefunction $\Psi_{electron}$ which explicitly depends on the electron coordinates. Thus, the total energy of the system can be written as the sum of electron energy and constant nuclear energy:

$$E_{total} = E_{electron} + E_{nuclei} \tag{4.6}$$

4.1.3. The Independent Electron Approximation: Now the primary problem in the structure of matter is reduced to solve the Schrödinger equation for a system of N interacting electrons in the Coulombic field generated by a collection of atomic nuclei. Even after the simplification of the Born-Oppenheimer equation, the solution of Eq. (4.3) remains difficult as it still corresponds to too many body eigenvalue problems. It is possible to get an exact solution only in the case of uniform electron gas or an atom with a small electron number.

In the independent electron approximation approach, the electron-electron interaction in the system is not considered, this approximation allows us to map the problem of many interacting electron systems onto a system of a non-interacting electron moving in an effective potential due to all other electrons. However, to achieve this mapping one can follow two different formulations (a) the wave function based approaches of Hartree [2], Hartree-Fock [3] formalism, and (b) the DFT-based approaches [4, 5]. Though the wave function-based approach is computationally heavy, and it is difficult to solve using the wave function approach for the bigger system. On the other hand, DFT is relatively simpler and computationally controllable compared to the wave function-based approach. In DFT, the many-electron wave-function is completely bypassed in favor of the electron density. This is the reason why DFT becomes the most important conceptual and practical advance in solving many-electron problems in physics and chemistry. The following discussions attempt to explain both the conceptual structure and some of the formalism of DFT.

4.1.4. Density Functional Theory (DFT): The term density functional theory refers to all methods that express the ground-state energy as a function of the electronic density $\rho(r)$. The DFT is presently the most successful (and also the most promising) approach to compute the electronic structure of matter. Its applicability ranges from atoms, molecules, and solids to nuclei and quantum and classical fluids. The idea of density functional theory can be attributed to the

Thomas-Fermi theory of electron density concept [6, 7], where the fundamental idea was to replace the many-body wave function Ψ(**r**) with the electron density ρ(**r**). In this way, a function of the 3N variable, where N is the number of electrons, can be reduced to a lower dimension. According to that model, the electron density can be written as:

$$\rho(\boldsymbol{r}) = N \int \psi(r_1, r_2, \dots, r_N)\psi^*(r_1, r_2, \dots, r_N) dr_1 dr_2 \dots dr_N \tag{4.7}$$

The Thomas-Fermi model, however, was too crude, because the approximation used for the kinetic energy of the electrons as well as errors in the exchange energy was unable to sustain bound states. Nevertheless, it had shown the pathway for the development of DFT by Hohenberg and Kohn in [6] to deal with many-electron problems more efficiently. In 1964, Hohenberg and Kohn put forth two crucial theorems [4] that provided a practical approach for reducing the many-electron problems to an effective one-electron problem. These two theorems are considered as the backbone for electronic structure calculations in condensed matter physics.

The primary advantages of taking electronic density as the basic variable are: (i) it is a function of 3 variables, unlike the wave-function which is a function of 3N variables and is simpler to tabulate and plot, (ii) it is a function in 3D space in which we live, and it provides better visualization, (iii) it is an experimental variable. In the next section, we discuss the mathematical formulation of the density of states briefly.

4.1.5. The Hohenberg- Kohn Theorem:

Theorem 1

*The electron density ρ(**r**) determines the external potential (to within an additive constant).*

Corollary 1

Electron density ρ(**r**) uniquely determines the Hamiltonian operator which can be obtained by solving the full many-body Schrödinger's equation.

Theorem 2

For any positive definite trial density ρ_t*, such that* $\int \rho_t(\boldsymbol{r})d\boldsymbol{r} = N$ *then* $(\rho_t) \geq E_0$.

Corollary 2

The functional E[ρ] alone is sufficient to determine the exact ground state energy and density. In general excited states of the electrons must be determined by other processes.

Proof of the Theorem 1:

Let the ground state of two N-electron systems characterized by two different external potentials (differing by more than an additive constant) $v_1(\mathbf{r})$ and $v_2(\mathbf{r})$. Let us further assume that, the corresponding two wave functions ψ_1 and ψ_2 yields the same ground-state electron charge density $\rho_0(\mathbf{r})$. Thus the corresponding Hamiltonians and Schrödinger's equation for the two N-electron systems is given by:

$$\begin{aligned} H_1\psi_1 &= E_1\psi_1 \\ H_2\psi_2 &= E_2\psi_2 \end{aligned} \tag{4.8}$$

One may use the variational principle and write the energy expression as:

$$E_1 = \langle\psi_1|H_1|\psi_1\rangle < \langle\psi_2|H_2|\psi_2\rangle \tag{4.9}$$

$$= \langle\psi_2|H_2|\psi_2\rangle + \langle\psi_2|H_1 - H_2|\psi_2\rangle \tag{4.10}$$

$$< E_2 + \int dr\rho(\boldsymbol{r})\,[v_1(\boldsymbol{r}) - v_2(\boldsymbol{r})] \tag{4.11}$$

On interchanging the suffices, we can write:

$$E_2 < E_1 + \int dr\rho(\boldsymbol{r})\,[v_2(\boldsymbol{r}) - v_1(\boldsymbol{r})] \tag{4.12}$$

Summation of the two inequality leads to a contradiction:

$$E_1 + E_2 < E_2 + E_1 \tag{4.13}$$

Thus, the theorem has been proven by *reductio ad absurdum*. Thus one may conclude that the assumption of identical density arising from two different external potentials is wrong. Hence a given ρ(**r**) corresponds to only one v(**r**), and since v(**r**) is fixed, the Hamiltonian and hence the ground state expectation value of any observable is unique functional of the ground state electron charge density.

Proof of the Theorem 2:

The proof of this theorem is very much straightforward. Let us consider, the many-body Hamiltonian $\mathbf{H} = \mathbf{T} + \mathbf{V} + \mathbf{V_{ext}}$ where **T** is the kinetic energy, **V** is the electron-electron interaction and $\mathbf{V_{ext}}$ is the external potential. For a given electron charge density ρ(**r**) total energy can be expressed as:

$$E(\rho) = \langle\psi[\rho]|H|\psi[\rho]\rangle \tag{4.14}$$

$$= \langle\psi[\rho]|T + V|\psi[\rho]\rangle + \langle\psi[\rho]|V_{ext}|\psi[\rho]\rangle \tag{4.15}$$

$$= F(\rho) + \int \rho(r)V_{ext}(\boldsymbol{r})d\boldsymbol{r} \tag{4.16}$$

Now using Rayleigh-Ritz variational principle to electron charge density we can obtain that:

$$F(\rho) + \int \rho(r)V_{ext}(\boldsymbol{r})d\boldsymbol{r} = E[\rho(\boldsymbol{r})] \geq E_0[\rho_0(\boldsymbol{r})] = \langle\psi|H|\psi\rangle \tag{4.17}$$

This implies a remarkable fact that the ground state properties of an interacting N electron system can be completely determined by the electron charge density ρ(**r**). So, the problem is reduced to find ρ(**r**) which minimizes the energy functional E[ρ(**r**)].

Now, to determine E[ρ(**r**)] one need to know the exact analytical form of F(ρ) which contains all the many-body effect. The kinetic and electron-electron functionals are unknown. If good approximations to these functionals could be found direct minimization of the energy would be possible. It was Kohn and Sham who specifically proposed a new approximation which can solve this shortcoming.

4.1.6. The Kohn-Sham Equation and Formulation of Modern DFT: The equations of Kohn and Sham, published in 1965, turn DFT into a practical tool [5]. The weakest part of the Thomas-Fermi theory [8] was the treatment of kinetic energy functionals, which was taken care of by Kohn-Sahm equations based on the Hohenberg-Kohn theorem. This equation provided an approximation of kinetic energy functional T(ρ) for the interacting electron system in terms of a non-interacting electron system having the same ground-state charge density ρ(**r**).

The total energy functional for the N interacting electron system can be written as, in terms of density has thus the generalized form:

$$E[\rho(\boldsymbol{r})] = F(\rho) + \int \rho(r) V_{ext}(\boldsymbol{r}) d\boldsymbol{r} \tag{4.18}$$

where F[ρ] is a universal function of density. Kohn-Shan separated this function into three different terms:

$$F(\rho) = T(\rho) + V_H(\rho) + E_{xc}^{total}[\rho] \tag{4.19}$$

where T(ρ) is the kinetic energy of the interacting electron, $V_H(\rho)$ is the electrostatic Coulomb energy of electrons and $E_{xc}^{total}[\rho]$ contains all the exchange and correlation effects. Within the Kohn-Sham formulation, the exact kinetic energy is replaced by the kinetic energy of a system of non-interacting particles having the same charge density with a new effective exchange-correlation term which is in general called the exchange-correlation (XC) energy functional $E_{XC}[\rho]$

$$E_{xc}(\rho) = E_{XC}^{total}[\rho] + T[\rho] - T_s[\rho] \tag{4.20}$$

where $T_s[\rho]$ represents the kinetic energy of non-interacting electrons. This approximation allows us to map many interacting electron systems onto an exactly equivalent system of non-interacting electrons living under an effective potential contributed by all other electrons and having the same ground-state charge density $\rho(\mathbf{r})$. The schematic representation of the situation is depicted in Figure 4.1. Thus the interacting many-electron problem is reduced to solving a set of self-consistent non-interacting one-electron equations known as Kohn-Sham equations.

For a system of N non-interacting electrons, the ground state charge density can be represented as a sum over one-electron orbitals φ_i as follows:

$$\rho(r) = \sum |\varphi_i|^2 \tag{4.21}$$

and henceforth the total energy functional for this non-interacting system may be evaluated as:

$$E_{KS}[\rho] = T_s[\rho(\boldsymbol{r})] + \int \boldsymbol{V}_{ext}(\boldsymbol{r})\rho(\boldsymbol{r})d\boldsymbol{r} + \frac{1}{2}\frac{e^2}{4\pi\epsilon_o}\iint \frac{\rho(\boldsymbol{r})\rho(\boldsymbol{r}')}{|\boldsymbol{r}-\boldsymbol{r}'|}d\boldsymbol{r}d\boldsymbol{r}' + E_{xc}\,[\rho(\boldsymbol{r})] \tag{4.22}$$

and the corresponding Hamiltonian is given by:

$$\boldsymbol{H}_{KS} = -\frac{\hbar^2}{2m}\boldsymbol{\nabla}^2 + V_{eff}(\boldsymbol{r}) \tag{4.23}$$

where,

$$\begin{aligned} V_{eff}(\boldsymbol{r}) &= V_{ext}(\boldsymbol{r}) + \frac{1}{2}\frac{E^2}{4\pi\epsilon_0}\int \frac{\rho(\boldsymbol{r}')}{|r-\boldsymbol{r}'|}dr' + \frac{\delta E_{xc}}{\delta\rho(\boldsymbol{r})} \\ &= V_{ext}(\boldsymbol{r}) + V_{Hartree}(\boldsymbol{r}) + V_{xc}(\boldsymbol{r}) \end{aligned} \tag{4.24}$$

Thus using Eq. (4.21), (4.22), (4.23), and (4.24) one can find the one-electron orbitals φ_i which minimize the energy and satisfy the following set of one-electron Schrödinger-like equations:

$$\left[-\frac{\hbar^2}{2m}\boldsymbol{\nabla}^2 + V_{eff}(\boldsymbol{r},\boldsymbol{\rho})\right]\varphi(\boldsymbol{r}) = \epsilon_i\varphi_i \tag{4.25}$$

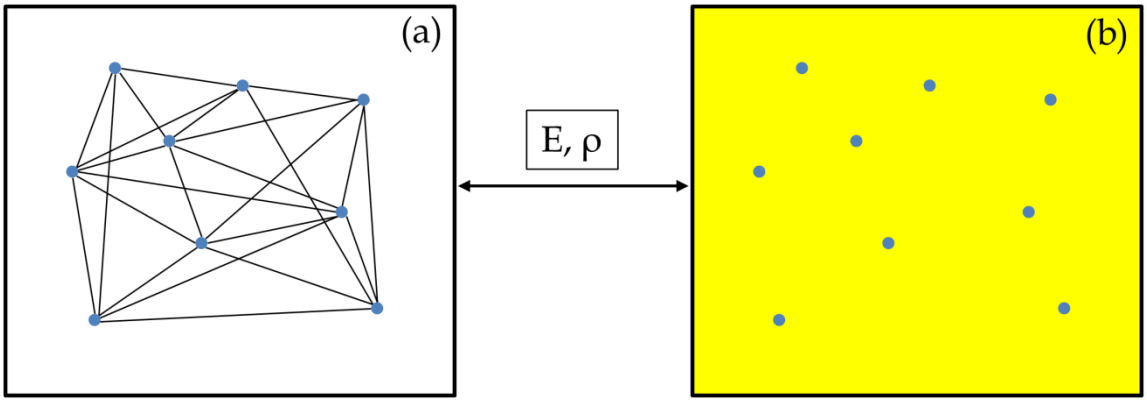

Figure 4.1: *Schematic Representation of a) interacting electrons, b) non-interacting electrons in a potential field as implemented in DFT formalism.*

From Eq. (4.25) it should be noted that the above set of one-electron equations can be solved if the effective potential V_{eff} is known. However, to know V_{eff} we have to know the charge density ρ(**r**). Now, ρ(**r**) depends on Kohn-Sham orbitals φ_i, which again depends on V_{ext} (**r**). So, the Kohn-Sham equations can't be solved straightforwardly. Thus the Kohn-Sham equations need to be solved self-consistently by applying iterative methods as follows-

1. Start with an initial guess for the charge density ρ(**r**).
2. Calculate the corresponding V_{eff} (**r**,ρ) and solve the Eq. (4.24) with appropriate boundary conditions to obtain the total energy ε_i and the one-electron orbitals φ_i.
3. From the φ_i, calculate the new charge density and repeat the iterative process until convergence is reached. The convergence is self-consistently achieved when the output charge density differs from the input charge density by a pre-assigned small value.

A flowchart summarizing the above steps is given in Figure 4.2.

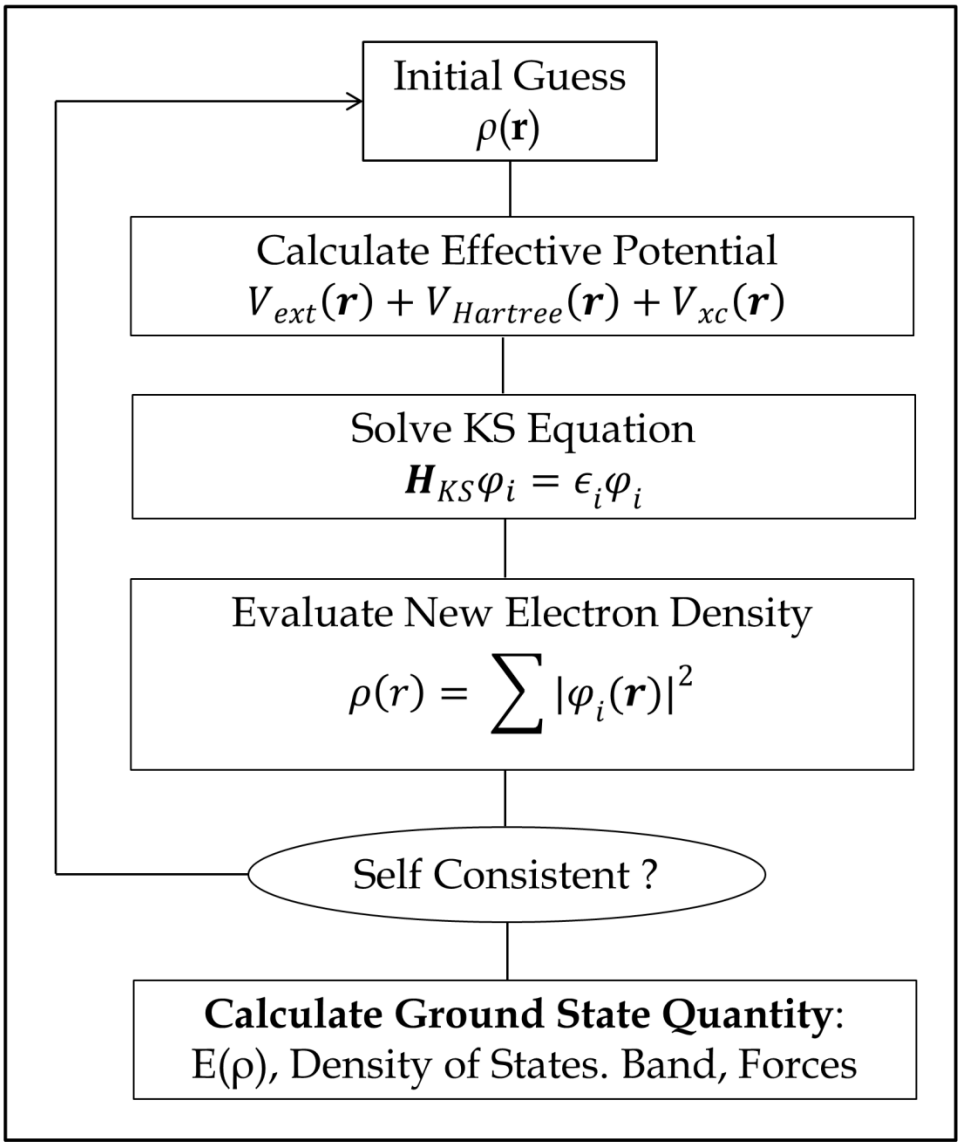

Figure 4.2: *Flowchart illustrating the iterative procedure to solve the Kohn-sham equations.*

4.1.7. Exchange Correlation Functional: Although DFT is accurate in principle, the main drawback of the Kohn-Sham formulation comes due to its inexplicit exchange-correlation term. The exact expression of the E_{XC} is complex and unknown. So, to solve the equation one needs to choose a good approximation of the exchange-correlation function.

In practice, the utility of the theory lies in the approximations used for E_{XC}. Even though the exact formulation of E_{XC} is very complex, great progress has been

made with a remarkably simple approximation to encounter the problem. Of the various approximation formulas, the local density approximation (LDA) and generalized gradient approximation (GGA) are the most commonly used approximation methods. The different approximate functionals for exchange-correlation are discussed next section.

4.1.7.1. Local Density Approximation (LDA): Local Density Approximation is one of the earliest and most widely used approximations for the exchange-correlation energy. The primary idea of the LDA approximation relies on the assumption that the exchange-correlation is a functional that depends only on the local value of the electron charge density. It was first introduced by Kohn and Sham in 1965, but the basic idea existed in the theory by Thomas-Fermi-Dirac. Under the LDA approximation, it is assumed that the charge density varies very slowly at any point **r** in space, so that the electron gas in a small volume element $d^3\mathbf{r}$ could be considered locally uniform.

LDA postulates that the exchange-correlation functional has the following form:

$$E_{XC}[\rho(r)] = \int \epsilon_{XC}^{LDA}[\rho(\boldsymbol{r})]\rho(\boldsymbol{r})d\boldsymbol{r} \tag{4.26}$$

Under the LDA formalism, an obvious choice is to take ϵ_{XC}^{LDA} to be the exchange and correlation energy density of the homogeneous electron gas of density ρ(**r**). This term can be further written as a sum of the exchange and correlation contributions:

$$\epsilon_{XC}^{LDA}[\rho(\boldsymbol{r})] = \epsilon_{X}^{LDA}[\rho(\boldsymbol{r})] + \epsilon_{C}^{LDA}[\rho(\boldsymbol{r})] \tag{4.27}$$

for any homogeneous electron gas, the exchange energy $\epsilon_{X}^{LDA}[\rho(\boldsymbol{r})]$ part can be formulated by the Dirac equation:

$$\epsilon_X^{LDA}[\rho(\boldsymbol{r})] = -\frac{3}{4}\left(\frac{3}{\pi}\right)^{\frac{1}{3}}\rho^{\frac{1}{3}} = -\frac{3}{4}\left(\frac{9}{4\pi^2}\right)^{\frac{1}{3}}\frac{1}{r_s} = -\frac{0.058}{r_s} \tag{4.28}$$

where $r_s = (3/4\pi\rho)^{1/3}$ is the mean inter-electron distance.

On the other hand, the functional form of correlation energy density $\epsilon_C^{LDA}[\rho(\boldsymbol{r})]$ is unknown and in 1980, Ceperley and Adler [9] provided an accurate estimate of $\epsilon_C^{LDA}[\rho(\boldsymbol{r})]$ for the homogeneous electron gas by numerical quantum Monte-Carlo simulations which yield essentially exact results with numerical accuracy. The resultant XC functional was later on parameterized by Perdew and Zunger [10], Perdew and Wang [11], etc. and are now known as LDA functionals.

The LDA approximation is expected to work well for systems in which the electronic charge density is varying slowly, but surprisingly it yields good results even in the case where the density is not slowly varying, for which this approximation hardly looks appropriate [12]. This can be attributed to two facts. First, the LDA underestimates the exchange energy and overestimates the correlation energy which leads to the cancellation of errors. Secondly, the electron-electron interaction is dependent only on the spherical average of the exchange-correlation hole and not on its detailed shape.

However, while the LDA approximation provides reasonable results for metallic systems, but for the semiconductor system, the bandgap is underestimated by a factor of 1/2 to 2/3 factors. The properties of insulators, particularly Mott insulators, are not described well using this formalism. Moreover, it cannot accurately predict activation energy barriers and is known to overestimate the binding energies. Intense efforts are going on to resolve the backlogs of this theory. We shall briefly describe the next step towards the improvement of LDA XC.

4.1.7.2. Generalized Gradient Approximation (GGA): We have seen that the LDA was derived by assuming that the electron density varies very slowly in space. Thus, it was argued that LDA could be improved if we expanded the exchange-correlation functional in terms of the gradient of the density in the Taylor series and truncated it to some order. Such an approximation is known as generalized gradient expansion approximation and was implemented by Herman *et al.* (1969) [13]. While GGA retains the core features of LDA, it also takes into account the spatial variations in the charge density which are important. The exchange-correlation energy within the GGA approximation can be written as:

$$\begin{aligned} E_{XC}^{GGA} &= \int \epsilon_{XC}[\rho(\boldsymbol{r}), |\nabla\rho(\boldsymbol{r})|]\rho(\boldsymbol{r})d\boldsymbol{r} \\ &= \int \epsilon_{XC}[\rho(\boldsymbol{r})]F_{XC}[\rho(\boldsymbol{r}), \nabla\rho(\boldsymbol{r})]\rho(\boldsymbol{r})d\boldsymbol{r} \end{aligned} \tag{4.29}$$

where the functional F_{XC} is called an enhancement factor. Depending on the choice of the functional form of enhancement factor F_{xc}, there are many forms of GGAs available which are being used over the years. One that has been widely used is by Perdew and Wang, known as PW86 and PW91 [14, 15]. Later on, Perdew *et al.* (1996) proposed another functional (PBE) [16], which retains important features of PW91. In the present thesis, we have mostly used GGA-PBE exchange-correlation functional, which is briefly described below.

In the case of PBE exchange-correlation functional, first, the enhancement factor F_{XC} over the local exchange is defined as:

$$E_{XC}^{PBE} = \int \epsilon_X^{LDA}[\rho(\boldsymbol{r})]F_{XC}(\rho, \zeta, s)\rho(\boldsymbol{r})d\boldsymbol{r} \tag{4.30}$$

where ρ is the local density, ζ is the relative spin-polarization and $s = \frac{\nabla\rho(r)}{2k_F\rho}$ is the dimensionless density gradient.

$$F_{XC}(s) = 1 + \mathrm{K} - \frac{\mathrm{K}}{1 + \mu s^2/\mathrm{K}} \tag{4.31}$$

where K and μ are empirically fitted to a database of ionization energies.

The correlation contribution to the energy is written as:

$$E_C^{PBE} = \int [\epsilon_c^{LDA}(\rho, \zeta) + H(\rho, \zeta, t)]\rho(\boldsymbol{r})d\boldsymbol{r} \tag{4.32}$$

with,

$$H(\rho, \zeta, t) = (\frac{e^2}{a_o})\gamma\phi^2 ln\{1 + \frac{\beta\gamma^2}{t}\left[\frac{1 + At^2}{1 + At^2 + At^4}\right]\} \tag{4.33}$$

in this equation $t = \frac{|\nabla\rho(\boldsymbol{r})|}{2\phi k_s \rho}$ is the dimensionless density gradient and $k_s = (\frac{4k_F}{\pi a_o})$ is the Thomas Fermi Screening wave number, and, $\phi(\zeta) = \frac{[(1+\zeta)^{2/3}+(1-\zeta)^{2/3}]}{2}$ is a spin scaling factor.

Function A has the form:

$$A = \frac{\beta}{\gamma}[\frac{exp(-\epsilon_C^{LDA}[\rho])}{\gamma\phi^3(e^2/a_o)} - 1]^{-1} \tag{4.34}$$

This GGA retains the correct features of LDA and combines them with the inhomogeneity features that are energetically most important. Although the GGA method works much precisely over LDA in terms of predicting the binding energies, electronic and magnetic properties of the materials, it does have a few drawbacks. The GGA approximation cannot describe the van der Waals (vdW) interaction. It is also known to overestimate the electric polarization for polar materials [17]. Finally, both GGA and LDA fail for strong electron-electron correlated systems and present research is continuing in search of a better functional.

4.1.7.3. LDA + U or GGA + U Method: It has been seen that LDA and GGA fail to give the correct ground state of strongly correlated systems such as transition metal oxides. LDA + U or GGA + U methods have been designed to correct this situation by constructing an orbital-dependent functional. The idea was taken from the Hubbard model [18, 19]. Suppose we have an orbital that already has one electron. If we put another electron in it, it will cost an energy U because of the electron-electron repulsion in that orbital. This idea when incorporated in LDA or GGA produces the LDA + U method. In the LDA + U or GGA + U method, strong

on-site Coulomb repulsion (generally term as U) is directly added to strongly localized orbitals such as *d* and *f* orbitals along with the LDA or GGA functional. The magnitude of the added interaction is determined by the parameter U.

Let us consider a system with a fluctuating number of *d* (or *f*) electrons, but the total number of electron $N = \sum_i n_i$ is constant. Within the LDA + U method total energy can be written as:

$$E = E^{LDA} + \frac{1}{2}U\sum_{i\neq j} n_i\, n_j - U\frac{N(N-1)}{2} \tag{4.35}$$

This orbital-dependent functional gives upper and lower Hubbard band separation equal to U and thus correctly describes the physics of Mott insulators. For example, it correctly gives the antiferromagnetic insulating ground states for many transition metal oxides and cuprate superconductors, which turn out to be metallic using LDA or GGA. However, the main problem of the LDA + U method is the choice of the value of U. Although U can be found ab initio by using the constrained DFT approach, it is overestimated by this method. Thus, the common way of finding U is to treat it as an adjustable parameter so that one finds good agreement between some calculated and experimental results.

4.1.7.4. Van der Waals (vdW) Corrections: Although the results of Kohn-Sham equations are very much robust i.e. it provides reasonably correct predictions for many properties of various systems [20]. However, the main disadvantage of all common GGA functionals, including hybrids, that they are not able to describe long-range electron correlations precisely that are responsible for vdW forces [21, 22]. The vdW interactions between atoms and molecules play a crucial role in many systems in which they maintain a balance with electrostatic and exchange-repulsion interactions. As a result of it, they control many important fundamental properties including the packing of crystals, the structures of DNA and proteins,

the orientation of molecules on surfaces or in molecular films, etc. So, it is very important to incorporate the vdW corrections in the DFT calculations.

Total exchange-correlation energy E_{xc} of a system including vdW correction can be written as:

$$E_{xc} = E_X^{GGA/LDA} + E_C^{GGA/LDA} + E_C^{NL} \tag{4.36}$$

where standard exchange and correlation components of LDA or GGA. Moreover, E_C^{NL} represents the nonlocal term describing the dispersion energy. Typically, E_C^{NL} is computed non-self-consistently i.e. it is simply an add-on to the self-consistent field (SCF). Even though this new add-on has very little effect on computed energy, it affects the computational forces calculated during geometry optimization.

Grimme finds the empirical dispersion correction term which is written below:

$$E_C^{NL} = -s_6 \sum_{i=1}^{N_{at}-1} \sum_{j=i+1}^{N_{at}} \frac{C_6^{ij}}{R_{ij}^6} f_{dmp}(R_{ij}) \tag{4.37}$$

Here, N_{at} is the number of atoms in the system, C_6^{ij} denotes the dispersion coefficient for atom pair ij, s_6 is a global scaling factor which depends only on the density functional used, and Rij is an interatomic distance.

To avoid near-singularities for small R, a damping function f_{dmp} has been used, which can be written as:

$$f_{dmp}(R_{ij}) = \frac{1}{1 + e^{-d(R_{ij}/R_r - 1)}} \tag{4.38}$$

where R_r is the sum of atomic vdW radii. The DFT-D2 method is implemented in the VASP software [23].

4.1.8. Basis Set: To solve the Kohn-Sham equations, a choice of an appropriate basis set to expand the one-electron Kohn-Sham orbitals is necessary. The choice of basis set is dependent on the attributes of the system under study. Over the years, various basis set methods have been developed for the prediction of the electronic properties of solids with reasonable accuracy. Depending on the choice of basis sets, different methods can be broadly classified into two categories:

4.1.8.1. Fixed Basis Set Methods: In this approach, the Kohn-Sham orbitals are expanded in terms of energy independent basis sets or fixed basis sets as in the tight-binding model using a linear combination of atomic orbitals (LCAO) [24], the orthogonalized plane wave-pseudopotential methods [25, 26], etc. Here one has to solve the following eigenvalue value equation:

$$(H - \epsilon O).C = 0 \tag{4.39}$$

to determine the eigenvalue ε and expansion coefficient C, where O is the overlap matrix. This method is computationally simple but the disadvantage is that the basis depends on the ionic positions, so Pulay corrections have to be added to the Helmann-Feynman forces.

4.1.8.2. Partial Wave Methods: In these methods, the Kohn-Sham orbitals are expanded in a set of energy and potential-dependent all-electron partial wave basis set as in the cellular method, the augmented plane wave method (APW) [27], and the Korrimga-Kohn-Rostoker (KKR) method [28, 29]. Here one has to solve the set of the equation of the following form:

$$M(\epsilon).C = 0 \tag{4.40}$$

This approach is accurate in the band structure calculation but the main shortcomings of this method are due to the complicated non-linear energy dependence of the secular equation, the solution of this kind of equation is computationally very heavy. To overcome this, in 1975 O. K. Andersen first proposed a unified approach considering the positive aspects of a fixed basis set

method and that of partial wave basis by linearization of energy-dependent of partial waves. Linear augmented plane wave (LAPW) [27] and linear muffin-tin orbital (LMTO) [30] methods are the linearized version of the APW and KKR methods respectively.

In this thesis, we have used two types of basis set methods for geometry optimization and electronic structure calculations. These are:

1. Plane-wave basis set pseudopotential method within the projected augmented wave (PAW) scheme.

2. The all-electron linearized augmented plane wave (LAPW) method.

A brief description of those above-mentioned methods is provided below:

4.1.9. Plane Wave Based Pseudopotential Methods:

4.1.9.1. Plane Wave Basis Set: Choice of the plane wave as a basis function to expand the single-particle Kohn-Sham orbitals is one of the common and widely used approaches in many first-principles method calculations due to the following reasons:

• The basis set is independent of the atomic position.

• The Hellmann-Feynman forces acting on the atoms and the stresses on the unit cell can be easily calculated in terms of the expectation value of the Hamiltonian with respect to the ionic coordinates. So no basis set correction to the force is needed.

• With this basis set, it is easy to change from a real-space representation (where the potential energy V has a diagonal representation) to momentum-space (where kinetic energy has diagonal representation) via a Fast Fourier Transform (FFT).

According to Bloch's theorem, the wave function of an electron moving in a potential generated by a periodic lattice can be written as a product of a plane wave $e^{ik.r}$ and a function $u_k(r)$ that has the periodicity of the lattice. Thus we can write:

$$\psi_k(\boldsymbol{r}) = e^{i\boldsymbol{k}.r} u_{\boldsymbol{k}}(\boldsymbol{r}) \tag{4.41}$$

Furthermore, the cell periodic part $u_k(r)$ of the electron wave-function can be expanded using a basis set of plane waves whose wave vectors are the reciprocal lattice vectors of the crystal. So, we can write $u_k(r)$ in the following way:

$$u_{\boldsymbol{k}}(\boldsymbol{r}) = \sum_{\boldsymbol{G}} c_{i,\boldsymbol{G}} e^{i\boldsymbol{G}.r} \tag{4.42}$$

where the reciprocal lattice vectors G are defined by $\mathbf{G}.l = 2\pi m$ for all l where l is a lattice vector and m is an integer. Therefore the full electron wave-function can be written as:

$$\psi_{\boldsymbol{k}}(\boldsymbol{r}) = \sum_{\boldsymbol{G}} c_{i,k+\boldsymbol{G}} e^{i(k+\boldsymbol{G}).r} \tag{4.43}$$

Thus, we can expand the electron wave-function at each **k** as a linear combination of discrete plane waves.

4.1.9.2. Pseudopotential Method: The electronic states of a large number of materials can be separated into two classes, such as, core states, which are localized in space and deep in energy and valence or conduction states which are spread out spatially as well as higher in energy. Since the core electrons are tightly bound to the nucleus and rapidly oscillating due to the orthogonality required within the valence state, a large number of plane waves are required to describe the accurate behavior of the core state's wave functions. This is one of the major problems of the plane wave basis. To overcome the problem, in 1940 C. Herring introduced the orthogonalized plane wave method [31, 32], where he described

core states by Bloch sums built from localized orbitals and valence states by plane waves, orthogonalized to the core states.

The pseudopotential approximation takes advantage of the fact that electrons in the core state do not play a significant role in determining the physical properties of materials such as chemical bonding, electronic structure, etc. Instead, these electrons partially screen the nucleus and thereby form an inert core along with the nucleus. Thus the atom can be represented as an ionic core that interacts with the valence electrons via a strong ionic potential. This allows separation of the core states and valence states, which is exploited in the pseudopotential approach by removing the core electrons and replacing the strong ionic potential with a weaker effective pseudopotential. The valence electrons are then described by a set of pseudo wave functions which are acted on by the effective pseudopotential. The pseudopotential and pseudo wave functions are constructed in such a way that they are identical to the true potential and true wave function, respectively beyond a certain cut-off radius.

The general procedure for obtaining the pseudo-potential is following,

The all-electron (AE) free atom Kohn-Sham radial equation is given by:

$$\left[-\frac{1}{2}\frac{d^2}{dr^2}+\frac{l(l+1)}{2r^2}+V_{eff}^{AE}[\rho^{AE}(\boldsymbol{r})]\right]\boldsymbol{r}R_{nl}^{AE}(\boldsymbol{r})=\in_{nl}^{AE}(\boldsymbol{r})R_{nl}^{AE}(\boldsymbol{r}) \tag{4.44}$$

where R_{nl}^{AE} is the radial part of the all-electron wave-function with angular momentum l. Within the spherical assumption of the Hartree and exchange-correlation potential, the effective potential V_{eff}^{AE} is written as:

$$V_{eff}^{AE}[\rho^{AE}(\boldsymbol{r})]=-\frac{Z}{r}+V_{Hartree}[\rho^{AE}(\boldsymbol{r})]+V_{xc}[\rho^{AE}(\boldsymbol{r})] \tag{4.45}$$

For a given distribution of electrons in the atomic energy levels, the free atom Kohn-Sham radial equation is then solved to obtain the radial wave function R_{nl}^{AE}.

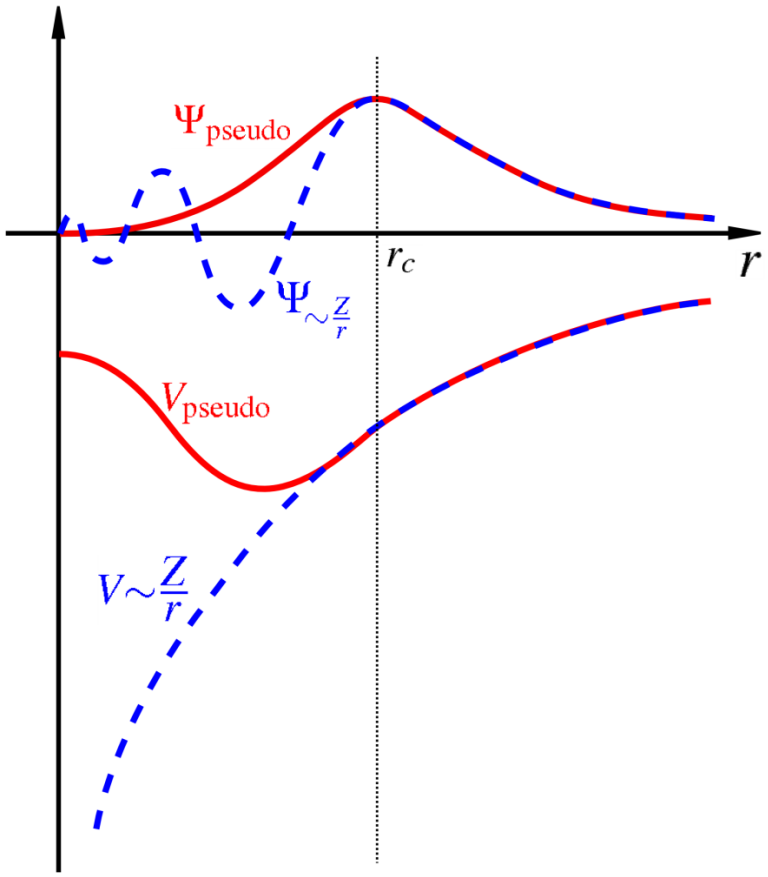

Figure 4.3: *Schematic diagram showing the basic idea of pseudopotential. The figure is taken from web:http://en.wikipedia.org/wiki/Pseudopotential.*

Next, generate a pseudo-wave function R_{nl}^{PS} corresponding to R_{nl}^{AE} imposing the following conditions,

(i) The pseudo wave function should be node-less inside the core region of a certain radius r_c.

(ii) It should coincide exactly with the true all-electrons (AE) wave function beyond a certain cutoff distance i.e. $R_{nl}^{PS} = R_{nl}^{AE}$ for $r \geq r_c$.

Knowing the pseudo-wave-function, the pseudo-potential can be obtained by inverting the radial Kohn-Sham equation for the pseudo-wave-function and the valence electronic density, given by:

$$V_{l,scr}^{PS} = \in_l^{PS} - \frac{l(l+1)}{2\boldsymbol{r}^2} + \frac{1}{2rR_l^{PS}(r)}\frac{d^2}{dr^2}[\boldsymbol{r}R_l^{PS}(\boldsymbol{r})] \tag{4.46}$$

The pseudopotential $V_{l,scr}^{PS}$ thus obtained takes into account the screening effect of the valence electrons. Finally to obtain the pseudopotential one has to subtract the Hartree and XC potential calculated only for the valence electrons. Therefore, considering the screening effect the pseudopotential takes the following form:

$$V_l^{PS} = V_{l,scr}^{PS} - V_{Hartree}[\rho^{PS}(\boldsymbol{r})] - V_{xc}[\rho^{PS}(\boldsymbol{r})] \tag{4.47}$$

The basic idea of pseudopotential is depicted in Figure 4.3. The cut-off radius $\mathbf{r}_c$ where pseudo and true wave-functions coincide is not an adjustable pseudopotential parameter. The outermost nodal surface of the true wave-function gives rise to the estimation of the smallest possible value of cut-off radius r_c and the pseudopotential corresponding this cut-off radius close to the minimum, is very realistic and at the same time very strong. If a very large cut-off radius is chosen, the pseudopotential will be smooth and almost angular momentum independent, and at the same time, it will be unrealistic. A smooth potential leads to fast convergence of plane-wave basis calculations. So choosing an optimal cut-off radius is critical to balance between basis-set size and pseudopotential accuracy.

A major drawback of the plane-wave pseudopotential method is that all information on the true wave-function close to the nuclei is lost which can play an important role in determining certain physical properties such as hyperfine splitting, electric field gradients, etc. Within the pseudopotential method, this problem can be addressed by the use of the projected augmented wave (PAW)

method proposed by P. Blöchl [33]. A different approach is on the all-electron approach of the linearized augmented plane wave method based on the choice of partial wave functions as basis sets. Both methods are discussed in the following sections.

4.1.10. Linearized Augmented Plane Wave (LAPW) Formalism: The LAPW is a method for solving the equations of DFT. It was first formulated by Slater in 1937 [34, 35]. Although pseudopotential methods are extremely useful in solving many problems, however, information inherently nears the nucleus they are not the method of choice. In such cases Augmented Plane Wave (APW) basis set can be more useful. LAPW formalism is a modification of the augmented plane wave (APW) method proposed by Slater. Modern implementations allow for several approximations to exchange and correlation (LDA, GGA, and LDA + U among others) and make no approximations to the shape of the crystal potential, unlike methods employing the atomic sphere approximation (ASA) which assume spherical symmetry around each atom. Like most modern electronic-structure methods, the LAPW method is a variational expansion approach that solves the equations of DFT by approximating solutions as a finite linear combination of basis functions.

Electrons that are far away from the nuclei behave as free particles. They can be described by plane waves. In contrast to regions close to the nuclei, the electrons behave in a localized manner at the nuclei site and therefore are more accurately described by atomic-like functions. In the APW method, this allows one to partition the system space into two parts viz. the ‘muffin-tin" (MT) spheres centered at each atom site and the remaining region called interstitial. The MT approximation was widely used in APW codes to elucidate the properties of transition metals and compounds.

An MT sphere (S_a) is a sphere of radius R_a constructed around each atom. These MT spheres are chosen in such a way that, they do not overlap and fill the space to the maximal extent. The remaining space outside the spheres is called the interstitial region (IS). Within the MT spheres, the potential is approximated to be spherically symmetric while in the interstitial region it is considered to be constant.

The APW basis functions are then defined as:

$$\phi_G^k(r,\epsilon) = f(x) = \begin{cases} \frac{1}{\sqrt{\Omega}} e^{i(k+G).r} & for\ r \in IS \\ \sum_{l,m} A_{lm}^{a,k+G} \varphi_l^a(r,\epsilon) Y_m^l(\theta',\varphi') & for\ r \in S_a \end{cases} \quad (4.48)$$

The position r inside the spheres is given with reference to the center of each sphere. φ_l^a is the solution to the radial Schrödinger equation for an isolated atom to the energy parameter ε. The coefficients $A_{lm}^{a,k+G}$ are determined by the requirement that the wave-functions have to be continuous at the boundary of the MT spheres. Thus by matching the plane waves outside the sphere to the function inside the sphere at the boundary the value of $A_{lm}^{a,k+G}$ can be obtained. In principle, since the expansion of the plane wave term of Eq. (4.48) contains a series of infinite terms, an infinite number of $A_{lm}^{a,k+G}$ can be found such that two functions can be matched. For practical purposes, however, a truncation at some value of l_{max} is required. A reasonably good condition is given by $R_a G_{max} = l_{max}$ where G_{max} provides the cut-off for the plane wave expansion.

Since φ_l^a depends on energy, so does the resultant Hamiltonian matrix H. Thus, solving the secular equation to obtain the energy eigenvalues becomes a nonlinear problem that is computationally more expensive and non-trivial. Linearization of the APW method i.e. LAPW [31] helps to get rid of this problem. The linearized version of the Augmented Plane Wave basis, following Andersen's linearization approach [36, 37], is expressed as:

$$\phi_G^k(r,\epsilon) = \begin{cases} \frac{1}{\sqrt{\Omega}} e^{i(k+G).r} & for\ r \in IS \\ \sum_{l,m} A_{lm}^{a,k+G} \varphi_l^a(r', \in_v) + B_{lm}^{a,k+G} \dot{\varphi}_l^a(r', \in_v) Y_m^l(\theta', \varphi')\ for\ r \in S_a \end{cases} \quad (4.49)$$

where the coefficients $A_{lm}^{a,k+G}$ and $B_{lm}^{a,k+G}$can be determined by matching these solutions in magnitude and slope at the sphere boundary. Although adding local orbitals increases the LAPW basis set size, still their number is quite small compared to the typical LAPW basis the set size of a few hundred functions. The problem with the APW method was the energy dependence of the basis set, which is removed in the LAPW method, however, at the cost of a somewhat larger basis set size.

4.1.11. The Projector Augmented Wave (PAW) Formalism: The projector augmented-wave (PAW) method was developed by Blochl in 1994 [33] as a method to accurately and efficiently calculate the electronic structure. The advantage of this formalism is it contains the numerical advantages of pseudopotential calculations while retaining the physics of all-electron calculations including the correct nodal behavior of the valence-electron wave functions and the ability to include upper core states in addition to valence states in the self-consistent iterations. Later Kresse and Joubert modified this PAW method and implemented it within the plane-wave code of Vienna Ab Initio Simulation Package (VASP) [38, 39]. Within this formalism, the drawback arising due to oscillations of valence-state wave-functions is addressed by transforming the physical wave-functions $\psi_n(\mathbf{r})$ into smooth auxiliary wave-functions $\tilde{\psi}_n(r)$ that can be represented in a plane wave expansion. This is achieved by defining a linear transformation operator $\boldsymbol{T}$ as:

$$T = 1 + \sum_a T^a \quad (4.50)$$

where T^a only acts in the augmentation spheres.

Augmentation spheres are constructs similar to the muffin-tin spheres defined around each atom i and have a radius $|r - R^a| < r_c^a$, where r_c^a is the cut-off radius, a is the atom site index and R_a is the position of the atoms i.

Then transformation **T** maps the smooth auxiliary wave-functions onto the true wave-functions by:

$$\psi_n(r) = \boldsymbol{T}\,\tilde{\psi}_n(r) \tag{4.51}$$

To evaluate the form of the operator **T**, one considers the all-electron partial wave basis functions $|\phi_i^a\rangle$. Let $|\tilde{\phi}_i^a\rangle$ be the auxiliary partial wave such that outside the augmentation spheres they are identical to the all-electron partial wave basis functions:

$$|\phi_i^a\rangle = |\tilde{\phi}_i^a\rangle \;\forall |r - R^a| > r_c^a \tag{4.52}$$

Then,

$$|\phi_i^a\rangle = \boldsymbol{T}|\tilde{\phi}_i^a\rangle \tag{4.53}$$

$$|\phi_i^a\rangle = (1 + \sum_{a'} \boldsymbol{T}^{a'})\,|\tilde{\phi}_i^a\rangle \tag{4.54}$$

$$|\phi_i^a\rangle = (1 + \boldsymbol{T}^a)\,|\tilde{\phi}_i^a\rangle \tag{4.55}$$

The above equation implies that:

$$\begin{aligned} \hat{T}^a\,|\tilde{\phi}_i^a\rangle &= |\phi_i^a\rangle - |\tilde{\phi}_i^a\rangle \\ &= \sum_j (|\phi_j^a\rangle - |\tilde{\phi}_j^a\rangle\langle\tilde{p}_j^a|\tilde{\phi}_i^a\rangle) \end{aligned} \tag{4.56}$$

where $\langle\tilde{p}_j^a|$ is the projector operator satisfying the condition $\langle\tilde{p}_j^a|\tilde{\phi}_i^a\rangle = \delta_{i,j}$

So, the operator **T** can be written as:

$$\boldsymbol{T} = 1 + \sum_j (|\phi_j^a\rangle - |\tilde{\phi}_j^a\rangle\langle\tilde{p}_j^a|\tilde{\phi}_i^a\rangle) \tag{4.57}$$

Thus, $\psi_n(r)$ can be reconstructed from $\tilde{\psi}_n(r)$ on operating **T** as:

$$\psi_n(r) = \tilde{\psi}_n(r) + \sum_j (|\phi_j^a\rangle - |\tilde{\phi}_j^a\rangle\langle\tilde{p}_j^a|\tilde{\phi}_i^a\rangle) \tag{4.58}$$

The smooth auxiliary wave-function $\tilde{\psi}_n(\mathrm{r})$ is identical to the all-electron wavefunctions $\psi_n(\mathrm{r})$ outside the augmented spheres. The auxiliary partial waves $|\tilde{\phi}_j^a\rangle$ are chosen such that they form the basis for $\tilde{\psi}_n(\mathrm{r})$ within the augmented sphere. Therefore it can be written as:

$$\tilde{\psi}_n(r) = \sum_i C_{ni}^a |\tilde{\phi}_i^a\rangle \tag{4.59}$$

Furthermore, it can be shown that the all-electron wave function $\psi_n(\mathrm{r})$ can be expanded in terms of all-electron partial waves $|\phi_j^a\rangle$ using the same coefficients C_{ni}^a.

The PAW formalism as implemented within the VASP software by Kresse and Joubert has been primarily used for the work described within this thesis.

4.2. Time-Dependent Density Functional Theory (TDDFT):

The DFT has been generalized to include time-dependent potentials and is known as TDDFT. This theory can be thought of as a reformulation of the time-dependent quantum mechanics in terms of time-dependent electron density $\rho(\mathbf{r},t)$. This approach has a great advantage over the wave function approach, as the many-body wave function is a function of N positions, where N is the number of electrons while the electron density is a function of one position only.

The main theoretical construction was done by Runge and Gross (1984) who gave a theorem known as Runge–Gross theorem [40], which is the analog of the Hohenberg–Kohn theorem for the time-dependent electron density $\rho(\mathbf{r},t)$. They showed that DFT can be extended to problems where a time-dependent external perturbation is present, such as the oscillating electric field of a laser. Runge–Gross theorem establishes a one-to-one correspondence between $\rho(\mathbf{r},t)$ and time-

dependent external potential $v_{\text{ext}}(\mathbf{r},t)$ for a given initial state. Similar to DFT, one can define a fictitious system of non-interacting electrons that has the same density $\rho(\mathbf{r},t)$ of the real system and which moves in a time-dependent effective potential $v_{\text{eff}}(\mathbf{r},t)$. This leads to an equation similar to the time-dependent Schrödinger equation, known as the time-dependent KS equation. A noninteracting system is defined in such a way that it reproduces the exact groundstate density of the interacting system. This means that we can calculate the exact density as the sum of squares of single-particle orbitals:

$$\rho(\boldsymbol{r},t) = \sum_{j=1}^{N} |\varphi_j(r)|^2 \tag{4.60}$$

where the orbitals satisfy the following equation:

$$\left[-\frac{\nabla^2}{2} + v_{eff}(\boldsymbol{r},t)\right]\varphi_j(r) = \varepsilon_j\varphi_j \tag{4.61}$$

This equation is called the time-dependent Kohn Sham equation [41, 42].

Here,

$$v_{eff}(\boldsymbol{r},t) = v_{ext}(\boldsymbol{r},t) + v_{XC}(\boldsymbol{r},t) + \int d^3r' \frac{\rho(\boldsymbol{r},t)}{|r-r'|} \tag{4.62}$$

Here $v_{XC}(\boldsymbol{r},t)$ is the time-dependent exchange-correlation potential, and $v_{ext}(\boldsymbol{r},t)$ is the external time-dependent field. The second term on the right-hand side of Eq. (4.62) is the time-dependent Hartree potential, describing the interaction of classical electronic charge distributions. The exchange-correlation potential $v_{xc}(\boldsymbol{r},t)$ is an unknown functional of $\rho(\boldsymbol{r},t)$ which has to be approximated. The functional derivative of exchange-correlation potential $\delta v_{xc}/\delta\rho$ is called the exchange-correlation kernel f_{XC}. The simplest approximation is the adiabatic local density approximation (ALDA) in which the exchange-correlation potential of the homogeneous electron-gas [9] with the instantaneous density is used to evaluate $v_{xc}(\boldsymbol{r},t)$, that is:

$$v_{XC}^{ALDA}(\boldsymbol{r},t) = v_{XC}^{unif}(n(\boldsymbol{r},t)) \tag{4.63}$$

This formalism has been applied to calculate excited-state energies and photo-absorption cross-sections of molecules and clusters. Hence one replaces the inhomogeneous electron system at each point $\boldsymbol{r}$ with a homogeneous electron gas having the density of the inhomogeneous system at $\boldsymbol{r}$. The rationale for this approximation is in the limit of slowly varying density. In practice, however, the macroscopic dielectric function calculated using this kernel has two well-known deficiencies: the quasiparticle gap is too small, and the physics of the bound electron-hole pair is missing. ALDA does not improve on the results obtained within the random phase approximation (RPA) which corresponds to the trivial kernel $f_{XC} = 0$.

4.2.1. Exchange Correlation Kernel: exchange-correlation potential is not sufficient to describe the change of electron density in the presence of an external potential. The change of electron density in the presence of an external potential requires the exchange-correlation kernel which is the functional derivative of the exchange-correlation potential with respect to the density. The search for improved TDDFT potentials and kernels is hence a subject of increasing interest. There is a large literature dealing with the inclusion of many-body effects into TDDFT kernels, to correctly reproduce excitonic features. In the present thesis, we have used two types of exchange-correlation kernel to calculate the excitonic property of systems, which are; a) Bootstrap (BOS) [43] and b) Long Range Contribution (LRC) [44].

4.2.1.1. Bootstrap Method [43]: We have adapted the Bootstrap kernel method as implemented by Gross *et al*. The exact relationship between the dielectric function ε and the kernel f_{xc} for a periodic solid can be written as:

$$\begin{aligned} \varepsilon^{-1}(\boldsymbol{q},\omega) &= 1 + v(\boldsymbol{q})\chi(\boldsymbol{q},\omega) \\ &= 1 + \chi_0(\boldsymbol{q},\omega)v(\boldsymbol{q})\{1 - [v(\boldsymbol{q}) + f_{xc}(\boldsymbol{q},\omega)]\chi_0(\boldsymbol{q},\omega)\}^{-1} \end{aligned} \tag{4.64}$$

In this equation, v is the bare Coulomb potential, χ is the full response function, and χ_0 is the response function of the noninteracting Kohn-Sham system. The frequency-independent approximation for the xc can be written as:

$$f_{XC}^{boot}(q,\omega) = -\frac{\epsilon^{-1}(q,\omega=0)v(\boldsymbol{q})}{\varepsilon_{GG'}^{0}(q,\omega=0)-1} = \frac{\epsilon^{-1}(q,\omega=0)}{\chi_{GG'}^{0}(q,\omega=0)} \tag{4.65}$$

where $\varepsilon_0 = 1 - v(\boldsymbol{q})\chi_0(\boldsymbol{q},\omega)$ is the dielectric function in RPA formalism [45]. The approximate functional is chosen in such a way that it satisfies two important requirements; a) f_{XC} has the exact long-wavelength behavior i.e.

$$f_{XC}(q \to 0) = \alpha_{XC}/q^2 \tag{4.66}$$

In the $\omega \to 0$ limits, the form of f_{XC} should yield static dielectric constants close to the RPA values, which are known to reproduce experiments reasonably well.

These equations are useful when either f_{XC} or ε is unknown. With the addition of the approximation given by Eq. (4.65), however, both f_{XC} and ε can be determined from knowledge of χ_0 exclusively. The *modus operandi* for doing so is to start by setting $f_{XC} = 0$ and then solving Eq. (4.64) to obtain ε^{-1}. This is then ''bootstrapped'' in Eq. (4.65) to find a new f_{XC}, and the procedure is repeated until self-consistency between the two equations at ω = 0 is achieved.

This Bootstrap kernel has two key advantages: first of all, the computation cost is very minimal, as the most expensive part is the calculation of χ_0, which needs to be calculated only once, and, most importantly no system-dependent external parameter is required.

4.2.1.2. Long Range Method [44]: The long-range component of the exchange-correlation kernel f_{XC} is completely absent from local density or generalized gradient approximations, but it is believed to be present in the "exact" f_{XC}. In the case of solids, the Hartree contribution is not sufficient to yield good absorption spectra (it then just gives rise to the crystal local field effects). In this case, taking

into account f_{XC} within Time-Dependent LDA (TDLDA) does not lead to a significant improvement. The reason for this failure can be traced back to the short-range nature of the TDLDA f_{XC}, while the "exact" f_{XC} is believed to be long-ranged, decaying in momentum space as $1/q^2$.

Therefore, when calculating electronic excitations in solids we have the Bethe-Salpeter equation (BSE), a precise but computationally demanding method, and at the same time, we are using TDDFT, a rather inexpensive method whose applicability is severely limited by the shortcomings of the TDLDA. Several attempts have been made to find a desirable f_{XC} which will be generally applicable. Improvements to the TDLDA might come through the inclusion of dynamical effects and/or long-range nonlocal terms. One of the simplest models used to consider the long-range effect is of the form:

$$f_{XC}^{static}(q) = -\alpha^{static}/q^2 \tag{4.67}$$

where α^{static} is a frequency-independent long-range component of the exchange-correlation kernel. Keeping only this contribution is sufficient to simulate the strong continuum exciton effect in the absorption spectrum. More detailed and accurate formulation involves introducing frequency dependence. To improve on this simplest of models, we can follow two paths: a) introduce a more complex spatial behavior, b) introduce frequency dependence. We have followed the later method in our time-dependent absorption calculations.

The frequency-dependent form of the model kernel is proposed as:

$$f_{xc}^{dyn}(\boldsymbol{q}, \omega) = -\frac{1}{q^2}(\alpha + \beta\omega^2) \tag{4.68}$$

the two parameters α and β of Eq. (4.68) can be related to physical quantities, like the dielectric constant and the plasma frequency. This approach is a promising alternative to the use of the significantly more complicated kernels proposed in

the literature for the efficient calculation of electronic excitations in complex systems made of semiconductors and insulators.

4.3. Phonon Calculations:

In material physics, a phonon is a collective excitation in a periodic, elastic arrangement of atoms or molecules that arises from oscillating atoms within a crystal [46]. Phonon is a unit of the vibrational energy of the solids (and some liquids also). As we know any solid crystal, consists of atoms bound into a specific repeating three-dimensional spatial pattern called a lattice. In the crystal lattice, the atoms behave as if they are connected by tiny springs, their own thermal energy or outside forces make the lattice vibrate. This eventually produces mechanical waves which can transmit heat and sound through the material. A packet of these waves can travel throughout the crystal with definite energy and momentum, so in quantum mechanical terms the waves can be treated as a particle, called a phonon. A phonon is a discrete unit or quantum of vibrational mechanical energy, similar to a photon in the quantum of electromagnetic or light energy. Phonons and electrons are the two main types of elementary particles or excitations in solids. Electrical properties of the systems are generated from electrons; similarly, phonons determine the thermal and acoustic properties of the systems. Moreover, phonons are essential in the phenomenon of superconductivity—a process in which certain metals lose all their electrical resistance at temperatures near to 0 K. At normal temperature electrons collide with impurities and face resistance forces as they move through a metal, which results in a frictional loss of energy. In superconducting material at the temperature below the critical temperature, electrons—which ordinarily repel each other, slightly attract each other through the intermediate effect of phonons. So, the electron-phonon interaction plays a very crucial role in a variety of physical phenomena. The electron-phonon interaction is one of the fundamental interactions of quasiparticles in solids. In particular in metals, low-energy

electronic excitations are strongly modified by the coupling to lattice vibrations, which affects many properties including transport and thermodynamic properties [47, 48]. So, it is very much essential to calculate the phonon mediated properties of the systems.

In crystals, it is presumed that atoms move around their equilibrium positions **r** ($l\kappa$) with displacements **u** ($l\kappa$), where l and κ are the labels of unit cells and atoms in each unit cell, respectively. Crystal potential energy Φ is assumed to be a function of the displacements of atoms. Φ can be expressed as [49],

$$\Phi = \Phi_0 + \sum_{l\kappa}\sum_{\alpha} \Phi_\alpha(l\kappa)\, u_\alpha(l\kappa) + \frac{1}{2}\sum_{ll'\kappa\kappa'}\sum_{\alpha\beta} \Phi_{\alpha\beta}(l\kappa, l'k')\, u_\alpha(l\kappa) u_\beta(l'k') + \frac{1}{3!}\sum_{ll'l''\kappa\kappa'\kappa''}\sum_{\alpha\beta\gamma} \Phi_{\alpha\beta\gamma}(l\kappa, l'k', l''k'')\, u_\alpha(l\kappa) u_\beta(l'k') u_\gamma(l''k'') + \cdots \tag{4.69}$$

where α, β, γ are the Cartesian indices. The coefficients of the series expansion, Φ_0, $\Phi_\alpha(l\kappa)$, $\Phi_{\alpha\beta}(l\kappa, l'k')$, $\Phi_{\alpha\beta\gamma}(l\kappa, l'k', l''k'')$ are the zeroth, first, second, and third order force constants, respectively. With small displacements at constant volume, the atomic vibrations of the system can be solved with the second-order terms as the harmonic approximation, and the higher order terms are treated by the perturbation theory.

First order force can be defined as:

$$F_\alpha(lk) = -\frac{\delta\Phi}{\delta u_\alpha(l\kappa)} \tag{4.70}$$

From Eq. (4.70), an element of second-order force constants $\Phi_{\alpha\beta}(l\kappa, l'k')$ is obtained by:

$$\frac{\delta^2\Phi}{\delta u_\alpha(l\kappa)\delta u_\beta(l'k')} = -\frac{\delta F_\beta(l'k')}{\delta u_\alpha(l\kappa)} \tag{4.71}$$

Now, the crystal symmetry is employed to improve the numerical accuracy of the force constants and to reduce the computational cost. More details on the calculation of force constants are shown in the following references [50, 51].

The dynamical property of atoms in the harmonic approximation is obtained by solving the eigenvalue problem of dynamical matrix D(**q**) [46, 52].

$$D(\boldsymbol{q})\boldsymbol{e}_{\boldsymbol{q}j} = \omega_{\boldsymbol{q}j}^2 \boldsymbol{e}_{\boldsymbol{q}j} \quad \text{or} \quad \sum_{\beta\kappa'} D_{\kappa k'}^{\alpha\beta}(\boldsymbol{q}) e_{\boldsymbol{q}j}^{\beta k'} = \omega_{\boldsymbol{q}j}^2 e_{\boldsymbol{q}j}^{\alpha\beta} \tag{4.72}$$

with,

$$D_{\kappa k'}^{\alpha\beta}(\boldsymbol{q}) = \sum_{l'} \frac{\Phi_{\alpha\beta}(0\kappa, l'k')}{\sqrt{m_k m_{k'}}} e^{i\boldsymbol{q}.[\boldsymbol{r}(l'k') - \boldsymbol{r}(0\kappa)]} \tag{4.73}$$

where, m_κ is the mass of the atom κ; **q** is the wave vector, and j is the band index. $\omega_{\mathbf{q}j}$ and $\mathbf{e}_{\mathbf{q}j}$ give the phonon frequency and polarization vector of the phonon mode labeled by a set {**q**,j} respectively. Here, D(**q**) is an Hermitian matrix, so its eigenvalues, $\omega_{\boldsymbol{q}j}^2$ are real. The matrix D(**q**) is a $3n_a \times 3n_a$ matrix [46], where n_a is the number of atom in a unit cell. Factor 3 comes from the freedom of the Cartesian indices for the crystal.

Therefore, $\mathbf{e}_{\mathbf{q}j}$ becomes a complex column vector with $3n_a$ elements, $\mathbf{e}_{\mathbf{q}j}$ is normalized to be 1, i.e., $\sum_{\alpha\kappa} |e_{\boldsymbol{q}j}^{\alpha\kappa}|^2 = 1$. Information of collective motion of atoms is given by the term $\mathbf{e}_{\mathbf{q}j}$. This may be realized as a set of atomic displacement vectors,

$$[\boldsymbol{u}(l1), \ldots, \boldsymbol{u}(l1)] = [\frac{A}{\sqrt{m_1}} \boldsymbol{e}_{\boldsymbol{q}j}^1 e^{i\boldsymbol{q}.\boldsymbol{r}(l1)}, \ldots, \frac{A}{\sqrt{m_{n_a}}} \boldsymbol{e}_{\boldsymbol{q}j}^{n_a} e^{i\boldsymbol{q}.\boldsymbol{r}(l\kappa)}] \tag{4.74}$$

where, A is the complex constant undetermined by Eq. (4.72), and $e_{qj}^{\kappa\ T} = \left(e_{\boldsymbol{q}j}^{xk}, e_{\boldsymbol{q}j}^{xk}, e_{\boldsymbol{q}j}^{xk}\right)$.

The phonon density of states is defined as:

$$g(\omega) = \frac{1}{N}\sum_{\boldsymbol{qj}} \delta(\omega - \omega_{\boldsymbol{qj}}) \tag{4.75}$$

where N is the number of unit cells in crystal. Divided by N, g(ω) is normalized so that the integral over frequency becomes $3n_a$. Atom specific phonon DOS projected along a unit direction vector $\hat{\boldsymbol{n}}$ is defined as:

$$g_k(\omega, \hat{n}) = \frac{1}{N}\sum_{\boldsymbol{qj}} \delta\big(\omega - \omega_{\boldsymbol{qj}}\big)|\hat{\boldsymbol{n}}.\boldsymbol{e}^{\kappa}_{\boldsymbol{qj}}|^2 \tag{4.76}$$

4.3.1. Electron-Phonon Coupling: Coulomb interaction is one of the fundamental interactions of quasiparticle in solids. Besides, the electron-phonon interaction is another important interaction in solids. It plays an important role for a variety of physical phenomena. Specifically, in metal, the low-energy electronic excitations are strongly altered by the coupling to lattice vibrations, which can influence their transport and thermodynamic properties. Electron-phonon coupling (EPC) also provides in a fundamental way an attractive electron-electron interaction, which is always present and, in many metals, is the origin of the electron pairing underlying the macroscopic quantum phenomenon of superconductivity.

The simplest process containing the electron-phonon interaction is the scattering of a single electron by a simultaneous creation or annihilation of a single phonon. A schematic of the process is shown in Figure 4.4. The probability for the scattering process is called the electron-phonon vertex *g*. We will briefly sketch its derivation starting from rather general grounds. As the ratio of ionic mass to electronic mass is very high, the dynamics of the ions and the electrons in the system can be systematically expressed in terms of a small parameter $= (m/M)^{1/4}$ which results in partial decoupling [53, 54]. To lowest order in κ, called the adiabatic or Born-Oppenheimer approximation, the total wavefunction of the coupled electron-ion system can be written as:

$$\Psi(\boldsymbol{r}, \boldsymbol{R}) = \chi(\boldsymbol{R})\psi(\boldsymbol{r}; \boldsymbol{R}) \tag{4.77}$$

where r and R denote the set of electron and ion coordinates, respectively. The electronic wavefunction follows the equation:

$$[T_e + V_{ee} + H_{e-i}(\boldsymbol{R})]\psi(\boldsymbol{r}; \boldsymbol{R}) = E_n(\boldsymbol{R})\, \psi(\boldsymbol{r}; \boldsymbol{R}) \tag{4.78}$$

where T_e and V_{ee} denote the kinetic energy and Coulomb interaction of the electron system, respectively. Eq. (4.78) depends parametrically on the ionic positions **R** via the electron-ion interaction H_{e-i}.

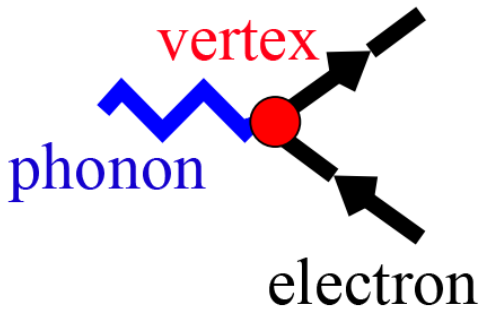

Figure 4.4: *Diagrammatic representation of the basic electron-phonon scattering process. Black lines represent electrons, the blue zigzag line a phonon, and the red circle the screened vertex.*

The electron-phonon vertex appears in first order beyond the adiabatic approximation. It induces off-diagonal matrix elements among the electronic eigenstates **n**, which can be expressed in the following ways:

$$< n|\delta_R V|n' > \tag{4.79}$$

The operator δ_{RV} denotes the linear change of the potential which an electron undergoes when an atom displace from its rest position: R = R_0 + u. If the potential V is the bare electron-ion potential V^0, then we can write $\delta_{RV} = \boldsymbol{u}.\nabla V^0|_{R_0}$. Eq. (4.79) represents the bare vertex. Though, in solids, and in particular in metals, other electron can screen the bare electron-ion potential. This screening process

can also modifies the vertex significantly. Within the limit of linear response theory, the form of the operator will be,

$$\delta_R V = u.\epsilon^{-1}\nabla V^0|_{R_0} \tag{4.80}$$

where, ε^{-1} is the inverse dielectric matrix [55], which is a measure of the screening.

Next, we will try to advance a systematic perturbative treatment of the mutual influence of the electronic and phononic subsystems in a solid. As we will see, electronic states are significantly influenced by lattice vibrations mostly in close vicinity of the Fermi energy. It is therefore appropriate to start with electrons moving in the static potential of a rigid ion lattice, without any renormalization by the lattice vibrations. At the same time, the bare vibrations of the ion lattice would be a bad starting point, because they are strongly altered by the screening of the electrons. This screening must be built into the description of the harmonic lattice vibrations which defines the noninteracting phonons. For the discussion of electron-phonon coupling effects in periodic solids, a good starting point is the Fröhlich Hamiltonian, which reads in second quantization:

$$H = H_e + H_{ph} + H_{e-ph} \tag{4.81}$$

In the present case, the electron system is described by noninteracting quasiparticles with dispersion ε_k. These quasiparticles are considered to be the stationary solutions of band electrons in a perfect periodic lattice, and include already the renormalization from Coulomb interaction:

$$H_e = \sum_{\kappa\nu\rho} \varepsilon_{\kappa\nu} c^{\dagger}_{\kappa\nu\rho}\, c_{\kappa\nu\rho} \tag{4.82}$$

Here $c_{\kappa\nu\rho}$ and $c^{\dagger}_{\kappa\nu\rho}$ are the annihilation and creation operators respectively, for an electronic state with momentum κ, band index ν, spin σ, and band energy $\varepsilon_{\kappa\nu}$.

The lattice Hamiltonian is expressed in terms of quantized harmonic vibrations, and represents noninteracting phonons:

$$H_{ph} = \sum_{qj} \omega_{qj}(b^{\dagger}_{qj}\, b_{qj} + \frac{1}{2}) \tag{4.83}$$

In this equation $b^{\dagger}_{qj}$ is the creation operator and b_{qj} is the annihilation operator for a phonon with momentum **q**, branch index j and energy ω_{qj}. The operator of atom displacements is expressed in terms of the phonon operators by,

$$u_{ls\alpha} = e^{i\boldsymbol{q}\boldsymbol{R}^{0}_{ls}} \frac{1}{\sqrt{N_q}} \sum_{\boldsymbol{qj}} A^{qj}_{s\alpha}\, (b_{qj} + b^{\dagger}_{-qj}) \tag{4.84}$$

where, $A^{qj}_{s\alpha} = \frac{\eta_{s\alpha}(\boldsymbol{q}j)}{\sqrt{2M_s\omega_{qj}}}$

Atoms are characterized by two indices denoting the unit cell (*l*) and the atoms inside a unit cell (*s*), respectively, with M_s the corresponding atom mass. α denotes Cartesian indices, and $\eta_{s\alpha}(\boldsymbol{q}j)$ is the eigenvector of the normal mode **q***j*. The number of points in the summation over **q** is N_q.

The third term describes the lowest-order coupling between electrons and phonons derived from Eq. (4.80). Using the relationship Eq. (4.84) it has the form:

$$H_{e-ph} = \sum_{\kappa\nu\nu'\sigma} \sum_{\boldsymbol{qj}} g^{\boldsymbol{qj}}_{k+q\nu',k\nu}\, c^{\dagger}_{\kappa+q\nu'\sigma}\, c_{\kappa\nu\rho}(b_{\boldsymbol{qj}} + b^{\dagger}_{\boldsymbol{qj}}) \tag{4.85}$$

$g^{\boldsymbol{qj}}_{k+q\nu',k\nu}$ is the electron-phonon matrix element and describes the probability amplitude for scattering an electron with momentum **k** from band υ to a state with

momentum **k** + **q** in band υ′ under the simultaneous absorption (emission) of a phonon with momentum **q** (−**q**) and branch index *j*.

$$g^{\boldsymbol{qj}}_{k+q\nu',k\nu} = \sum_{s\alpha} A^{\boldsymbol{qj}}_{s\alpha} \langle \boldsymbol{k}+\boldsymbol{q}\nu' | \delta^{q}_{s\alpha} V | \boldsymbol{k}\nu\sigma \rangle \tag{4.86}$$

Here again the screened first-order variation enters the matrix elements. They are independent of spin for nonmagnetic ground states.

This general form of the Fröhlich Hamiltonian will be the starting point for the many-body perturbation outlined in the next Sections. To simplify the treatment, we will use a compact notation combining momentum and band/branch index into a single symbol: *k* = (**k**ν), k′ = (**k′**ν′), and q = (**q***j*). The EPC matrix elements are then denoted as:

$$g^{q}_{k',k} = g^{\boldsymbol{qj}}_{\boldsymbol{k'}\nu',\boldsymbol{k}\nu} \delta_{\boldsymbol{k'},\boldsymbol{k}+\boldsymbol{q}} \tag{4.87}$$

which implicitly takes into account momentum conservation.

4.4. Quantum Transport Calculations:

DFT quantum transport calculations are executed by using the Atomistic Toolkit 15.1 package [56], with the GGA-PBE exchange correlation [57, 58]. We have employed the double-zeta plus polarization (DZP) basis set for the device calculation and the expansion of electronic density. During the simulation, vdW corrections are taken into account by following the DFT-D2 method. For geometry optimization, the real-space energy cutoff is kept as 200 Hartree with the maximum force of 0.01 eV/Å. For quantum transport properties in the two-probe model, DFT coupled nonequilibrium Green's function (NEGF) method [59] is employed [60].

The total system can be divided into three parts: left electrodes, central region, and right electrodes. The implementation relies on the so-called screening approximation. In this approximation, it is assumed that the properties of the left and right regions, the electrodes, can be described by solving a bulk problem for the fully periodic electrode cell. The criterion to fulfill the screening is a small current flow through the system so that the electrode regions can be described by an equilibrium electron distribution.

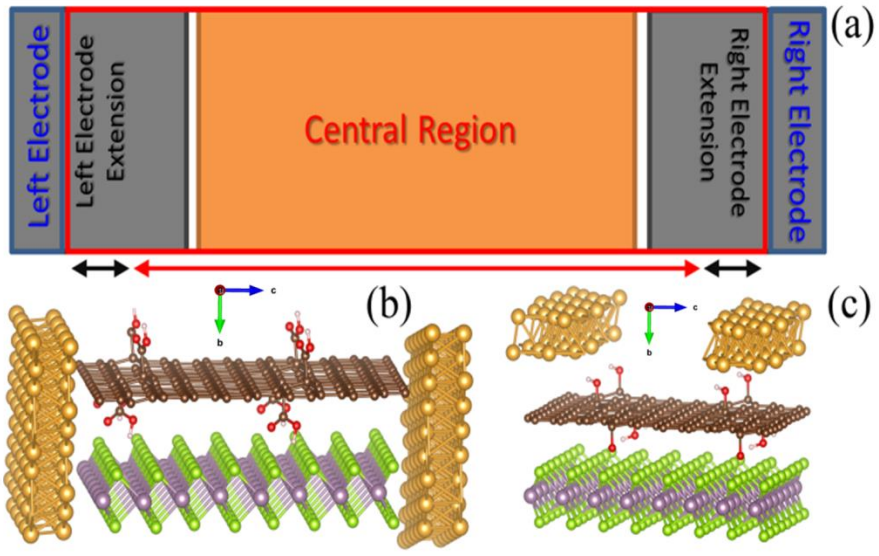

Figure 4.5: *a) Geometry of a device configuration with two electrodes (two-probe configuration). In the left and right electrode regions, the system is periodic in the transport direction (the C direction). The central region seamlessly connects the left and right electrode regions, and the part of the central region where the atom positions follow the periodic arrangement of the electrodes is called the left and right electrode extension. b) Schematic diagram of the Lateral contact device and c) vertical contact device.*

Figure 4.5a illustrates how the electrode regions must be extended into the central region, to screen out the perturbations from the scatterer (in this case the Graphene Oxide/$MoSe_2$ heterostructure) inside the device. In our case, we have extended the electrodes 5-10 Å into the central region which is usually sufficient to extend. The left and right regions are equilibrium systems with periodic boundary conditions, and the properties of these systems are obtained using a conventional

electronic structure calculation. The main difficulty to calculate the properties of a device system lies in the calculation of the non-equilibrium electron distribution in the central region of the system. To solve this difficulty, it is assumed that the system is in a steady state such that the electron density of the central region remains constant in time. The electron density is given by the occupied eigenstates of the system. Now, the chemical potential is different in the two electrodes. Consequently, the contribution from each electrode to the total electron density in the central region should be calculated separately.

The contribution from the left (ρ_L) and right (ρ_R) electrodes can be obtained by calculating the scattering states, which are the eigenstates of the system when scattering boundary conditions are used. A schematic diagram, showing a left moving scattering state with origin in the right electrode is presented in Figure 4.6.

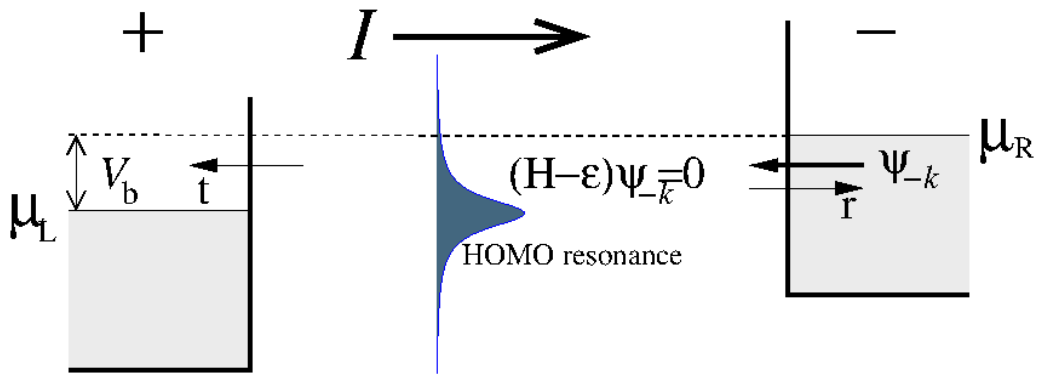

Figure 4.6: *Overall electron distribution in a device configuration is represented schematically. The figure illustrates a left moving scattering state with origin in the right electrode. The chemical potential of left and right electrodes is μ_L and μ_R respectively.*

The left and right regions have an equilibrium electron distribution with chemical potentials μ_L and μ_R, related through the applied bias, $\mu_R - \mu_L = eV_b$. It is assumed that the electrons with energies in the bias window has potential greater than μ_L and higher than μ_R i.e. $\mu_L \leq \varepsilon \leq \mu_R$. In this condition, the system gives rise to a steady-state electrical current with a left moving scattering state whose origin is in the right electrode.

The left and right electrode electron density can be expressed by adding up the occupied scattering states as:

$$\rho(r) = \rho^L(r) + \rho^R(r) \tag{4.88}$$

The scattering states of the system was calculated by first calculating the Bloch states in the electrodes and subsequently solving the Schrödinger equation of the central region using the Bloch states as matching boundary conditions:

$$\rho^L(r) = \sum_{\alpha} |\psi_\alpha(r)|^2 f\left(\frac{\varepsilon_\alpha - \mu_L}{kT}\right), \tag{4.89}$$

$$\rho^R(r) = \sum_{\alpha} |\psi_\alpha(r)|^2 f\left(\frac{\varepsilon_\alpha - \mu_R}{kT}\right), \tag{4.90}$$

It is possible to calculate the non-equilibrium electron density using the non-equilibrium Green's function (NEGF) method, instead of using the scattering state. We have used QuantumATK software in which the NEGF method is implemented. The electron density is given in terms of the electron density matrix. The density matrix has been divided into the left and right contributions:

$$D = D^L + D^R \tag{4.91}$$

The left density matrix contribution is calculated using the NEGF method as [60]:

$$D^L = \int \varphi^L(\varepsilon) f\left(\frac{\varepsilon - \mu_L}{k_B T_L}\right) d\varepsilon \tag{4.92}$$

where,

$$\varphi^L(\varepsilon) \equiv \frac{1}{2\pi} G(\varepsilon) \Gamma^L(\varepsilon) G^\dagger(\varepsilon) \tag{4.93}$$

is the spectral density matrix. Note that while there is a non-equilibrium electron distribution in the central region, the electron distribution in the electrode is described by a Fermi function f with an electron temperature T_L.

The expression of Γ^L is given as:

$$\Gamma^L = \frac{1}{i}(\Sigma^L - (\Sigma^L)^\dagger) \tag{4.94}$$

In Eq. (4.93) the term G is denoted as retarded Green's Function and Γ^L is the broadening function of the left electrode. Γ^L is a function of the left electrode self-energy. A similar equation exists for the right density matrix contribution.

The retarded Green's function matrix is defined as:

$$G(\varepsilon) = \frac{1}{(\varepsilon + i\delta_+)S - H} \tag{4.95}$$

where δ_+ is an infinitesimal positive number. S and H are the overlaps and Hamiltonian matrices respectively, of the entire system.

The Green's function is only required for the central region and can be calculated from the Hamiltonian of the central region by adding the electrode self-energies:

$$G(\varepsilon) = [(\varepsilon + i\delta_+)S - H - \Sigma^L(\varepsilon) - \Sigma^R(\varepsilon)]^{-1} \tag{4.96}$$

Therefore, the calculation of the Green's function of the central region at specific energy requires the inversion of the Hamiltonian matrix of the central region. In QuantumATK, this matrix is stored in a sparse format, and the inversion is done using an O(N) algorithm [61].

In terms of the density matrix, $\boldsymbol{D}$, the electron density of the central region is given by:

$$\rho(r) = \sum_{ij} D_{ij}\phi_i(\boldsymbol{r})\phi_j(\boldsymbol{r}) \tag{4.97}$$

The Green's function of the central region gives the density matrix of the central region, $\boldsymbol{D_{CC}}$, however, to calculate the density correctly close to the central cell boundaries the terms involving, $\boldsymbol{D_{LL}}$, $\boldsymbol{D_{LC}}$, $\boldsymbol{D_{CR}}$, $\boldsymbol{D_{RR}}$ are also needed. These terms are called spill-in terms. In the ATK formalism, all the spill-in terms are included for calculating electron density [62]. This gives added stability and well-behaved convergence in the device algorithm [62].

In the next step, the aim was to calculate the effective potential as the sum of the exchange-correlation and electrostatic Hartree potentials. The calculation of the exchange-correlation potential is straightforward since it is a local or semi-local function of the density. However, the calculation of the electrostatic Hartree potential requires some additional consideration for a device system. The calculation details to determine Hartree potential is described below:

The Hartree potential of a system is defined up to an arbitrary constant. In a device setup the Hartree potentials of the two electrodes are aligned through their chemical potentials (i.e. their Fermi levels) since these are related by the applied bias:

$$\mu_R - \mu_L = eV_b \tag{4.98}$$

Here μ_R and μ_L are the right and left electrode Fermi level respectively. This shift the left and right electrode Fermi levels relative to each other is a basic mode of operation for electronic devices.

The Hartree potential of the central region is obtained by solving the Poisson equation, using the bulk-like Hartree potentials of the electrodes as boundary conditions at the interfaces between the electrodes and the central region. There are several methods used to solve the Poisson equation of a device system.

A device system is an open system where the charge can flow in and out of the central region from the left and right reservoirs. So the particle number is not conserved here. In this case, it is necessary to use grand canonical potential to describe the energetics of the system [63] as:

$$\Omega[n] = \varepsilon[n] - eN_L\mu_L - eN_R\mu_R \tag{4.99}$$

where $N_{L/R}$ is the number of electrons contributed to the central region from the left/right electrode. Now, the central region will be charged neutral due

to the screening approximation. So, if the ionic charge in the central region is considered as $\boldsymbol{N}$, then we can write $\boldsymbol{N}$ in this way:

$$N = N_L + N_R \tag{4.100}$$

So, at no applied bias, we can obtain from Eq. (4.99) that, $\mu_L = \mu_R$ and the particle terms in Ω will be constant when atoms are moved in the central region. But at finite bias voltage the particle terms Ω will be important. In this case, the expression of force will be:

$$F_i = \frac{\partial \Omega[n]}{\partial \boldsymbol{R}_i} \tag{4.101}$$

The calculation of this force is identical to the calculation of the equilibrium force. However, in the non-equilibrium case, the density and energy density matrix is calculated with the NEGF framework [62-64].

Once the self-consistent non-equilibrium density matrix has been determined, it is possible to calculate various transport properties of the system. One of the most important quantities is the transmission spectrum, from which current and differential conductance can be obtained. We define the fraction of a scattering state k which propagates through a device using the transmission amplitude t_k. The transmission coefficient at energy ε is obtained by summing up the transmission amplitude from all the states at this energy:

$$T(\varepsilon) = \sum_k t_k^\dagger \, t_k \partial(\varepsilon - \varepsilon_k) \tag{4.102}$$

The transmission coefficient may also be obtained from the retarded Green's function using the following equation:

$$T(\varepsilon) = G(\varepsilon)\Gamma^L(\varepsilon)G^\dagger(\varepsilon)\Gamma^R(\varepsilon) \tag{4.103}$$

In the present thesis work, we have constructed two types of contact geometry for the devices, viz., lateral and vertical contacts with metallic atoms (shown in Figure 4.5). In general, we have used gold (Au) or silver (Ag) as a

contact in the entire thesis work. The channel length was optimized to ensure zero contributions from the inter-electrode transmissions. The direction of placement of the electrodes is taken as *c*-axis and along *a*-axis direction the system is infinite due to periodic boundary conditions. The Monkhorst-Pack *k*-point grid for the lateral and vertical contact devices is taken as 5 × 5 × 50. The temperature is kept at 300 K and the real-space density mesh cutoff is 200 Hartree with the maximum force of 0.01 eV/Å used for geometry optimization. At the boundary of the electrode and the drain-channel, Dirichlet boundary conditions are used to provide charge-neutrality between the source and the drain. Both spin-polarized and non-spin polarized modes of transport are studied and the corresponding transmission coefficients are calculated by averaging over a $k_x \times k_y$ mesh of 10 × 10 in a direction perpendicular to the current transmission. Moreover, all the calculations were performed at zero bias (zero voltage at left and right electrodes) as well as finite bias (where the left and right electrode voltages are different).

4.5. Formation of Heterostructures:

We have designed the heterostructure by the coincidence site lattice (CSL) method, as implemented in the QuantumATK 15.1 package [65, 66]. The CSL method is a geometrical construction based on the geometry of the lattice. In general two lattices do not match due to lattice mismatch. If a (fixed) fraction of lattice sites are coincident, then the expectation is that the boundary structure will be more regular than a general boundary. For minimization of interfacial mutual rotational strain, a survey was performed through the grid $m\mathbf{v}_1 + n\mathbf{v}_2$, with the vectors $\mathbf{v}_1$ and $\mathbf{v}_2$ being the basis vectors of the fixed lattice (L1), so that for the maximum value of the integers *m* and *n*, the supercell of both of the lattices has the lowest mismatch. The rotation of the second lattice is limited to those values that bring a (lattice) point into coincidence with a different point in the first lattice. The geometry is such that the rotated point (in the rotated lattice (L2)) and the superimposed point (in the fixed lattice 1) are related by a mirror plane in the

unrotated state. Next, the mutual strain is minimized by varying the mutual rotation angle between the L1 and L2 surfaces around the stacking direction in increments of one degree.

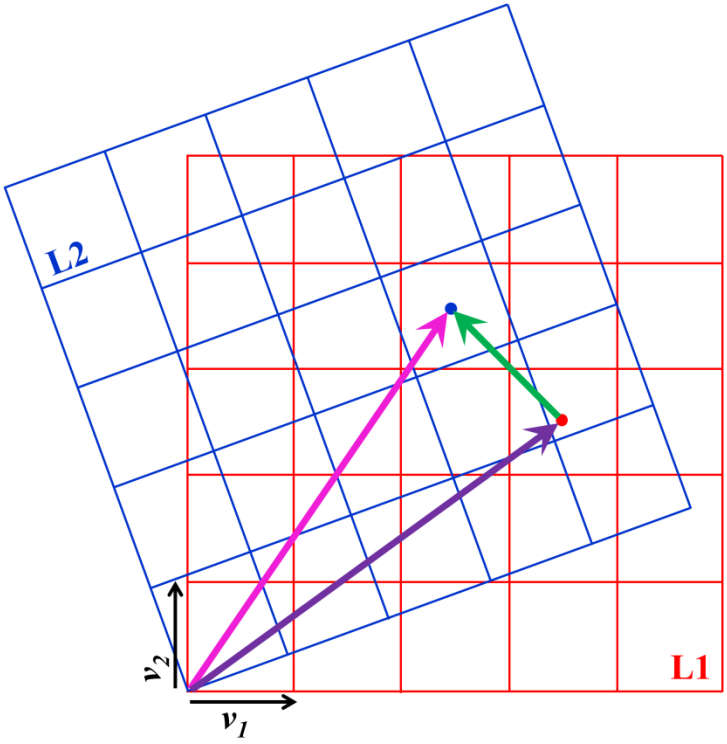

Figure 4.7: *A schematic of CSL method is shown here. CSL are obtained by generating a superposition of two periodic lattices. One of the lattices was rotated (L2) with respect to the other (L1), generating coincident points between the lattices for each rotation angle.*

Here, the blue lattice was obtained from the red one by some transformation; in this case by a simple rotation. The red point with the purple vector pointing to it is an arbitrary point in lattice L1 (in particular center of a lattice L1 cell). After the transformation, it is now the blue point at the apex of the pink and green arrows in lattice L2. It is still about in the center of a cell in lattice L2, but for the particular transformation shown, it is also about in the center of a lattice L1 cell. So, there is a coincidence of equivalence points. For perfect coincidence, the blue point denotes coinciding equivalence points.

References

[1] M. Born, R. Oppenheimer, Zur quantentheorie der molekeln, *Ann. Phys.* 389 (1927) 457.

[2] D. R. Hartree, The wave mechanics of an atom with a non-Coulomb central field. Part I. Theory and methods, *Math. Proc. Camb. Philos. Soc.* 24 (1928) 89.

[3] V. Fock, Näherungsmethode zur Lösung des quantenmechanischen Mehrkörperproblems, *Z. Physik* 61 (1930) 126.

[4] P. Hohenberg, W. Kohn, Inhomogeneous electron gas, *Phys. Rev.* 136 (1964) B864.

[5] W. Kohn, L. J. Sham, Self-consistent equations including exchange and correlation effects, *Phys. Rev.* 140 (1965) A1133.

[6] L. H. Thomas, The calculation of atomic fields, *Math. Proc. Cam. Philos. Soc.* 23 (1927) 542.

[7] E. Fermi, Un metodo statistico per la determinazione di alcune priorieta dell'atome, *Rend. Accad. Naz. Lincei* 6 (1927) 32.

[8] E. H. Lieb, B. Simon, The Thomas-Fermi theory of atoms, molecules and solids, *Adv. Math.* 23 (1977) 22.

[9] D. M. Ceperley, B. J. Alder, Ground state of the electron gas by a stochastic method, *Phys. Rev. Lett.* 45 (1980) 566.

[10] J. P. Perdew, A. Zunger, Self-interaction correction to density-functional approximations for many-electron systems, *Phys. Rev. B* 23 (1981) 5048.

[11] J. P. Perdew, Y. Wang, Accurate and simple analytic representation of the electron-gas correlation energy, *Phys. Rev. B* 45 (1992) 13244.

[12] R. O. Jones, O. Gunnarsson, The density functional formalism, its applications and prospects, *Rev. Modern Phys.* 61 (1989) 689.

[13] F. Herman, J. P. Van Dyke, I. B. Ortenburger, Improved statistical exchange approximation for inhomogeneous many-electron systems, *Phys. Rev. Lett.* 22 (1969) 807.

[14] J. P. Perdew, W. Yue, Accurate and simple density functional for the electronic exchange energy: Generalized gradient approximation, *Phys. Rev. B* 33 (1986) 8800.

[15] J. P. Perdew, Y. Wang, Accurate and simple analytic representation of the electron-gas correlation energy, *Phys. Rev. B* 45 (1992) 13244.

[16] J. P. Perdew, K. Burke, M. Ernzerhof, Generalized gradient approximation made simple, *Phys. Rev. Lett.* 77 (1996) 3865.

[17] Y. Umeno, B. Meyer, C. Elsässer, P. Gumbsch, Ab initio study of the critical thickness for ferroelectricity in ultrathin Pt/$PbTiO_3$/Pt films, *Phys. Rev. B* 74 (2006) 060101.

[18] J. Hubbard, B. H. Flowers, Electron correlations in narrow energy bands, *P. Roy. Soc. Lond. Math. Phys. Sci.* 276 (1963) 238.

[19] V. Bach, E. H. Lieb, J. P. Solovej, Generalized Hartree-Fock theory and the Hubbard model, *J. Stat. Phys.* 76 (1994) 3.

[20] W. Koch, M. C. Holthausen, A chemist's guide to density functional theory, *John Wiley & Sons*, Grünstadt, Germany, 2015.

[21] P. Hobza, J. šponer, T. Reschel, Density functional theory and molecular clusters, *J. Comp. Chem.* 16 (1995) 1315.

[22] S. Kristyán, P. Pulay, Can (semi) local density functional theory account for the London dispersion forces?, *Chem. Phys. Lett.* 229 (1994) 175.

[23] S. Grimme, Semiempirical GGA-type density functional constructed with a long-range dispersion correction, *J. Comp. Chem.* 27 (2006) 1787.

[24] J. C. Slater, G. F. Koster, Simplified LCAO method for the periodic potential problem, *Phys. Rev.* 94 (1954) 1498.

[25] D. Vanderbilt, Soft self-consistent pseudopotentials in a generalized eigenvalue formalism, *Phys. Rev. B* 41 (1990) 7892.

[26] G. Kresse, J. Hafner, Norm-conserving and ultrasoft pseudopotentials for first-row and transition elements, *J. Phys Cond. Matt.* 6 (1994) 8245.

[27] T. L. Loucks, Augmented plane wave method; a guide to performing electronic structure calculations, *W.A. Benjamin*, New York, USA, 1967.

[28] J. Korringa, On the calculation of the energy of a Bloch wave in a metal, *Physica* 13 (1947) 392.

[29] J. Korringa, Early history of multiple scattering theory for ordered systems, *Phys. Rep.* 238 (1994) 341.

[30] O. K. Andersen, O. Jepsen, Explicit, first-principles tight-binding theory, *Phys. Rev. Lett.* 53 (1984) 2571.

[31] C. Herring, A new method for calculating wave functions in crystals, *Phys. Rev.* 57 (1940) 1169.

[32] C. Herring, A. G. Hill, The theoretical constitution of metallic beryllium, *Phys. Rev.* 58 (1940) 132.

[33] P. E. Blöchl, Projector augmented-wave method, *Phys. Rev. B* 50 (1994) 17953.

[34] J. C. Slater, Statistical exchange-correlation in the self-consistent field, *Adv. Quant. Chem.*, *Elsevier*, Massachusetts, 1972.

[35] J. C. Slater, Wave functions in a periodic potential, *Phys. Rev.* 51 (1937) 846.

[36] O. K. Andersen, Linear methods in band theory, *Phys. Rev. B* 12 (1975) 3060.

[37] D. D. Koelling, G. O. Arbman, Use of energy derivative of the radial solution in an augmented plane wave method: Application to copper, *J. Phys. F: Metal Phys.* 5 (1975) 2041.

[38] G. Kresse, J. Furthmüller, Efficient iterative schemes for ab initio total-energy calculations using a plane-wave basis set, *Phys. Rev. B* 54 (1996) 11169.

[39] G. Kresse, D. Joubert, From ultrasoft pseudopotentials to the projector augmented-wave method, *Phys. Rev. B* 59 (1999) 1758.

[40] E. Runge, E. K. Gross, Density-functional theory for time-dependent systems, *Phys. Rev. Lett.* 52 (1984) 997.

[41] M. Levy, Electron densities in search of Hamiltonians, *Phys. Rev. A* 26 (1982) 1200.

[42] E. H. Lieb, Density functionals for Coulomb systems in R. M. Dreizler, J. da Providência, Density functional methods in physics, *Springer US*, Boston, USA, 1985.

[43] S. Sharma, J. Dewhurst, A. Sanna, E. Gross, Bootstrap approximation for the exchange-correlation kernel of time-dependent density-functional theory, *Phys. Rev. Lett.* 107 (2011) 186401.

[44] S. Botti, A. Fourreau, F. Nguyen, Y. O. Renault, F. Sottile, L. Reining, Energy dependence of the exchange-correlation kernel of time-dependent density functional theory: A simple model for solids, *Phys. Rev. B* 72 (2005) 125203.

[45] O. Johns, A consistent RPA formalism, *Z. Physik* 253 (1972) 269.

[46] G. P. Srivastava, The physics of phonons, *Taylor & Francis Group*, New York, USA, 1990.

[47] A. Lanzara, P. Bogdanov, X. Zhou, S. Kellar, D. Feng, E. Lu, T. Yoshida, H. Eisaki, A. Fujimori, K. Kishio, Evidence for ubiquitous strong electron–phonon coupling in high-temperature superconductors, *Nature* 412 (2001) 510.

[48] R. Heid, Density functional perturbation theory and electron phonon coupling in E. Pavarini, E Koch, U. Schoolwock, Emergent phenomena in correlated matter, (Lecture note of the autamn school, Institute of Advanced Simulation, Forschungszentrumm Jülich), Jülich, Germany, 2013.

[49] A. Togo, I. Tanaka, First principles phonon calculations in materials science, *Scr. Mater.* 108 (2015) 1.

[50] A. Togo, L. Chaput, I. Tanaka, Distributions of phonon lifetimes in Brillouin zones, *Phys. Rev. B* 91 (2015) 094306.

[51] L. Chaput, A. Togo, I. Tanaka, G. Hug, Phonon-phonon interactions in transition metals, *Phys. Rev. B* 84 (2011) 094302.

[52] J. M. Ziman, Electrons and phonons: The theory of transport phenomena in solids, *Clarendon Press*, Virginia, 1960.

[53] M. Born, R. Oppenheimer, Zur Quantentheorie der Molekeln, *Ann. Phys.* 389 (1927) 457.

[54] G. Chester, A. Houghton, Electron-phonon interaction in metals: The harmonic approximation, *Proc. Phys. Soc.* 73 (1959) 609.

[55] S. K. Sinha, Electron-phonon interaction and phonon dispersion relations using the augmented plane wave method, *Phys. Rev.* 169 (1968) 477.

[56] V. Brouet, W. Yang, X. Zhou, Z. Hussain, N. Ru, K. Shin, I. Fisher, Z. Shen, Fermi surface reconstruction in the CDW state of $CeTe_3$ observed by photoemission, *Phys. Rev. Lett.* 93 (2004) 126405.

[57] D. R. Smith, S. Schultz, P. Markoš, C. Soukoulis, Determination of effective permittivity and permeability of metamaterials from reflection and transmission coefficients, *Phys. Rev. B* 65 (2002) 195104.

[58] J. M. Soler, E. Artacho, J. D. Gale, A. García, J. Junquera, P. Ordejón, D. Sánchez-Portal, The SIESTA method for ab initio order-N materials simulation, *J. Phys. Cond. Matter* 14 (2002) 2745.

[59] S. Datta, The non-equilibrium Green's function (NEGF) formalism: An elementary introduction, *Digest. International Electron Devices Meeting, IEEE*, (2002) 703.

[60] M. Brandbyge, J. L. Mozos, P. Ordejón, J. Taylor, K. Stokbro, Density-functional method for nonequilibrium electron transport, *Phys. Rev. B* 65 (2002) 165401.

[61] D. E. Petersen, H. H. B. Sørensen, P. C. Hansen, S. Skelboe, K. Stokbro, Block tridiagonal matrix inversion and fast transmission calculations, *J. Comput. Phys.* 227 (2008) 3174.

[62] D. Stradi, U. Martinez, A. Blom, M. Brandbyge, K. Stokbro, General atomistic approach for modeling metal-semiconductor interfaces using density functional theory and nonequilibrium Green's function, *Phys. Rev. B* 93 (2016) 155302.

[63] T. N. Todorov, Local heating in ballistic atomic-scale contacts, *Phil. Mag. B* 77 (1998) 965.

[64] R. Zhang, I. Rungger, S. Sanvito, S. Hou, Current-induced energy barrier suppression for electromigration from first principles, *Phys. Rev. B* 84 (2011) 085445.

[65] S. Smidstrup, T. Markussen, P. Vancraeyveld, J. Wellendorff, J. Schneider, T. Gunst, B. Verstichel, D. Stradi, P. A. Khomyakov, U. G. Vej-Hansen, M. E. Lee, S. T. Chill, F. Rasmussen, G. Penazzi, F. Corsetti, A. Ojanperä, K. Jensen, M. L. N. Palsgaard, U. Martinez, A. Blom, M. Brandbyge, K. Stokbro, QuantumATK: An integrated platform of electronic and atomic-scale modelling tools, *J. Phys. Condens. Matter* 32 (2019) 015901.

[66] S. Smidstrup, D. Stradi, J. Wellendorff, P. A. Khomyakov, U. G. Vej-Hansen, M. E. Lee, T. Ghosh, E. Jónsson, H. Jónsson, K. Stokbro, First-principles Green's-function method for surface calculations: A pseudopotential localized basis set approach, *Phys. Rev. B* 96 (2017) 195309.

Chapter 5

Spectroscopic and Computational Studies on the Role of Surface Defects of UV Light Harvesting Nanomaterials

5.1. Introduction:

Recent work into nanoparticles (NPs) and nanohybrids (NHs) are highly fascinating due to the unique properties of nanosize structures in comparison to their larger counterparts [1]. The main advantage of NP is the high surface to volume ratio, as a result of it, the active surface area of NP is higher than bulk. NP has wide ranges of applications in various fields, such as medicine, textiles, agriculture, optics, food packaging, cosmetics, automobile, domestic refrigerator, dye-sensitized solar cells, photocatalysis, aerospace, and construction [2-8]. Besides, NP appears to be better in most of the applications compared to its microparticle system. Because of their distinct optical, magnetic, and electrical properties from their bulk counterpart, NPs are commonly used to fabricate biosensors, photocatalytic materials, magnetic storage devices, etc. Nanoscience and nanotechnology are not new fields but developments within many disciplines and a fusion of principles and ideas across different fields [9]. At present, one of the key objectives of nanotechnology is to reduce environmental pollution and danger to human health.

On the other hand, as the nanoparticle has an improved surface-to-volume ratio, it is possible to alter its different properties by manipulating the surface composition of NP [10]. However, NP has an inherent surface defect that limits its activity. The surface defect of the nanoparticle can decrease its performance in different fields. So, if we can modulate the inherent surface defect of the NP wisely, it is possible to heighten its different properties. For example, the

passivation of surface defects of NP by using surfactants is an efficient method to increase device performances of metal oxide nanoparticles based on hybrid solar cells [11]. While tailoring particle surface is a challenging task, chemists have a well-equipped toolbox to provide functionality through synthesis or post-synthesis [12, 13].

With the blessing of rapid industrialization came the bane of accumulating pollutants, contaminating groundwater reservoirs. Thus, procuring clean water became one of the biggest obstacles. Due to higher cost and many other notional side effects, modern wastewater treatment methods such as chlorination, ozonation, etc. are less suitable for large-scale applications. On the contrary, photocatalysis based on NP-based semiconductors is an environmentally sustainable green technique for environmental pollutant degradation and water purification. Among several different photocatalysts, ZnO and TiO_2 were extensively studied due to their good oxidizing capabilities for organic pollutant decomposition, chemical stability, non-toxicity, natural abundance, eco-friendliness, and affordable prices [14-19]. Although ZnO has some advantages over TiO_2, the presence of several bulk and surface defects in ZnO limits its use for various applications over TiO_2. Thus the defect state manipulation could be used as a method for tuning the photocatalysis and other applications of ZnO over TiO_2. For ZnO nanostructures, a rich variety of defect chemistry is known to be present, viz. zinc vacancy (V_{Zn}), oxygen vacancy (V_O), zinc interstitial (Zn_i), oxygen interstitial (O_i), or antisite oxygen (O_{Zn}) [20]. Common defects such as V_O present in ZnO crystal generally aggravate ZnO's photocatalytic activity. Therefore finding an effective method for repairing such defects is extremely crucial [21].

To understand the role of defect state in the activity of ZnO NP, it is paramount to recognize the different defects (and their roles) present in ZnO [20]. Defect state modulation can drastically affect the properties of ZnO. The optical

response of ZnO, for example, can be modified within the visible spectral region by regulating the rates of intrinsic defects, making it an excellent photodetector in the sub-UV regime. Such levels of intrinsic defects establish located states within the bandgap that affect optical absorption and carrier dynamics [22]. Although defect modulates the activity, still the type and sources of the defects in indigenous undoped ZnO remain controversial. Regarding defect state alteration, a critical issue is the doping of ZnO with another dopant cation. Doping on ZnO can also introduce the defect states within the bandgap of ZnO [23-25]. A complete analysis is however missing which elaborately explains the impact of surface defect state mediated defect and doping state mediated defect on the activity of ZnO NP. Therefore, a detailed mechanistic investigation of the role of defect state on the activity of ZnO is needed.

In the first work of this chapter, we have synthesized ZnO NPs of various sizes (5 nm and 30 nm). Defect states of pristine ZnO have been modulated by cationic dopant (Mn^{2+}) and anionic healer (Cl-ion). The formation of ZnO NP and Mn-doped ZnO NP are characterized using X-ray diffraction techniques. The morphology and elemental analysis have been done using high-resolution electron microscopy (HRTEM, FEG-SEM) and EDAX. We have further studied the UV-Vis absorption and emission spectra of ZnO of different sizes. Picosecond resolved time-correlated single-photon counting (TCSPC) has been utilized to confirm the Mn-doping and Cl attachment. The manifestation of the modulation of the defect states in the NPs for their photocatalytic activity through ROS generation has also been explored. First principles computational calculations have been carried out on similarly constructed nanostructures to recognize the appearance and absence of defect modulated energy levels. It is found that the introduction of doping in the ZnO increases the deep level of trap states within the bandgap of ZnO, while, attachment of chlorine on the surface of ZnO decreases the defect mediated state

of ZnO. This present study implies that modulation of the defect states is very crucial for the application of the NPs in photocatalysis.

As the surface modification of ZnO via chloride ion can give better defect state healing, it is possible to tune its various other properties by modulation of the surface defect. Moreover, there is a scope to enhance other properties of ZnO by proper tuning of the surface defect with other halide ions. Therefore, it is necessary to investigate the effects of other halide ions on ZnO NP. This motivates the other work in this chapter where we have explored the possibility of surface modification of ZnO NP using different halide ions.

NP has a propensity to agglomerate enormously. In liquid media, the stability of NP is very hard to control [26]. Therefore, it is essential to keep the NP dissolute in an aqueous medium for biological and environmental applications. Hence arresting the NP agglomeration is paramount. Many factors are controlling the stability of NP in the aqueous medium. Until now surface modulation using ligand functionalization is one of the foremost strategies to improve the liquid media stability of NP [26, 27]. Surface modification of NP can modulate a multitude of functionalities, including enhanced magnetization properties. Previous work by Kittisltved *et al.* has reported the role of capping agent of Mn-ZnO for room temperature ferromagnetism [28]. They reported that the capping agent which introduces *p*-type doping in the system raises room-temperature ferromagnetism, while the capping agent which introduces *n*-type doping does not introduce room temperature ferromagnetism. Similar to modulating magnetic properties, the surface of the nanoparticle can be changed to tune its different properties. So, modifying the ZnO NP surface by a simple one-step method to monitor its functionality is extremely desirable.

In the next work of the chapter, we have reported a comparative study of halide ions functionalization at the surface defect of ZnO NP to find a halide-ZnO

hybrid structure which is non-toxic, water-stable, higher photocatalytic activity, and enhanced magnetic activity. ZnO NP's photoelectrochemical characteristics for water oxidation reaction were assessed by linear sweep voltammetry (LSV), photocurrent spectra measurements, and incident photon measurements to current conversion efficiency (IPCE) measurements. It is found that the photocurrent or photocatalytic activity of ZnO is mainly manifested by the bandgap excitation of the semiconductor. A detailed study of photocatalytic activity of halide-ZnO and its mechanism to degrade model textile dye methyl orange (MO) under light illumination has been investigated. Magnetic behavior of different halide-ZnO at room temperature and the low-temperature is also explored. Ab initio density functional calculation was performed on a model nanocluster and halide attached nanocluster to realize the original mechanism behind higher photocatalytic and magnetic properties.

5.2. Results and Discussion:

5.2.1. Enhanced Charge Separation through Modulation of Defect-state in Wide Band-gap Semiconductor for Potential Photocatalysis Application: Ultrafast Spectroscopy and Computational Studies [29]: To explore the impact of ZnO's defect state manipulation through the interaction of different types of ions, we have synthesized bare, cation doped, and anion-attached ZnO NP. To confirm the formation of the ZnO NP XRD study of the as-synthesized ZnO NP and Mn-ZnO NP has been carried out. Figure 5.1a depicts the XRD patterns of ZnO (black) and Mn-ZnO (red), which reveals that the XRD pattern of ZnO and Mn-ZnO are similar and consistent with the reported wurtzite structure [30]. The FESEM image of ZnO and Mn-doped ZnO (Figure 5.1b) indicates insignificant changes to the grain size. The chemical composition of the Mn-doped ZnO was confirmed by EDAX analysis as shown in Figure 5.1c. It is found that the Mn^{2+} doping load into the ZnO crystal lattice is approximately 2.3 weight%. Elemental mapping of the Mn-doped ZnO system confirms the homogeneity of Zn, O, and Mn within the

system as evident from Figure 5.1d. High-resolution transmission electron microscope images of ZnO and Mn-doped ZnO samples further confirms the crystallinity of the synthesized NPs. Figure 5.1e and 5.1f show the HRTEM image of ZnO and Mn-doped ZnO (5 nm), whereas Figure 5.1g and 5.1h shows the same for 30 nm NPs. For 5 nm ZnO and Mn-doped ZnO NPs, the fringe width is 0.264 and 0.262 nm respectively, which refers to the distance between (002) planes [31, 32]. At the same time, the fringe width for 30 nm ZnO and Mn-doped ZnO NPs are 0.278 and 0.286 nm respectively, which is consistent with the spacing between (100) planes of ZnO [32].

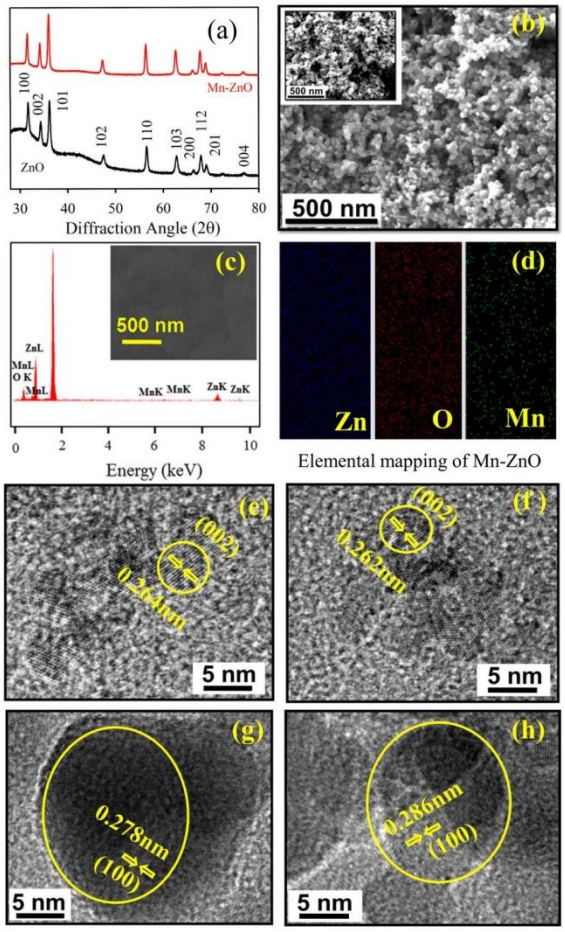

Figure 5.1: *a) XRD pattern of ZnO (black) and Mn-doped ZnO (red). b) FESEM image of 30 nm ZnO NP. Inset shows the SEM image of 30 nm Mn-doped ZnO NP, c) EDAX spectrum of Mn-doped ZnO 30 nm NP. d) Elemental mapping images of Mn-doped ZnO NP are shown for Zn (blue), O (red), and Mn (green). High Resolution TEM of e) ZnO (5nm NP), f) Mn-doped ZnO (5nm NP), g) ZnO (30 nm NP), and h) Mn-doped ZnO (30 nm NP).*

To investigate the optical properties of the pristine ZnO, and anion and cation modulated ZnO, steady-state absorption and emission spectroscopy has been carried out for all systems. Figure 5.2a shows the UV-visible absorption spectra of ZnO (black) indicating peaks at 336 nm corresponds to bandgap ~3.7 eV. However, after Mn-doped (red) there is approximately 10 nm blue shift of

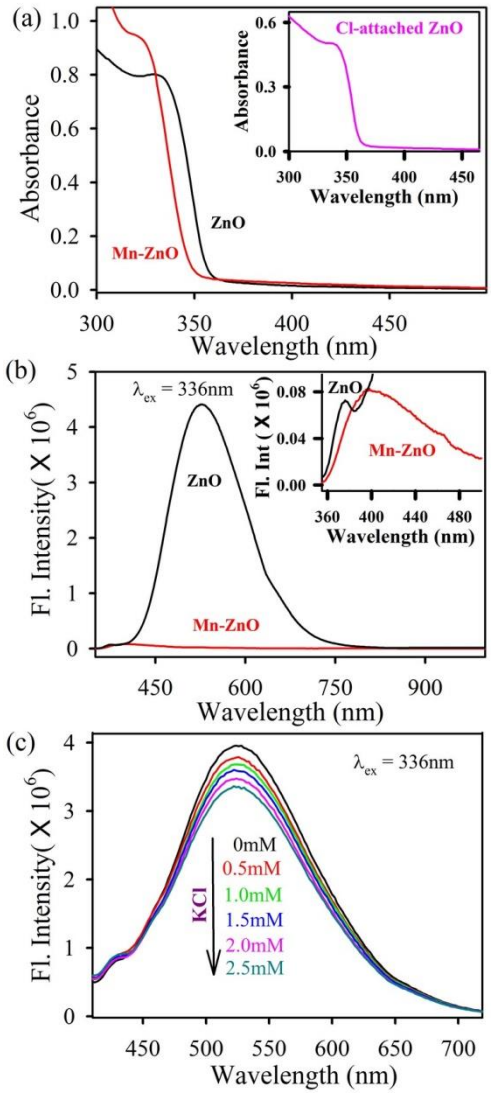

Figure 5.2: *a) Absorption spectra of ZnO (black), Mn-doped ZnO (red). Inset shows the absorption spectra of chloride attached ZnO. b) Emission spectra of ZnO and Mn-doped ZnO (red) indicate a significant decrease in intensity after doping. Inset shows the bandgap emission spectra of the same samples. The excitation wavelength is 336 nm. c) Depicts the change in emission spectra of ZnO by the addition of increasing concentration of KCl. The excitation wavelength is 336 nm.*

absorption peak. The change in absorption spectra indicates substitutional doping of Mn^{2+} in crystal lattice [33]. On the other hand, there is no clear peak shift in the case of Cl-attached ZnO (inset) which indicates while chloride ions are expected to get attached at the surface of ZnO NP. The modification of the absorption edge towards the blue end of the spectra by Mn doping implies an increase in the bandgap as a result of an increase in the population of all states close to the conduction band [34, 35].

ZnO of size 5 nm shows a very intense and broad emission band in the green region upon excitation above the band-edge (λ_{ex} = 336 nm) which comes due to the defect states found near the surface of the system (Figure 5.2b). The wide emission consists of two bands: one coming from the dually charged vacancy center V_0^{++} at 555 nm (P_2) and the other coming from the single charged vacancy center V_0^{+} at 500 nm (P_1) [1, 36]. Besides, another narrow emission band near the UV region comes due to the bandgap emission. However, the defect state emission intensity of ZnO decreases drastically upon Mn-doping. As Mn^{2+} ion enters inside the lattice of ZnO, it introduces many deep levels of defects inside the bandgap which provide many competitive pathways for electron-hole recombination [37]. Our first principles calculation also reveals the increment of defect states after Mn-doping inside ZnO NP. The inset of Figure 5.2b shows the band-gap emission of ZnO and Mn-doped ZnO. There is very little change in the intensity of bandgap emission. The surface defect emission of ZnO after Cl-attachment has been shown in Figure 5.2c. Increasing the Cl concentration in the system reduces the strength of the green luminescence. The computational calculation also predicts surface attachment of chloride ions reduces the oxygen vacancy states [38]. In addition to that, the introduction of some new non-radiative relaxation pathways due to Cl-attachment can reduce visible luminescence [39]. The fluorescence decay profile of the ZnO NPs and in the presence and absence of dopant ion was obtained upon excitation with 375 nm laser and monitored at 530 nm (Figure 5.3a). The

decrement of the average lifetime of Mn-doped ZnO NPs and Cl-attached ZnO NPs can be ascribed to a significant electronic interaction [37] between ZnO

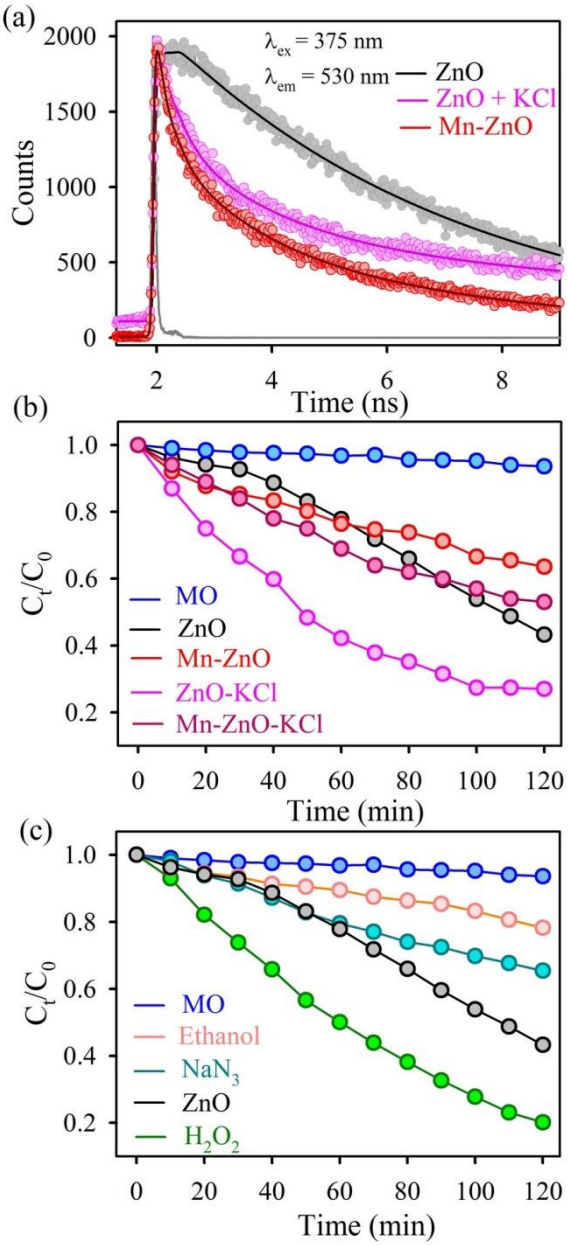

Figure 5.3: *a) The picosecond-resolved fluorescence transients of ZnO (black), chloride attached ZnO (pink) Mn-doped ZnO (red). The excitation wavelength is 375 nm and the decay profile was collected at 530 nm. b) Photocatalytic degradation of MO in the presence of ZnO (black), Mn-doped ZnO (red) Cl attached ZnO (pink) and Cl attached Mn-doped ZnO (dark red) under UV light irradiation. c) Photocatalytic degradation of MO by ZnO (black) and in presence of sodium azide (cyan), ethanol (fade red), and H_2O_2 (green) under UV light irradiation.*

and the corresponding attached ions. An additional faster component of 0.3 ns has been generated in both of the modulated systems, which contributes nearly 50% of the total decay. The electronic cross-talking indeed demonstrates the successful interaction of ZnO either with dopant Mn^{2+} ions or with the surface attached chloride ions. The details of the spectroscopic parameters and the fitting parameters of the fluorescence decays are tabulated in Table 5.1.

***Table 5.1**: Excited state lifetimes of ZnO, Cl attached ZnO and Mn-doped ZnO.**

System	τ_1 (ns)	τ_2 (ns)	τ_3 (ns)	τ_{avg} (ns)
ZnO	_	3.4 (3 %)	5.3 (97 %)	5.3
Cl-attached ZnO	0.3 (41 %)	1.9 (36 %)	14.2 (23%)	4.1
Mn-doped ZnO	0.3 (53 %)	3.4 (42 %)	15.0 (5 %)	2.4

**The values in parentheses represent the relative weight percentages of the time components. PL emissions were detected at 530 nm upon excitation at 375 nm.*

To manifest the interfacial charge transfer dynamics in the modulated ZnO, we have studied the photocatalytic activity of ZnO and its derivative systems. The photocatalytic activity of different systems has been studied under UV light irradiation using methyl orange (MO) as a model pollutant. Cl-ZnO shows much higher photocatalytic activity (~70% degradation in 2 hr.) than pristine ZnO (~55%). On the contrary, Mn-doped ZnO exhibits much lower ~30% MO degradation. As Mn^{2+} ion enters inside the ZnO crystal, it creates lots of defect states inside the bandgap of ZnO, as a result of it the dopant impurities can create large capture cross-section for excitons, which acts as trap states [40, 41]. Further attachment of chloride ion on Mn-doped ZnO, the catalytic activity increased to ~45%. When the chloride ion is attached to the surface Mn-doped ZnO, the trap states are partially healed resulting in increased photocatalytic activity. However, attachment of Cl-ion in ZnO reduces the photoinduced electron-hole recombination rate and excited state electron availability becomes higher, which

subsequently produces (in the presence of oxygen and water) highly oxidative radicals ROS (including h^+, $OH\cdot$, etc), that can degrade the organic pollutants.

To further investigate the reaction mechanism, the effects of ROS scavengers and initiator on the degradation of MO were examined. The effects of a ROS scavenger (sodium azide) and initiator (H_2O_2) on the degradation efficiency of MO are shown in Figure 5.3c. The photocatalytic activity of ZnO reduces to 35% in the presence of sodium azide (NaN_3), whereas the activity increases to 80% in the H_2O_2 environment. These observations indicate that the photocatalytic degradation process follows the ROS mechanism [42]. To obtain further insight regarding the mechanism of change in catalytic activities of ZnO under Mn-doping and Cl-attached ZnO, we have analyzed the electronic structure of ZnO-cluster under various experimentally plausible conditions. We have constructed a $Zn_{50}O_{50}$ cluster in a cubical box of side ~23 Å. The orbital projected (OPDOS) density of states for the optimized $Zn_{50}O_{50}$ cluster in pristine form and presence of different types for oxygen vacancies are plotted in Figure 5.4 (a, b and c), herein, studied the influence of surface and core oxygen vacancies. For bulk ZnO, where Zn^{2+} with valence configuration $3d^{10}4s^0$ is in tetrahedral coordination with O^{2-} ligands ($2s^22p^6$), there is a band-gap of ~3.3 eV. Nevertheless, there are shallow surface states near Fermi level (E_F) in this ($Zn_{50}O_{50}$ cluster) due to the shift in near-surface coordination and surface reconstruction, which constitute partially unfilled Zn-3*d* and O-2*p* levels of the Zn and O surface atoms. However, in this ($Zn_{50}O_{50}$ cluster), due to the change of coordination near-surface and surface reconstruction, there are shallow surface states near Fermi level (E_F), constituting partially unfilled Zn-3*d* and O-2*p* levels of surface Zn and O atoms. The theoretically obtained bandgap of ZnO nanocluster is approximately ~0.8 eV (shown in Figure 5.4a), which is well-known to be underestimated for density functional calculations. However, a scaling of the theoretical value of band-gap to

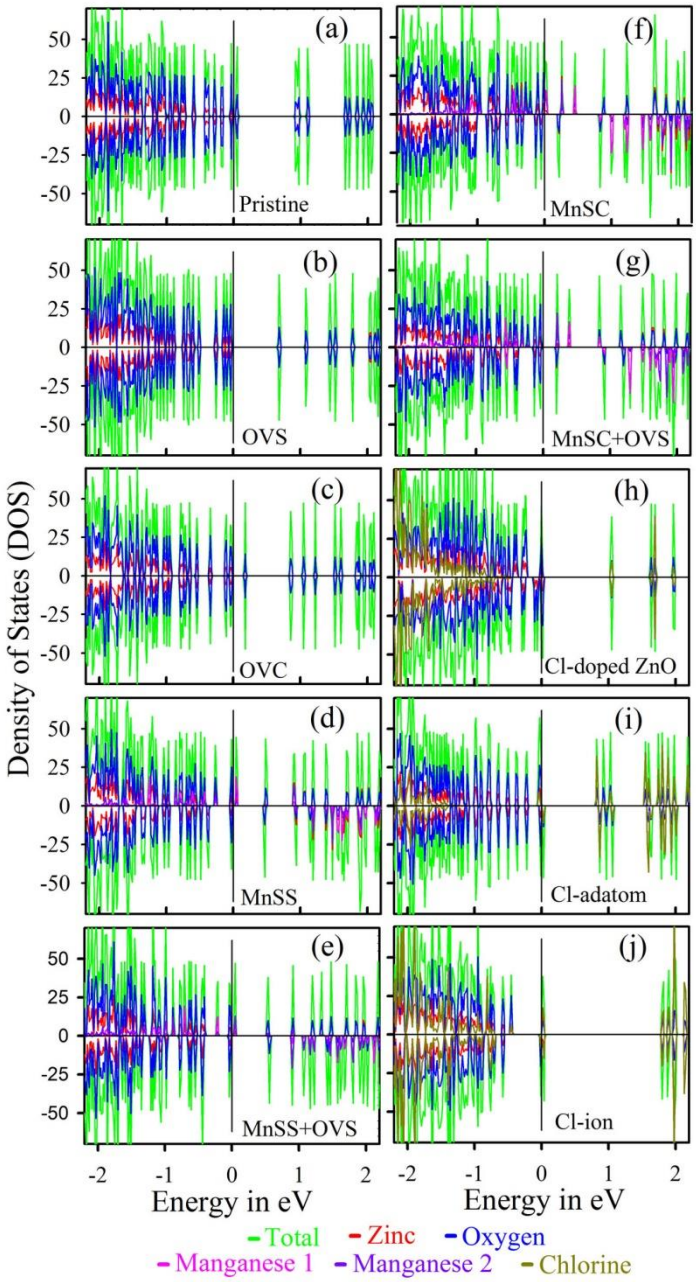

Figure 5.4: *Atom (APDOS) and orbital projected (OPDOS) density of states of a) ZnO Nanocluster, b) ZnO Nanocluster with oxygen vacancy on the surface (OVS), and c) ZnO Nanocluster with oxygen vacancy in the core (OVC). Mn-doped ZnO; d) both of the Mn is on the surface (MnSS), e) both of the Mn is on the surface with the nearest neighbor oxygen vacancy on the surface (MnSS+OVS), f) one Mn is on the surface and another one is in the core (MnSC) and g) one Mn is on the surface and another one is in core with the nearest neighbor oxygen vacancy on the surface (MnSC+OVS). h) Cl-attached ZnO Nanocluster, i) ZnO Nanocluster with oxygen vacancy on the surface, and a nearby Cl-adatom, and j) ZnO Nanocluster with oxygen vacancy on the surface and a nearby Cl-ion. The DOS is plotted for all Zn-3d and all O-2p levels.*

the experimentally obtained value (3.3 eV) may provide a quantitative estimate of the position of various orbital states. However, a qualitative comparison with all feasible experimental conditions also helps one to estimate the existence of shallow levels and deep trap states in the system. We have further investigated the role of several oxygen vacancies in the ZnO system i.e. oxygen vacancy in the surface (OVS) or oxygen vacancy in the core (OVC). OPDOS of OVS and OVC is represented in Figure 5.4b and 5.4c respectively. In both of these cases, there is a shift of Fermi-level (E_F) towards the conduction band, signifying *n*-type doping. In addition to that, there are deep trap states within band-gap due to defect, which is apparent from the comparison of Figures 5.4 (a, b and c). It is found that the formation of OVS is energetically stable than OVC, which is very much consistent with the experimental findings. The experimental probability of occurrence for OVS in nano-sized structures is more relevant than that of OVC. It may also be noted that the trap state generated in the case of OVS (Figure 5.4b) is about 2.63 eV (considering the scaling factor as described above) away from the valance band and very much consistent with the experimentally observed P_1 (2.5 eV from valance band) state in the NPs [1]. The charge density distribution of pristine ZnO and ZnO-OVS has been depicted in Figure 5.5a and 5.5b respectively. The reallocation of surface charges in the presence of OVS is apparent from Figure 5.5b.

The effects of Mn-doping in the $Zn_{50}O_{50}$ cluster were further investigated for four such experimentally possible situations, viz. (1) Two Mn (Mn1 and Mn2), substituting two nearest neighbors (*nn*) surface Zn atoms (MnSS); (2) MnSS with nearest neighbor surface oxygen vacancy (MnSS + OVS); (3) Two Mn substituting one Zn at the core and one at the surface (MnSC), and (4) MnSC with nearest neighbor surface oxygen vacancy (MnSC + OVS). We found the formation of MnSS is energetically more favorable than the MnSC (either with or without OVS). In all cases, nearest neighbor Mn-atoms are ferromagnetically aligned. The

corresponding AP and OPDOS for ferromagnetic alignment are plotted in Figure 5.4 (d-g). Due to the high surface reconstruction, the magnetic moments obtained

Table 5.2: *The number of trap states, the position of trap state, and the nature of the trap state of several configurations of ZnO, Mn-doped ZnO, and chloride attached ZnO.*

System	No. of Trap State	Position of Trap state (eV)	Nature of trap state
ZnO pristine	-	Nil	Nil
ZnO + OVS	1	0.63	Surface defect
ZnO + OVC	1	0.24	Surface defect
MnSS	1	0.37	Deep
MnSS + OVS	1	0.41	Deep
MnSC	4	0.12, 0.16, 0.36, 0.72	Deep
MnSC + OVS	2	0.15, 0.35	Deep
Cl-attached	1	0.93	Deep
Cl-ad atom	0	Nil	Shallow acceptor
Cl-ion	0	Nil	Shallow acceptor

by Mn1 and Mn2 are also higher for surface Mn atoms. The Mn-doped experimental systems would be essentially a mixture of all four of the above configurations. For MnSS cases, the relative shift of E_F is towards the conduction band, indicating an *n*-type charge transfer from Mn1 and Mn2 -3*d* levels to Zn-3*d* and O-2*p* empty states. Highly hybridized Mn1 and Mn2-3*d*, Zn-3*d* and O-2*p* states manifest the charge transfer (shown in Figure 5.4d and 5.4e and also from the corresponding charge-density plot in Figure 5.5c and 5.5d). On the other hand, there is *p*-type doping and a reverse charge transfer from Zn-3*d* filled states to Mn-3*d* levels for MnSC cases, as can be seen from Figure 5.4f and 5.4g. Another important aspect of Mn doping within the ZnO cluster is the introduction of many deep label traps states (for all four probable cases) within the conduction band and valance band as depicted in Figure 5.4 (d–g). Such deep trap states absorb carriers and operate as recombination generation centers, thereby reducing photocatalytic activity, which has also been experimentally found. The details of trap states are tabulated in Table 5.2. To model carrier trapping, we made a total energy

comparison for MnSS and MnSC cases, after increasing the total number of electrons in the system. An increase in the number of electrons raises the total energy of the system, which suggests the stability of the system decreases with an increased number of carriers.

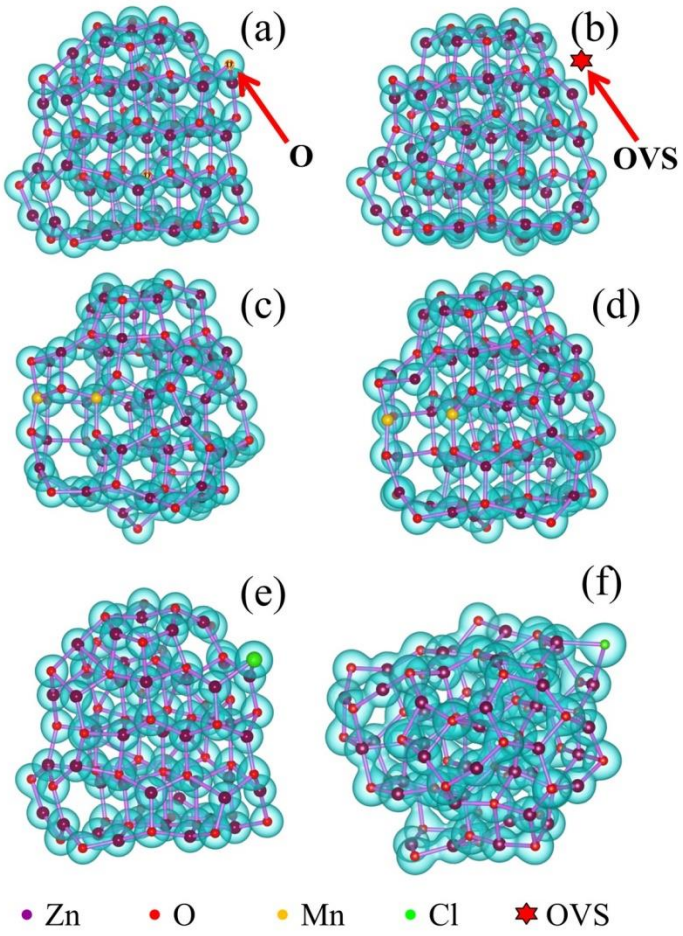

Figure 5.5: *Charge density plot of a) ZnO Nanocluster, b) ZnO Nanocluster with Oxygen vacancy on the surface, c) MnSS d) MnSS+OVS e) ZnO Nanocluster with oxygen vacancy on the surface and a nearby Cl-adatom, and f) ZnO Nanocluster with oxygen vacancy on the surface and a nearby Cl-ion. Magenta and red indicate Zinc and Oxygen respectively. Yellow and green indicate Mn atoms and Cl atom respectively. The red star symbol stands for oxygen vacancy state at surface.*

To understand the increased photocatalytic activities for chloride attached systems, we have considered three situations, viz., (1) Cl-atom substituting an O-atom on the surface of $Zn_{50}O_{50}$ cluster, (2) Cl-adatom near an OVS on the same cluster, (3) Cl-ion near an OVS on the same cluster. All the above-mentioned cases

show *p*-type doping in the ZnO cluster, where the E_F is shifting towards the valence band. The OPDOS of different Cl-based systems are plotted in Figure 5.4 (h-j). Cl-ion near an OVS shows the highest *p*-type doping. In case (1), there is very little charge transfer from the surface of Zn-3*d* and O-2*p* to Cl-3*p*, which produces very little magnetic moment (0.3μ_B) within the system. This is due to partial filling of the unfilled surface states of pristine ZnO nanocluster which is generated as a result of surface reconstruction after geometrical optimization. For case (2) and (3), in presence of an OVS, both the Cl adatom and Cl^- ion settle at the OVS place, and chemical bonding have been generated with the nearest Zn atoms. This means that surface oxygen vacancies can be suitable for Cl-doping sites within the cluster. In these two cases, the Cl-3*p* induced shallow acceptor levels are produced very close to the valence band (within ~0.1 eV). These acceptor levels are strongly hybridized with the levels Zn-3*d* and O-2*p*, implying a partial exchange

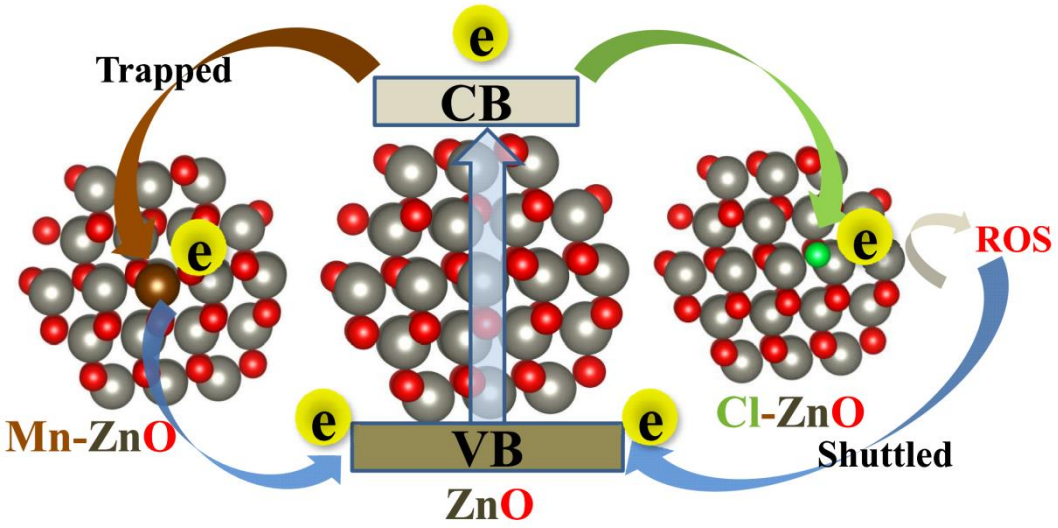

Scheme 5.1: *Schematic representation of various electron shuttling pathways in structurally modulated ZnO nanostructure leading to dissimilar photocatalytic activity.*

of the charge from those levels to Cl-3*p*. Surface charge rearrangement will be also apparent from the charge-density plots as shown in Figure 5.5e and 5.5f for cases (2) and (3) respectively. Case (3) shows the highest magnetic moment among all other cases (0.8 μ_B), due to a higher amount of charge transfer. Moreover, this

configuration is energetically most favorable condition. The existence of shallow acceptor levels and the absence of deep trap-states for Cl-attached systems could be the underlying cause behind the increase in photocatalytic activity in the Cl-attached ZnO system. All these three cases, contrary to the Mn-doped system, acquire better stability with the increase of the total number of electrons within the system.

5.2.2. Halide Modulated Functionality of Wide Bandgap Zinc Oxide Semiconductor Nanoparticle [43]: In the previous work, we investigated the role of Cl-ion towards healing the surface defect of ZnO NP. This motivates to investigate the interaction of ZnO with other halide ions. Herein, we have modulated the surface of synthesized ZnO NP with different halide ions (namely Cl, F, I).

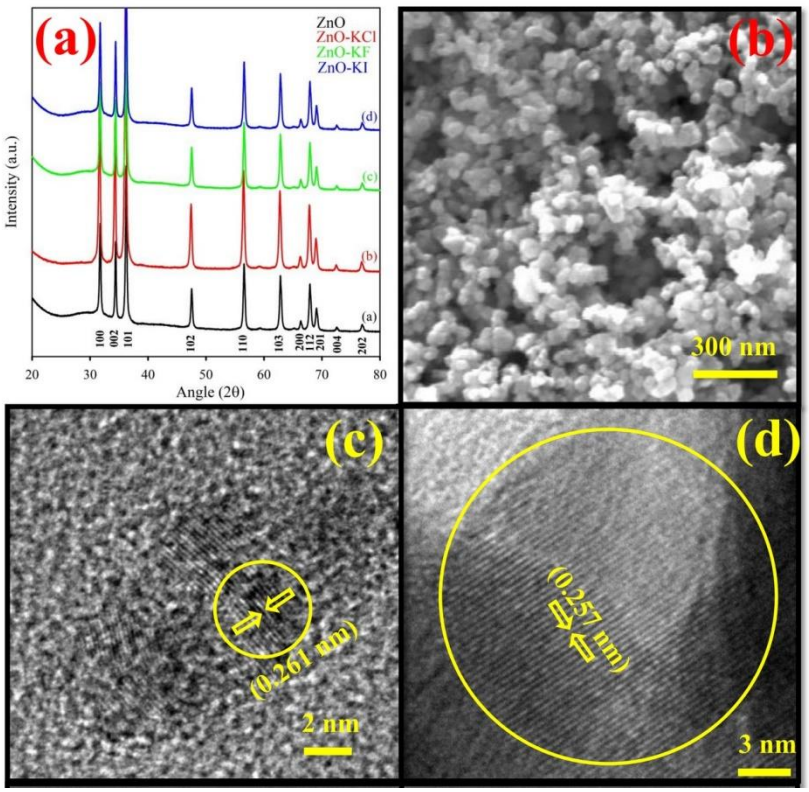

Figure 5.6: *a) XRD image of pristine 30 nm ZnO NP and other halides ZnO-NP, b)SEM image of ZnO NP, HRTEM images of c)5nm ZnO NP d)30 nm NP.*

Figure 5.6a shows the XRD image of ZnO NP and other halide-ZnO NP [44]. All the XRD peaks are well-indexed to the hexagonal wurtzite pattern. No other impurity peaks are observed, which confirms that the growth of the sample is a single-phase. There is no impurity phase generated after halide ion treatment on ZnO NP. The morphology of as-synthesized ZnO NP is shown in Figure 5.6b, acquired using FESEM. The synthesized ZnO NP is homogeneous and spherical. The clear crystal lattice of ZnO NP (of different sizes) as obtained from high-resolution transmission electron microscopy confirms the good crystallinity of the NP. Figure 5.6c and 5.6d show typical HRTEM images of ZnO NPs of size 5 nm and 30 nm respectively, with spherical morphology. We have calculated the fringe widths of 5 nm and 30 nm ZnO system, which are 0.261 and 0.257 nm respectively, corresponds to (002) plane of ZnO crystal [45].

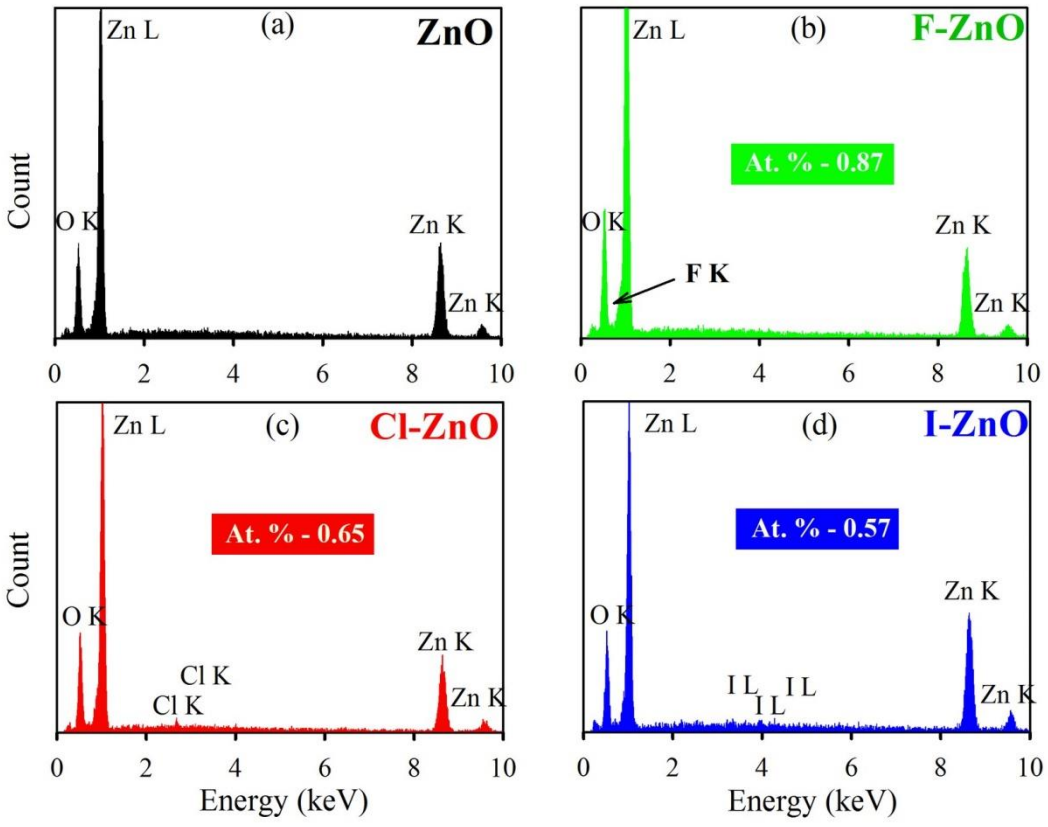

Figure 5.7: *The energy-dispersive X-ray spectroscopy (EDS) spectrum of a) pure ZnO, b) F ZnO,c) Cl-ZnO and d) I-ZnO.*

Next, to confirm the presence of different halide ion in the system, we have carried out energy dispersive analysis of X-rays (EDAX) over a selected area of the ZnO NP and halide-ZnO NP. The EDAX image of all systems is depicted in Figure 5.7. We found, 0.87 atomic % of F is attached to ZnO whereas 0.65 and 0.57 atomic % of Cl and I respectively, have been attached to ZnO NP. To further confirm the homogeneity of the system, energy dispersive mapping has been done for all systems. Figure 5.8 shows the EDS-mapping of halide-ZnO systems, which shows that all the elements are uniformly distributed within the systems.

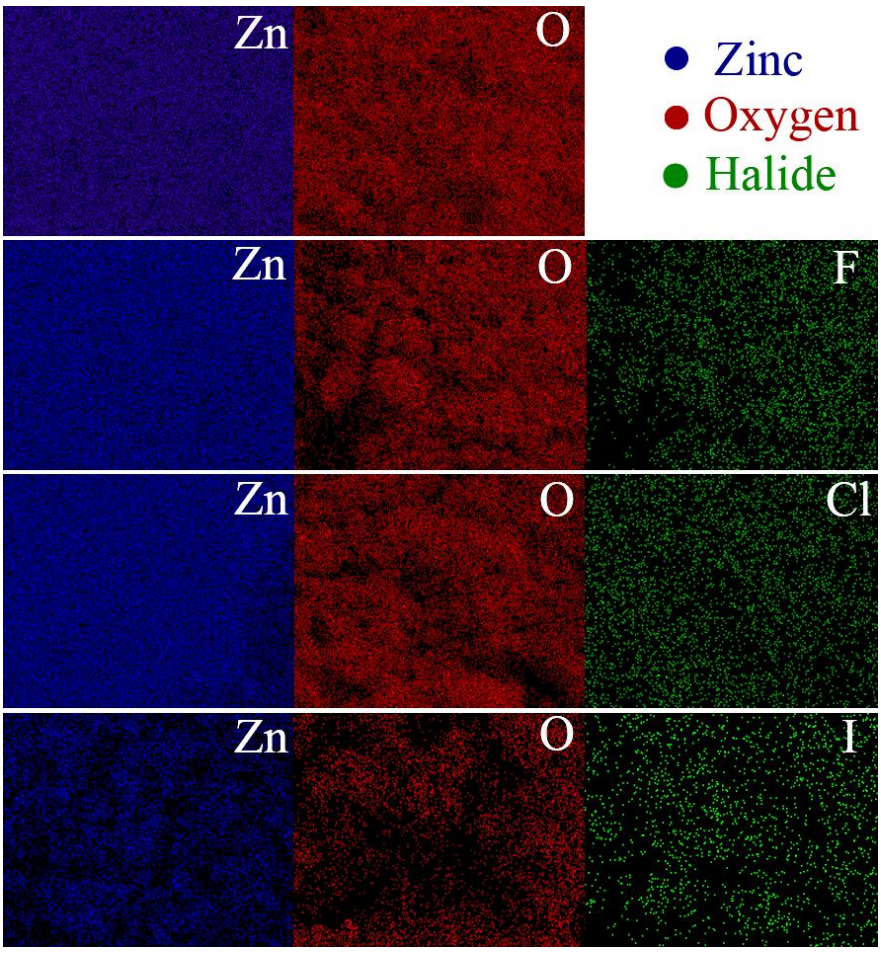

Figure 5.8: *Elemental mapping of NPs: a) pure ZnO, b) F-ZnO,c) Cl-ZnO and d) I-ZnO.*

Figure 5.9a corresponds to the UV-Vis absorbance spectra of 5nm ZnO NP and halide-ZnO NP. The absorption peak of ZnO NP is found around 350 nm [46] corresponds to the bandgap of 3.5 eV. Halide-ZnO NP absorbance peaks are also

found to be approximately 350 nm. Upon halide attachment in the ZnO NP, a small change in the absorption band (~2-4 nm) is observed without altering the basic shape and strength of the spectra. This shift in absorption spectra comes due to the change of the electronic structure of ZnO upon the interaction with halides on the surface. Halide treatment on ZnO modulates the surface states of ZnO NP and generates new states near the band edge, which is highly hybridized by Zn- *d* orbital with O- *p* orbital and halide *p* orbital. These additional states eventually alter the optical bandgap of the modified systems. Figure 5.9b shows that the absorbance of ZnO NP and halide-ZnO NP of size 30 nm. The pure ZnO NP shows an absorption peak at 376 nm which corresponds to a bandgap of ~3.3 eV [47] which is lesser than of ~5 nm NP as expected. Inset shows the enlarged view of the bandgap region which reveals very little change in bandgap for halide-ZnO NP.

We further checked the stability of the systems in an aqueous medium. To study the solubility of ZnO NP before and after surface modification, the UV-Vis absorption peak maxima (λ = 376 nm) of the ZnO (of size ~30 nm) is monitored in kinetic mode for 30 min. Figure 5.9c shows the relative solubility study of ZnO and halide-ZnO systems in an aqueous medium. It is observed that ZnO modulated with halide ion shows greater stability in the aqueous medium compared to pure ZnO NP. After 30 min, only 6% of F-ZnO and 9% of Cl-ZnO are precipitated from the water in comparison to pure ZnO (54%). To investigate the increment of solubility we have studied the first principles DFT calculations of the systems. It is found that halide ion attachment in the system increases the polarity of the system. Due to the high polarity of halide, the treated ZnO surface became hydrophilic. The grafting of halide ions on the surface of ZnO NP will cause repulsive force between NPs, thereby preventing the aggregation of modified ZnO NP in water.

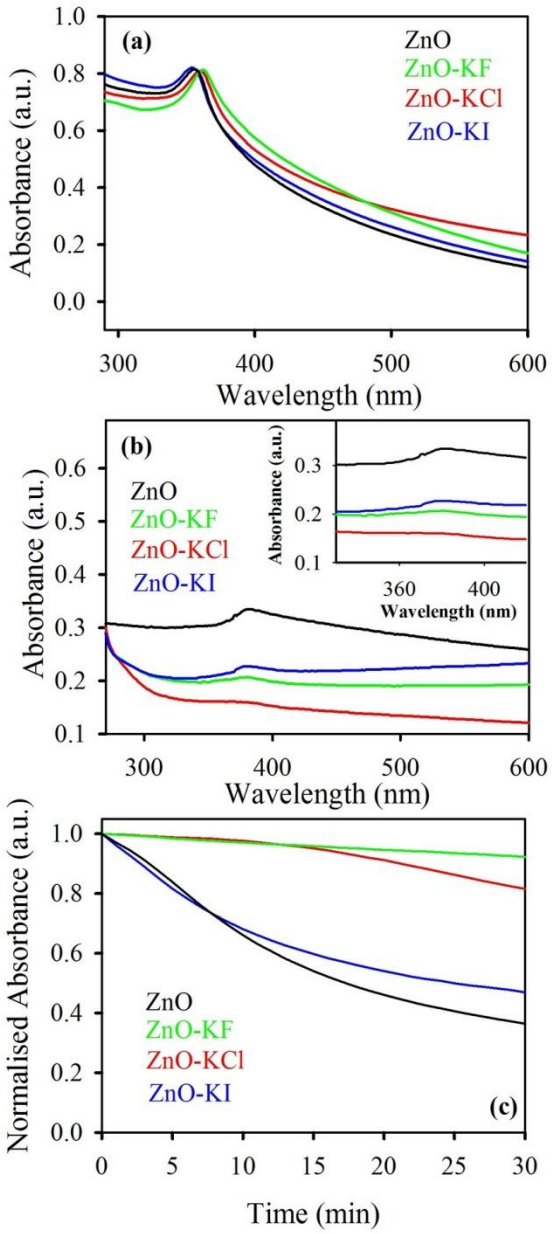

Figure 5.9: *a) UV-Vis absorbance of 5nm ZnO NP and halide-ZnO NP, b) UV-Vis absorbance of 30 nm ZnO NP and halide-ZnO NP, inset shows the enlarged view of the band-gap region, c) stability of ZnO and other halide-ZnO from the absorbance at 376 nm in the water at 30 min. time window.*

Figure 5.10a displays the room temperature fluorescence spectra of ZnO NP (of size ~5 nm), upon excitation at bandgap. As we have discussed earlier, it is well known that ZnO NP exhibits dual emission in the ultraviolet and visible regions when excited by their bandgap energy. Direct band to band

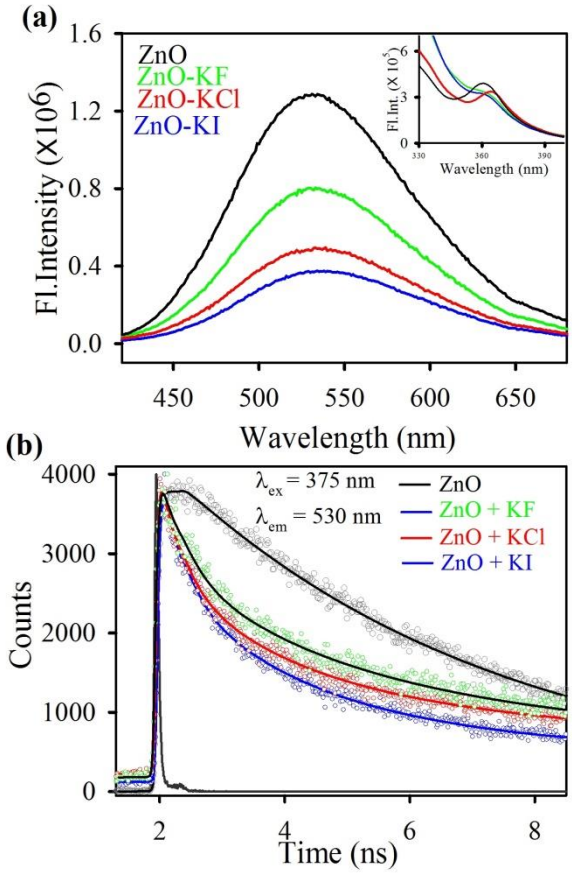

Figure 5.10: *a) Room-temperature emission spectra of ZnO NP and halide-ZnO NP, the excitation wavelength was 375 nm (inset shows band-band emission of the NPs), b) the picosecond resolved fluorescence transient of ZnO NP and halide ZnO NP are shown. The excitation wavelength was 375 nm and the collection wavelength was 530 nm.*

emission occurs due to the recombination of excitonic centers in ZnO, which was also observed in both ZnO NP and halide-ZnO NP at around 395 nm. There is a slight shift in bandgap emission after halide attachment on ZnO NP (inset of Figure 5.10a). Due to surface defects, another broad emission band is observed in the blue-green region, with a peak near 530 nm [48, 49]. Incorporation of halogen ions at the surface of ZnO resulted in significant fluorescence quenching. After halide treatment of ZnO NP, halide dopants usually occupied O-related defects in the ZnO matrix (such as O-vacancy or replacement of O_2^- lattice ions) leading to a reduction in surface defects. As a result of it, a heavy reduction of defect state emission intensity occurs in the halide-ZnO system [38] (shown in Figure 5.10a).

The fluorescence quenching is maximum in the case of iodide and lowest in fluoride. However, although the I-ZnO system shows fluorescence quenching, this quenching is not coming due to surface defect modulation. Rather, a deep level of trap state has been generated in this particular case. We have elaborately discussed this in the first principal analysis section.

Table 5.3: *Excited state lifetimes of ZnO and halide-ZnO. PL emissions were detected at 530 nm upon excitation at 375 nm. The values in parentheses represent the relative weight percentages of the time components. PL emissions were detected at 530 nm upon excitation at 375 nm.*

System	τ_1 (ns)	τ_2 (ns)	τ_3 (ns)	τ_{avg} (ns)
ZnO	-	3.4 (4)	15.3 (96)	5.4
F-ZnO	0.3 (32)	1.5 (31)	9.3 (37)	3.9
Cl-ZnO	0.2 (33)	1.1 (37)	9.2 (30)	3.2
I-ZnO	0.1 (40)	1.2 (35)	7.7 (25)	2.4

The size of the halide ion plays an important role in the defect state emission quenching. The time-resolved fluorescence decay profile of ZnO and different halide-ZnO NP (of ~5 nm) were collected at 530 nm wavelength (shown in Figure 5.10b) using a 375 nm picosecond laser. For all halide-ZnO systems, a new faster component of ~0.2 - 0.3 ns is generated. The detail of the spectroscopic and fitting parameter of excited state decay is listed in Table 5.3. The reduction in the average lifetime of halide-ZnO comes due to mutual charge transfer between NP and halide ions. The excited state quenching decay pattern of halide-ZnO resembles the ground state quenching pattern.

We have studied the photoelectrochemical (PEC) activity of ZnO to get information on photoinduced hydrogen generation in presence of light. The PEC efficiency of ZnO NP, in the electrolytic medium, is performed using a periodically chopped UV-visible light. Figure 5.11a shows the linear sweep voltammetry (LSV) result of ZnO with a potential bias varying from -0.4 V to 1 V (versus Ag / AgCl) with intermittent illumination of light, suggesting substantial

photo-activity of ZnO against water oxidation [50]. The maximum obtained photocurrent to be 0.4 mA/cm^2, appeared at 0.8 V bias which arises due to water oxidation reaction at the photoanode. The chronoamperometric plot of the ZnO

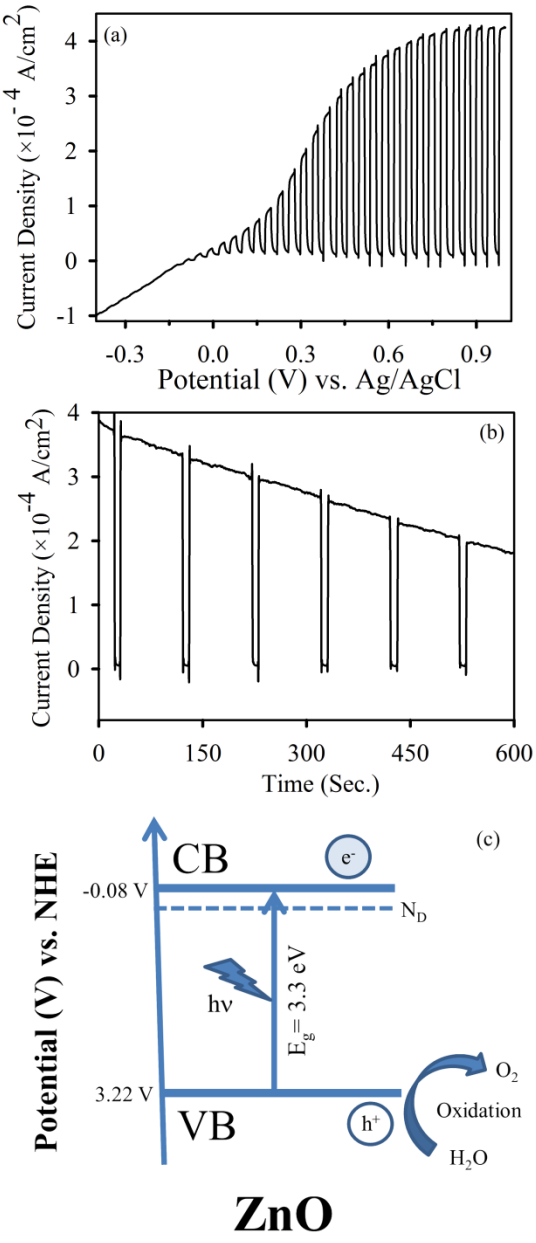

Figure 5.11: *a) Linear sweep voltammetry of ZnO electrode in 0.1 M Na_2SO_4–PBS buffer (pH 7) solution (for water oxidation) under UV-Vis light (intensity: 100 mW /cm^2). b) Current-time response (chronoamperometry) curve of the ZnO electrode at an applied potential of 0.8 V. c) Schematic representation of the band-alignment of ZnO nanostructure. This band-alignment allows for a better water oxidation reaction.*

thin film under a constant light illumination is depicted in Figure 5.11b. ZnO NP shows a fairly stable behavior for the PEC water oxidation reaction [51, 52]. The host semiconductor ZnO produced approximately 9.3 µmol of oxygen in 10 min., which is higher than previously reported literature [53, 54]. This type of higher production rate of the system can be very beneficial in practical water purification purposes [55]. Figure 5.11c depicts the schematic energy band diagram of ZnO, which reveals that the conduction band (CB) position at -0.08 V and that of the valence band (VB) at +3.14 V, measured at pH 7 working solution. Pourbaix water diagram reveals that the redox potential of the photoexcited electron isn't enough ($H_2O \rightarrow H_2$, E_0 = -0.410 V, in pH 7 condition) to inaugurate the photoelectrochemical H_2 evaluation reaction [56]. On the other side, the redox potential of the photo-generated holes (+3.14 V) is large enough to cause the water oxidation reaction (H_2O often O_2, E_0 = +0.80 V) at pH 7.

This result motivates us to further investigate the photocatalytic activity of the ZnO NP and halide-ZnO NP. We have studied the photodegradation of ZnO NP and halide-ZnO NP using MO as a model pollutant in the presence of UV light (< 380 nm). The detailed photocatalytic mechanism of ZnO can be explained stepwise [57-59]: at first, the organic pollutant is dispersed in the aqueous medium and comes into contact with the surface of the photocatalyst. Photo-induced electron-hole pair (e^-/h^+) is produced on ZnO NP in presence of light. This tremendously reactive e^-/h^+ pair produces hydroxyl radicals (•OH) and superoxide ($O^{2-\bullet}$) radicals respectively using redox reaction. The superoxide radical forms H_2O_2 which produces extremely reactive oxidizing agent hydroxyl radical (E^0 = +3.06 V) which destroys the contaminant dye molecules adsorbed at the ZnO surface and produces a various intermediate compound, which is finally converted to CO_2, H_2O, and other harmless products. However, the biggest disadvantage of ZnO as a photocatalyst is the rapid recombination rate of the photoexcited electron-hole pair and defect mediated photoexcited electron

capturing which reduces the photocatalytic degradation rate [57]. We attach halide on the surface of the ZnO NPs to resolve such disadvantages. The halide ion works similarly to the ZnO semiconductor that Au nanoparticle serves with the ZnO or TiO_2 [60, 61]. Halides are attached to the surface of the ZnO NP, shuttles the photo-excited electrons, and prevents it from being captured by the defect state of the ZnO NPs. The combination of those two effects leads to a reduction in the excited state electron-hole recombination process and the excited state electrons become more available, which results in higher photocatalytic efficiency.

A comparative study of the photocatalytic activity of the F-ZnO NP, Cl-ZnO NP, and I-ZnO NP for degradation of MO with respect to ZnO NP shows that F-ZnO, Cl-ZnO, and I-ZnO degrades 70%, 76%, and 50% MO respectively in 2hr. in comparison to control ZnO (~55%). When halide ions are attached to ZnO, the surface defect state of ZnO NP decreases, subsequently the photocatalytic activities of the system increased. It is found from fluorescence spectroscopy, that the quenching of the defect state emission of Cl-ZnO is higher than that of F-ZnO, which indicates that Cl-ZnO can restore the surface defect of ZnO NP higher than F-ZnO, thus Cl-ZnO exhibits greater catalytic activity than F-ZnO. However, we found I-ZnO shows a decrement in photocatalytic activity. In other cases halides (Cl, F) acquired the excited electrons from ZnO and shuttles it to the medium that enhances the overall catalytic activity, but in the case of I-ZnO, the electron is trapped and becomes unavailable. As iodine has the highest ionic radius and lowest electron density among the other stable halides, it can take the excited electron from ZnO and trap it to its surface, and the electron became inaccessible for catalytic reaction, which results in no increment in photocatalytic activity [62].

We also explored the photocatalytic behavior of ZnO in the presence of a known radical initiator (H_2O_2) and radical quencher (NaN_3) separately (Figure 5.12b) to explore the catalytic pathway. In the presence of UV irradiation, H_2O_2 increases the generation of $^{\bullet}OH$ which eventually increases the photocatalytic

activity of ZnO. This demonstrates the role of ROS in the degradation of MO. Radical quencher like NaN_3 acts as an efficient electron trapping agent, leading to a decrement of photocatalytic activity. The overall photocatalytic efficiency of ZnO is reduced after adding NaN_3, whereas efficiency is increased to 80% in the presence of H_2O_2. This result indicates that the photocatalytic process follows the ROS generation mechanism [63].

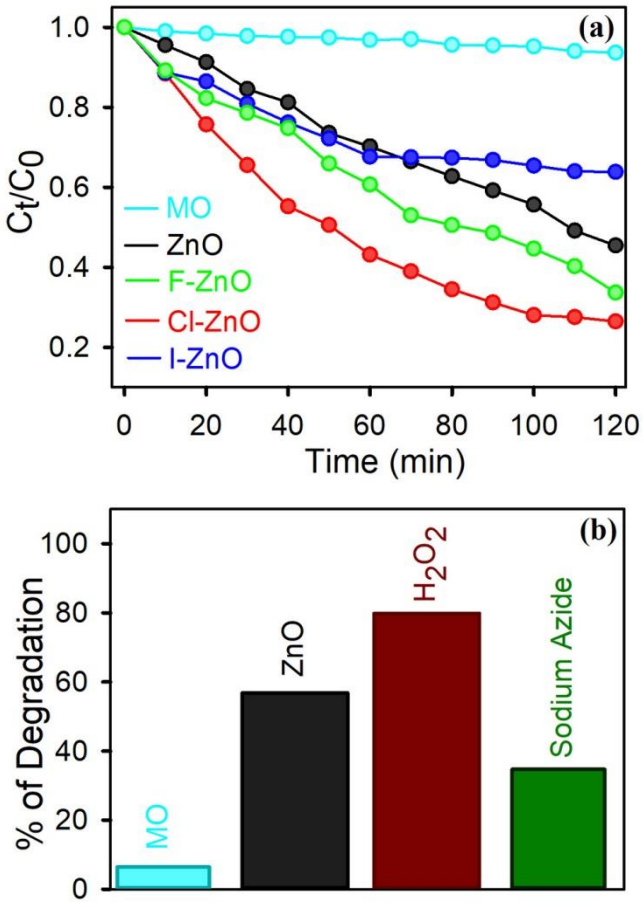

Figure 5.12: *a) Photocatalytic degradation of MO by ZnO and halide-ZnO under UV light irradiation, b) Photocatalytic degradation ZnO in the presence of H_2O_2 and NaN_3 under UV light irradiation.*

To better understand the role of the semiconductor and the dye (methyl orange) in the photocatalytic degradation process, the photocatalytic experiment was conducted at various wavelengths keeping other parameters unchanged. Figure 5.13a shows the photocatalytic performance of ZnO and Cl-ZnO under

different wavelengths for 1 hr. light exposer. It is seen from the action spectra that the photocatalysis process mainly occurs via bandgap excitation (~375 nm) of the semiconductor. The rate of catalytic activity starts decreasing gradually, upon excitation of lower energy than the bandgap of the semiconductor. Insignificant photocatalysis activity at the wavelength 460 nm (at MO absorbance maxima) indicates that photocatalysis is not influenced by the pollutant dye MO [64].

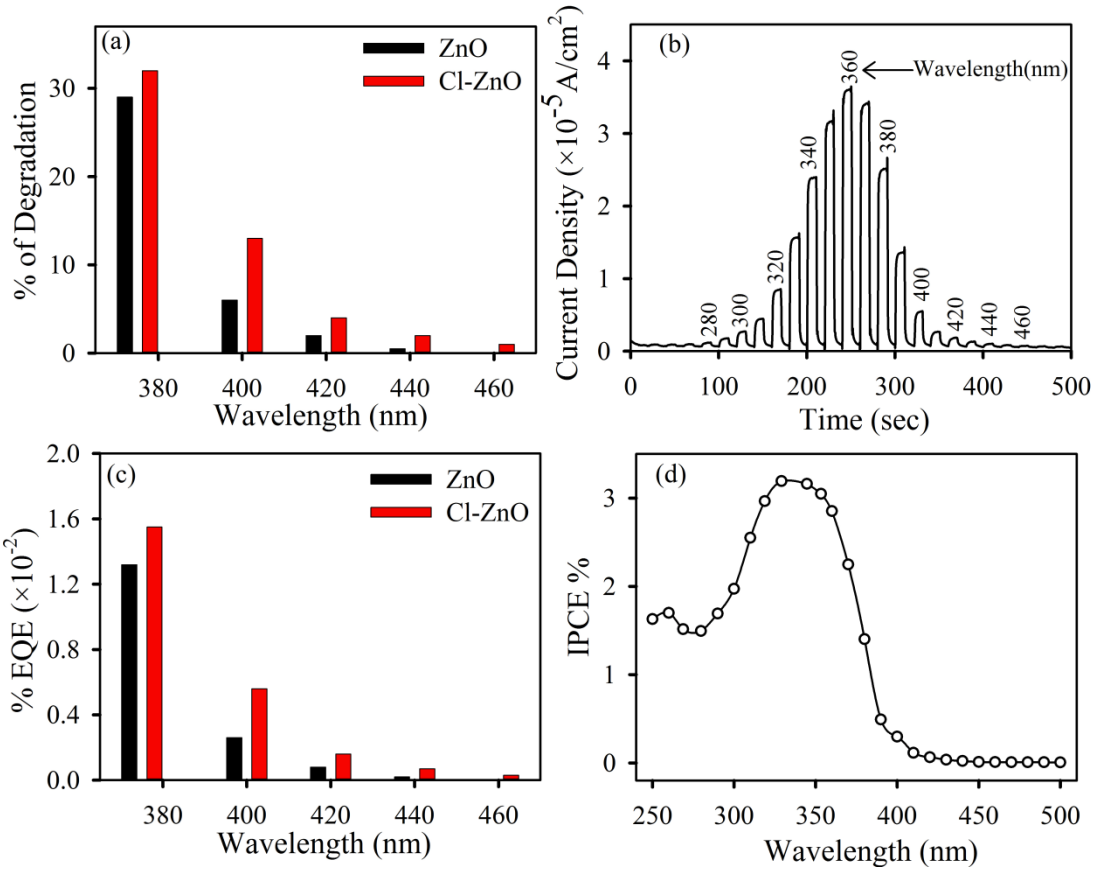

Figure 5.13: *a) Wavelength dependent photocatalytic activity of ZnO and Cl-ZnO b) action spectra of ZnO in 0.1 M Na_2SO_4–PBS (pH 7) at applied potential 0.8 V vs. Ag/AgCl reference electrode, c) external quantum efficiency of ZnO and Cl-ZnO, and d) % IPCE of ZnO in 0.1 M Na_2SO_4–PBS (pH 7) at applied potential 0.8 V vs. Ag/AgCl reference electrode.*

Figure 5.13b displays the PEC action spectra of ZnO (for water oxidation reaction), as measured from the photocurrent spectrum at varying wavelengths (from 250 nm to 500 nm). The wavelength-dependent photocurrent measurement is useful to determine the onset wavelengths of the photocatalyst for the

degradation of the organic compounds. The appearance of photocurrent at ~410 nm in the PEC action spectra indicates the photoelectrochemical or 'true' bandgap of the semiconductor as 3.02 eV. The highest value of the photocurrent happens at the bandgap excitation (360 nm) of the semiconductor demonstrating photocatalysis predominantly occurs due to the bandgap excitation of the ZnO.

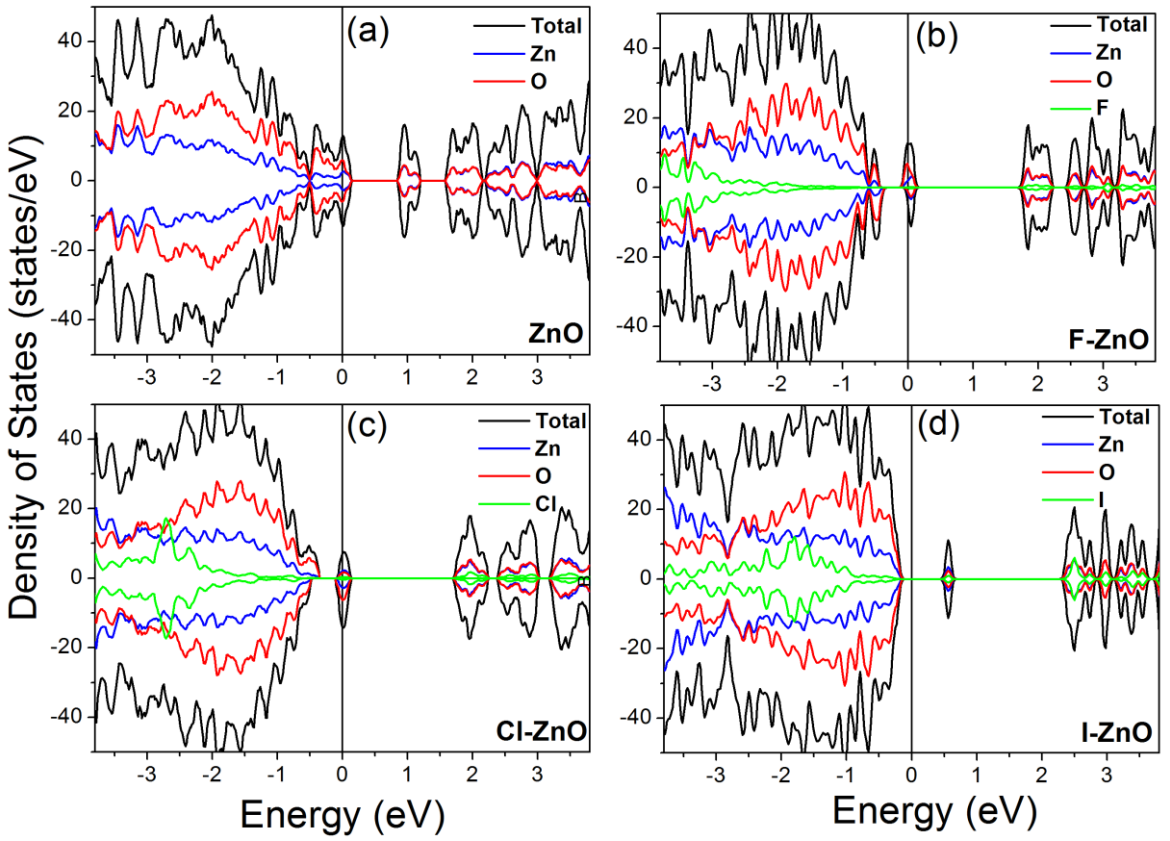

Figure 5.14: *Orbital projected (OPDOS) and atom projected density of states (APDOS) of the systems a) ZnO OVS b) F-ZnO, c) Cl-ZnO, and d) I-ZnO.*

We further simulate different experimental situations using density functional theory to probe the inside of catalytic reactions for different systems. A $Zn_{50}O_{50}$ cluster is taken and various halide ions are attached to it. We studied the electronic change of cluster after different halide ion attachment. The presence of surface oxygen vacancy (OV) during synthesis is a very eminent experimental fact for ZnO NP. In the previous work, we have already shown using theoretical modeling that, the formation of surface OV is energetically much stable than core

OV [29]. As we already discussed in the experimental section, the halide ions introduced in the system settle close to the surface of the OV and create bonding states with the nearest neighbor (nn) Zn ions. Here, we have compared the electronic structure of the $Zn_{50}O_{50}$ cluster with a surface OV with a single negatively charged F, Cl, and I ions. In bulk ZnO, Zn^{2+} with valence configuration $3d^{10}4s^0$ is in tetrahedral coordination with O^{2-} ligands ($2s^22p^6$), there is a band-gap of ~3.3 eV. The atom and orbital projected density of states (DOS) are plotted in Figure 5.14 for (a) $Zn_{50}O_{49}$ cluster (with OV) and with (b) F^-, (c) Cl^-, (d) I^- ions near-surface OV.

It is observed that many surface states have been generated near Fermi level, in the $Zn_{50}O_{49}$ cluster, constituting partially unfilled Zn-3*d* and O-2*p* hybridized levels of surface Zn and O atoms. These states come due to the alteration of tetrahedral coordination near the surface edge of ZnO due to surface rebuilding. We found the bandgap ~0.8 eV, which is well-known to be underestimated for ground-state DFT calculations [65]. Due to 2*p*-3*d* hybridization of the Zn^{2+} ion nn to the OV with the neighboring O^{2-} ions, minimal spin polarization, and substantial low moment generated by the nn ions to the surface OV. After halide ion attachment near OV, there is a generation of *n*-type doping of the $Zn_{50}O_{49}$ cluster which indicates electron comes from halide to the ZnO system. It is observed that the amount of *n*-type doping is the maximum for the Cl-ZnO system among all. For F^- and Cl^-, strong orbital hybridization of Zn-3*d*, O-2*p* and F-2*p*/Cl-3*p* states results in partially filled spin-polarized levels at E_F. The calculated bond lengths for different halide ions with the nn Zn ion are F^- (2.07 Å), Cl^- (2.29 Å), and I^- (2.55 Å), bearing the correct trend of being larger for larger ionic radii. The Zn-F and Zn-Cl bond-lengths are close to the Zn-O bond length (1.97 Å). As I^- has a larger ionic size, it does not settle at the surface OV place easily. Also, among these three, due to the large Zn-I bond distance, I^- have the lowest charge sharing with nn Zn. Thus, the presence of I^-, unlike other halide ions, only has

contributions in the antibonding regime, resulting in deep trap-states. Thus I^- has almost no role in healing surface defect of ZnO, rather it generates more deep level trap states. Although F^- has the lowest Zn^{2+}-F^- bond distance, it has a lesser electron affinity than Cl^- due to its smaller ionic radii. Moreover, screening effects are also stronger for larger ionic radii. As a result, Cl-3*p* levels hybridize more asymmetrically with the Zn-3*d* and O-2*p* than F-2*p*. This results in higher spin-polarization and ionic moment for Cl-ZnO, which follows the experimental trends. We found the ionic moments and photocatalytic activities of Cl-ZnO are higher than F-ZnO, whereas the deep gap states present in I^- attached system acts as carrier-trap leading to less photocatalytic and magnetic activity.

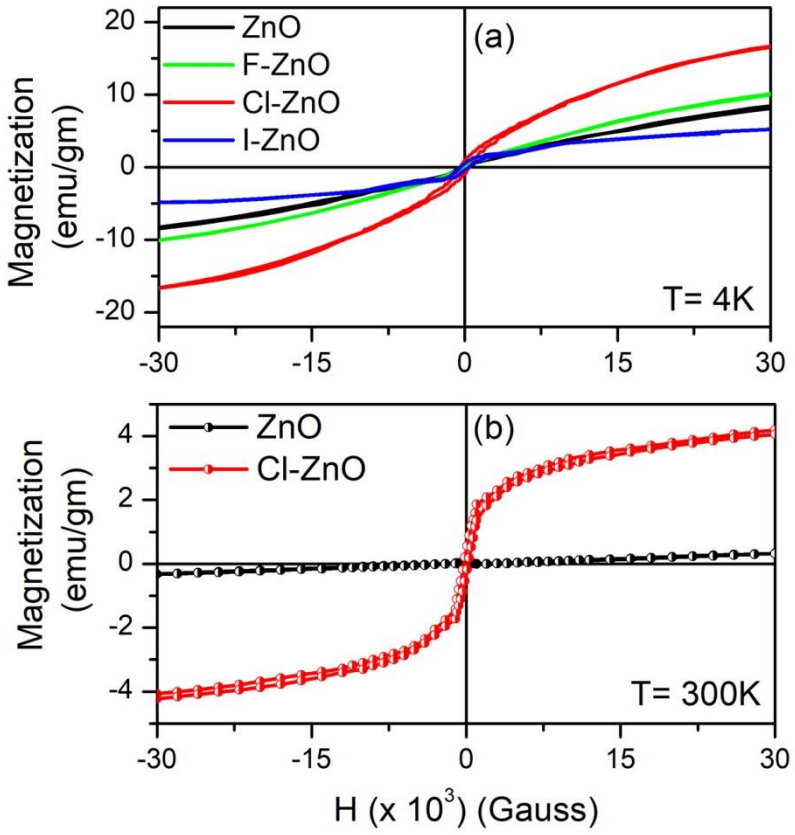

Figure 5.15: *a) Mass normalized M-H curves of ZnO NP and halide-ZnO at 4K. b) M-H loops with the mass-normalized magnetization value of ZnO and Cl-ZnO at room temperature.*

For the realization of different potential devices in oxide-based diluted magnetic semiconductor systems, the occurrence of long-distance ferromagnetic

ordering has been extensively studied. According to the previously reported literature, it can be observed that the magnetic moment of ZnO NP is negligible, which is caused by surface defects (such as surface OV) [66]. Many efforts have been done to increase the photocatalytic activity of ZnO NP by modifying the surface of ZnO NP. In the next section, we have investigated the magnetic properties of the halide-ZnO systems. As obtained from the theoretical calculations, due to the increase in the electron affinity of the attached halide ions and the resulting *p-d* hybridization, for the NP attached to the halide, the magnetic moment of the ZnO NP increases [66]. We have measured the magnetic moment of different systems using the SQUID magnetometer. It is found that per ion magnetic moments of the systems match closely to the theoretically obtained magnetic moment values (tabulated in Table 5.4).

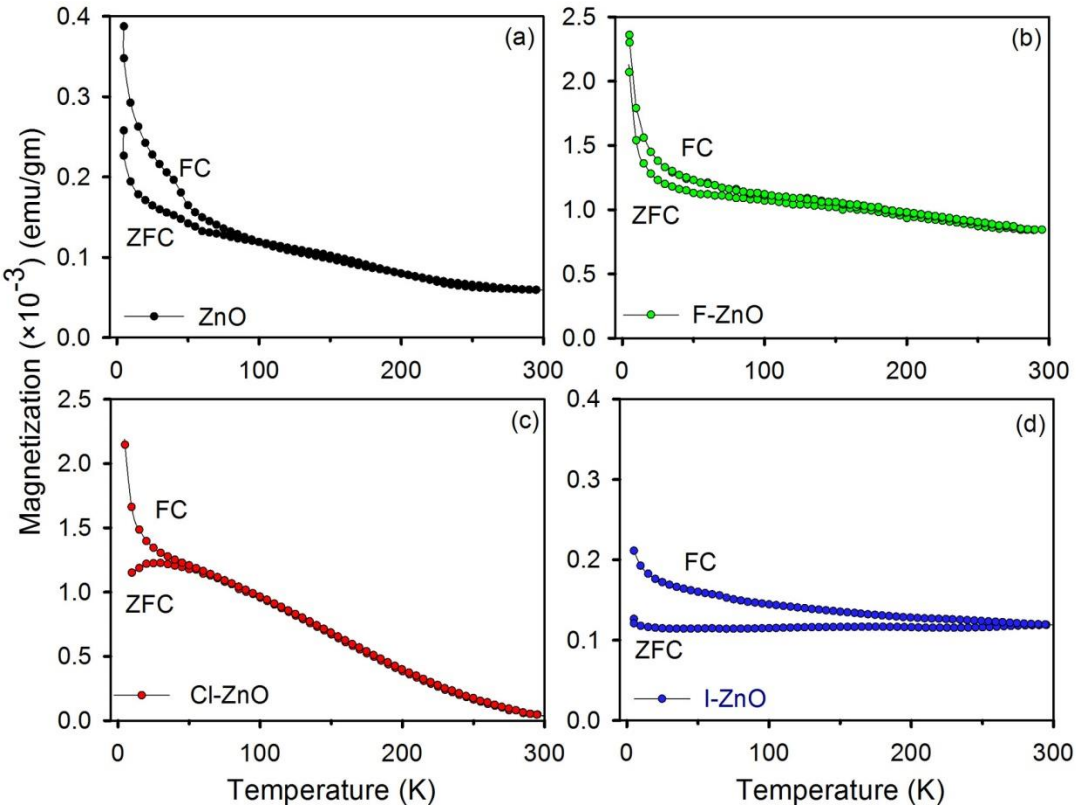

Figure 5.16: *The mass-normalized magnetization measured in zero field-cooled (ZFC) and field-cooled (FC) modes. It is evident from the comparison of the scales of the figures that halide treatment leads to an increase in magnetization in the system.*

Figure 5.15a represents the magnetization versus applied field hysteresis loop behavior at 5 K, indicating the presence of ferromagnetic (FM) long-range order. However, only Cl-ZnO sustains the hysteresis behavior at room temperature (Figure 5.15b). We have calculated the effective magnetic moment from magnetization versus temperature graph in field cooled (FC) conditions. The effective magnetic moment was calculated using Curie constant (*C*) following the equation [67]:

$$\mu_{eff} = (3kC/N)^{1/2} = (8C)^{1/2}\mu_B \qquad (5.1)$$

where k is the Boltzman constant, N is the Avogadro number and μ_B is the Bohr magneton. A mismatch between the zero-field cooled (ZFC) and FC graph specifies the magnetic irreversibility and the long-range order in halide attached systems, as can be seen from Figure 5.16.

Table 5.4: *The magnetic moment of ZnO and halide-ZnO, a comparison of theoretical and experimental results are tabulated here.*

System	Magnetic Moment (in μ_B)	
	Theoretical (per atom)	**Experimental**
ZnO	1×10^{-3}	2.3×10^{-4}
F-ZnO	4.3×10^{-3}	1.2×10^{-3}
Cl-ZnO	6.4×10^{-3}	1.3×10^{-3}
I-ZnO	1×10^{-4}	2×10^{-4}

5.3. Conclusion:

In summary, it has been observed that, by modulating the surface defect of a wide bandgap semiconductor ZnO, using chloride ion, it is possible to considerably improve its activity. Time-resolved fluorescent study reveals electronic interaction between Cl to ZnO which confirms the formation of Cl-ZnO

NP. We have studied the photocatalytic activity of structurally modulated ZnO NPs in the presence of ultraviolet light. It is found that, in Cl-ZnO, chloride can at the surface of ZnO shuttle the photo-excited electrons. As a result excited state electrons became more available, which increases ROS generation and higher photocatalytic activity. However, in the case of Mn-doped ZnO, Mn^{2+} can act as a trapping site for the excitons, which reduces the available excited state electrons. As a consequence of it, the photocatalytic activity reduces in Mn-doped ZnO. In addition to chloride ion, trap states of Mn-doped ZnO could also be restored resulting in greater photocatalytic efficiency.

Moreover, we further investigated the role of other halide ions towards the surface defect state modulation of ZnO to investigate its enhanced multifunctional activity. We observe surface modulation of ZnO by different halides modifies water stability, photocatalytic activity, and magnetism. Halide-treated ZnO shows higher aqua-stability compared to pristine ZnO. At the same time, Cl-ZnO and F-ZnO show higher photocatalytic activity in the presence of UV light. Moreover, the magnetic result of halide-ZnO is also very promising, the attachment of certain halide ions on ZnO NP will modulate its electronic structure drastically, and it will produce ferromagnetic-like behavior even in the absence of magnetic ions. Of them, only Cl-ZnO produces substantial room temperature ferromagnetism. Due to higher electron affinity, Cl-ZnO shows the highest amount of magnetism compared to the halide-ZnO. So, Cl-ZnO shows both enhanced photocatalytic activity and room temperature ferromagnetic property. Thus, modulation of surface defects through certain halide ion was shown to be responsible for improved physical properties of ZnO, demonstrating its utility for the functionalization of ZnO NP.

References

[1] A. Makhal, S. Sarkar, T. Bora, S. Baruah, J. Dutta, A. K. Raychaudhuri, S. K. Pal, Dynamics of light harvesting in ZnO nanoparticles, *Nanotechnology* 21 (2010) 265703.

[2] R. Dastjerdi, M. Montazer, A review on the application of inorganic nano-structured materials in the modification of textiles: Focus on anti-microbial properties, *Colloids Surf. B: Biointerfaces* 79 (2010) 5.

[3] L. Zhang, F. Gu, J. Chan, A. Wang, R. Langer, O. Farokhzad, Nanoparticles in medicine: Therapeutic applications and developments, *Clin. Pharmacol. Ther.* 83 (2008) 761.

[4] R. Ravichandran, Nanotechnology applications in food and food processing: Innovative green approaches, opportunities and uncertainties for global market, *Int. J. Green Nanotech.: Phys. Chem.* 1 (2010) 72.

[5] R. Sathyavathi, M. B. Krishna, S. V. Rao, R. Saritha, D. N. Rao, Biosynthesis of silver nanoparticles using coriandrum sativum leaf extract and their application in nonlinear optics, *Adv. Sci. Lett.* 3 (2010) 138.

[6] F. Bonet, S. Grugeon, R. H. Urbina, K. Tekaia-Elhsissen, J. M. Tarascon, In situ deposition of silver and palladium nanoparticles prepared by the polyol process, and their performance as catalytic converters of automobile exhaust gases, *Solid State Sci.* 4 (2002) 665.

[7] O. Gohardani, M. C. Elola, C. Elizetxea, Potential and prospective implementation of carbon nanotubes on next generation aircraft and space vehicles: A review of current and expected applications in aerospace sciences, *Prog. in Aerospace Sci.* 70 (2014) 42.

[8] N. Zhou, V. López-Puente, Q. Wang, L. Polavarapu, I. Pastoriza-Santos, Q. H. Xu, Plasmon-enhanced light harvesting: Applications in enhanced photocatalysis, photodynamic therapy and photovoltaics, *RSC Adv.* 5 (2015) 29076.

[9] D. R. Baer, P. E. Burrows, A. A. El-Azab, Enhancing coating functionality using nanoscience and nanotechnology, *Prog. Org. Coat.* 47 (2003) 342.

[10] O. Koshkina, D. Westmeier, T. Lang, C. Bantz, A. Hahlbrock, C. Würth, U. Resch-Genger, U. Braun, R. Thiermann, C. Weise, Tuning the surface of nanoparticles: Impact of poly (2-ethyl-2-oxazoline) on protein adsorption in serum and cellular uptake, *Macromol. Biosci.* 16 (2016) 1287.

[11] S. Shao, K. Zheng, T. N. Pullerits, F. Zhang, Enhanced performance of inverted polymer solar cells by using poly (ethylene oxide)-modified ZnO as an electron transport layer, *ACS Appl. Mater. Interfaces* 5 (2013) 380.

[12] E. Boisselier, D. Astruc, Gold nanoparticles in nanomedicine: Preparations, imaging, diagnostics, therapies and toxicity, *Chem. Soc. Rev.* 38 (2009) 1759.

[13] N. V. Konduru, K. M. Murdaugh, A. Swami, R. J. Jimenez, T. C. Donaghey, P. Demokritou, J. D. Brain, R. M. Molina, Surface modification of zinc oxide nanoparticles with amorphous silica alters their fate in the circulation, *Nanotoxicology* 10 (2016) 720.

[14] A. Fujishima, K. Honda, Electrochemical photolysis of water at a semiconductor electrode, *Nature* 238 (1972) 37.

[15] B. O'Regan, M. Gratzel, A low-cost, high-efficiency solar cell based on dye-sensitized colloidal TiO_2 films, *Nature* 353 (1991) 737.

[16] N. Serpone, A. V. Emeline, Semiconductor photocatalysis — Past, present, and future outlook, *J. Phys. Chem. Lett.* 3 (2012) 673.

[17] O. Legrini, E. Oliveros, A. M. Braun, Photochemical processes for water treatment, *Chem. Rev.* 93 (1993) 671.

[18] M. A. Fox, M. T. Dulay, Heterogeneous photocatalysis, *Chem. Rev.* 93 (1993) 341.

[19] M. R. Hoffmann, S. T. Martin, W. Choi, D. W. Bahnemann, Environmental applications of semiconductor photocatalysis, *Chem. Rev.* 95 (1995) 69.

[20] A. Kohan, G. Ceder, D. Morgan, C. G. van de Walle, First-principles study of native point defects in ZnO, *Phys. Rev. B* 61 (2000) 15019.

[21] M. Y. Guo, A. M. C. Ng, F. Liu, A. B. Djurisic, W. K. Chan, H. Su, K. S. Wong, Effect of native defects on photocatalytic properties of ZnO, *J. Phys. Chem. C* 115 (2011) 11095.

[22] R. M. Sheetz, I. Ponomareva, E. Richter, A. N. Andriotis, M. Menon, Defect-induced optical absorption in the visible range in ZnO nanowires, *Phys. Rev. B* 80 (2009) 195314.

[23] D. P. Norton, Y. Heo, M. Ivill, K. Ip, S. Pearton, M. F. Chisholm, T. Steiner, ZnO: Growth, doping & processing, *Mater. Today* 7 (2004) 34.

[24] L. Schmidt-Mende, J. L. MacManus-Driscoll, ZnO – Nanostructures, defects, and devices, *Mater. Today* 10 (2007) 40.

[25] W. Zhu, S. Kitamura, M. Boffelli, E. Marin, E.D. Gaspera, M. Sturaro, A. Martucci, G. Pezzotti, Analysis of defect luminescence in Ga-doped ZnO nanoparticles, *Phys. Chem. Chem. Phys.* 18 (2016) 9586.

[26] M. Iijima, H. Kamiya, Surface modification for improving the stability of nanoparticles in liquid media, *KONA Powder Part. J.* 27 (2009) 119.

[27] L. Guerrini, R.A. Alvarez-Puebla, N. Pazos-Perez, Surface modifications of nanoparticles for stability in biological fluids, *Materials (Basel)* 11 (2018) 1154.

[28] K. R. Kittilstved, D. R. Gamelin, Activation of high-T_c ferromagnetism in Mn^{2+}-doped ZnO using amines, *J. Am. Chem. Soc.* 127 (2005) 5292.

[29] T. K. Maji, D. Bagchi, P. Kar, D. Karmakar, S. K. Pal, Enhanced charge separation through modulation of defect-state in wide band-gap semiconductor for potential photocatalysis application: Ultrafast spectroscopy and computational studies, *J. Photochem. Photobiol. A: Chem.* 332 (2017) 391.

[30] S. S. Kumar, P. Venkateswarlu, V. R. Rao, G. N. Rao, Synthesis, characterization and optical properties of zinc oxide nanoparticles, *Int. Nano Lett.* 3 (2013) 1.

[31] M. Alias, R. Aljarrah, H. Al-Lamy, K. Adem, Investigation the effect of thickness on the structural and optical properties of nano ZnO films prepared by dc magnetron sputtering, *Int. J. Appl. Innovat. in Engineer. Manag.* 2 (2013) 2319.

[32] A. Bagabas, A. Alshammari, M.F. Aboud, H. Kosslick, Room-temperature synthesis of zinc oxide nanoparticles in different media and their application in cyanide photodegradation, *Nanoscale Res. Lett.* 8 (2013) 1.

[33] T. L. Tan, C. W. Lai, S. B. Abd Hamid, Tunable band gap energy of Mn-doped ZnO nanoparticles using the coprecipitation technique, *J. Nanomater.* 2014 (2014) 1.

[34] E. Burstein, Anomalous optical absorption limit in InSb, *Phys. Rev.* 93 (1954) 632.

[35] T. Moss, The interpretation of the properties of indium antimonide, *Proc. Phys. Soc. London, Sect. B* 67 (1954) 775.

[36] S. Sardar, S. Chaudhuri, P. Kar, S. Sarkar, P. Lemmens, S. K. Pal, Direct observation of key photoinduced dynamics in a potential nano-delivery vehicle of cancer drugs, *Phys. Chem. Chem. Phys.* 17 (2015) 166.

[37] Y. H. Lu, W. H. Lin, C. Y. Yang, Y. H. Chiu, Y. C. Pu, M. H. Lee, Y. C. Tseng, Y. J. Hsu, A facile green antisolvent approach to Cu^{2+}-doped ZnO nanocrystals with visible-light-responsive photoactivities, *Nanoscale* 6 (2014) 8796.

[38] Y. J. Choi, K. M. Kang, H. S. Lee, H. H. Park, Non-laminated growth of chlorine-doped zinc oxide films by atomic layer deposition at low temperatures, *J. Mater. Chem. C* 3 (2015) 8336.

[39] Y. Gong, T. Andelman, G. F. Neumark, S. O'Brien, I. L. Kuskovsky, Origin of defect-related green emission from ZnO nanoparticles: Effect of surface modification, *Nanoscale Res. Lett.* 2 (2007) 297.

[40] J. Han, P. Mantas, A. Senos, Defect chemistry and electrical characteristics of undoped and Mn-doped ZnO, *J. Am. Ceram. Soc.* 22 (2002) 49.

[41] M. G. Nair, M. Nirmala, K. Rekha, A. Anukaliani, Structural, optical, photo catalytic and antibacterial activity of ZnO and Co doped ZnO nanoparticles, *Mater. Lett.* 65 (2011) 1797.

[42] S. Sarkar, A. Makhal, T. Bora, K. Lakhsman, A. Singha, J. Dutta, S. K. Pal, Hematoporphyrin–ZnO nanohybrids: Twin applications in efficient visible-light

photocatalysis and dye-sensitized solar cells, *ACS Appl. Mater. Interfaces* 4 (2012) 7027.

[43] T. K. Maji, P. Kar, H. Mandal, C. Bhattacharya, D. Karmakar, S. K. Pal, Halide-modulated functionality of wide band gap zinc oxide semiconductor nanoparticle, *ChemistrySelect* 3 (2018) 6382.

[44] M. J. Akhtar, M. Ahamed, S. Kumar, M. A. M. Khan, J. Ahmad, S. A. Alrokayan, Zinc oxide nanoparticles selectively induce apoptosis in human cancer cells through reactive oxygen species, *Int. J. Nanomedicine* 7 (2012) 845.

[45] A. Bagabas, A. Alshammari, M. F. Aboud, H. Kosslick, Room-temperature synthesis of zinc oxide nanoparticles in different media and their application in cyanide photodegradation, *Nanoscale Research Lett.* 8 (2013) 1.

[46] S. Sardar, P. Kar, H. Remita, B. Liu, P. Lemmens, S. K. Pal, S. Ghosh, Enhanced charge separation and FRET at heterojunctions between semiconductor nanoparticles and conducting polymer nanofibers for efficient solar light harvesting, *Sci. Rep.* 5 (2015) 1713.

[47] T. K. Kundu, N. Karak, P. Barik, S. Saha, Optical properties of ZnO nanoparticles prepared by chemical method using poly (vinyl alcohol) (PVA) as capping agent, *Int. J. Soft Comput. Eng.* 1 (2011) 19.

[48] A. van Dijken, E. A. Meulenkamp, D. Vanmaekelbergh, A. Meijerink, The kinetics of the radiative and nonradiative processes in nanocrystalline ZnO particles upon photoexcitation, *J. Phys. Chem. B* 104 (2000) 1715.

[49] A. Makhal, S. Sarkar, T. Bora, S. Baruah, J. Dutta, A. Raychaudhuri, S. K. Pal, Dynamics of light harvesting in ZnO nanoparticles, *Nanotechnology* 21 (2010) 265703.

[50] M. Zhong, Y. Li, I. Yamada, J. J. Delaunay, ZnO-$ZnGa_2O_4$ core-shell nanowire array for stable photoelectrochemical water splitting, *Nanoscale* 4 (2012) 1509.

[51] H. Mandal, S. Shyamal, P. Hajra, A. Bera, D. Sariket, S. Kundu, C. Bhattacharya, Development of ternary iron vanadium oxide semiconductors for applications in photoelectrochemical water oxidation, *RSC Adv.* 6 (2016) 4992.

[52] H. Mandal, S. Shyamal, P. Hajra, B. Samanta, P. Fageria, S. Pande, C. Bhattacharya, Improved photoelectrochemical water oxidation using wurtzite ZnO semiconductors synthesized through simple chemical bath reaction, *Electrochim. Acta* 141 (2014) 294.

[53] Y. Wang, Y. Wang, R. Jiang, R. Xu, Cobalt phosphate–ZnO composite photocatalysts for oxygen evolution from photocatalytic water oxidation, *Ind. Eng. Chem. Res.* 51 (2012) 9945.

[54] A. Xiong, T. Yoshinaga, T. Ikeda, M. Takashima, T. Hisatomi, K. Maeda, T. Setoyama, T. Teranishi, K. Domen, Effect of hydrogen and oxygen evolution cocatalysts on photocatalytic activity of GaN:ZnO, *Eur. J. Inorg. Chem.* 2014 (2014) 767.

[55] M. Zhong, Y. Li, I. Yamada, J. J. Delaunay, ZnO–$ZnGa_2O_4$ core–shell nanowire array for stable photoelectrochemical water splitting, *Nanoscale* 4 (2012) 1509.

[56] K. Zeng, D. Zhang, Recent progress in alkaline water electrolysis for hydrogen production and applications, *Prog. Energy Combust. Sci.* 36 (2010) 307.

[57] C. B. Ong, L. Y. Ng, A. W. Mohammad, A review of ZnO nanoparticles as solar photocatalysts: Synthesis, mechanisms and applications, *Renew. Sustain. Energy Rev.* 81 (2018) 536.

[58] M. Samadi, M. Zirak, A. Naseri, E. Khorashadizade, A. Z. Moshfegh, Recent progress on doped ZnO nanostructures for visible-light photocatalysis, *Thin Solid Films* 605 (2016) 2.

[59] K. M. Lee, C. W. Lai, K. S. Ngai, J. C. Juan, Recent developments of zinc oxide based photocatalyst in water treatment technology: A review, *Water Res.* 88 (2016) 428.

[60] S. S. Rayalu, D. Jose, M. V. Joshi, P. A. Mangrulkar, K. Shrestha, K. Klabunde, Photocatalytic water splitting on Au/TiO_2 nanocomposites synthesized through various routes: Enhancement in photocatalytic activity due to SPR effect, *Appl. Catal., B* 142-143 (2013) 684.

[61] S. Sarkar, A. Makhal, T. Bora, S. Baruah, J. Dutta, S. K. Pal, Photoselective excited state dynamics in ZnO-Au nanocomposites and their implications in photocatalysis and dye-sensitized solar cells, *Phys. Chem. Chem. Phys.* 13 (2011) 12488.

[62] F. Barka-Bouaifel, B. Sieber, N. Bezzi, J. Benner, P. Roussel, L. Boussekey, S. Szunerits, R. Boukherroub, Synthesis and photocatalytic activity of iodine-doped ZnO nanoflowers, *J. Mater. Chem.* 21 (2011) 10982.

[63] Y. Nosaka, A. Y. Nosaka, Generation and Detection of Reactive Oxygen Species in Photocatalysis, *Chem. Rev.* 117, (2017),11302.

[64] P. Kar, T. K. Maji, R. Nandi, P. Lemmens, S. K. Pal, In-Situ hydrothermal synthesis of Bi–$Bi_2O_2CO_3$ heterojunction photocatalyst with enhanced visible light photocatalytic activity, *Nano-Micro Lett.* 9 (2017) 18.

[65] M. Khuili, N. Fazouan, H. A. E. Makarim, G. E. Hallani, E. H. Atmani, First principle study of structural, electronic, optical and electrical properties of Ga doped ZnO with GGA and mBJ approximations, *J. Phys. Conf. Series* 758 (2016) 012024.

[66] C. Peng, Y. Wang, Z. Cheng, G. Zhang, C. Wang, G. Yang, Tuning magnetism by biaxial strain in native ZnO, *Phys. Chem. Chem. Phys.* 17 (2015) 16536.

[67] X. Xu, L. Jiang, J. Shen, Z. Chen, Z. Xu, Relationship between spin state of Co ions and thermopower in $La_{1-x}Sr_xCoO_3$ ($0 \leqslant x \leqslant 0.5$), *Phys. Lett. A* 351 (2006) 431.

Chapter 6

Spectroscopic and Ab Initio Studies on Organic-Inorganic Nanohybrid for Visible Light Harvesting

6.1. Introduction:

The development of new functional materials with enhanced solar light harvesting property has been known as an essential strategy for sustainable energy resources and to solve the growing energy crisis throughout the world [1-3]. Additionally, severe environmental pollution issues have prompted people to find potential solutions to clean up the water and environmental pollution through solar energy.

The way to realize efficient solar energy conversion is the development of a high-yielding system whose absorption spectra overlap with the solar spectrum. The developed material should have an effective photoexcited charge-segregation mechanism to arrest the electron-hole recombination process and sufficient energy of charges to perform the preferred chemical reactions [4-7]. Organic-inorganic nanohybrid (NH) is a newly developed hybrid material, composed of organic dyes and inorganic nanoparticles, and has been widely used in photocatalysis [8]. It is possible to fulfill the above mentioned primary criteria of solar light harvesting by developing proper organic-inorganic NH.

Although oxide-based semiconductors, (for example TiO_2, ZnO) have been used widely as photoresponsive materials, they are limited in performance, because of their wide bandgap nature which limits its activity in the UV region and their low-efficiency in charge separation [9, 10]. Therefore, a tremendous effort has been made to sensitize oxide-based semiconductors in the visible spectral range via doping or surface-tuning using different dyes [11, 12]. However, the use of inorganic dyes based on ruthenium is not efficient for photocatalytic

applications because it is very expensive as well as toxic, which can produce secondary contamination during catalysis [13-15]. In contrast, the use of porphyrin or phthalocyanine based dyes is very efficient as a light harvester for practical photocatalytic application due to low cost and less toxicity. The coupling of these dyes with oxide-based semiconductors has proven to be an effective strategy, which can not only absorb a wider range of sunlight but also significantly promote the separation of photo-generated charges, thereby greatly improving the efficiency of solar light harvesting [16-20]. This motivates us to work on dye-sensitized oxide-based NH systems.

In this chapter, we have successfully developed (Cu)PP-TiO_2 NH where copper metallated protoporphyrin (PP) is attached to porous TiO_2 microspheres ((Cu)PP-TiO_2) through covalent bonding. It is observed that (Cu)PP-TiO_2 NH shows admirable photocatalytic activity in the presence of visible light, for the degradation of toxic metal Cr(VI). A detailed electron microscopic and optical spectroscopic characterization of the synthesized nanohybrid has also been performed. The recyclability of the (Cu)PP-TiO_2 NH is confirmed, even in the presence of interfering Cr(III) and Fe(III), the toxic Cr(VI) ions can be repeatedly reduced, which shows that the material has practical long-term stability. We have embedded the (Cu) PP-TiO_2 NH on a stainless-steel metal mesh (SSM) (size 2 cm × 2 cm, pore size 150 μm × 200 μm) to construct a prototype device. This device would not only diminish the soluble Cr(VI) ions, also filter out suspended particulates containing reduced Cr(III). To our understanding, the developed strategy will be beneficial to the detoxification of chromium in water samples in the real world.

Besides, the demand for magnetic nanoparticle (NP) photocatalyst is increasing progressively. This kind of system has the advantage that it can be separated very easily using an external magnetic field. In recent times, the search for magnetic photocatalysts has progressed so that it can be effectively separated

from pure water using an external magnetic field [21-25], substituting the tiresome centrifugation procedure to isolate the catalyst from the medium [26, 27]. Concurrently, the photochemical water splitting method is one of the most promising technologies for producing hydrogen from solar energy, to establish sustainable, renewable, and green energy. One of the most essential standards for making a photoelectrochemical cell (PEC) is to design efficient however cost-effective material-based cells. However, there are still a few inexpensive materials that are effective in photocatalysis and solar hydrogen production using photoelectrochemical water splitting. Still, a cost-effective material that has an efficient conversion rate in both photocatalysis and solar hydrogen generation field is sparse in the community. Hematite (α-Fe_2O_3) is a capable material that can be used for higher photocatalytic activity and efficient hydrogen generation due to its unique electronic band structure. Moreover, this material is cheap, non-toxic, environment-friendly, and has very high chemical stability and pronounced abundance [28-30]. Despite these encouraging characteristics, the application of this material is still inadequate because of its low carrier mobility and fast electron-hole recombination rate. Making a hybrid system, by using hematite that can arrest the recombination rate and increase charge separation, can be very much useful for its high performance. This motivates us to work on the hybrid system based on α-Fe_2O_3 for higher photocatalytic activity and hydrogen generation.

In another work of this chapter, we prepared a novel NH using Fe_2O_3 and phthalocyanine (PC) and investigated its application in different fields. NH system can efficiently reduce the charge carrier recombination rate of the system. As a result, the NH exhibits higher photocatalytic activity and serves as a better photoanode material for photoelectrochemical water splitting. To confirm the NH formation, different spectroscopic tools including Raman Spectroscopy and picosecond-resolved fluorescence spectroscopy has been used. The hybrid system

shows higher magnetic property as well as enhanced visible-light induced photocatalytic and photocurrent properties. The first principles DFT calculation has been performed to probe the insight of the increased activity. Furthermore, the NH has been embedded on the surface of an SSM and the activity of the immobilized catalyst has been measured. This developed strategy will be beneficial for application in the real-world water purification process.

6.2. Results and Discussion:

6.2.1. Development of a Photo-Catalytic Converter for Potential Use in the Detoxification of Cr(VI) Metal in Water from Natural Resources [31]: In the current work, we have developed a new strategy to sensitize porous TiO_2 NP by protoporphyrin IX with copper (II) ion to synthesize a functional NH for visible light photocatalysis application. XRD pattern of as-synthesized TiO_2 microsphere (after annealing at 400°C) is depicted in Figure 6.1a which is consistent with the tetragonal anatase phase [32]. Figure 6.1b shows FESEM images of the TiO_2 microsphere indicates TiO_2 microspheres are perfectly spherical (average diameter of 1-1.5 μm) and composed of interrelated nanocrystals (Figure 6.1c). HRTEM image of TiO_2 microspheres (Figure 6.1d) shows the pore size is approximately 10-12 nm in the boundary of two interconnected NPs in the microsphere (Figure 6.1e-f). HRTEM image of TiO_2 shows lattice fringe width ~0.352 nm corresponds to (101) plane of anatase TiO_2.

We have used Fourier-transform infrared (FTIR) spectroscopic to calculate the interaction between PP and TiO_2 microsphere present in NH. Free PP shows two characteristic antisymmetric (asym) and symmetric (sym) stretching vibration peaks for the carboxylic group located at 1698 and 1402 cm^{-1} respectively (Figure 6.2a). Here the difference in the stretching frequency ($\Delta = \gamma_{asym} - \gamma_{sym}$) of the carboxylic group can be used as a marker of PP binding on the NP surface [33]. After binding with the TiO_2 microsphere, there is a change in stretching frequency

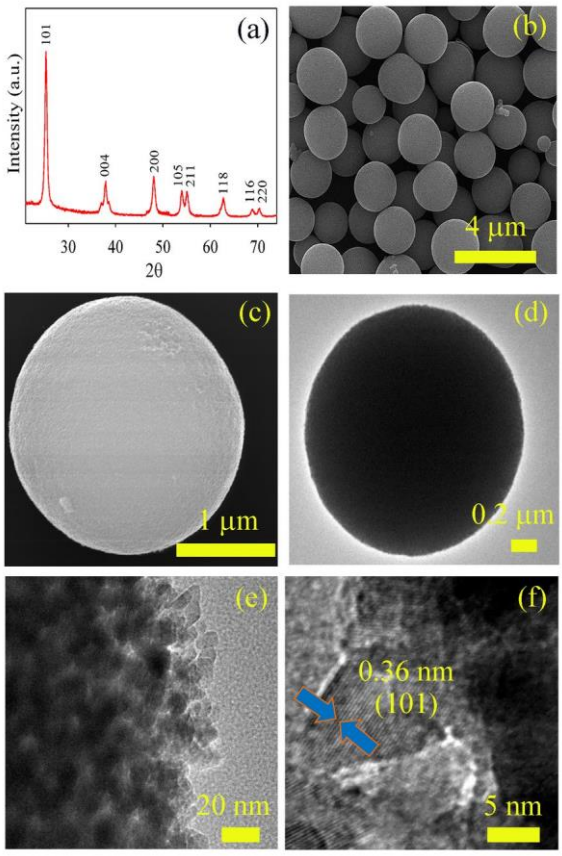

Figure 6.1: *a) XRD pattern of TiO_2 microspheres, b) and c) FESEM images of TiO_2 microspheres. d) TEM, e), and f) HRTEM images of TiO_2 microspheres.*

of the carboxylic group (γ_{asym} = 1634 cm^{-1} and γ_{sym} = 1403 cm^{-1}), consequently the Δ value of PP changes from 296 cm^{-1} to 231 cm^{-1} indicating bidentate covalent binding of PP on host TiO_2 surface [34]. The incorporation of metal ions in the PP moiety has been confirmed by the disturbance of the N-H stretching frequency (Figure 6.2b). N-H stretching frequency for free PP is found to be at 3441 cm^{-1}. However, there is no change in N-H stretching frequency in PP-TiO_2 indicating PP anchors on TiO_2 through the carboxylic functional group only. Contrastingly, perturbation of N-H stretching frequency is modulated in the presence of metal ions (Cu^{2+}, Fe^{3+}, and Cr^{3+}) attachment with PP, confirming the successful binding of the metal ions to the PP through the central pyrrole nitrogen atoms.

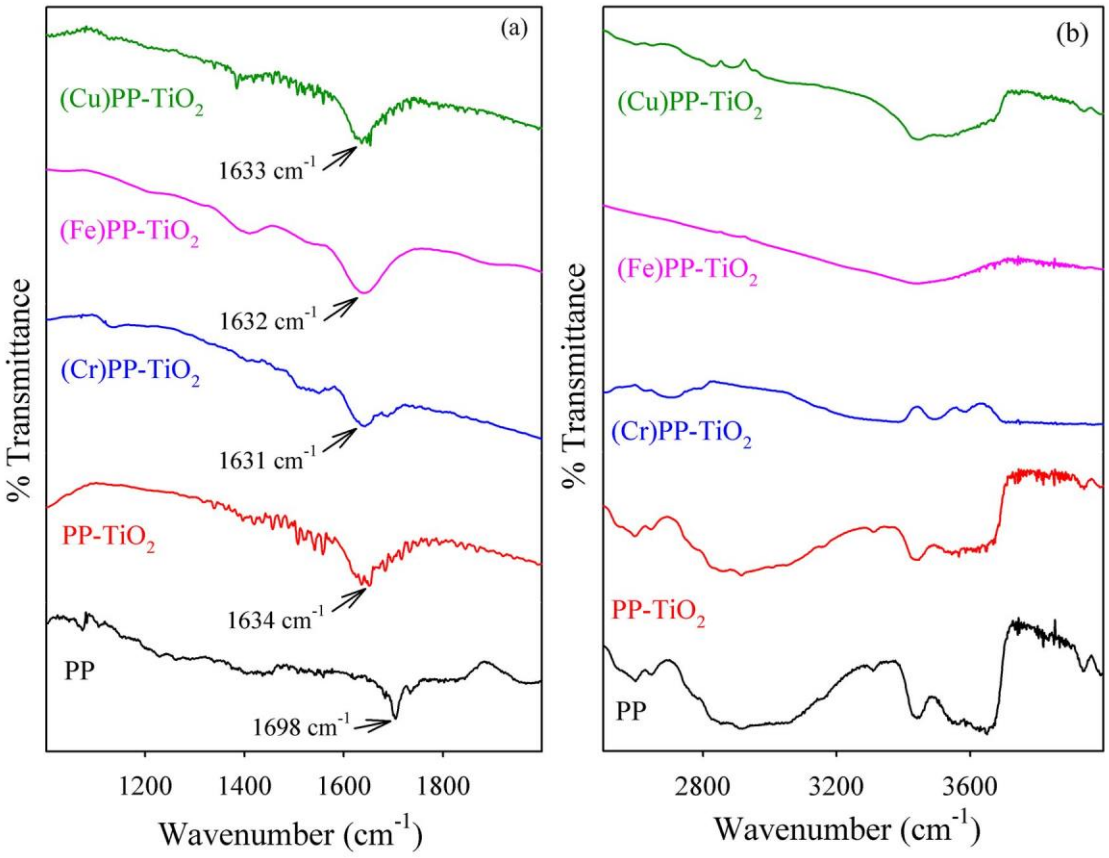

Figure 6.2: *a) FTIR spectra of PP, PP-TiO_2, (Cr)PP-TiO_2, (Fe)PP-TiO_2, and (Cu)PP-TiO_2. b) FTIR spectra of PP, PP-TiO_2, (Cr)PP-TiO_2, (Fe)PP-TiO_2, and (Cu)PP-TiO_2.*

The absorption spectrum of PP and PP-TiO_2 NH is depicted in Figure 6.3a. PP having extensively delocalized π electrons exhibits a Soret band at 409 nm along with Q bands between 500-700 nm [35, 36]. The formation of J and H type of aggregates for PP in DMSO-water is evident from the spectra [37, 38]. After attachment of PP on the TiO_2 surface, there is a redshift in the Soret band which is due to the disappearance of aggregation, indicating an interaction between carboxylic groups of PP with TiO_2 [34, 39]. Fluorescence spectra of PP and metal-PP upon excitation at the Soret band are shown in Figure 6.3b. However, after metalation emission intensity of PP is significantly decreased indicating excited state charge transfer transitions responsible for fluorescence quenching [40, 41].

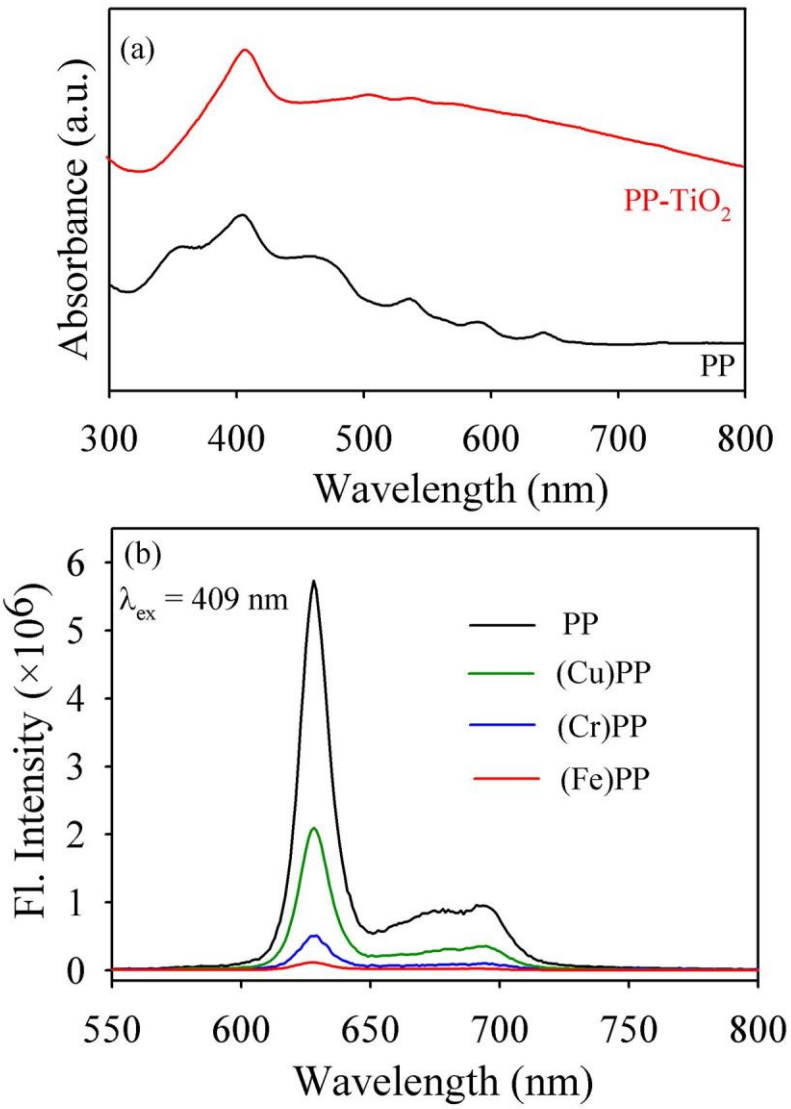

Figure 6.3: *a) UV-Vis absorption spectra of PP and PP-TiO_2. b) Room-temperature PL spectra of PP, (Cu)PP, (Cr)PP, and (Fe)PP.*

The photocatalytic activity of NHs is explored in the presence of visible light. We observed the reduction of Cr(VI) in aqueous solutions in the presence of NH. Figure 6.4a shows the decrement of UV-Vis absorption spectra of DPC-Cr(VI) complex solution (monitored at ~540 nm) under visible light illumination in the presence of (Cu)PP-TiO_2. Photocatalytic reduction of Cr(VI) in the presence of PP-TiO_2 and Cr-PP-TiO_2 is depicted in Figure 6.4b. Prior to illumination, the solution was stirred in the dark for 30 minutes to achieve the adsorption equilibrium of the

toxic Cr(VI) on the NH. The decrement in absorbance is almost negligible in the dark. In the presence of visible light, PP-TiO_2 NH shows a 60% photoreduction of Cr(VI) in 1 hr. Upon incorporation of copper(II) metal ion within the porphyrin moiety, the photocatalytic reduction of (Cu)PP-TiO_2 NH enhanced to ~100% in 1hr, which is better than other previously reported literature [42-46]. The stability

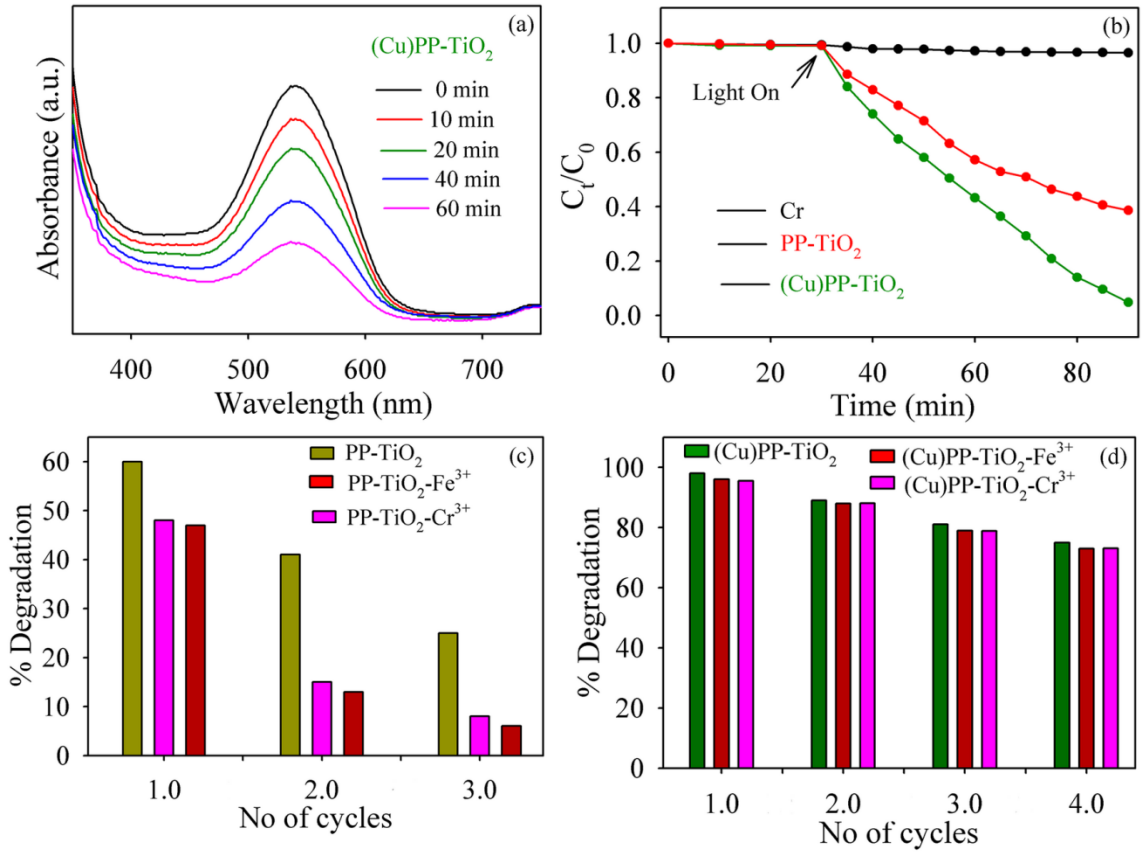

Figure 6.4: *a) UV-Vis absorption spectra for the photocatalytic reduction of Cr(VI) by (Cu)PP-TiO_2 under visible-light. b) Photocatalytic reduction of Cr(VI) under visible-light in the presence and absence of NH. c) Recyclability study by PP-TiO_2 in presence of Fe^{3+} and Cr^{3+} ions for the reduction of Cr(VI). d) Recyclability study by (Cu)PP-TiO_2 in the presence of Fe^{3+} and Cr^{3+} ions for the reduction of Cr(VI).*

of the photocatalysts is a major issue from the application point of view, as it could cut the cost of the respective process [47, 48]. We further studied the recyclability of (Cu)PP-TiO_2 and PP-TiO_2 NHs in the presence and absence of water dissolved Fe^{3+} (0.07 mM) and Cr^{3+} (0.07 mM) ions. The metal ions concentration used in this study is above the WHO prescribed limit present in groundwater. It is observed

that the recyclability of PP-TiO_2 NH decreases after each cycle in the presence of other dissolved metal ions as evident from Figure 6.4c. On the contrary, (Cu)PP-TiO_2 NH exhibits excellent recyclability up to four cycles (Figure 6.4d). The activity remains intact even in the presence of the dissolved metal. Therefore, (Cu)PP-TiO_2 not only gives better photocatalytic activity but also gives efficient recyclability.

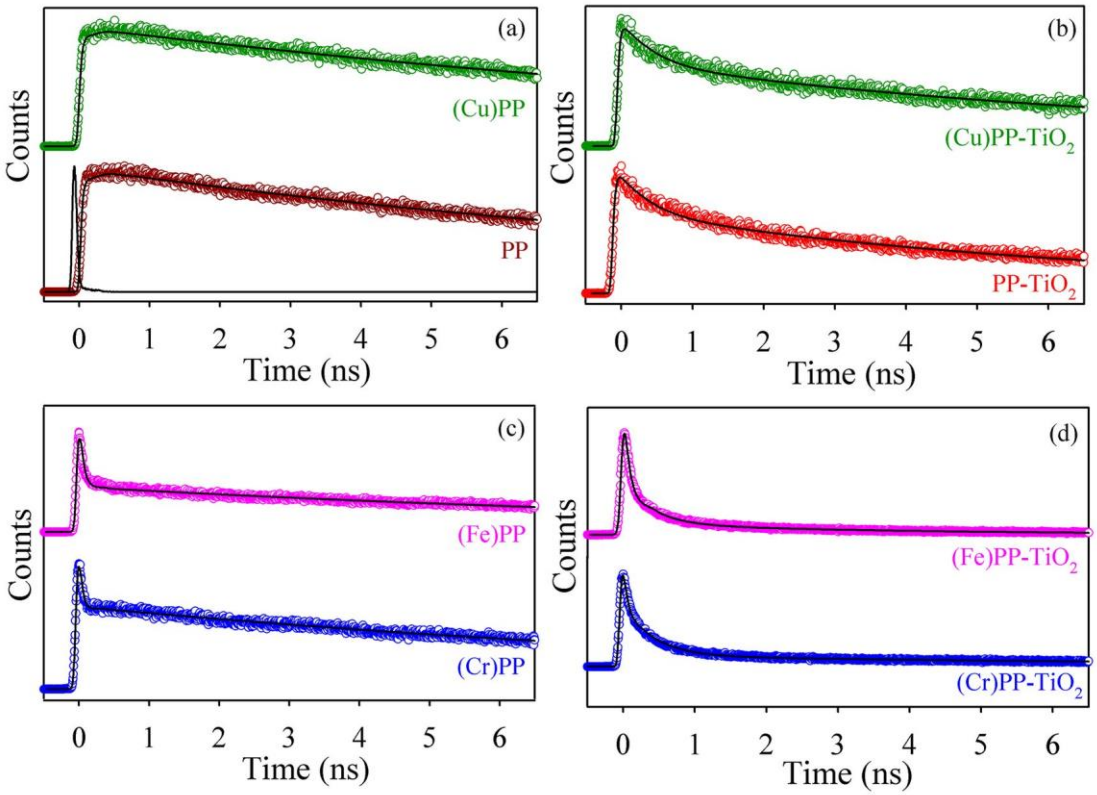

Figure 6.5: *Fluorescence decay profiles of a) PP (violet)and (Cu)PP (dark green), b) PP-TiO_2 (red) and (Cu)PP-TiO_2 (dark green), c) (Cr)PP (blue) and (Fe)PP (pink), d) (Cr)PP-TiO_2 (blue), (Fe)PP-TiO_2 (Pink) detected at 630 nm upon excitation at a wavelength of 409 nm.*

To understand the mechanism of higher photocatalytic activity, we have studied the ultrafast dynamics of the systems. Picosecond resolved fluorescence spectroscopies of all the system is presented in Figure 6.5. We observe an additional faster component in (Fe)PP and (Cr)PP system, which indicates the excited state electron transfer from PP to metals ions (Fe^{3+} and Cr^{3+}). However, in the case of (Cu)PP, the timescale is comparable to PP, which rule out the

possibility of electron transfer from PP to Cu. We assume an additional inter system electron migration pathway has been generated for Fe-PP and Cr-PP systems. The associated time constants are tabulated in Table 6.1. Further, we have analyzed the excited state decay of different metal-PP attached TiO_2 systems. In the PP-TiO_2 system, an additional faster component is generated which may be ascribed to the excited state electron transfer from PP to TiO_2 NP (Figure 6.5). Although the fluorescence transient of (Cu)PP-TiO_2 is comparable with PP-TiO_2, fluorescence transient of (Cr)PP-TiO_2 and (Fe)PP-TiO_2 are faster compared to PP-TiO_2. This result indicates, an additional electron migration pathway from PP to Cr^{3+}/Fe^{3+} ions modulates the photocatalytic activity of PP-TiO_2, as it significantly reduces the availability of electron on the conduction band of TiO_2.

Table 6.1: *Lifetimes of picosecond time-resolved PL transients of different samples detected at 630 nm PL maxima upon excitation at 409 nm wavelength.**

System	τ_1 (ps)	τ_2 (ps)	τ_3 (ps)	τ_{avg} (ns)
PP	12200 (100)			12.2
Cu-PP	12100 (100)			12.1
Cr-PP	39 (70)	12100 (30)		3.65
Fe-PP	50 (68)	12100(32)		3.9
PP-TiO_2	420 (39)	7245 (61)		4.53
Cu-PP-TiO_2	420 (39)	8519 (61)		5.36
Cr-PP-TiO_2	45 (67)	414 (28)	8583 (9)	0.77
Fe-PP-TiO_2	50 (72)	370 (24)	7865 (4)	0.43

* *The values in parentheses represent the relative weight percentages of the time components.*

We purposefully incorporated metal ions (Fe^{3+} and Cu^{2+}) within the porphyrin moiety to check the catalytic activity of different metal attached PP-TiO_2 system. The photocatalytic activity of different hybrid systems was studied under visible light illumination as illustrated in Figure 6.6a. There is an insignificant reduction of Cr(VI) in the presence of visible light without any

catalyst. We found the catalytic activity of (Cu)PP-TiO_2 is higher (100%) comparable to PP-TiO_2 (60%). However, the photocatalytic activity of (Cr)PP-TiO_2 and (Fe)PP-TiO_2 reduces greatly compared to both PP-TiO_2. As evident from the excited state fluorescence spectroscopy, due to excited state electron transfer from PP to Cr^{3+}/Fe^{3+} the availability of electron in the conduction band decreases. Consequently, the catalytic activity of PP-TiO_2 in presence of Cr^{3+} or Fe^{3+} ion decreases. In the presence of Cu(II) metal ions in the PP moiety, the increased photocatalytic activity is related to the additional structural stability of the (Cu)PP-TiO_2 NH against photobleaching. The structural stability eventually leads to the generation of more electrons that are responsible for the enhancement in the photoreduction ability of Cr(VI).

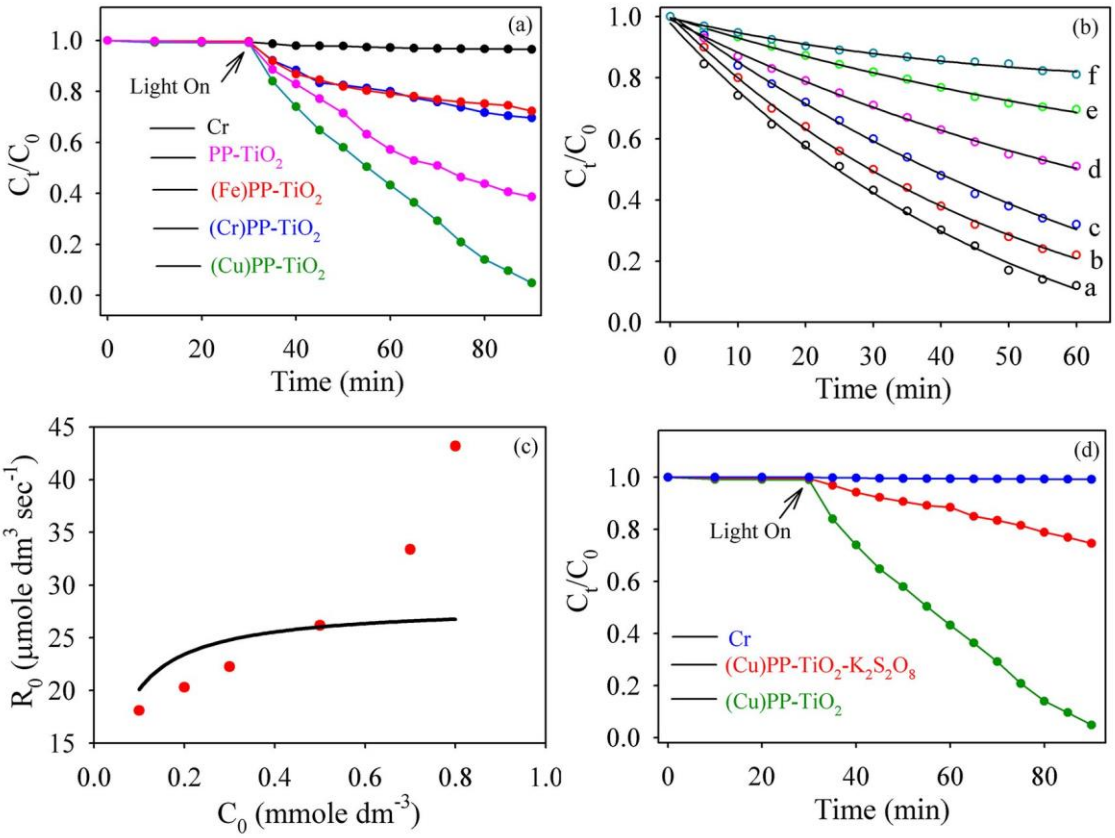

Figure 6.6: *a) Photocatalytic reduction of Cr (VI) under visible-light in the presence and absence of NHs. b) C_t/C_0 vs. time with different concentrations of Cr(VI) under visible-light by (Cu)PP-TiO_2. c) Langmuir–Hinshelwood plot of photocatalytic reduction for Cr(VI) using (Cu)PP-TiO_2 (where solid line is the model fitting and solid circles are experimental data). d) Photocatalytic reduction of Cr(VI) by (Cu)PP-TiO_2 in the presence of $K_2S_2O_8$.*

Such enhancement in photocatalytic activity due to the presence of copper metal within the PP moiety is reported in several pieces of literature [36, 41, 49].To find out the effect of the surface on photocatalysis, we further performed Langmuir–Hinshelwood (L–H) kinetics study, using different concentrations of Cr(VI) as shown in Figure 6.6b. A significant deviation of the model (solid line) from experimental data (as shown in Figure 6.6c) ruled out the role of surface in the photodegradation of Cr (VI) under visible light illumination. To substantiate the photocatalytic reaction mechanism, we have used $K_2S_2O_8$ as a scavenger for photo-generated electrons [50, 51]. The Photoreduction of Cr(VI) under visible light illumination has been performed using (Cu)PP-TiO_2 NH in the presence and absence of $K_2S_2O_8$. In the presence of $K_2S_2O_8$, the catalytic activity of (Cu)PP-TiO_2 reduces significantly (Figure 6.6d). Based on the above discussion and previously reported literature work [51-53], it is concluded that photocatalytic reduction of Cr(VI) reactions is a distal rather surface-mediated L-H type.

To explore real-world applications, we have fabricated NHs on an SSM for the removal of toxic metal present in drinking water (Figure 6.7a). Surface morphology of bare SSM and SSM coated with TiO_2 microspheres were identified from FESEM images. Low magnification images of bare mesh and TiO_2 microsphere coated mesh are shown in Figure 6.7b and 6.7c-d respectively. High magnification images of TiO_2 microspheres coated mesh (Figure 6.7e) shows uniform distribution of TiO_2 microspheres ranging from 1-1.5 μm. After the TiO_2 fabrication on the mesh, we have successfully sensitized the microspheres with PP and (Cu)PP. The photocatalytic reduction of Cr(VI) under visible light illumination has been studied using mesh embedded NHs. A control study has been carried out in the absence of any photocatalyst. We found in the presence of visible light, there is only 2% degradation of Cr(VI) without any photocatalyst. However, PP-TiO_2 exhibit 35% photocatalytic ability in visible light. At the same

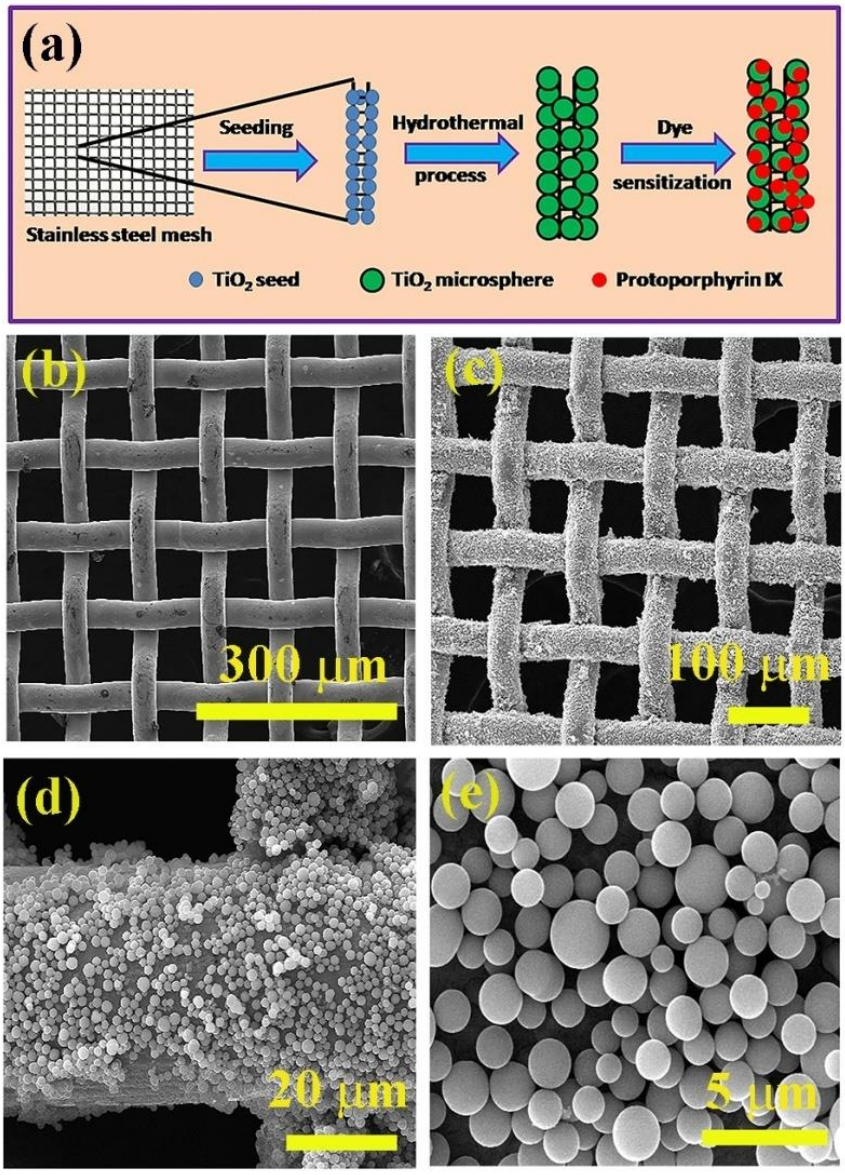

Figure 6.7: *a) Schematic representation of TiO_2 microsphere synthesis on SSM. b) SEM images of bare SSM. SEM images of TiO_2 on mesh in low magnification (c and d) and high magnification e).*

condition (Cu)PP-TiO_2 exhibits 50% degradation of Cr(VI) (Figure 6.8). From the perspective of practical applications, the photocatalytic nanomaterials based on the mesh can effectively remove pollutants through physical (filtering) and chemical (photocatalytic) processes.

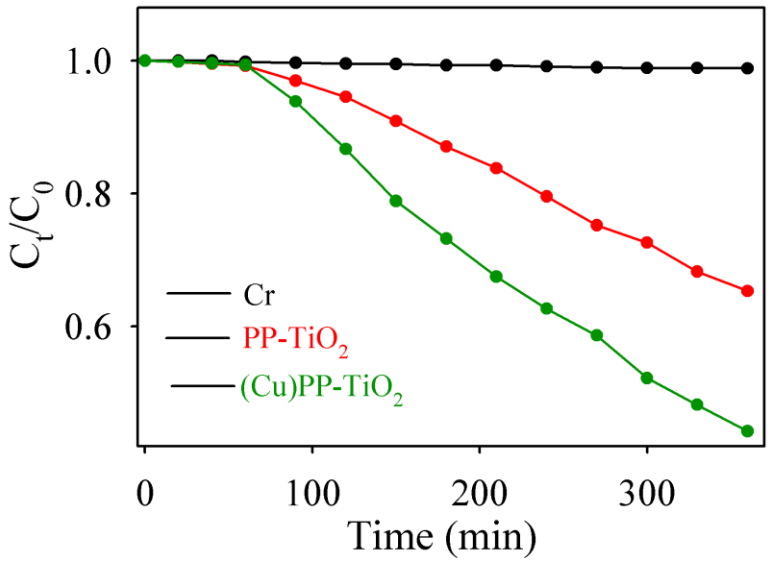

Figure 6.8: *Photocatalytic reduction of Cr(VI) by PP-TiO_2 and (Cu)PP-TiO_2 and only Cr on the mesh under visible light illumination.*

The earlier report shows that a mesh-based system can be effective for higher photocatalytic degradation [54, 55]. In comparison to reports, we showed that our approach is not only cost-effective but also offer the decontamination of drinking water in a promising and feasible way (Scheme 6.1).

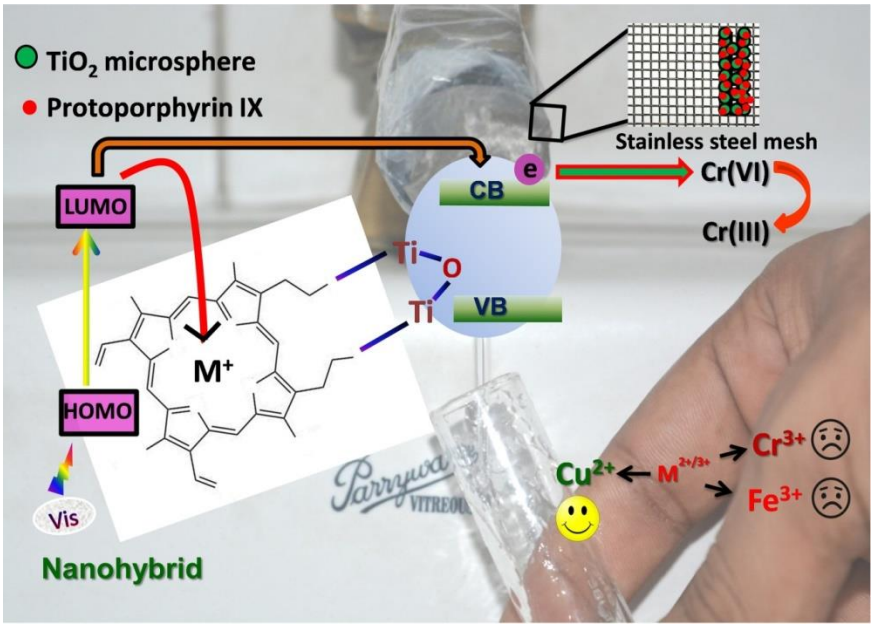

Scheme 6.1: *Schematic representation of photocatalytic reduction of Cr(VI) by (Cu)PP-TiO_2 NH in the presence of water dissolved metal ions (Fe^{3+} and Cr^{3+}) under visible-light illumination.*

6.2.2. Development of a Magnetic Nanohybrid for Multifunctional Application: From Immobile Photocatalysis to Efficient Photoelectrochemical Water Splitting: A Combined Experimental and Computational Study [56]: In this work, we have synthesized Fe_2O_3 NP and modified its surface using phthalocyanine ligand. The formation of nanohybrid is confirmed via XRD analysis. The XRD pattern of the as-synthesized Fe_2O_3 NPs is depicted in Figure 6.9. All the diffraction peaks obtained from the NP is very sharp (corresponds to good crystallinity) and can be matched to a rhombohedral phase of α-Fe_2O_3 (hematite, JCPDS No. 33-0664) [29, 57]. No impurity peak in the XRD pattern is observed, demonstrating the high purity of the synthesized NPs. The XRD peak of Fe_2O_3-PC NH shows the same diffraction pattern as pristine Fe_2O_3 NP which confirms that the crystallinity of α-Fe_2O_3 remains intact after PCs attachment.

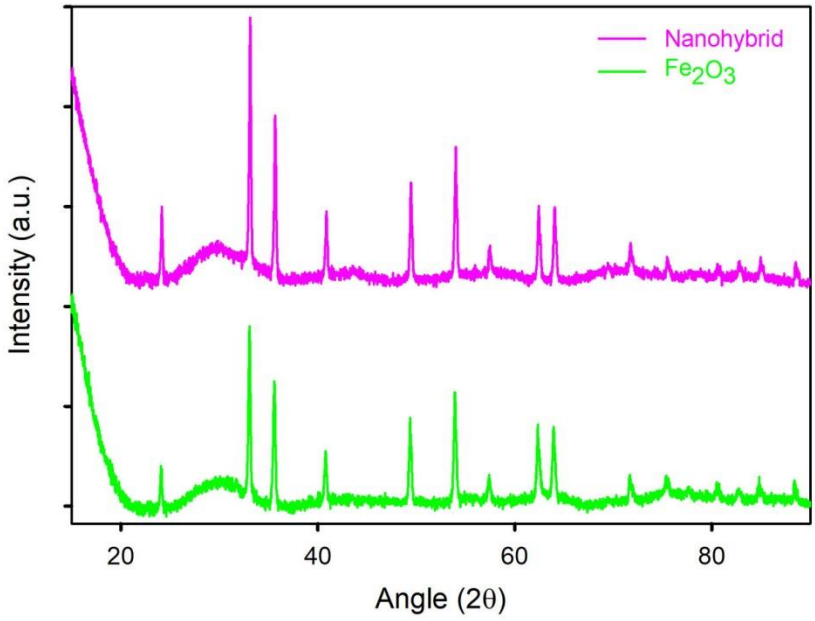

Figure 6.9: *Powder XRD image of Fe_2O_3 and Fe_2O_3-PC NH.*

To get a confirmation about the nanohybrid formation, Raman spectroscopy has been carried out in Fe_2O_3 and NH system. The Raman spectra of α-Fe_2O_3 NP, PC, and NH systems are depicted in Figure 6.10. Raman spectra of the α-Fe_2O_3

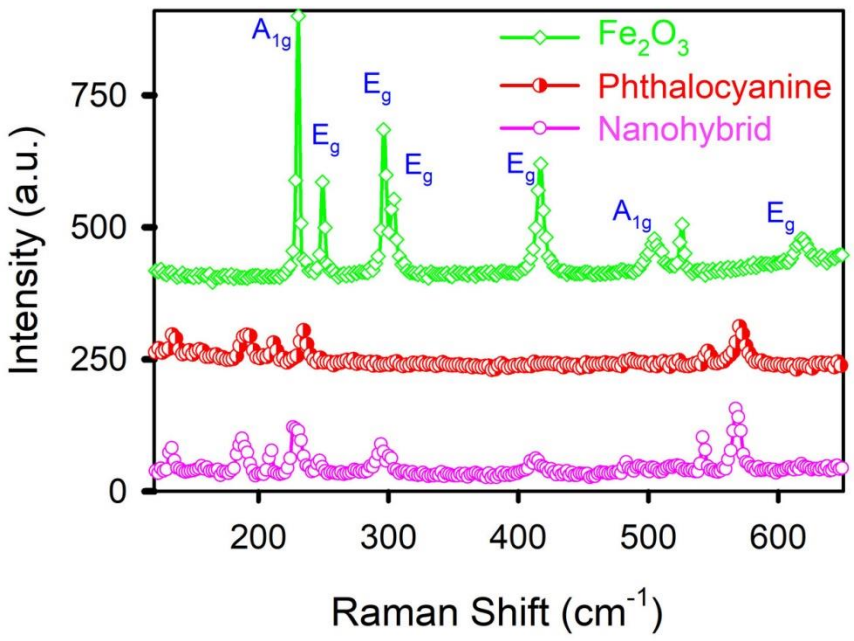

Figure 6.10: *Raman spectra of Fe_2O_3, phthalocyanine, and nanohybrid.*

NPs shows seven significant peaks, two A_{1g} modes (226 cm^{-1} and 497 cm^{-1}) and five E_g modes (245 cm^{-1}, 293 cm^{-1}, 298 cm^{-1}, 412 cm^{-1}, and 613 cm^{-1}) [58, 59]. A_{1g} modes of Fe_2O_3 are correlated to symmetric stretching vibrations of Fe–O bond, while E_g modes come due to symmetric bending vibrations of Fe–O bond. The peak positions obtained for our case fit well with the standard data of the hematite system [59-61]. This further endorses the formation of high-quality crystalline hematite (α-Fe_2O_3) NPs. The Raman data of NH shows that there is structural heterogeneity, in which the characteristic Raman peaks of Fe_2O_3 and PC coexist. Also, the A_{1g} mode of Fe_2O_3 (at ~497 cm^{-1}) and the E_g mode (at ~613 cm^{-1}) of Fe_2O_3 are suppressed after PC attachment while other modes stay intact in the NH. Compared with the original Fe_2O_3 NP, slight changes in the phonon energy of NH are observed. These shifts are related to the change of chemical bond length caused by the bonding between PC and Fe_2O_3 which confirms the successful formation of NH.

To confirm that PCs are conjugated to the α-Fe_2O_3 (hematite) a TGA-DTA analysis has been performed on NH. Due to the evaporation of the solvent, an

initial weight loss of 6% occurred at 130 °C to 180 °C. The complete decomposition of PC happens around 400 °C which is ascribed to a sharp weight loss of ~6 % near 400 °C indicating the loss of the peripheral group and the core ring of PC. We can infer that around 6 weight% dye has been conjugated in the NH system.

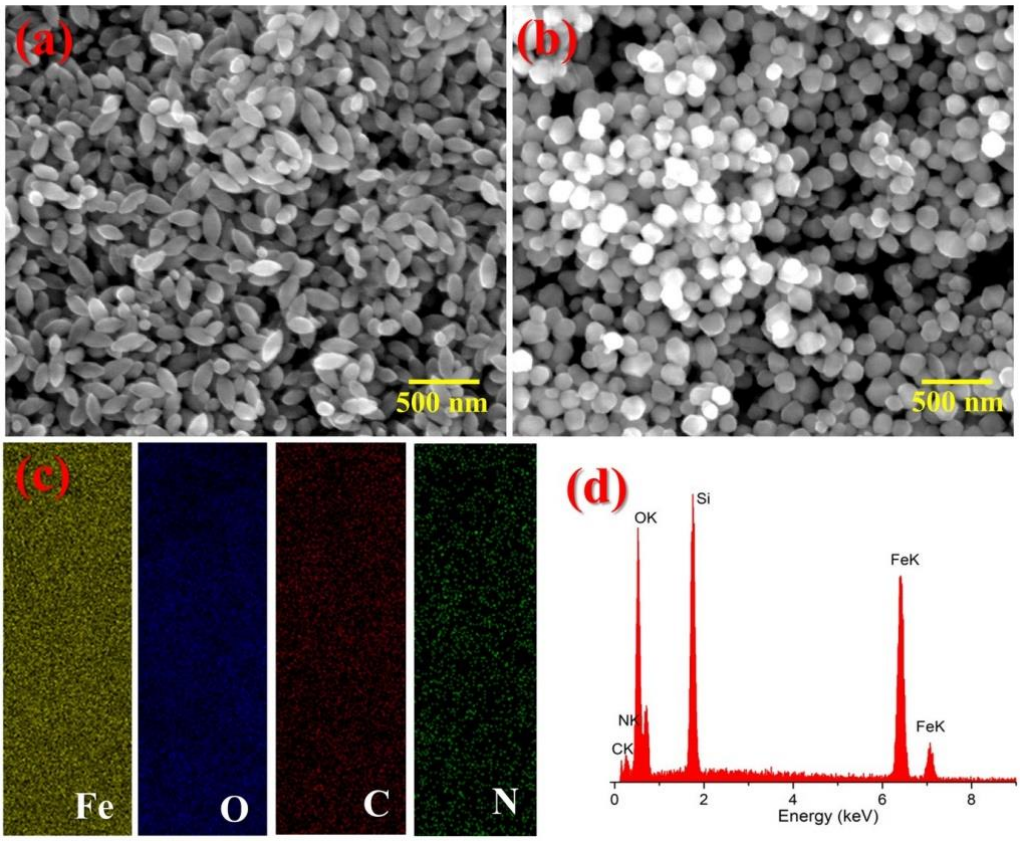

Figure 6.11: *FESEM image of a) a-Fe_2O_3 NP and b) a-Fe_2O_3-PC NH, c) Mapping of different elements of NH confirms the presence of a-Fe_2O_3 and PC, d) EDAX image of NH.*

The morphology of the NP is investigated using the FESEM image (shown in Figure 6.11a). As-synthesized α-Fe_2O_3 NP shows individual spindle-like structures making an assembly [62, 63]. After surface functionalization by ligand attachment, the morphology of α-Fe_2O_3 changes vividly [64]. NH displays a spherical structure after surface functionalization (shown in Figure 6.11b). This change in size and morphology is due to the surface etching of the ligand PC [65]. Figure 6.11c shows the EDS mapping image of Fe, O, C, and N in NH, which endorses the

homogeneity and presence of PC in the NH system. The EDS image of NH is also presented in Figure 6.11d which shows the presence of components of PC.

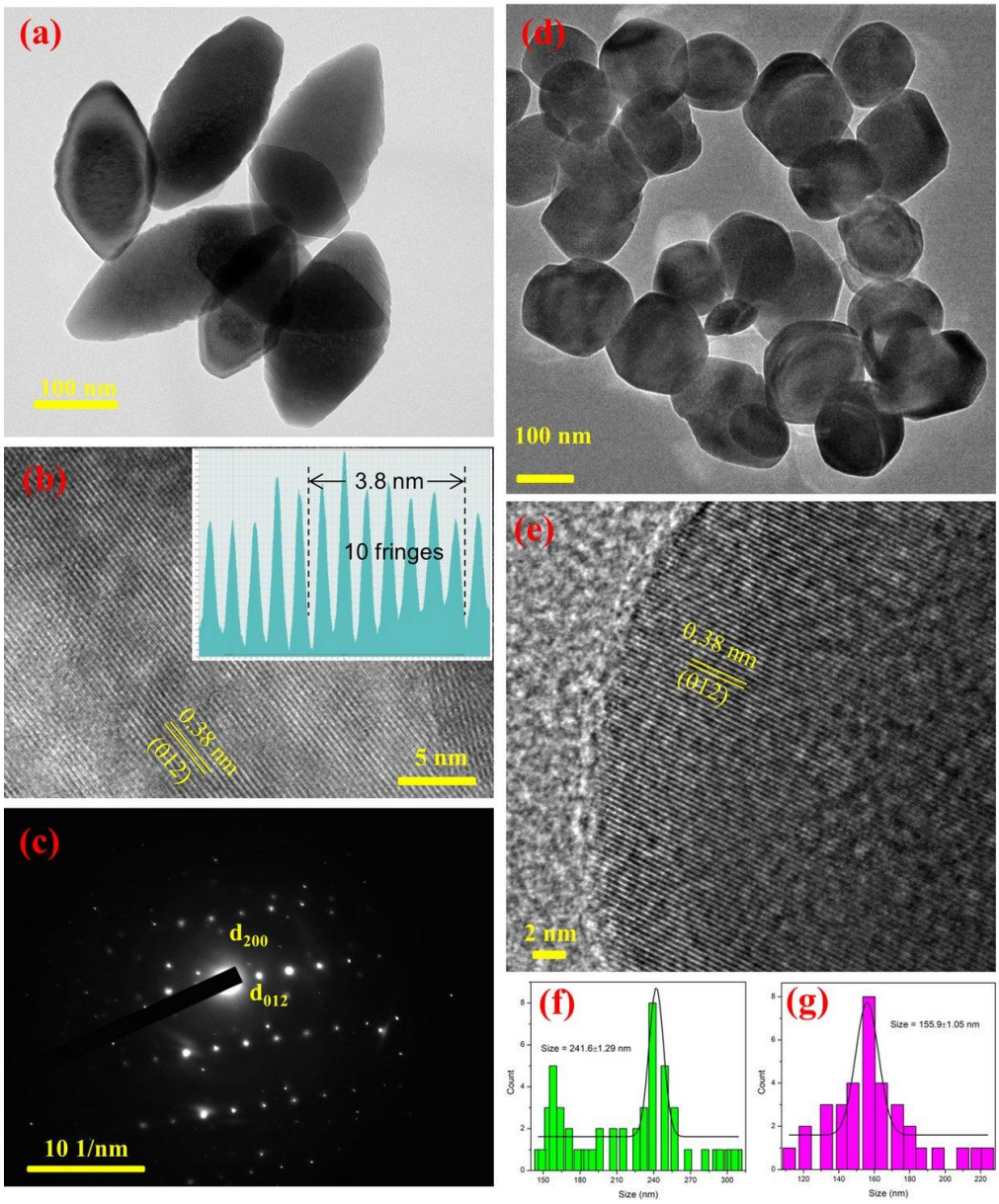

Figure 6.12: *a) TEM image of a-Fe_2O_3, b) HRTEM image of a-Fe_2O_3 NP and c) SAED pattern of the system. d) TEM image of a-Fe_2O_3-PC NH, e) HRTEM image of the NH, f) and g) shows the particle size distribution of a-Fe_2O_3 and a-Fe_2O_3-PC NH respectively.*

TEM images of Fe_2O_3 NP and Fe_2O_3-PC NH are depicted in Figure 6.12. Figure 6.12a displays the TEM image of Fe_2O_3 with the spindle-like structure which resembles the SEM image. The high-resolution TEM image (HRTEM) of the

NP (depicted in Figure 6.12b) reveals a continuous fringe with fringe distance ~0.38 nm which corresponds to the (012) plane of the NP [66]. The SAED image, displayed in Figure 6.12c, indicates the formation of a good quality crystalline structure. The change of surface morphology (from spindle to spherical) of Fe_2O_3 NP after surface modification by PC can also be observed from TEM images (Figure 6.12d). The HRTEM image of NH (Figure 6.12e) displays a well-defined and sharp fringe with a fringe width of ~0.38 nm corresponds to (012) plane of hematite. This result suggests that, although the morphology of the structure has changed due to the binding of the ligand, the crystallinity of F_2O_3 remains unchanged even after the surface functionalization. The particle size distribution of the NP and NH are depicted in Figure 6.12f and 6.12g respectively. The average particle size of the Fe_2O_3 system has reduced from ~241.6±1.29 nm to 155.9±1.05 nm after surface modification due to surface etching.

To investigate the interaction between Fe_2O_3 NPs and PCs, various spectroscopic characterizations of the systems has been performed. The absorption spectra of all systems are depicted in Figure 6.13a. Pure Fe_2O_3 NP shows a broad absorption in the visible region with peak maxima at ~566 nm along with a weak absorption band near ~450 nm. The absorption of Fe_2O_3 NP in the visible region (400-600 nm) is mainly generated by the couple excitations produced by two magnetically attached adjacent Fe^{3+} cations. The highest absorption peak is ascribed due to the collective effect of an electronic transition from $^6A_1$ to $^4T_2$ (^4G) and pair excitation of $^6A_1$ + $^6A_1$ - $^4T_2(^4G)$ + $^4T_2(^4G)$. The contribution in the absorption band near ~450 nm comes from the pair exciton $^6A_1$- ^4E, $^4A_1$ of magnetically coupled neighboring Fe^{3+}-Fe^{3+}cations [62, 63]. Characteristic Q band absorption of PC is shown at ~670 nm which is ascribed to the π-π^* transition from the highest occupied molecular orbital (HOMO) to the lowest unoccupied

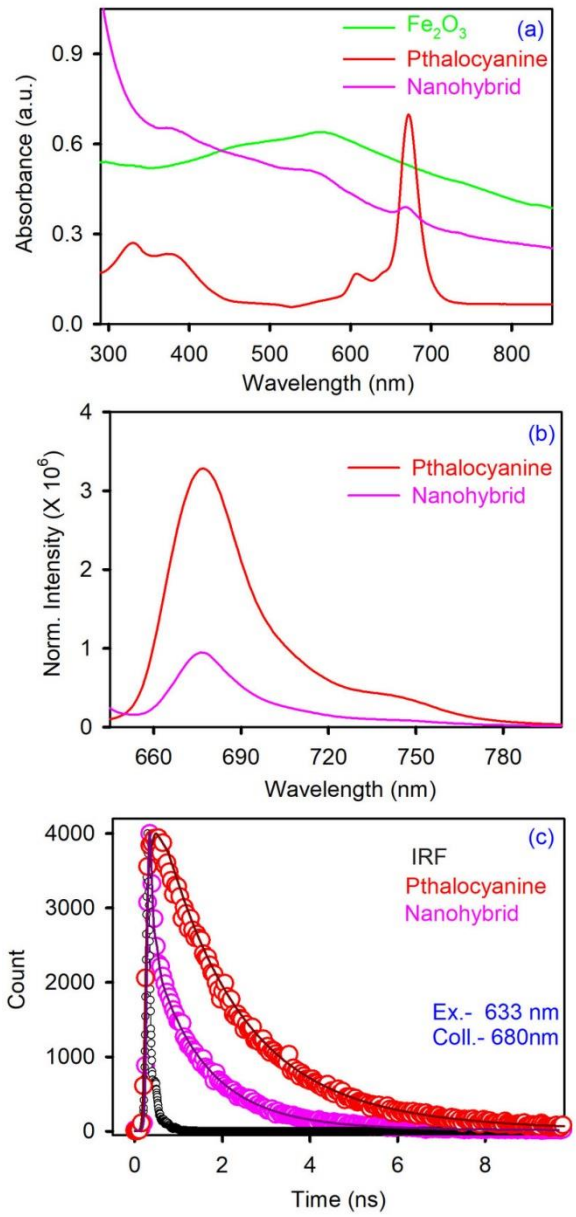

Figure 6.13: *a) Absorption spectra of a-Fe_2O_3, PC, and NH, b) steady-state emission spectra of PC and NH, c) time-resolved decay of PC and NH.*

molecular orbital (LUMO) of the PC ring whereas the absorption near 300-400 nm is recognized to the soret band [67]. In NH characteristic peaks of both Fe_2O_3, NP and PC are observed. However, the characteristic peak of Fe_2O_3 NPs in the visible region experiences a substantial blue shift which corresponds to the decrease in particle size. The bandgap transformed plot using the Kubelka-Munk function vs.

photon energy has been plotted in Figure 6.14 [68, 69]. The Tauc plot of Fe_2O_3

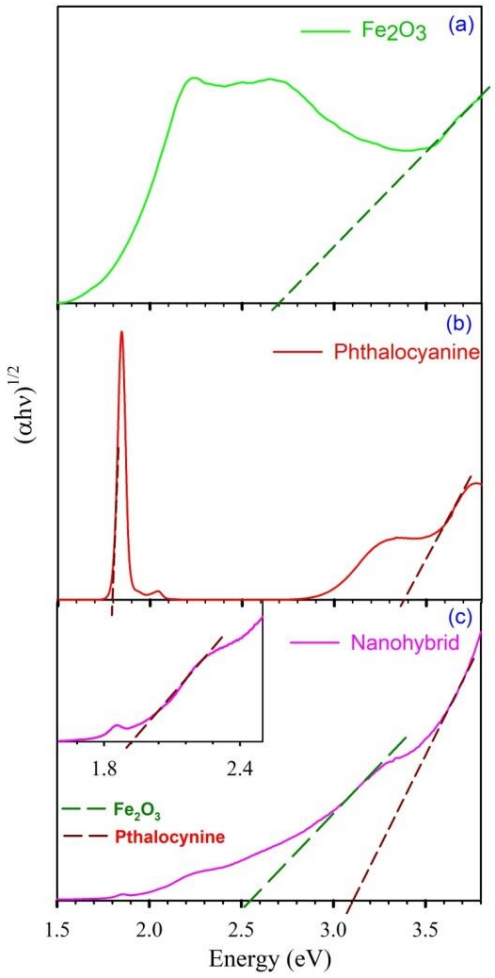

Figure 6.14: *A plot of transformed Kubelka-Munk function vs. the energy of light for a) pristine a-Fe_2O_3, b) PC, and c) nanohybrid.*

approximately estimates the bandgap of Fe_2O_3 which is ~2.68 eV. The Tauc plot of PC clearly shows two bandgaps approximately at 1.8 eV which corresponds to the characteristic absorption of PC. Another band is observed at ~3.37 eV which is generated due to higher-order transition in the PC system. Figure 6.14c depicted the bandgap transformation Tauc plot of Fe_2O_3 PC NH which shows three peaks. The contributions from Fe_2O_3 come ~2.55 eV whereas 1.9 eV and 3.1 eV peaks feature to PC. The steady-state fluorescence spectra (depicted in Figure 6.13b) shows there is quenching in PC emission in the hybrid system. The probable reason for the static fluorescence quenching of PC in the presence of Fe_2O_3 NP is

the electron transfer from the LUMO of PC to the host Fe_2O_3 NP. To get the direct evidence of electron relocation from PC to Fe_2O_3 NP, we have utilized picosecond resolution excited state fluorescence spectroscopy. We have examined the decay profile of PCs and NH systems (using 633 nm LASER) as shown in Figure 6.13c. PC shows a double exponential decay mode, corresponding to the inter-system crossover and the normal exciton lifetime of the system [70]. But in the NH system, a tri-exponential decay pattern is observed. An additional faster component of ~48 ps is generated in the hybrid system which comes due to an ultrafast photo-induced electron transfer from PC to Fe_2O_3 NP. The sensitization process changes the electronic behavior of Fe_2O_3 and PC via modulating the recombination rate of the exciton [31, 71]. The detailed lifetime components of the systems are tabulated in Table 6.2.

Table 6.2: *Fluorescence Lifetime of different systems.**

System	τ_1 (ps)	τ_2(ps)	τ_3(ps)	τ_{avg}(ps)
α-Fe_2O_3	-	1700 (87.6)	3769.6 (12.3)	1955.4
α-Fe_2O_3-PC	46.4 (81.4)	1149 (17.3)	3768 (1.3)	254.8

**value inside parenthesis shows the contribution of the corresponding components.*

We have measured magnetic properties using a superconducting quantum interference device (SQUID) magnetometer (Figure 6.15). The field (H) dependence of magnetization measured at temperatures 5 K and 300 K are plotted in Figure 6.15a and 6.15b respectively. Although it is well known that the original Fe_2O_3 system has a large number of antiferromagnetic sequences, we have obtained measurable small magnetization in Fe_2O_3 NP. This magnetization comes due to uncompensated moments because of the presence of surface states in the NP, as a result, the spins of the Fe^{3+} ions at the surface are canted [72]. Compared with the Fe_2O_3 NP system, NH exhibits a significant increase in saturation

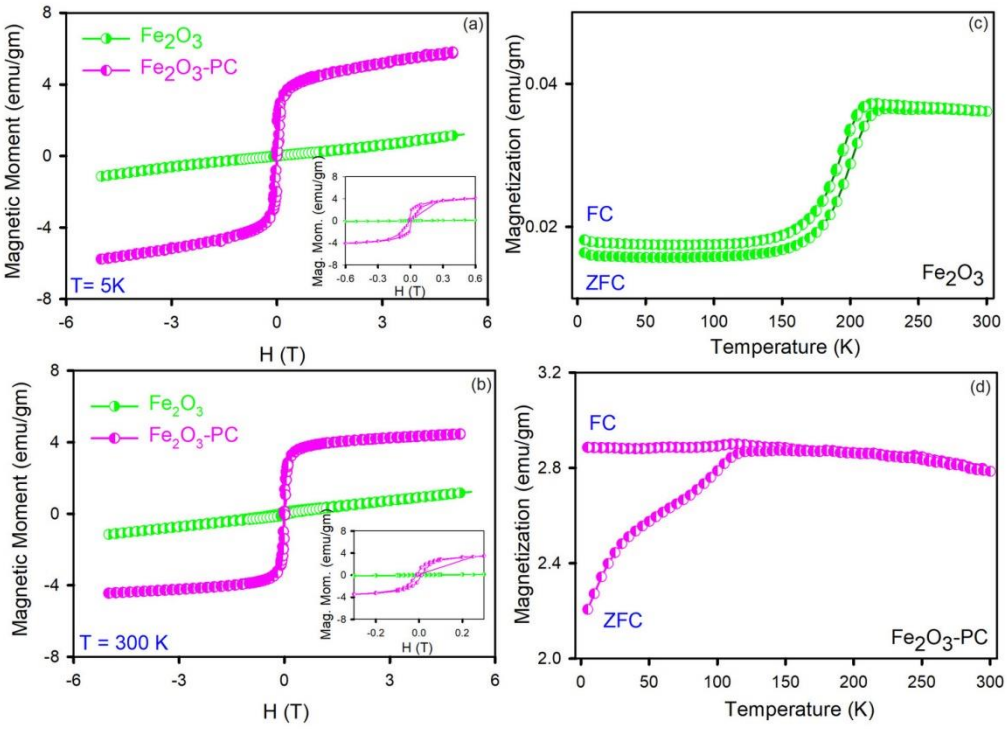

Figure 6.15: *M-H hysteresis curve of a) a-Fe_2O_3 NP, b) a-Fe_2O_3 -PC NP and FC-ZFC curve of c) a-Fe_2O_3 NP, d) a-Fe_2O_3 -PC NH.*

magnetization (M_S) at two temperatures (low temperature and room temperature), and a clear hysteresis phenomenon appears. Even with the maximum available applied field, the magnetization of the system increases monotonically, which means that the canted spins on the NH surface are not saturated. This increment of magnetic properties comes due to the heavy surface remodeling and a large amount of charge transfer between ligand to metal during the formation of NH. As a result, NH shows ferromagnetic nature displaying a finite hysteresis loop [73]. The temperature dependence of magnetization for the samples is studied in both zero-field-cooled (ZFC) and field cooled (FC) conditions for two different field values. The ZFC-FC magnetization curve of pristine Fe_2O_3 NP and NH are presented in Figure 6.15c and 6.15d (field value H= 1000 Oe). The ZFC-FC curve of NP shows the nature of being concave outwards, which confirms the low carrier density and carrier locality in the system [72, 74]. The splitting between ZFC and FC curves becomes negligible at approximately 225 K, which corresponds to the

blocking temperature (T_B) of the system [75]. Due to the Morin transition (spin-flip transition), the rise of the FC and ZFC curves both start at ~200 K, during which the magnetization changes from perpendicular to the *c* axis to parallel to the *c* axis.

Table 6.3: *Magnetic Properties of the Fe_2O_3-PC NH.*

Temperature (K)	**System**	**Saturation Magnetization (M_S) (emu/gm)**	**Remanent magnetization (M_R) (emu/gm)**	**Coercivity (H_C) (Oe)**
4 K	α-Fe_2O_3	1.13	0.02	664
	α-Fe_2O_3-PC	-	1.13	134
300 K	α-Fe_2O_3	1.07	0.1	956
	α-Fe_2O_3-PC	4.5	0.73	120

The temperature dependence of magnetization exhibits sharp changes from Fe_2O_3 NP to NH. T_B moves to a lower temperature (140 K) in the NH system, and below T_B, the ZFC magnetization curve drops sharply, with a small hump around 50 K, while the FC magnetization curve remains almost constant below 5 K, which shows the presence of long-range order in the system. Moreover, Morin transition was completely suppressed for NH, signifying that the attachment with the ligand in NH restricts the spin-flipping. The effective magnetic moments are tabulated in Table 6.3. The saturation magnetization (M_S) of the NH is found to be ~4.56 emu/gm at T = 300 K and increases with lowering T. Larger coercively H_C (134 Oe and remnant magnetization (M_R) indicate noticeable ferromagnetic behavior at 5 K, which remains almost intact at 300 K. Per formula magnetic moment of the NH is obtained approximately ~1.2 μ_B, which is much higher than the Fe_2O_3 NP (~0.2 μ_B). The enhancement of the magnetic moment is due to surface reconstruction and charge mismatch on the Fe_2O_3 surface in the presence of ligand [72, 76], which also matches the theoretical calculation described in the later section.

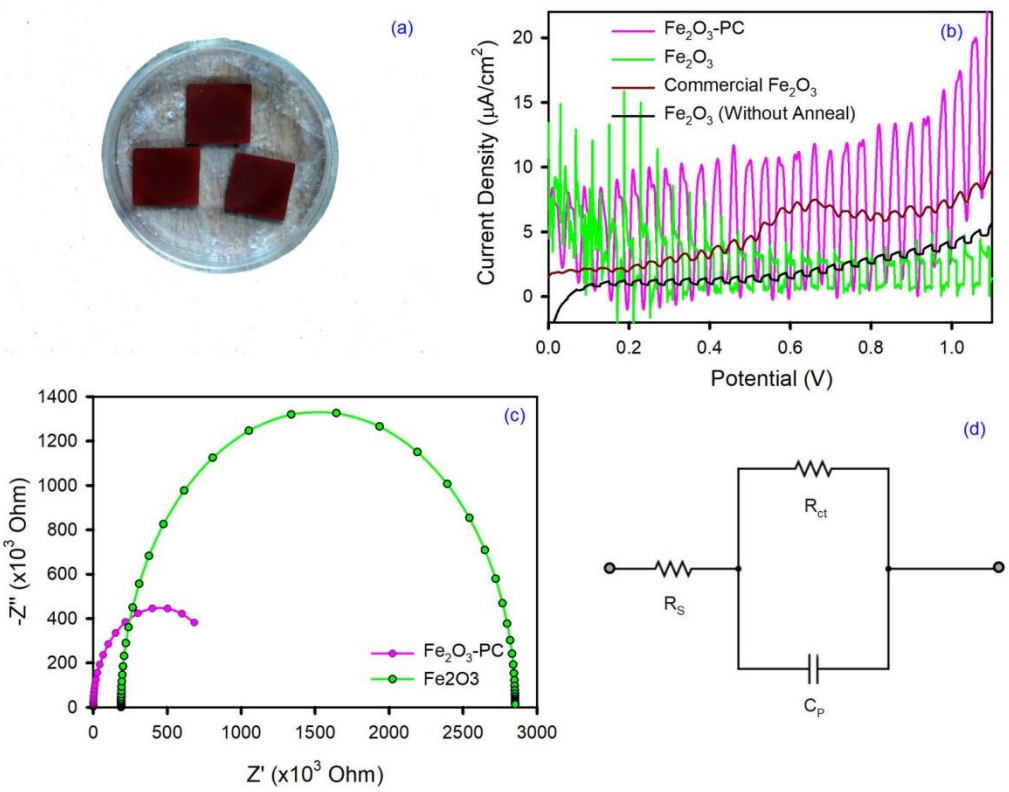

Figure 6.16: *a) Pictorial image of a cell prepared by a-Fe_2O_3 NP, b) Photocurrent density of different systems a-Fe_2O_3, a-Fe_2O_3-PC NH, Commercial a-Fe_2O_3 and as-synthesized a-Fe_2O_3 (without annealing), c) Nyquist plot of a-Fe_2O_3 and a-Fe_2O_3-PC measured at open circuit condition, d) an equivalent circuit that produces the Nyquist plot.*

The photoconductivity of the NH has been carried out to recognize the role of photoinduced charge separation to the net photocurrent. The linear sweep voltammograms (LSV) is recorded on pristine Fe_2O_3 NPs and Fe_2O_3-PC NH. It is found that in the dark condition the current is negligible for both systems. Although Fe_2O_3 has a broad visible absorption band, it has low photocurrent density particularly due to the fast recombination rate of the photo-generated electron-hole pairs. The adhesion of PC and Fe_2O_3 can significantly improve the PEC performance of Fe_2O_3 NP. The images of the NH deposited ITO cells are shown in Figure 6.16a. The photocurrent density of the Fe_2O_3-PC NH has been doubled up to compare with pristine Fe_2O_3 NP (Figure 6.16b), suggesting that interaction of PC with Fe_2O_3 improves charge separation of Fe_2O_3-PC nanocomposite. Consequently, NH shows higher PEC performance. We have

compared the photocurrent of commercially bought Fe_2O_3 and as-synthesized Fe_2O_3 NP (without annealing). The photocurrent output and stability of both the system are much lower than that of either Fe_2O_3 (annealed) or Fe_2O_3-PC NH.

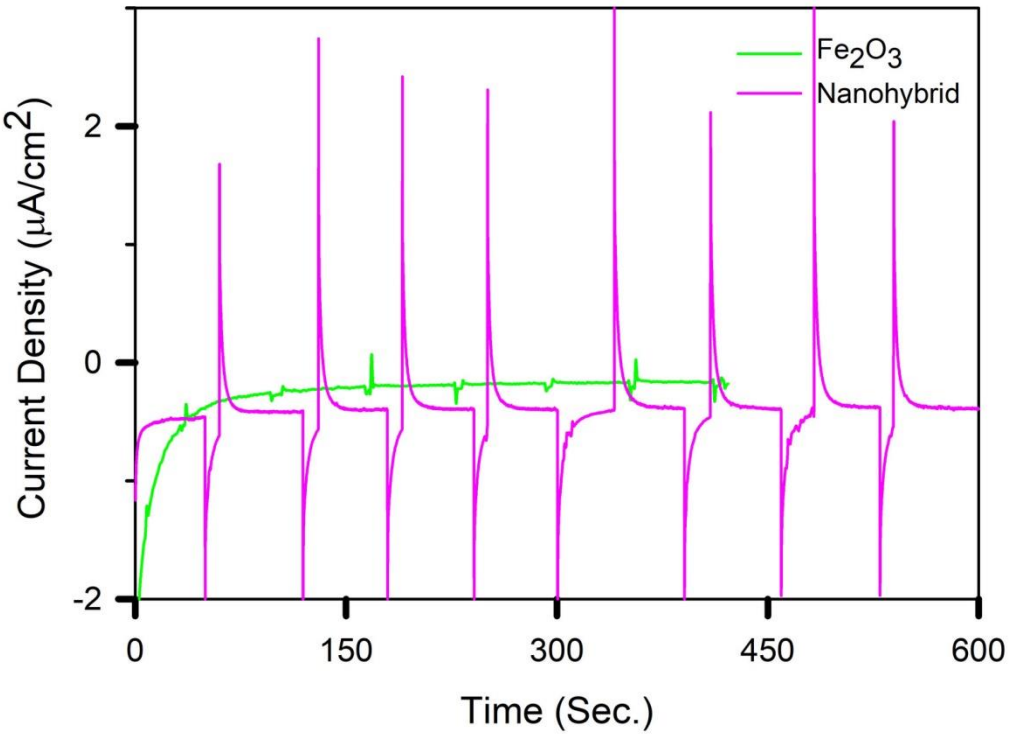

Figure 6.17: *Current-time response (chronoamperometry) curve of the pristine a-Fe_2O_3 and NH for 10 minutes under the fixed illumination of light.*

The photoelectric flux of the newly synthesized Fe_2O_3 NP (no annealing treatment) is almost negligible, which means that to get a better photocurrent output NP needs to be annealed at a higher temperature. During annealing, the crystallinity of the system increases with the lowering of defects and impurities, resulting in improvement in photocurrent. It is found that commercial Fe_2O_3 also gives negligible photocurrent. The stability of the photocurrent is another key issue for an effective photoelectrochemical water splitting process. To check the stability of the NH, continuous photocurrent was measured for 10 min. in 0.1 M Na_2SO_4 (pH7 PBS) holding the electrodes at a potential of 0.8 V. The chronoamperometric plots of the NH films and pristine system under the fixed illumination of light (intensity

100 mW/cm^2) for 10 min. is depicted in Figure 6.17. NH shows a fairly stable nature for photoelectrochemical water oxidation. The electrochemical impedance spectra were recorded within the frequency range of 100 kHz to 20 MHz using ac amplitude of 10 mV at a fixed potential of 0.8 V under UV-Vis illumination. Figure 6.16c and 6.16d show the Nyquist plot obtained at similar experimental conditions using Fe_2O_3 and Fe_2O_3-PC films. The corresponding equivalent circuit diagram is shown in Figure 6.16d to estimate the circuit parameters, where R_s, the solution (ohmic) resistance, R_{ct} is the charge-transfer resistance across the photocatalyst-electrolyte interface and C_P is the associated capacitance. The calculated R_{ct} value of NH is 2.5 times lower than the pristine Fe_2O_3 NP. Due to the facile transfer of photogenerated holes across the photocatalyst-electrolyte interface hybrid material exhibits higher photocurrent.

Further, we have used the NH as a visible light photocatalyst. As we discussed earlier, although Fe_2O_3 has a bandgap in the visible range, the photocatalytic activity of Fe_2O_3 is very limited due to its fast charge recombination rate [77]. Our newly developed NH is designed to prevent the rapid recombination process of Fe_2O_3. We have monitored the degradation of model contaminant Methylene Blue (MB) under visible light irradiance as depicted in Figure 6.18a. The photocatalytic activity of NH is compared with as-synthesized Fe_2O_3 and commercially available hematite (Figure 6.18b). A major increase in catalytic efficiency has been observed in the NH compared to other systems. The catalytic rate constants are shown in Figure 6.18c. The insets show the images of the aqueous solution before and after the experiments, clearly showing the degradation of MB in the presence of the catalyst. Figure 6.18d shows the image of photocatalyst with and without the presence of a magnetic field after keeping the photocatalyst in place for 30 minutes, which shows that NH can be easily separated using a small magnetic field, making it easy to recover the active

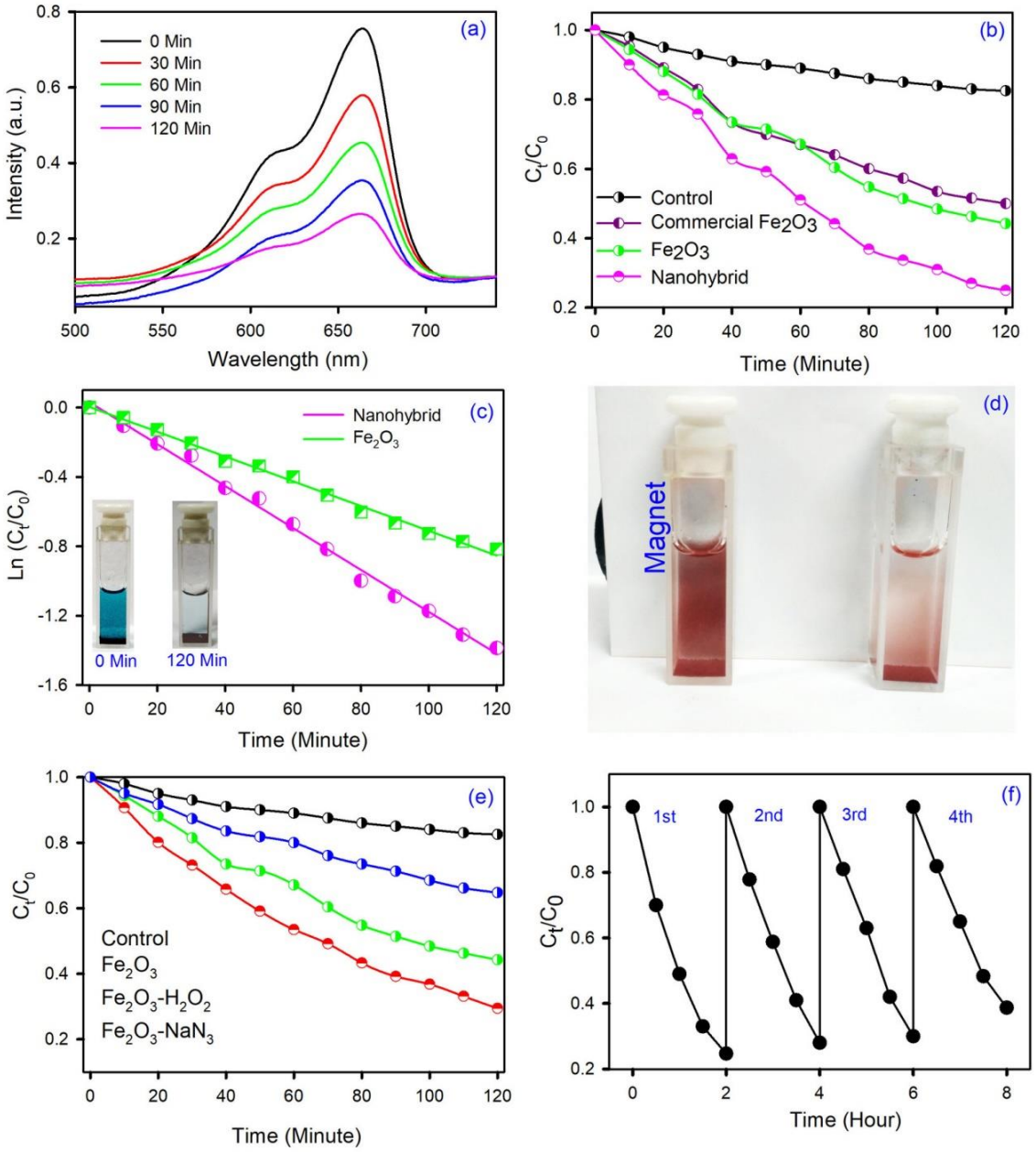

Figure 6.18: *a) Photocatalytic degradation curve of MB in presence of NH, b) visible light photocatalytic degradation of different systems, c) degradation rate of NH and a-Fe_2O_3 NP, inset shows the initial and final state of MB contained water, d) effect of magnetic attraction of the NH in presence of a magnetic environment, e) photocatalytic degradation rate of a-Fe_2O_3 in presence of radical initiator (H_2O_2 and radical quencher (NaN_3), f) photocatalytic repeatability test of NH.*

photocatalyst from the aqueous medium after the catalytic experiment. The details of the photocatalytic rate constants for different systems are given in Table 6.4.

Table 6.4: *Photocatalytic degradation rate and rate constant of different systems.*

System	% degradation in 2 hr.	Rate Constant (min^{-1})	Rate constant (min^{-1} mg^{-1} L $\times 10^{-3}$)
MB Control	12	0.001	0.01
Commercial Fe_2O_3	49	0.0061	0.006
Fe_2O_3	56	0.007	0.007
Fe_2O_3-PC	75	0.012	0.012

Intending to investigate the role of reactive oxygen species (ROS) in the photocatalytic process, we have used well known radical quencher and activator (sodium azide and H_2O_2). It is found that photocatalytic activity has reduced in presence of NaN_3 whereas the activity increased in the presence of H_2O_2 (Figure 6.18e). The results suggest that the photocatalysis procedure is mainly facilitated through the ROS generation mechanism [78]. For practical application, the repeatability of the photocatalyst has always been an important factor. NH showed good photocatalytic activity up to four cycles (Figure 6.18f), indicating the catalyst has excellent stability.

To explore the specific areas and the porosity of the as-synthesized NP and NH we have performed BET gas sorption measurement. N_2 adsorption-desorption isotherms and pore size distributions (of Fe_2O_3 NP and NH calculated using the B.J.H. method) are shown in Figure 6.19. These isotherms are classified as type II, which indicates that the synthesized NPs are slightly porous or macroporous [79]. The Fe_2O_3-PC NP shows a higher BET surface area (34.04 m^2/gm) compared to the pristine one (29.57 m^2/gm). In the NH system, the aggregation between the individual Fe_2O_3 NP decreases in the presence of PC which is the reason for the higher surface area. The pore diameter of the Fe_2O_3 and NH was found to be 1.66 nm and 1.88 nm respectively.

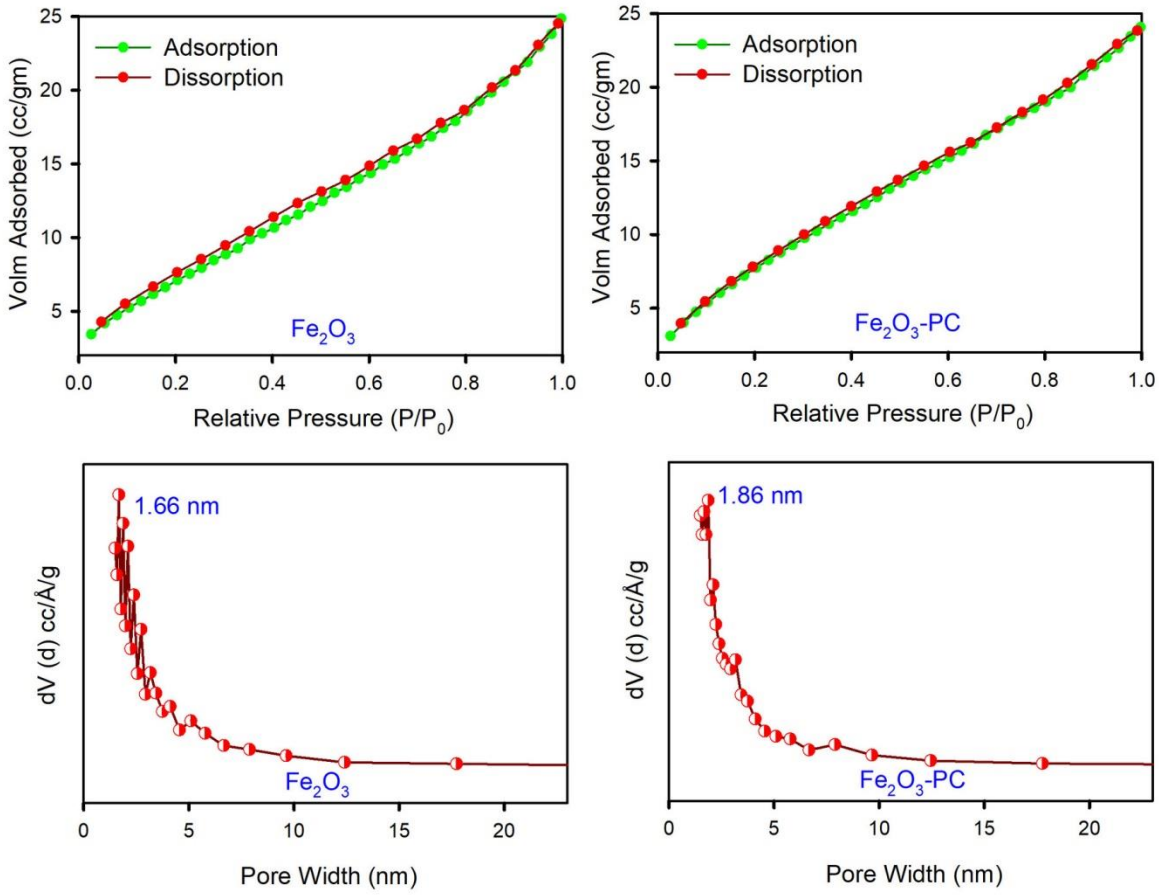

Figure 6.19: *Adsorption desorption curve and pore size of a-Fe_2O_3 and a-Fe_2O_3 -PC.*

Scheme 6.2 describes a schematic diagram of the proposed visible light catalytic mechanism. The band alignment of Fe_2O_3 and PC is such that the combined system forms a type II heterojunction. This kind of band alignment is very much efficient for charge separation [28, 80-82]. In presence of visible light, the excited-state electrons travel from the LUMO of PC to the conduction band of Fe_2O_3 whereas the holes move from the valence band of Fe_2O_3 to the HOMO of PC. As a result, an efficient electron-hole delocalization process happens in the interface which results in better photocatalytic activity in Fe_2O_3-PC NH.

To utilize the NH in real-life applications, we have performed the photocatalytic activity of NH after embedding it in the SSM. Fe_2O_3 NP was embedded on the surface of the mesh using the hydrothermal technique. The color

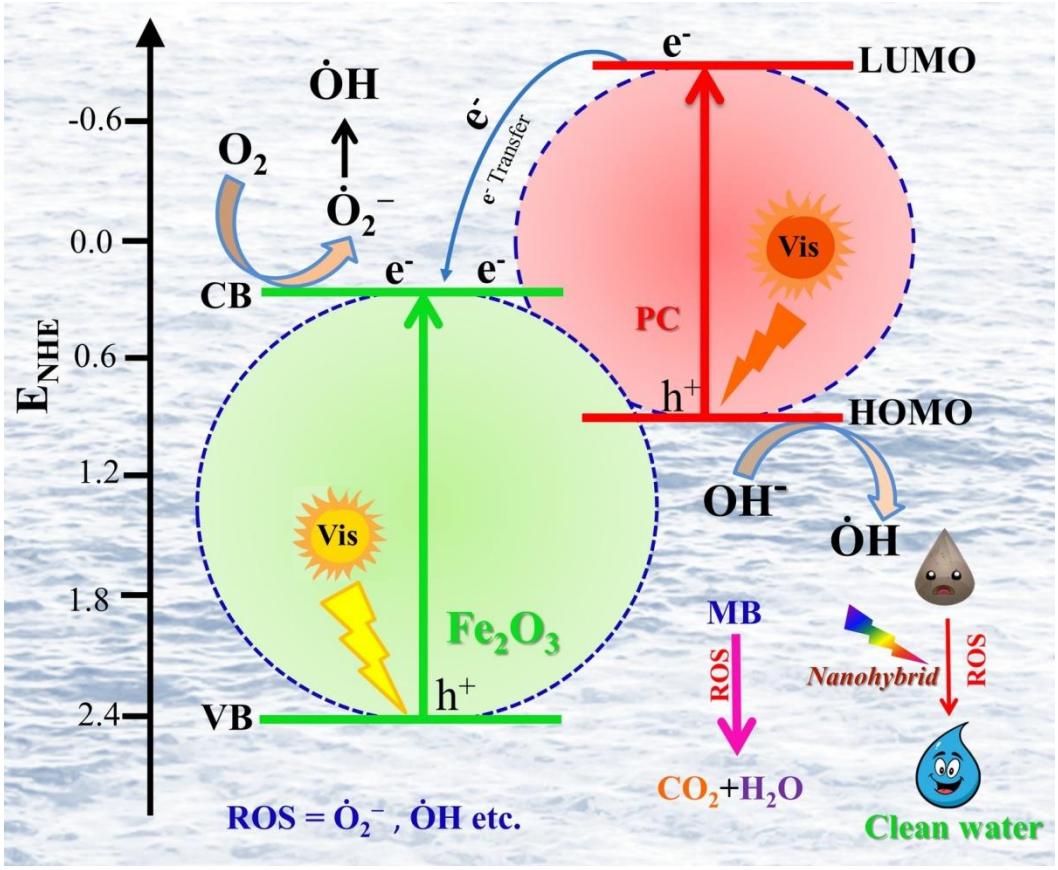

Scheme 6.2: *Relative band positions and charge transfer mechanism of the nanohybrid.*

of the mesh turns silvery white to darkish red after the deposition. The morphology of SSM before and after Fe_2O_3 treatment was studied by scanning electron microscope. Figures 6.20a and 6.20b show the SEM image of bare SSM with different magnification. Figure 6.20c and d show the SEM images of SSM after keeping them for one month at ambient conditions. There is almost no change in SSM after keeping them in ambient condition. Even after one month, there is almost no coating of rust (which is a type of $Fe_{2-x}O_{3+x}$). But after hydrothermal treatment for 36 hr. we observed the surface of the SSM substrate is entirely covered with spindle-like structures of Fe_2O_3 with a size of approximately ~200 nm. The enlarged image of the mesh shows the homogeneous distribution of NP (Figure 6.20e) attached to the top of the mesh. This Fe_2O_3 embedded mesh was

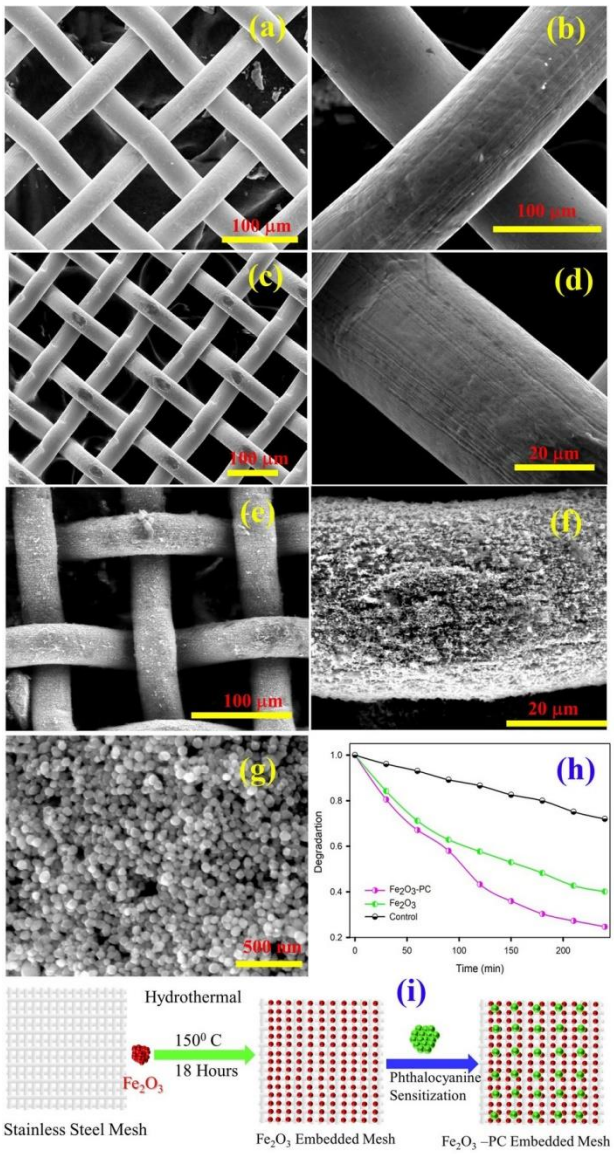

Figure 6.20: *SEM image of a) and b) bare stainless steel mesh, c) and d) stainless steel mesh after keeping in ambient condition for one month, e) and f) stainless steel mesh after embedded with a-Fe_2O_3 NP using the hydrothermal method, g) high-resolution SEM image of NP embedded on the mesh, h) photocatalysis of a-Fe_2O_3 NP, NH, and control system, i) schematic image of the whole embedded process.*

then sensitized by PC. The photocatalytic activity of Fe_2O_3 and Fe_2O_3-PC embedded SSM is shown in Figure 6.20h. We found NH degrades 50% MB in 4 hr. compared to 35% degradation by Fe_2O_3. A schematic process of the Fe_2O_3 decoration on the SSM and sensitization process is described in Figure 6.20i. This kind of mesh-based photocatalytic system has a dual-action mechanism for the

pollutant removal process. Photocatalyst eliminates the contaminant by chemical degradation process, at the same time, mesh acts as a physical filter to remove the contaminants [31]. An important consequence of the current work is that this system can be used on a large scale as this kind of immobile system is easily separable after the cleaning process. The NH loaded mesh can be easily formed into a different shape and applied to use as a continuous flow reactor.

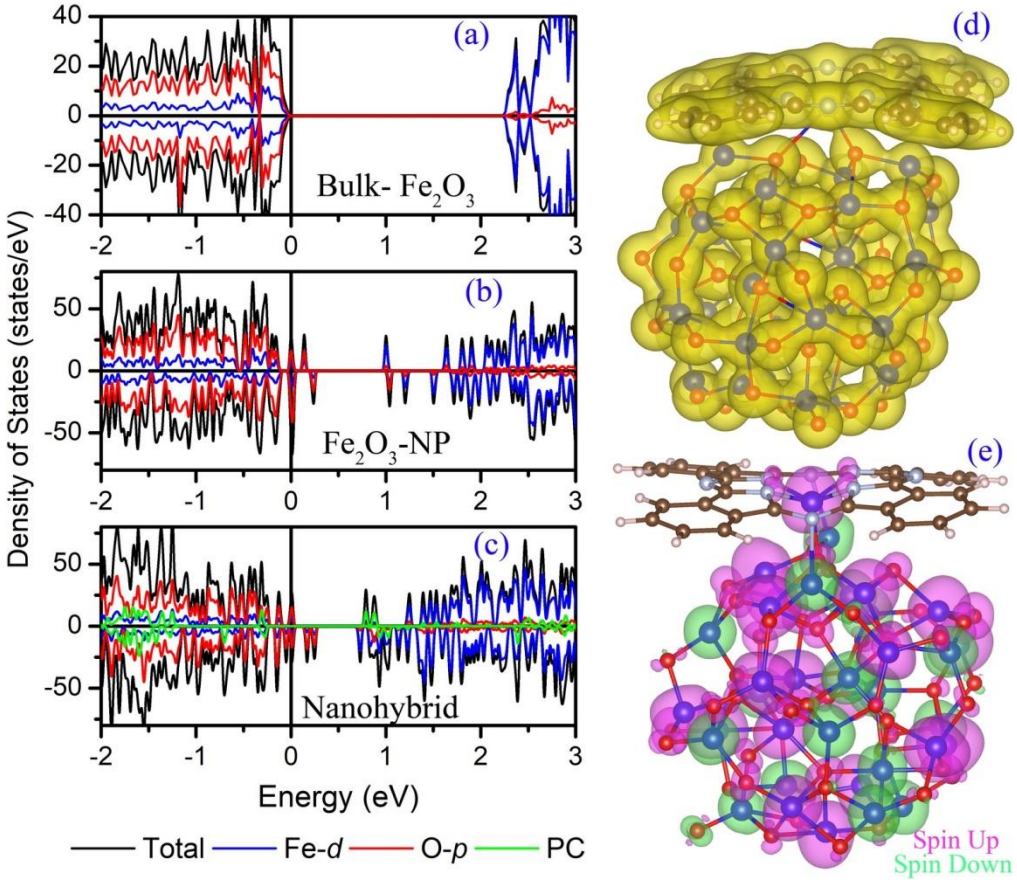

Figure 6.21: *Orbital projected density of states (OPDOS) of a) bulk a-Fe_2O_3, b) a-Fe_2O_3-NP, and c) a-Fe_2O_3-PC NH, d) charge density plot of NH, and e) spin density plot of NH system.*

Aiming to find insight into the reason for enhanced activity in the Fe_2O_3-PC NH system, we have carried out the first principles DFT study. A Fe_2O_3 nanocluster is created from bulk Fe_2O_3 and PC ligand is attached to it. Structural optimization of the pristine Fe_2O_3 NP and Fe_2O_3-PC NH was carried out using GGA-PBE formalism. Hematite belongs to the trigonal space group, and it has different magnetic configurations. All possible magnetic configurations of Fe_2O_3

have been investigated and found antiferromagnetic (AFM) configuration to be energetically most stable which is consistent with previously reported literature [83, 84]. Although the experimentally observed bandgap of the hematite Fe_2O_3-NP is ~2.2 eV, the GGA calculated band gap was found ~0.2 eV [85]. This deviation of the band gap from the experimental result is due to the incapability of GGA functional to accurately calculate the CBM incorporating the strongly correlated Fe- 3*d* electrons. To overcome this problem, we have used the GGA+U approach with a U-J value ~5 eV (U= 5.5 eV and J = 0.5 eV), where the bandgap was found ~2.2 eV, which is consistent with experimentally obtained bandgap [85, 86]. These parameter values are kept intact for the rest of the calculations. The orbital projected density of states (OPDOS) of the bulk Fe_2O_3 is depicted in Figure 6.21a. The GGA+U OPDOS of Fe_2O_3 reveals that valance band maxima are contributed by hybridized 2*p* character of O and 3*d* character of Fe atom, whereas conduction band minima is mainly contributed by Fe-3*d* character indicating a *p*-*d* transition [85] which is consistent with spectroscopic descriptions [87]. Next, we investigated the electronic structure of Fe_2O_3 NP and the NH. The binding energy of the NH has been calculated from the formula written below-

$$E_B = E_{NH} - E_{Fe_2O_3} - E_{PC} \tag{6.1}$$

The calculated binding energy of the NH is approximately -21 meV/atom, indicating the formation of NH is thermodynamically favorable. The OPDOS of Fe_2O_3 NP (shown in Figure 6.21b) depicts a visible reduction in bandgap in the density of states of the NP. Due to surface reconstruction during NP formation, lots of surface states have been generated, which results in a change in the bandgap. Few states are generated within the bandgap of the NP which is caused by the 2*p* character of surface O-atoms and 3*d* character of surface Fe atoms. While valance band minima are mainly dominated by O-*p* orbital, conduction band maxima are dominated by Fe-*d* character which is comparable to the bulk system [87]. The up channel and down channel of the DOS is asymmetric due to the effect of spin tilting after surface reconstruction. This is one of the prime reasons for

increment in the magnetic moment in the nano Fe_2O_3 structures. Per molecule magnetic moment in NP increased to 0.28 μ_B, which is higher compared to the bulk system. There is an *n*-type doping in the NH system after ligand attachment, which indicates the possibility of ligand to metal charge transfer (LMCT) from PC to Fe_2O_3 NP. This result follows the experimental trend. The OPDOS of the NH is depicted in Figure 6.21c. It is found that the conduction band maximum is highly hybridized by the Fe-3*d*, O-2*p* character along with the *p* character of PC. After the formation of NH the conduction band edge of Fe_2O_3 is moved towards the valence bands significantly reducing the bandgap, which could favor an easier electron transfer across the bandgap [86]. From the charge density diagram of the system (as shown in Figure 6.21d), the delocalization of the charge can be observed more clearly. The figure shows that there is a large charge overlap between the Fe_2O_3 and the PC system, indicating the possibility of net charge transfer between the two systems. As a result of efficient charge transfer, we observe the high catalytic activity in the NH system. The spin density plot of the NH is presented in Figure 6.21e reveals the asymmetric spin distribution in the NH system. The magnetic moment has been increased in NH due to the charge transfer between PC and Fe_2O_3, and asymmetric spin canting at the surface. This result is consistent with the experimentally obtained increment in the magnetic moment in NH.

6.3. Conclusion:

In summary, we developed (Cu)PP-TiO_2 NH which can reduce Cr(VI) in the presence of visible light. Compared with PP-TiO_2, (Cu)PP-TiO_2 NH shows much higher photocatalytic activity and recyclability. Besides, the presence of dissolved metal ion (Cr^{3+} and Fe^{3+}) decreases the photocatalytic efficiency of PP-TiO_2 significantly. However, the enhanced photostability of (Cu)PP-TiO_2 shows almost the same performance in the presence of dissolved metal ion (Cr^{3+} and Fe^{3+}) in water. We have also developed a prototype for practical applications. (Cu)PP-TiO_2 NH fabricated on SSM can reduce toxic metal Cr(VI) efficiently in the

presence of visible light. The newly developed hybrid material acted as a chemical cleaning mediator to detoxify toxic Cr(VI) into non-toxic Cr(III), and the host mesh serves as a physical strainer to remove the photo-reduced products. This double cleaning effect of the prototype can effectively separate the product (basically suspended particles) from the water and prevent the further reduction of Cr(III) to Cr(VI) in the natural/physiological environment. This novel prototype will serve as a promising tool for water purification applications to tackle hazards from aqua-chromium.

Moreover, we have described the novel synthesis strategy of a multipurpose NH using magnetic NP (Fe_2O_3) which can provide enhanced photocatalytic activity and photoelectrochemical activity. The photoinduced electron-hole separation is higher in the hybrid system. Compared with pristine Fe_2O_3, the wider light absorption and more effective delocalization of charge in NH produce higher photocurrent and photocatalytic activity. Excitation electrons from LUMO of PC to CB of Fe_2O_3 can stimulate the photoactivity induced by visible light. PC hybridization on the Fe_2O_3 shows multiple enhanced activities (photocatalytic and photocurrent). In addition, NH has been implanted on the top of the SSM, and their photocatalytic activity (in the presence of visible light) has been studied, which is very promising. We believe that the present work can be worthwhile in the direction of magnetic catalysts having higher charge separation which can be used as both mobile and immobile catalysts.

References

[1] S. Chu, A. Majumdar, Opportunities and challenges for a sustainable energy future, *Nature* 488 (2012) 294.

[2] J. A. Turner, Sustainable hydrogen production, *Science* 305 (2004) 972.

[3] X. Chen, C. Li, M. Gratzel, R. Kostecki, S. S. Mao, Nanomaterials for renewable energy production and storage, *Chem. Soc. Rev.* 41 (2012) 7909.

[4] N. Serpone, A. V. Emeline, Semiconductor photocatalysis—Past, present, and future outlook, *J. Phys. Chem. Lett.* 3 (2012) 673.

[5] Z. Hai, N. El Kolli, D. B. Uribe, P. Beaunier, M. Jose-Yacaman, J. Vigneron, A. Etcheberry, S. Sorgues, C. Colbeau-Justin, J. Chen, H. Remita, Modification of TiO_2 by bimetallic Au-Cu nanoparticles for wastewater treatment, *J. Mater. Chem. A* 1 (2013) 10829.

[6] E. Kowalska, K. Yoshiiri, Z. Wei, S. Zheng, E. Kastl, H. Remita, B. Ohtani, S. Rau, Hybrid photocatalysts composed of titania modified with plasmonic nanoparticles and ruthenium complexes for decomposition of organic compounds, *Appl. Catal. B* 178 (2015) 133.

[7] H. Nishi, T. Torimoto, T. Tatsuma, Wavelength and efficiency-tunable plasmon-induced charge separation by the use of Au-Ag alloy nanoparticles, *Phys. Chem. Chem. Phys.* 17 (2015) 4042.

[8] Y. Chen, M. Yue, Z. H. Huang, L. N. Wang, F. Kang, Monolithic organic/inorganic ternary nanohybrids toward electron transfer cascade for enhanced visible-light photocatalysis, *RSC Adv.* 5 (2015) 23174.

[9] M. D. Hernandez-Alonso, F. Fresno, S. Suarez, J. M. Coronado, Development of alternative photocatalysts to TiO_2: Challenges and opportunities, *Energy Environ. Sci.* 2 (2009) 1231.

[10] J. Schneider, M. Matsuoka, M. Takeuchi, J. Zhang, Y. Horiuchi, M. Anpo, D. W. Bahnemann, Understanding TiO_2 photocatalysis: Mechanisms and materials, *Chem. Rev.* 114 (2014) 9919.

[11] J. Tao, T. Luttrell, M. Batzill, A two-dimensional phase of TiO_2 with a reduced bandgap, *Nat. Chem.* 3 (2011) 296.

[12] X. Chen, L. Liu, P.Y. Yu, S. S. Mao, Increasing solar absorption for photocatalysis with black hydrogenated titanium dioxide nanocrystals, *Science* 331 (2011) 746.

[13] L. M. Peter, The Grätzel Cell: Where Next?, *J. Phys. Chem. Lett.* 2 (2011) 1861.

[14] J. W. Dobrucki, Interaction of oxygen-sensitive luminescent probes Ru(phen)32+ and Ru(bipy)32+ with animal and plant cells in vitro: Mechanism of phototoxicity and conditions for non-invasive oxygen measurements, *J. Photochem. Photobiol. B* 65 (2001) 136.

[15] J. N. Demas, D. Diemente, E. W. Harris, Oxygen quenching of charge-transfer excited states of ruthenium(II) complexes. Evidence for singlet oxygen production, *J. Am. Chem. Soc.* 95 (1973) 6864.

[16] M. T. Mayer, Y. Lin, G. Yuan, D. Wang, Forming heterojunctions at the nanoscale for improved photoelectrochemical water splitting by semiconductor materials: Case studies on hematite, *Acc. Chem. Res.* 46 (2013) 1558.

[17] J. S. Jang, H. G. Kim, J. S. Lee, Heterojunction semiconductors: A strategy to develop efficient photocatalytic materials for visible light water splitting, *Catal. Today* 185 (2012) 270.

[18] A. Kongkanand, K. Tvrdy, K. Takechi, M. Kuno, P. V. Kamat, Quantum dot solar cells. Tuning photoresponse through size and shape control of CdSe−TiO_2 architecture, *J. Am. Chem. Soc.* 130 (2008) 4007.

[19] D. R. Baker, P. V. Kamat, Photosensitization of TiO_2 nanostructures with CdS Quantum dots: Particulate versus tubular support architectures, *Adv. Funct. Mater.* 19 (2009) 805.

[20] Y. Wang, Q. Wang, X. Zhan, F. Wang, M. Safdar, J. He, Visible light driven type II heterostructures and their enhanced photocatalysis properties: A review, *Nanoscale* 5 (2013) 8326.

[21] C. Haw, W. Chiu, S. Abdul Rahman, P. Khiew, S. Radiman, R. Abdul Shukor, M. A. A. Hamid, N. Ghazali, The design of new magnetic-photocatalyst nanocomposites ($CoFe_2O_4$–TiO_2) as smart nanomaterials for recyclable-photocatalysis applications, *New J. Chem.* 40 (2016) 1124.

[22] H. Yao, M. Fan, Y. Wang, G. Luo, W. Fei, Magnetic titanium dioxide based nanomaterials: Synthesis, characteristics, and photocatalytic application in pollutant degradation, *J. Mater. Chem. A* 3 (2015) 17511.

[23] F. Shi, Y. Li, Q. Zhang, H. Wang, Synthesis of Fe_3O_4/C/TiO_2 magnetic photocatalyst via vapor phase hydrolysis, *Int. J. Photoenergy* 2012 (2012) 8.

[24] A. Kumar, Shalini, G. Sharma, M. Naushad, A. Kumar, S. Kalia, C. Guo, G. T. Mola, Facile hetero-assembly of superparamagnetic Fe_3O_4/$BiVO_4$ stacked on biochar for solar photo-degradation of methyl paraben and pesticide removal from soil, *J. Photochem. Photobiol. A: Chem.* 337 (2017) 118.

[25] A. Habibi-Yangjeh, M. Mousavi, K. Nakata, Boosting visible-light photocatalytic performance of g-C_3N_4/Fe_3O_4 anchored with $CoMoO_4$ nanoparticles: Novel magnetically recoverable photocatalysts, *J. Photochem. Photobiol. A: Chem.* 368 (2019) 120.

[26] A. Fernández, G. Lassaletta, V.M. Jiménez, A. Justo, A.R. González-Elipe, J. M. Herrmann, H. Tahiri, Y. Ait-Ichou, Preparation and characterization of TiO_2 photocatalysts supported on various rigid supports (glass, quartz and stainless steel): Comparative studies of photocatalytic activity in water purification, *Appl. Catal. B: Environ.* 7 (1995) 49.

[27] A. A. Aziz, K. S. Yong, S. Ibrahim, S. Pichiah, Enhanced magnetic separation and photocatalytic activity of nitrogen doped titania photocatalyst supported on strontium ferrite, *J. Hazard Mater.* 199-200 (2012) 143.

[28] Y. Xu, G. Zhang, G. Du, Y. Sun, D. Gao, α-Fe_2O_3 nanostructures with different morphologies: Additive-free synthesis, magnetic properties, and visible light photocatalytic properties, *Mater. Lett.* 92 (2013) 321.

[29] M. Tadic, M. Panjan, V. Damnjanovic, I. Milosevic, Magnetic properties of hematite (α-Fe_2O_3) nanoparticles prepared by hydrothermal synthesis method, *Appl. Surf. Sci.* 320 (2014) 183.

[30] K. Kamada, N. Soh, Enhanced visible-light-induced photocatalytic activity of α-Fe_2O_3 adsorbing redox enzymes, *J. Asian Ceram. Soc.* 3 (2015) 18.

[31] P. Kar, T. K. Maji, P. K. Sarkar, P. Lemmens, S. K. Pal, Development of a photo-catalytic converter for potential use in the detoxification of Cr(VI) metal in water from natural resources, *J. Mater. Chem. A* 6 (2018) 3674.

[32] B. Liu, H. C. Zeng, Carbon nanotubes supported mesoporous mesocrystals of anatase TiO_2, *Chem. Mater.* 20 (2008) 2711.

[33] G. B. Deacon, R. J. Phillips, Relationships between the carbon-oxygen stretching frequencies of carboxylato complexes and the type of carboxylate coordination, *Coord. Chem. Rev.* 33 (1980) 227.

[34] P. Kar, S. Sardar, E. Alarousu, J. Sun, Z. S. Seddigi, S. A. Ahmed, E. Y. Danish, O. F. Mohammed, S. K. Pal, Impact of metal ions in porphyrin-based applied materials for visible-light photocatalysis: Key information from ultrafast electronic spectroscopy, *Chem. Eur. J.* 20 (2014) 10475.

[35] A. Marcelli, I. Jelovica Badovinac, N. Orlic, P. R. Salvi, C. Gellini, Excited-state absorption and ultrafast relaxation dynamics of protoporphyrin IX and hemin, *Photochem. Photobiol. Sci.* 12 (2013) 348.

[36] S. Sardar, P. Kar, S. K. Pal, The impact of central metal ions in porphyrin functionalized ZnO/TiO_2 for enhanced solar energy conversion, *J. Mat. NanoSci.* 1 (2014) 19.

[37] S. Verma, A. Ghosh, A. Das, H. N. Ghosh, Ultrafast exciton dynamics of J- and H-aggregates of the porphyrin-catechol in aqueous solution, *J. Phys. Chem. B* 114 (2010) 8327.

[38] N. C. Maiti, S. Mazumdar, N. Periasamy, J- and H-aggregates of porphyrin−surfactant complexes: Time-resolved fluorescence and other spectroscopic studies, *J. Phys. Chem. B* 102 (1998) 1528.

[39] G. Granados-Oliveros, E. A. Páez-Mozo, F. M. Ortega, C. Ferronato, J. M. Chovelon, Degradation of atrazine using metalloporphyrins supported on TiO_2 under visible light irradiation, *Appl. Catal. B: Environ.* 89 (2009) 448.

[40] S. Sarkar, A. Makhal, T. Bora, K. Lakhsman, A. Singha, J. Dutta, S. K. Pal, Hematoporphyrin–ZnO nanohybrids: Twin applications in efficient visible-light photocatalysis and dye-sensitized solar cells, *ACS Appl. Mater. Interfaces* 4 (2012) 7027.

[41] P. Kar, T. K. Maji, J. Patwari, S. K. Pal, Can a light harvesting material be always common in photocatalytic and photovoltaic applications?, *Mater. Chem. Phys.* 200 (2017) 70.

[42] Q. Wu, J. Zhao, G. Qin, C. Wang, X. Tong, S. Xue, Photocatalytic reduction of Cr(VI) with TiO_2 film under visible light, *Appl. Catal. B: Environ.* 142–143 (2013) 142.

[43] X. F. Lei, X. X. Xue, H. Yang, Preparation and characterization of Ag-doped TiO_2 nanomaterials and their photocatalytic reduction of Cr(VI) under visible light, *Appl. Surf. Sci.* 321 (2014) 396.

[44] J. Yang, J. Dai, J. Li, Visible-light-induced photocatalytic reduction of Cr(VI) with coupled Bi_2O_3/TiO_2 photocatalyst and the synergistic bisphenol A oxidation, *Environ. Sci. Pollut. Res.* 20 (2013) 2435.

[45] X. Liu, L. Pan, T. Lv, Z. Sun, C. Sun, Enhanced photocatalytic reduction of Cr(VI) by ZnO–TiO_2–CNTs composites synthesized via microwave-assisted reaction, *J. Mol. Catal. Chem.* 363–364 (2012) 417.

[46] X. Liu, L. Pan, T. Lv, G. Zhu, Z. Sun, C. Sun, Microwave-assisted synthesis of CdS-reduced graphene oxide composites for photocatalytic reduction of Cr(VI), *ChemComm* 47 (2011) 11984.

[47] P. Kar, T. K. Maji, R. Nandi, P. Lemmens, S. K. Pal, In-situ hydrothermal synthesis of Bi–$Bi_2O_2CO_3$ heterojunction photocatalyst with enhanced visible light photocatalytic activity, *Nano-Micro Lett.* 9 (2016) 18.

[48] P. Kar, S. Sardar, S. Ghosh, M. R. Parida, B. Liu, O. F. Mohammed, P. Lemmens, S. K. Pal, Nanosurface engineering of Mn_2O_3 for potential light-harvesting application, *J. Mater. Chem. C* 3 (2015) 8200.

[49] X. Zhao, Y. Wang, W. Feng, H. Lei, J. Li, Preparation of Cu(II) porphyrin-TiO_2 composite in one-pot method and research on photocatalytic property, *RSC Adv.* 7 (2017) 52738.

[50] Y. Zhang, Z. Chen, S. Liu, Y. J. Xu, Size effect induced activity enhancement and anti-photocorrosion of reduced graphene oxide/ZnO composites for degradation of organic dyes and reduction of Cr(VI) in water, *Appl. Catal. B: Environ.* 140–141 (2013) 598.

[51] L. Shao, J. Li, X. Liang, T. Xie, S. Meng, D. Jiang, M. Chen, Novel β-In2.77S4 nanosheet-assembled hierarchical microspheres: Synthesis and high performance for photocatalytic reduction of Cr(VI), *RSC Adv.* 6 (2016) 18227.

[52] X. Wang, S. O. Pehkonen, A. K. Ray, Removal of aqueous Cr(VI) by a combination of photocatalytic reduction and coprecipitation, *Ind. Eng. Chem. Res.* 43 (2004) 1665.

[53] D. K. Padhi, K. Parida, Facile fabrication of α-FeOOH nanorod/RGO composite: A robust photocatalyst for reduction of Cr(VI) under visible light irradiation, *J. Mater. Chem. A* 2 (2014) 10300.

[54] S. Jung, K. Yong, Fabrication of CuO-ZnO nanowires on a stainless steel mesh for highly efficient photocatalytic applications, *ChemComm* 47 (2011) 2643.

[55] C. J. Chang, P. Y. Chao, K. S. Lin, Flower-like BiOBr decorated stainless steel wire-mesh as immobilized photocatalysts for photocatalytic degradation applications, *Appl. Surf. Sci.* 494 (2019) 492.

[56] T. K. Maji, M. N. Hasan, S. Ghosh, D. Wulferding, C. Bhattacharya, P. Lemmens, D. Karmakar, S. K. Pal, Development of a magnetic nanohybrid for multifunctional application: From immobile photocatalysis to efficient photoelectrochemical water splitting: A combined experimental and computational study, *J. Photochem. Photobiol. A: Chem.* 397 (2020) 112575.

[57] X. Liu, K. Chen, J. J. Shim, J. Huang, Facile synthesis of porous Fe_2O_3 nanorods and their photocatalytic properties, *J. Saudi Chem. Soc.* 19 (2015) 479.

[58] J. F. Lu, C. J. Tsai, Hydrothermal phase transformation of hematite to magnetite, *Nanoscale Res. Lett.* 9 (2014) 230.

[59] T. Szatkowski, M. Wysokowski, G. Lota, D. Pęziak, V. V. Bazhenov, G. Nowaczyk, J. Walter, S. L. Molodtsov, H. Stöcker, C. Himcinschi, Novel nanostructured hematite–spongin composite developed using an extreme biomimetic approach, *RSC Adv.* 5 (2015) 79031.

[60] N. M. A. Rashid, C. Haw, W. Chiu, N. H. Khanis, A. Rohaizad, P. Khiew, S. A. Rahman, Structural and optical properties analysis of single crystalline hematite (α-Fe_2O_3) nanocubes prepared by one-pot hydrothermal approach, *CrystEngComm* 18 (2016) 4720.

[61] J. f. Lu, C. J. Tsai, Hydrothermal phase transformation of hematite to magnetite, *Nanoscale Res. Lett.* 9 (2014) 230.

[62] R. Nandi, S. Mishra, T. K. Maji, K. Manna, P. Kar, S. Banerjee, S. Dutta, S. Sharma, P. Lemmens, K. D. Saha, S. K. Pal, A novel nanohybrid for cancer theranostics: Folate sensitized Fe_2O_3 nanoparticles for colorectal cancer diagnosis and photodynamic therapy, *J. Mater. Chem. B* 5 (2017) 3927.

[63] S. Mitra, S. Das, K. Mandal, S. Chaudhuri, Synthesis of a α-Fe_2O_3 nanocrystal in its different morphological attributes: Growth mechanism, optical and magnetic properties, *Nanotechnology* 18 (2007) 275608.

[64] H. Pan, S. Low, N. Weerasuriya, B. Wang, Y. S. Shon, Morphological transformation of gold nanoparticles on graphene oxide: Effects of capping ligands and surface interactions, *Nano Converg.* 6 (2019) 2.

[65] Q. Li, M. Rellán-Piñeiro, N. Almora-Barrios, M. Garcia-Ratés, I. N. Remediakis, N. López, Shape control in concave metal nanoparticles by etching, *Nanoscale* 9 (2017) 13089.

[66] A. Ivanova, E. Slavinskaya, O. Stonkus, R. Gulyaev, T. Glazneva, A. Noskov, A. Boronin, Highly active and durable Pd/Fe_2O_3 catalysts for wet CO oxidation under ambient conditions, *Catal. Sci. Technol.* 6 (2016) 3918.

[67] K. P. Priyanka, S. Sankararaman, K. M. Balakrishna, T. Varghese, Enhanced visible light photocatalysis using TiO_2/phthalocyanine nanocomposites for the degradation of selected industrial dyes, *J. Alloys. Compd.* 720 (2017) 541.

[68] X. C. Dai, M. H. Huang, Y. B. Li, T. Li, B. B. Zhang, Y. He, G. Xiao, F. X. Xiao, Regulating spatial charge transfer over intrinsically ultrathin-carbon-encapsulated photoanodes toward solar water splitting, *J. Mater. Chem. A* 7 (2019) 2741.

[69] L. Yang, B. Kruse, Revised Kubelka–Munk theory. I. Theory and application, *J. Opt. Soc. Am. A* 21 (2004) 1933.

[70] W. H. Chen, K. E. Rieckhoff, E. M. Voigt, M. L. W. Thewalt, Double fluorescence lifetimes of metal-free phthalocyanine in a mixed-solvent Shpol'skii matrix at 4.2 K, *Mol. Phys.* 67 (1989) 1439.

[71] M. Gharagozlou, S. Naghibi, Sensitization of ZnO nanoparticles by metal–free phthalocyanine, *J. Lumin.* 196 (2018) 64.

[72] D. Karmakar, S. Mandal, R. Kadam, P. Paulose, A. Rajarajan, T. K. Nath, A. K. Das, I. Dasgupta, G. Das, Ferromagnetism in Fe-doped ZnO nanocrystals: Experiment and theory, *Phys. Rev. B* 75 (2007) 144404.

[73] R. D. Zysler, D. Fiorani, A. M. Testa, L. Suber, E. Agostinelli, M. Godinho, Size dependence of the spin-flop transition in hematite nanoparticles, *Phys. Rev. B* 68 (2003) 212408.

[74] S. Das Sarma, E. H. Hwang, A. Kaminski, Temperature-dependent magnetization in diluted magnetic semiconductors, *Phys. Rev. B* 67 (2003) 155201.

[75] S. Mørup, C. Frandsen, F. Bødker, S. N. Klausen, K. Lefmann, P. A. Lindgård, M. F. Hansen, Magnetic properties of nanoparticles of antiferromagnetic materials, *Springer Netherlands*, Dordrecht, Netherlands, 2003.

[76] B. Issa, I. M. Obaidat, B. A. Albiss, Y. Haik, Magnetic nanoparticles: Surface effects and properties related to biomedicine applications, *Inter. J. Mol. Sci.* 14 (2013) 21266.

[77] A. G. Joly, G. Xiong, C. Wang, D. E. McCready, K. M. Beck, W. P. Hess, Synthesis and photoexcited charge carrier dynamics of β-FeOOH nanorods, *Appl. Phys. Lett.* 90 (2007) 103504.

[78] T. K. Maji, P. K. Sarkar, P. Kar, B. Liu, P. Lemmens, D. Karmakar, S. K. Pal, A combined experimental and computational study on a nanohybrid material for potential application in NIR photocatalysis, *Appl. Catal. A: Gen.* 583 (2019) 117124.

[79] K. S. Singh, Reporting physisorption data for gas/solid systems with special reference to the determination of surface area and porosity, *Pure Appl. Chem.* 57 (1985) 603.

[80] M. Gorgoi, D. R. T. Zahn, "Band bending" in copper phthalocyanine on hydrogen-passivated Si (111), *Org. Electron.* 6 (2005) 168.

[81] A. G. Tamirat, J. Rick, A. A. Dubale, W. N. Su, B. J. Hwang, Using hematite for photoelectrochemical water splitting: A review of current progress and challenges, *Nanoscale Horiz.* 1 (2016) 243.

[82] T. Teranishi, M. Sakamoto, Charge separation in type-II semiconductor heterodimers, *J. Phys. Chem. Lett.* 4 (2013) 2867.

[83] X. Huang, S. K. Ramadugu, S. E. Mason, Surface-specific DFT + U approach applied to α-Fe_2O_3(0001), *J. Phys. Chem. C* 120 (2016) 4919.

[84] S. Chaudhury, C. Varadachari, K. Ghosh, Ab initio studies on hematite surface and the adsorption of phosphate, *J. Theor. Chem.* 2014 (2014) 1.

[85] G. Rollmann, A. Rohrbach, P. Entel, J. Hafner, First-principles calculation of the structure and magnetic phases of hematite, *Phys. Rev. B* 69 (2004) 165107.

[86] N. Dzade, A. Roldan, N. de Leeuw, A density functional theory study of the adsorption of benzene on hematite (α-Fe_2O_3) surfaces, *Minerals* 4 (2014) 89.

[87] J. Zaanen, G. Sawatzky, J. Allen, Band gaps and electronic structure of transition-metal compounds, *Phys. Rev. Lett.* 55 (1985) 418.

Chapter 7

Experimental and Computational Studies on Inorganic-Inorganic Nanohybrid for Efficient NIR Light Harvesting

7.1. Introduction:

In heterostructure material, two or more different materials of different compositions meet at interfaces [1]. This type of hybrid system is expected to put a great impact on the future design and development of multifunctional materials with defined purposes [1-4]. Numerous new ideas have been initiated for synthesizing different types of heterostructures such as metal-metal [5], metal-polymer [6], organic-inorganic heterostructure [7], and inorganic-inorganic heterostructure [8]. Novel with enhanced physical and chemical properties can be found in the newly developed heterostructure which comes due to strong interactions between the two counterparts [4]. The current trend in material science advances towards the inorganic semiconductor–semiconductor hybrid system in which the hybridization of two different inorganic materials makes a new material, which can have enhanced property compare to pristine counterparts [9, 10]. This motivates us to work on inorganic-inorganic nanohybrid (NH) systems. In our coupled inorganic-inorganic semiconductor NHs, enhanced activity can be described as the result of transfer of electrons and holes from one semiconductor to another.

In this chapter, we have prepared an inorganic-inorganic NH heterojunction using two different inorganic semiconductors. The work aimed to utilize the NIR part of the solar light efficiently using a combination of two inorganic semiconductors. Although UV and visible part of the solar spectrum has been widely used to harvest solar light, very little work has been reported to

harvest near-infrared (NIR) light. Moreover, UV and visible light contain only 51% of the total solar spectrum. So, to improve the efficiency of photocatalytic reactions, it is highly desirable to develop new strategies to make full use of the residual solar spectrum. Although there are many difficulties, such as low photon energy conversion rate and high thermal effect [11, 12] the main benefit of NIR is its high penetration depth and higher available time [13]. Recently works have explored the possibility of harvesting NIR light and utilize it in the photocatalytic reaction [14-18]. Many approaches have been explored to efficiently harvest NIR light including up-conversion, Surface Plasmon Resonance (SPR) material incorporation, bandgap engineering, etc [19-22]. An appropriate combination of materials with proper band-gap alignment can harvest NIR light which can accelerate NIR induced photocatalysis [21, 23, 24]. In the present work we have used band-gap engineering mechanism in a novel inorganic heterostructure to harvest NIR light.

Photocatalysis can be demonstrated as the acceleration of a reaction in the presence of a photon by adding a substance (catalyst) [25, 26]. Since the discovery of photocatalysis [27] in 1972, an enormous amount of investigation has been done to decontaminate water using heterogeneous photocatalytic reactions [25, 28-33]. Though NIR contains almost half of the solar spectrum, the uses of NIR light in the photocatalytic field are not very promising as the low photon energy of NIR light has very little efficiency to harvest solar light [15, 34]. A lot of research has been devoted to converting more solar energy to photochemical energy [23, 35-37]. Recently, semiconductor heterostructure has gained a lot of interest in the photocatalytic research field as the efficient formation of the hybrid system can maximize solar spectra harvesting. Many other properties including electronic, magnetic, optical can be highly tuned in the hybrid system [38-40], which can be very beneficial for application purposes.

In the present case, a modulated band-alignment of the hybrid system, achieved by the synergistic effect of NIR active material with an efficient photocatalyst produces a favorable charge transfer pathway that separates the photoinduced charge and also reduces the recombination process. We have used a wide bandgap semiconductor ZnO and low bandgap semiconductor CuS [41] to form an NH heterostructure. Compared to other NIR active nanoparticles (NPs), CuS has much higher photo-stability [42]. Here, we report the wet chemical synthesis of a novel CuS-ZnO NH following a two-step synthesis process. In the first step, we synthesize a biological ligand (cysteine) capped CuS (Cys-CuS) NP. Next, CuS NP is attached to previously prepared ZnO NP using the cysteine linker. The formation of NH has been duly verified by Raman spectroscopy. The newly developed NH can halt the fast charge recombination rate of CuS. First principles DFT calculations have been employed to ratify the charge-transfer pathway. Our predicted band alignment shows that the hybrid system forms a type II heterojunction in the nanohybrid. Upon excitation by NIR light, the excited state electron of CuS moves to the conduction band of ZnO which eventually leads to better charge separation in the hybrid system. The photocatalytic property of the hybrid has been investigated in the presence of NIR light illumination. In this chapter, the photocatalytic activity of the CuS-ZnO NH has been investigated in the presence of NIR light. We observe that the photocatalytic activity of the hybrid system in the presence of NIR light, increases compare to pristine CuS NP.

7.2. Results and Discussion:

7.2.1. A Combined Experimental and Computational Study on a Nanohybrid Material for Potential Application in NIR Photocatalysis [43]: Bandgap engineering by combining a low bandgap semiconductor (LBS) with a wide bandgap semiconductor (WBS) to form a hybrid heterostructure could be a proficient NIR harvesting photocatalyst. In this kind of combination low-bandgap material harvest the NIR light, consequently, the electron-hole separation process

occurred in that system. The light-induced excited electron goes to the conduction band of LBS. In the LBS-WBS based heterostructure system, excited electron transfer from the conduction band (CB) of LBS transfer to CB of WBS. WBS separates the excited state electron which is coming from LBS, hence, the available time of excited state electron became much longer.

Here, we show a novel inorganic-inorganic NH CuS-ZnO, bound by an inorganic ligand cysteine, which consists of a combination of LBS (CuS) with WBS (ZnO). This newly synthesized hybrid material shows enhanced photocatalytic activity in presence of the NIR part of the solar spectrum. Cys-capped CuS NP was synthesized in an ethanol medium by using copper acetate ($(CH_3COO)_2Cu$) and sodium sulfide (Na_2S) in a water-ethanol mixture. Here, *L*-cysteine was used as a capping agent. In the hybrid system, ZnO NPs of different sizes were attached to CuS using other ends of the Cys ligand. We use XRD measurement to determine the phase purity and crystallinity of NP and NH (Figure 7.1).

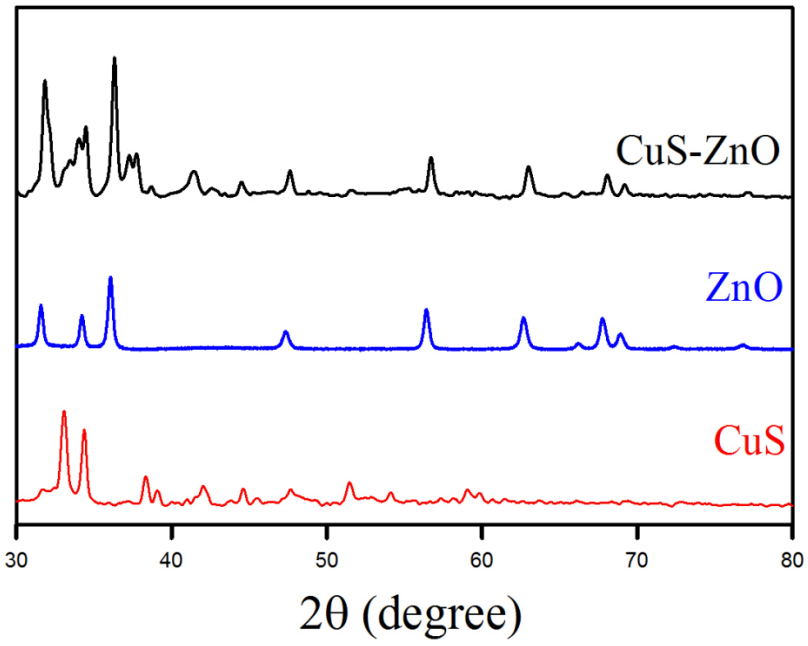

Figure 7.1: *XRD patterns of cysteine capped CuS NP, ZnO NP, and CuS-ZnO nanohybrid.*

The diffraction peaks perfectly point to the hexagonal phase of covellite-type CuS [44, 45]. In the case of ZnO, precise diffraction peaks are obtained which matches the diffraction pattern of wurtzite ZnO [46]. The XRD pattern of NH includes the characteristic peak of both CuS and ZnO. Though, there is a little shift in the XRD peak of CuS in CuS-ZnO with respect to pristine CuS. Previous literature study reveals that, copper sulfide has at least 5 stable phases at normal temperature (CuS (covellite), $Cu_{1.75}S$ (anilite), $Cu_{1.8}S$ (digenite), $Cu_{1.95}S$ (djurleite), Cu_2S (chalcocite)) [47, 48]. This shift of XRD peak may come due to the formation of a new phase Cu_xS which is generated during the time of NH synthesis. However, the intensities of those peaks are so low that, it can be ignored safely.

The morphological distribution of the NP and NH has been investigated using FESEM analysis as depicted in Figure 7.2a and b. The distribution of NP in the NH did not change significantly. Figures 7.2c and 7.2d also show the distribution of CuS and CuS-ZnO in different magnifications. There is also no noticeable change in the morphology of the NH compared to pristine CuS. Energy Dispersive Spectroscopy (EDS) of CuS and CuS-ZnO NH has been performed (shown in Figure 7.2e and 7.2f respectively) to estimate the elements of the systems. Elemental analysis shows the presence of copper (Cu) and sulfur (S) in Figure 7.2e whereas Figure 7.2f shows the presence of zinc (Zn) and oxygen (O) element along with copper (Cu) and sulfur (S) in the hybrid system. The High-resolution transmission electron microscopy (HRTEM) images of the NP and NH are depicted in Figure 7.3. Clear lattice fringes are observed for the HRTEM image of CuS NP (Figure 7.3a), which confirms the good quality of the crystallinity of the NP. The obtained interplanar distances of CuS NPs are ~3.07 Å which corresponds to the [102] plane of CuS [44, 49]. The calculated lattice fringe of ZnO (Figure 7.3b) is approximately 2.62 Å correlated to the [002] plane of ZnO [50]. HRTEM image of CuS-ZnO NH is shown in Figure 7.3c. There is an overlap between the image of ZnO and CuS NP, which indicates the attachment of these two NPs. We measured

the selected area electron diffraction (SAED) configuration of the NH (shown in Figure 7.3d). From the SAED pattern of hybrid, two distinct diffraction patterns

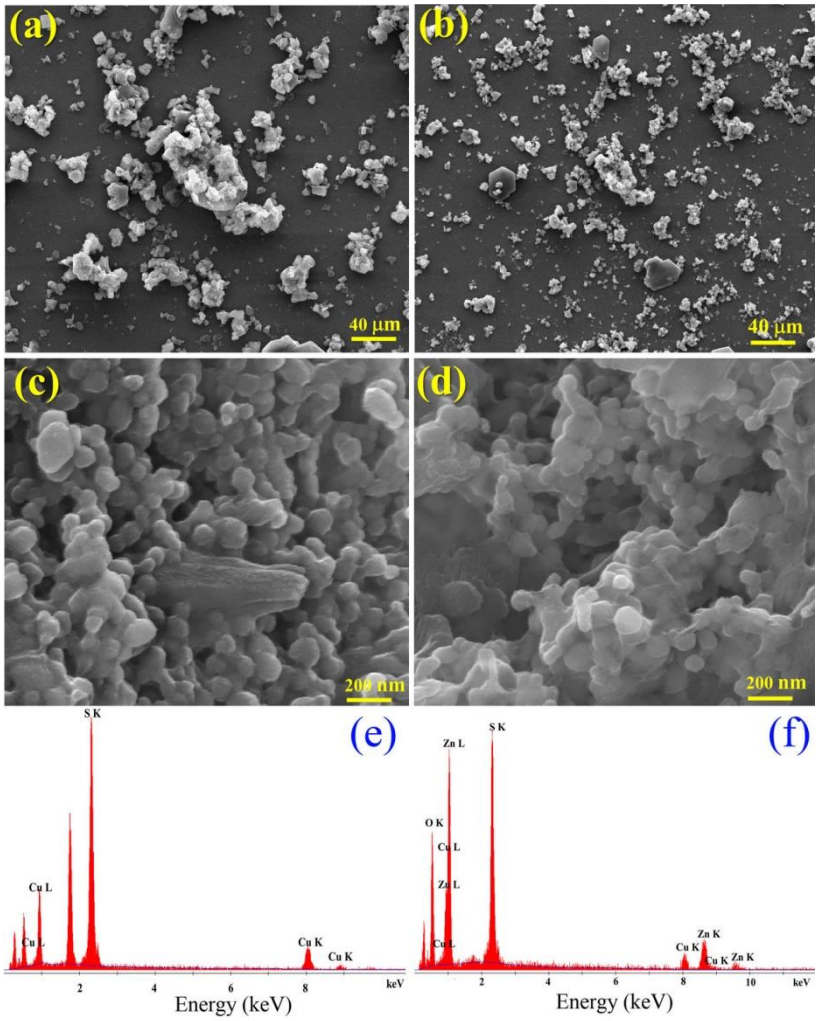

Figure 7.2: *FESEM image of a) CuS and b) CuS-ZnO respectively shows the particle distribution, c) and d) shows the same images of CuS NP and CuS-ZnO NH with higher magnification, e) and f) shows the EDS spectra of CuS and CuS-ZnO respectively.*

(corresponds to CuS and ZnO) are visible which are overlapping with each other. The fringe widths of CuS and ZnO calculated from the SAED image pattern are 3.06 Å and 2.67 Å, respectively, corresponding to the [102] phase of CuS and the [002] phase of ZnO.

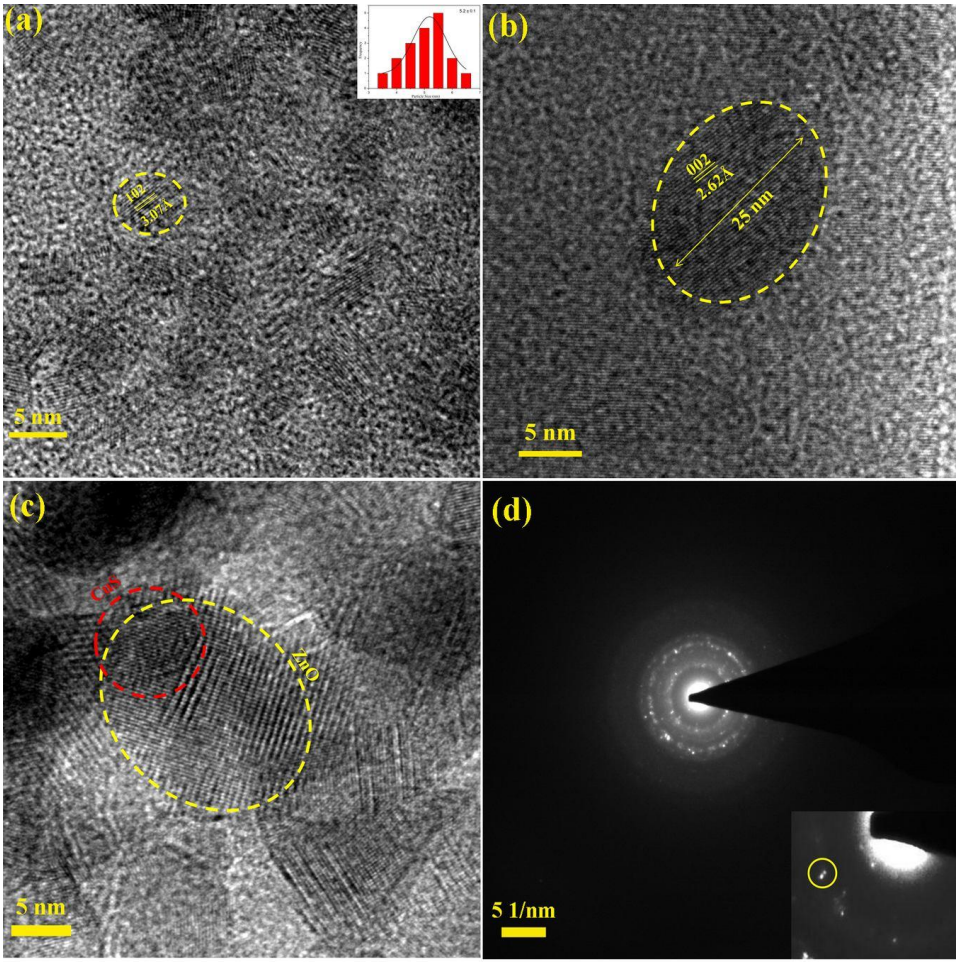

Figure 7.3: *HRTEM images of a) CuS NP and b) ZnO NP respectively show very good crystallinity, c) HRTEM images of CuS-ZnO NH, shows the overlap between the NPs, and d) SAED images of the NH. Inset shows two prominent spots within the diffraction ring.*

We further investigate the absorption spectra of CuS, ZnO, and CuS-ZnO hybrid system (shown in Figure 7.4). It is evident from Figure 7.4 that CuS displays a strong absorption peak in the NIR region (starting from ~700 nm to ~1100 nm) which is a common characteristic of covellite CuS [41, 51]. The inset displays the NIR absorption peak of CuS around ~980 nm. It is found that the as-synthesized CuS NP is fairly stable upon light exposer. This NIR absorption band of CuS produces from the localized surface plasmon resonance (SPR) and inter-band transition of electrons from valance state to an unoccupied state of CuS. Depending on the synthesis condition, the absorption band of covellite CuS differs from 970 nm to 1050 nm. However, CuS has a very fast carrier recombination rate,

so it is very much essential to reduce the recombination rate to get higher activity in presence of NIR light. Herein, we attach CuS with a WBS ZnO to reduce its fast charge recombination by relocating the excited state charge from CuS to ZnO. The absorption peak of ZnO shows a peak of around 372 nm corresponding to a bandgap of 3.3 eV. The absorption spectrum of CuS-ZnO NH shows the mutual effect of both CuS and ZnO. The spectrum shows two distinct peaks at 371 nm and 980 nm which are coming due to the contribution of ZnO and CuS respectively. This suggests that the newly prepared CuS-ZnO NH can absorb NIR light efficiently which can be very much promising in various NIR based optoelectronic applications.

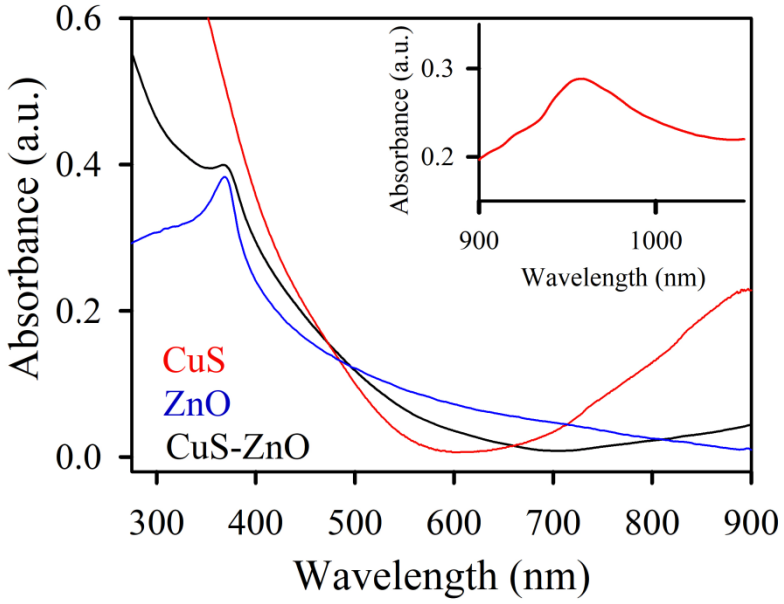

Figure 7.4: *UV-Vis absorption spectrum of CuS NP, ZnO NP, and CuS-ZnO heterostructure. (Inset shows the absorption spectrum of CuS NP in the NIR region).*

Moreover, to further confirm the formation of the heterostructure, we have carried out Raman Spectroscopy of the systems. Raman spectra collected from CuS, ZnO, and CuS-ZnO NH in the wavenumber region of 350−650 cm^{-1} are depicted in Figure 7.5a. As evidenced by Figure 7.5a, CuS NP displays a very noticeable peak at 472 cm^{-1}, which is coming due to the covalent S–S bond stretching vibration modes of CuS NP [52]. The Raman spectrum of the ZnO NP

shows vibration peaks at 380, 437, and 579 cm^{-1} [53, 54]. The main characteristic peak of ZnO at 437 cm^{-1} corresponds to a non-polar optical $E_{2(high)}$ phonon mode of

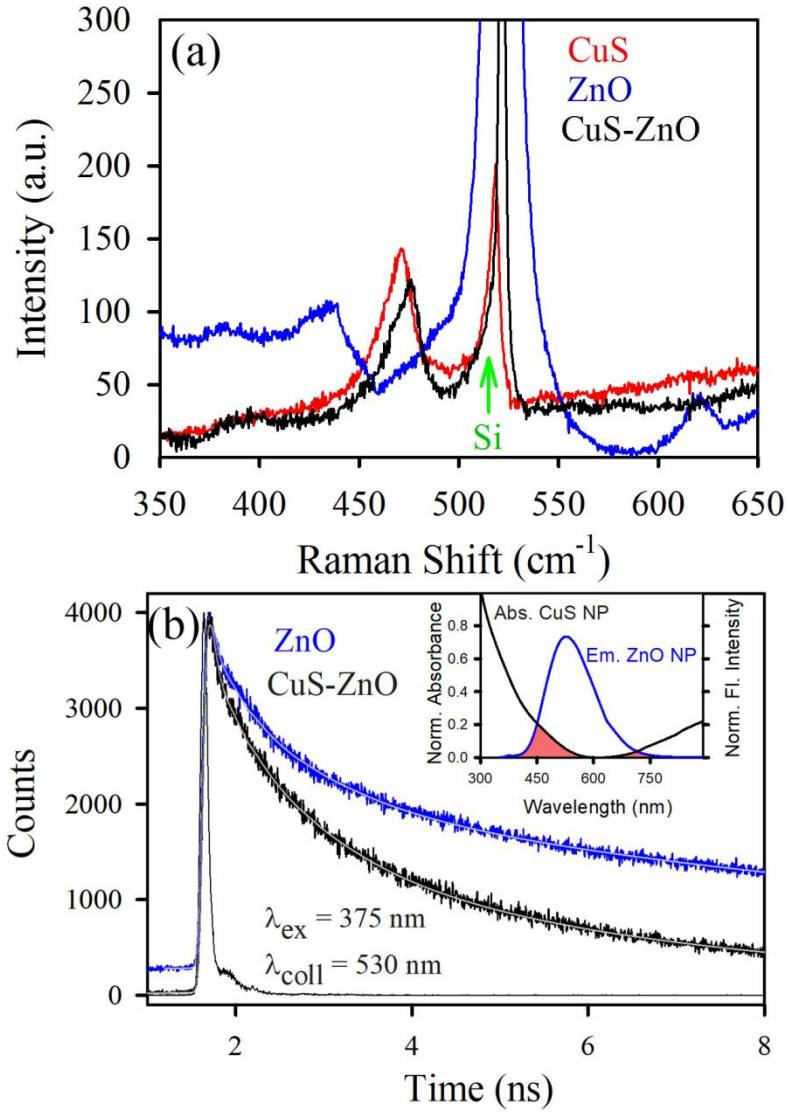

Figure 7.5: *a) Raman fingerprint patterns of CuS, ZnO, and CuS-ZnO Heterostructure, b) Picosecond-resolved PL transients of ZnO NPs (5nm) and CuS-ZnO Heterostructure collected at $\lambda_{collect}$ = 530 nm upon λ_{ex} = 375 nm. Inset shows the spectral overlap of the absorbance of CuS and emission of ZnO NP.*

ZnO [53, 55]. This peak comes from the vibration of the oxygen-deficient state of ZnO [53]. The peak intensity of $E_{2(high)}$ mode (437 cm^{-1} peaks) of ZnO has been suppressed after the formation of NH, keeping other modes intact. This result

indicates the passivation of surface states of ZnO after attachment with CuS, suggesting a successful formation of NH by surface attachment of ZnO with CuS NP [55]. After the formation of NH, the other peaks of CuS and ZnO remain intact, indicating that the structure and crystalline properties of ZnO and CuS remain good.

ZnO of size 5 nm shows a strong surface defect state mediated emission around 530 nm [56]. The excited state transient spectra of ZnO NP at 530 nm upon excitation with a 375 nm laser is shown in Figure 7.5b. The defect mediated emission of ZnO is considerably quenched after attachment with CuS, which indicates there is an electronic interaction between CuS and ZnO via surface defect states. This implies the reduction of surface defect states of ZnO NP, which reinforces the result acquired in Raman spectroscopy. It is found that the defect state emission of ZnO and the absorption of CuS have significant spectral overlap, which indicates the possibility of energy transfer from the donor ZnO NP to the acceptor CuS part. The excited state PL quenching of ZnO NP upon attachment with CuS NP can further be rationalized using Förster Resonance Energy Transfer (FRET) mechanism [57, 58]. The extend of quenching in the time-resolved emission signal is supported with the interparticle distance (CuS-ZnO) to be around ~2.7 nm [58]. This observation establishes the electronic attachment and energy transfer between LBS CuS and WBS material ZnO. The details of the spectroscopic parameters of the excited state fluorescence decay of ZnO and NH are tabulated in Table 7.1.

Table 7.1: *Lifetimes of picosecond time-resolved PL transients of ZnO NP and CuS-ZnO NH detected at 530 nm PL maxima upon excitation at 375 nm wavelength.*

System	τ_1 (ns)	τ_2 (ns)	τ_3 (ns)	τ_{avg} (ns)
ZnO	-	0.36 (5.62)	7.49 (94.38)	3.6
CuS-ZnO	0.14 (3.44)	0.96 (15.4)	4.66 (81.02)	1.7

To study the photocatalytic activity of the system, the newly developed NH was exposed to NIR light ($\lambda > 650$ nm and intensity ~3.47×10^4 Lux). We have used a tungsten halogen lamp as a light source for the photocatalysis measurement. A high-pass filter of 650 nm was utilized to notch the light of wavelength < 650 nm. The spectrum of the light source is showed in Figure 7.6b. After using NIR light to excite the NH, the excited state electrons of CuS have been transferred to the CB of ZnO, which facilitates the separation of electrons and holes. At the same time, holes are also produced in the valence band (VB) of CuS. This charge separation phenomenon is reflected in the photocatalytic efficiency of the system. Photoinduced separated electron-hole can combine with oxygen and H_2O, and produce superoxide or hydroxyl radical which degrades the pollutants. This excited state electron-hole pair decomposes the model pollutant methyl orange (MO) in the aqueous system. In the presence of NIR light, the efficiency of photocatalytic degradation of MO using different photocatalyst is shown in Figure 7.6a. Pure CuS degrades only ~15% of MO under 4 hr. irradiation times, whereas the new NH shows a better photodecomposition rate of MO (~39%) under the same irradiation time. All the photocatalytic results are tabulated in Table 7.2. To establish the pathway of the photocatalytic activity, we have put a well-known radical initiator H_2O_2 and radical quencher sodium azide (NaN_3) in the system (shown in Figure 7.6b). It is well known that H_2O_2 acts as an electron acceptor and as a source of the reactive oxygen species (ROS) radical as well as enhances the ROS generation activity of the NP [59]. We observe, in the presence of H_2O_2 the photocatalytic activity of CuS has increased manifold. On the other hand, in the presence of NaN_3, the catalytic activity reduced significantly. Those results indicate that the photocatalytic activity predominantly occurs through the ROS generation mechanism, which degrades the pollutants [59, 60]. One of the main drawbacks of NIR light is its high heating capacity. To nullify the heating effect of NIR light in photocatalysis, we have done the whole photocatalysis experiment in

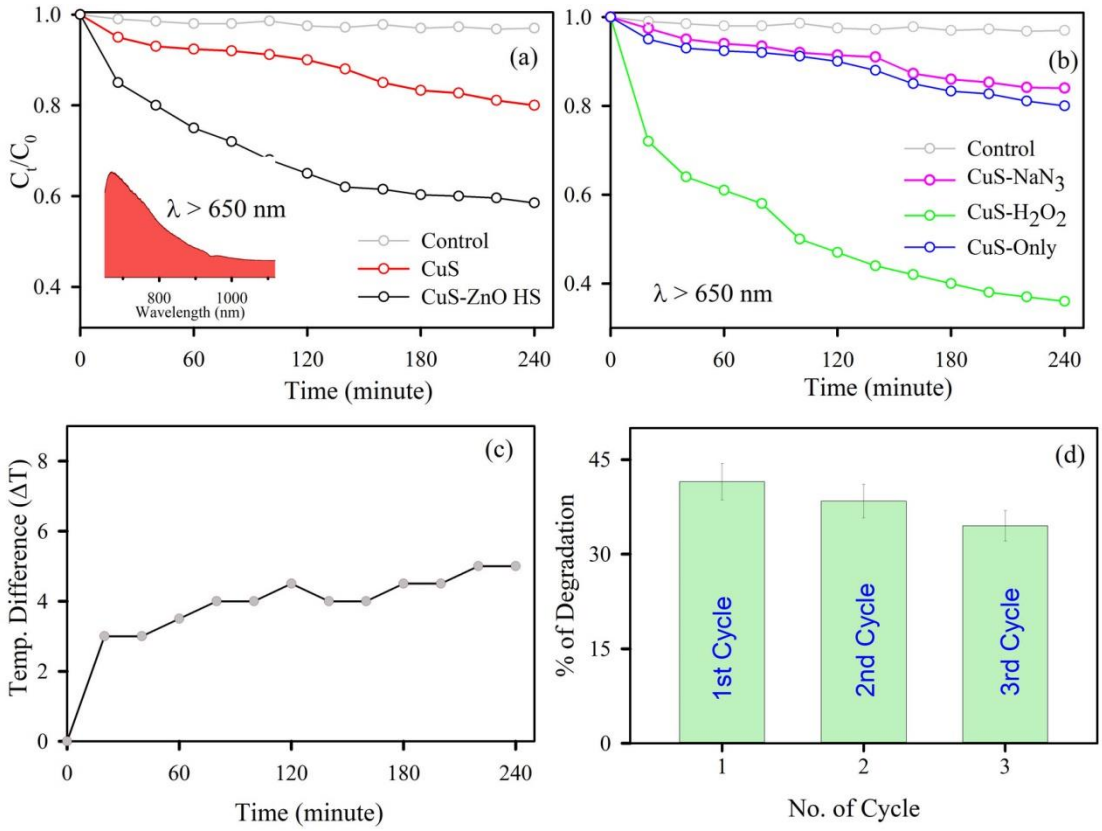

Figure 7.6: *a) Photocatalytic degradation of MO in presence of CuS NP and CuS-ZnO NH under NIR light illumination (λ > 650 nm). The inset shows the spectrum of light-source used for photocatalytic activity. b) Photodegradation of MO over CuS and CuS-ZnO under conventional condition, presence of H_2O_2 and NaN_3 into the solution. c) Temperature difference of the solution with respect to irradiation time, and d) reclibility result of CuS-ZnO NH.*

a water-bath and monitored the temperature of the system at the time of NIR light exposition. The temperature difference before and after the NIR exposer has been plotted in Figure 7.6c. There is an insignificant rise of temperature in the system (~6°C) after 4 hr. of NIR light illumination. This result confirms that the temperature does not play any role in the improved catalytic activity. So, the photocatalytic process is completely reliant on the activity of photocatalyst under light exposition. Moreover, the photocatalytic efficiency of CuS-ZnO NH was retained after 3 cycles (shown in Figure 7.6d) which confirms its reusability and photocatalytic stability. The surface area plays a crucial role in photocatalytic activity. To understand the effect of surface area in the catalytic activity, we have calculated the BET surface area by multipoint BET method using adsorption data.

CuS and ZnO have a BET surface area of 17.22 m^2/gm and 14.78 m^2/gm respectively. In the case of NH, an insignificant increment of specific surface area (17.30 m^2/gm) has been observed. Therefore, the surface area does not play any vital role in the enhanced photocatalytic process. A higher charge separation mechanism in the hybrid system plays the main role in the higher photocatalytic activity. Due to efficient charge separation in CuS-ZnO NH, excited state electrons of CuS move to the conduction band of ZnO. This excited state electron generates reactive oxygen species (like $\dot{O}_2^-$ etc). This activated ROS eventually kills the organic pollutant and generates some non-toxic elements (CO_2, H_2O). Simultaneously, the holes produce active ȮH radicals by reacting with water which also kills the pollutant in the water.

Table 7.2: *Amount of photo-degradation of MO in the presence of different systems under the illumination of NIR light (λ > 650 nm).*

System	Control	CuS	CuS-ZnO	CuS-H_2O_2	CuS-NaN_3
% of degradation	3	15	39	45	13

To probe the mechanism behind the superior catalytic activity in CuS-ZnO NH, we have explored the electronic structure of NH using first principles density functional theory calculations. Using ab initio calculations, we have carried out an extensive analysis of electronic structure, spin polarization, charge transfer process, and band alignment of CuS, ZnO, and CuS-ZnO NH. The calculated atom projected density of states (APDOS) of CuS is shown in Figure 7.7a. Experimental results of the previous section show that CuS is a low bandgap material, which is consistent with the APDOS plot [61]. The non-zero DOS at the Fermi level (E_F) leads to the metallicity of the system. The APDOS of CuS NP shows that the highest occupied molecular orbital (HOMO) and the lowest unoccupied molecular orbital (LUMO) are mainly composed of the highly hybrid S-3*p* orbital and the Cu-3*d* orbital, confirming the covalent nature of the system (Figure 7.7a) [61]. ZnO NP

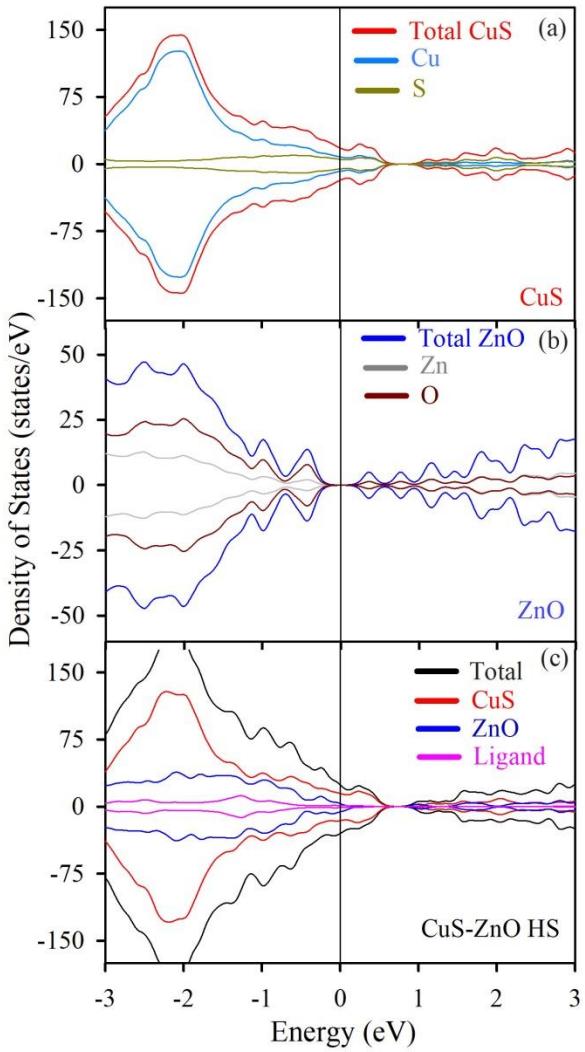

Figure 7.7: *Atom projected density of states (APDOS) of a) CuS NP, b) ZnO NP, and c) ligand attached CuS-ZnO NH.*

is a well-known wide bandgap semiconductor. From an experimental point of view, it is easy to have surface oxygen vacancies in ZnO NP [46]. The APDOS of the cluster is presented in Figure 7.7b. The VB maximum of ZnO is primarily filled with O-2*p* states. CB minima of ZnO are equally hybridized by cationic Zn-4*d* and anionic O-2*p* states. Besides, some gap states are produced within the bandgap, due to oxygen vacancy in the ZnO cluster. Interestingly, cysteine attached CuS-ZnO NH shows many new electronic properties compared to the pristine CuS. The APDOS of CuS-ZnO NH is depicted in Figure 7.7c. In the hybrid system, the metallic character of CuS near E_F remains intact. However, a considerable number

of states were created due to cysteine near E_F asserting the possibility of accumulation of charges. In the hybrid system, the E_F moves to the VB which stipulates *p*-type doping in the system, suggests the possibility of transferring charges from CuS to ligand and ZnO. The charge density plot

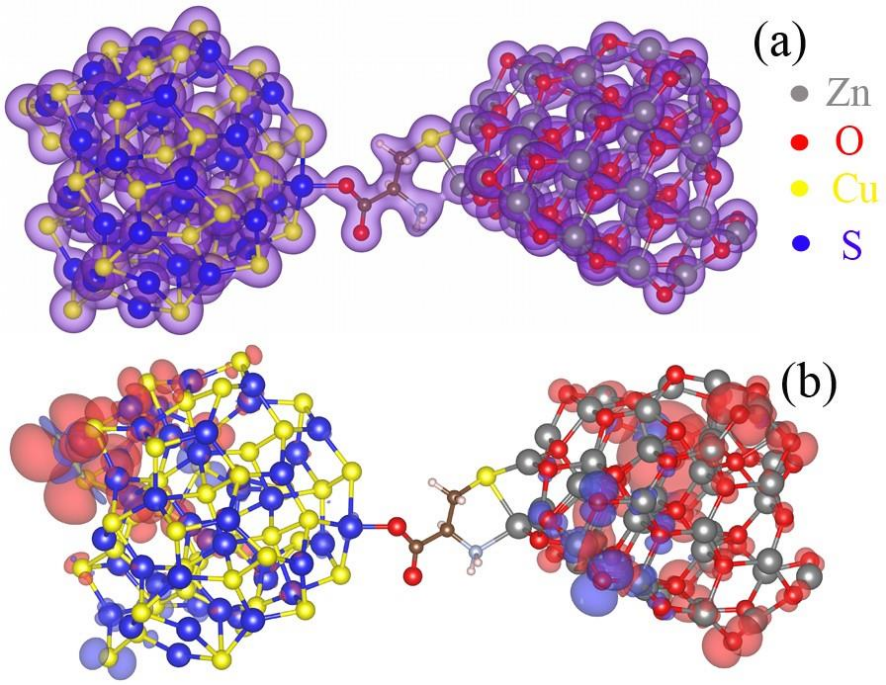

Figure 7.8: *a) Isosurface plots of charge density of CuS-ZnO heterostructure. Cu, S, Zn, O atoms are denoted by yellow, blue, grey, and red color respectively, b) spin density plot of CuS-ZnO heterostructure. Red color shows up-spin density while blue color shows down-spin density contribution.*

(Figure 7.8a) of NH confirms that there is an overlap of charge density of CuS, ligand, and ZnO. The edge states, where the ligand is attached to CuS and ZnO, are delocalized, indicates there is a possibility of charge transfer within the NH. Another important outcome of the electronic structure of the hybrids system is neither CuS nanocluster nor ZnO nanocluster separately shows magnetization, but after forming NH, due to the effect of mutual charge exchanges, it shows magnetic behavior. APDOS of NH exhibits asymmetry in up and down spin channels near E_F. The spin density distribution of the NH can be seen in Figure 7.8b, showing that the magnetic moment is distributed primarily through the ZnO nanocluster

surface oxygen atom. Magnetic moments mainly originated from the *d*-orbitals of Cu and Zn and *p*-orbital of S and O.

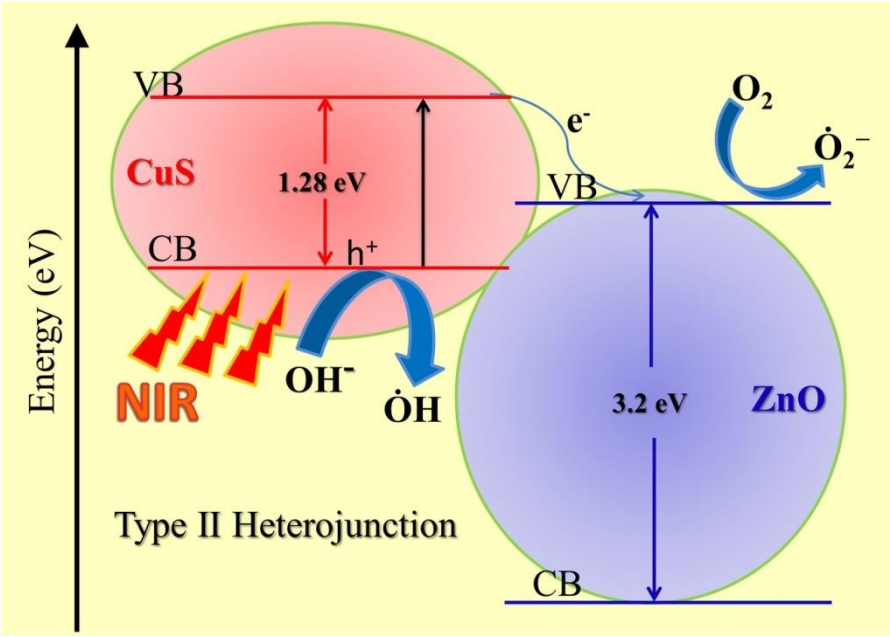

Scheme 7.1: *Theoretically predicted band alignment of CuS-ZnO heterostructure using density functional theory.*

The schematic representation of the heoretically determined energy band diagram of CuS-ZnO is given in Scheme 7.1. It is clear from the band alignment of the NH that, it forms a type–II heterojunction [62-64]. Whenever the NH is exposed to NIR light, the electron travels from VB of CuS to CB of CuS. That excited electron further goes into the CB of ZnO. As a result of these synergic effects, the efficient process of separating charges occurs within NH which results in increased photocatalytic activity.

Moreover, we have calculated the optical absorbance of CuS, ZnO, and CuS-ZnO NH using DFT as implemented in ATK software (shown in Figure 7.9) [65]. This result is consistent with the experimental absorption spectra. The measured absorption spectrum reveals a broad absorption band close to the NIR region that distributes from NIR to distant IR [66]. This result indicates that CuS is a potential NIR absorber. In the present case, to match with the experimental

condition a ZnO nanocluster with oxygen vacancy in surface (OVS) has been taken for calculation purposes. This ZnO NP has an absorbance peak around ~380 eV due to the transition from LUMO to HOMO. However, due to OVS, many

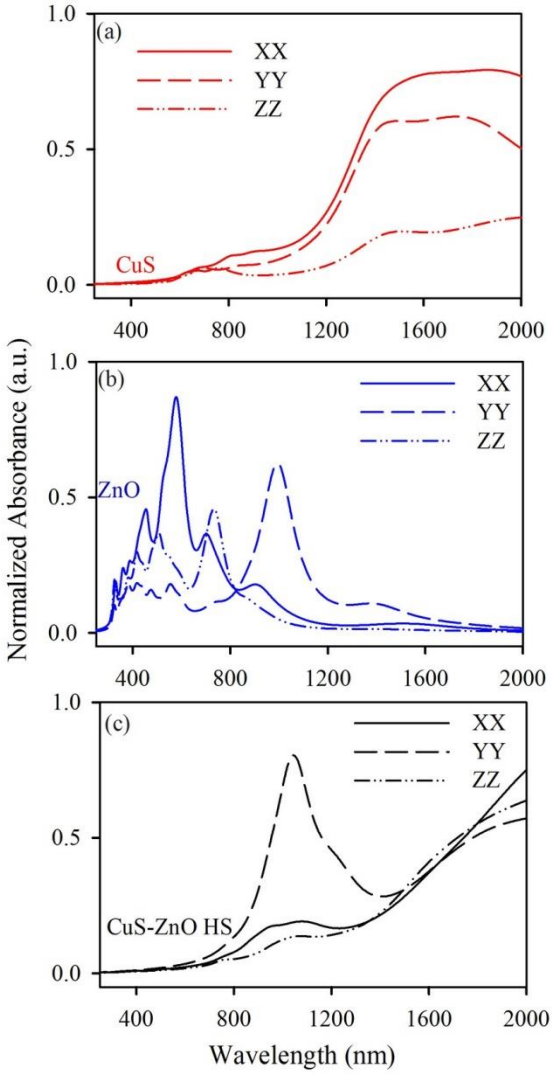

Figure 7.9: *Optical absorbance plot of a) CuS NP, b) ZnO NP, and c) CuS-ZnO NH using DFT calculation.*

midgap trap states have been generated resulting in the generation of other absorbance peaks. The transition from HOMO and trap states leads primarily to those peaks. In the case of CuS-ZnO, the absorption spectrum is somewhat different from its pristine identity. In NH, CuS NP is attached to the ZnO through a ligand on the surface oxygen vacant state of ZnO. As a result of the reduction of

the defect state of ZnO at surface generating due to the oxygen vacancy, the absorption peak in the visible region due to oxygen vacancy state is subsided in the NH. An absorption peak in the NIR region is also observed in the NH, which is contributed by CuS.

According to the above study, it can be concluded that CuS generates electron-hole pairs upon illumination of NH with simulated NIR light source. Because of its advantageous electronic bandgap arrangement, the excited state electrons are passed to the CB of ZnO, as indicated by our first principles theoretical analysis, which effectively reduces the recombination cycle of charges. Therefore, efficient separation of charge carrier of the NH significantly improves photocatalytic activity under NIR light exposer in comparison to its pristine equivalents.

7.3. Conclusion:

In short, a new type of near-infrared harvesting nanohybrid CuS-ZnO has been successfully prepared using a narrow bandgap semiconductor CuS and wide bandgap semiconductor ZnO, through a simple wet chemical synthesis method. The formation of NH has been established using various spectroscopic tools including picosecond resolved technique and Raman spectroscopy. Low bandgap semiconductor CuS shows a sharp absorption band in the NIR region, which effectively captures the NIR part of solar light. The first principles DFT calculation reveals the hybrid system as a type II heterostructure. Consequently, enhanced photocatalytic activity in the hybrid system comes due to efficient excited state charge delocalization from the conduction band of CuS to ZnO. The current work shows an inventive strategy to use the NIR part of the solar spectrum for efficient photocatalytic degradation using a novel NH. This novel work may promote the development of research on the harvesting and application of near-infrared solar light in a new direction.

References

[1] S. M. Paek, J. M. Oh, J. H. Choy, A lattice-engineering route to heterostructured functional nanohybrids, *Chem. Asian J.* 6 (2011) 324.

[2] J. H. Choy, J. H. Park, J. B. Yoon, Multilayered SiO_2/TiO_2 nanosol particles in two-dimensional aluminosilicate catalyst−support, *J. Phys. Chem. B* 102 (1998) 5991.

[3] J. H. Choy, S. J. Kwon, G. S. Park, High-T_c superconductors in the two-dimensional limit:$[(Py\text{-}C_nH_{2n+1})_2HgI_4]$-$Bi_2Sr_2Ca_{m-1}Cu_mO_y$ (m= 1 and 2), *Science* 280 (1998) 1589.

[4] N. B. Saleh, A. Afrooz, J. H. Bisesi, N. Aich, J. Plazas-Tuttle, T. Sabo-Attwood, Emergent properties and toxicological considerations for nanohybrid materials in aquatic systems, *Nanomaterials* 4 (2014) 372.

[5] K. Liu, K. Nagodawithana, P. C. Searson, C. L. Chien, Perpendicular giant magnetoresistance of multilayered Co/Cu nanowires, *Phys. Rev. B* 51 (1995) 7381.

[6] M. Bognitzki, H. Hou, M. Ishaque, T. Frese, M. Hellwig, C. Schwarte, A. Schaper, J.H. Wendorff, A. Greiner, Polymer, metal, and hybrid nano and mesotubes by coating degradable polymer template fibers (TUFT process), *Adv. Mater.* 12 (2000) 637.

[7] Y. Guo, Q. Tang, H. Liu, Y. Zhang, Y. Li, W. Hu, S. Wang, D. Zhu, Light-controlled organic/inorganic *p*−*n* junction nanowires, *J. Am. Chem. Soc.* 130 (2008) 9198.

[8] D. J. Milliron, S. M. Hughes, Y. Cui, L. Manna, J. Li, L. W. Wang, A. P. Alivisatos, Colloidal nanocrystal heterostructures with linear and branched topology, *Nature* 430 (2004) 190.

[9] N. Zhang, C. Han, X. Fu, Y. J. Xu, Function-oriented engineering of metal-based nanohybrids for photoredox catalysis: Exerting plasmonic effect and beyond, *Chem.* 4 (2018) 1832.

[10] H. Liu, X. Chen, L. Deng, X. Su, K. Guo, Z. Zhu, Preparation of ultrathin 2D MoS_2/graphene heterostructure assembled foam-like structure with enhanced electrochemical performance for lithium-ion batteries, *Electrochim. Acta* 206 (2016) 184.

[11] S. M. Schieke, P. Schroeder, J. Krutmann, Cutaneous effects of infrared radiation: From clinical observations to molecular response mechanisms, *Photodermatol. Photoimmunol. Photomed.* 19 (2003) 228.

[12] D. Barolet, F. Christiaens, M. R. Hamblin, Infrared and skin: Friend or foe, *J. Photochem. Photobiol. B* 155 (2016) 78.

[13] M. V. Padalkar, N. Pleshko, Wavelength-dependent penetration depth of near infrared radiation into cartilage, *Analyst* 140 (2015) 2093.

[14] X. Y. Kong, W. L. Tan, B. J. Ng, S. P. Chai, A. R. Mohamed, Harnessing Vis–NIR broad spectrum for photocatalytic CO_2 reduction over carbon quantum dots-decorated ultrathin Bi_2WO_6 nanosheets, *Nano Res.* 10 (2017) 1720.

[15] W. Fan, H. Bai, W. Shi, Semiconductors with NIR driven upconversion performance for photocatalysis and photoelectrochemical water splitting, *CrystEngComm* 16 (2014) 3059.

[16] S. Ganguli, C. Hazra, M. Chatti, T. Samanta, V. Mahalingam, A highly efficient UV–Vis–NIR active Ln^{3+}-doped $BiPO_4$/$BiVO_4$ nanocomposite for photocatalysis application, *Langmuir* 32 (2015) 247.

[17] L. Wondraczek, E. Tyystjärvi, J. Méndez-Ramos, F.A. Müller, Q. Zhang, Shifting the sun: Solar spectral conversion and extrinsic sensitization in natural and artificial photosynthesis, *Adv. Sci.* 2 (2015) 1500218.

[18] L. Yang, B. Liu, T. Liu, X. Ma, H. Li, S. Yin, T. Sato, Y. Wang, A P25/$(NH_4)_x$ WO_3 hybrid photocatalyst with broad spectrum photocatalytic properties under UV, visible, and near-infrared irradiation, *Sci. Rep.* 7 (2017) 45715.

[19]. L. Wang, X. Xu, Q. Cheng, S. X. Dou, Y. Du, Near-infrared-driven photocatalysts: Design, construction, and applications, *Small* (2019) 1904107.

[20] Q. Tian, W. Yao, W. Wu, C. Jiang, NIR light-activated upconversion semiconductor photocatalysts, *Nanoscale Horiz.* 4 (2019) 10.

[21] D. Li, S. H. Yu, H. L. Jiang, From UV to near-infrared light-responsive metal–organic framework composites: Plasmon and upconversion enhanced photocatalysis, *Adv. Mater.* 30 (2018) 1707377.

[22] Q. Tian, W. Yao, W. Wu, J. Liu, Z. Wu, L. Liu, Z. Dai, C. Jiang, Efficient UV–Vis-NIR responsive upconversion and plasmonic-enhanced photocatalyst based on lanthanide-doped $NaYF_4/SnO_2/Ag$, *ACS Sustain. Chem. Eng.* 5 (2017) 10889.

[23] Y. Sang, H. Liu, A. Umar, Photocatalysis from UV/Vis to near-infrared light: Towards full solar-light spectrum activity, *ChemCatChem* 7 (2015) 559.

[24] X. Zhao, Y. Wang, W. Feng, H. Lei, J. Li, Preparation of Cu(II) porphyrin-TiO_2 composite in one-pot method and research on photocatalytic property, *RSC Adv.* 7 (2017) 52738.

[25] K. Kabra, R. Chaudhary, R. L. Sawhney, Treatment of hazardous organic and inorganic compounds through aqueous-phase photocatalysis: A review, *Ind. Eng. Chem. Res.* 43 (2004) 7683.

[26] K. M. Lee, C. W. Lai, K. S. Ngai, J. C. Juan, Recent developments of zinc oxide based photocatalyst in water treatment technology: A review, *Water Res.* 88 (2016) 428.

[27] A. Fujishima, K. Honda, Electrochemical photolysis of water at a semiconductor electrode, *Nature* 238 (1972) 37.

[28] R. Georgekutty, M. K. Seery, S. C. Pillai, A highly efficient Ag-ZnO photocatalyst: Synthesis, properties, and mechanism, *J. Phys. Chem. C* 112 (2008) 13563.

[29] S. G. Kumar, L. G. Devi, Review on modified TiO_2 photocatalysis under UV/visible light: Selected results and related mechanisms on interfacial charge carrier transfer dynamics, *J. Phys. Chem. A* 115 (2011) 13211.

[30] M. Umar, H. A. Aziz, Photocatalytic degradation of organic pollutants in water in M. N. Rashed, Organic pollutants-monitoring, risk and treatment, *InTech*, London, UK, 2013.

[31] Y. Wang, Q. Wang, X. Zhan, F. Wang, M. Safdar, J. He, Visible light driven type II heterostructures and their enhanced photocatalysis properties: A review, *Nanoscale* 5 (2013) 8326.

[32] J. M. Herrmann, Heterogeneous photocatalysis: Fundamentals and applications to the removal of various types of aqueous pollutants, *Catal. Today* 53 (1999) 115.

[33] X. Zong, H. Yan, G. Wu, G. Ma, F. Wen, L. Wang, C. Li, Enhancement of photocatalytic H_2 evolution on CdS by loading MoS_2 as cocatalyst under visible light irradiation, *J. Am. Chem. Soc.* 130 (2008) 7176.

[34] L. Dou, W. H. Chang, J. Gao, C. C. Chen, J. You, Y. Yang, A selenium-substituted low-bandgap polymer with versatile photovoltaic applications, *Adv. Mater.* 25 (2013) 825.

[35] X. Wu, S. Yin, Q. Dong, B. Liu, Y. Wang, T. Sekino, S. W. Lee, T. Sato, UV, visible and near-infrared lights induced NO_x destruction activity of (Yb, Er)-$NaYF_4$/C-TiO_2 composite, *Sci. Rep.* 3 (2013) 2918.

[36] X. Wu, S. Yin, Q. Dong, T. Sato, Blue/green/red colour emitting up-conversion phosphors coupled C-TiO_2 composites with UV, visible and NIR responsive photocatalytic performance, *Appl. Catal. B: Environ.* 156 (2014) 257.

[37] Y. Asakura, Y. Anada, R. Hamanaka, T. Sato, K. I. Katsumata, X. Wu, S. Yin, Multifunctionality in coating films including Nb-doped TiO_2 and Cs_xWO_3: Near infrared shielding and photocatalytic properties, *Nanotechnology* 29 (2018) 224001.

[38] T. K. Maji, K. K. Tiwary, D. Karmakar, Achieving tunable doping of $MoSe_2$ based devices using GO@$MoSe_2$ heterostructure, *AIP Conf. Proc.* 1832 (2017) 120019.

[39] R. K. Yadav, J. Aneesh, R. Sharma, P. Abhiramnath, T. K. Maji, G. J. Omar, A. K. Mishra, D. Karmakar, K. V. Adarsh, Designing hybrids of graphene oxide and gold nanoparticles for nonlinear optical response, *Phys. Rev. Appl.* 9 (2018) 044043.

[40] R. Sharma, J. Aneesh, R. K. Yadav, S. Sanda, A. R. Barik, A. K. Mishra, T. K. Maji, D. Karmakar, K. V. Adarsh, Strong interlayer coupling mediated giant two-photon absorption in $MoSe_2$/graphene oxide heterostructure: Quenching of exciton bands, *Phys. Rev. B* 93 (2016) 155433.

[41] Y. T. Kwon, G. D. Lim, S. Kim, S. H. Ryu, T. Y. Hwang, K. R. Parka, Y. H. Choa, *J. Mater. Chem. C* 6 (2018) 754.

[42] M. Yin, Z. Li, E. Ju, Z. Wang, K. Dong, J. Ren, X. Qu, Multifunctional upconverting nanoparticles for near-infrared triggered and synergistic antibacterial resistance therapy, *ChemComm* 50 (2014) 10488.

[43] T. K. Maji, P. K. Sarkar, P. Kar, B. Liu, P. Lemmens, D. Karmakar, S. K. Pal, A combined experimental and computational study on a nanohybrid material for potential application in NIR photocatalysis, *Appl. Catal. A: Gen.* 583 (2019) 117124.

[44] M. Tanveer, C. Cao, Z. Ali, I. Aslam, F. Idrees, W. S. Khan, F. K. But, M. Tahir, N. Mahmood, Template free synthesis of CuS nanosheet-based hierarchical microspheres: An efficient natural light driven photocatalyst, *CrystEngComm* 16 (2014) 5290.

[45] S. S. Kalanur, H. Seo, Tuning plasmonic properties of CuS thin films via valence band filling, *RSC Adv.* 7 (2017) 11118.

[46] T. K. Maji, D. Bagchi, P. Kar, D. Karmakar, S. K. Pal, Enhanced charge separation through modulation of defect-state in wide band-gap semiconductor for potential photocatalysis application: Ultrafast spectroscopy and computational studies, *J. Photochem. Photobiol. A: Chem.* 332 (2017) 391.

[47] J. Podder, R. Kobayashi, M. Ichimura, Photochemical deposition of Cu_xS thin films from aqueous solutions, *Thin Solid Films* 472 (2005) 71.

[48] D. Koch, R. McIntyre, The application of reflectance spectroscopy to a study of the anodic oxidation of cuprous sulphide, *J. Electroanal. Chem.* 71 (1976) 285.

[49] M. Tanveer, C. Cao, I. Aslam, Z. Ali, F. Idrees, W. S. Khan, M. Tahir, S. Khalid, G. Nabi, A. Mahmood, Synthesis of CuS flowers exhibiting versatile photo-catalyst response, *New J. Chem.* 39 (2015) 1459.

[50] D. Jiang, L. Cao, W. Liu, G. Su, H. Qu, Y. Sun, B. Dong, Synthesis and luminescence properties of core/shell ZnS:Mn/ZnO nanoparticles, *Nanoscale Res. Lett.* 4 (2008) 78.

[51] Z. Zha, S. Wang, S. Zhang, E. Qu, H. Ke, J. Wang, Z. Dai, Targeted delivery of CuS nanoparticles through ultrasound image-guided microbubble destruction for efficient photothermal therapy, *Nanoscale* 5 (2013) 3216.

[52] A. G. Milekhin, N. A. Yeryukov, L. L. Sveshnikova, T. A. Duda, E. E. Rodyakina, V. A. Gridchin, E. S. Sheremet, D. R. Zahn, Combination of surface- and interference-enhanced Raman scattering by CuS nanocrystals on nanopatterned Au structures, *Beilstein J. Nanotechnol.* 6 (2015) 749.

[53] P. Jiang, J. J. Zhou, H. F. Fang, C. Y. Wang, Z. L. Wang, S. S. Xie, Hierarchical shelled ZnO structures made of bunched nanowire arrays, *Adv. Funct. Mater.* 17 (2007) 1303.

[54] M. Procek, T. Pustelny, A. Stolarczyk, Influence of external gaseous environments on the electrical properties of ZnO nanostructures obtained by a hydrothermal method, *Nanomaterials* 6 (2016) 227.

[55] S. Sarkar, A. Makhal, T. Bora, K. Lakhsman, A. Singha, J. Dutta, S. K. Pal, Hematoporphyrin–ZnO nanohybrids: Twin applications in efficient visible-light photocatalysis & dye-sensitized solar cells, *ACS Appl. Mater. Interfaces* 4 (2012) 702.

[56] A. Makhal, S. Sarkar, T. Bora, S. Baruah, J. Dutta, A. Raychaudhuri, S. K. Pal, Dynamics of light harvesting in ZnO nanoparticles, *Nanotechnology* 21 (2010) 265703.

[57] J. R. Lakowicz, Principles of fluorescence spectroscopy, *Springer,* New York, USA, 2006.

[58] S. Sardar, P. Kar, H. Remita, B. Liu, P. Lemmens, S. K. Pal, S. Ghosh, Enhanced charge separation and FRET at heterojunctions between semiconductor

nanoparticles and conducting polymer nanofibers for efficient solar light harvesting, *Sci. Rep.* 5 (2015) 17313.

[59] A. Giri, N. Goswami, M. Pal, M. T. Z. Myint, S. Al-Harthi, A. Singha, B. Ghosh, J. Dutta, S. K. Pal, Rational surface modification of Mn_3O_4 nanoparticles to induce multiple photoluminescence and room temperature ferromagnetism, *J. Mater. Chem. C* 1 (2013) 1885.

[60] P. Kar, T. K. Maji, R. Nandi, P. Lemmens, S. K. Pal, In-situ hydrothermal synthesis of Bi–$Bi_2O_2CO_3$ heterojunction photocatalyst with enhanced visible light photocatalytic activity, *Nano-Micro Lett.* 9 (2016) 18.

[61] A. Morales-García, A. L. Soares Jr, E. C. Dos Santos, H. A. de Abreu, H. A. Duarte, First-principles calculations and electron density topological analysis of covellite (CuS), *J. Phys. Chem. A* 118 (2014) 5823.

[62] B. Peng, G. Yu, X. Liu, B. Liu, X. Liang, L. Bi, L. Deng, T. C. Sum, K. P. Loh, Ultrafast charge transfer in MoS_2/WSe_2 *p–n* Heterojunction, *2D Mater.* 3 (2016) 025020.

[63] S. Tongay, W. Fan, J. Kang, J. Park, U. Koldemir, J. Suh, D. S. Narang, K. Liu, J. Ji, J. Li, R. Sinclair, J. Wu, Tuning interlayer coupling in large-area heterostructures with CVD-grown MoS_2 and WS_2 monolayers, *Nano Lett.* 14 (2014) 3185.

[64] Y. Wei, F. Wang, W. Zhang, X. Zhang, The electric field modulation of electronic properties in a type-II phosphorene/PbI_2 van der Waals heterojunction, *Phys. Chem. Chem. Phys.* 21 (2019) 7765.

[65] S. Smidstrup, D. Stradi, J. Wellendorff, P. A. Khomyakov, U. G. Vej-Hansen, M. E. Lee, T. Ghosh, E. Jónsson, H. Jónsson, K. Stokbro, First-principles Green's-function method for surface calculations: A pseudopotential localized basis set approach, *Phys. Rev. B* 96 (2017) 195309.

[66] L. Xiao, J. Wu, J. Ran, Y. Liu, W. Qiu, F. Lu, F. Shao, D. Tang, P. Peng, Near-infrared radiation absorption properties of covellite (CuS) using first-principles calculations, *AIP Adv.* 6 (2016) 085122.

Chapter 8

Computational Studies on the Interlayer Modulation of Graphene Analogous Heterostructure

8.1. Introduction:

Heterostructure (HS) systems in which materials of different compositions meet at interfaces [1] comprise a relatively new, yet already immense, area of materials science; they are expected to greatly influence the future design and development of materials with defined functions [1-4]. Many new ideas have been proposed for synthesizing different types of heterostructures such as metal-metal [5], metal-polymer [6], organic-inorganic [7], and inorganic-inorganic heterostructure [8]. Completely novel or improved physical and chemical properties can be found in the newly developed heterostructure which comes due to strong interactions between the two counterparts [4].

Since the discovery of Graphene in 2004, enormous research has been carried out on two-dimensional (2D) materials due to many interesting properties of 2D based systems such as high mechanical strength, high charge carrier mobility, high thermal conductivity, and broadband optical absorption [9-11]. One of the main advantages of the 2D nanostructure is a very high surface area and large interface structure. As a result of the large interface area, research interest on heterostructure based on the 2D system is increasing significantly for designing new-age hybrid material that can provide many enhanced physical, chemical, and mechanical properties [12-15]. The combination of different layered constituents may produce heterogeneous and functional materials whose interfaces yield completely different types of 2D electronic systems. These hybrid heterostructures have potential applications in advanced quantum electronics applications due to

their novel architectures. To realize more controllable device functions, precise tunability of the system is a very important issue of scientist's concerns. It is possible to tune many exotic properties in the 2D heterostructure system very precisely [16]. This kind of advantage motivates us to work on 2D inorganic-inorganic heterostructure systems. In the coupled inorganic-inorganic 2D heterostructure, the improved efficiency of the hybrid system is explained as the result of a vectorial transfer of electrons and holes from one system to another.

Transition metal dichalcogenides (TMDCs) are atomic thin semiconductors composed of a sandwich structure of the transition metal layer (i.e., Mo, W, etc.) in between the two chalcogen layers (S, Se etc.). Monolayers of TMDC shows a direct bandgap around 1.5–1.8 eV, which is very much suitable for their application in nanoelectronic devices [17-19]. Moreover, TMDC can almost overcome the shortcomings of Graphene-based devices. MoS_2 is one of the most studied TMDC materials due to its numerous advantages [18-21]. $MoSe_2$ is the selenium counterpart of MoS_2, having a direct monolayer optical gap of ~1.58 eV at room temperature, which is less than MoS_2 (1.9 eV), having an optimal range for optical device utility. $MoSe_2$ also has shown its potentiality in the new-generation optoelectronic devices application due to its several advantageous properties [22]. However, pristine TMDC material has several shortcomings (like low mobility due to interface-induced scattering effects). So, it is essential to modulate the surface of TMDC with functional ligands or some other material to produce an engineered hybrid system which can overcome the problem.

An extraordinary privilege of 2D heterostructure with van der Waals (vdW) stacking systems is the uninhibited materialization of the combination of disparate systems to obtain the tailor-made *best of both* properties. These kinds of vdW layered materials consist of in-plane covalently bonded atomic layers that interact weakly with other constituents in the out-of-plane direction. Such HS paves the way for the generation of devices with unique characteristics. To modify the

intrinsic properties of the inorganic TMDC rendering new characteristics, specific molecular groups can be employed. There are several studies in the literature depicting a modification of doping, transport, and optical properties of the TMDC underneath by placing a top layer of Graphene (G) or Graphene Oxide GO [16, 23-26]. Controlling the doping by growing a bilayer heterostructure is relatively easier to handle. Depending on the oxygen concentration of the attached GO layer, Musso *et al.* have demonstrated a lowering of the *p*-type Schottky barrier height for the GO/MoS_2 system [16]. These previous studies have not dealt with the fine tunability of doping and their impact on non-collinear magnetism, static and time dependent optical properties, and realistic-device transport. Our aim of the work is to address the impact of oxygen ligand on the optical and transport properties of the 2D TMDC system.

In this chapter, we have chosen a prototype HS, wherein we demonstrate a custom-made modification of the electronic properties of the pristine $MoSe_2$ system. We intend to overcome the drawbacks in the electrical and electronic properties of $MoSe_2$ by integrating it with a GO layer at the top of it. The interlayer coupling of these two layers can be modulated depending on the concentration and types of the functional ligands on the GO layer as can also be seen from prior works [16, 27, 28]. Interlayer coupling of these two layers can be modulated depending on the concentration and types of the functional ligands on GO. The impact of carrier doping on the electronic structure of the HS is discussed in detail. In the next section, modulation of the interlayer coupling and thereby obtained effects on the static and time dependent optical properties are investigated. The following section elaborates on the formation of different contact geometry, interfacial effects, and device transport properties. The outcome of these studies suggests the promising potential of the present HS in future optoelectronic device applications.

8.2. Results and Discussion:

8.2.1. Intricate Modulation of Interlayer Coupling at Graphene Oxide (GO)/$MoSe_2$ Interface: Application in Time-dependent Optics and Device Transport [29]: To study the electronic properties of GO/$MoSe_2$ interface, we have initially constructed a Graphene (G)/$MoSe_2$ interface by joining the two lattices by Co-incidence Site Lattice (CSL) Method, as implemented in the Atomistic Toolkit 15.1 package. In all our calculations, the lowest strain is ~0.66%, when the mutual rotation between a stacking of 5×5×1 G on a 4×4×1 $MoSe_2$ surface about the *z*-axis is ~19°. The GO surface was constructed from the 5×5×1 surface of G with varying concentrations of hydroxyl (OH) and carboxyl (COOH) functional ligands. We have constructed four different types of GO surfaces, viz., (1) with single OH (G-OH), (2) single COOH (G-COOH), (3) lesser concentrations of both OH and COOH (G-Low), and (4) higher concentrations (G-High) of both ligands. To avoid strain-induced buckling of the GO layer, the functional groups are placed symmetrically on both sides of the G surface [16, 28]. To demonstrate the role of these functional groups in modulating interlayer coupling, we have constructed five HS by following the CSL method to minimize the interfacial strain, viz., (A) G/$MoSe_2$ interface (HS1), (B) G-OH/$MoSe_2$ (HS2), (C) G-COOH/$MoSe_2$ (HS3), (D) G-Low/$MoSe_2$ (HS4), and (E) G-High/$MoSe_2$ (HS5). We designate HS2, HS3, HS4, and HS5 as OH, COOH, Low and High in all the figures for an easy correlation with the ligand details. For $MoSe_2$ ML, the most common defect is the Se-vacancy (SeV). The doping trend for all these HS is also investigated in the presence of ~3% SeV and the doping trend is mentioned in Table 8.1. Since the presence of SeV only modifies the obtained doping, we do not discuss the results in the present study. The ionic positions of the individual interfaces are relaxed to obtain the lowest energy configuration. A vacuum of ~15 Å is introduced at the top and bottom of the interface to avoid periodic replication from the adjacent supercell. The structures of all GO/$MoSe_2$ interfaces (HS2-HS5) are presented

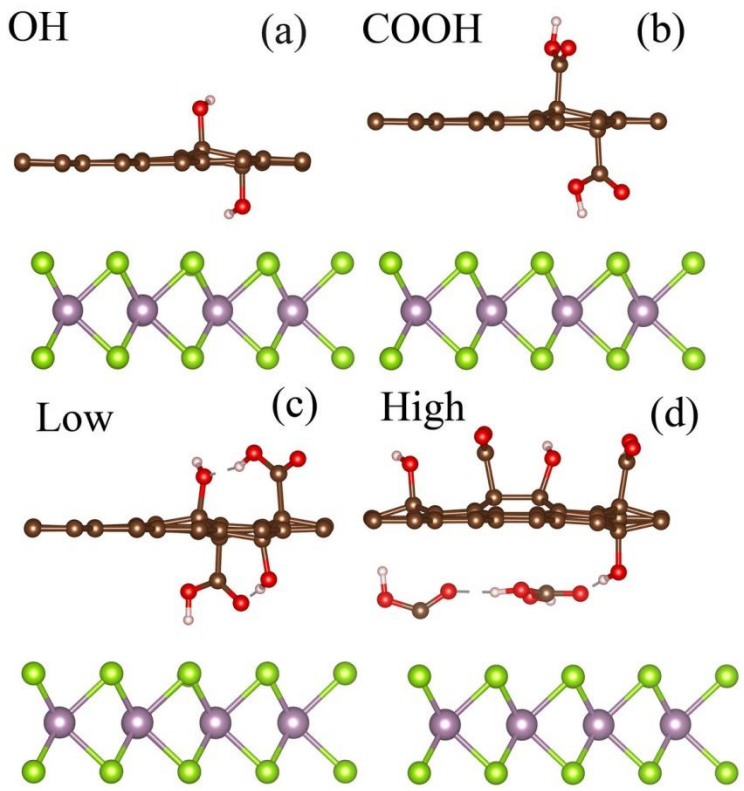

Figure 8.1: *Structural geometry of GO/$MoSe_2$ HS. a) OH, b) COOH, c) Low, and d) High.*

in Figure 8.1 (a-d). The detailed analysis of the electronic structure of the GO/$MoSe_2$ heterostructure (HS) is performed by using GGA-PBE + spin-orbit coupling (SOC) calculations. For such systems lacking inversion symmetry, the effect of SOC is significant. We start with a comparison of the GGA and GGA + SOC bandstructure of $MoSe_2$ 4×4×1 monolayer (ML) surface. Figure 8.2a and 8.2b depict the band-structure and atom (APDOS) and orbital projected (OPDOS) density of states of ML $MoSe_2$ surface respectively. The peak of the DOS at approximately -1.1 eV corresponds to the σ-bonded Se-4p_z and Mo-4d_{xz} and 4d_{yz} orbitals. The states at the top of the valence band (VB) and bottom of the conduction band (CB) in the bonding and antibonding region are mostly constituted of σ-bonded Se-4p_x, 4p_y and Mo-d_{xy}, $d_{x^2-y^2}$ and d_{3z^2-1} orbitals. We obtained a bandgap ~1.47 eV of the system, using GGA formalism. For $MoSe_2$, the chalcogen (Se) ligand field-effect is more prominent than its Sulfur counterpart,

making the bands wider and thereby reducing the bandgap in comparison to MoS_2. The band structure along Γ-M-K-Γ high symmetry path clearly shows the direct band-gap at K-point. Figures 8.2c and 8.2d present the band-structure and DOS of the same system respectively after incorporating SOC. The band structure reveals a spin-splitting for both VB and CB. Whereas for the VB splitting, the valley dependence of the spin-splitting is the dominant cause, the CB splitting is a combined effect of the larger negative component of SOC for Se and a smaller positive contribution from Mo-*d* orbitals [30]. Since the incorporation of SOC renders the magnetic moments to be non-collinear, the adjacent DOS of Figure 8.2d has directionally projected components. The *x*, *y*, and *z* component projected DOS and their resultant is depicted in the figure. For the 2D ML system, the *z*-component of the DOS is the most prominent. The calculated band gap of 1.47 eV for non-SOC case reduces to 1.36 eV for SOC. The ubiquitous effects of SOC for such systems render its inclusion for all further calculations of HS. For HS1-HS5 and their corresponding SeV cases, as described in the prior section, there is a reduction of ground state energy for GGA + SOC, in comparison to GGA. Placement of GO over the underneath $MoSe_2$ layer is capable of regulating the doping of the combined system. The type and concentration of different ligands on the top GO layer control the interlayer charge transfer and thus controls the doping of the combined system. We have observed that the calculated Fermi-level (E_F) of the combined system is undergoing significant shifts for different HS systems. For HS2, with a single OH ligand at the bottom and top of the G-layer, the E_F is shifting towards the conduction band, implying *n*-type doping. If the ligand is changed to a single COOH attached to both sides of the G-layer (HS3), the E_F shifts towards the valence band, indicating *p*-type doping. In the next step, we have increased the number of functional ligands attached to the G-layer keeping a 1:1 ratio of the OH and COOH groups and found that the gradual increase in *p*-type shifts of E_F is monotonic only until an optimum concentration of

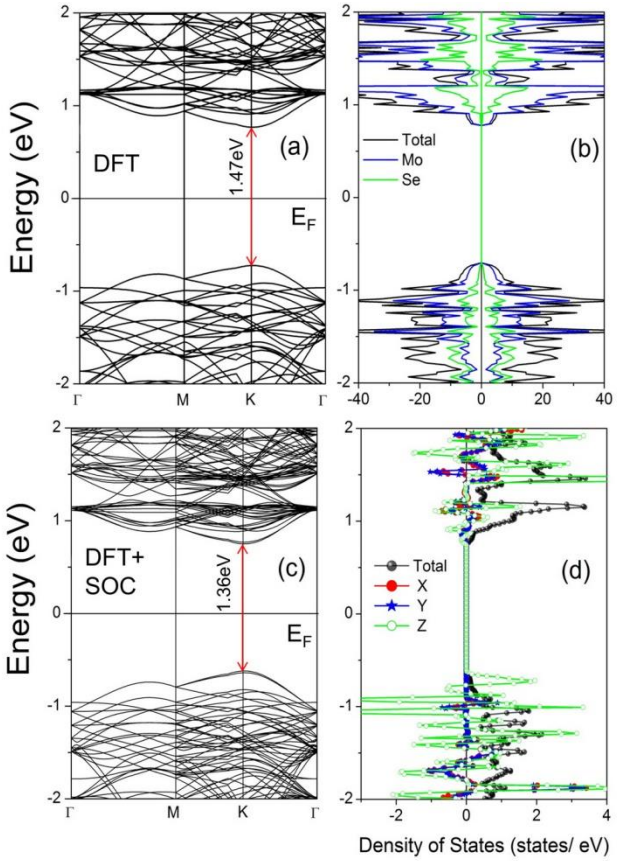

Figure 8.2: *a) GGA-PBE band structure and b) atom projected density of states (APDOS) of pure $MoSe_2$ structure, c) corresponding band structure, and d) x, y, z spin components-projected DOS of $MoSe_2$ after incorporating SOC. For better visibility of the total DOS, the components are magnified by an appropriate factor.*

functional ligands. We denote the highest *p*-type doped system HS4 as Low. Uncontrolled increase of ligand concentrations leads mostly to two detrimental effects for *p*-type doping, viz., 1) large buckling of the G-layer, disturbing the vdW stacking and 2) proximity induced mutual charge transfer between the ligands. For HS5 (High), although the trend of *p*-type doping is retained, the extent of doping is less in comparison to HS4. The relative shift of E_F to the pristine $MoSe_2$ and the nature of doping are listed in Table 8.1 for GGA + SOC cases. The trend of doping remains the same for both GGA and GGA + SOC cases. The presence of SeV is well-known to introduce *n*-type doping. All of these systems show a reduction of *p*-type doping in presence of SeV, as described in the supporting

information. In the successive sections, we will cogitate the reasoning behind the modulated doping of the combined systems.

Table 8.1: *Relative shift of E_F with respect to pristine $MoSe_2$. + and – denotes the direction of the shift of E_F towards CB and VB respectively.*

System	No vacancy		With SeV	
	Shift of E_F (eV)	*Type of doping*	*Shift of E_F (eV)*	*Type of doping*
OH	+0.399	*n*-type	+0.473	*n*-type
COOH	-0.721	*p*-type	-0.747	*p*-type
Low	-1.182	*p*-type	-0.981	*p*-type
High	-0.994	*p*-type	N/A	*Not Stable*

To understand the manifestation of ligand concentration on the electronic band-structure of the system, the atomically projected band structures are investigated for three most interesting cases: (1) For G/$MoSe_2$ (HS1), (2) G-OH/$MoSe_2$ (HS2) – the maximal *n*-doped case, and (3) G-Low/$MoSe_2$ (HS4) – the maximal *p*-doped case, as presented in Figure 8.3 (a-c). In each figure, the fatbands indicating total Mo, Se, and C characters are shown in different colors. All these band structures are normalized to the corresponding calculated E_F. For all three HS, the intersecting Dirac cones of Graphene bands got split due to vdW interactions with $MoSe_2$. For HS1 (Figure 8.3a), there is a direct bandgap between the Dirac cones of G at K-point ~0.32 eV. After attachment of ligands, the Dirac cones of G are gradually detaching from the CB and VB, introducing a modulation of the band-gap magnitude, nature, and position. Placement of ligands renders local destruction of hexagonal symmetry and the introduction of change like hybridization from sp^2 to sp^3. For HS2 (Figure 8.3b), the presence of OH on both sides of G introduces a high degree of hybridization of Mo-4d_{3z^2-1} and C-2p_z at VBM. The part of the Dirac cone at the CB is separated downwards and the bandgap becomes indirect at an intermediate position between K to Γ with a value of 0.64 eV. This Graphene-derived donor level appears at around ~0.1 eV below the CB, implying the occurrence of *n*-type doping for HS1. For HS4 (Figure 8.3c),

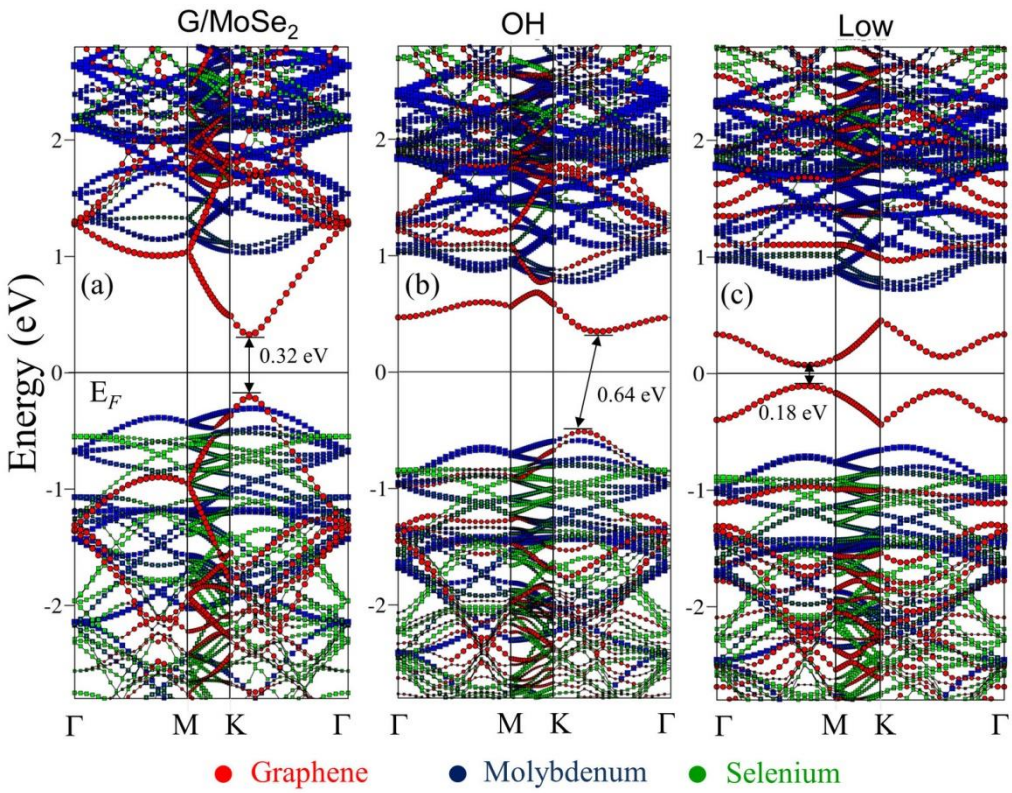

***Figure* 8.3:** *The atom projected fatbands for a) G/$MoSe_2$ (HS1), b) G-OH/$MoSe_2$ (HS2) and c) G-Low/$MoSe_2$ (HS4). Fatband color code is mentioned in the figure. The figures are normalized with respect to the calculated Fermi-level of the respective systems.*

due to the symmetric placement of both types of ligands and the increased extent of sp^3 hybridization, two symmetrically split C-2p_z Dirac cones are placed around E_F. In this case, the Graphene-derived acceptor level appears within ~0.18 eV of the valence band, suggesting *p*-type doping. The comparative extent of doping will be more evident from the quantitative charge-transfer, as presented in the consecutive section. The direct band-gap of 0.18 eV is now situated between Γ to M. A closer look at Figure 8.3 (a-c) also reveals that the presence of G and GO on top of $MoSe_2$ leads to a drastic variation of the effective mass of carriers, as calculated from the band structure and presented in Table 8.2. In the case of HS1, there is a reduction of effective mass to 0.12 from the value of 0.66 for pristine $MoSe_2$, stipulating high carrier mobility for the combined system. The addition of ligands to the G-layer results in flattening of bands and thereby leads to an increase in effective mass. For HS2, the effective mass is less than the pristine

system (0.55), supporting the *n*-type shift of E_F. For HS4, the increase of effective mass to the value 1.05 exactly corresponds with the obtained *p*-type doping and thus the primary presence of heavier carriers like holes in the system.

Table 8.2: *The effective mass of the systems calculated from bandstructure*

System	$MoSe_2$	G/$MoSe_2$	OH	Low
Effective Mass	0.66	0.12	0.55	1.05

Interestingly, for all three HS, the difference between valance band maxima (VBM), and conduction band minima (CBM) of $MoSe_2$ layer remains intact along with their unaltered position in K-space between K to Γ. Thus, controlling the ligand concentration in the GO layer, albeit capable of modulating carrier-induced electrical properties of GO/$MoSe_2$ HS systems, the fundamental band structure of $MoSe_2$ remains almost intact.

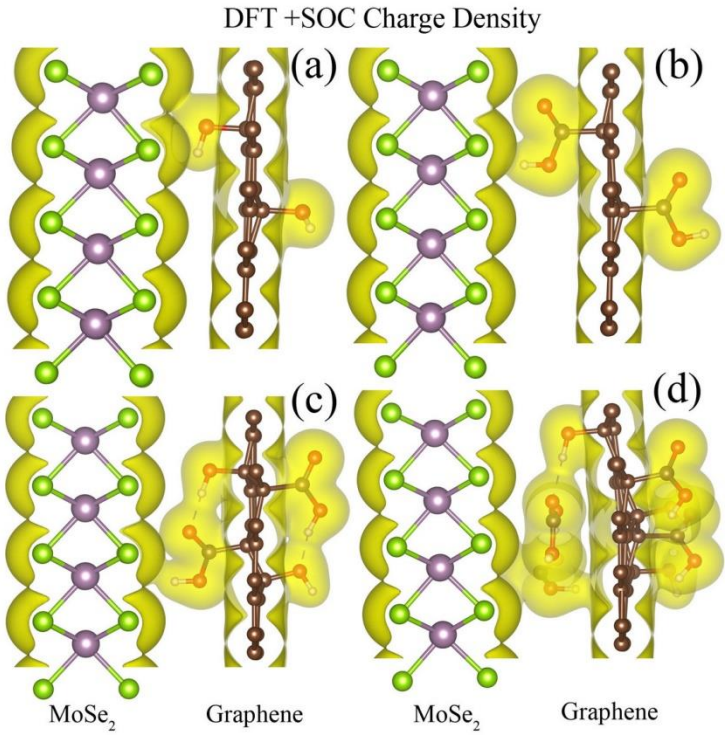

Figure 8.4: *Converged DFT+SOC charge density plots for a) HS2 b) HS3 c) HS4, and d) HS5. Overlapping between the constituent layers indicates the mutual charge transfer. Violet and green represent Mo and Se atoms respectively whereas brown represent carbon atoms. Oxygen atoms are denoted by red color.*

We have observed that the presence of ligands at the G-surface can tune the inter-layer charge-transfer and thereby can also control the doping of the underneath $MoSe_2$ layer. Interlayer charge-transfer between the component layers of the HS will be evident from the charge density plots presented in Figure 8.4 and the subsequent analysis. The type of doping and direction of charge transfer is entirely dependent on the ligand type and concentration. For HS2, where there is a single OH group on both sides of G, $MoSe_2$ experiences an *n*-type doping and the corresponding positive shift of the E_F in comparison to the pristine system.

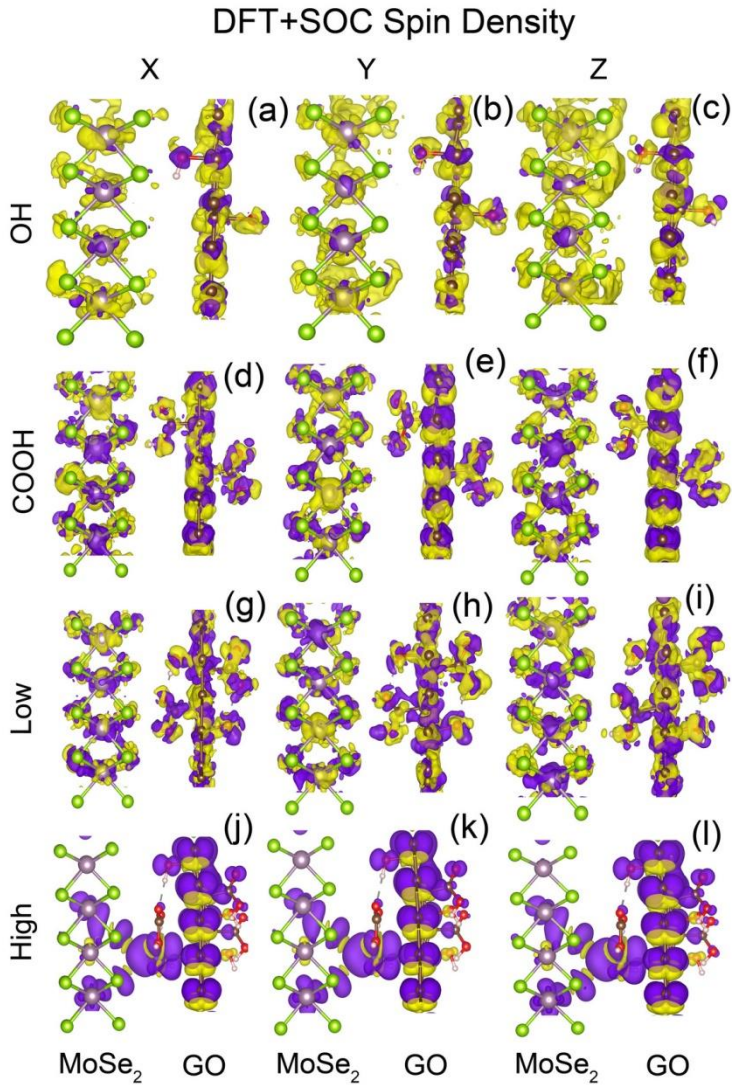

Figure 8.5: *Spin Density plots for HS2 for a) x, b) y, c) z-projected components, HS3 d)x, e) y, f) z, HS4 g) x, h) y , i) z and HS5 j) x , k) y , l) z.*

Due to the lower concentration of ligands, the buckling of the G layer is less. The simultaneous satisfaction of electron affinity of Oxygen of OH ligand from H and C of G-layer promotes the excess electron to flow towards $MoSe_2$. The direction of charge transfer reverses in the case of HS3, where a more polar functional group, COOH is attached to both sides of G. This results in a larger buckling due to the 3D nature of the C-C bond between G and COOH culminating in a local conversion of hybridization from sp^2 to sp^3. Moreover, the higher oxygen content of COOH and its buckling induced vicinity to the $MoSe_2$ ML expedites more hybridization of the *p*-levels of O and Se, leading to the electron transfer from $MoSe_2$ to GO. The E_F of the combined system shifts towards the valence band and the system acquires *p*-type doping. For both HS4 and HS5, significant charge transfer occurs from $MoSe_2$ to the GO layer, as can be seen from Figure 8.4. Using Bader-analysis, we have tried to quantify the amount of charge transfer for HS2 (maximum *n*-type) and HS4 (maximum *p*-type). As is evident from Figure 8.4, large buckling of the G-layer and mutual charge transfer between the ligands with increasing concentration of the ligands leads to the reduction of the *p*-type doping. However, the pernicious outcome of increasing ligand concentration is seen to have interesting effects on the SO-coupled non-collinear magnetic properties of the system. From HS2-HS5, with increasing ligand concentration, the *x*, *y*, and *z* components of the magnetic moment gradually increase, as presented in Table 8.3. We have also presented a comparative spin-density plot in Figure 8.5, which exhibits an increase in the spin-density of the systems with increasing ligand concentration for all three components. HS5, possessing the highest concentration of dopants, has the highest magnetic moment. For the GO layer, the manifestation of increment of spin-density is more due to its buckling. The same order of magnitudes of magnetic moments for all the three components suggests the absence of any directional magnetic anisotropy. Therefore, increasing the concentration of the dopants is observed to be capable of incorporating magnetic functionalization.

Table 8.3: *Magnetic moment table of the system with and without spin-orbit coupling.*

System	Magnetic Moment (SOC) (μ_B)			Mag. (Non-SOC) (μ_B)
	X Comp.	Y Comp.	Z Comp.	
OH	-0.0007	-0.0007	-0.0008	-0.0001
COOH	0.0003	0.0003	0.0004	0.0003
Low	0.0005	0.0005	0.0006	0.0007
High	1.0755	1.0719	1.3029	2.002

Next, we have compared the optical absorbance of different HS using static DFT and TDDFT and computed the excitonic positions from the calculations. For static DFT, we have used the Kubo-Greenwood formula to calculate the susceptibility tensor and the real as well as the imaginary part of the dielectric tensor. For a one-to-one comparison of the PDOS and the optical absorbance, GGA + SOC PDOS and the corresponding optical spectra are plotted at consecutive columns of Figure 8.6 for all five HS along with $MoSe_2$. The first column presents a comparison of the normalized DOS for $MoSe_2$ along with HS1-HS5. In GO, an increase of ligand concentration leads to an increase of the hybridization of ligand *p*-orbital with π-orbitals of G, breaking the sp^2 bonding chain of G. As a result of this buckling, the intersecting Dirac cones corresponding to the G-band structure opens up with the appearance of in-gap levels. For all the three *p*-type doped cases HS3-HS5, there is a gradual shrinking of bandgap and appearance of acceptor levels near VB, as can be seen from Figure 8.6. The position of acceptor level is closest to VB for HS4 (G-Low) case, supporting the fact that this is the most *p*-type doped system. G-High (HS5) possesses a bandgap very close to zero. The initial peak in the absorbance spectrum of $MoSe_2$ (Figure 8.6a) is at 1.5 eV due to the inter-band transitions from VBM to CBM, corresponding to the optical band gap, which essentially is the same as the electronic band-gap for the static DFT calculations, without the correction of exciton binding energy. The transitions are mostly from the Se-4p_x, 4p_y –hybridized Mo-4d_{xy}, 4$d_{x^2-y^2}$ and 4d_{3z^2-1} filled states at VBM to the unfilled states at CBM having almost the same character [31-33].

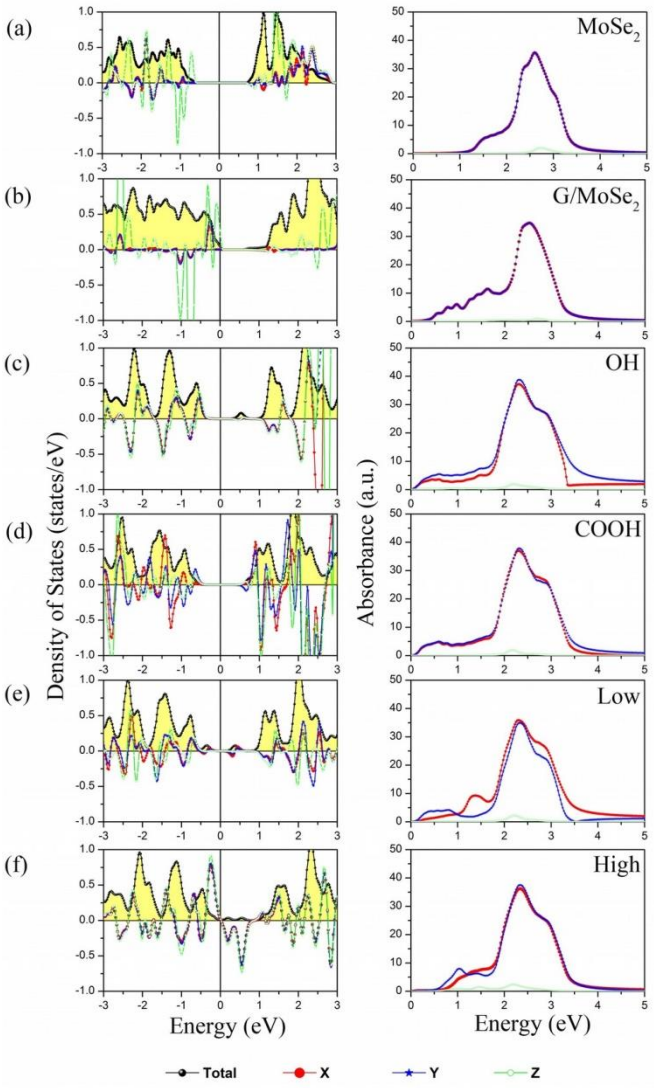

***Figure* 8.6:** *The SO coupled x, y, z spin component-projected PDOS and corresponding absorption coefficients of GO/$MoSe_2$ with different ligand concentration, a) $MoSe_2$, b) HS1, c) HS2, d) HS3, e) HS4, and f) HS5. Red, blue, and green color represent x, y, z directions respectively. For better visibility with respect to the total DOS, the components are magnified by an appropriate factor.*

Mutual charge-transfer between G and $MoSe_2$ via the functional ligands, albeit the appearance of mid-gap states, does not modify the difference of VBM and CBM of the original $MoSe_2$ layer, as is also seen in Figure 8.3. The highest peak in absorbance occurs at ~2.5 eV, corresponding to the transition from the strong bonding levels of $MoSe_2$ consisting of Se-4p_z hybridized Mo-4d_{xy}, 4$d_{x^2-y^2}$, and 4d_{3z^2-1} levels to the unfilled Se-4p_x, 4p_y hybridized levels of the same orbital Mo-character [34]. From the PDOS plot (Figure 8.6a), it will be evident that the contribution to

the *z*-component is more at the bonding regime. For HS1, due to the presence of G, the bandgap is reduced, the outcome of which is revealed in the absorbance spectrum with the appearance of additional peaks before 1.5 eV. There is, however, no change in the highest peak position of the absorbance for HS1 (~2.5 eV), implying that the presence of an overlayer G does not have much impact on bonding orbitals.

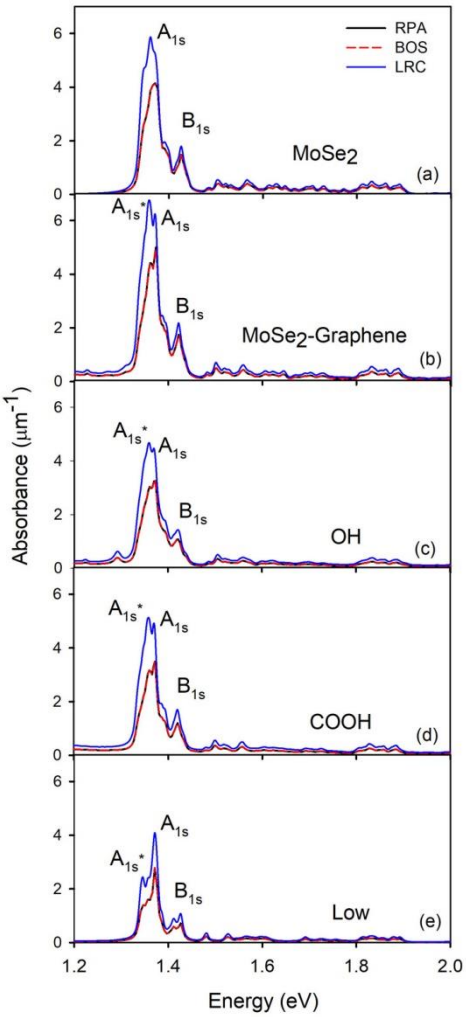

Figure 8.7: *The comparison of absorbance of different GO/$MoSe_2$ HS with pristine $MoSe_2$ using different TDDFT mechanisms (BOS and LRC) and RPA calculations.*

To obtain an idea about the excitonic mechanism in such HS, we have also investigated the time dependent optical properties of these systems using the TDDFT approach as implemented in ELK code [35]. We have used both the

Bootstrap (BOS) [23] and long-range contribution (LRC) kernel [36] to compute the TDDFT optical properties. Bootstrap in two different methodologies is tested for the present system, viz., Bootstrap (BOS), and Random Phase Approximation Bootstrap or RPA-Bootstrap (RBO) [37, 38]. Figure 8.7 represents a summary of the absorption coefficient calculated using the above-mentioned TDDFT methodologies along with the RPA calculations for different GO/$MoSe_2$ HS. Calculations are carried out for $MoSe_2$ ML, G/$MoSe_2$ interface (HS1), G-OH/$MoSe_2$ (HS2), G-COOH/$MoSe_2$ (HS3), and G-Low/$MoSe_2$ (HS4). Closer scrutiny of all the plots suggests that the optical properties calculated by using RPA calculations and Bootstrap (BOS) kernels do not differ much. We have next computed the optical properties by using the LRC TDDFT kernel, where the frequency-dependent dynamic XC kernel is used. After using the LRC kernel, there is a significant enhancement in the absorbance peaks and also the appearance of new satellite peaks, which may be attributed to the presence of excitons and charged excitons. For $MoSe_2$, the presence of A_{1s} and B_{1s} exciton positions, as calculated from TDDFT spectra are at 1.37 and 1.42 eV respectively (Figure 8.7), without the presence of any charged excitons. The corresponding experimental values are 1.59 and 1.65 eV [39]. In comparison to $MoSe_2$, its interface with G (HS1) has a red-shifted A_{1s} peak (1.35 eV). Interestingly, the addition of functional ligands to the G-layer does not introduce any energy shift for the A_{1s} peak. The unchanged peak position for A_{1s} supports the well-known phenomena of band-gap renormalization [40]. The change in the electron-hole interaction for 1*s* exciton obtained after modifying the electrostatic screening by the introduction of different functional ligands at the interface is nullified by the modification of electron-electron interaction and thereby resulting change in the quasiparticle band-gap. For B_{1s}, the absorption spectrum of HS1 is minutely red-shifted compared to ML $MoSe_2$. In addition to that, on adding ligands, a satellite peak ~20 meV below the A_{1s} peak position generates, which is denoted as A_{1s}^*. This peak may be present due to the occurrence of charged excitons in such systems [41].

Although both experimental and theoretical accomplishment of anticipated doping pattern by forming the 2D-2D HS is feasible, the behavior of the HS after placement of electrical contacts may undergo drastic changes. The contact geometry and electronic properties of interfaces of metal contacts with the HS of two semiconducting systems have their roles to play. We intend to explore the transport behavior of the HS for lateral and vertical placement of contacts with a commonly used metal like gold (Au). A model device configuration having two electrodes, electrode extension, and a central region is shown in Scheme 8.1. The geometry of the lateral and vertical contacts for the real system and the corresponding coordinate system will be evident from Scheme 8.1b and 8.1c respectively. Before calculating the transport properties, we intend to investigate the electronic structure of all HS with lateral and vertical interfaces with Au. The OPDOS and APDOS for the laterally and vertically contacted systems are plotted in Figure 8.8 for all four HS along with the pristine system. For lateral contacts, the edge Mo and Se atoms covalently bond with Au. The Mo and Se atoms inside the channel, on the other hand, have no hybridization with Au. Au 6*s* delocalized electrons are transferred to both Mo-4*d* and Se-4*p* states leading to almost the same weightage of highly hybridized Mo and Se-induced deep bonding levels. The situation alters for the vertical interface, where both of the bonding and antibonding DOS are dominated by Se-4*p* levels (Figure 8.8). In this case, the charge transfer from Au-6*s* to Mo-4*d* occurs via Se-4*p* leading to filled Mo-4*d* states below -1 eV and above 1 eV. The *p*-type Schottky barrier (SB) is shorter than the *n*-type ones for the lateral case, whereas the *n*-type one is shorter for the vertical interface. In the presence of GO, there is a little modification at the lateral interface. The transferred charges of Au-6*s* are now shared between the edge atoms of $MoSe_2$ and GO resulting in complete delocalization of Mo, Se, and GO levels and introducing metallic behavior in the system. On the contrary, for vertical interfaces, the intermediate GO layer reduces hybridization of Se and Au levels and results in the disappearance of highly hybridized peaks of Au and Se

between 0 to -1 eV which was present in the ML-$MoSe_2$ system. As a result, near E_F, there are delocalized levels of GO and Au. For all four HS (HS2-HS4), the hybridization of Mo and Se levels is regained for vertical interfaces, where both bonding and antibonding levels are dominated by Mo-4*d* states.

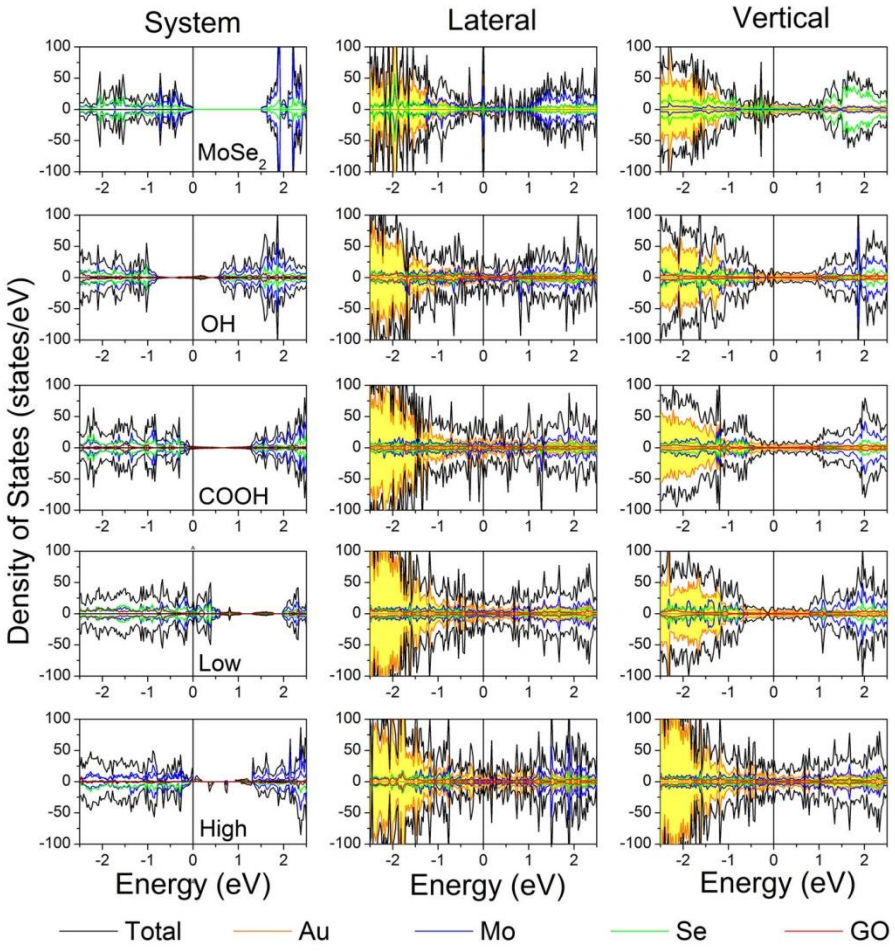

Figure 8.8: *The APDOS for the pristine system and different GO/$MoSe_2$ HS and the corresponding DOS for lateral and vertical interfaces with Au. For the first column, the energy scale is normalized by the difference of E_F of the corresponding system minus the E_F of the pristine $MoSe_2$ to make the n and p-type shift evident.*

For lateral contacts, the side interfaces are constructed from gold with a strain on the gold layer less than 5% on both sides. For vertical contacts, the relaxed structure of the interface is considered as the channel and after swapping the *b* and *c* axis, both sides of this channel are periodically extended to construct the left and right electrodes. Consequently, for both types of devices, self-

consistent quantum transport calculations are carried out to have an idea of the transmission coefficient and the I-V characteristics as a function of the source to drain bias. Figure 8.9 (a–f) depicts a comparison of the transport characteristics of lateral and vertical contact devices for non-spin polarized as well as spin-polarized quantum transport calculations. A comparison of the transmission coefficients

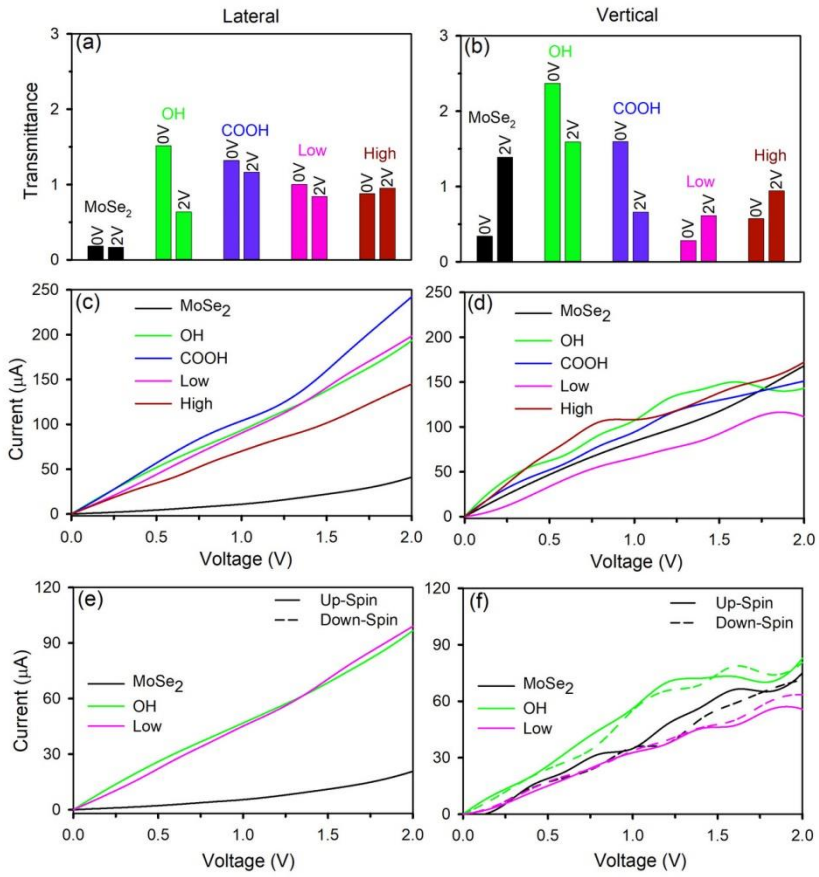

Figure 8.9: *Γ –point transmission of HS and pristine system at 0 V and 2 V bias for a) lateral and b) vertical contact. Comparison of I-V characteristics of HS and pure system with c) lateral and d) vertical contact configurations normalized by channel length are plotted. The spin-polarized I-V characteristic of HS and pure system with e) lateral and f) vertical contact configurations.*

for minimum (0V) and maximum (2V) bias voltages for both types of contacts reveals that the achieved nature of doping after combining GO with $MoSe_2$ does not extrapolate for devices. The systems studied in the present work are different from common TMDC systems in many aspects. As can be seen from Figure 8.9a and b, with lateral Au contacts, all of the HS from HS2-HS5 are lower resistive and

possess higher transmission coefficients for both bias voltages in comparison to ML-$MoSe_2$, confirming *n*-type doping with increasing ligand concentration. For vertical contacts, on the contrary, the transmission coefficients follow the expected *p*-type doping trend. The overall current value is lower than the lateral ones, as can be seen from the I-V characteristics plots for both non-spin-polarized and spin-polarized transports in Figure 8.9 (c–f). With optimal *p*-type doping for G-Low/$MoSe_2$ (HS4) system, the corresponding vertical contact device is the most resistive one with the current lower than the pristine system for both bias values. Therefore, for GO/$MoSe_2$ HS with optimal *p*-type doping, vertical contact devices are seen to be more effective to retain the achieved doping type even in the presence of metal contacts. Another significant attribute of vertical contact is the dependence of transport properties on spin-polarization, which is absent for lateral contacts. As observed in the prior section, the presence of more ligands on the top GO layer may turn the HS magnetic due to the spin-polarized nature of the introduced carriers (electrons/holes). This HS with a dense population of ligands may be utilized as a channel material for spintronics applications. To obtain a spin-dependent transport for those devices, vertical contact can be utilized. Carrier-induced doping patterns can be retained for vertical contact, leading to the simultaneous preservation of carrier-induced magnetic properties.

Figure 8.10 presents the interpolated contour plots of the transmission coefficients at the (k_x, k_y) plane perpendicular to the direction of carrier transport for the transmission coefficients corresponding to the pristine system (a and b), HS2 (c and d), and HS4 (e and f) for lateral and vertical contact respectively. To obtain an idea of transmission across the full cross-section of the device perpendicular to the direction of current flow, the transmission maps are drawn symmetrically around Γ, from $-k_x$ to $+k_x$ and $-k_y$ to $+k_y$ region. For lateral contacts in the pristine system, the central region around Γ is broad and having an overall

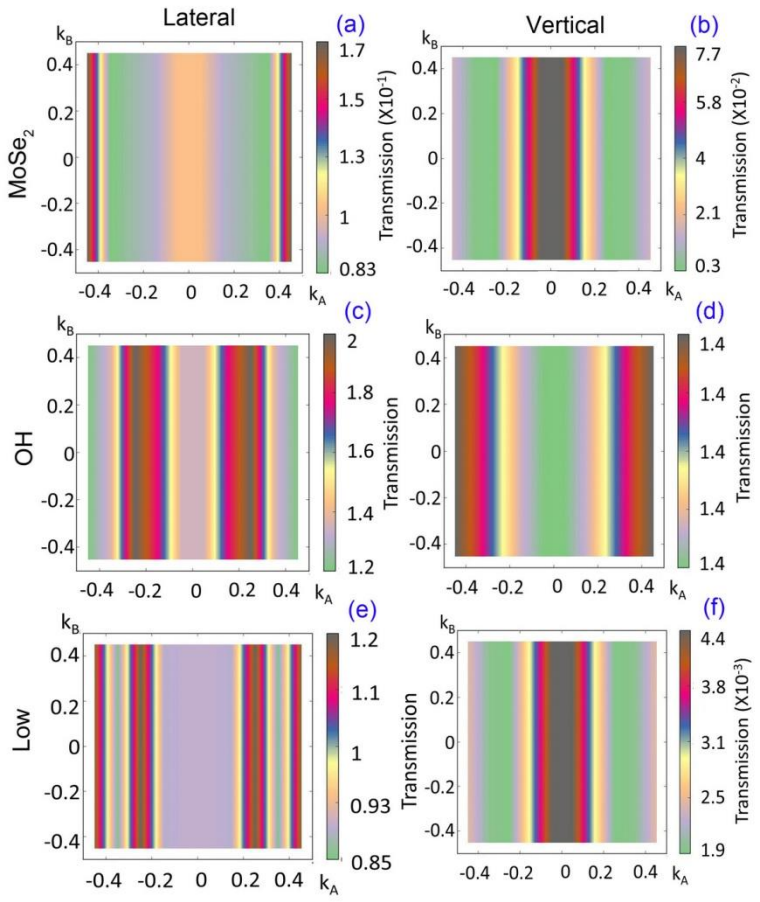

Figure 8.10: *Interpolated contour plot of the transmission coefficients in reciprocal space at zero bias for pristine $MoSe_2$ a) lateral and b) vertical contact, for HS2 c) lateral and d) vertical contact, for HS4 e) lateral and f) vertical contact. The center of the plot is the Γ point.*

better transmission than the vertical system with highly transmitting edges in *k*-space. For vertical contacts, on the contrary, the transmission is more for the central region of *k*-space than the edges. For HS2 lateral contacts (with OH), the edges in the *k*-space are having lower transmission than intermediate regions (Figure 8.10c). For vertical contacts, the variation of transmission is very less, as can be seen from the scale, although having higher values at the edges (Figure 8.10d) in *k*-space. For HS4, the vertical contact (Figure 8.10f) induces a significant reduction of two orders of magnitude of transmission coefficients in comparison with HS2 (Figure 8.10d) in the same contact geometry, as is evident from the color scale. The overall symmetry of the transmission contour plot about Γ–point is attributed to the orthorhombic symmetry of the constructed device.

For the present type of HS, the functional ligands on GO modulate the interlayer coupling and thereby control the doping of the underneath $MoSe_2$ ML. The inter-layer vertical charge transfer is responsible for controlling doping which lowers the height of the SB at the metal-semiconductor junction and thus proves to be more effective to retain the obtained doping. Lateral contacts, on the other hand, having chemical bonding and orbital overlap for both GO and $MoSe_2$ layer, are disruptive for the doping obtained via inter-layer charge transfer.

8.3. Conclusion:

In summary, we have investigated the role of functional ligands in modulating the interlayer coupling and the consequential control on the type of doping for various HS of GO/$MoSe_2$ obtained after varying the concentration and type of ligands. The summary of the electronic property investigations implies that for GO/$MoSe_2$ system, the optical properties are mainly determined by the almost intact band-structure of $MoSe_2$, whereas the electrical transport properties can be attributed to the modification of Graphene bands due to the presence of ligands. Other key inspections accomplished in the present work are 1) comprehensive observation of interconnection of variation of interlayer interactions and the corresponding modification of electronic structure; 2) study of static and time-dependent optical properties encompassing the exciton dynamics behavior of the HS; 3) scrutinizing realistic device transports for the system in both lateral and vertical contact geometry indicating that for the present HS, where the carrier density modifications are obtained through vertical charge transfer, vertical/top contacts are more effective to replicate the obtained doping pattern. These observations provide an efficient insight into the electronic structure of the system and thus enable effective utilization of these systems for optoelectronic and nano-electronic device applications like photo-transistor or photo-detectors.

References

[1] S. M. Paek, J. M. Oh, J. H. Choy, A lattice-engineering route to heterostructured functional nanohybrids, *Chem. As. J.* 6 (2011) 324.

[2] J. H. Choy, J. H. Park, J. B. Yoon, Multilayered SiO_2/TiO_2 nanosol particles in two-dimensional aluminosilicate catalyst−support, *J. Phys. Chem. B* 102 (1998) 5991.

[3] J. H. Choy, S. J. Kwon, G. S. Park, High-T_c superconductors in the two-dimensional limit:$[(P_y\text{-}C_nH_{2n+1})_2HgI_4]$-$Bi_2Sr_2Ca_{m-1}Cu_mO_y$ (m= 1 and 2), *Science* 280 (1998) 1589.

[4] N. B. Saleh, A. Afrooz, J. H. Bisesi, N. Aich, J. Plazas-Tuttle, T. Sabo-Attwood, Emergent properties and toxicological considerations for nanohybrid materials in aquatic systems, *Nanomaterials* 4 (2014) 372.

[5] K. Liu, K. Nagodawithana, P. C. Searson, C. L. Chien, Perpendicular giant magnetoresistance of multilayered Co/Cu nanowires, *Phys. Rev. B* 51 (1995) 7381.

[6] M. Bognitzki, H. Hou, M. Ishaque, T. Frese, M. Hellwig, C. Schwarte, A. Schaper, J. H. Wendorff, A. Greiner, Polymer, metal, and hybrid nano and mesotubes by coating degradable polymer template fibers (TUFT process), *Adv. Mater.* 12 (2000) 637.

[7] Y. Guo, Q. Tang, H. Liu, Y. Zhang, Y. Li, W. Hu, S. Wang, D. Zhu, Light-controlled organic/inorganic *p-n* junction nanowires, *J. Am. Chem. Soc.* 130 (2008) 9198.

[8] D. J. Milliron, S. M. Hughes, Y. Cui, L. Manna, J. Li, L. W. Wang, A. P. Alivisatos, Colloidal nanocrystal heterostructures with linear and branched topology, *Nature* 430 (2004) 190.

[9] K. S. Novoselov, D. Jiang, F. Schedin, T. J. Booth, V. V. Khotkevich, S. V. Morozov, A. K. Geim, Two-dimensional atomic crystals, *Proc. Natl. Acad. Sci. U.S.A* 102 (2005) 10451.

[10] K. S. Novoselov, A. K. Geim, S. V. Morozov, D. Jiang, Y. Zhang, S. V. Dubonos, I. V. Grigorieva, A. A. Firsov, Electric field effect in atomically thin carbon films, *Science* 306 (2004) 666.

[11] M. J. Allen, V. C. Tung, R. B. Kaner, Honeycomb carbon: A review of Graphene, *Chem. Rev.* 110 (2010) 132.

[12] J. Azadmanjiri, J. Wang, C. C. Berndt, A. Yu, 2D layered organic–inorganic heterostructures for clean energy applications, *J. Mater. Chem. A.* 6 (2018) 3824.

[13] M. Y. Li, C. H. Chen, Y. Shi, L. J. Li, Heterostructures based on two-dimensional layered materials and their potential applications, *Mater. Today* 19 (2016) 322.

[14] S. Bertolazzi, D. Krasnozhon, A. Kis, Nonvolatile memory cells based on MoS_2/graphene heterostructures, *ACS Nano* 7 (2013) 3246.

[15] K. Kośmider, J. W. González, J. Fernández-Rossier, Large spin splitting in the conduction band of transition metal dichalcogenide monolayers, *Phys. Rev. B* 88 (2013) 245436.

[16] T. Musso, P.V. Kumar, A. S. Foster, J. C. Grossman, Graphene oxide as a promising hole injection layer for MoS_2-based electronic devices, *ACS Nano* 8 (2014) 11432.

[17] Q. H. Wang, K. Kalantar-Zadeh, A. Kis, J. N. Coleman, M. S. Strano, Electronics and optoelectronics of two-dimensional transition metal dichalcogenides, *Nat. Nanotech.* 7 (2012) 699.

[18] B. Radisavljevic, M. B. Whitwick, A. Kis, Integrated circuits and logic operations based on single-layer MoS_2, *ACS Nano* 5 (2011) 9934.

[19] K. Roy, M. Padmanabhan, S. Goswami, T. P. Sai, G. Ramalingam, S. Raghavan, A. Ghosh, Graphene–MoS_2 hybrid structures for multifunctional photoresponsive memory devices, *Nat. Nanotech.* 8 (2013) 826.

[20] M. M. Furchi, D. K. Polyushkin, A. Pospischil, T. Mueller, Mechanisms of photoconductivity in atomically thin MoS_2, *Nano Lett.* 14 (2014) 6165.

[21] Z. Wang, B. Mi, Environmental applications of 2D molybdenum disulfide (MoS_2) nanosheets, *Environ. Sci. Tech.* 51 (2017) 8229.

[22] X. Lei, K. Yu, Z. Tang, Z. Zhu, Synthesized $MoSe_2/TiO_2$ heterogeneous structure as the promising photocatalytic material: Studies from theory to experiment, *J. Appl. Phys.* 121 (2017) 044303.

[23] S. Sharma, J. Dewhurst, A. Sanna, E. Gross, Bootstrap approximation for the exchange-correlation kernel of time-dependent density-functional theory, *Phys. Rev. Lett.* 107 (2011) 186401.

[24] K. Roy, M. Padmanabhan, S. Goswami, T. P. Sai, G. Ramalingam, S. Raghavan, A. Ghosh, Graphene-MoS_2 hybrid structures for multifunctional photoresponsive memory devices, *Nat. Nano* 8 (2013) 826.

[25] A. Ebnonnasir, B. Narayanan, S. Kodambaka, C.V. Ciobanu, Tunable MoS_2 bandgap in MoS_2-graphene heterostructures, *Appl. Phys. Lett.* 105 (2014) 031603.

[26] D. Pierucci, H. Henck, J. Avila, A. Balan, C. H. Naylor, G. Patriarche, Y. J. Dappe, M. G. Silly, F. Sirotti, A. T. C. Johnson, M. C. Asensio, A. Ouerghi, Band alignment and minigaps in monolayer MoS_2-Graphene van der Waals heterostructures, *Nano Lett.* 16 (2016) 4054.

[27] T. K. Maji, K. K. Tiwary, D. Karmakar, Achieving tunable doping of $MoSe_2$ based devices using GO@$MoSe_2$ heterostructure, 1832, *AIP Conf. Proceed.* (2017) 120019.

[28] P. Johari, V.B. Shenoy, Modulating optical properties of graphene oxide: Role of prominent functional groups, *ACS Nano* 5 (2011) 7640.

[29] T. K. Maji, K. Vaibhav, S. K. Pal, K. Majumdar, K. V. Adarsh, D. Karmakar, Intricate modulation of interlayer coupling at the graphene oxide/$MoSe_2$ interface: Application in time-dependent optics and device transport, *Phys. Rev. B* 99 (2019) 115309.

[30] K. Kośmider, J. W. González, J. Fernández-Rossier, Large spin splitting in the conduction band of transition metal dichalcogenide monolayers, *Phys. Rev. B* 88 (2013) 245436.

[31] R. Sharma, J. Aneesh, R. K. Yadav, S. Sanda, A. Barik, A. K. Mishra, T. K. Maji, D. Karmakar, K. Adarsh, Strong interlayer coupling mediated giant two-photon absorption in $MoSe_2$/graphene oxide heterostructure: Quenching of exciton bands, *Phys. Rev. B* 93 (2016) 155433.

[32] N. Dong, Y. Li, Y. Feng, S. Zhang, X. Zhang, C. Chang, J. Fan, L. Zhang, J. Wang, Optical limiting and theoretical modelling of layered transition metal dichalcogenide nanosheets, *Sci. Rep.* 5 (2015) 14646.

[33] K. Wang, Y. Feng, C. Chang, J. Zhan, C. Wang, Q. Zhao, J. N. Coleman, L. Zhang, W. J. Blau, J. Wang, Broadband ultrafast nonlinear absorption and nonlinear refraction of layered molybdenum dichalcogenide semiconductors, *Nanoscale* 6 (2014) 10530.

[34] Y. Pan, S. Li, M. Ye, R. Quhe, Z. Song, Y. Wang, J. Zheng, F. Pan, W. Guo, J. Yang, Interfacial properties of monolayer $MoSe_2$–metal contacts, *J. Phys. Chem. C* 120 (2016) 13063.

[35] B. Sahoo, K. S. P. Devi, S. Dutta, T. K. Maiti, P. Pramanik, D. Dhara, Biocompatible mesoporous silica-coated superparamagnetic manganese ferrite nanoparticles for targeted drug delivery and MR imaging applications, *J. Colloid Interface Sci.* 431 (2014) 31.

[36] J. Kang, W. Liu, D. Sarkar, D. Jena, K. Banerjee, Computational study of metal contacts to monolayer transition-metal dichalcogenide semiconductors, *Phys. Rev. X* 4 (2014) 031005.

[37] S. Rigamonti, S. Botti, V. Veniard, C. Draxl, L. Reining, F. Sottile, Estimating excitonic effects in the absorption spectra of solids: Problems and insight from a guided iteration scheme, *Phys. Rev. Lett.* 114 (2015) 146402.

[38] Y. M. Byun, C.A. Ullrich, Excitons in solids from time-dependent density-functional theory: Assessing the Tamm-Dancoff approximation, *Computation* 5 (2017) 9.

[39] S. Mouri, W. Zhang, D. Kozawa, Y. Miyauchi, G. Eda, K. Matsuda, Thermal dissociation of inter-layer excitons in $MoS_2/MoSe_2$ hetero-bilayers, *Nanoscale* 9 (2017) 6674.

[40] G. Gupta, S. Kallatt, K. Majumdar, Direct observation of giant binding energy modulation of exciton complexes in monolayer $MoSe_2$, *Phys. Rev. B* 96 (2017) 081403.

[41] Y. Lin, X. Ling, L. Yu, S. Huang, A. L. Hsu, Y. H. Lee, J. Kong, M. S. Dresselhaus, T. Palacios, Dielectric screening of excitons and trions in single-layer MoS_2, *Nano Lett.* 14 (2014) 5569.

Chapter 9

Computational and Optical Studies on the Interface of MoS_2 and High *k* Dielectric Oxides for Potential Device Application

9.1. Introduction:

The relevancy of two-dimensional (2D) materials in the field of ultra-scaled logic devices have gained a lot of attention in recent ages over the conventional channel materials like Si, Ge, etc. 2D materials are considered for high-performance logic devices due to their atomic thickness, which offers better scalability in comparison to Si and III–V channel FET [1]. 2D materials, such as Graphene (G) [2, 3], transition metal dichalcogenides (TMDCs), and hexagonal boron nitride (h-BN), offer interesting opportunities for the implementation of transistors for digital and high-frequency electronics owing to their intrinsic physical attributes like dangling bond free surface containing natural passivation [4], tunable optimal band-gap [5], advanced carrier control [6, 7] and the possibility of modulating electro-optical properties by forming combinatorial van der Waal (vdW) stacks [8-11]. However, electronic device utilization of TMDC systems like MoS_2 encounters several challenges. To address these challenges a deep understanding of the interfacial chemistry, physics of band alignment and contact-engineering at the metal-semiconductor interfaces are very much required [12-15].

In most of the device systems, the high contact resistance at metal−semiconductor junctions hinders their performance of the device significantly. Electronic device utilization of TMDC systems like MoS_2 poses several challenges on charge transport and contact-engineering at the metal-

semiconductor interfaces. Moreover, as a result of the charge redistribution across the interface, the presence of the interfacial dipoles causes a significant modification of the band-bending across the interface. To attain an efficient mechanism for higher carrier injection and channel transport in TMDC devices, many new strategies have been adopted. Tuning the contact resistances at the metal-semiconductor junction to control the metal-induced gap states (MIGS) and Fermi-level Pinning (FLP) is one of the efficient mechanism for higher carrier injection [13, 16-21]. Dielectric screening of the scattering centers resulting from the interfacial carrier traps by using a high-*k* dielectric or 2D insulators is another technique to improve efficiency [22-26]. As a result of its interface of TMDC and high-*k* dielectric transition metal oxides (TMO) had gained a lot of interest in the scientific community due to the proficient impact of TMO in reducing the contact resistance as well as restraining the FLP for the metal-TMDC contacts. The MOS_2/TiO_2 interfaces are also commonly used for the betterment of photo-electrochemical and photo-catalytic performances of MoS_2 [27-31]. Though most of the TMDC/TMO based works have been carried out by small area exfoliated flakes or small area CVD, for large-area growths of both MoS_2 and anatase−TiO_2 (A−TiO_2), the interface is yet not investigated.

In the present work, we have grown large-area TMDC/TMO interfaces, by using different techniques. Here we have grown a pulsed laser deposited (PLD) MoS_2 thin film. On top of it, the TiO_2 layer has been grown using different techniques (PLD and atomic layer deposition (ALD)). TiO_2 grown by two different techniques show different electronic and optical properties at the interface. In the present case, we found upon deposition of the TiO_2 layer (for both techniques), on the top of MoS_2 the system undergoes *p*-type doping. Structural characterizations are done by using micro-Raman (MR) and cross-sectional transmission electron micrograph (TEM). The binding energy (BE) shifts of the core-level spectra of Mo-3*d* and S-2*p* for both MoS_2/TiO_2 (PLD) and MoS_2/TiO_2 (ALD) have been

investigated using the XPS technique. Our first principles DFT calculation also validates the doping nature obtained by the XPS study. It is found that in the heterostructure, the type of doping has a strong dependence on the surface termination of the TMO layer. An extensive optical analysis including the excited state dynamical optical properties, the transient absorption spectra, and the non-linear responses of the heterostructures have been explored. Finally, we measured the four-probe photo-transport for both of these systems and then demonstrated a top-gate photo-transistor from the MoS_2/TiO_2 (PLD) system.

9.2. Results and Discussion:

9.2.1. Combinatorial Large-area MoS_2/Anatase-TiO_2 Interface: A Pathway to Emergent Optical and Opto-electronic Functionalities: We have prepared MoS_2 samples using the PLD technique. The approximate thickness of the MoS_2 sample was found to be ~28 nm corresponds to 30 layers of MoS_2. Depending upon the number of pulses three types of MoS_2 have been grown: a) 400 pulses, b) 600 pulses, and c) 1000 pulses. For the PLD deposition of TiO_2, the number of pulses needed for the growth of continuous TiO_2 film is found to be 3600 (thickness ~80 nm). Another interface MoS_2/TiO_2 (ALD) is grown after using the cyclic gas-surface self-limiting reactions in the ALD setup by using Titatinum isopropoxide precursor for uniform deposition of 2 nm at 250° °C temperature. We denote MoS_2 (PLD)/TiO_2 (ALD) as HS1 and MoS_2 (PLD)/TiO_2 (PLD) as HS2. The surface roughness of MoS_2 decreases by an order of magnitude after the deposition of TiO_2. PLD deposited TiO_2 layer is found to be polycrystalline. The detail of surface roughness is shown in Table 9.1.

Table 9.1: *Thickness measurement and surface roughness table.*

System	Thickness (nm)	Surface Roughness (nm)
MoS_2-1000P	28.2	2.61
TiO_2-3600P	20.8	1.18
Heterostructure	136	0.86

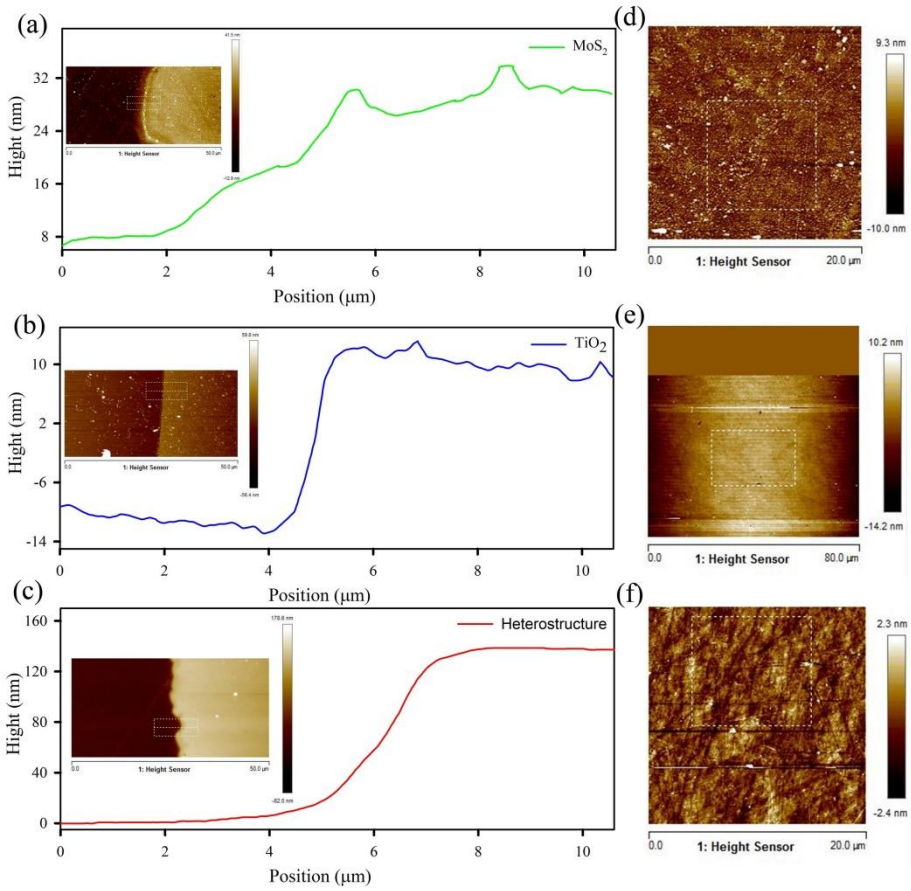

Figure 9.1: *Thickness of different deposited systems a) MoS_2 1000 pulse, b) TiO_2 3600 pulse, c) MoS_2 (1000P)/TiO_2 (3600P). Surface roughness measurement of a) MoS_2 1000 pulse, b) TiO_2 3600 pulse, c) MoS_2 (1000P)/TiO_2 (3600P).*

The micro-Raman spectra (using 532 nm laser) of pristine MoS_2 (400, 600, 1000 pulses) and the corresponding HS1 and HS2 systems are depicted in 9.2. We have taken an average of several Raman Spectra over a large area (400 μm × 400 μm) to confirm the uniformity of the deposited samples. MoS_2 shows two characteristic peaks for the in-plane Mo–S vibration (E^1_{2g}) and out-of-plane S-vibration (A^1_g). Raman frequencies can be used as an indicator of the layer thickness. For MoS_2, with the increment of thickness, the difference between E^1_{2g} mode and A^1_g mode increase [32], which is also obtained in our present study. The detailed Raman peak position of all systems is tabulated in Table 9.2.

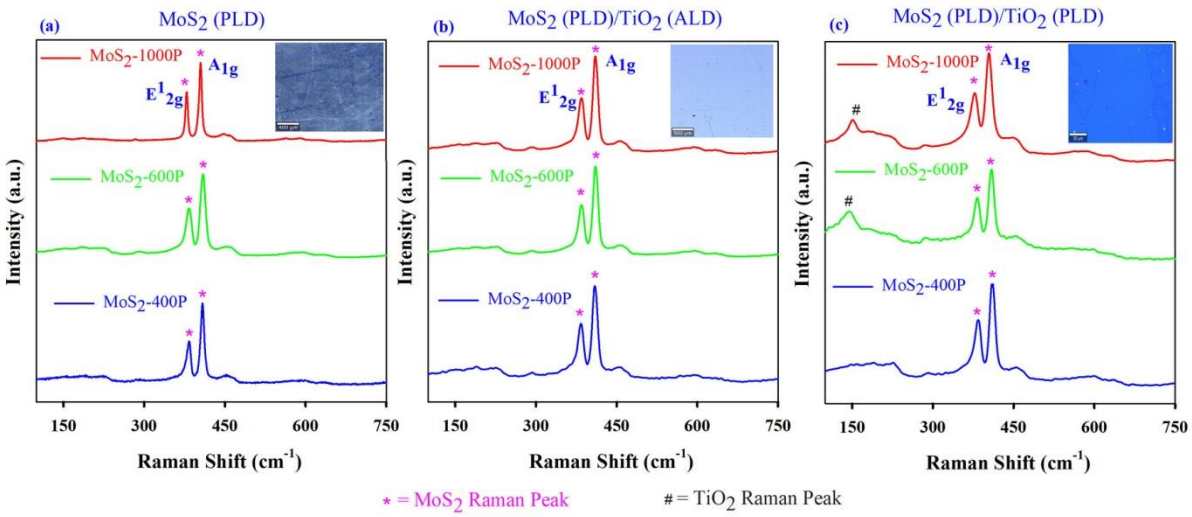

Figure 9.2: *Micro-Raman spectra of a) MoS_2 (PLD), b) MoS_2 (PLD)/TiO_2 (ALD), and c) MoS_2 (PLD)/TiO_2 (PLD) for difference thicknesses of MoS_2 (400, 600, 1000 pulses) and same thickness of TiO_2 (3600 pulses) for PLD samples.*

In the presence of amorphous TiO_2 (ALD deposition), there is a blue shift in the MoS_2 peak position which is consistent with the earlier literature [33]. In this case, due to the amorphous nature of TiO_2, the signature peak of TiO_2 is not visible in the Raman spectra (Figure 9.2b) [34]. However, in the case of polycrystalline TiO_2 in PLD, there is an overall red-shift, indicating the detrimental effect of the interfacial strain on both the in-plane and out-of-plane vibrations for the thicker TiO_2 layer. TiO_2 deposited by PLD shows the characteristic peak of the anatase phase of TiO_2 at ~150 cm^{-1} as a result of the better crystallinity of the TiO_2 layer [34].

Table 9.2: *Raman Peak of different systems.*

System	Peak	MoS_2	HS1	HS2
MoS_2 1000P	E^1_{2g}	379.1	384.8	376.9
	A_{1g}	405.6	410.6	405.4
MoS_2 600P	E^1_{2g}	383.3	384.6	382.3
	A_{1g}	408.9	410.5	409.3
MoS_2 400P	E^1_{2g}	383.5	384.6	383.7
	A_{1g}	408.3	409.3	410.6

We have performed the cross-sectional high-resolution transmission electron microscopic (HRTEM) of MoS_2 (1000) and HS2 (1000) films on quartz. The layered nature of the MoS_2 structure is visible from Figure 9.3a. HRTEM image of

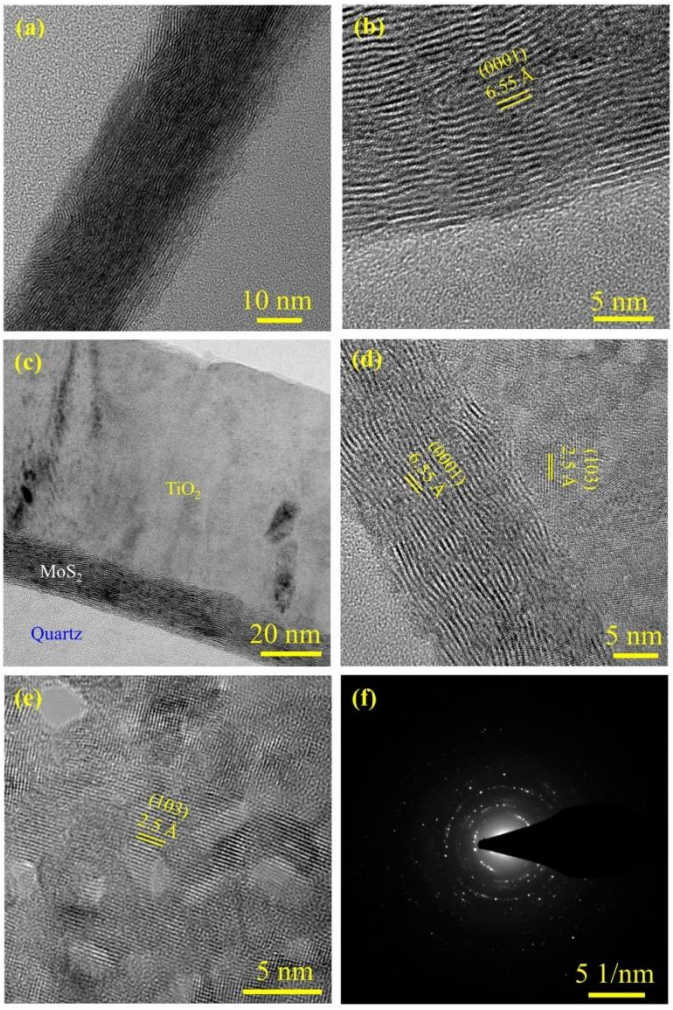

Figure 9.3: *a) Cross-sectional TEM image of PLD-grown MoS_2 (1000), b) HRTEM image of MoS_2 (1000), c) cross-sectional micrograph of HS2 (1000) (see text), showing Quartz, MoS_2, and TiO_2, d) HRTEM image of HS2 (1000), e) HRTEM image of TiO_2 layer of HS2 (1000), and f) SAED image of HS2 (1000).*

MoS_2 is depicted in Figure 9.3b. The calculated lattice fringe of the system is ~0.655 nm which corresponds to the [0001] plane of MoS_2. The cross-sectional TEM image of HS2 is presented in Figure 9.3c. Corresponding HRTEM image is depicted in Figure 9.3d, which shows the crystalline and polycrystalline nature of the PLD-

grown MoS_2 and A-TiO_2 respectively. We have calculated the fringe-width of MoS_2 (~0.64 nm corresponds to [0001] plane) and TiO_2 (~0.25 nm corresponds to [103] plane) in the HS1 system. However, a realistic HRTEM image of the MoS_2 PLD layer indicates the presence of discontinuous edges. These edges can be passivized by the TiO_2 layer, improving the overall crystallinity of the combined hetero-structure. This will also be evident from the selected area electron diffraction (SAED) images, containing both spots and ring patterns, as seen in Figure 9.3f which is consistent with previous literature [33, 35].

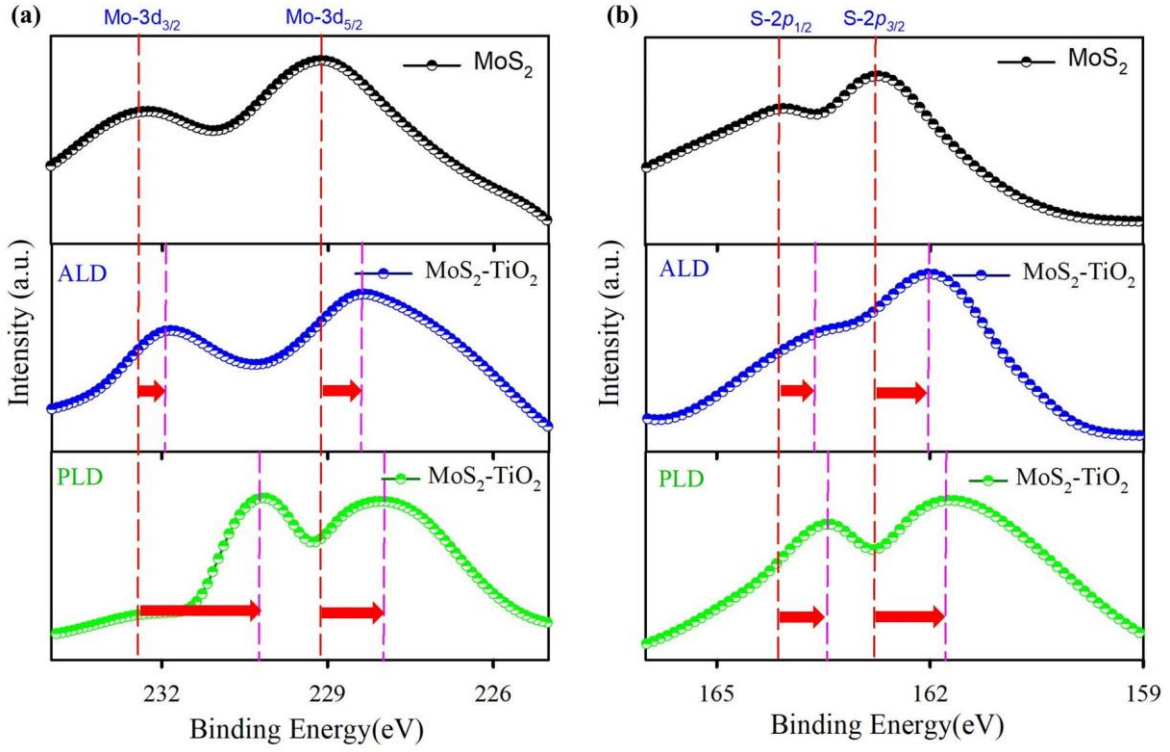

Figure 9.4: *XPS spectra depicting the core level shifts for MoS_2 (1000P)/TiO_2 systems: a) comparison of Mo-3d levels for pristine MoS_2, HS1 (see text) and HS2 (see text); b) same comparison for S-2p levels.*

The standard identification technique adopted to find out the nature of doping in 2D HS is the measurement of the BE shifts in the XPS spectra for core level electrons [36-39]. To obtain an idea of the elemental composition and the corresponding valence configuration, high-resolution photoelectron spectroscopy of the films is performed with hard X-rays in an energy range of 2-15 keV. In a

similar way like the Raman spectra, the resultant XPS data for each film is obtained by averaging over several scans at various places of the respective film. The details of the measurement are presented in the experimental section. The comparative plots for the BE of the core levels, viz., Mo $3d_{5/2}$, Mo $3d_{3/2}$, S $2p_{3/2}$, and S $2p_{1/2}$ for the pristine MoS_2 and both HS1 and HS2 with MoS_2 deposited with 1000 pulses is depicted in Figure 9.4. For both the heterostructures, after TiO_2 deposition on it, the BE of both Mo-3*d* and S-2*p* undergoes a shift towards lower energy implying a shift of the Fermi-level towards the valence band and thereby indicating *p*-type doping, which differs from the prior results in the literature for the exfoliated MoS_2 and ALD TiO_2 [33, 35, 38]. The shifts in BE for different HS are presented in Table 9.3.

To understand the detail of electronic behavior at the interface of MoS_2 and TiO_2, we have elaborately investigated the interface of MoS_2/TiO_2 using DFT calculation. There is a significant difference between the interface created from micron-sized exfoliated MoS_2 and a fast deposition of amorphous TiO_2 by ALD [33, 35, 38, 39] with the large-area epitaxial growth processes used in the present study. While the large-area interfaces are grown with longer deposition times, there are provisions of a gradual relaxation of the interfacial strains with increasing thickness of the top layer by mutual rotation of the constituting surfaces at the interfacial region. We have constructed a large area interface after stacking a (2 × 2 × 1) supercell of 2H-MoS_2 ($P6_3/mmc$) with a (2 × 2 × 1) supercell of A-TiO_2 ($I4_1/amd$) by the co-incidence site lattice (CSL) method, as implemented in the Atomistic Tool Kit 15.1 package [40, 41]. The mutual strain is minimized by varying the mutual rotation angle between the MoS_2 and TiO_2 surface cells around the stacking direction (*c*-axis for the present case). In all the calculations, the minimized mutual strain is found to be ~0.87%, when the mutual rotational angle between the two surfaces is ~46°. Figure 9.5 represents the two possibilities of surface termination of the TiO_2 layer on MoS_2, viz. a) O-termination, and b) Ti-

termination. The electronic structures of these two interfaces are investigated with the help of GGA-PBE + SOC calculations, as implemented in the Vienna Ab Initio Simulation Package (VASP) [42].

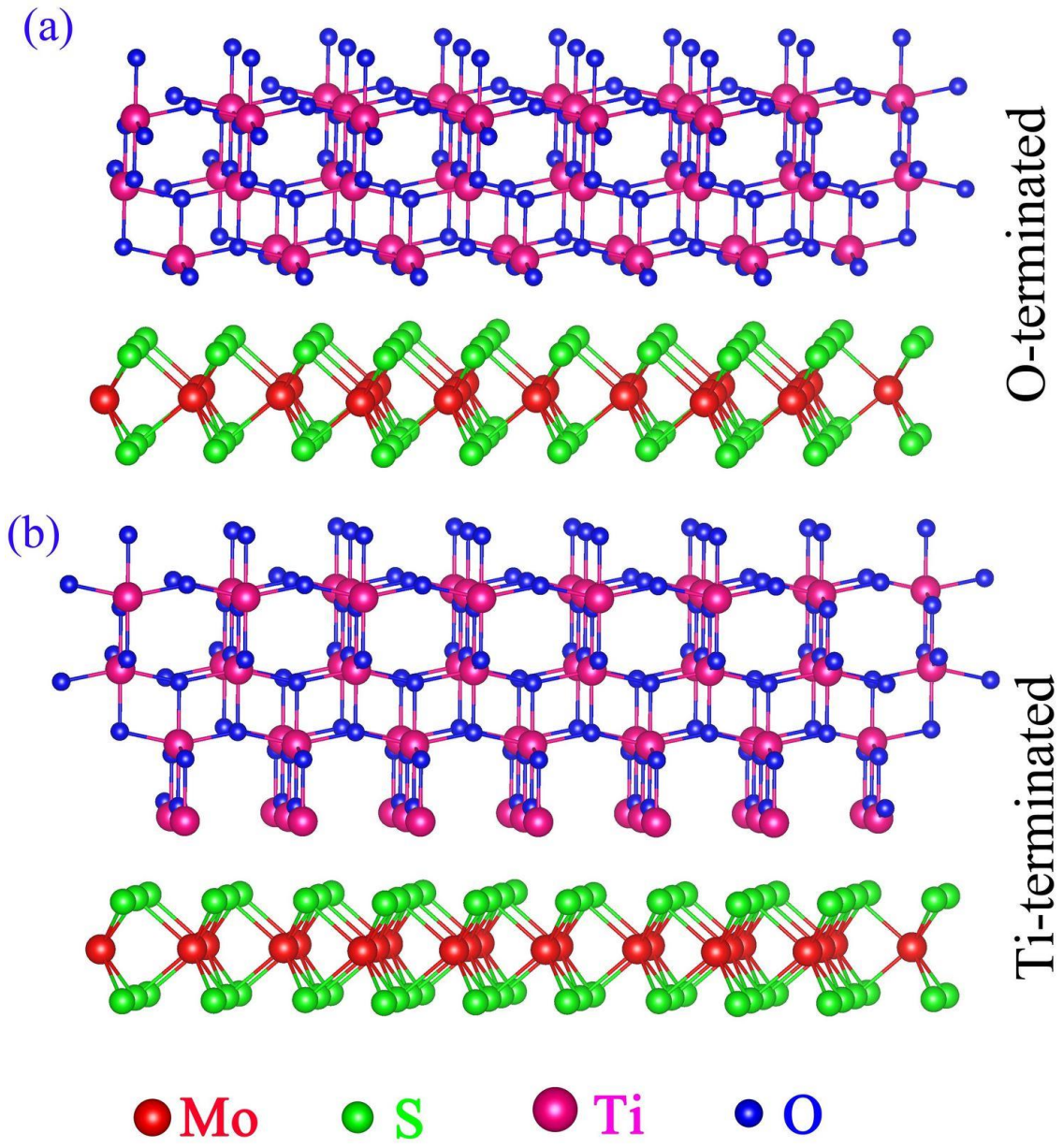

Figure 9.5: *Structural image of a) O-terminated MoS_2/TiO_2 heterostructure and b) Ti-terminated MoS_2/TiO_2 heterostructure.*

It is very common to have a vacancy in nanostructure during the formation. We have taken care of the impact of the presence of vacancies for these two

interfaces, where, for the O-terminated interface, the interfacial S (at MoS_2) and O (at TiO_2) vacancies are designated as SV and OV respectively. Similarly, for the Ti-terminated one, the S (at MoS_2) and Ti (at TiO_2) vacancies are denoted as SV and TiV respectively. Surface termination and interfacial vacancy play a great impact on the electronic structure and doping nature of the system. Ti-terminated surfaces are heavily *n*-type doped with a significant shift of E_F towards the conduction band (CB) revealing a metallic nature. The O-terminated system shows *p*-type doping with a shift of Fermi towards the valance band (VB). Interestingly, in the O-terminated system, the system is semiconducting in one spin channel and metallic in the other one, representing perfect half-metallic behavior. The Fermi-level shifts for all these interfaces are presented in Table 9.3. To compare with experimental doping, we have presented the result of the O-terminated system only.

Table 9.3: *Shift of E_F versus surface termination for different systems.*

System	Shift of E_F (eV)	Type of doping
O-terminated	-0.10	*p*-type
O-terminated + SV	-0.11	*p*-type
O-terminated + OV	-0.12	*p*-type
Ti-terminated	+1.53	*n*-type
Ti-terminated + SV	+1.54	*n*-type
Ti-terminated + TiV	+1.72	*n*-type

The orbital projected band structure and corresponding density of states for the O-terminated heterostructure and SV, OV systems are represented in Figure 9.6. The vertical up and down panels constitute the layer-projected MoS_2 and TiO_2 fatbands with the corresponding orbital contributions as Mo-*d* (red), S-*p* (green), Ti-*d* (magenta), and O-*p* (blue) respectively. It is found that the overall

semiconducting nature of MoS_2 is protected, and the direct-band gap resulting from Mo-*d* orbitals (red bands in the upper panel of Figure 9.6a) remains unaltered in the HS with a *k*-space shift of the conduction band minima (CBM) in between the Γ-M high-symmetry directions. There is a heavy hybridization of the Mo-*d* and S-*p* characters of MoS_2, both at valence band maxima (VBM) and CBM.

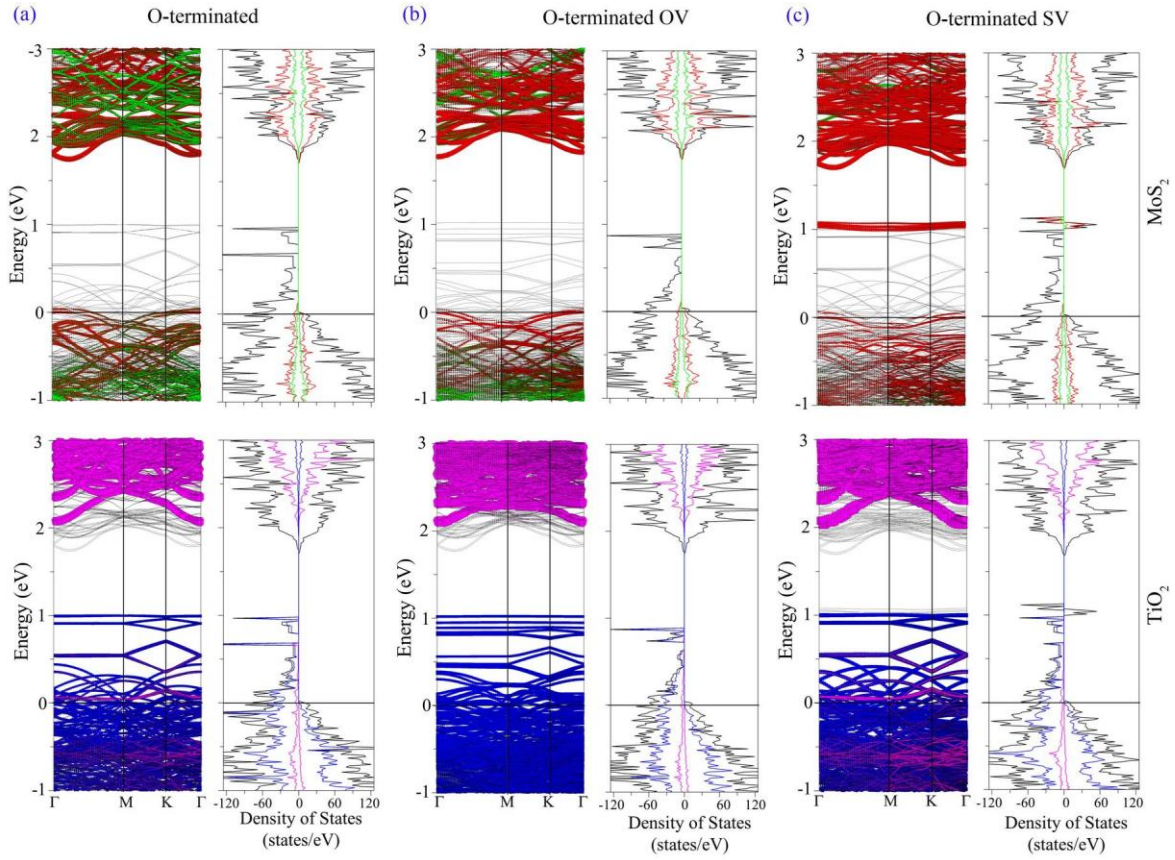

Figure 9.6: *Layer-projected fatbands for MoS_2 (upper panel) and TiO_2 (lower panel) and the corresponding partial density of states (DOS) for a) O-terminated MoS_2/TiO_2 systems, b) O-terminated MoS_2/TiO_2 systems with O-vacancy (OV) and c) O-terminated MoS_2/TiO_2 systems with S-vacancy (SV). The color code used for orbital projections is Mo-d (red), S-p (green), Ti-d (magenta), and O-p (blue).*

On the other hand, for TiO_2, the Ti-*d* orbital contributions are prominent at CBM with the O-*p* orbitals contributing near VBM. TiO_2 results in the acceptor levels within ~0.5 eV of the valence band of MoS_2 (blue bands in the lower panel of Figure 9.6a). This kind of generation of acceptor level is due to charge transfer

from MoS_2 to TiO_2. It also leads to the generation of localized mid-gap states at ~1 eV. The DOS result reveals that states near E_F are contributed by the up channel of TiO_2 which leads to the half-metallic nature of the interface. We further investigated the effect of the vacancy in the electronic structure of the systems.

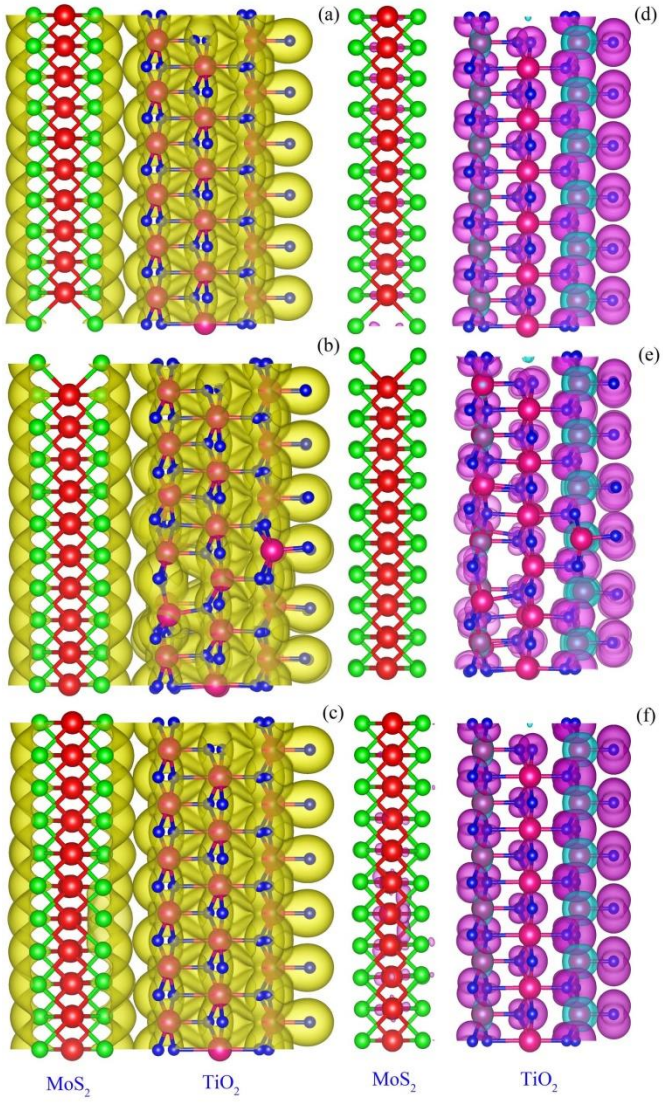

Figure 9.7: *Charge densities of different systems a) O-terminated MoS_2/TiO_2, b) same with OV, c) same with SV and corresponding spin densities of different systems d) O-terminated MoS_2/TiO_2, e) same with OV, and f) same with SV.*

In the presence of OV, some mid-gap states are generated (near ~1 eV) which comes from the O-*p* character (Figure 9.6b). Moreover, SV leads to the generation

of midgap states which come from the contribution of S-*p* states. The incorporation of spin-orbit coupling (SOC) leads to the splitting of VBM as well as CBM. However, unequal splitting of the bands at both the band-edges may lead to the occurrence of satellite peaks adjacent to the primary excitons. Converged charge and spin-densities for the O-terminated interfaces are depicted in Figure 9.7. Most of the charge and spin-densities are observed to be located around the TiO_2 layer. The decrement of charge in MoS_2 layers establishes the *p*-type nature of the heterostructure. The magnetic nature due to spin imbalance comes solely due to TiO_2.

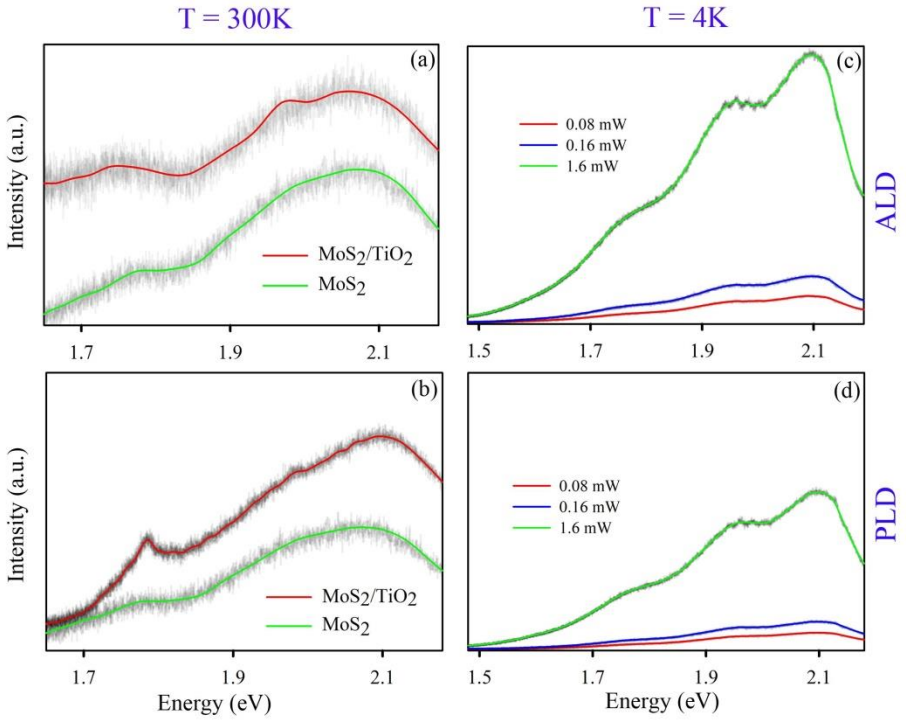

Figure 9.8: *Comparative PL spectra of a) HS1 (1000) and MoS_2 (1000) at 300 K, b) HS2 (1000) and MoS_2 (1000) at 300 K, c) HS1 (1000) at 4 K for three different laser powers, and d) HS2 (1000) at 4 K for three different laser powers.*

The photoluminescence (PL) spectra were collected for MoS_2 (1000), HS1 (1000), and HS2 (1000) with a laser of 532 nm wavelength and spot size of 20 μm diameter. In monolayer MoS_2, due to the SOC induced VB splitting and the enhanced Coulomb interactions, multi-exciton interactions are surviving even at

room temperature [43, 44]. Although, MoS_2 has both interlayer and intra-layer exciton, the intra-layer excitons, having an order of magnitude higher radiative decay rate, contribute the most to the PL signal. The comparative PL spectra for all the systems (1000 pulse), is depicted in Figure 9.8. In all cases, the intensity and

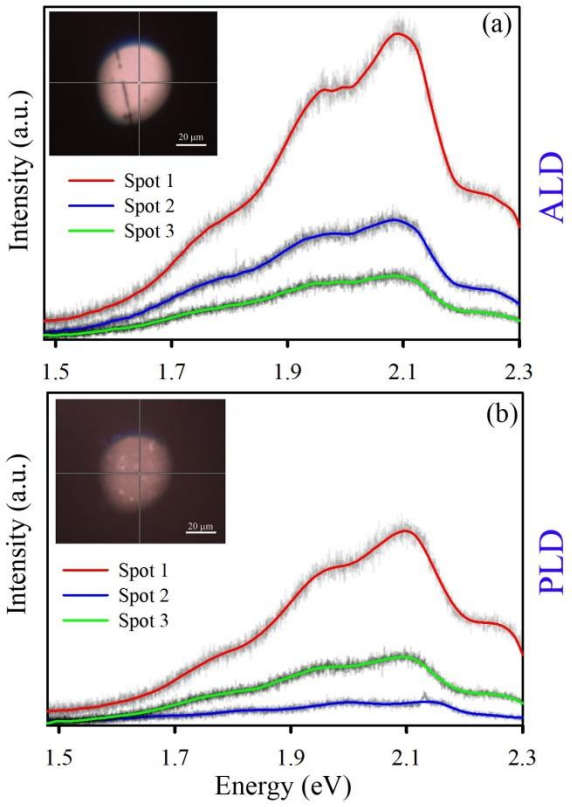

Figure 9.9: *Photoluminescence spectra of a) MoS_2 (PLD)/TiO_2 (ALD) at 4 K at 3 different random places (inset shows a typical image of a spot) and b) MoS_2 (PLD)/TiO_2 (PLD) at 4 K at 3 different random places (inset shows a typical image of a spot).*

line width of B exciton is higher, which are attributed to the proximity of the electron-hole pairs in 2D systems possessing larger densities of excitons, leading to mutually driven correlated inter-excitonic interactions [45]. PL spectra of HS1 (1000) and MoS_2 (1000) is depicted at 300K, revealing an A and B exciton peaks at ~1.77 and ~2.08 eV. There is a red and blue shift respectively in A and B exciton which can be attributed to the multi-layered nature and weak vdW stacking due to the presence of defects and surface edges, as is also evident from the TEM images. We found an extra saddle-point peak ~0.1 eV away from B exciton. There

are two possibilities for the generation of this peak, a) SOC splitting at CBM, and

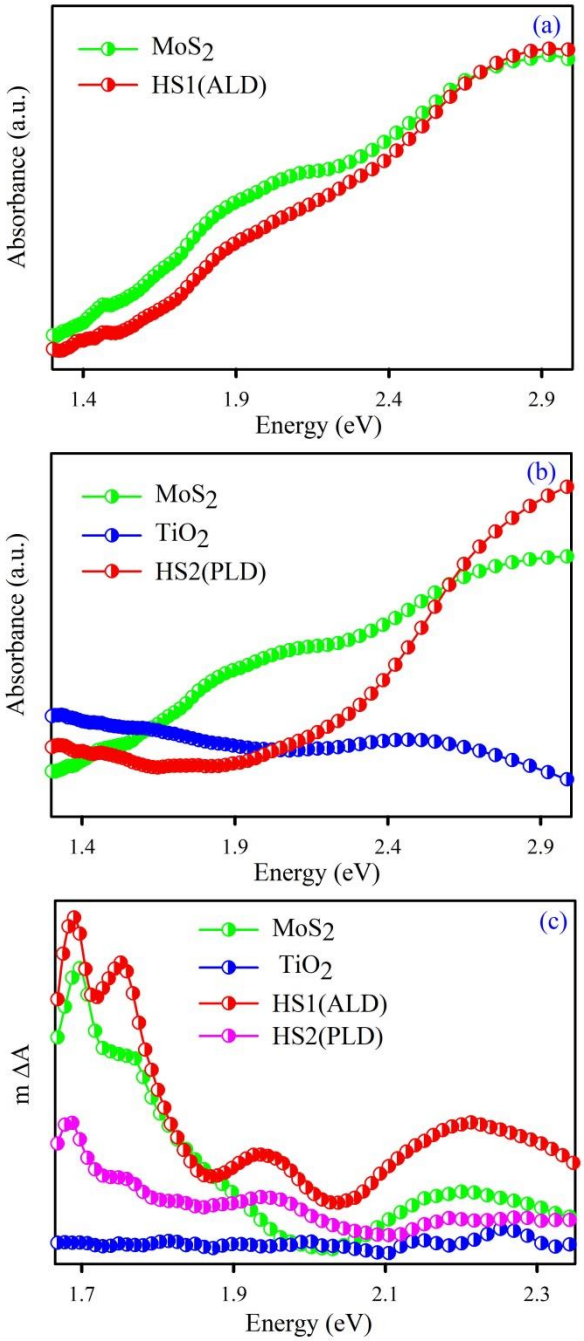

Figure 9.10: *Steady-State Absorbance of a) HS1 (ALD), b) HS2 (PLD), and c) comparison of Transient Absorption of heterostructures after 2 ps delay.*

b) the presence of TiO_2 generated acceptor levels, which may accommodate the de-excited electrons from CBM. In Figure 9.8b the saddle-point peak is not evident

here because of the stronger B exciton. However, low-temperature PL for three different power (Figure 9.8c and d) shows the noticeable presence of all three peaks (A exciton at ~1.76 eV, B exciton at ~2.09 eV, and saddle point peak at ~1.96 eV). A comparison with the PL of pristine MoS_2 reveals an overall increase of PL intensity in the HS with HS1 (ALD) having a stronger intensity than HS2 (PLD). So, the low temperature and room temperature PL shows detail of the excitonic interactions. Moreover, to confirm the uniformity of the system, PL spectra have been taken at different spots of the films (shown in Figure 9.9). It is found that there is no change in peak position at different positions except the peak intensity, which reveals the uniformity of the film. We measured the ground-state absorption spectra of different systems, as depicted in Figure 9.10. Closer scrutiny of the overall absorbance in Fig 9.10 reveals that the quenched nature of the A and B excitons in MoS_2 multi-layered films and HS2 (1000). HS1 (1000) manifests more prominent A and B exciton features.

Next, we have examined the exciton dynamic of the MoS_2 and HS system probed by using ultrafast (picosecond-resolved) transient absorption (TA) spectroscopy. In this case, the system is excited with a pump photons of 3.1 eV, and the changes in the absorbance are measured by using a probe signal ranging from 1.79 to 2.6 eV. The contour plot of TA for MoS_2 (1000), TiO_2 (3600), HS1 (1000), and HS2 (1000) is depicted in Figure 9.11 (a-d) respectively where the pump-probe delay is plotted against the energy of the probe beam. The color of the contour represents the differential absorbance (ΔA). The differential absorbance as a function of pump-probe delay is depicted in Figure 9.11 (e-g). The figures show bleach at the exciton position due to the filling up of the excited state and a time delay-induced absorption below the exciton position due to the presence of the trap states. The time-scales for the exciton decay and the trap state filling are represented in Table 9.4.

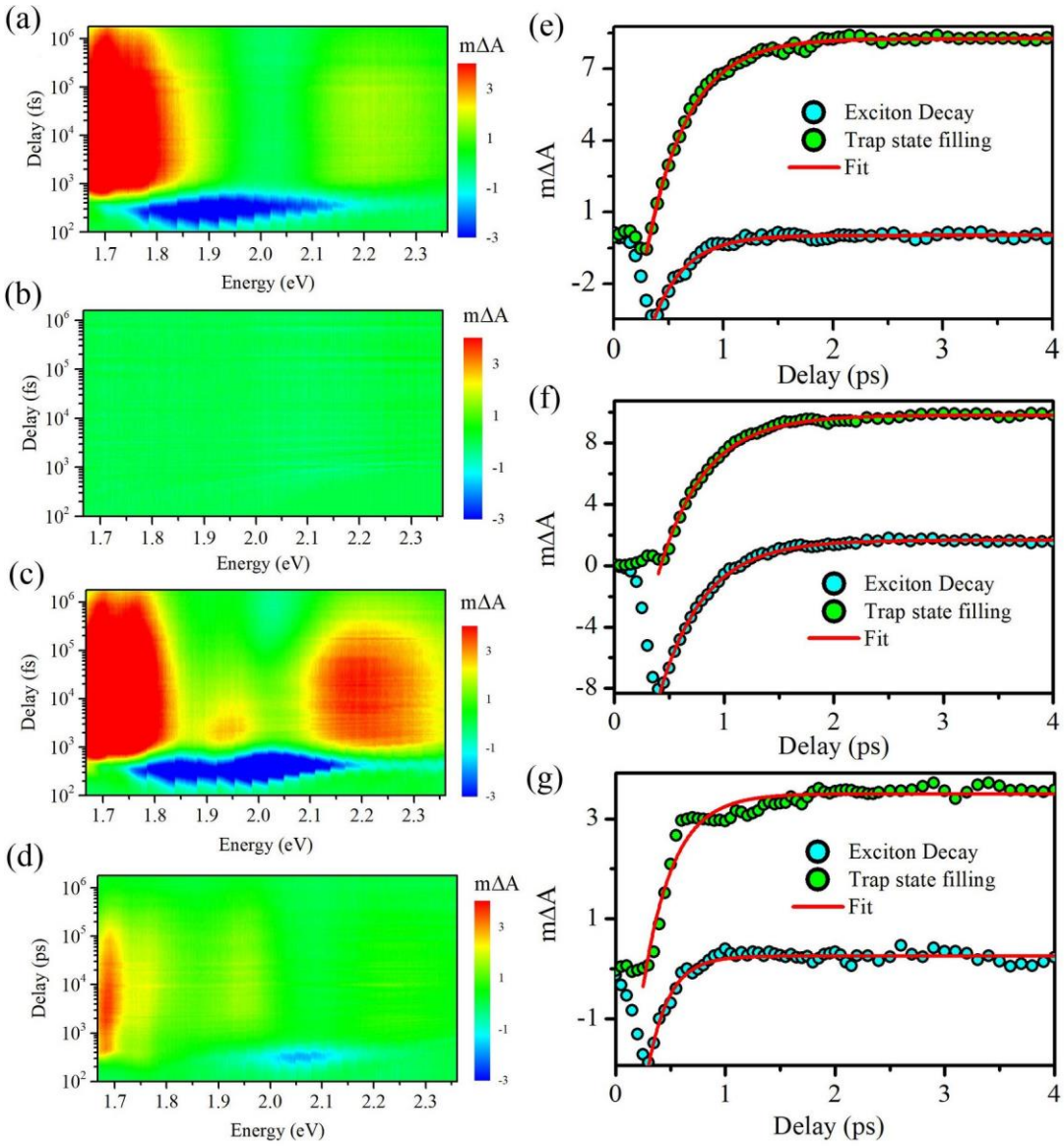

Figure 9.11: *Contour plots (see text) of TA measurements for a) MoS_2 (1000), b) TiO_2 (3600), c) HS1 (1000), and d) HS2 (1000). Kinetics for A-exciton decay at 2 eV and trap state filling at 1.73 eV for e) MoS_2 (1000), f) HS1 (1000), and g) HS2 (1000).*

MoS_2 (1000) shows a broad exciton band, where the A and B exciton ranges from 1.75 eV to 2.21 eV (Figure 9.11a). The exciton decay is followed by the trap state absorption at ~1.69 eV. It is found that the exciton decay time (0.29 ± 0.01 fs) is smaller than the trap state build-up time (0.33 ± 0.01 fs). TiO_2 shows no excitonic band (Figure 9.11b). In the case of HS1, two distinct excitons are observed which correspond to A and B excitons of MoS_2. The intensity of B exciton is larger which

follows the PL results. Additionally, there is a growth of escalation of the sub-bandgap as well as higher energy delocalized trap states, which indicates that after the dissociation of excitons, the carriers may be delocalized from MoS_2 to the acceptor levels of TiO_2 near VB. On the contrary, for HS2, there is a heavy quenching in exciton signal suggesting the reduction of carriers from the MoS_2 to TiO_2. This result indicates the *p*-type doping behavior of the system. As seen from Table 9.4, HS1 manifests a longer lifetime of excitons than HS2, which can be ascribed to the presence of larger interlayer charge transfer and greater density of mid-gap traps.

Table 9.4: *Exciton decay and trap build-up times for different systems.*

Sample	Exciton decay (ps)	Trap build-up (ps)
MoS_2 (1000)	0.29 ± 0.01	0.33 ± 0.01
HS1 (1000)	0.41 ± 0.01	0.42 ± 0.01
HS2 (1000)	0.19 ± 0.01	0.22 ± 0.02

To analyze the possibility of third-order non-linearity and mid-gap states within the system, we have studied nanosecond-resolved open aperture *Z*-scan spectra. In this measurement, we excited the systems with a 1064 nm laser and compare the possibilities of the two-photon absorption (TPA) for different systems. Higher intensities of sub-bandgap excitations indicate a higher density of the mid-gap levels, which can be attributed to the presence of vacancies in the respective HS. Normalized transmittance as a function of *z*-scan positions has been depicted in Figure 9.12a for MoS_2 (1000), TiO_2 (3600), and HS1 (1000) systems. For both MoS_2 and TiO_2, 1064 nm corresponds to a sub-bandgap excitation. We found the monotonically increased normalized transmittance for MoS_2 and TiO_2 till the focal point (z = 0) which shows the usual characteristic of saturable absorption (SA) for both systems [46, 47]. However, in the case of HS1 (1000), the SA decreases heavily compared to other systems, which corresponds to a lower

density of mid-gap traps. A similar comparison for HS2 (1000) is shown in Figure 9.12b. It is observed that there is a significant enhancement of SA in HS2 (1000) which proves the presence of the mid-gap state in the HS2 (1000). This result follows the TA exciton dynamics, where the exciton signals were highly quenched for HS2 (1000) due to the depletion of carriers from MoS_2 and their subsequent transfer to TiO_2. The normalized transmittances for different peak intensities are plotted in Fig 9.13 for (a) MoS_2 (1000), (b) TiO_2 (3600), (c) HS1 (1000) and (d) HS2 (1000). Although the power dependence is very obvious which has been reflected in the case of MoS_2, TiO_2, and HS2; the HS1 system shows very little dependence on different powers, because of the reduced extent of TPA.

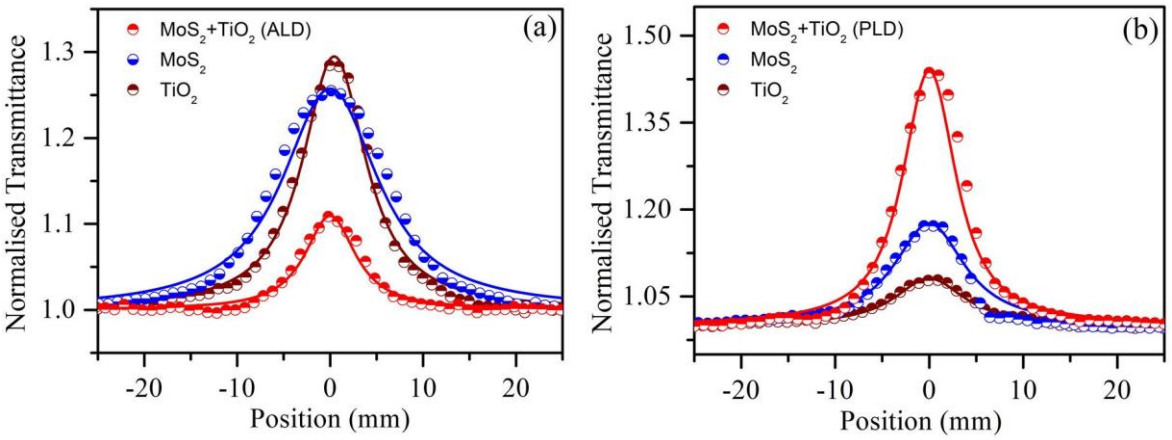

Figure 9.12: *Comparative normalized transmittance as a function of position in open-aperture Z scan at a peak intensity of 15 MW/cm² at 7 ns, 1064 nm pulse excitation for a) HS1 (1000), MoS_2 (1000), TiO_2 (3600) and b) HS2 (1000), MoS_2 (1000), TiO_2 (3600). The solid lines represent theoretical fitting.*

Thus above discussion concludes, PLD-grown HS2 (1000) acts as a better potential saturable absorber material in comparison to ALD-grown heterostructure HS1 (1000) having a prominent non-linear response for the sub-bandgap (1064 nm) excitation.

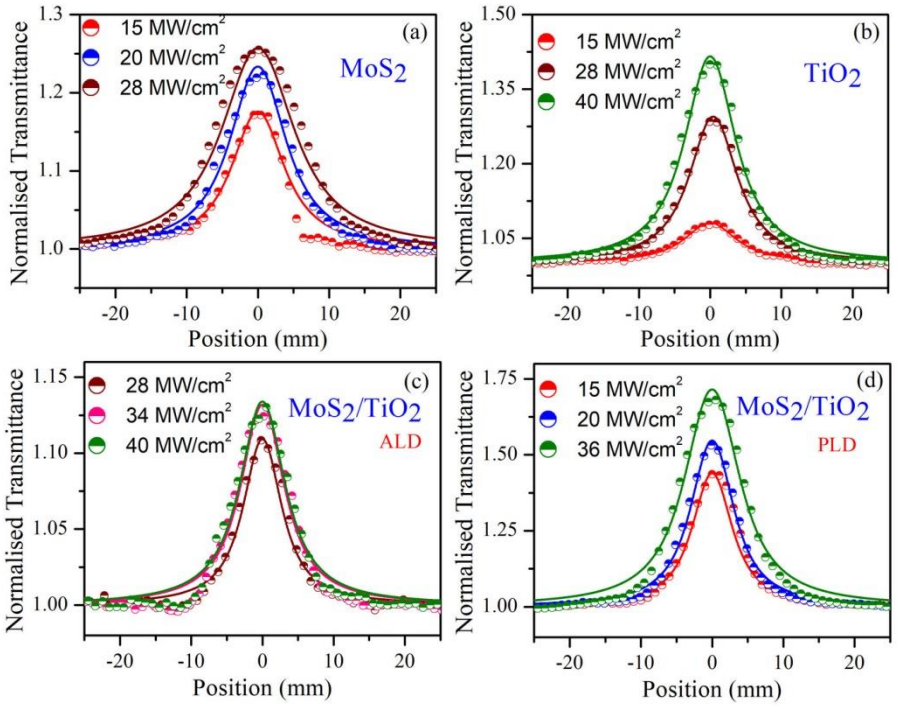

Figure 9.13: *Normalized transmittance as a function of position in open aperture Z scan at 7 ns, 1064 nm pulse excitation with different peak intensities for a) MoS_2, b) TiO_2, c) MoS_2/TiO_2 (ALD) (HS1), and d) MoS_2/TiO_2 (PLD) (HS2) respectively.*

Next, to analyze the applicability of such large-area HS for optoelectronic applications, we have measured the four-probe photo-transport. We use Ni contact, as it shows the betterment of Schottky barrier heights [48]. Ni contacts of 500 μm diameter are deposited by thermal evaporation on all systems using a shadow mask array. Four-probe photo-transport of all the systems is measured where channel-width normalized currents (in mA) are plotted as a function of voltages (in volt) as depicted in Figure 9.14. The linear relationship of current-versus-voltage confirms the ohmic nature of the Ni-contact for the MoS_2 (PLD) and HS1. However, in the case of HS2 (1000), the I-V characteristics become non-linear with increasing voltage. In comparison to MoS_2, the reduction of current is insignificant for HS1 (Figure 9.14b). On the other hand, for the HS2 system, there are three orders of magnitude reduction of current. Theoretically, we have established the presence of acceptor level-induced *p*-type doping and a direct band-gap nature for such HS.

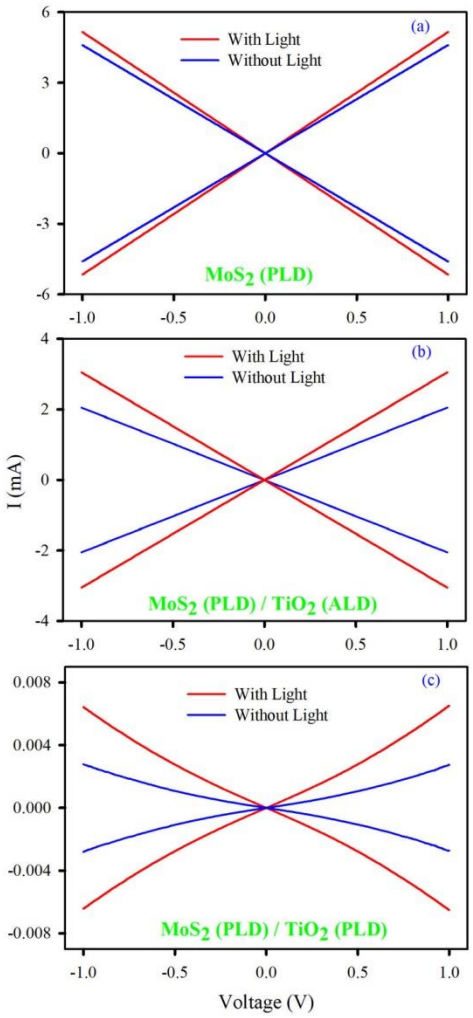

Figure 9.14: *Four-probe I-vs-V characteristics of different systems a) MoS_2 (1000), b) HS1 (1000), and c) HS2 (1000).*

Afterward, we have analyzed the potential of MoS_2/TiO_2 large-area HS in producing large-area phototransistor by fabricating a top-gated device by using the ionic gel as a gate. From the previous result, it can be inferred that HS2 shows maximal photoresponse, for that reason we have tested the device applicability for HS2. Room-temperature ionic liquids are well-known [49-51] for their potential application as a dielectric gate for controlling the electronic properties of semiconductors. Usually, field-effect transistors (FET) are designed after using oxide gate dielectrics, offering high operating voltage windows and higher power consumption, rendering them inappropriate for modern-age low-power

integrated electronics. The ion-gel dielectric gated FET can overcome these limitations by forming electric double-layer (EDL) capacitors under an external electric field, due to its large specific capacitance (> 1 μF/cm²).

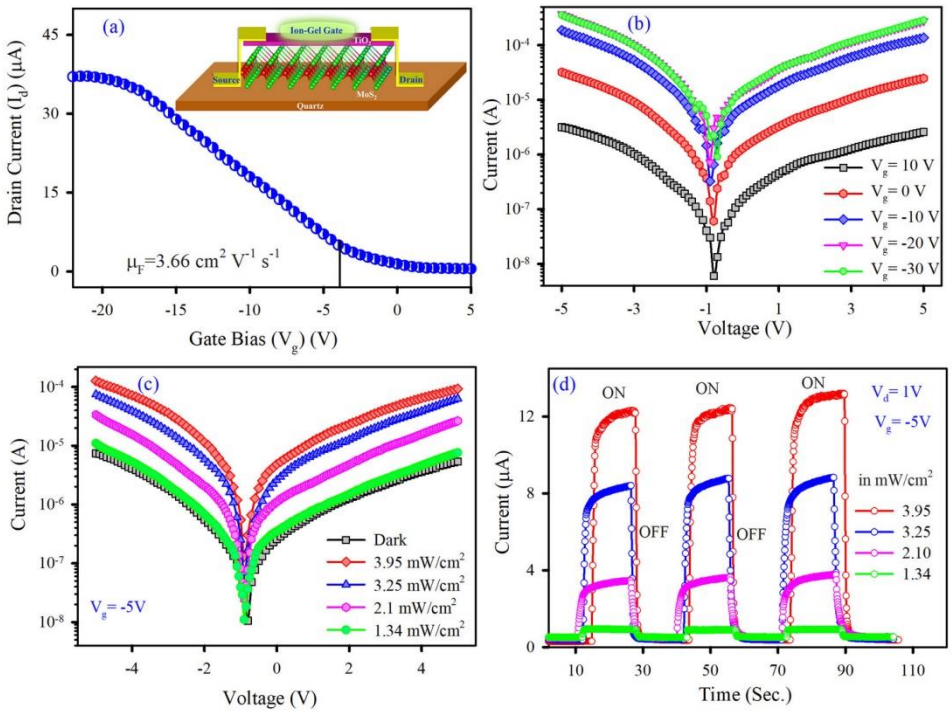

Figure 9.15: *Phototransistor characteristics of large-area devices from HS. a) Drain current versus gate voltage characteristics implicating a p-type nature, b) Drain current versus channel voltage plot for different gate biases, c) current versus voltage photo-response under dark and different illuminating conditions, and d) photo-transistor on-off behavior with different illuminating power.*

Here, we have investigated the photo-response characteristics of HS2 based device by simultaneous illumination and gate bias, using ion-gel gate dielectrics. Polyethylene oxide (PEO) and Lithium perchlorate ($LiClO_4$) precursors are used to prepare the gate dielectrics. The transfer characteristic (I_d - V_g curves) of the transistor at a fixed drain voltage (V_d = 1V) shows a usual FET behavior (Figure 9.15a). A *p*-type channel characteristic has been observed indicating a hole transport through the HS2 (1000) channel whose characteristic is opposite to the common 2D-MoS_2 based *n*-type FET channel. The off-state current (I_{off}) of the FET is ~0.53 μA, and the channel current increases sharply leading to an ON condition,

as V_g decreases below a threshold voltage (V_{th}) of -3.5 V and then saturates at ~37 μA (I_{on}) after a gate bias of approximately -18 V. The low turn-on voltage (-3.5 V) of the fabricated FET, which is coming due to high specific capacitance of the dielectric ion-gel, allows the work function of the channel to be readily modulated at low operating voltages. The resulting on/off ratio (I_{on}/I_{off}) is found to be ~75 in between -20 V to 5 V operating voltages. Under the application of a negative gate bias (V_g) to the channel material (MoS_2/TiO_2), the resultant electric field drives the Li^+ ions towards the gate electrode and the ClO_4^- ions near the channel surface, forming a nanoscale thickness gate capacitor, known as an EDL. The large capacitance of the EDL, leading to a large surface carrier density and induced holes in the *p*-type channel, effectively enhances the electric current through the channel between source and drain electrodes. The field-effect mobility has been extracted by using the following expression:

$$\mu = \frac{\nabla I_d}{\nabla V_g} \times \frac{L}{W C_{sp} V_d} \tag{9.1}$$

where L is the channel length (1 mm), W is the channel width (2 mm), and C_{sp} is the specific capacitance of the dielectric gel, about ~3 μF/cm² [51]. From the data presented in Figure 9.15a, the field-effect mobility was estimated as ~3.66 $cm^2V^{-1}s^{-1}$. The output characteristics (I_d *vs* V_d) of the ion-gel-gated MoS_2/TiO_2 heterostructure FET is measured for different fixed gate voltages (V_g) and presented in Figure 9.15b. The large degree of current modulation in the device, obtained after changing the V_g values, indicates that the field-effect behavior of the fabricated transistor is dominated by the HS2 (1000) channel and not by the contacts.

The current-voltage (I_d –V_d) characteristics of the fabricated device for a fixed gate bias (-V_g >V_{th}) are shown in Figure 9.15c under dark and various illuminating powers. We observed a symmetric I-V curve, which signifies the formation of a similar junction between Au and HS2 (1000) hybrid at both source

and drain end. Upon 325 nm UV illumination, a substantial upsurge of the current level is found. This increment is coming due to the photo-generated carriers which indeed lead to the improvement of the field-effect mobility in the channel. Synergic effect of the dielectric gate and UV illumination results in substantial enhancement (~10 times) of the dark current for V_d > ±2 V. We further analyzed

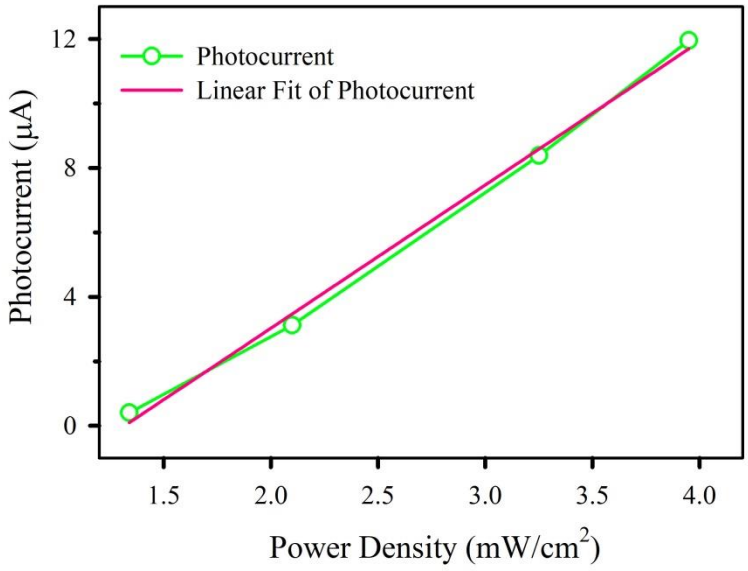

Figure 9.16: *Linear dependence of photocurrent and power density.*

the photo-switching characteristics of the fabricated EDL-FET system upon pulse illumination with 325 nm laser with various power densities (Figure 9.15d). The rapid and periodic changes in the current level for dark and illuminated conditions signify the outstanding reproducibility and stability of the photodetectors. The results also demonstrate that the absence of persistent photo-current and non-fluctuating current levels with time. Furthermore, with increasing illumination intensity, the photocurrent response has been increased. We have investigated the variation of photocurrent with incident optical intensity. Figure 9.16 shows that the rate of photo-carrier generation is proportional to the absorbed photon flux. Responsivity is a key-feature of a photodetector. We have calculated the Responsivity of the present system which is found to be ~3025 A/W for 3.95 mW/cm^2 (@325 nm laser wavelength) illumination.

Thus, in the EDL-FET device, electron-hole pairs are generated in the HS2 (1000) channel under illumination and EDL induced positive charges in the channel, which, through the capacitive coupling of the applied negative gate bias, effectively increases the carrier concentration, leading to an enhanced photocurrent. The gate bias is also advantageous to the neutralization of the charged vacancies, which in turn reduces the potential scattering leading to the enhanced field-effect mobility, resulting in an efficient collection of photo-carriers.

9.3. Conclusion:

In summary, we have studied the electronic and optical impacts of different growth techniques on large area interfaces of MoS_2/A-TiO_2 HS. It is found that PLD produces a polycrystalline TiO_2 layer with enhanced thickness, whereas ALD results in an amorphous and thinner TiO_2 layer. For both cases, we found *p*-type doping in the MoS_2 system. Remarkably, both of these interfaces emanate *p*-type doping of the MoS_2 under-layer with the increasing trend of the extent of doping with the thickness of the TiO_2 layer. This *p*-type doping is further validated by the first principles DFT calculations. Depends upon the surface termination of TiO_2 the properties of the heterostructures change completely. Moreover, the steady-state and ultrafast optical responses reveal that MoS_2/TiO_2 (PLD) interface has many mid gap states which are opposite to the MoS_2/TiO_2 (ALD) interface. The *z*-scan two-photon absorption of these two interfaces indicates the application of the MoS_2 (PLD)/TiO_2 (PLD) interface as a potential saturable absorber having a significant non-linear response. Finally, we have demonstrated the utilization of this interface in large-area phototransistors having significant hole-mobility and photoresponse. In summary, we have thoroughly studied the different types of large-area interfaces of MoS_2/TiO_2 using experimental and theoretical investigation and demonstrate its application as a potential phototransistor material.

References

[1] L. Liu, S. B. Kumar, Y. Ouyang, J. Guo, Performance limits of monolayer transition metal dichalcogenide transistors, *IEEE Trans. Electron Devices* 58 (2011) 3042.

[2] K. S. Novoselov, A. K. Geim, S. V. Morozov, D. Jiang, Y. Zhang, S. V. Dubonos, I. V. Grigorieva, A. A. Firsov, Electric field effect in atomically thin carbon films, *Science* 306 (2004) 666.

[3] S. Andleeb, J. Eom, N. Rauf Naz, A. K. Singh, MoS_2 field-effect transistor with graphene contacts, *J. Mater. Chem. C* 5 (2017) 8308.

[4] J. Kang, W. Liu, D. Sarkar, D. Jena, K. Banerjee, Computational study of metal contacts to monolayer transition-metal dichalcogenide semiconductors, *Phys. Rev. X* 4 (2014) 031005.

[5] M. Chhowalla, H. S. Shin, G. Eda, L. J. Li, K. P. Loh, H. Zhang, The chemistry of two-dimensional layered transition metal dichalcogenide nanosheets, *Nat. Chem.* 5 (2013) 263.

[6] G. Fiori, F. Bonaccorso, G. Iannaccone, T. Palacios, D. Neumaier, A. Seabaugh, S. K. Banerjee, L. Colombo, Electronics based on two-dimensional materials, *Nat. Nanotechnol.* 9 (2014) 768.

[7] B. W. H. Baugher, H. O. H. Churchill, Y. Yang, P. Jarillo-Herrero, Intrinsic electronic transport properties of high-quality monolayer and bilayer MoS_2, *Nano Lett.* 13 (2013) 4212.

[8] T. K. Maji, K. Vaibhav, S. K. Pal, K. Majumdar, K. V. Adarsh, D. Karmakar, Intricate modulation of interlayer coupling at the graphene oxide/$MoSe_2$ interface: Application in time-dependent optics and device transport, *Phys. Rev. B* 99 (2019) 115309.

[9] C. H. Lee, G. H. Lee, A. M. van der Zande, W. Chen, Y. Li, M. Han, X. Cui, G. Arefe, C. Nuckolls, T. F. Heinz, J. Guo, J. Hone, P. Kim, Atomically thin *p–n* junctions with van der Waals heterointerfaces, *Nat. Nanotechnol.* 9 (2014) 676.

[10] G. Iannaccone, F. Bonaccorso, L. Colombo, G. Fiori, Quantum engineering of transistors based on 2D materials heterostructures, *Nat. Nanotechnol.* 13 (2018) 183.

[11] A. K. Geim, I. V. Grigorieva, Van der Waals heterostructures, *Nature* 499 (2013) 419.

[12] J. R. Durán Retamal, D. Periyanagounder, J. J. Ke, M. L. Tsai, J. H. He, Charge carrier injection and transport engineering in two-dimensional transition metal dichalcogenides, *Chem. Sci.* 9 (2018) 7727.

[13] C. Kim, I. Moon, D. Lee, M. S. Choi, F. Ahmed, S. Nam, Y. Cho, H. J. Shin, S. Park, W. J. Yoo, Fermi level pinning at electrical metal contacts of monolayer molybdenum dichalcogenides, *ACS Nano* 11 (2017) 1588.

[14] Y. Wang, J. C. Kim, R. J. Wu, J. Martinez, X. Song, J. Yang, F. Zhao, A. Mkhoyan, H. Y. Jeong, M. Chhowalla, Van der Waals contacts between three-dimensional metals and two-dimensional semiconductors, *Nature* 568 (2019) 70.

[15] A. Rai, H. C. Movva, A. Roy, D. Taneja, S. Chowdhury, S. K. Banerjee, Progress in contact, doping and mobility engineering of MoS_2: An atomically thin 2D semiconductor, *Crystals* 8 (2018) 316.

[16] V. Heine, Theory of surface states, *Phys. Rev.* 138 (1965) A1689.

[17] A. Allain, J. Kang, K. Banerjee, A. Kis, Electrical contacts to two-dimensional semiconductors, *Nat. Mater.* 14 (2015) 1195.

[18] S. Das, H. Y. Chen, A. V. Penumatcha, J. Appenzeller, High performance multilayer MoS_2 transistors with scandium contacts, *Nano Lett.* 13 (2013) 100.

[19] S. L. Li, K. Tsukagoshi, E. Orgiu, P. Samorì, Charge transport and mobility engineering in two-dimensional transition metal chalcogenide semiconductors, *Chem. Soc. Rev.* 45 (2016) 118.

[20] Y. Liu, P. Stradins, S. H. Wei, Van der Waals metal-semiconductor junction: Weak Fermi level pinning enables effective tuning of Schottky barrier, *Sci. Adv.* 2 (2016) e1600069.

[21] Z. Yu, Z. Y. Ong, Y. Pan, Y. Cui, R. Xin, Y. Shi, B. Wang, Y. Wu, T. Chen, Y. W. Zhang, G. Zhang, X. Wang, Realization of room-temperature phonon-limited carrier transport in monolayer MoS_2 by dielectric and carrier screening, *Adv. Mater.* 28 (2016) 547.

[22] Y. Y. Illarionov, G. Rzepa, M. Waltl, T. Knobloch, A. Grill, M. M. Furchi, T. Mueller, T. Grasser, The role of charge trapping in MoS_2/SiO_2 and MoS_2/hBN field-effect transistors, *2D Mater.* 3 (2016) 035004.

[23] K. Dolui, I. Rungger, S. Sanvito, Origin of the *n*-type and *p*-type conductivity of MoS_2 monolayers on a SiO_2 substrate, *Phys. Rev. B* 87 (2013) 165402.

[24] W. Bao, X. Cai, D. Kim, K. Sridhara, M. S. Fuhrer, High mobility ambipolar MoS_2 field-effect transistors: Substrate and dielectric effects, *Appl. Phys. Lett.* 102 (2013) 042104.

[25] P. Bolshakov, P. Zhao, A. Azcatl, P. K. Hurley, R. M. Wallace, C. D. Young, Electrical characterization of top-gated molybdenum disulfide field-effect-transistors with high-*k* dielectrics, *Microelectron. Eng.* 178 (2017) 190.

[26] H. Liu, D. Y. Peide, MoS_2 dual-gate MOSFET with atomic-layer-deposited Al_2O_3 as top-gate dielectric, *IEEE Electron Device Lett.* 33 (2012) 546.

[27] Y. Lin, P. Ren, C. Wei, Fabrication of MoS_2/TiO_2 heterostructures with enhanced photocatalytic activity, *CrystEngComm* 21 (2019) 3439.

[28] B. Chen, Y. Meng, J. Sha, C. Zhong, W. Hu, N. Zhao, Preparation of MoS_2/TiO_2 based nanocomposites for photocatalysis and rechargeable batteries: Progress, challenges, and perspective, *Nanoscale* 10 (2018) 34.

[29] Q. A. Drmosh, A. Hezam, A. H. Y. Hendi, M. Qamar, Z. H. Yamani, K. Byrappa, Ternary $Bi_2S_3/MoS_2/TiO_2$ with double Z-scheme configuration as high performance photocatalyst, *Appl. Surf. Sci.* 499 (2020) 143938.

[30] M. Mehta, A. P. Singh, S. Kumar, S. Krishnamurthy, B. Wickman, S. Basu, Synthesis of MoS_2-TiO_2 nanocomposite for enhanced photocatalytic and photoelectrochemical performance under visible light irradiation, *Vacuum* 155 (2018) 675.

[31] T. Wei, W. M. Lau, X. An, X. Yu, Interfacial charge transfer in MoS_2/TiO_2 heterostructured photocatalysts: The impact of crystal facets and defects, *Molecules* 24 (2019) 1769.

[32] C. Lee, H. Yan, L. E. Brus, T. F. Heinz, J. Hone, S. Ryu, Anomalous lattice vibrations of single and few-layer MoS_2, *ACS Nano* 4 (2010) 2695.

[33] Y. Pak, W. Park, S. Mitra, A. A. Sasikala Devi, K. Loganathan, Y. Kumaresan, Y. Kim, B. Cho, G. Y. Jung, M. M. Hussain, Enhanced performance of MoS_2 photodetectors by inserting an ALD processed TiO_2 interlayer, *Small* 14 (2018) 1703176.

[34] Q. Zhang, L. Ma, M. Shao, J. Huang, M. Ding, X. Deng, X. Wei, X. Xu, Anodic oxidation synthesis of one-dimensional TiO_2 nanostructures for photocatalytic and field emission properties, *J. Nanomater.* 2014 (2014) 1.

[35] W. Park, J. W. Min, S. F. Shaikh, M. M. Hussain, Stable MoS_2 field-effect transistors using TiO_2 interfacial layer at metal/MoS_2 contact, *Phys. Status Solidi A* 214 (2017) 1700534.

[36] L. Yang, K. Majumdar, H. Liu, Y. Du, H. Wu, M. Hatzistergos, P. Y. Hung, R. Tieckelmann, W. Tsai, C. Hobbs, P. D. Ye, Chloride molecular doping technique on 2D materials: WS_2 and MoS_2, *Nano Lett.* 14 (2014) 6275.

[37] J. D. Lin, C. Han, F. Wang, R. Wang, D. Xiang, S. Qin, X. A. Zhang, L. Wang, H. Zhang, A. T. S. Wee, W. Chen, Electron-doping-enhanced trion formation in monolayer molybdenum disulfide functionalized with cesium carbonate, *ACS Nano* 8 (2014) 5323.

[38] N. Kaushik, D. Karmakar, A. Nipane, S. Karande, S. Lodha, Interfacial *n*-doping using an ultrathin TiO_2 layer for contact resistance reduction in MoS_2, *ACS Appl. Mater. Interfaces* 8 (2016) 256.

[39] A. Nipane, D. Karmakar, N. Kaushik, S. Karande, S. Lodha, Few-layer MoS_2 *p*-type devices enabled by selective doping using low energy phosphorus implantation, *ACS Nano* 10 (2016) 2128.

[40] S. Smidstrup, T. Markussen, P. Vancraeyveld, J. Wellendorff, J. Schneider, T. Gunst, B. Verstichel, D. Stradi, P. A. Khomyakov, U. G. Vej-Hansen, M. E. Lee, S. T. Chill, F. Rasmussen, G. Penazzi, F. Corsetti, A. Ojanperä, K. Jensen, M. L. N. Palsgaard, U. Martinez, A. Blom, M. Brandbyge, K. Stokbro, QuantumATK: An integrated platform of electronic and atomic-scale modelling tools, *J. Phys. Condens. Matter* 32 (2019) 015901.

[41] S. Smidstrup, D. Stradi, J. Wellendorff, P. A. Khomyakov, U. G. Vej-Hansen, M. E. Lee, T. Ghosh, E. Jónsson, H. Jónsson, K. Stokbro, First-principles Green's function method for surface calculations: A pseudopotential localized basis set approach, *Phys. Rev. B* 96 (2017) 195309.

[42] G. Kresse, J. Furthmüller, Efficient iterative schemes for ab initio total-energy calculations using a plane-wave basis set, *Phys. Rev. B* 54 (1996) 11169.

[43] T. Korn, S. Heydrich, M. Hirmer, J. Schmutzler, C. Schüller, Low-temperature photocarrier dynamics in monolayer MoS_2, *Appl. Phys. Lett.* 99 (2011) 102109.

[44] T. Elsaesser, J. Shah, L. Rota, P. Lugli, Initial thermalization of photoexcited carriers in GaAs studied by femtosecond luminescence spectroscopy, *Phys. Rev. Lett.* 66 (1991) 1757.

[45] S. Sim, J. Park, J. G. Song, C. In, Y. S. Lee, H. Kim, H. Choi, Exciton dynamics in atomically thin MoS_2: Interexcitonic interaction and broadening kinetics, *Phys. Rev. B* 88 (2013) 075434.

[46] R. Sharma, J. Aneesh, R. K. Yadav, S. Sanda, A. R. Barik, A. K. Mishra, T. K. Maji, D. Karmakar, K. V. Adarsh, Strong interlayer coupling mediated giant two-photon absorption in $MoSe_2$/Graphene oxide heterostructure: Quenching of exciton bands, *Phys. Rev. B* 93 (2016) 155433.

[47] R. K. Yadav, J. Aneesh, R. Sharma, P. Abhiramnath, T. K. Maji, G. J. Omar, A. K. Mishra, D. Karmakar, K. V. Adarsh, Designing hybrids of graphene oxide and gold nanoparticles for nonlinear optical response, *Phys. Rev. Appl.* 9 (2018) 044043.

[48] G. Gupta, S. Kallatt, K. Majumdar, Direct observation of giant binding energy modulation of exciton complexes in monolayer $MoSe_2$, *Phys. Rev. B* 96 (2017) 081403.

[49] C. E. Clement, D. Jiang, S. K. Thio, S. Y. Park, A study of dip-coatable, high-capacitance ion gel dielectrics for 3D EWOD device fabrication, *Materials* 10 (2017) 41.

[50] M. Taghavikish, S. Subianto, Y. Gu, X. Sun, X. S. Zhao, N. R. Choudhury, A poly(ionic liquid) gel electrolyte for efficient all solid electrochemical double-layer capacitor, *Sci. Rep.* 8 (2018) 10918.

[51] S. Mondal, R. Ram Ghimire, A. Raychaudhuri, Enhancing photoresponse by synergy of gate and illumination in electric double layer field effect transistors fabricated on *n*-ZnO, *Appl. Phys. Lett.* 103 (2013) 231105.

Chapter 10

First Principles Studies on Bimetallic, Metal/Weyl Semimetal Heterostructure, and Topological Material

10.1. Introduction:

Depends on the bandgap of the systems, materials can be classified into three types; metal, semiconductor, and insulators. Metals are known to be conducted because of overlapping of the conduction band (CB) and valance band (VB) and insulator are non-conducting due to finite bandgap in the systems, however, a semiconductor has a bandgap in between metals and insulators. Although insulators are nonconducting, they can be categorized into different classes according to the topology of their bandstructure. Topological insulator (TI) is a type of system, where the usual ordering of CB and VB of a normal insulator system has been inverted in presence of strong spin-orbit coupling. This inverted bandstructure gives metallic surface states within the insulator system. Similar to the surface states of TIs, different other systems also encompass surface states. Weyl semimetals (WSMs) are one of the many exotic semi-metallic systems which have surface states. The symmetry protected surface states come from the special energy band of the materials. The energy band in a specific momentum space region would obey Dirac or Weyl equation. TIs and topological semimetals are all new types of quantum materials that are distinguished by surface states induced by the topology of the bulk band structure.

Recently, Metal/Metal or Metal/Semimetal heterojunctions have attracted substantial curiosity due to their importance in basic science as well as in different technological applications [1-7]. The interface created by the bimetallic system is one of the key problems for the investigation of the underlying mechanism of enhanced activity. Current amelioration on bimetallic nanostructures (NS) [4-7]

has instigated a lot of activities in multi-revisited phoenix field, superconductivity, with the concurrent genesis of controversies. The first and foremost impact of such studies is, to ignite the expectation to accomplish the long-prophesized goal of near-room temperature superconductivity. Higher superconducting critical temperature [8-10] and large-area epsilon-near-zero (ENZ) systems [11, 12] are two long-standing goals of the scientific arena. Inspired by the recent experimentally observed strongly correlated phenomena in bimetallic Drude nanostructure systems [4-7], we have explored different probable bimetallic face-centered cubic (FCC) combinations starting from the large-area interface to different nanostructure system, having resemblance with the experimentally studied systems. Different combinations of noble metals are used in the plasmonic circuit [13-16] and many other fields including the designing of different metamaterials. Artificially designed metamaterials are extensively used for different enhanced properties, compared to the pristine one. Engineered metamaterial has different applications in different fields including electromagnetic [17], microwave [18], and optical [19] purposes.

Using different computational techniques, including density functional theory (DFT), time-dependent DFT (TDDFT), phonon and DFT-coupled quantum transport, we propose the following strongly correlated prospects of potential bimetallic nanostructures like Au/Ag and Pt/Pd: 1) for 2D doped and embedded nanostructures of these systems, DFT-calculated non-trivial band-structure and Fermi-surface topology can illustrate the presence of instabilities like charge density waves or spin density wave; 2) the fascinated optical property calculated using TDDFT formalism for these systems indicate morphology induced band-localization leading to ENZ behavior of both real and imaginary parts of the dielectric response in the ultra-violet to visible (UV-Vis) optical range; 3) low-energy intra-band plasmonic band are completely suppressed for embedded and doped nanostructures which was present in the single metallic system; 4) the

phonon dispersion of the nanostructure system shows the existence of soft phonons and dynamic instability; 5) quantum transport calculations performed on the simplest devices made from these bimetallic systems have shown that for certain selected device geometries, high-transmittance cavities are produced over cross-section area. We predict that such systems may reveal many fascinating properties in the field of physics and optics promoting relevant applications in many diverse fields.

Topological semimetals define a class of gapless electronic phases exhibiting topologically stable crossings of energy bands. Weyl fermions are massless opposite chiral quasiparticles with spin 1/2 and the material containing this particle is called WSM [20, 21]. In 1929, Hermann Weyl simplified the famous Dirac Hamiltonian for zero mass and proposed Weyl Hamiltonian by considering massless particles. The simplified form of Dirac Hamiltonian endorsed by Weyl can be written as [22]:

$$H_W = \pm c\ (\sigma_x p_x + \sigma_y p_y + \sigma_z p_z) \tag{10.1}$$

Basically in the massless case, the Dirac equation decouples to two simplified equations where each equation describes a two-component chiral Weyl fermion with chirality ±1 [23]. Generally, a two-component Weyl fermion defined by the Weyl equation arises in solids when two non-degenerate energy bands touch at a point $\boldsymbol{k_0}$ in the momentum space [23]. This condition cannot be fulfilled when Kramers degeneracy holds at every momentum $\boldsymbol{k}$. So, in this case, either time reversal or inversion symmetry needs to be broken. In time reversal symmetry, a particle moves in the opposite momentum direction with opposite spin i.e. E (k,↑) = E (-k,↓) [24]. However, in inversion symmetry, the particle should move in opposite momentum direction with the same spin i.e. E (k,↑) = E (-k,↑). Eq. 10.1 describes a pseudo-magnetic monopole in the momentum space Barry curvature [25]. Likewise, the Berry curvature vanishes when both symmetries are present. Hence, the symmetry properties of the Berry curvature

describe a more proper argument way of demonstrating that the existence of Weyl points requires at least one of these symmetries to be broken. When the TRS and inversion symmetry coexists, a pair of degenerate Weyl points may exist, leading to the related Dirac semimetal (DSM) phase. So a DSM can be considered as two copies of WSMs [26]. According to the broken symmetry, the degeneracy of the Dirac point will be lifted which will lead to two Weyl points. Consequently, an energy contour crossing the Weyl points, exhibits an unclosed line that starts from one Weyl point and ends at the other with opposite chirality, which is called a Fermi arc [25-27]. Chiral anomaly is also another exotic phenomenon that appears only in the case of WSM when Weyl points are separated in momentum space [25, 27]. The Dirac points are splitted into two Weyl points in presence of a magnetic field which leads to the chiral anomaly. The characteristic of WSM with a gapless metal is topological invariant, which is different from the classification of topological phases of insulators [26]. Despite having rich physics, metal contact attachment on WSM can introduce many new fundamental properties [3, 28-30].

Furthermore, a TI is a material that behaves as an insulator in its interior but whose surface contains conducting states [31]. TIs have non-trivial symmetry-protected topological order [32]. The insulating bulk of TI hosts inverted bands in presence of spin-orbital coupling (SOC). In that case, the VB goes above the conduction band and CB drops below the VB. This is how they reverse the role. SOC plays an important role in topological materials. SOC causes an insulating material to acquire protected surface states in the TI systems. So, the surface states play a crucial role in the TI systems. By modulating the surface state it is highly possible to tune the properties of the systems.

Artificially engineered metamaterials are widely used for designing newer material properties, different from the inherited attributes of the consisting components, for innovative applicability in electromagnetic [17], microwave [18], and optical [19] purposes. Metal/Semimetal heterojunctions have gained a lot of

interest in recent years due to their substantial importance in basic science and technological applications in various fields [1-7]. Depending on the configuration of the Metal/Semimetal system (i.e. Metal/Semimetal single interface or Metal/Semimetal/Metal/Semimetal … stack system) the properties of the Weyl system change drastically.

Weyl semimetal TaAs, a congenial host to the massless Weyl fermions, spontaneously lacks the inversion symmetry and thus effectuates topologically stable Weyl nodes, resembling magnetic monopoles in momentum space [33-36]. Weyl nodes in a crystalline system always appear in pairs of opposite chirality at two distinctly separated *k*-points, so that, their annihilation by simple translational symmetry preserving perturbations, are prevented, rendering the topological stability of the system [37]. The hallmark signature of WSM is the presence of Fermi-arcs on the surface, joining two Weyl nodes of opposite chirality [38-42]. WSMs are well known to have the anomalous nature of their DC transport related to the absence of backscattering and weak antilocalization [40, 43, 44], as a consequence of the presence of topological surface states having a well-defined spin. Another interesting chiral property of WSM is the chiral anomaly, where, in the presence of electric and magnetic fields, the particle number corresponding to a particular valley is not conserved [44], culminating intervalley pumping of electrons between two nodes of opposite chirality [1, 44-47].

Besides the exciting fundamental physics, topological systems like Cd_3As_2 [2] and TaAs [3, 28-30] showed mesoscopic superconducting phase and high transport spin polarization in the presence of metallic point contacts like Ag. However, regarding the emergence of superconducting phases in TaAs, the debate about pairing symmetry still exists. Two opposite theory has been established in this regards. In one work, Wang *et al.* had suggested unconventional *p*-wave superconductivity [29, 48]. In another work, Gayen *et al.* had demonstrated an *s*-wave conventional nature [30]. Unsolved disagreements over the fundamental

existence of superconductivity and the need to consider the interfacial proximity effects have prompted the ongoing analysis of the large-area interfaces of the TaAs Weyl semimetal system with two well-known Au and Ag noble metals.

The primary outcomes of the present work can be listed as follows: 1) Ab initio DFT calculations on the interfacial systems have demonstrated an increment of the interface-induced spin-polarization and contact-induced transport spin-polarization of TaAs in the proximity of noble metals; 2) in contrast to the single interface, for vertically stacked cases, the broken inversion symmetry of the system introduces a *z*-directional band-dispersion, resulting in an energetically separated series of Weyl cones; 3) quantum transport calculations on different device geometries reveal the importance of contact geometry for spin-transport in TaAs devices. Lateral contacts are found to be more effective to obtain a uniform and effective spin transport; 4) the phonon dispersion behavior of Metal/TaAs (with lateral contact configuration) displays a closure of band-gap with the associated increase of phonon-density of states for the acoustic modes in the proximity of noble metals, indicating the occurrence of phonon-mediated correlated phenomena. TIs are unique quantum materials which are insulating in their interior but have a topologically protected conducting state at their surface. The origin of the topologically protected states is spin-orbital coupling interaction and time-reversal symmetry. The conducting surface states of TI are very much unique compared to other known electronic systems. These states may have many special properties that could be useful for various ranges of applications such as spin-momentum locking, photodetector, magnetic device, near-infrared transparency, and ultra-broadband plasmon excitation.

Antimony Trisulfide (Sb_2S_3 or stibnite) belongs to the semiconducting chalcogenide group V_2VI_3 compound, which is considered the second generation of TI. Stibnite is believed to be one of the most important V-VI group materials as it has a wide range of applications in diverse fields such as thermoelectric cooling

devices, solar energy harvesting, optoelectronic device, photovoltaic device application [49-53]. Those unique properties arise mainly due to a very high absorption coefficient (> 10^5 cm^{-1}), protected conducting surface state, and having bandgap value in the visible region range (1.65 eV to 2.5 eV) [53].

So far, extensive studies have been carried out on the electronic, thermoelectric, and optical properties of the Sb_2S_3 system. The phonon dispersion property of Sb_2S_3 is also investigated extensively by Liu *et al*. But, as the Sb_2S_3 system belongs to the second generation of TI, the surface plays a big role in its property. So increment of the surface can change many elementary properties of the present system. Until now, studies have been carried out on the fundamental properties of the stibnite, but a rigorous discussion on the change of electronic and optical property of stibnite with increasing surface to volume ratio is limited in the scientific literature.

In the last work of this chapter, we intend to study a comparison of the electronic behavior of stibnite for bulk and nanorod after a substitution doping with Se at S-site. We have used first-principles DFT calculations to extract the electronic structure of bulk Sb_2S_3 and Sb_2S_3 nanorod and its various doping profiles.

10.2. Results and Discussion:

10.2.1. Intriguing Electronic and Optical Prospects of FCC Bimetallic Two-dimensional Heterostructures: Epsilon Near-zero Behavior in UV-vis range [54]: We have prepared a [111] sliced *trilayer* of Au and Ag with the lattice parameter $\frac{a}{\sqrt{2}}$ in a hexagonal Brillouin Zone (BZ), where *a* is the lattice parameter of their respective FCC unit cell. We have investigated the electronic structure of several combined systems including the base trilayer structures i.e. a) Au-111, b) Ag-111, c) Au/Ag-111 (large area interface designed using Ag-111 and Au-111 with a lattice mismatch of 0.12%), d) Ag-nanocluster embedded on Au-matrix, and e) Ag-

doped Au heterostructure which is essentially a 2D heterostructure (where some Ag atoms have been doped inside the Au matrix). A vacuum slab of 20 Å thicknesses was added for systems d) and e) to avoid the *z* directional periodicity.

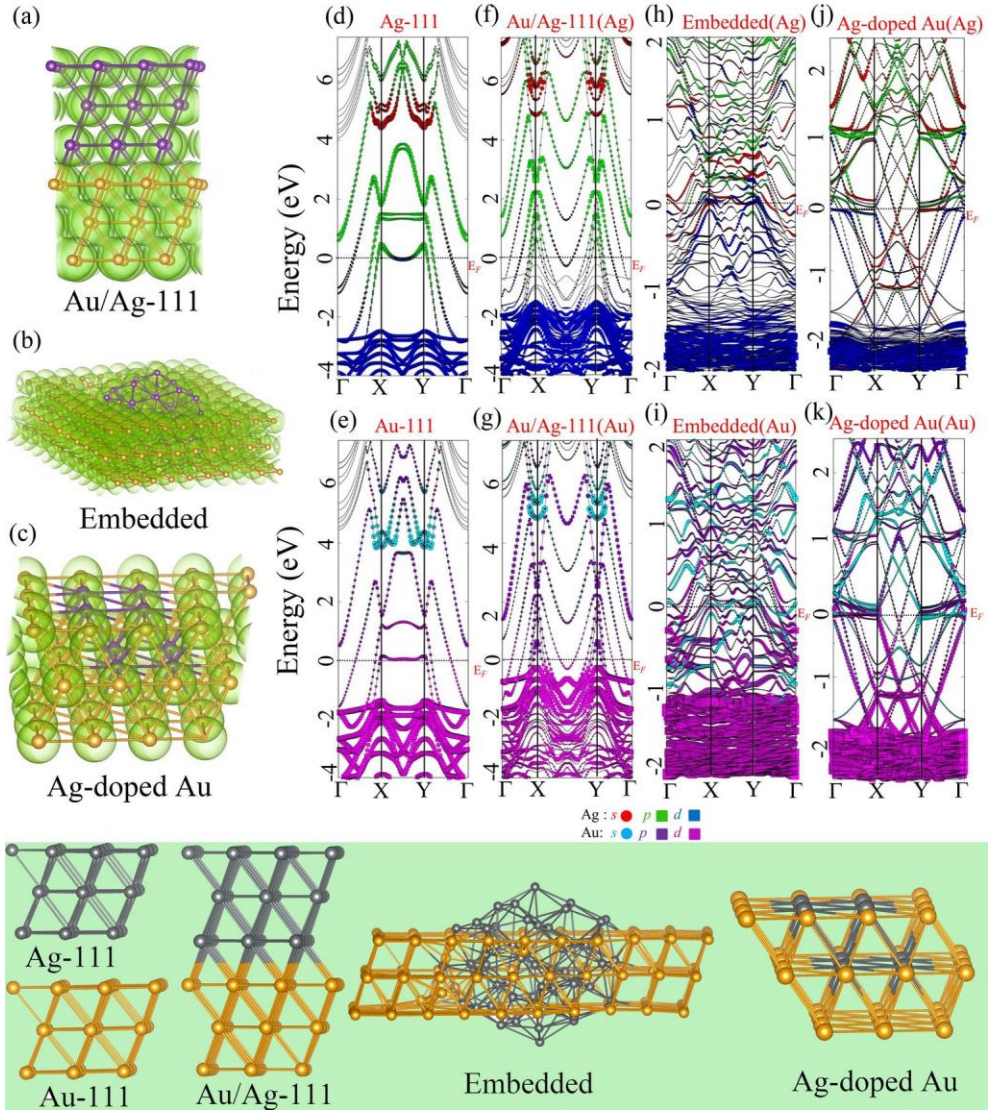

Figure 10.1: *Converged charge densities for a) Au/Ag-111, b) Embedded, c) Ag-doped Au systems. The orbital projected fatbands for d) Ag-111 e) Au-111, orbital projection of f) Ag in Au/Ag-111 system, g) Au in Au/Ag-111 system, h) Ag in Embedded system and i) Au in Embedded system, j) Ag in Ag-doped Au system, and k) Au in Ag-doped Au system with the respective orbital characters denoted in the figure. The lowest highlighted row depicts the structures 1-5.*

All the systems were structurally optimized using DFT as implemented in Vienna Ab Initio Simulation Packages (VASP) to find the ground state configuration. Figure 10.1 (a-c) shows the structure and charge density plot of Au/Ag-111,

Embedded, and Ag-doped Au heterostructure. We have incorporated spin-orbital coupling in all calculations. The orbital projected fatbands of different systems are depicted in Figure 10.1 (d-k). Corresponding hexagonal BZ is depicted in Figure 10.4d. To circumvent the *z*-directional periodic interaction between replica images, a vacuum layer of 20 Å thickness was added between them. All these systems are checked for their surface energy convergence and ground state stability. The last row of Figure 10.1 depicts the structures of the systems 1-5. Figure 10.1 (*d*–*k*) delineates the orbital-projected spin-orbitally coupled (SOC) electronic fatbands for all the five structurally relaxed systems along with high-symmetry directions within the hexagonal BZ, as depicted in Figure 10.2d. The first column of Figure 10.1 represents the converged charge densities for systems 3, 4, and 5. The outcomes of the investigation of electronic band structure are summarized as follows:

A) In comparison to the bulk bands, Ag-111 and Au-111 surface shows the existence of flat-bands marginally above the Fermi energy (E_F) between X-Y, demonstrating mostly *p-d* (Figure 10.1d) and *s-d* (Figure 10.1e) hybridized characters respectively. The occupied 5*d* levels of the Au-111 system are situated 0.7 eV higher than the Ag-4*d* level.
B) For the case of the Au/Ag-111 system (Figure 10.1f and 10.1g), the *s-d* hybridized electron of Au is transferred to the *p-d* hybridized levels of Ag, which results in an upshift for the Au-5*d* levels between the energy range 0 to -2 eV. Bader charge analysis results show the nature and amount of charge transfer between Au and Ag (presented in Table 10.1). From Table 10.1. It is very much clear that there is *p*-type doping in the Au matrix. Moreover, it is found that, near Fermi level, most of the bands are *p-d* hybridized for both Ag and Au and the system, being devoid of localized flat-bands due to inter-layer electron transfer from Au-111 to Ag-111, retaining the individual Fermi-liquid (FL) nature of Au or Ag. The

disappearance of flatbands and the resulting FL character implies the absence of correlated electron behavior, as is also experimentally seen for large interfaces [55].

C) For the embedded NS, it is observed that there is a reduction of bandwidth for near-E_F bands. Near Fermi level, flatter bands from X to Y contain *s-p-d* orbital characters. Correlated behavior induced by flatness raises the possibility of driving the system into the Non-Fermi liquid (NFL) regime. These bands have also instigated the system to lose its inherent mirror symmetry of the band-structure, as existent in systems 1-3, with a Γ-centered mirror plane passing through the hexagonal vertex. The partial DOS (PDOS) of the systems is depicted in Figure 10.2. The PDOS shows the existence of partially-filled Au-5*d* levels at E_F.

Table 10.1: *Bader charge chart of different systems.*

System	Total Charge (ideal)	Total Charge Bader	Ag Part		Au Part	
			Ideal Charge	Bader Charge	Ideal Charge	Bader Charge
Au/Ag-111	378	383.46	141	168.78	237	214.68
Embedded	20439	20001.45	2585	2534.65	17854	17466.80
Ag-doped Au	3536	3607.74	376	371.54	3160	3236.20

D) The symmetric nature of band-dispersion, as shown in system a-c, is retained in the system (e) (Figure 10.1j and 10.1k), where the 4*d* and 5*d* levels are heavily localized within the high symmetry zone Γ-X and Γ-Y, signifying an NFL nature. The band-topology within the X-Y symmetry level shows *s-p* hybridized levels. Bands within X-Y symmetry are nearly linearly dispersed with an approximate electron-hole symmetry illustrating Dirac-cone like characteristics near E_F. It is very much evident from the band-structure that, a small fluctuation or perturbation can open up the

bandgap in the doped system. These highly localized electrons in flat-bands eventually display ENZ property in this system.

E) For the case of Embedded system and Ag-doped Au system, highly localized flat-bands may be responsible for endorsing NFL like behavior, which was also observed previously in hole-doped cuprates [56, 57], where localized flat-band induced NFL behavior was observed at the large region of the BZ. Average effective masses (near flat-band region) for all the systems are depicted in Table 10.2. It is observed that the effective mass for Embedded and Doped systems is much higher than the other three large-area systems.

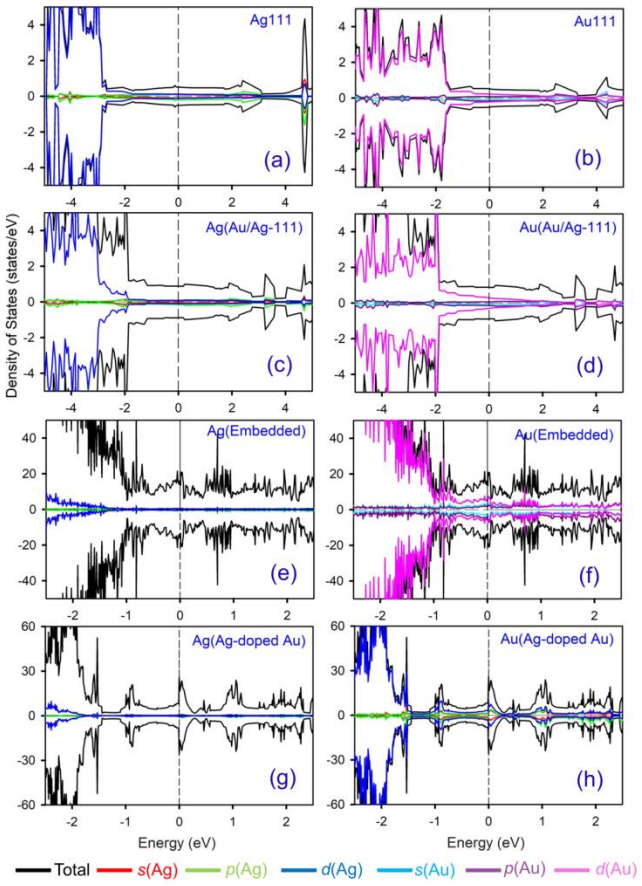

Figure 10.2: *Orbital Projected DOS for a) Ag111, b) Au111, c) contribution of Ag in Au/Ag-111, d) contribution of Au in Au/Ag-111, e) contribution of Ag in embedded, f) contribution of Au in embedded, g) contribution of Ag in Ag-doped Au, and h) contribution of Au in Ag-doped Au.*

F) Moreover, we have carried out this investigation for another bimetallic system Pt/Pd. It is observed that bimetallic Pt/Pd systems also display similar results to Au/Ag systems. In this case, we have developed two types of system a) Pt-111/Pd-111 large area interfaces and Pd-doped Pt nano-system. In contrary to the Au/Ag system, Pt/Pd system shows interesting optical properties for both nanostructure and large area interfaces. Figure 10.3 depicts the orbital projected fat band of the Pt/Pd combined system. In the Pd doped Pt system, partially occupied *d*-bands of both Pt and Pd generate flat-bands near Fermi-level.

G) Thus, for this kind of Metal/Metal combined nanostructure systems carrier-localization induced orbital chemistry is very much proficient in stimulating the correlated NFL nature for these systems.

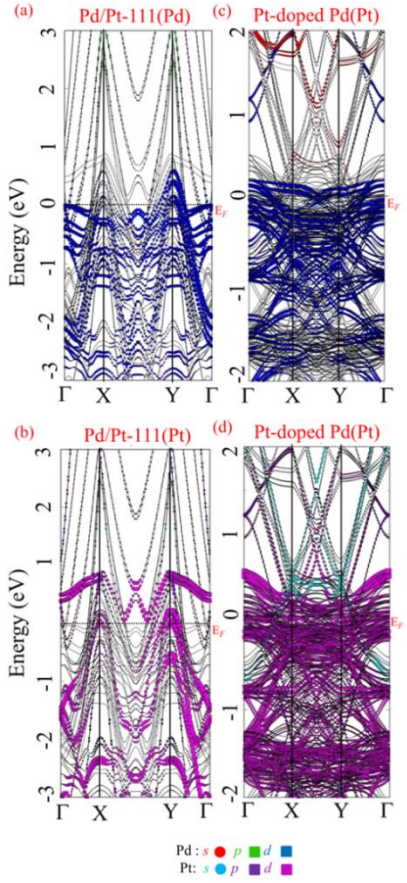

Figure 10.3: *The orbital projected fatbands for orbital components of a) Pd in Pt/Pd-111 system, b) Pt in Pt/Pd-111 system, c) Pd in Pd-doped Pt system and d) Pt in Pd-doped Pt system.*

The coexistence of Fermi-surface nesting (FSN) and the occurrence of charge/spin-density waves (CDW/SDW) in metals resulted from Peierl's concept of instability for the 1D periodic half-filled framework [58]. Instabilities such as CDW/SDW conceive of new periodicity within an electronic system that is either compatible (commensurate) or incompatible (incommensurate) with the periodicity of the lattices [59]. In presence of any perturbation from the ground state [60], the occupied ($\boldsymbol{k}$) and unoccupied ($\boldsymbol{k'}$) electronic levels interact with each other and as a synergistic effect of both a superposed density wave $\boldsymbol{q.R}$ generated, where $\boldsymbol{q} = \boldsymbol{k}-\boldsymbol{k'}$ and $\boldsymbol{R}$ symbolizes direct lattice position. CDW is represented by a doubly occupied density wave, at the same time SDW constitutes orbitals, singly-occupied with different spin states. Fermi pockets are contours of Fermi energy in the BZ. A Fermi pocket which is formed by filling the states using electrons is called an electron pocket, whereas if the Fermi surface encloses an empty region, then it is called a hole pocket. Moreover, in the presence of an FSN, electron and hole pockets are connected by $\boldsymbol{q}$ vector which is almost degenerate for all $\boldsymbol{k}$ near an FS sheet. For metallic structures with restricted dimensionality, a nested FS shows

Table 10.2: *Effective masses of carriers (DFT) and plasma frequencies (TDDFT) for different systems are presented. The inverse relationship between these two quantities is evident.*

System	Effective Mass (DFT)	Plasma Frequency (TDDFT) (eV)
Ag111	0.40	0.70
Au111	0.50	0.50
AuAg111	0.06	0.30
Embedded	1.17	0.04
Doped	2.89	0.06

the presence of CDW/SDW, whereby the nested portions of FS are removed by opening a gap. A recent reclassification [61-63] of CDW infers that for Type I CDW, the origin of CDW may be solely electronic FSN and as an outcome of it lattice distortion may be created. However, type II CDWs are controlled by electron-phonon coupling (EPC). Reduced dimensionality is an important

criterion for obtaining the FSN-driven CDW to produce a perfectly divergent response function. In that kind of system, whenever the symmetry of the system is broken macroscopically by doping or any other way, there is a reconstruction of the FS which results in forming electron and hole pockets, embodying closed orbits for quasiparticles [64]. Furthermore, there are conflicting studies about the FSN, in addition to CDW/SDW, that are primarily responsible for the generation of unconventional superconducting pairing in Fe-pnictides induced by spin/orbital fluctuation [65-67].

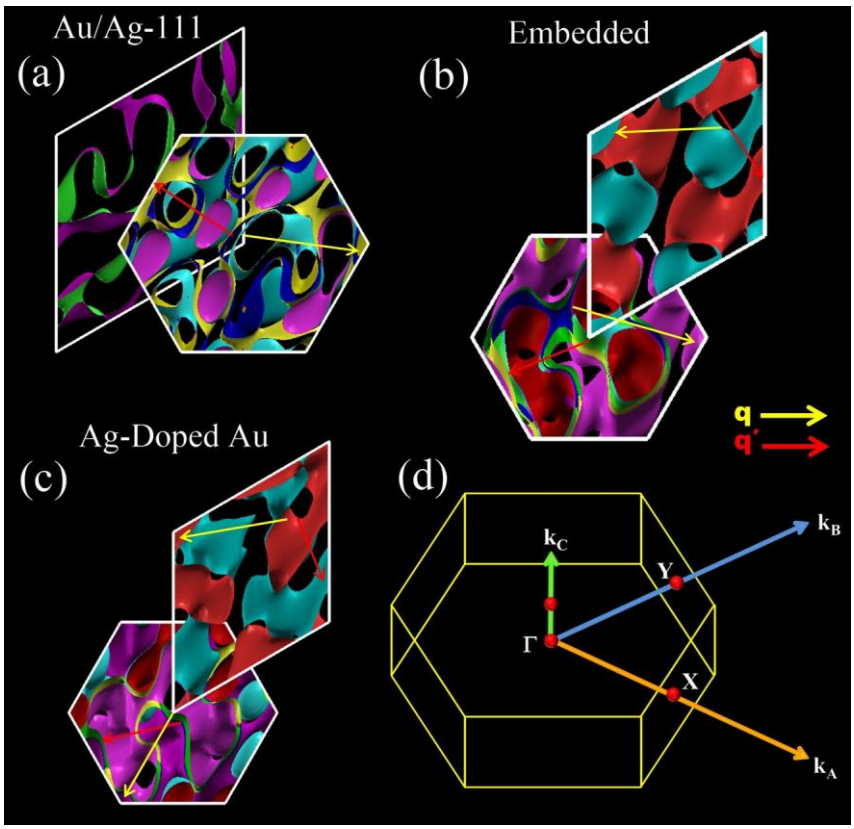

Figure 10.4: *Merged Fermi Surface sheets corresponding to all bands crossing E_F for a) Au/Ag-111 b) Embedded, c) Ag-doped Au systems within the hexagonal BZ. The rhombus represents the unit cell in the reciprocal lattice, d) Hexagonal BZ with high-symmetry directions.*

Reliance on the perfection of nesting on the superconducting pairing strength [68] has encouraged us to analyze the FS topology for systems (c), (d), and (e). The subsequent FS is complex for all three cases and consists of multiple separate sheets containing the electron and hole pockets indicating massive FS

reconstruction. 2D projection of the merged FS sheets within the BZ is depicted in Figure 10.4. The superimposed bottom/top rhombus represents a single FS sheet within the unit cell *k*-space. The rhombus tip inside the BZ is the Γ-point. The key features of the analysis of FS can be listed as follows:

A) In Figure 10.4a, for Au/Ag-111, there is partial nesting between Γ-centered hole pocket to the small electron pockets at the corner of the BZ with $\boldsymbol{q}$ (yellow arrow). There is another incomplete nesting identified by $\boldsymbol{q'}$ towards some BZ (red arrow) mid-sides. Partial nesting and electron-hole asymmetry leads to the inequality of size/shape of electron and hole pockets and also connote the systems lacking potential for CDW.
B) FSN is more complex for the embedded system (Figure 10.4b), due to the *z*-directional dispersion of the sheets. Near Γ, the hole pockets nest with electron pockets at the mid-side ($\boldsymbol{q'}$) and also at the corners ($\boldsymbol{q}$).
C) As the doped system is essentially having 2D nature, the Γ-centered hole pocket nests perfectly with all the electron pockets located at the corners ($\boldsymbol{q}$) and also at the mid-sides ($\boldsymbol{q}'$) (Figure 10.4c).

The reconstruction of FS and nesting-like features suggests that embedded and doped systems are potentially promising for CDW/unconventional superconductivity applicants. However, in all these systems, the FSN is incommensurate, with the nesting vectors $\boldsymbol{q} = \frac{a}{\sqrt{2}}$ and $' = \frac{\sqrt{3}a}{2\sqrt{2}}$, with a being the lattice parameter of the original lattice. The periodic reproduction of the FS, which retains the hexagonal symmetry, is also verified in the 2D plane in the extended BZ.

For metallic structures, a finite probability of intra-band transitions contributes to the so-called Drude-like term only at the long-wavelength limit, in addition to the inter-band transitions. In the next section, we have calculated the dynamical dielectric response and the electron-energy loss (EELS) function using

TDDFT formalism. These results give an idea about the low-energy optical and plasmonic properties of the heterostructure systems and their interconnection with the orbital chemistry.

Calculation of dynamical optical properties involves many body perturbative approach to the solution of Bethe-Saltpeter equation (BSE) using the single-particle Green's function, where the dielectric function is written in terms of the exchange-correlation (xc) kernel as: $\epsilon^{-1}_{GG'}(q,\omega) = \delta_{GG'} + v_{GG'}(q)\chi'(q,\omega)$, where $v_{GG'}(q)$ is the bare Coulomb potential, a function of wave vector q and $\chi'(q,\omega)$ being the full response function dependent on q and frequency ω. $\chi'(q,\omega)$ is related to the non-interacting density-density response function $\chi^0(q,\omega)$ as $\chi'(q,\omega) = \frac{v_{GG'}(q)\chi^0_{GG'}(q,\omega)}{1-\left[v_{GG'}(q)+f^{dyn}_{xc}(q,\omega)\right]\chi^0_{GG'}(q,\omega)}$, where the frequency-dependent dynamical exchange-correlation kernel is $f^{dyn}_{xc}(q,\omega) = -\frac{1}{q^2}(\alpha + \beta\omega^2)$, with α and β being system-dependent parameters. In the computational methodology section, details of the inter- and intra-band calculations are described [69-74]. The calculated real (ε_1) and imaginary (ε_2) parts of ε are presented in Figure 10.5, along with the corresponding refractive index and the dynamical electron energy loss spectra (EELS), as calculated from $\varepsilon_{loss} = -\Im\left[\epsilon^{-1}_{GG'}(q,\omega)\right]$.

The dynamical optical responses for all the five systems and their interdependence with the chemistry of localized band-carriers have been examined. The first and second columns of Figure 10.5 depict the real and imaginary parts of dynamical dielectric response functions of all the systems. For bulk systems (Ag-111, Au-111, and Au/Ag-111) the effects of intra-band transitions endorse the Drude-like near zero negative and positive divergence of ε_1 and ε_2 respectively. The close comparison of ε_1 and ε_2 of all these systems demonstrates that the optical property of embedded and doped systems are fascinating compared to other systems. For both of these systems, ε_1 and ε_2 experience a transition to an infinitesimal value in the UV-Vis energy range, after a

near-zero positive-divergence, revealing the massive deteriorating effects of intra-band transitions due to localization of carriers. Thus in the case of nanostructure-based on these two metal, flat-band induced NFL nature, presence of localized carriers with higher effective masses, and ENZ behavior in the ultra-violate range works conjointly. When two simple Drude-like systems (such as Au and Ag) are combined into a specific NS, all intra-band effects caused by carrier positioning can be suppressed. This behavior promotes the beneficial use of these NS in the field of non-linear optics, where there is a gigantic quest for ENZ materials underway [75, 76]. The third column of Figure 10.5 shows the refractive index of the systems which reveals that; the embedded and doped systems have a large non-linear refractive index. Therefore it can be used as optical switching material. The near-perpendicular departure of emitted light often encourages their use as optical interconnectors. The calculated plasma frequencies for all the systems using TDDFT are tabulated in Table 10.2. Plasma frequency has an inverse relationship with the effective mass. The values of plasma frequencies for embedded and doped systems are much lower than the other three systems indicating the localization-induced NFL behavior, which is consistent with the DFT prediction of localized orbital chemistry. The last column of Figure 10.5 depicts the time-dependent EELS which shows the dynamics of both low-energy intra-band and high-energy inter-band plasmons. For thinner Au and Ag systems, the surface plasmon interband resonance peaks are known to shift to higher energies [77, 78]. The inter-band plasmonic peak for trilayer Au-111 and Ag-111 systems are found at ~3 eV and ~2.8 eV respectively. Intra band plasmonic transition peaks of corresponding systems are shown in the respective insets. The intra-band plasmonic transition peak value resembles the calculated plasma frequencies in Table 10.2. For the nanostructured system (embedded and doped) all intra-band plasmonic oscillations are frozen and a single peak of inter-band plasmon has appeared. Such blocked intra-band plasmons for engineered heterostructure tally well with the highly localized electronic band-structure and

diverging properties of dynamical response, where intra-band effects are suppressed for systems d) and e). It is worth mentioning that experimental research has also observed the suppression effect of nanostructured components on plasmon resonance [7].

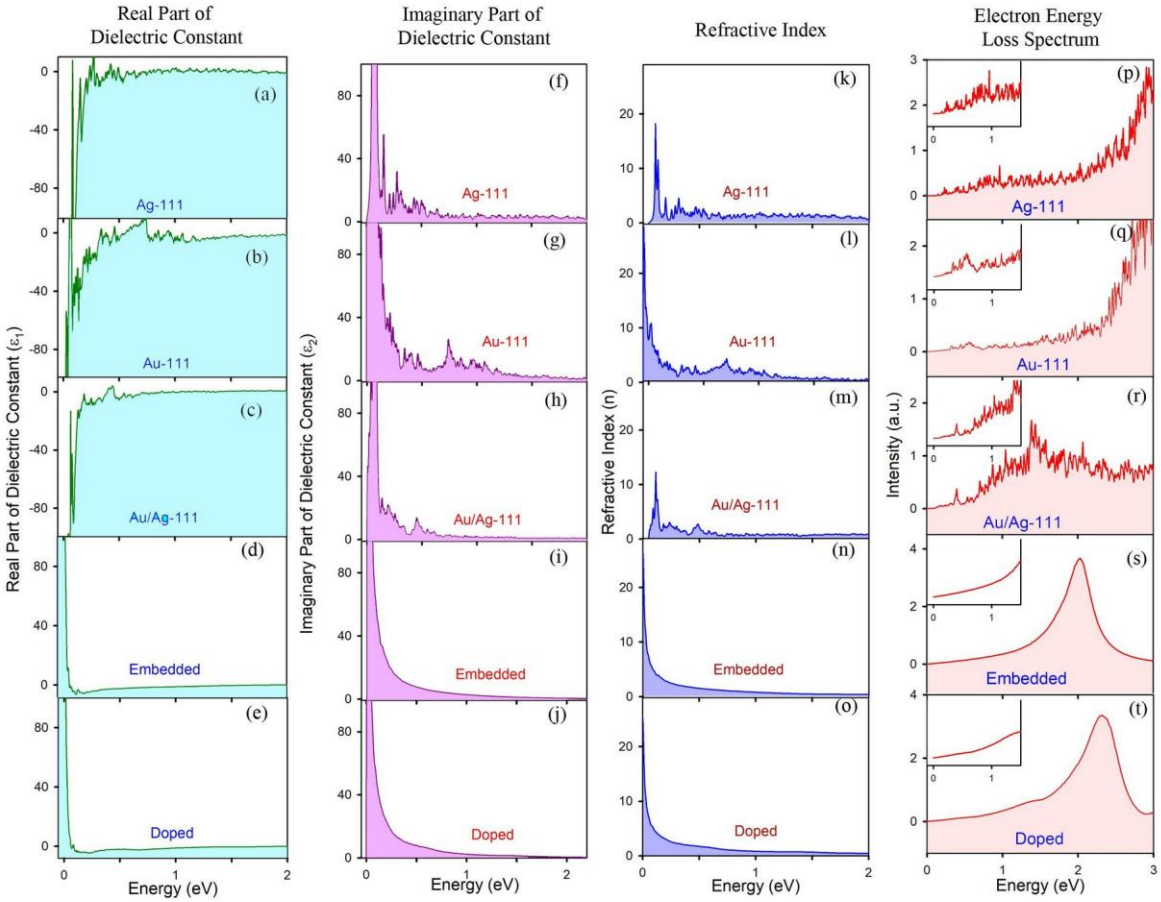

Figure 10.5: *Real (ε_1) and imaginary (ε_2) parts of dielectric constant (ε), refractive index (n), and EELS plot for different systems.*

The dielectric functions for the Pt/Pd systems are also investigated to view the other Metal/Metal systems. We found that, in the case of Pt/Pd bimetallic heterostructure system, the dielectric functions show the ENZ property for both large-area interfaces and doped systems (depicted in Figure 10.6).

Further, to find the occurrence of instabilities, we have explored the phonon dispersion and the corresponding density of states for four model systems

(based on Au and Ag). We have made the infinite surface of a) Au-111, b) Ag-111, c) Au-111 with 33% Ag doping (Low) and d) Au-111 with 66% Ag doping (High). By infinite surface, we denote the absence of a vacuum layer on top of the [111] cut surface. All the systems are geometrically optimized to the ground state. The phonon dispersion and the phonon DOS are depicted in Figure 10.7. Unlike Au-111 and Ag-111 system, doped systems exhibit the generation of soft phonons. As seen from Figure 10.7 (c, d), and 10.7 (g, h) dynamical instabilities [79, 80] are observed along with the full high-symmetry directions Γ-X-Y-Γ. The maximal negative value is observed at Γ point, signifying that the instability may have

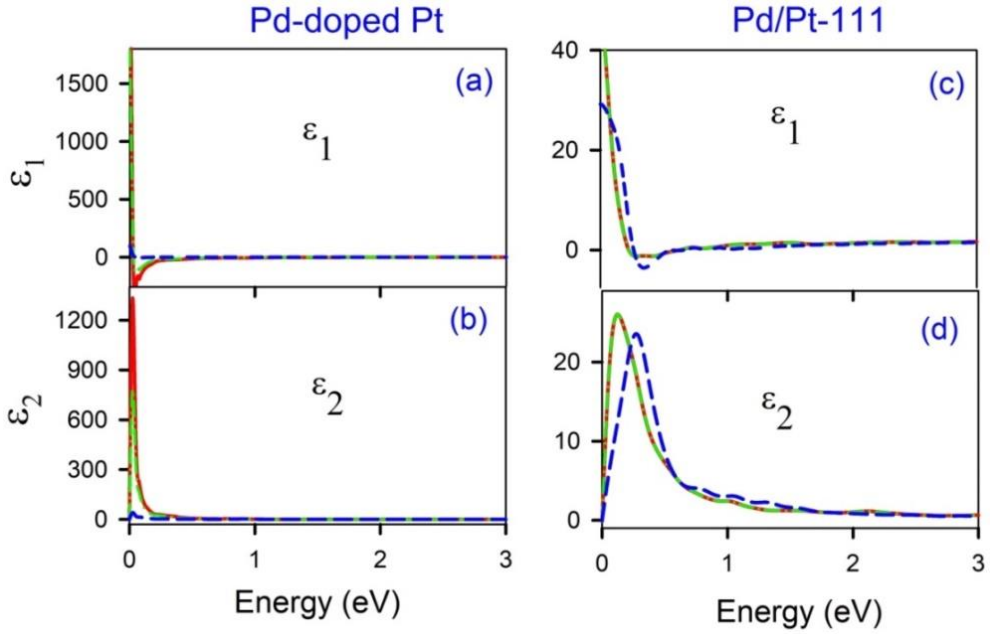

Figure 10.6: *Real and Imaginary part of the dielectric constant of the Pd-doped and Pd/Pt-111 system.*

created at the Γ point. The imaginary phonon modes with a negative frequency attributed to structural metastability created in the system, where permanent displacements of the ionic positions may be achieved through the lattice distortions [81]. Even though the nested FS (discussed earlier) points toward an unconventional pairing, the computed electron-phonon coupling constant (EPC) has shown an order of magnitude change, as also experimentally observed for the doped cuprate systems [82]. The calculated EPC for Au-111, Ag-111, and low-

doped systems are 0.03, 0.002 and 0.68 respectively. Localized peaks have been observed approximately ± 10 meV in the phonon density of states for both Ag-doped Au systems. This indicates the contribution of the corresponding modes in coupling with the charge carriers. Moreover, as the Ag doping degree increases, in the second case, the phonon bands became more localized between X and Y, and the softness is higher.

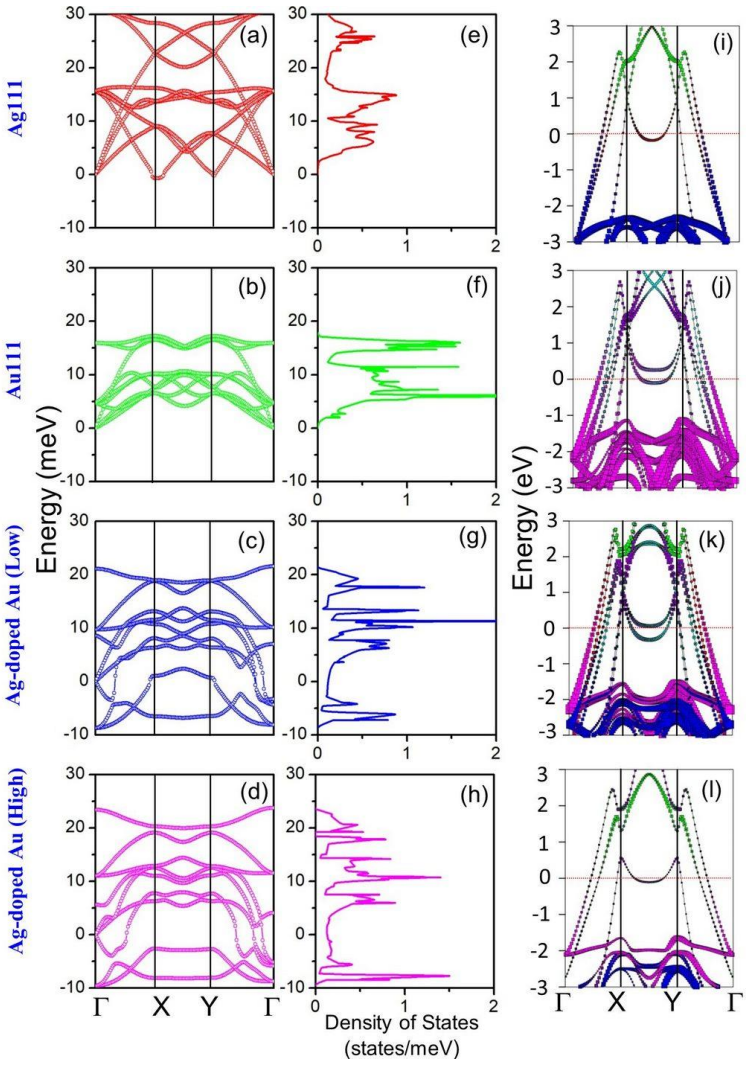

Figure 10.7: *Phonon dispersion for a) Au111, b) Ag111, c) Ag-doped Au (Low) and d) Ag-doped Au (High) systems. The corresponding phonon DOS is shown in e), f) g), h) respectively. Electronic fat-bands of i) Au111, j) Ag111, k) Ag-doped Au (Low) and l) Ag-doped Au (High) system with similar legends for orbital fatness as Figure 10.1.*

The resistivity measurements done experimentally in earlier experimental work [5-7], have influenced to investigate of the room-temperature DFT-coupled quantum transport properties of the simplest possible device geometries designed out of these two metals, where the trilayer surface of Au(Ag) will constitute a channel with lateral contacts of Ag(Au). We have designed two types of systems, a) Au channel with Ag contact and b) Ag channel with Au contact. The key findings of the quantum transport calculations on both devices can be enlisted as below:

A) The I-V transport characteristics, shown in Figure 10.8a, suggest that the absolute current value will be higher for the second device. There is a spin-dependency in the transport property.

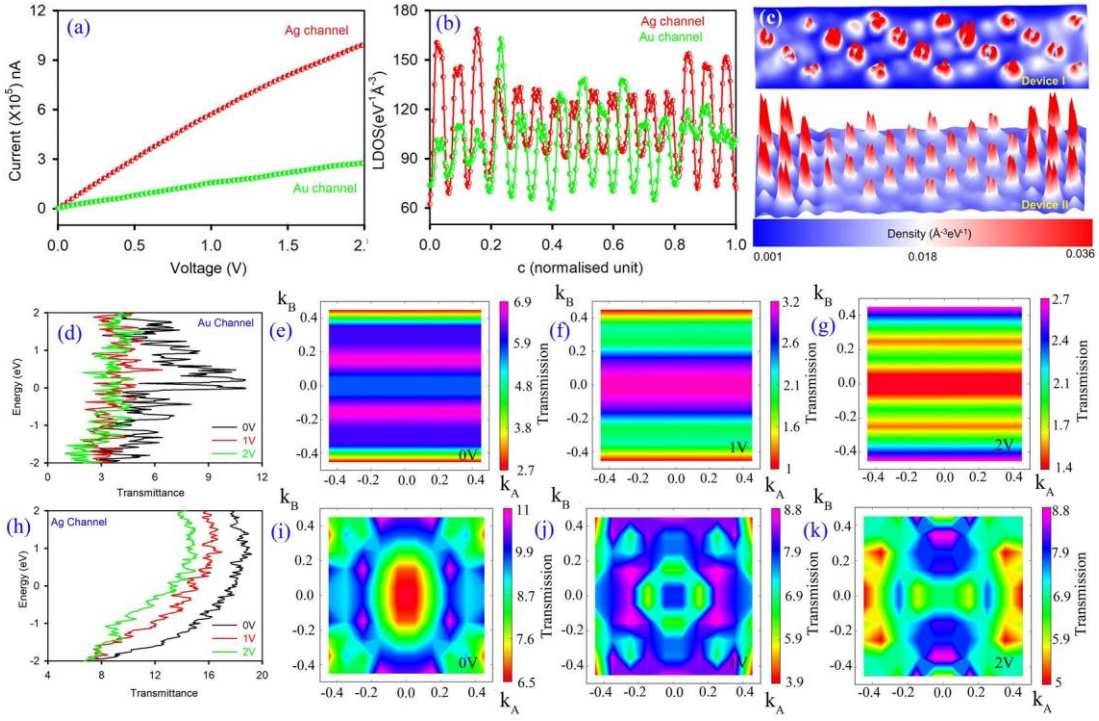

Figure 10.8: *a) Comparative I-V characteristics for I) Au channel with Ag contact, and II) Ag channel with Au contact, b) 1-D projected LDOS for the device I and II, and c) 3D colored plot for LDOS of device I and device II. Transmittance plot for d) device I (see text) and corresponding interpolated Γ-centered contour plots corresponding to bias voltages e) 0V, f) 1V and g) 2V, transmittance plot for h) device II and corresponding interpolated contour plot for bias voltages i) 0V, j) 1V and k) 2V.*

B) The 2D projection of the local DOS (LDOS) in the b-c plane passing through the center of the device-BZ (Γ point) with respect to the current-transport (c) axis is depicted in Figure 10.8b. A comparison of LDOS for the two device configurations indicates that device I (Au channel) shows more DOS at the channel, has lesser interfacial backscattering at the contacts. From the 3D LDOS diagram (Figure 10.8c), the contribution from the incident and reflected states from the contact-channel interfaces will also be manifested. This result is consistent with the 2D LDOS features where we observed more interfacial scattering for device II.

C) The nature of electrical transports will be more elusive from the interpolated transmission contour plots through the central *a-b* plane (perpendicular to the current transport), passing through the Γ-point for different biases along with the total integrated transmission spectra with respect to energy. In the case of the Au-channel system, near around the Γ-point highly transmitting zone starts reducing with increasing bias. On the contrary, edges start transmitting more. The integrated energy transmission plot (depicted in Figure 10.8d) also indicates a decrease in overall transmission across the core region with an increase in the applied bias.

D) In the case of the Ag channel device, the transmission color-maps have more complexities (Figure 10.8i, j, and k). In this system, many highly transmitting pockets have been created over the Γ-centered cross-sectional area of the device. In this case, also, the overall transmission across the core region decreases with higher bias. The transmission at the edge is much higher than the central region which follows the same trend as found in a device I.

Therefore, the above analysis concludes that the transport characteristic for the simplest possible device is far more complex than anticipated. Experimentally synthesized NS systems [5-7] will contain much more complexities due to the presence of defects, grain boundaries, and different sample morphologies.

Interfacial and defect mediated scattering impacts can worsen the situation many more times.

10.2.2. Broken Inversion Symmetry and Related Interface-induced Effects at Weyl-system TaAs in Proximity of Noble Metals: Bulk TaAs shows body-centered (BC) tetragonal lattice structure with space group $I4_1md$. The system shows a lack of inversion symmetry. Moreover, the C_4 rotational symmetry is also broken for its [001] surface [38, 39, 42]. In the present study, we have built the bilayer metal interfaces [111] (Au-111 and Ag-111) surfaces with the [3×3×2] supercell of TaAs. In the case of vertical Metal/TaAs interfaces, the average interfacial strain is reduced to 1.4% after a mutual rotation between TaAs and Metal-111 surface by ~29° by using the Co-incident site lattice (CSL) technique

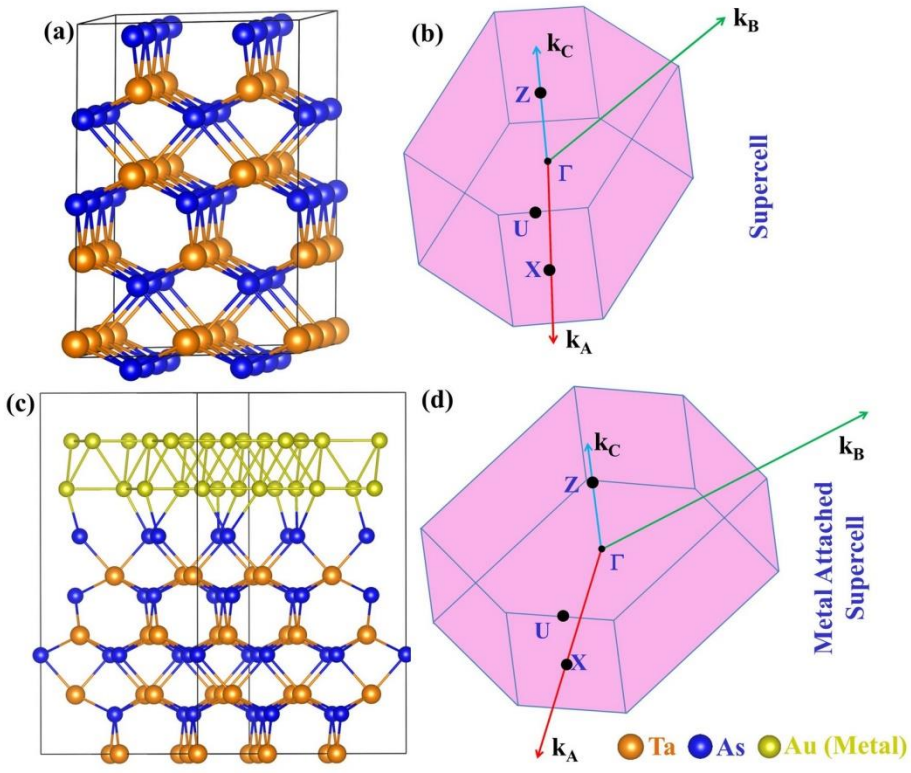

Figure 10.9: *a) Structural image of TaAs supercell in P_1 symmetry, b) Brillouin Zone, and high symmetry points of the supercell, c) structural image of TaAs/Au heterostructure, d) Brillouin Zone and high symmetry points of the heterostructure in P_1 symmetry.*

as employed in ATK [83, 84]. In the interface system, the symmetry of the TaAs system transformed from BC-tetragonal lattice to a triclinic (P_1). The structural image and corresponding BZ with the high-symmetry points of supercell and interfaces are depicted in Figure 10.9. To circumvent the z-directional periodic repetition, a vacuum of 15 Å in the *z*-direction has been added for the single interface systems. On the other hand, for stacked interfaces, the TaAs/Metal system repeats itself periodically along z-direction without any vacuum (shown in Figure 10.9c).

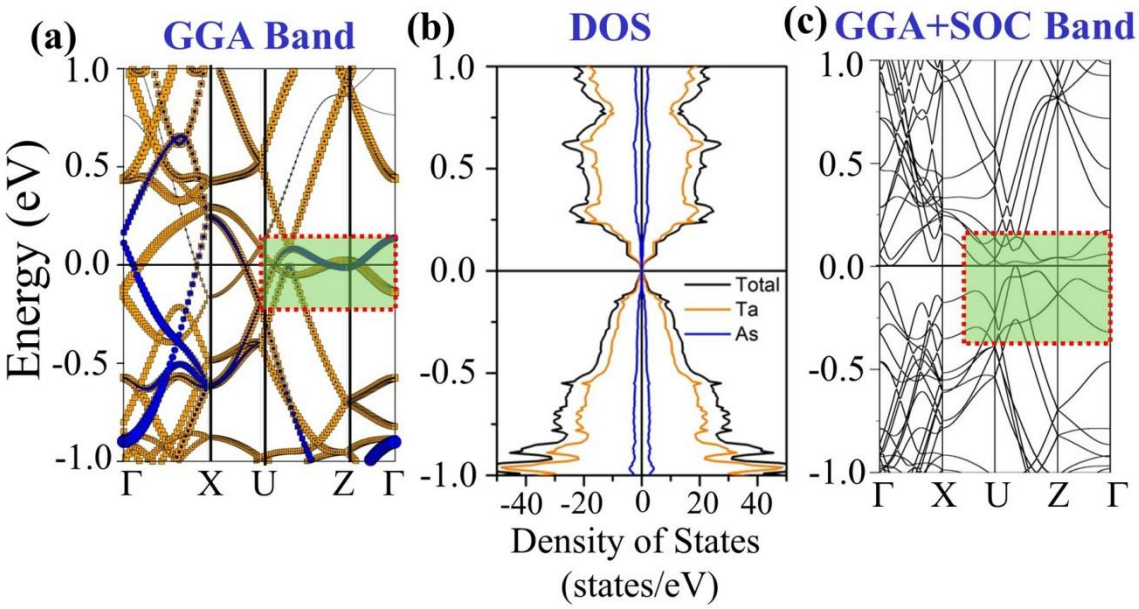

Figure 10.10: *Orbital Projected a) band-structure and b) DOS of TaAs supercell using GGA, c) GGA+SOC gapped band structure of the same supercell.*

The orbital projected band structure of the TaAs supercell along high symmetry directions of (shown in Figure 10.9b) is showed in Figure 10.10a. There are non-degenerate 3D band-crossings along with X-U and U-Z high symmetry points, exhibiting a Weyl-cone like feature. Bands near the Fermi level are highly hybridized by Ta-5*d* and As-4*p* character, as can be seen from the fatband figure (Figure 10.10a). Figure 10.10b represents the orbital projected DOS of the TaAs supercell, near E_F, the DOS shows the conventional semi-metal like behavior [85].

Upon incorporation of spin-orbit coupling the expected splitting of Weyl cones has been observed, producing a fully gapped band structure [41, 42].

Next, we have investigated the TaAs/Au or TaAs/Ag single interface systems with the vacuum. For TaAs/Au or TaAs/Ag single interfaces, the presence of vacuum abolishes the periodicity in the *z*-direction, shows 2D-like degenerate bands along the high symmetry zone X-U and Z-Γ, having almost minimal *z*-directional dispersion as shown in Figure 10.11a.

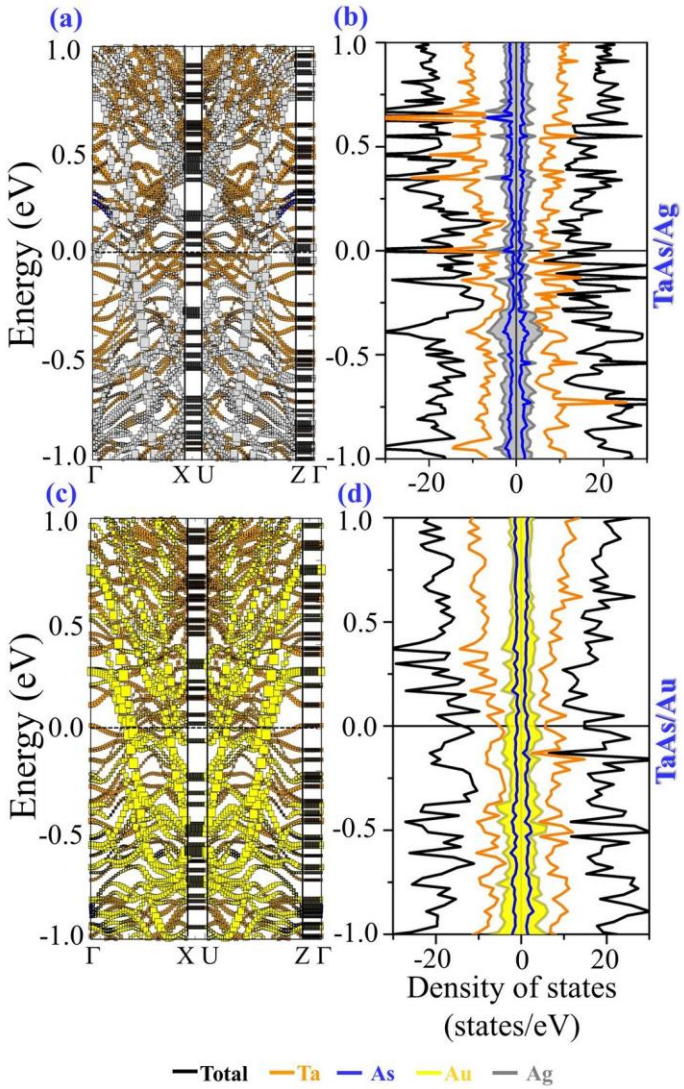

Figure 10.11: *a) Band structure and the corresponding b) orbital Projected DOS of TaAs/Ag single interface with vacuum, and c) the band structure and corresponding d) orbital Projected DOS of TaAs/Au single interface with a vacuum using GGA.*

Consequently proximity-induced inter-layer charge transfer several properties have been modulated as observed from DOS and band structures. The result shows the destruction of the Weyl-cone feature, higher spin polarization, and doping of the TaAs layer underneath the metal. Charge transfer from the delocalized orbital of metal (Au/Ag) to TaAs exhibits *n*-type doping for both the TaAs/Metal systems. Pristine TaAs shows AFM spin-orientation for the magnetic ground state, producing almost zero magnetic moments (Figure 10.11). However, proximity with metals at the interfaces presents spin-polarization in the heterostructure system because of the transfer of carriers from the delocalized *s-d* hybridized metal layer and the TaAs layer. The ground state magnetic configuration for both the Metal/TaAs single interfaces shifts to ferromagnetic (FM). The ground-state magnetic configuration, magnetic moments, and type of doping of the interfacial systems have been depicted in Table 10.3. Although a single interface system shows higher spin polarization, the broken inversion

Table 10.3: *Magnetic Moments, nature of doping, and ground-state configuration of different stack systems.*

	System	Magnetic Moment (μ_B)	Nature of doping	Ground State Configuration
Single Interface	TaAs	0.7520	-	AFM
	Ag-TaAs	2.6760	*n*-type	FM
	Au-TaAs	3.9020	*n*-type	FM
Stacked Interface	TaAs	0	-	AFM
	Ag-TaAs	-0.0013	*p*-type	AFM
	Au-TaAs	-0.0081	*n*-type	FM

symmetry of the interfacial system does not make the presence of Weyl cones because of the presence of a gigantic vacuum slab for the TaAs/Au and TaAs/Ag single interfaces. The confinement effect in the reciprocal space along *z*-direction destructs the Weyl feature. However, the non-degenerate band-crossings and the corresponding nodal features can be reestablished upon the formation of vertically stacked interfaces (TaAs/Metal/TaAs/Metal…) where the vacuum has been

slashed. Figure 10.12 represents the atom-projected band-structures and DOS for the stacked interfaces. The most interesting effect of stacked interfaces to the single interface is the restoration of non-degenerate band-crossings and nodal features along X-U for both the systems, as can be seen from Figure 10.12(a), (b), (d), and (e). The 3D band-crossings are sustained upon the application of SOC. Another important feature of the stack interface system is, the Weyl crossings along X-U are distributed along with the full energy-axis range. It suggests that the system will retail its band-crossing characteristics by sufficient doping-induced Fermi-level change with the aid of applied bias.

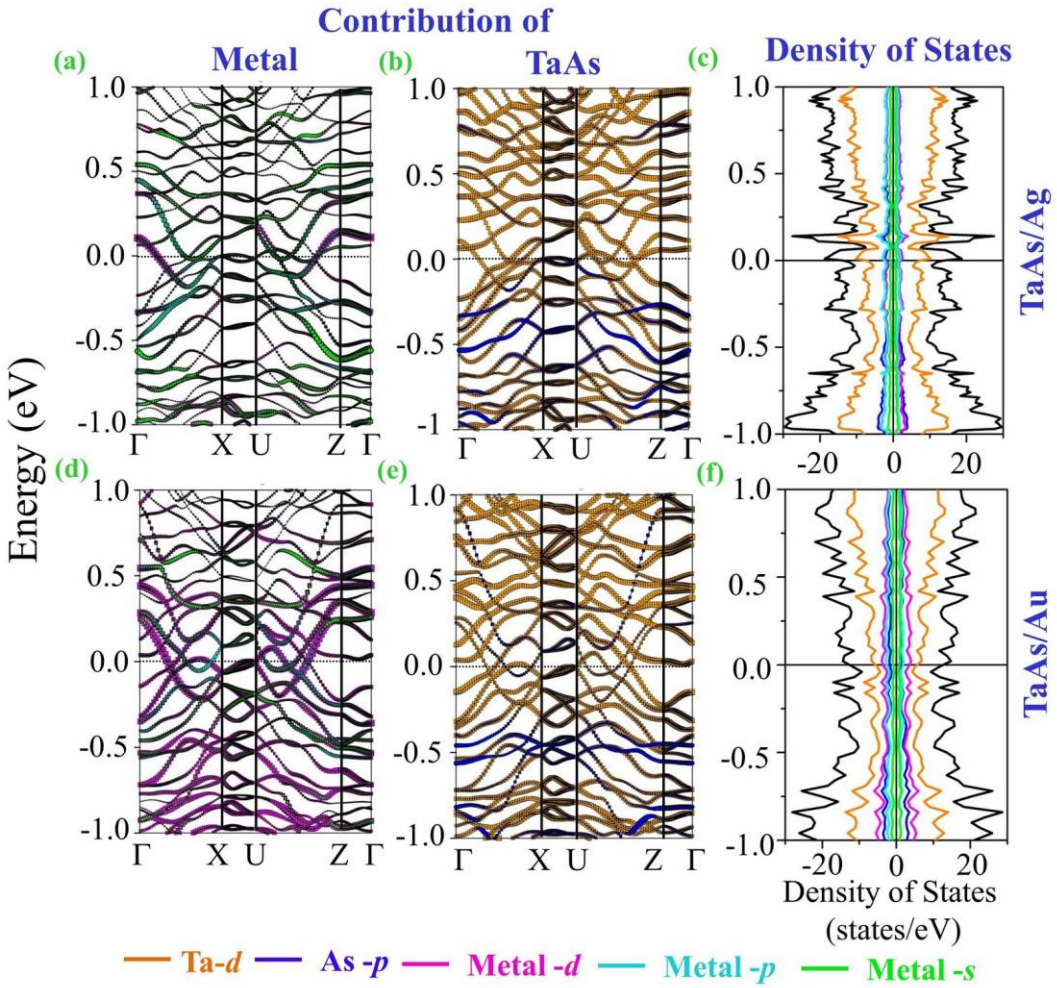

Figure 10.12: *Orbital Projected bands of different systems a) TaAs contribution in TaAs/Ag, b) Ag contribution in TaAs/Ag, and c) the corresponding DOS. Orbital Projected bands of d) TaAs contribution in TaAs/Au, e) Au contribution in TaAs/Au, and f) the corresponding DOS.*

The doping nature and the magnetic ground states of the stacked interface have shown a changed result compared to the single interfaces. The TaAs/Ag stacked interface shows *p*-type doping and AFM configuration of the spin-magnetic moments, as can be seen from Table 10.3. The hole-doped antiferromagnetism in TaAs/Ag system may render it to be a potential correlated system. Here holes are doped into the TaAs layer. However, here Ta-*5d* levels are less correlated. This kind of system is different from the other hole-doped antiferromagnetic systems like the cuprates and pnictides [86-90], where more correlated and localized Cu-3*d* or Fe-3*d* orbitals play a prominent role. On the other hand, TaAs/Au system shows an *n*-type FM ground state with a small magnetic moment.

Moreover, according to the Kramers theorem, in the presence of both time-reversal symmetry (TRS) and inversion symmetry (IS), the full band-structure is doubly degenerate at all *k*-points. Thus, by respecting any one of the symmetries and breaking the other, non-degenerate band crossings can be materialized, producing topologically stable *k*-space separated Weyl nodes at the same energy. If both the symmetries are simultaneously broken, the *k* space-separation and thus obtained topological stability of the Weyl node remains intact. However, the pairs of Weyl nodes now occur at two different energies, deviating slightly from the nodal semimetal [91]. For pristine TaAs, the TRS is preserved but IS is broken, as a result of it, broken IS leads to the 3D non-degenerate band crossing under the application of SOC. As we mentioned earlier, in the proximity of Noble metals, spin-polarization has been introduced. The resulting spin-polarization implied a spontaneous breaking of the time-reversal symmetry in this system. Furthermore, as a result of broken IS, the band-crossing-induced nodal features arise along X-U. The simultaneous presence of nodal feature and spin-polarization suggests the coexistence of both broken TRS and IS for TaAs/Ag or TaAs/Au stacked interfacial systems [26, 88-91]. A closer inspection of the nodal points has shown

their existence at different energy values. Near E_F, the energy differences between the two nodal points are ~0.08 eV and ~0.2 eV for GGA and GGA+SOC bands respectively. In addition to that, there is an appearance of magnetic nature within the system due to the presence of other delocalized bands crossing E_F.

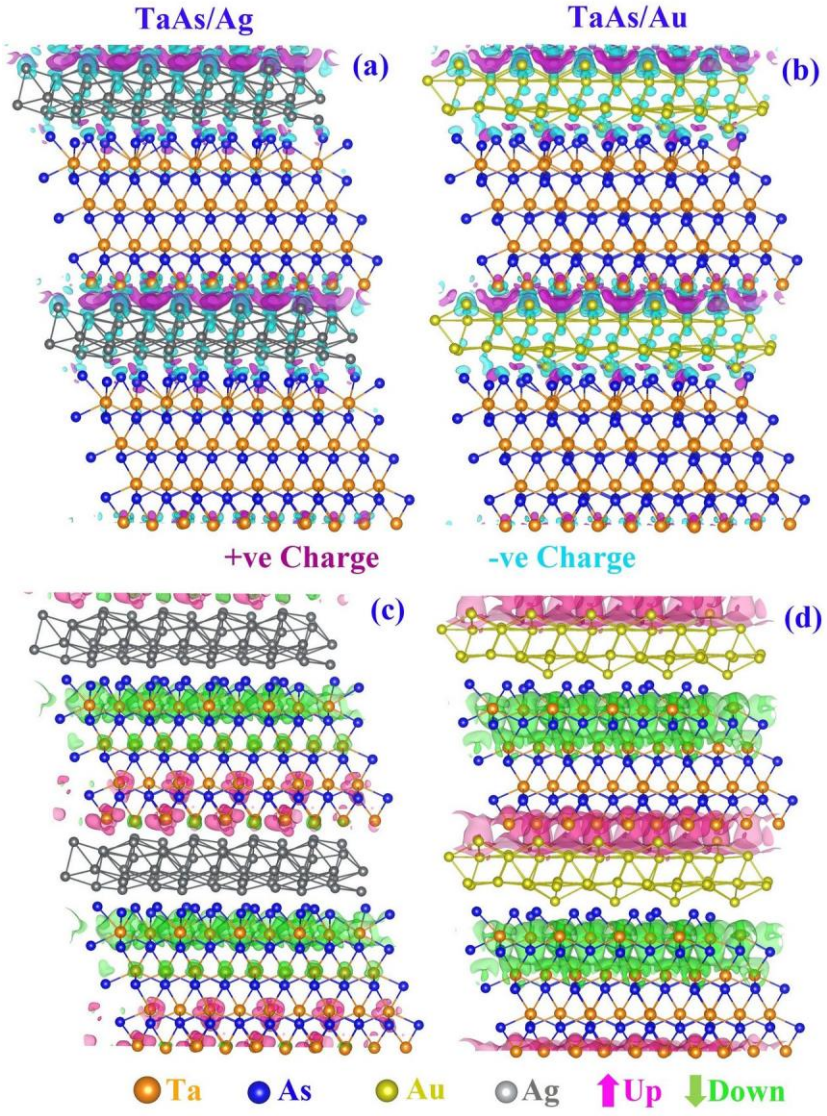

Figure 10.13: *Charge density difference plot of stacked interfaces a) TaAs/Ag and b) TaAs/Au and spin density plot of c) TaAs/Ag and d) TaAs/Au. The color coding for different atoms is Ta-d – orange, As-p – blue, Ag – grey, and Au – yellow. Positive and negative charges are denoted by purple and cyan color respectively. The spin-up and spin-down spin-densities are designated by magenta and green colors respectively.*

The orbital-projected band structures, as presented in Figure 10.12a, b, d, and e, display a strong hybridization of metal *s*-*d* hybridized bands (magenta and green) with the As-4*p* (blue) levels, as the As-layer is directly connected with the metal layer. The DOS for TaAs/Ag (Figure 10.12c) shows very sharp peaks near E_F, having a contribution from Ta-5*d* (orange) and As-4*p* (blue), whereas Figure 10.12f (TaAs/Au) depicts an itinerant electronic nature. The charge density difference plot of the system has been depicted in Figure 10.13a and b which shows a significantly visible charge-difference density at the metal-semimetal interface. The spin-density plots (Figure 10.13c and Figure 10.13d) also support the fact of an increase of spin-polarization for stacked interfaces with respect to the pristine system. It is found from point-contact spectroscopy that, the transport spin-polarization of TaAs increases in presence of plasmonic metal (Au or Ag) tip contact [2, 3]. In the next section, we have investigated the

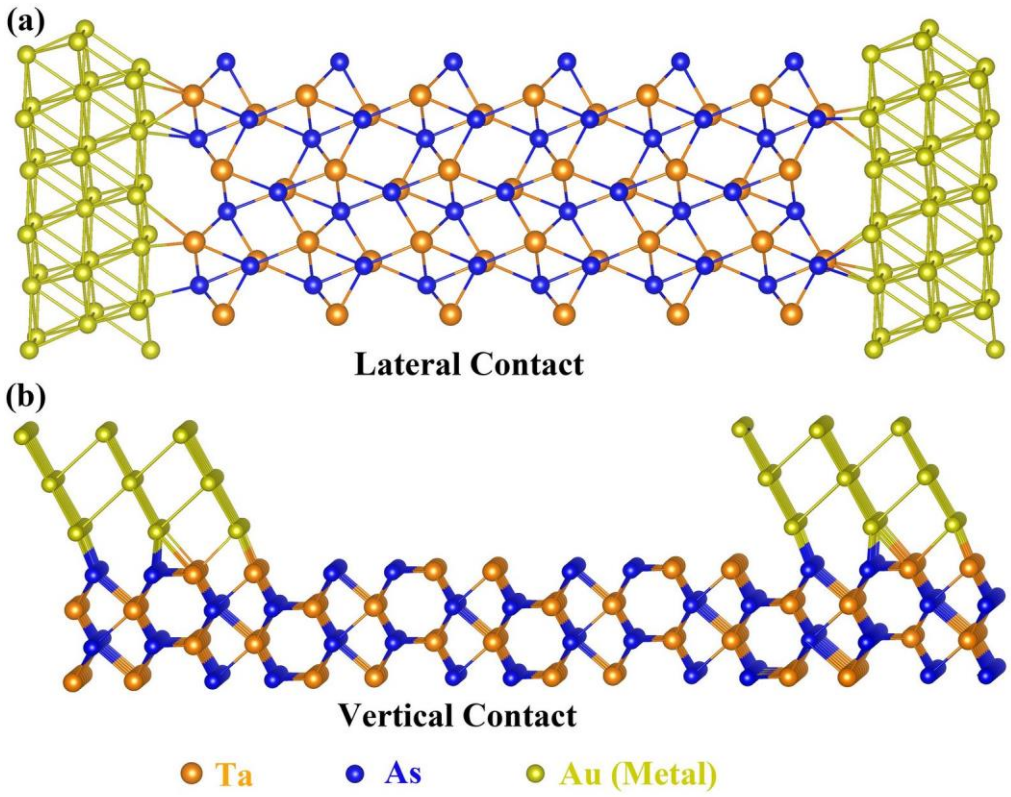

Figure 10.14: *Structural representation of a) TaAs with lateral metal contact and b) TaAs with vertical metal contact.*

transport properties of two probe devices made out of TaAs as channel and Au/Ag as lateral or vertical contacts using the NEGF method. The schematic constructions of lateral and vertical contact devices are shown in Figure 10.14a and 10.14b. Figure 10.15 represents the current (I) *vs.* voltage (V) characteristics for the lateral and vertical contact systems with Au and Ag contacts at room temperature. In room temperature transport characteristics, transport spin-polarization is more prominent for lateral contacts. On the contrary, vertical contact does not show spin polarization. So, to get spin-polarized activity certain device geometry (lateral contact) is more effective.

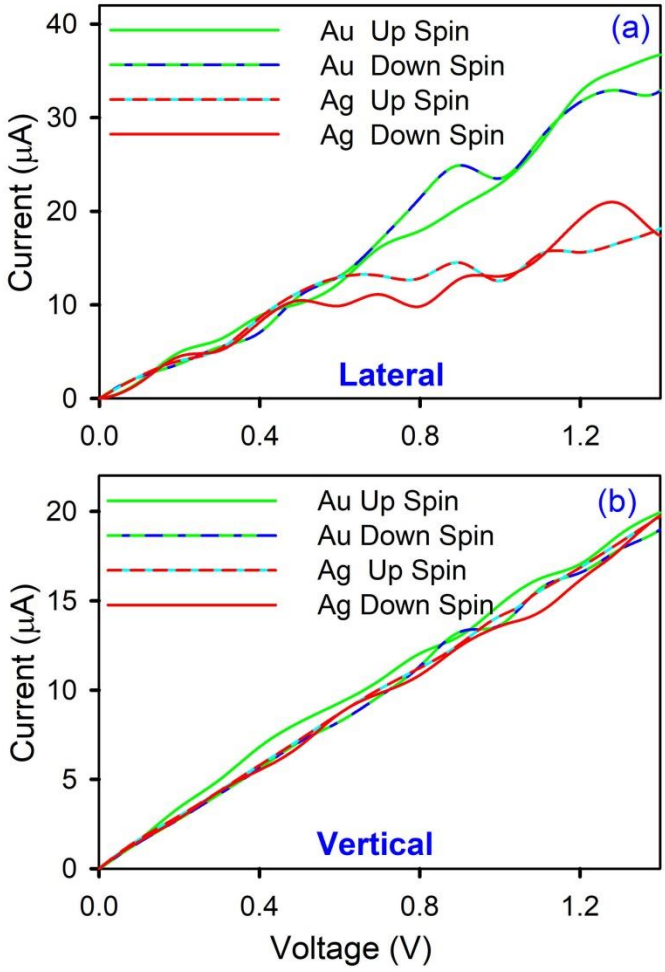

Figure 10.15: *Transport characteristics for a) lateral contacts b) vertical contact geometries for both TaAs/Ag and TaAs/Au.*

A comparison of the percentage of transport spin polarization has been plotted in Figure 10.16. We have plotted for different bias voltages, calculated from its absolute value $P_t = (I\uparrow - I\downarrow)/(I\uparrow + I\downarrow)$ for 5 K and 300 K for both lateral and vertical contact geometry, where $I\uparrow$ and $I\downarrow$ are the spin-up and spin-down currents respectively. For both systems, the value of P_t is an order of magnitude more for lateral contacts with a trend of increase in polarization after decreasing temperature. On the contrary, for vertical contacts, P_t at room temperature is more.

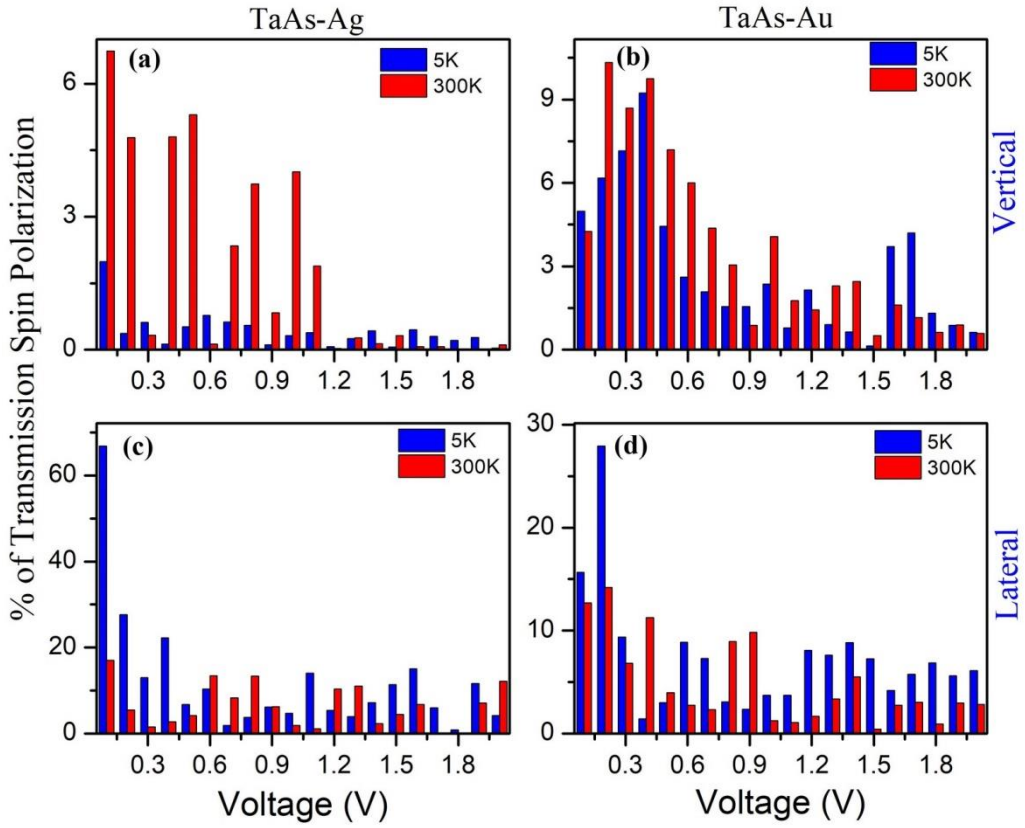

Figure 10.16: *Percentage of transport spin polarization of a) TaAs/Ag lateral, b) TaAs/Au lateral, c) TaAs/Ag vertical, and d) TaAs/Au vertical contact geometries.*

The Total (up-spin + down-spin) transmission spectra and the corresponding interpolated color-maps at 1V applied bias on the Γ-centered K_A- K_B plane perpendicular to the transport axis has been presented in Figure 10.17. Lateral contacts have shown a uniform transmission across the transport axis. On the other hand, vertical contacts show various transmission zones. The average

transmission is higher in Ag-contacts for lateral devices, whereas it is almost similar for the vertical contacts for both Ag and Au.

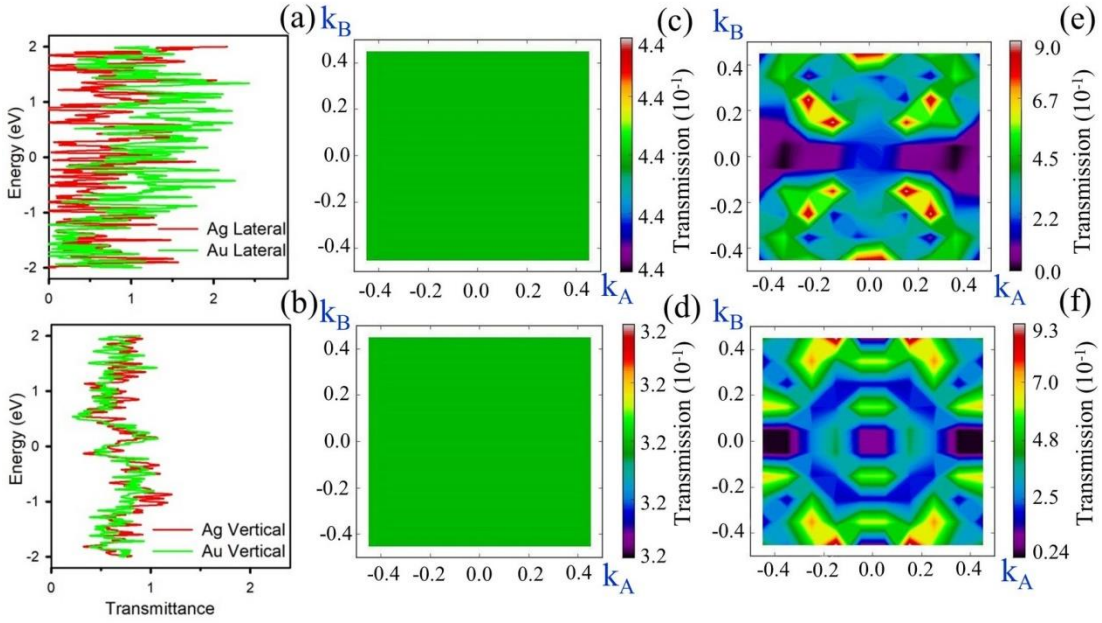

Figure 10.17: *The transmittance of a) lateral TaAs/Ag and TaAs/Au, b) vertical TaAs/Ag and TaAs/Au, transmission color map of c) Ag-lateral, d) Au-lateral, e) Ag-vertical, and f) Au-vertical.*

The local density of states (LDOS), presented in Figure 10.18, however, shows the difference of transport between the two types of devices along the device transport axis. Whereas the lateral contacts show less interfacial scattering at contacts, implying smoother transmission, the vertical contacts have more scattering near the contact boundary. Overall, lateral contacts are more effective in spin-transport in terms of its capability to retain the injected spin-polarization. Thus, while measuring device transport, the type of contact metal and the geometry of contacts have a tremendous impact on spin-polarized device transport.

Since, the lateral contact with the metal layer bonded with both Ta and As are more promising in producing better transport spin polarization, we intend to investigate the nature of the phonon dispersion of TaAs in presence of lateral Au or Ag metal contact. To obtain the nature of the phonon dispersion of TaAs in

presence of Au or Ag metal layer, we have created a smaller system resembling the stacked interface as shown in the first column of Figure 10.19. The band

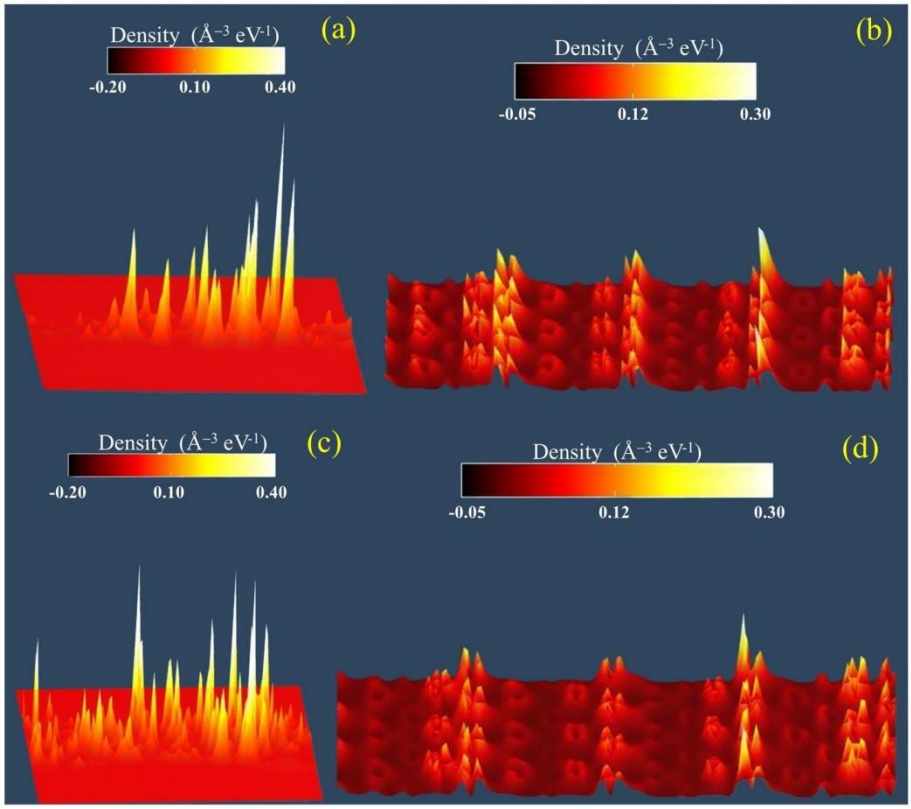

Figure 10.18: *Local density of states (LDOS) for a) Ag-lateral, b) Ag- vertical, c) Au-lateral, and d) Au- vertical contact devices.*

dispersion for bulk TaAs matches with the previous literature [92, 93]. We found the well-dispersed acoustic modes are mainly contributed by the vibration of the heavier Ta-ions and localized optical modes are generated due to vibrations of the lighter As-ions. There is a clear bandgap of ~2.4 eV between optical modes and acoustic modes. It is well-known that due to mass-discrepancy of the contributing ions phonon band-gap occurs [94]. However, in the presence of metal contact with TaAs (stacked interfaces), phonon band-gap vanishes and a significant amount of phonon bands has been generated in the acoustic frequency range, as depicted in Figure 10.19. The density of acoustic phonon bands also induces a corresponding increase of phonon DOS for both metal-stacking systems. The phonon DOS in the acoustic range almost doubles in association with localized peaks. This designates

that the electron-phonon interaction of TaAs/Au and TaAs/Ag may increase at

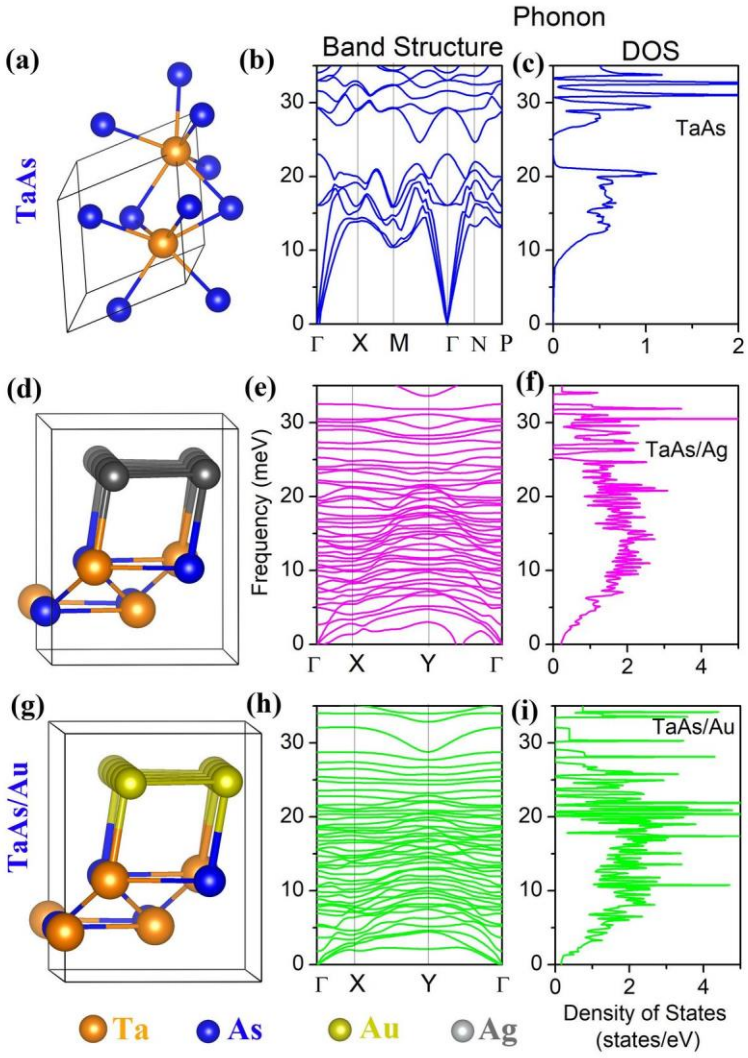

Figure 10.19: *a) Structural representation of TaAs, b) corresponding phonon band structure, and c) DOS of TaAs. d) Structural representation of TaAs/Ag, e) the corresponding phonon band structure and f) DOS of TaAs/Ag. g) Structural representation of TaAs/Au, h) corresponding phonon band structure, and i) DOS of TaAs/Au.*

the stacked interface. Such an increase may be conducive to the occurrence of phonon mediated correlated phenomena, as demanded in reference [35]. Thus, metal plays a great impact on the phonon dispersion and densities of TaAs, signifying the appearance of phonon-induced correlated behavior within the system.

10.2.3. Doping Induced Carrier and Band-gap Modulation in Bulk Versus Nano for Topological Insulators: A Test Case of Stibnite: Bulk crystalline structure used for the host semiconductor is a 120 atom $Sb_{48}S_{72}$ supercell of size ~12×12×22 $Å^3$, whereas Nanorod system consists of a 100-atom assembly of $Sb_{40}S_{60}$, placed in a rectangular box of size ~15×50×22 $Å^3$. For bulk systems, Se-doping sites are randomly chosen, whereas Nanorod doping sites are intentionally kept on the surface. Se-doping, in principle, should be associated with a size-induced chemical pressure because of the difference in the ionic radii of Se^{2-} (1.84 Å) and S^{2-} (1.7 Å). After structural relaxation, the Nanorod is observed to undergo huge surface reconstruction. As a result, the Sb-S-Sb bond angle near the Nanorod surface is ~15° higher than the bulk. A direct consequence of this surface-induced strain is manifested in the direct bandgap of the system. The band-gap of all Nanorod systems is one order of magnitude smaller than the bulk. The bandgap of doped and the pristine systems are listed in Table 10.4. Besides, Se incorporation within the system leads to an increase of bond-length for both Nanorod and bulk.

Table 10.4: *Variation of Bandgap of Sb_2S_3 upon doping with different concentration of Se atom.*

Bulk		Nanorod	
Doping concentration	Bandgap (in eV)	Doping concentration	Bandgap (in eV)
0%	1.18	0%	0.17
2.77%	1.13	3%	0.17
5.5%	1.13	6%	0.17
10%	1.09	10%	0.16

The impact of Se-doping on the electronic structure of bulk Sb_2S_3 and Nanorod has been shown in the APDOS Figure 10.20 and 10.21 respectively.

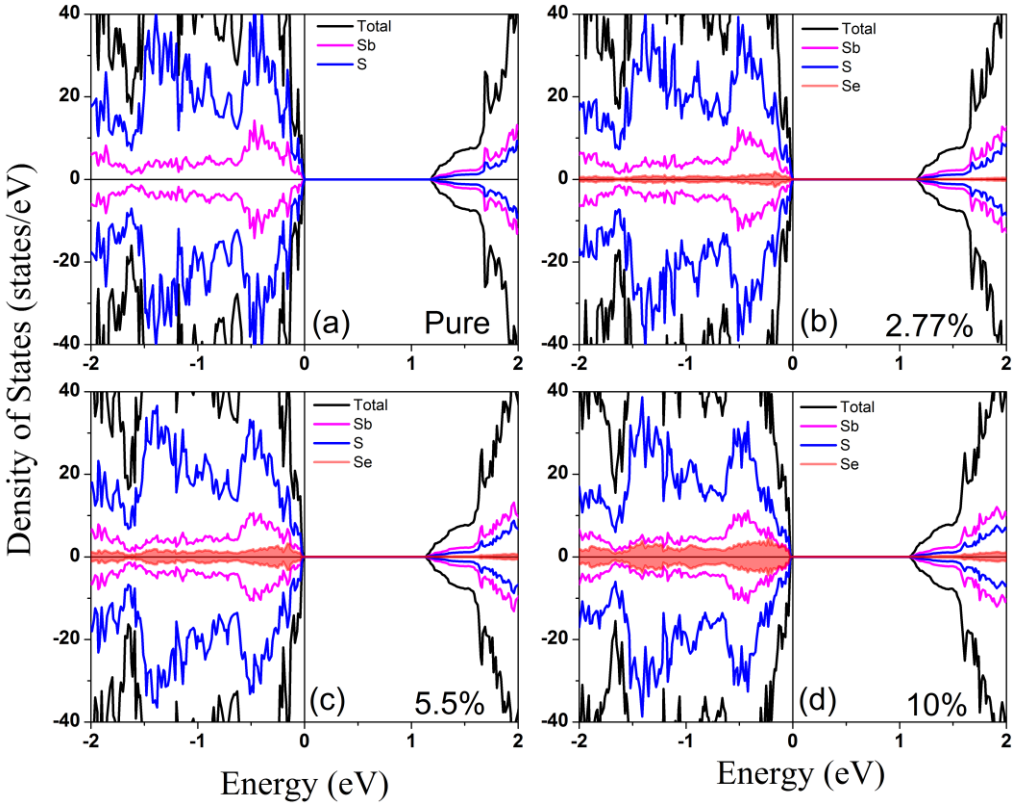

Figure 10.20: *APDOS of a) pure Sb_2S_3 bulk structure and b) 2.77%, c) 5%, and d) 10% Se doped systems respectively.*

For both systems, Se doping percentage is varied from ~3 – 10%. Bulk Sb_2S_3 is semiconducting with a bandgap of ~1.18 eV, with highly hybridized Sb-5*p* and S-3*p* states, mostly contributing to the bottom of the CB and top of the VB. The highest occupied valance bands below E_F is mainly dominated by S-3*p* states with a lesser contribution of Sb-5*p*, whereas the bottom of the conduction band has an almost equal weightage of Sb-5*p* and S-3*p* states [95]. The spin up and spin down components of the DOS are symmetrical, indicating that the pure system is non-magnetic. From the DOS of Se-doped Sb_2S_3, strong *p-p* hybridization is observed between Se-4*p* and Sb-5*p* orbitals. The amount of charge transfer is more from Sb-5*p* to Se-4*p* than to S-3*p* because of the higher electron affinity of Se than S. The presence of filled 3*d* orbitals in Se leads to more effective shielding than S.

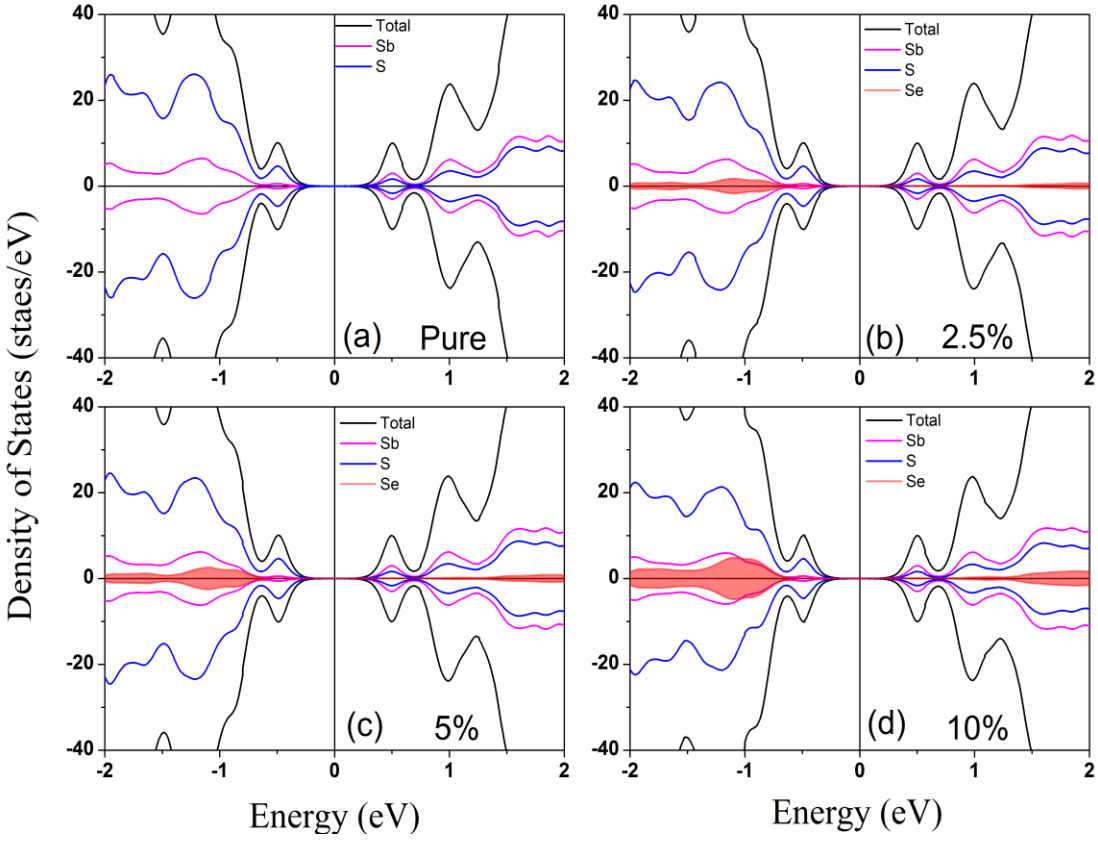

Figure 10.21: *APDOS plot of a) pure Sb_2S_3 bulk structure and b) 2.5%, c) 5% and d) 10% Se doped systems.*

The charge density plot for Sb_2S_3 and Se-doped Sb_2S_3 is presented in Figure 10.22. The charge density plot also shows that there is a huge charge accumulation in the Se center which supports the result of DOS. Therefore, with increasing concentration of Se, the system manifests more *p*-type doping. Interestingly, for the nano-system, there is an enormous surface reconstruction that happened upon structural optimization. This surface reconstruction results in the accumulation of charge near the surface of the Sb_2S_3.

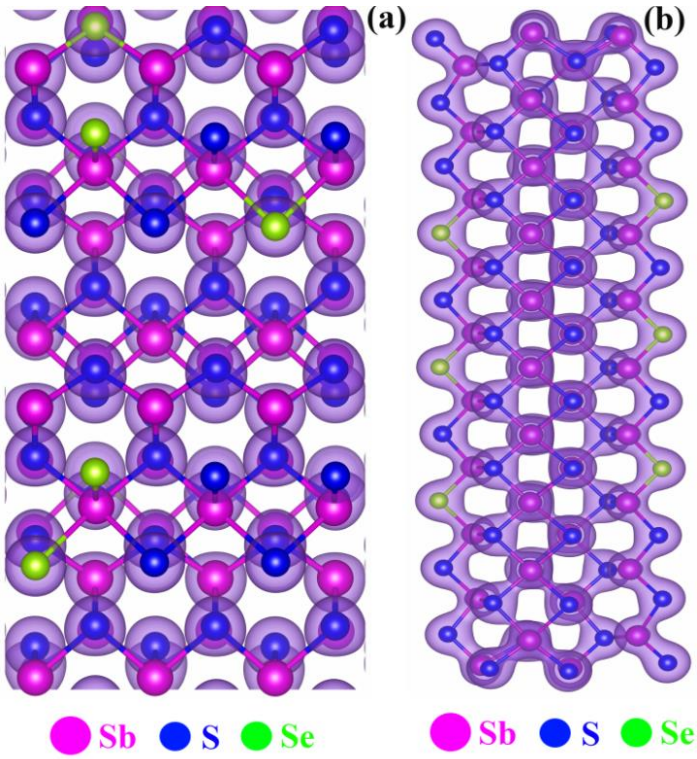

Figure 10.22: *Charge density plot of a) Bulk doped Sb_2S_3 and b) doped Sb_2S_3 Nanorod.*

10.3. Conclusion:

In summary, we have explored the electronic, optical, vibrational, and transport properties and their interdependence with the correlated orbital chemistry of Au-Ag nanostructures to find a clear view of the present experimental scenario. This elaborate study has the following significant results: A) DFT + SOC calculations reveal the interconnectivity of localized orbital chemistry and flat-band induced NFL nature for the embedded or doped NS, which can endorse the strongly correlated phenomena in such NS. This result follows the experimental trends. B) Presence of complete FSN for such NS indicates the possibility of the presence of CDW/SDW type instabilities; C) the dynamic optical response obtained by TDDFT shows that for those specific NS, the value of the dynamic dielectric response is close to zero in the UV-vis energy range; D) the calculated EELS of the nanostructure specifies the existence of plasmons in the frozen low energy band; E) the phonon dispersion curve of the

model system shows that there is dynamic instability in the doped system. In the case of Au-111 or Ag-111 system, there was no negative frequency whereas we found the negative frequency in the embedded and doped system; F) quantum transport result on the simplest model device shows that there is much complexity in the transport properties of Ag/Au based device. Thus, this elaborate study emphasizes the interdependence of nano-structural morphology, localized orbital chemistry, higher carrier effective mass, prediction of FSN-induced CDW/SDW, NEZ behavior, suppression of intra-band plasmonics, and complex quantum transport to highlight the fact that for selective NS morphologies, localized orbital chemistry may lead to the exotic electronic properties widely different from the individual components. A detailed study on more of these systems may produce interdisciplinary interest, linking physical chemistry with physics and materials science.

Moreover, we have investigated the modulation of electronic properties for single and stacked interfaces of the Weyl semimetal TaAs with Noble metal Au and Ag to study the proximity effects at the Noble Metal/Semimetal interfaces. 1) For both of the Metal/TaAs stacked interface systems, there is a simultaneous breaking of both inversion symmetry and time-reversal symmetry. 2) Although pristine TaAs show non-magnetic behavior, TaAs/Au and TaAs/Ag show electron-doped FM and hole-doped AFM ground-states respectively. 3) The transport property of the Metal/Semimetal system displays a heavy increment of transport spin-polarization both at room temperature and low temperature. On average, lateral contacts provide more uniform transport and more spin-polarization with lowering of temperature and are therefore more efficient in spin-transport. 4) The phonon-dispersion for the lateral-contact systems indicates a shrinking phonon bandgap and a boost in the density of state acoustic phonons.

In the last work, we have done a comparative analysis of the electronic structure of bulk Sb_2S_3 and its nanosystems. The effects of Se doping in Sb_2S_3 bulk

and nanosystem is also investigated using first principles DFT calculations. The bandgap changes one order of magnitude while going from the bulk to the Nanorod system due to the strain induced by the surface. Se-doping leads to *p*-type doping nature in bulk whereas in contrary to Nanorod Se doping leads to *n*-type doping. Moreover, it was found that, in the case of nanosystem, there is a huge charge accumulation on the surface of the Sb_2S_3. The present investigation gives a new perspective for the successful regulation of topological insulators' bandgap and doping existence.

References

[1] S. L. Adler, Axial-vector vertex in spinor electrodynamics, *Phys. Rev.* 177 (1969) 2426.

[2] L. Aggarwal, A. Gaurav, G. S. Thakur, Z. Haque, A. K. Ganguli, G. Sheet, Unconventional superconductivity at mesoscopic point contacts on the 3D Dirac semimetal Cd_3As_2, *Nat. Comm.* 15 (2016) 32.

[3] L. Aggarwal, S. Gayen, S. Das, R. Kumar, V. Süß, C. Felser, C. Shekhar, G. Sheet, Mesoscopic superconductivity and high spin polarization coexisting at metallic point contacts on Weyl semimetal TaAs, *Nat. Comm.* 8 (2017) 13974.

[4] M. Hooda, P. Kumar, V. Balakrishnan, C. Yadav, Observations of zero electrical resistance of Au-Ag thin films near room temperature, *arXiv preprint arXiv:1906.00708* (2019).

[5] S. Islam, R. Mahadevu, S. K. Saha, P. S. Mahapatra, B. Bhattacharyya, D. K. Thapa, T. P. Sai, S. Patil, A. Pandey, A. Ghosh, Current-voltage characteristics in Ag/Au nanostructures at resistive transitions, *arXiv preprint arXiv:1906.02291* (2019).

[6] D. K. Thapa, S. Islam, S. K. Saha, P. S. Mahapatra, B. Bhattacharyya, T. P. Sai, R. Mahadevu, S. Patil, A. Ghosh, A. Pandey, Coexistence of diamagnetism and vanishingly small electrical resistance at ambient temperature and pressure in nanostructures, *arXiv preprint arXiv:1807.08572* (2019).

[7] D. K. Thapa, S. K. Saha, B. Bhattacharyya, G. P. Rajasekar, R. Mahadevu, A. Pandey, Unconventional optical response in engineered Au-Ag nanostructures, *arXiv preprint arXiv:1906.05342* (2019).

[8] H. Urayama, H. Yamochi, G. Saito, K. Nozawa, T. Sugano, M. Kinoshita, S. Sato, K. Oshima, A. Kawamoto, J. Tanaka, A new ambient pressure organic superconductor based on BEDT-TTF with T_c higher than 10 K (T_c= 10.4 K), *Chem. Lett.* 17 (1988) 55.

[9] S. I. Uchida, High temperature superconductivity: The road to higher critical temperature, *Springer*, Uchida, Japan, 2014.

[10] A. W. Sleight, J. Gillson, P. Bierstedt, High-temperature superconductivity in the $BaPb_{1-x}Bi_xO_3$ system, *Solid State Commun.* 88 (1993) 841.

[11] A. Alu, M. G. Silveirinha, A. Salandrino, N. Engheta, Epsilon-near-zero metamaterials and electromagnetic sources: Tailoring the radiation phase pattern, *Phys. Rev. B* 75 (2007) 155410.

[12] R. Maas, J. Parsons, N. Engheta, A. Polman, Experimental realization of an epsilon-near-zero metamaterial at visible wavelengths, *Nat. Photonics* 7 (2013) 907.

[13] C. Dellagiacoma, T. Lasser, O.J.F. Martin, A. Degiron, J. J. Mock, D. R. Smith, Simulation of complex plasmonic circuits including bends, *Opt. Express* 19 (2011) 18979.

[14] M. Hochberg, T. Baehr-Jones, C. Walker, A. Scherer, Integrated plasmon and dielectric waveguides, *Opt. Express* 12 (2004) 5481.

[15] J. L. West, N. J. Halas, Engineered nanomaterials for biophotonics applications: Improving sensing, imaging, and therapeutics, *Annu. Rev. Biomed. Eng.* 5 (2003) 285.

[16] H. A. Atwater, A. Polman, Plasmonics for improved photovoltaic devices, *Nat. Mater.* 9 (2010) 205.

[17] M. Matthew, Analysis and design of metamaterials, (Doctoral dissertation, ETH Zurich), Zurich, Switzerland, 2010.

[18] B. Jokanović, R. H. Geschke, T. S. Beukman, V. Milošević, Metamaterials: Characteristics, design and microwave applications, *SAIEE Afr. Res. J.* 101 (2010) 82.

[19] P. Chaturvedi, Optical metamaterials: Design, characterization and applications, (Doctoral dissertation, University of Illinois at Urbana-Champaign), Urbana, Illinois, USA, 2009.

[20] Y. L. Fu, C. K. Li, Z. J. Zhang, H. B. Sang, W. Cheng, F. S. Zhang, Electronic properties of defects in Weyl semimetal tantalum arsenide, *Chin. Phys. B* 27 (2018) 097101.

[21] O. Deb, D. Sen, Generating surface states in a Weyl semimetal by applying electromagnetic radiation, *Phys. Rev. B* 95 (2017) 144311.

[22] H. Weyl, Elektron and Gravitation, *Z. Phys.* 56 (1929) 330.

[23] H. Gao, J. W. Venderbos, Y. Kim, A. M. Rappe, Topological semimetals from first principles, *Annu. Rev. Mater. Res.* 49 (2019) 153.

[24] J. S. Lamb, J. A. Roberts, Time-reversal symmetry in dynamical systems: A survey, *Physica D* 112 (1998) 1.

[25] M. Z. Hasan, S. Y. Xu, I. Belopolski, S. M. Huang, Discovery of Weyl fermion semimetals and topological Fermi arc states, *Ann. Rev. Cond. Matt. Phys.* 8 (2017) 289.

[26] B. Yan, C. Felser, Topological materials: Weyl semimetals, *Ann. Rev. Cond. Matt. Phys.* 8 (2017) 337.

[27] S. Jia, S. Y. Xu, M. Z. Hasan, Weyl semimetals, Fermi arcs and chiral anomalies, *Nat. Mater.* 15 (2016) 1140.

[28] H. Wang, H. Wang, Y. Chen, J. Luo, Z. Yuan, J. Liu, Y. Wang, S. Jia, X. J. Liu, J. Wei, Tip induced unconventional superconductivity on Weyl semimetal TaAs, *Sci. Bull.* 62 (2016) 425.

[29] H. Wang, H. Wang, Y. Chen, J. Luo, Z. Yuan, J. Liu, Y. Wang, S. Jia, X. J. Liu, J. Wei, Reply to Comment on" Tip induced unconventional superconductivity on Weyl semimetal TaAs", *arXiv preprint arXiv:1607.02886* (2016).

[30] S. Gayen, L. Aggarwal, G. Sheet, Comment on" Tip induced unconventional superconductivity on Weyl semimetal TaAs"[arXiv: 1607.00513], *arXiv preprint arXiv:1607.01405* (2016).

[31] C. L. Kane, E. J. Mele, Z_2 topological order and the quantum spin hall effect, *Phys. Rev. Lett.* 95 (2005) 146802.

[32] R. Shankar, Topological insulators: A review, *arXiv preprint arXiv:1804.06471* (2018).

[33] S. M. Young, S. Zaheer, J. C. Teo, C. L. Kane, E. J. Mele, A. M. Rappe, Dirac semimetal in three dimensions, *Phys. Rev. Lett.* 108 (2012) 140405.

[34] Z. Wang, Y. Sun, X. Q. Chen, C. Franchini, G. Xu, H. Weng, X. Dai, Z. Fang, Dirac semimetal and topological phase transitions in A_3Bi (A= Na, K, Rb), *Phys. Rev. B* 85 (2012) 195320.

[35] Z. Wang, H. Weng, Q. Wu, X. Dai, Z. Fang, Three-dimensional dirac semimetal and quantum transport in Cd_3As_2, *Phys. Rev. B* 88 (2013) 125427.

[36] B. J. Yang, N. Nagaosa, Classification of stable three-dimensional Dirac semimetals with nontrivial topology, *Nat. Comm.* 5 (2014) 4898.

[37] G. Chang, S. Y. Xu, H. Zheng, C. C. Lee, S. M. Huang, I. Belopolski, D. S. Sanchez, G. Bian, N. Alidoust, T. R. Chang, Quasi-particle interferences of the Weyl semimetals TaAs and NbP, *Phys. Rev. Lett.* 116 (2015) 066601.

[38] S. Y. Xu, I. Belopolski, D. S. Sanchez, C. Zhang, G. Chang, C. Guo, G. Bian, Z. Yuan, H. Lu, T. R. Chang, Experimental discovery of a topological Weyl semimetal state in TaP, *Sci. Adv.* 1 (2015) 1501092.

[39] B. Lv, H. Weng, B. Fu, X. Wang, H. Miao, J. Ma, P. Richard, X. Huang, L. Zhao, G. Chen, Experimental discovery of Weyl semimetal TaAs, *Phys. Rev. X* 5 (2015) 031013.

[40] X. Huang, L. Zhao, Y. Long, P. Wang, D. Chen, Z. Yang, H. Liang, M. Xue, H. Weng, Z. Fang, Observation of the chiral-anomaly-induced negative magnetoresistance in 3D Weyl semimetal TaAs, *Phys. Rev. X* 5 (2015) 031023.

[41] H. Weng, C. Fang, Z. Fang, B. A. Bernevig, X. Dai, Weyl semimetal phase in noncentrosymmetric transition-metal monophosphides, *Phys. Rev. X* 5 (2015) 011029.

[42] S. M. Huang, S. Y. Xu, I. Belopolski, C. C. Lee, G. Chang, B. Wang, N. Alidoust, G. Bian, M. Neupane, A. Bansil, Theoretical discovery/prediction: Weyl

semimetal states in the TaAs material (TaAs, NbAs, NbP, TaP) class, *Nat. Comm.* 6 (2015) 7373.

[43] S. Parameswaran, T. Grover, D. Abanin, D. Pesin, A. Vishwanath, Probing the chiral anomaly with nonlocal transport in three-dimensional topological semimetals, *Phys. Rev. X* 4 (2014) 031035.

[44] H. B. Nielsen, M. Ninomiya, The Adler-Bell-Jackiw anomaly and Weyl fermions in a crystal, *Phys. Rev. B* 130 (1983) 389.

[45] J. S. Bell, R. Jackiw, A PCAC puzzle: $\pi_0 \rightarrow \gamma\gamma$ in the σ-model, *Nuovo Cimento A* 60 (1969) 47.

[46] M. Stone, F. Gaitan, Topological charge and chiral anomalies in fermi superfluids, *Annal. Phys.* 178 (1987) 89.

[47] G. Volovik, Peculiarities in the dynamics of superfluid ^{3}He-A: Analog of chiral anomaly and of zero-charge, *Sov. Phys. JETP Lett.* 65 (1987) 1193.

[48] P. Wang, A theory of nonequilibrium steady states in quantum chaotic systems, *J. Stat. Mech. Theory Expt.* 2017 (2017) 093105.

[49] A. D. DeAngelis, K. C. Kemp, N. Gaillard, K. S. Kim, Antimony (III) sulfide thin films as a photoanode material in photocatalytic water splitting, *ACS Appl. Mater. Interfaces* 8 (2016) 8445.

[50] D. B. Salunkhe, S. S. Gargote, D. P. Dubal, W. B. Kim, B. R. Sankapal, Sb_2S_3 nanoparticles through solution chemistry on mesoporous TiO_2 for solar cell application, *Chem. Phys. Lett.* 554 (2012) 150.

[51] R. Boughalmi, A. Boukhachem, M. Kahlaoui, H. Maghraoui, M. Amlouk, Physical investigations on Sb_2S_3 sprayed thin film for optoelectronic applications, *Mater. Sci. Semicond. Process.* 26 (2014) 593.

[52] T. Ben Nasr, H. Maghraoui-Meherzi, N. Kamoun-Turki, First-principles study of electronic, thermoelectric and thermal properties of Sb_2S_3, *J. Alloys Compd.* 663 (2016) 123.

[53] E. Zimmermann, T. Pfadler, J. Kalb, J. A. Dorman, D. Sommer, G. Hahn, J. Weickert, L. Schmidt-Mende, Toward high-efficiency solution-processed planar heterojunction Sb_2S_3 solar cells, *Adv. Sci.* 2 (2015) 1500059.

[54] T. K. Maji, K. Vaibhav, R. Hawaldar, K. Adarsh, S. K. Pal, D. Karmakar, Intriguing electronic and optical prospects of FCC bimetallic heterostructures: Large area interface versus embedded and doped nanostructures, *Phys. Chem. Chem. Phys.* 22 (2020) 16314.

[55] A. Biswas, S. Parmar, A. Jana, R. J. Chaudhary, S. Ogale, Absence of superconductivity in pulsed laser deposited Au/Ag modulated nanostructured thin films, *arXiv preprint arXiv:1808.10699* (2018).

[56] D. S. Dessau, Z. X. Shen, D. M. King, D. S. Marshall, L. W. Lombardo, P. H. Dickinson, A. G. Loeser, J. DiCarlo, C. H. Park, A. Kapitulnik, W. E. Spicer, Key features in the measured band structure of $Bi_2Sr_2CaCu_2O_{8+\delta}$: Flat bands at E_F and Fermi surface nesting, *Phys. Rev. Lett.* 71 (1993) 2781.

[57] H. Maeda, Y. Tanaka, M. Fukutomi, T. Asano, A new high-T_c oxide superconductor without a rare earth element, *Jpn. J. Appl. Phys.* 27 (1988) L209.

[58] J. P. Pouget, The Peierls instability and charge density wave in one-dimensional electronic conductors, *C. R. Phys.* 17 (2016) 332.

[59] V. Brouet, W. Yang, X. Zhou, Z. Hussain, N. Ru, K. Shin, I. Fisher, Z. Shen, Fermi surface reconstruction in the CDW state of $CeTe_3$ observed by photoemission, *Phys. Rev. Lett.* 93 (2004) 126405.

[60] M. H. Whangbo, E. Canadell, P. Foury, J. P. Pouget, Hidden Fermi surface nesting and charge density wave instability in low-dimensional metals, *Science* 252 (1991) 96.

[61] S. Dugdale, Life on the edge: A beginner's guide to the Fermi surface, *Phys. Scr.* 91 (2016) 053009.

[62] X. Zhu, Y. Cao, J. Zhang, E. Plummer, J. Guo, Classification of charge density waves based on their nature, *Proc. Natl. Acad. Sci.* 112 (2015) 2367.

[63] M.D. Johannes, I. Mazin, Fermi surface nesting and the origin of charge density waves in metals, *Phys. Rev. B* 77 (2008) 165135.

[64] S. Chakravarty, H. Y. Kee, Fermi pockets and quantum oscillations of the Hall coefficient in high-temperature superconductors, *Proc. Natl. Acad. Sci.* 105 (2008) 8835.

[65] M. Sunagawa, T. Ishiga, K. Tsubota, T. Jabuchi, J. Sonoyama, K. Iba, K. Kudo, M. Nohara, K. Ono, H. Kumigashira, Characteristic two-dimensional Fermi surface topology of high-T_c iron-based superconductors, *Sci. Rep.* 4 (2014) 4381.

[66] R. Arita, H. Ikeda, Is Fermi-surface nesting the origin of superconductivity in iron pnictides?: A fluctuation–exchange-approximation study, *J. Phys. Soc. Jpn.* 78 (2009) 113707.

[67] M. L. Cohen, P. W. Anderson, Comments on the maximum superconducting transition temperature, *AIP Conf. Proc.* 4 (1972) 17.

[68] K. Terashima, Y. Sekiba, J. Bowen, K. Nakayama, T. Kawahara, T. Sato, P. Richard, Y. M. Xu, L. Li, G. Cao, Fermi surface nesting induced strong pairing in iron-based superconductors, *Proc. Natl. Acad. Sci.* 106 (2009) 7330.

[69] S. Botti, A. Fourreau, F. Nguyen, Y. O. Renault, F. Sottile, L. Reining, Energy dependence of the exchange-correlation kernel of time-dependent density functional theory: A simple model for solids, *Phys. Rev. B* 72 (2005) 125203.

[70] M. Dadsetani, A.R. Omidi, Ab initio study on optical properties of glycine sodium nitrate: A novel semiorganic nonlinear optical crystal, *RSC Adv.* 5 (2015) 90559.

[71] J. Harl, The linear response function in density functional theory, (Doctoral dissertation, University of Vienna), Vienna, Austria, 2008.

[72] R. Bauer, A. Schmid, P. Pavone, D. Strauch, Electron-phonon coupling in the metallic elements Al, Au, Na, and Nb: A first-principles study, *Phys. Rev. B* 57 (1998) 11276.

[73] Y. Pan, S. Li, M. Ye, R. Quhe, Z. Song, Y. Wang, J. Zheng, F. Pan, W. Guo, J. Yang, Interfacial properties of monolayer $MoSe_2$–metal contacts, *J. Phys. Chem. C* 120 (2016) 13063.

[74] K. Liu, K. Nagodawithana, P. C. Searson, C. L. Chien, Perpendicular giant magnetoresistance of multilayered Co/Cu nanowires, *Phys. Rev. B* 51 (1995) 7381.

[75] I. Liberal, N. Engheta, Erratum: Near-zero refractive index photonics, *Nat. Photonics* 11 (2017) 264.

[76] M. Z. Alam, I. De Leon, R. W. Boyd, Large optical nonlinearity of indium tin oxide in its epsilon-near-zero region, *Science* 352 (2016) 795.

[77] K. B. Mogensen, K. Kneipp, Size-dependent shifts of plasmon resonance in silver nanoparticle films using controlled dissolution: Monitoring the onset of surface screening effects, *J. Phys. Chem. C* 118 (2014) 28075.

[78] I. Zorić, M. Zäch, B. Kasemo, C. Langhammer, Gold, platinum, and aluminum nanodisk plasmons: Material independence, subradiance, and damping mechanisms, *ACS Nano* 5 (2011) 2535.

[79] P. Modak, A. K. Verma, Pressure induced multi-centre bonding and metal–insulator transition in $PtAl_2$, *Phys. Chem. Chem. Phys.* 21 (2019) 13337.

[80] T. Yildirim, Ferroelectric soft phonons, charge density wave instability, and strong electron-phonon coupling in BiS_2 layered superconductors: A first-principles study, *Phys. Rev. B* 87 (2013) 020506.

[81] J. Yang, X. Wen, H. Xia, R. Sheng, Q. Ma, J. Kim, P. Tapping, T. Harada, T. W. Kee, F. Huang, Y. B. Cheng, M. Green, A. Ho-Baillie, S. Huang, S. Shrestha, R. Patterson, G. Conibeer, Acoustic-optical phonon up-conversion and hot-phonon bottleneck in lead-halide perovskites, *Nat. Commun.* 8 (2017) 14120.

[82] Z. An-Min, Z. Qing-Ming, Electron—phonon coupling in cuprate and iron-based superconductors revealed by Raman scattering, *Chin. Phys. B* 22 (2013) 087103.

[83] T. K. Maji, K. Vaibhav, S. K. Pal, K. Majumdar, K. Adarsh, D. Karmakar, Intricate modulation of interlayer coupling at the graphene oxide/$MoSe_2$ interface:

Application in time-dependent optics and device transport, *Phys. Rev. B* 99 (2019) 115309.

[84] S. Smidstrup, T. Markussen, P. Vancraeyveld, J. Wellendorff, J. Schneider, T. Gunst, B. Verstichel, D. Stradi, P. A. Khomyakov, U .G. Vej-Hansen, QuantumATK: An integrated platform of electronic and atomic-scale modelling tools, *J. Phys. Cond. Mat.* 32 (2019) 015901.

[85] C. C. Lee, S. Y. Xu, S. M. Huang, D. S. Sanchez, I. Belopolski, G. Chang, G. Bian, N. Alidoust, H. Zheng, M. Neupane, Fermi surface interconnectivity and topology in Weyl fermion semimetals TaAs, TaP, NbAs, and NbP, *Phys. Rev. B* 92 (2015) 235104.

[86] M. Wang, C. Zhang, X. Lu, G. Tan, H. Luo, Y. Song, M. Wang, X. Zhang, E. Goremychkin, T. Perring, Doping dependence of spin excitations and its correlations with high-temperature superconductivity in iron pnictides, *Nat. Comm.* 4 (2013) 2874.

[87] E. H. da Silva Neto, P. Aynajian, A. Frano, R. Comin, E. Schierle, E. Weschke, A. Gyenis, J. Wen, J. Schneeloch, Z. Xu, S. Ono, G. Gu, M. Le Tacon, A. Yazdani, Ubiquitous interplay between charge ordering and high-temperature superconductivity in cuprates, *Science* 343 (2014) 393.

[88] E. Liu, Y. Sun, N. Kumar, L. Muechler, A. Sun, L. Jiao, S. Y. Yang, D. Liu, A. Liang, Q. Xu, J. Kroder, V. Süß, H. Borrmann, C. Shekhar, Z. Wang, C. Xi, W. Wang, W. Schnelle, S. Wirth, Y. Chen, S. T. B. Goennenwein, C. Felser, Giant anomalous Hall effect in a ferromagnetic kagome-lattice semimetal, *Nat. Phys.* 14 (2018) 1125.

[89] Q. Xu, E. Liu, W. Shi, L. Muechler, J. Gayles, C. Felser, Y. Sun, Topological surface Fermi arcs in the magnetic Weyl semimetal $Co_3Sn_2S_2$, *Phys. Rev. B* 97 (2018) 235416.

[90] L. Muechler, E. Liu, J. Gayles, Q. Xu, C. Felser, Y. Sun, Emerging chiral edge states from the confinement of a magnetic Weyl semimetal in $Co_3Sn_2S_2$, *Phys. Rev. B* 101 (2020) 115106.

[91] A. A. Zyuzin, S. Wu, A. A. Burkov, Weyl semimetal with broken time reversal and inversion symmetries, *Phys. Rev. B* 85 (2012) 165110.

[92] J. Buckeridge, D. Jevdokimovs, C. Catlow, A. Sokol, Bulk electronic, elastic, structural, and dielectric properties of the Weyl semimetal TaAs, *Phys. Rev. B* 93 (2016) 125205.

[93] T. Ouyang, H. Xiao, C. Tang, M. Hu, J. Zhong, Anisotropic thermal transport in Weyl semimetal TaAs: A first principles calculation, *Phys. Chem. Chem. Phys.* 18 (2016) 16709.

[94] H. Kim, First-principles calculations of the lattice instability and the symmetry-lowering modulation of PtSi, *J. Korean Phys. Soc.* 66 (2015) 612.

[95] I.L. Validžić, M. Mitrić, N. Abazović, B. Jokić, A. Milošević, Z. Popović, F. Vukajlović, Structural analysis, electronic and optical properties of the synthesized Sb_2S_3 nanowires with small band gap, *Semicond. Sci. Technol.* 29 (2014) 035007.

Chapter 11

Combined Experimental and Computational Studies on Organic-Inorganic Nanohybrid Heterostructure for their Manifold Applications

11.1. Introduction:

Organic-inorganic nanohybrids (NHs) composed of organic and inorganic components have attracted intense attention in various field systems due to their favorable physicochemical properties [1, 2]. Organic materials are readily synthesized, can provide inorganic materials with remarkably improved stability, and can be polyfunctionalized to allow tailoring of the resulting optical, electronic, and chemical properties [2-4]. Completely novel or improved physical and chemical properties can result from strong interactions between the organic and inorganic units. This organic-inorganic NH can be used in various fields including solar light harvesting [5], drug delivery systems [6], enhanced medicinal activity [7], sensing application [8], etc.

Metal-organic complexes (MOCs) are a class of organic-inorganic hybrid substances composed of metal linked with organic moiety [9]. In recent times, MOC has rapidly grown as one of the most dynamic areas of coordination chemistry research fields due to its enormous potential application in various fields including storage, catalysis, sensing, optoelectronics, adsorption, biomedical imaging, enhanced medicinal activity, and so forth [7, 10-13]. Although MOC has many diverse applications, sometimes toxic metal-contaminated organometallic compounds can be very much harmful to the human body. Upon contact with biological fluids, various transformations can take place on the MOC containing toxic metal, which can be harmful to the human body [14, 15]. The metal exchange

technique (MET) is a beneficial strategy to modify the MOC by exchanging the metal node, which can change the property of the organometallic compound [16, 17].

Heavy metals related pollutions are extremely dangerous, as it directly affects human physiology. It also enters the living organisms including microbes and plants through the food-chain. Mercury is reckoned as the most toxic heavy metal among all [18]. One of the most recurrent sources of mercury pollution is an aqueous stable oxidized divalent mercuric ion (Hg^{2+}), possessing high stability in normal environmental conditions [19]. Contaminated and untreated industrial wastes are the main source of stable Hg pollutants, entering the human food chain, mostly via usable water [20]. Those toxic metals have a high tendency to chelate with essential food elements, and through the food chain, it directly enters the human body causing hazardous health effects. Curcumin is a very well-known chelating agent as the turmeric powder is rich in curcuminoids, proteins, and carbohydrates [21]. There are a lot of available metal-binding sites within Curcumin [22]. The Metal chelating tendency of Curcumin sometimes exhibits adverse effects when it undergoes complexation with toxic heavy metal ions like lead, mercury, cadmium, and arsenic. The water-soluble form of mercury (Hg^{2+}) can easily contaminate Curcumin at the time of cultivation or transport. Moreover, contaminated Curcumin used in beauty products may cause toxic metal contamination to the skin [23]. In the present work, we have shown a possible way to exchange the toxic Hg from the Hg-Curcumin complex with another chelating metal, copper, via a simple chemical metal exchange technique. With proper Cu concentration and incubation time, it is possible to replace most of the Hg from the complex. It is found that the LD50 value of Hg is manifold higher than Cu [14]. The daily consumption limit of Hg is 20 μg/day whereas for Cu the consumption limit is ~4mg/day [24]. Although it has been reported that Cu shows very little toxicity; but at a lower concentration of Cu, it is almost harmless to the body [24-

26]. Moreover, being a vital part of several enzymes, Cu is an essential micronutrient up to a certain concentration [26].

The surface plasmon resonance (SPR) band of Ag-NP can be heavily modulated in presence of Hg^{2+} ions. This property can be utilized to detect free Hg^{2+} ions efficiently in an aqueous medium [19]. We have used this mechanism to detect free Hg ions in the aqueous medium after the transmetalation reaction. In summary, a relatively cost-effective and field-deployable technique has been used to detect the free Hg from the Curcumin complex.

Organic-inorganic NHs are becoming popular for their potential biological applications including diagnosis and treatment of cancerous cells [27]. Great efforts have been made to design and fabricate versatile NHs that can be useful in the field of drug delivery [4, 28]. Nowadays, with the demanding requirements for personalized therapy, great efforts have been made to monitor the response of treatment and the concept of theranostics offers new opportunities. In this regard, Organic-inorganic NHs could be promising candidates for the new generation biomaterials.This motivates us to work on the development of an NH for the diagnosis and therapy of colorectal cancer. Target specific delivery of a drug in the case of PDT is the most important part of the efficacy of the treatment [29]. In this regard, folic acid (FA) is a stable and cheap ligand which can target cancer cell via folate receptor (FR) [30]. Taking advantage of FRs targeting cancer cells is a well-known strategy due to the overexpression of FR in a variety of cancer cells including breast, kidney, colon, ovaries, cervix, and renal cell carcinomas [31-40]. In this work, we developed a simple one-step hydrothermal synthesis of FA templated water-soluble magnetic iron oxide nanoparticles (NPs) (FA-Fe_2O_3). Detailed spectroscopic characterization was performed with the help of FTIR, UV-Vis, fluorescence, Raman and time-resolved fluorescence spectroscopy (TCSPC). Picosecond resolved Förster resonance energy transfer (FRET) was used to confirm the attachment of FA to Fe_2O_3 at the molecular level. Photoinduced

enhanced ROS generation of FA-Fe_2O_3 with respect to Fe_2O_3 was monitored by dichlorofluorescein (DCFH) oxidation. Magnetic property measurements were done using VSM. Anti-cancer activity and cellular uptake studies have been done on human colorectal carcinoma (HCT 116) cell line. We have performed a relaxometry study and MRI study of synthesized FA-Fe_2O_3 to consider its potential use as an MRI contrast agent for diagnosis.

11.2. Results and Discussion:

11.2.1. A Combined Spectroscopic and Ab initio Study on Transmetalation of a Polyphenol for Potential Purification Strategy of Food Additive [41]: Curcumin (commonly known as turmeric) is a yellow chemical produced by Curcuma longa which has many applications. Curcumin has many void spaces within the system, because of that, it is prone to metal chelation. However, the metal complexation of Curcumin causes a significant transformation in their electronic structures. As a result of it, colorimetric changes may be observed in metal Curcumin with respect to pure Curcumin. From this change, it is possible to detect the purity of Curcumin. But, the problem arises when metalation in Curcumin doesn't change the color. In that case, another spectroscopic tool is required to detect the contamination. In our present work, we are keen to detect and decontaminate toxic Hg from the Curcumin complex. The main problem of Hg-Curcumin contamination is Hg-Curcumin complex cannot be distinguished from Curcumin by simple visualization, because of the same color. Figure 11.1a shows the colorimetric image of Hg-Curcumin and Curcumin of the same concentration. There is an almost insignificant difference in the color of those systems. The absorbance of Curcumin and Hg-Curcumin is depicted in Figure 11.1b. The absorption peak of Curcumin is at 424 nm due to π-π^* transition, whereas Hg-Curcumin shows absorption maxima at 427 nm. There is no significant change in the absorption of Hg-Curcumin after complexation. Hence, it is very much challenging to detect as well as remove Hg from the Curcumin complex to avoid

hazardous contamination. In the present work, we have described a new strategy to detect and decontaminate toxic Hg from the Hg-Curcumin complex. The steady-state emission spectra of Curcumin and Hg-Curcumin at a constant optical density (OD) are shown in Figure 11.1c. A significant decrement of emission intensity of Curcumin is found after metal attachment, indicating the generation of new non-radiative processes. The fluorescence quenching of Curcumin in the presence of Hg metal puts a clear indication of attachment of Curcumin with metal. Picosecond resolved fluorescence decay of Curcumin and Hg-Curcumin has been recorded to further confirm the attachment of metal in the Curcumin complex. Figure 11.1d depicts the decay profile of Curcumin and Hg-Curcumin in a glycerol medium. The decay profile of Curcumin shows a bi-exponential component whose shorter component (446 ps) corresponds to solvation dynamics and longer component (1.08 ns) comes due to excited-state intramolecular hydrogen atom transfer within the system [42]. An additional faster component of ~100 ps has been generated after the metalation of Curcumin. The shorter lifetime could be attributed to the photoinduced electron transfer process from Curcumin to metal ions [43]. The positively charged metal ion in the metal Curcumin complex behaves as an electron acceptor and the ligand Curcumin in the metallo-Curcumin complex acts as an electron donor to the metal in the complex system [44]. The detail of the time scale has been tabulated in Table 11.1.

Table 11.1: *Picosecond resolved fluorescence transient data of Curcumin and metallo–Curcumin sample. Numbers in parentheses indicate relative contributions.*

System	τ_1 (ps)	τ_2 (ps)	τ_3 (ps)	τ_{avg} (ps)
Curcumin	-	446 (65.51)	1081 (34.49)	664.96
Hg-Curcumin	85 (58.82)	274 (35.29)	855 (5.88)	197.00
Cu-Curcumin	126 (66.22)	521(31.08)	2457 (2.70)	311.70
Cu-Hg-Curcumin	87 (59.25)	342 (33.33)	1309 (7.41)	262.51

Herein, we use a wet chemical transmetalation method to replace Hg metal attached with Cu metal in the metal-Curcumin complex. The transformation process was evaluated by allowing the Hg-Curcumin to react in the aqueous solution of copper (II) acetate. The pictorial image of Hg-Curcumin, Cu-Curcumin, and Cu-treated Hg-Curcumin with the same concentration is displayed in Figure 11.2a. The color of Hg-Curcumin is light yellow and Cu-Curcumin is deep brown, whereas Cu-treated Hg-Curcumin shows color in between. The absorbance

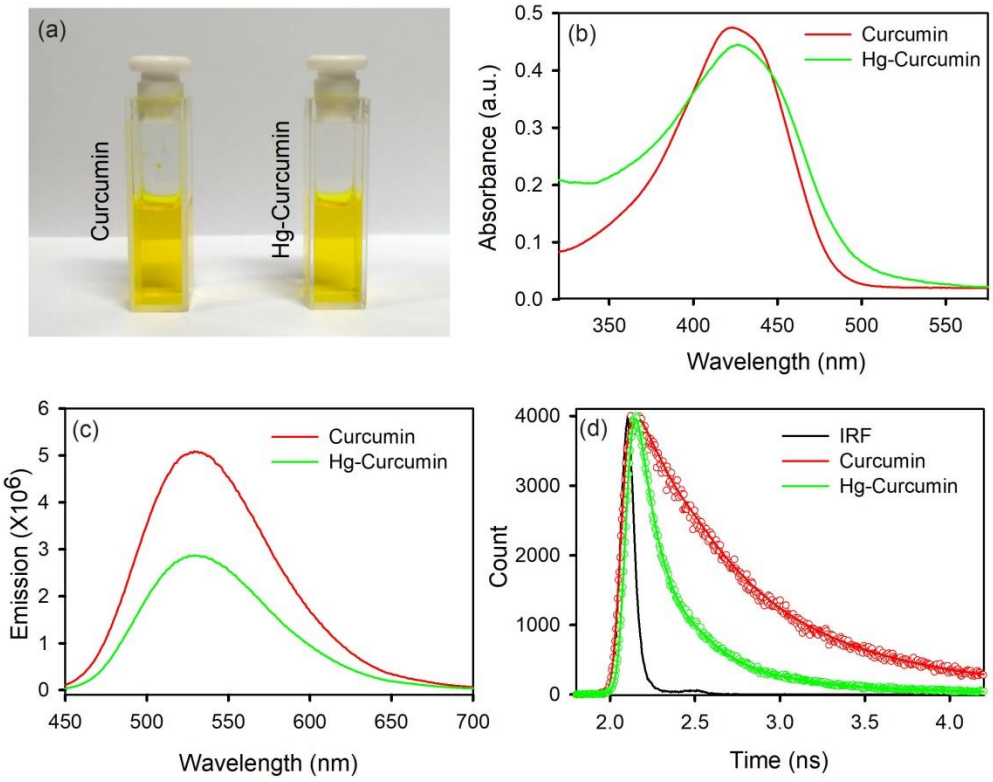

Figure 11.1: *a) Pictorial image of Hg-Curcumin and Curcumin, b) Absorption spectra of Curcumin and Hg-Curcumin, c) Emission spectra of Curcumin, and Hg-Curcumin and d) time-resolved fluorescence decay of Curcumin and Hg-Curcumin.*

spectra of pure Hg-Curcumin, Cu-Curcumin, and Cu-treated Hg-Curcumin complex is depicted in Figure 11.2b. It is very much evident from Figure 11.2b that there is a significant change in the absorption spectra of Hg-Curcumin and Cu-Curcumin. Cu-Curcumin shows a red-shifted absorption peak at ~447 nm. This redshift can be attributed to the generation of new electronic states at lower

energy. Another reason for the shift may be the participation of the carbonyl group in metal Curcumin complex formation [45]. However, Cu-treated

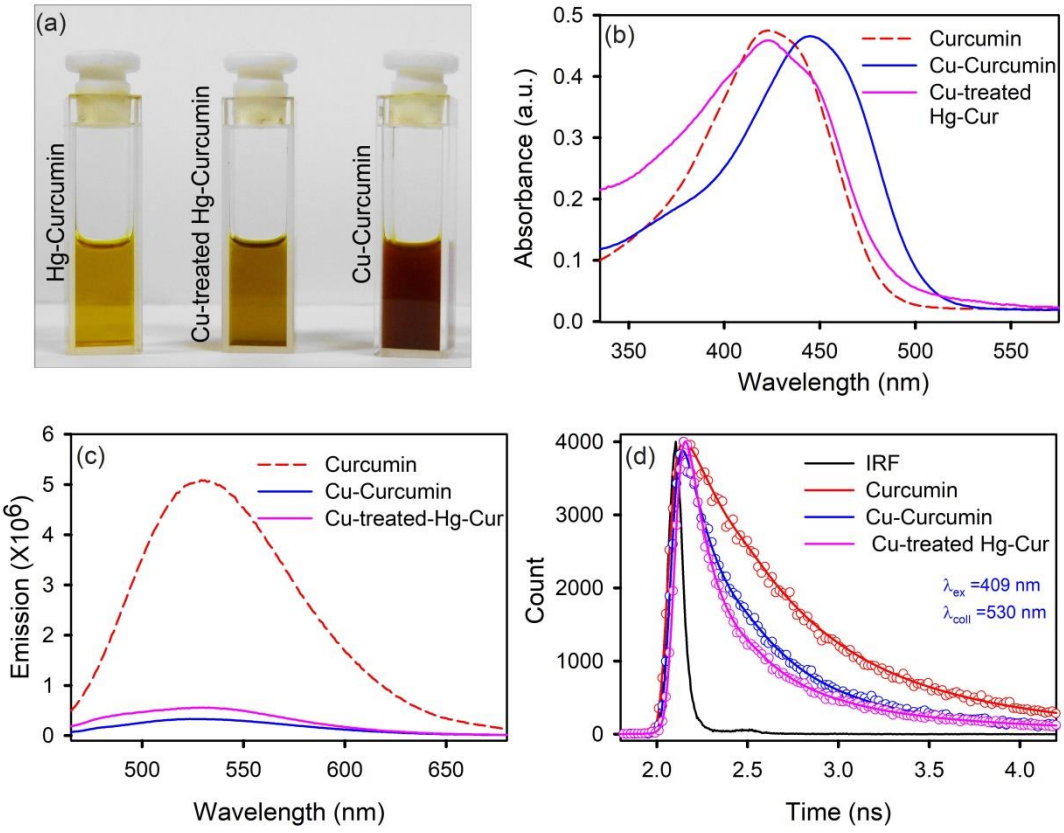

Figure 11.2: *a) Pictorial image of Hg-Curcumin, Cu-treated Hg-Curcumin and Cu-Curcumin, b) Absorption spectra of Curcumin, Cu-Curcumin, and Cu-treated Hg-Curcumin, c) Emission spectra of Curcumin, Hg-Curcumin, Cu-Curcumin, d) Excited state fluorescence decay of Curcumin, Cu-treated Hg-Curcumin, and Cu-Curcumin.*

Hg-Curcumin shows two peaks at ~424 nm and ~445 nm corresponds to the contribution of both Hg-Curcumin and Cu-Curcumin respectively. This observation suggests that, after the transmetalation reaction, a part of Hg-Curcumin converts to Cu-Curcumin. The OD normalized steady-state emission spectra of Cu-treated Hg-Curcumin and Cu-Curcumin are shown in Figure 11.2c. As discussed earlier, metallation in Curcumin reduces the steady-state quenching significantly. The excited state decay of Cu-Curcumin and Cu-treated Hg-Curcumin is shown in Figure 11.2d. It is to be noted that, the decay pattern of Cu-

treated Hg-Curcumin looks like the decay of Cu-Curcumin. This result indicates that Hg-Curcumin turns to Cu-Curcumin via transmetalation reaction in presence of Cu.

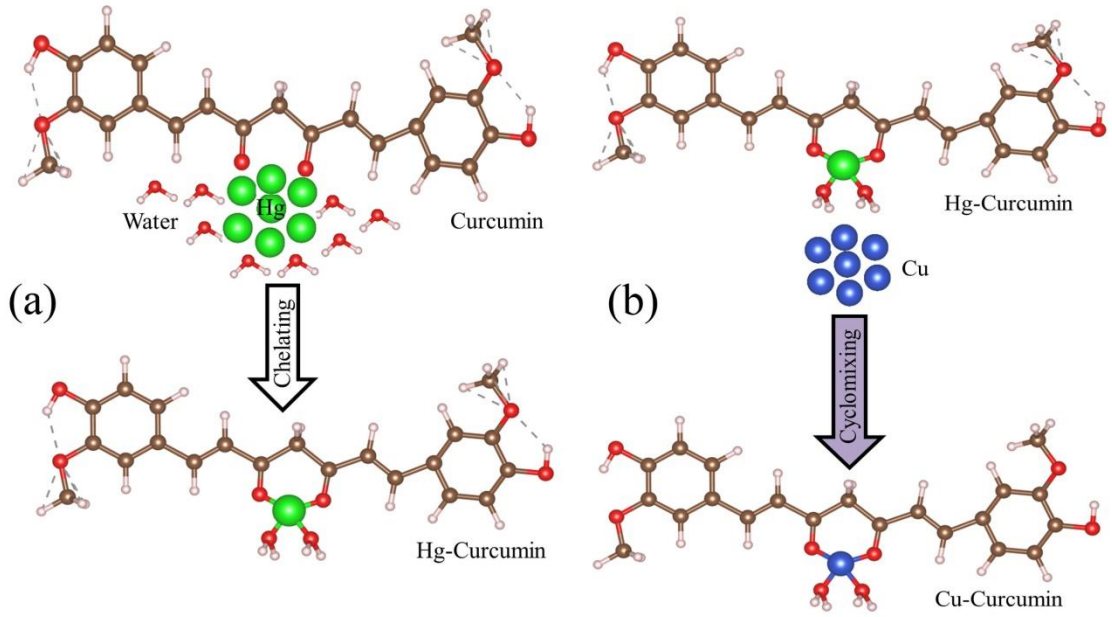

Scheme 11.1: *a) Natural way to Hg chelation with Curcumin to make Hg-Curcumin complex, b) Pictorial representation of Cu replacement in Hg–Curcumin which results in the formation of Cu–Curcumin.*

The probable complexation reaction of Hg ion with Curcumin is shown in scheme 11.1a. According to the activity series of metal in chemistry, copper is more reactive than mercury. Hence, for a single-replacement reaction (where one element replaces another element in a compound), Cu can replace Hg in a compound system [46]. Crystal field theory (CFT) describes electrostatic interaction between a transition metal and ligands, which originates due to the attraction between the positively charged metal cation center and negatively charge ligand site [47]. CFT can approximately illustrate the strength of the metal-ligand bonds of the system. According to CFT, the stability of the metal-ligand complexes increases with increasing ionic potential. Cu^{2+} is a d^9 system which exhibits much higher stability, as six-coordinate Cu^{2+} complexes undergo Jahn-Teller distortion to form a system of lower symmetry and lower energy [48]. The

transmetalation process can also be explained using the Lewis acid-base theory [49]. According to HSAB (hard and soft (Lewis) acids and bases) theory, hard acid reacts faster with hard base and forms much stronger bonds among themselves. In the present case, Hg^{2+} is a soft acid whereas Cu^{2+} is harder acid, and beta-diketone of Curcumin is a hard base. So according to HSAB theory, attachment of Cu^{2+} with Curcumin is much more favorable compared to Hg^{2+}. The above discussion establishes that for Cu metal, the formation of the metal-organic complex is energetically more stable than that of Hg metal. The graphical representation of the metal exchange process is described in Scheme 11.1b. Cu ion removes hazardous Hg metal from Curcumin, and at the same time, after the metal exchange process newly synthesized material (Cu-Curcumin) has much higher antioxidant activity than pure Curcumin [7]. So, it is possible to convert a heavily toxic contaminated material to a much lesser toxic one and health-friendly material using a simple transmetalation process.

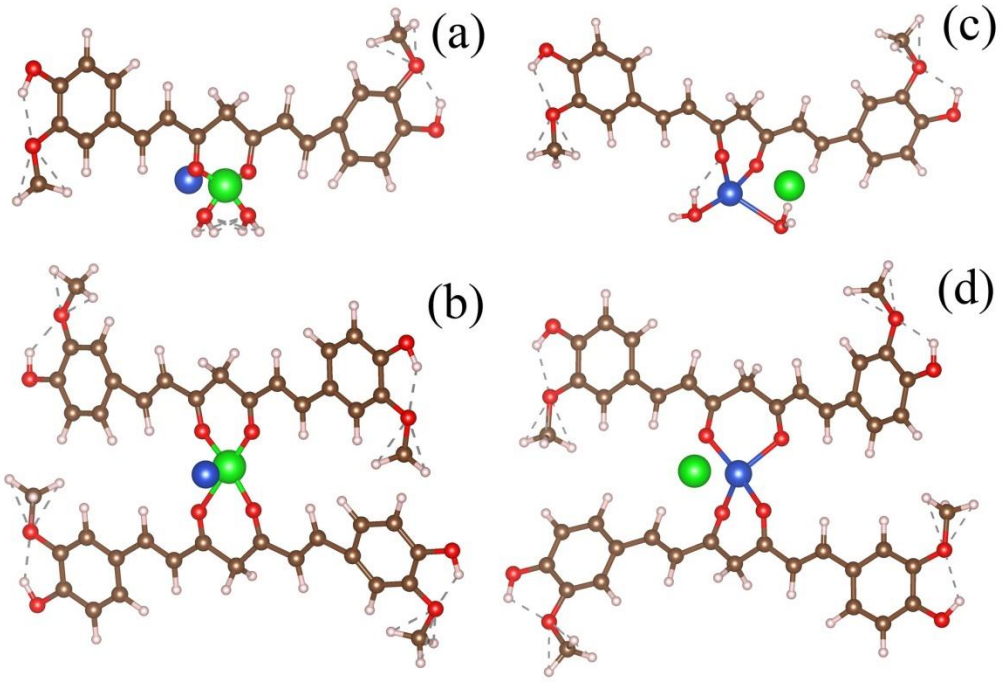

Figure 11.3: *Initial structure of a) monodentate and b) bidentate Hg-Curcumin in Cu environment. Energy optimized final structure of the systems shows Cu-ion replacing Hg from Curcumin in c) monodentate and d) bidentate Metal-Curcumin systems.*

To simulate the experimental condition, we have taken Hg-Curcumin in the aqueous environment. Deprotonation of the hydroxyl group in the curcumin system leads to the formation of a bidentate β-diketonate moiety, which has a strong tendency to chelates with transitional metal ions in two probable geometries forming monodentate (1:1) and bidentate (1:2) complexes [50]. We have considered both the possibility of metal chelation. In monodentate condition, one metal ion is attached with one Curcumin and in bidentate condition; one metal ion is attached with two Curcumin (Figure 11.3a and 11.3b). Free Cu-ion is placed in the vicinity of the Hg-Curcumin. Figure 11.3a and 11.3b show the initial structure of the system for monodentate and bidentate condition respectively. It is clear from the figure that in Hg-Curcumin Hg is attached to Curcumin, and Cu is free within the system. Next, this complex system is allowed to undergo complete structural relaxation via the minimization of force and energy using density functional theory. The energy-optimized relaxed systems are reproduced in Figures 11.3c and 11.3d. The final optimized structure shows that the Cu ion replaces the Hg from the Hg-Curcumin and makes the Cu-Curcumin complex. The bond length shown in Table 11.2 shows that the distance of Hg from the Curcumin chain has increased, whereas, the distance of Cu has decreased. The theoretically calculated formation energy for Cu-Curcumin is -1.4 eV where is formation energy for Hg-Curcumin is 0.4 eV. So, the formation of Cu-Curcumin is energetically favorable than Hg-Curcumin. Mercury is a filled d^{10} system, whereas Cu is just one electron away from a filled *d*-orbital. Hence, the unfilled *d*-orbital of Cu has a higher affinity to fill itself and thus endorses easier chelation with Curcumin than Hg. These free Hg ions removed from Curcumin, come to the medium and increase the amount of Hg ion in the medium. It is possible to detect the increment of Hg ion in the medium using the different experimental techniques to verify the detoxification of Curcumin via metal-exchange.

Table 11.2: *The distance of Cu and Hg atom from the Curcumin chain.*

System	Distance from Curcumin chain	
	Initial (Å)	Final Optimized (Å)
Hg	1.32	3.73
Cu	2.39	1.92

To detect free Hg^{2+} ion in the medium we employed the surface plasmon resonance (SPR) band of Ag NP as a probe. Citrate capped Ag NP has been synthesized by using a wet chemical synthesis route. Figure 11.4a shows the TEM image of citrate capped Ag NP which is spherical. Average particle

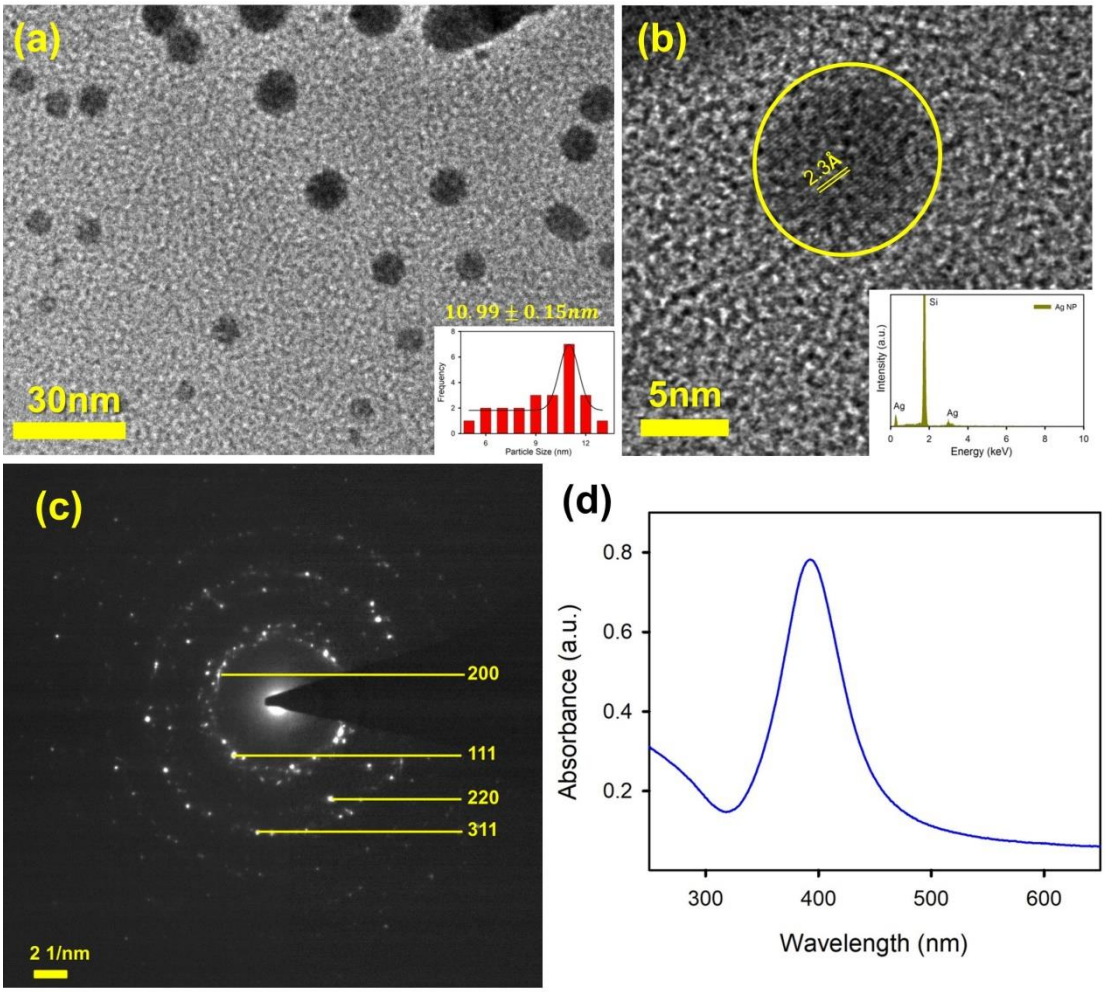

Figure 11.4: *a) TEM image of Ag Nanoparticle, b) HRTEM image of Ag NP showing the fringe distance 2.3Å, inset shows the X-Ray EDS image of Ag NP c) SAED image of Ag NP. d) Absorption spectra of Ag NP.*

size of the NP is found ~9.12 ± 0.09 nm (particle distribution is shown in the inset of Figure 11.4a). To get detailed crystallographic information about the structure we have taken the HRTEM image of the Ag NP. The inter-planar distance calculated from fringes-width is around 0.23 nm, which corresponds to the [111] lattice plane of Ag NP [51]. The inset of Figure 11.4b shows the EDS spectra of Ag NP, which confirms the presence of the Ag element in the system. A selected area electron diffraction (SAED) pattern of Ag NP is depicted in Figure 11.4c. The diffraction rings on the SAED patterns correspond to the face-centered cubic (FCC) structure of the Ag NP. The spacing of diffraction rings is 0.20, 0.23, 0.14, and 0.12 nm, which relate to the (200), (111), (220) and (311) lattice planes of FCC Ag NP respectively [52]. As synthesized yellow-colored citrate capped Ag NP shows an absorption peak at ~395 nm (shown in Figure 11.4d) [53]. This absorption peak comes due to the excitation of surface plasmon resonance (SPR band) vibrations of Ag NP. The average particle size calculated from the absorbance band is roughly ~11 nm [54], which is consistent with the particle size obtained from TEM images.

To perform the sensing experiments, the initial concentration of Ag NP is taken ~0.15 nM for all cases. To understand how Hg^{2+} ion interacts with the SPR band of the Ag NP, a control study was carried out without adding anything within the system. The absorbance spectrum of Ag NP in medium remained constant (data not are shown) for more than 1 hr. indicating that without the presence of any ion, the SPR peak of Ag NP remains invariant with time. To detect the mercury in solutions, a time dependent spectral study of the SPR spectra of Ag NP has been performed before and after introducing Hg^{2+} in the medium. There is an instant change in the SPR peak of Ag-NP in the presence of Hg^{2+} ion (depicted in Figure 11.5a). In addition to the suppression in the intensity of the SPR band, the band undergoes an overall blueshift instantly after the addition of Hg^{2+} ion. In presence of Hg^{2+} ions, Ag NP aggregates with each other and forms the Ag-Hg-Ag

complex [55-57]. As a result of it, aggregated Ag NP loses the SPR band (decrease in absorbance), and overall particle size increases [56]. Due to the hydrophobic effect, citrate capped Ag NP starts forming aggregation in the presence of cationic Hg^{2+} ion [56], as an effect of that average particle size increases.

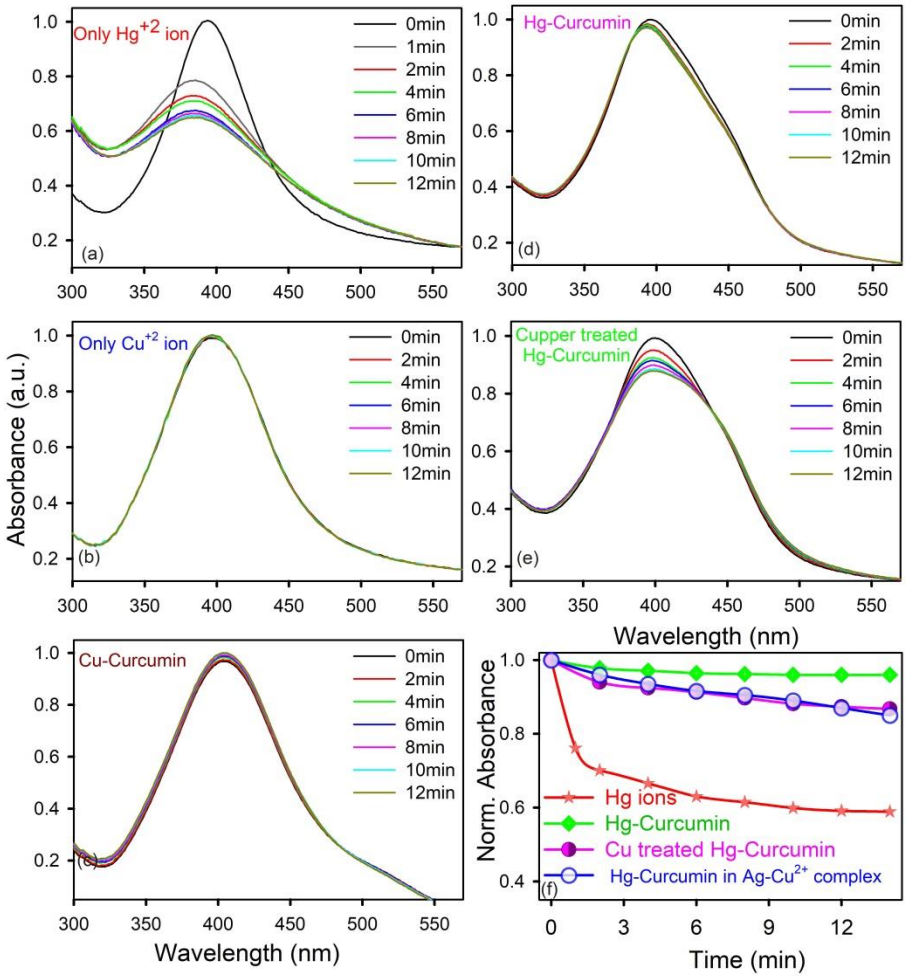

Figure 11.5: *Temporal variations of the SPR spectra of Ag NP immersed in the aqua-methanolic solution in presence of a) only Hg^{2+} ion, b) only Cu^{2+} ion, c) Cu-Curcumin, d) Hg-Curcumin, and e) Cu-treated Hg-Curcumin. Absorbance at zero time is normalized to 1.0 in each case, f) relative variations of the SPR spectra of Ag NP with respect to time, immersed in the aqua-methanolic solution in presence of Hg^{2+} ion, Hg-Curcumin, and Cu-treated Hg-Curcumin.*

To realize how the SPR band of the NP is affected by the free Hg^{2+} ion removed from the Hg-Curcumin complex, first, we have studied the effect of SPR band quenching with free Hg^{2+} ion. We found amalgamation or partial oxidation

of Ag NP in the presence of Hg^{2+} ion is very fast and completes within 14 min. (Figure 11.5a). So, the fast response time and simple technique make this method an efficient probe to detect Hg^{2+} ions in a real-life system. On the other hand, in presence of Cu^{2+} ion and Cu-Curcumin, the SPR band of Ag NP remains unaltered. Moreover, mercury interacts differently with the SPR band when it is in a complex form with other particles as compared to free-standing Hg^{2+} ion. In the Hg-Curcumin system, Hg is chelated with Curcumin. So, in the Hg-Curcumin complex system, there are negligible free Hg ions available in the system. It is observed that in presence of Hg-Curcumin there is an insignificant reduction of SPR band. However, upon Cu-treatment in Hg-Curcumin, Cu-ion squeezes out

Table 11.3: *Relative degradation of SPR of Ag NP after 14 min. and 1 hr.*

System	**Relative O.D. degradation of Ag SPR**	
	After 14 min.	After 1 hr.
Free Hg^{2+} ion	41%	58%
Hg-Curcumin	4%	5.5%
Cu-Hg-Curcumin	14%	47%

the Hg ion from the Hg-Curcumin complex and makes it free in the aqueous solution. As a result of it, in the case of Cu-treated Hg-Curcumin, the SPR band of Ag NP again started shrinking (Figure 11.5e). The trend of decrement is similar to the decrement of free Hg^{2+} ions. Cu-treated Hg-Curcumin has a greater impact on SPR peak than Hg-Curcumin because of released free Hg ions from Curcumin after being replaced by Cu. Moreover, we examined the time required for Cu^{2+} ion to replace Hg^{2+} ion from the Hg-Curcumin complex. At first, free Cu^{2+} ion is intermixed with the Ag-NP, then Hg-Curcumin is added in that Cu^{2+}-Ag NP system. The relative changes in the absorption spectra of different systems with respect to time are shown in Figure 11.5f. It is evident from the figure that, for free Hg^{2+} ion, the suppression rate of the SPR band is highest (41% in 12 min.). The

suppression rate is almost negligible in the case of Hg-Curcumin. Interestingly, Cu-treated Hg-Curcumin shows a higher suppression rate compared to Hg-Curcumin. Nearly 15% of the SPR band has been decreased in the treated Curcumin in 14 min. We further monitored the SPR peak of different systems after 1 hr. of incubation time. It is observed that, in 1 hr. SPR peak of Hg^{2+} ion diminishes 58% whereas in the case of Cu-treated Hg-Curcumin there is 47% suppression of SPR peak after 1 hr. The presence of Cu^{2+} ion in the system pulls out more Hg atoms from the Curcumin with increasing reaction time. The amount of suppression is tabulated in Table 11.3. To get further quantitative detail about how much Cu is replacing the Hg from Hg-Curcumin, we have performed the EDS measurement of those samples (shown in Figure 11.6).

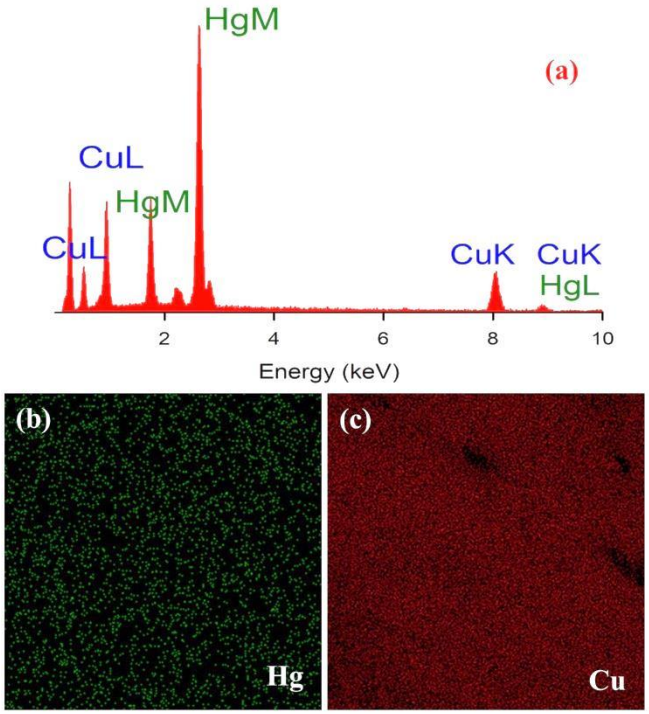

Figure 11.6: *a) X-Ray dispersive EDS spectrum of Cu-treated Hg-Curcumin. Mapping image of b) Hg and c) Cu in the Cu-treated Hg-curcumin system.*

Cu-treated Hg-Curcumin was washed several times before EDS measurement to ensure that there was no free Hg or Cu ion present in the system. Our modified system shows the presence of both Hg and Cu. We observe, after

Cu-treatment in the Hg-Curcumin complex, 75% of Hg-Curcumin converted to Cu-Curcumin. EDS mapping of the Cu-treated Hg-Curcumin has been performed to get information about the elemental distribution after the reaction. The elemental mapping of Hg and Cu has been shown in Figure 11.6b and 11.6c. From those figures, it is confirmed that, in the Cu-treated Hg-Curcumin complex system, the amount of Cu element is higher than Hg, which indicates that, Cu replaces Hg in the system. The elemental amounts are presented in Table 11.4. This result is consistent with the result obtained by using the Ag SPR quenching detection method.

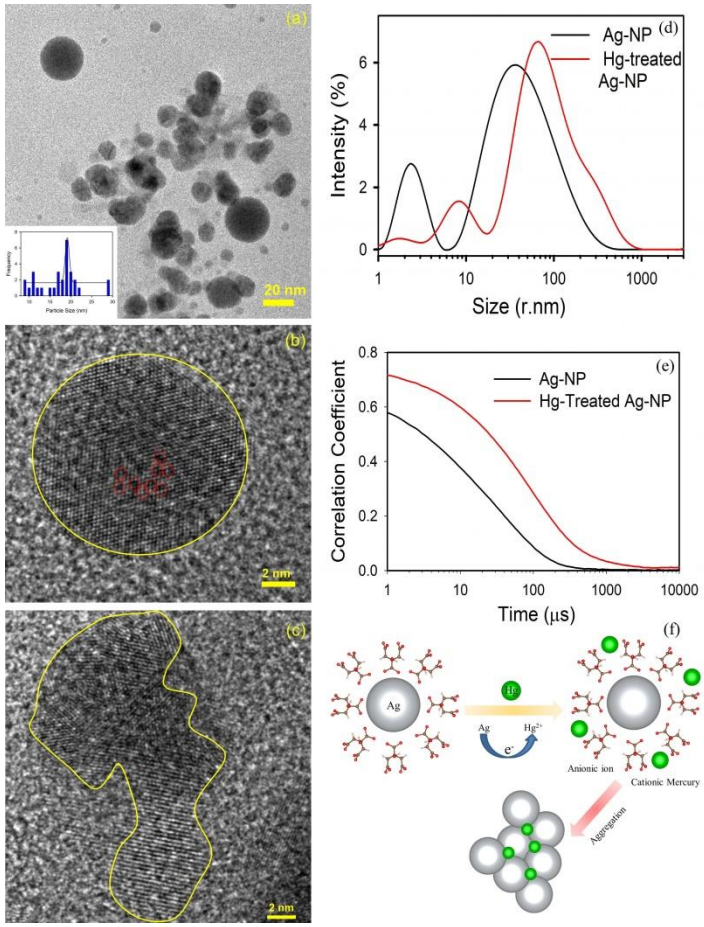

Figure 11.7: *a) TEM image of Ag NP after amalgamation with Hg^{2+} ions, b) HRTEM image of Ag NP after treatment. Hg ions are decorated (marked by the red dot) inside the Ag NP, c) HRTEM image of agglomeration of Ag NP. d) Size of Ag NP measured before and after detection, e) correlation coefficient of Ag NP before and after treatment, f) schematic mechanism of aggregation of Ag NP in the presence of cationic mercury ion.*

To examine the change of particle size, we have done TEM imaging of the Ag NP after the interaction with Hg. Figure 11.7a shows the TEM imaging of Ag NP after interacting with Hg. The measured average particle size of Ag NP is found ~19.62 nm, which is larger than the synthesized Ag NP. Figure 11.7b shows the HRTEM image of Ag NP after agglomeration with free Hg^{2+} ion. A distinct contrast difference (red marked area) has been observed within the Ag NP, which was absent in the pure Ag NP. We suggest there is a possibility of decoration of Hg^0/Hg^{2+} particle on the surface of Ag NP during the time of the amalgamation process. The possible amalgamation/aggregation mechanism is shown in Scheme 11.2.

Table 11.4: *Relative atomic % of Cu and Hg atom for different systems measured using EDS.*

System	Relative atomic %	
	Cu	Hg
Hg-Curcumin	0.1	99.9
Cu-Curcumin	0.0	100.0
Cu-Hg-Curcumin	75.1	24.9

The aggregation of Ag NP after the interaction with cationic Hg^{2+} ion is visible in Figure 11.7c. The hydrodynamic diameter (d_H) of the particle is measured using DLS. The average d_H measured for synthesized Ag NP is ~16.8 nm (Figure 11.7d) which is slightly larger than the particle size obtained from TEM. The average d_H of the Ag NP increases to ~23.2 nm upon amalgamation with Hg^{2+} ion. The autocorrelation coefficient is also plotted in Figure 11.7e. The decay of Ag NP is much rapid than Hg-treated Ag NP, which is consistent with the size increment after the interaction. The schematic representation of the aggregation mechanism of Ag NP in the presence of Hg ion is illustrated in Figure 11.7f.

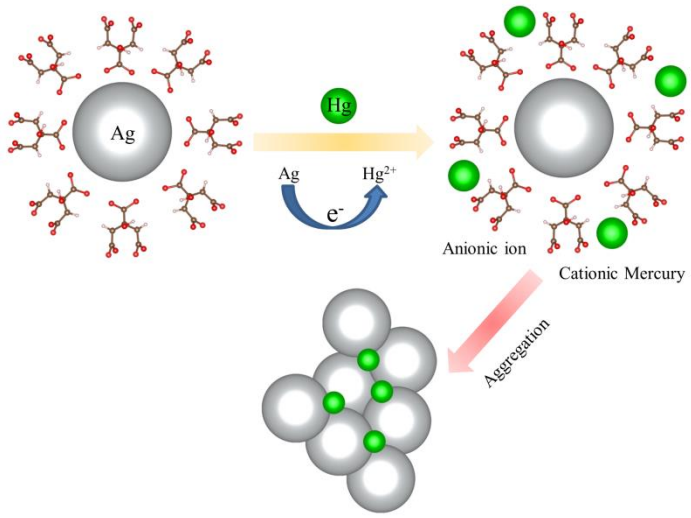

Scheme 11.2: *Possible aggregation mechanism of Ag NP in the presence of cationic mercury ion.*

In summary, a simple wet chemical transmetalation technique was developed to remove the toxic Hg metal from the contaminated Curcumin complex by employing Cu ions. We assume, Cu ion turns the Hg-Curcumin complex into the Cu-Curcumin complex and makes Hg free in the medium. The free Hg ion is detected by utilizing the SPR band of Ag NP. Using the first principles density functional theory calculation, we have corroborated our experimental findings. This result suggests that the proposed mechanism may have a great potential to decontaminate the heavily toxic Hg from any polyphenol complex.

11.2.2. A Novel Nanohybrid for Cancer Theranostics: Folate Sensitized Fe_2O_3 Nanoparticle for Colorectal Cancer Diagnosis and Photodynamic Therapy [58]: Organic-inorganic based NH became very much useful for their applications in biological field including diagnosis and treatment of cancerous cells. Injection of drugs followed by irradiation of light of appropriate wavelength on the targeted place (damaged tissue) stimulates the drug, which produces reactive oxygen species (ROS) and induces cell death. In this regard, target-specific delivery of a drug is very much important for an efficient result. In the present work, we have

developed a magnetic NP-based hybrid drug using Fe_2O_3 and folic acid which can serve the present purposes.

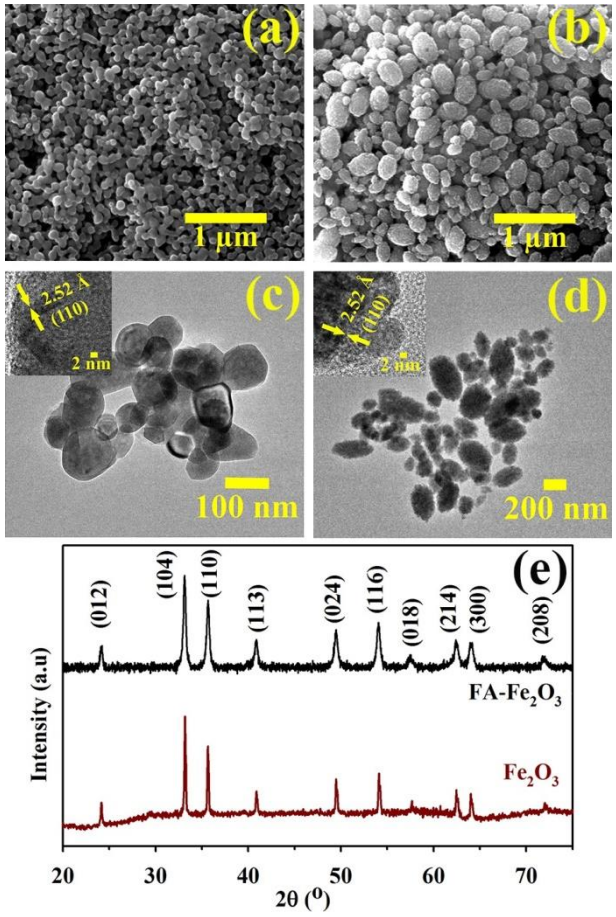

Figure 11.8: *FESEM image of a) Fe_2O_3 and (b) FA-Fe_2O_3. HRTEM image of c) Fe_2O_3 and d) FA-Fe_2O_3. Inset of c) and d) show corresponding HRTEM images at higher magnification. e) XRD pattern of Fe_2O_3 and FA-Fe_2O_3.*

Figure 11.8a and 11.8b depict the FESEM image of as-prepared Fe_2O_3 and FA-Fe_2O_3 respectively. Fe_2O_3 has a branched network like morphology having a segment length of 300-500 nm and width 50-70 nm. FA-Fe_2O_3 has a nano-egg like morphology of length 150-200 nm and width 60-110 nm. Figure 11.8c and 11.8d represents the corresponding HRTEM images of Fe_2O_3 and FA-Fe_2O_3, while insets show corresponding HRTEM image at higher magnification. For both the samples fringe distance is 2.52 Å which corresponds to the spacing between (110) planes of α-Fe_2O_3 [59]. Powder X-ray diffraction pattern of FA-Fe_2O_3 and Fe_2O_3 has been

shown in Figure 11.8e. The diffraction pattern matches with International Centre for Diffraction Data (ICDD) card no 33-0664, which corresponds to α-Fe_2O_3 [59]. XRD pattern and fringe distance from HRTEM image imply crystal structure of α-Fe_2O_3 remains intact after FA templated synthesis.

Figure 11.9a depicts FTIR spectra of FA, Fe_2O_3, and FA-Fe_2O_3. Two sharp peaks at 472 cm^{-1} and 550 cm^{-1} are the characteristics of Fe-O stretching in the Fe_2O_3 spectrum. The lower frequency absorption remains unchanged but the higher one gets shifted to higher frequency 570 cm^{-1} in FA-Fe_2O_3, which indicates a change in size during FA templated synthesis of Fe_2O_3 [60]. The sharp peak at 1699 cm^{-1} corresponds to the C=O stretching of the carboxylic acid group of FA. In FA-Fe_2O_3, the C=O stretching perturbed into two peaks, one remains at 1699 cm^{-1} and another at 1684 cm^{-1}. This perturbation may be due to one of the free carboxylic acids of FA in FA-Fe_2O_3 and another one gets covalently attached with Fe_2O_3 [61]. Peaks in between 1485-1519 cm^{-1} corresponding to phenyl and pterin ring of FA [62]. Raman spectra of Fe_2O_3 and FA-Fe_2O_3 are depicted in Figure 11.9b. Fe_2O_3 shows peaks at 228 cm^{-1} and 500 cm^{-1} corresponding to A_{1g} phonon modes and four E_g phonon modes at 248, 296, 413, and 612 cm^{-1}. Another 2 longitudinal optical (2LO) phonon mode at 1324 cm^{-1} [63]. The longitudinal optical (LO) phonon mode which is Raman forbidden is not observed in the case of Fe_2O_3 [63]. But the LO phonon modes are observed in the case of FA-Fe_2O_3 at 662 cm^{-1}, the same mode was also observed by Onari *et al* [64]. This variation may come due to calcination at higher temperatures leading to better crystallinity of Fe_2O_3 than that of un-calcined FA-Fe_2O_3 [63].

The differences in UV-Vis absorption spectra of Fe_2O_3 and FA-Fe_2O_3 has been depicted in Figure 11.9c. FA has two well-known absorption bands at 360 and 280 nm [65]. Three possible electronic transitions are observed in the case of Fe_2O_3 absorption spectra, absorption arising in the range of 200-400 nm mainly due to ligand to metal charge transfer transition (LMCT) from oxygen to iron, the

absorption band at 445 nm is attributed mainly to pair excitation from $^6A_1 \rightarrow {}^4E$, $^4A_1$ of magnetically coupled Fe^{3+}-Fe^{3+} system and sharp band at 568 nm is due to the electronic transition from $^6A_1$ to $^4T_2(^4G)$ along with pair excitation of $^6A_1+{}^6A_1 \rightarrow {}^4T_2(^4G)+{}^4T_2(^4G)$ [66-68]. In the case of FA-Fe_2O_3, the LMCT band in the wavelength range 200-400 nm and the absorption band at 445 nm get triggered, surprisingly another one at 568 nm becomes sedate due to FA functionalization of Fe_2O_3. The significant spectral overlap of emission of FA with the absorption of Fe_2O_3 has been shown in Figure 11.9d. Steady-state fluorescence quenching of FA was observed in presence of Fe_2O_3 upon excitation at 283 nm and 375 nm has shown in the insets of Figure 11.9e and 11.9f, respectively.

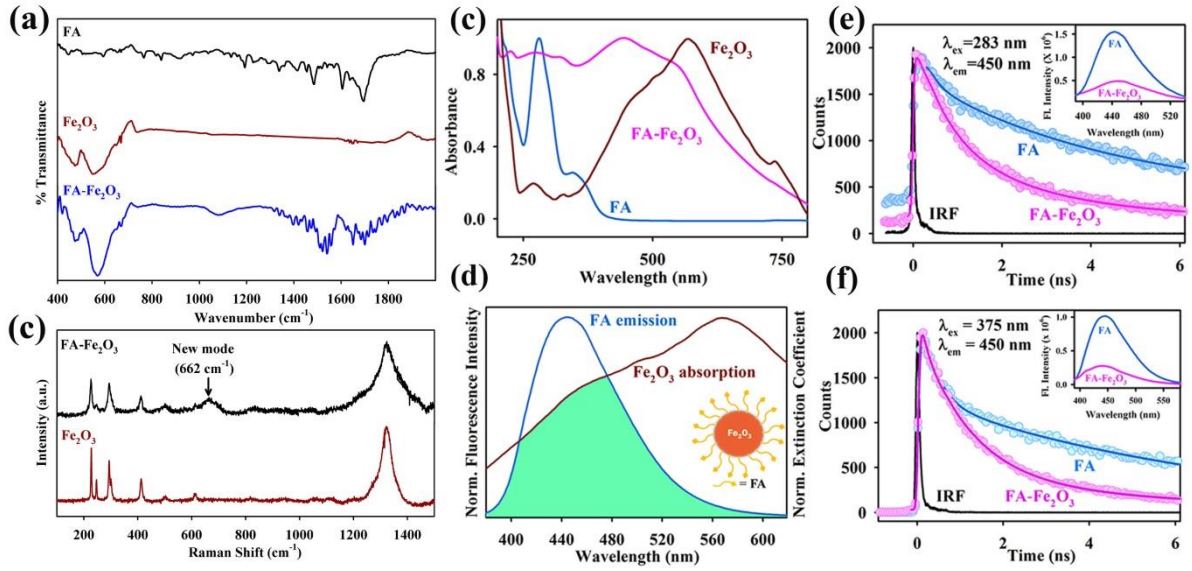

Figure 11.9: *a) FTIR spectra of FA, Fe_2O_3, and FA-Fe_2O_3. b) Raman spectra of FA-Fe_2O_3 and Fe_2O_3. c) Absorption spectra of FA, Fe_2O_3, and FA-Fe_2O_3. d) The spectral overlap between emission of FA and absorption of Fe_2O_3. The picosecond-resolved fluorescent transient spectra of FA in the absence and presence of Fe_2O_3, recorded at 450 nm upon excitation at e) 283 nm and f) 375 nm, respectively. Inset shows corresponding steady-state PL spectra.*

Picosecond resolved fluorescent transients were recorded for both FA and FA-Fe_2O_3 at 450 nm upon excitation at 283 nm and 375 nm as shown in Figure 11.9e and 11.9f, respectively, and the corresponding time scales are tabulated in Table 11.5. We employed a well-known FRET strategy to confirm the molecular level attachment of FA with Fe_2O_3. The fluorescence lifetime of FA is found to be

quenched in the presence of Fe_2O_3 NP, which suggests a non-radiative energy transfer process from the donor (FA) to the acceptor (Fe_2O_3). The donor-acceptor distances (r_{DA}) have been calculated to be 1.11 nm and 1.13 nm for the excitation at 283 nm and 375 nm, respectively, and all the other calculated FRET parameters are shown in Table 11.5. This molecular cross-talking between FA and Fe_2O_3 suggests an alteration in activities.

Table 11.5. *Lifetimes of the picosecond-resolved fluorescent transient of FA and FA-Fe_2O_3.* *

Picosecond resolved fluorescence transient lifetimes	**System**	**λ_{ex} (nm)**	**λ_{em} (nm)**	**τ_1(ns)**	**τ_2(ns)**	**τ_3 (ns)**	**τ_{avg}(ns)**
	FA	283	450	0.25 (35%)	4.50 (65%)	-	3.0
		375	450	0.28 (51%)	6.35 (49%)	-	3.3
	FA-Fe_2O_3	283	450	0.12 (14%)	0.78 (49%)	2.78 (37%)	1.4
		375	450	0.25 (33%)	1.30 (54%)	6.23 (13%)	1.6
FRET parameters of FA-Fe_2O_3		**λ_{ex} (nm)**	**λ_{em} (nm)**	**J (λ) ($M^{-1}cm^{-1}$ nm^4)**	**E (in %)**		**r_{DA} (nm)**
		283	450	3.75×10^{13}	54.0		1.11
		375	450	3.75×10^{13}	52.0		1.13

* *The values in parentheses represent the relative weight percentages of the time components. The reported lifetimes carry ~5% uncertainties.*

Magnetic properties measurement of FA-Fe_2O_3 using vibrating sample magnetometer (VSM) shows magnetic field-dependent magnetization (M vs. H) at 80 K and 300 K shows hysteresis feature with coercivity 0.43 T and 0.053 T, respectively (Figure 11.10a). Insets of Figure 11.10a depict M_{ZFC} curve decreases and M_{FC} rises slowly as a function of decreasing temperature reveals strong ferromagnetic property and the blocking temperature was 332 K.

In vitro ROS generation was evaluated using well known DCFH assay, in which [69] DCFH is oxidized to fluorescent DCF by reacting with ROS, and thus

ROS generation monitored using fluorescence of DCF at 520 nm. FA-Fe_2O_3 was assessed for its capability to generate ROS in the presence of a range of visible light excitation (blue: 460 ± 15, green: 540 ± 15, and red: 640 ± 15 nm). The maximum ROS generation was observed in the presence of blue light (data not shown). This is attributed to the absorption band at 445 nm in Fe_2O_3, which becomes stimulated in presence of FA. We further evaluated ROS generation in the presence of Fe_2O_3 with control under blue light irradiation, which reveals enhanced ROS generation in the case of FA-Fe_2O_3 (Figure 11.10b). The swift nature of ROS generation gets saturated within 15 min, indicating a good signature for PDT application.

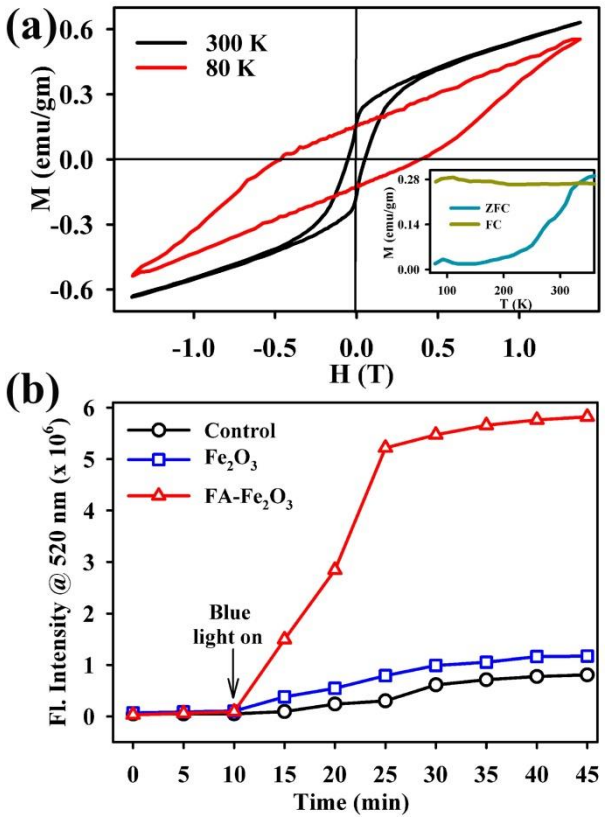

Figure 11.10: *a) Field dependent magnetization (M vs. H) of FA-Fe_2O_3 at 300 K and 80 K. Bottom right inset shows the temperature dependence of M_{ZFC} and M_{FC} curves measured at H =1.6 T. b) DCFH oxidation with respect to time in addition of Fe_2O_3, FA-Fe_2O_3, and control under dark with subsequent blue light irradiation.*

To check the cytotoxicity of the NH (FA-Fe_2O_3) and individual ingredients (FA and Fe_2O_3) HCT 116 cells were subjected to MTT assay without blue light

exposure (Figure 11.11a). HCT 116 cells were incubated with FA, Fe_2O_3 and FA-Fe_2O_3 of different concentrations (0.01, 0.1, 1, 10, 50 and 100 μg/ml). Native FA and Fe_2O_3 do not have significant cytotoxicity up to a concentration of 1 μg/ml. However, in the case of FA-Fe_2O_3, cell viability was reduced to 70.68% at the same concentration (Figure 11.11a). After 1 μg/ml concentration the effect of FA-Fe_2O_3 on cell viability of HCT 116 cells was almost reached saturation. To determine the optimum cytotoxicity with the lowest concentration of FA-Fe_2O_3 in absence of blue light, another screening was done using FA-Fe_2O_3 of concentration up to 1μg/ml. Figure 11.11b depicts the optimum cell viability was found to be 70.26% at 0.1 μg/ml concentration of FA-Fe_2O_3. As FA is a well-known nutrient, it does not have significant cytotoxicity, we have excluded FA from the next part of our cellular study. Next, to ascertain the enhanced intracellular ROS activity of FA-Fe_2O_3 in presence of blue light, HCT 116 cells were incubated with 0.1 μg/ml of FA-Fe_2O_3 and were exposed to blue light for the different time duration (5-45 min.). A gradual decrease in the cell viability was observed with an increase in blue light exposure time (in 5, 10, 15, 30, and 45 min. of light exposure cell viability was 63.63%, 42.32%, 21.34%, 18.47%, and 16.63%, respectively) as compared to the FA-Fe_2O_3 treated cells without light exposure (Figure 11.11b and 11.11c). A light dose of 15 min. shows the maximum effect on cell death (Cell viability 21.34%) and after that the effect is minimal, suggesting a rapid ROS activity of FA-Fe_2O_3 in HCT 116 cells as consistent with extracellular ROS generation. The in vitro PDT experiment illustrates the photodynamic effect of FA-Fe_2O_3 and also suggests a direct indication of photosensitized cytotoxicity of FA-Fe_2O_3 NH in HCT 116 cells. The intracellular ROS generation experiment was done using cell-permeable dye DCFH-DA. HCT 116 cells were incubated with Fe_2O_3 and FA-Fe_2O_3 of different concentrations (0.01, 0.1, 1, 10, 50, and 100 μg/ml) to determine ROS activities without blue light exposure. As shown in Figure 11.11d, Fe_2O_3 does not have significant ROS activity without blue light exposure. Moreover, Fe_2O_3 has minimal ROS activity in extracellular conditions (as shown in Figure 11.10b) in the presence

of blue light. Hence Fe_2O_3 have been excluded for further experiment. Figure 11.11d depicts FA-Fe_2O_3 treated cells show a moderate increase in DCF fluorescence intensity with respect to the Fe_2O_3 treated cells. Another screening was done in the absence of light with 0-1 μg/ml of FA-Fe_2O_3. Figure 11.11e depicts moderate intracellular ROS activity of the NH in absence of blue light at a concentration of 0.1 μg/ml. The initial cytotoxicity study showed 0.1 μg/ml of FA-Fe_2O_3 have an optimum effect on cell viability in the absence of blue light. To ascertain the intracellular ROS level in the presence of blue light with an optimum dose of FA-Fe_2O_3, cells were treated with 0.1 μg/ml FA-Fe_2O_3. Treated cells were exposed to blue light for the differential time duration (5, 10, 15, 30, and 45 min.). Figure 11.11f depicts ROS generation was gradually increased with increasing blue light exposure time (1.42, 1.88, 3.69, 4.11, and 4.15 fold in 5, 10, 15, 30, and 45 min., respectively). The trend in intracellular ROS generation reached saturation with 15 min. of light exposure, which is consistent with both extracellular ROS generation and photo-induced cytotoxicity assay. Considerable light-induced enhanced intracellular ROS activity and optimum dark toxicity of 0.1 μg/ml dose of FA-Fe_2O_3 indicate its potential in PDT.

Earlier reports have shown that amongst the numerous free radicals, the hydroxyl radical is a commonly found cellular free radical that is produced through oxidative stress, causes cell death [29]. For the assessment of the type of ROS produced within the cell by light-sensitized FA-Fe_2O_3, a flow cytometric study of intracellular ROS generation was conducted using a specific fluorescent probe HPF, a marker for hydroxyl radical [70]. Pretreated cells with 0.1 μg/ml of FA-Fe_2O_3 was exposed to a different light dose of 5, 10, and 15 min. A gradual ($p < 0.05$) increase in HPF fluorescence intensity was observed (2.67, 4, 5.17 fold in 5, 10, and 15 min., respectively) with increasing light exposure time (Figure 11.11g and 11.11h). The observation reveals that enhanced cytotoxicity upon blue light

exposure is due to the generation of hydroxyl radical within the cell in presence of FA-Fe_2O_3.

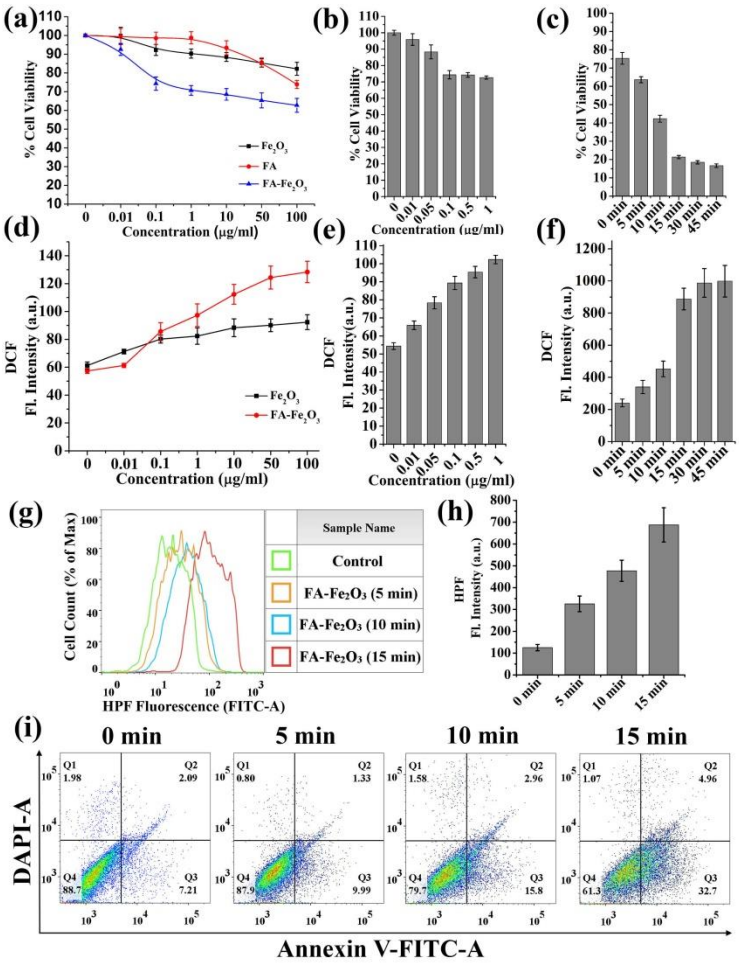

Figure 11.11: *HCT 116 cells were treated with a requisite amount of drugs for 24 hr. before various experiments. a) MTT assay quantified cell viability with different concentrations of FA, Fe_2O_3, and FA-Fe_2O_3 in absence of blue light. b) The same at different concentrations of only FA-Fe_2O_3. c) Light-induced cytotoxicity after treatment with 0.1 µg/ml of FA-Fe_2O_3 followed by blue light irradiation with different time duration (0-45 min.). d) Fe_2O_3 and FA-Fe_2O_3 treated dose-dependent (0-100 µg/ml) intracellular ROS level in terms of DCF fluorescence intensity without blue light treatment. e) FA-Fe_2O_3 treated dose-dependent (0-1 µg/ml) intracellular ROS level in terms of DCF fluorescence intensity without blue light treatment. f) Intracellular ROS measurement after treatment with 0.1 µg/ml FA-Fe_2O_3 followed by time dependent (0-45 min.) blue light exposure. g) Intracellular hydroxyl radical (ȮH) determination by HPF staining after treatment with FA-Fe_2O_3 followed by time dependent (0-15 min.) blue light exposure, using flow cytometer. h) Flow Jo analyzed data of hydroxyl radical (ȮH) determination. i) Flow cytometric analysis of Annexin V–FITC/DAPI binding level in FA-Fe_2O_3 (0.1µg/ml) treated cells with different blue light exposure time.*

It is well known that phosphatidylserine (PS), a phospholipid component of the cell membrane, are translocated in the membrane and externalized during apoptosis [71]. Annexin-V is a specific PS-binding protein that can be used to detect the apoptotic cells when conjugated with a specific fluorophore. On the other hand DNA binding dye DAPI was used along with annexin V to assess the degree of apoptosis and necrosis. To find out the underlying mechanism of the photodynamic effect of FA-Fe_2O_3 on HCT 116 cells, a flow cytometric technique was used using Annexin V-FITC/DAPI. The percent viable cell population in FA-Fe_2O_3 treatment without light exposure was 88.7% following mild early apoptosis of 7.21%, late apoptosis of 2.09%, and necrosis of 1.98%. Interestingly, the percent of the apoptotic (early and late) population was progressively increased with the time of exposure (5, 10, and 15 min.) of light in FA-Fe_2O_3 pretreated cells (Figure 11.11i). With 15 min. exposure of light, the viable cells were reduced to 61.3% following the enhancement of early/late apoptotic and necrotic population of 32.7%, 4.96%, and 1.07%, respectively.

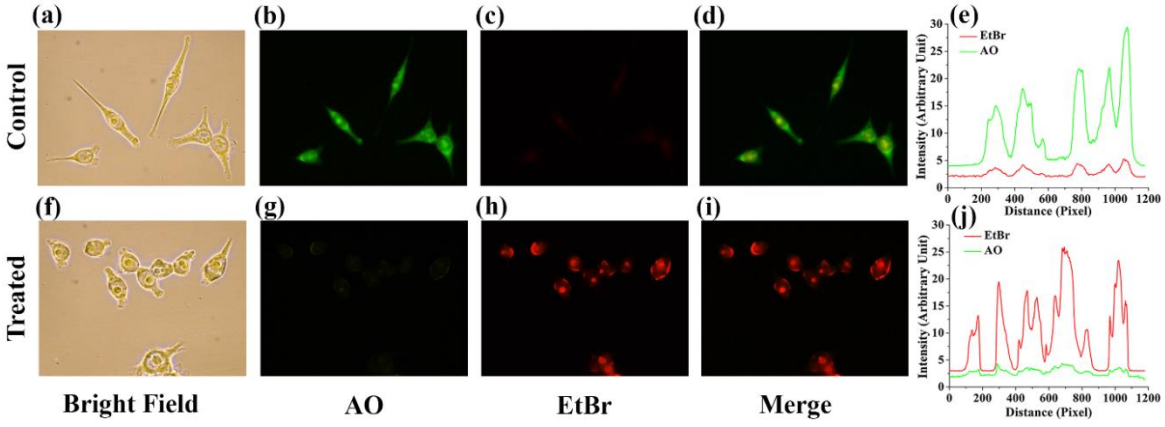

Figure 11.12: *Morphological changes of FA-Fe_2O_3 (0.1 µg/ml for 24h) treated HCT 116 cells followed by blue light exposure (15 min.). a) and f) control and treated cells under the bright field. b) and g) AO stained control and treated cells. c) and h) EtBr stained of control and treated cells. (d) and (i) Merged image of AO and EtBr stained cells. e) and j) Change in AO and EtBr fluorescence intensity of control and treated cell.*

To further confirm the degree of apoptosis and necrosis upon treatment with FA-Fe_2O_3 in presence of light, fluorescence microscopic analysis was

conducted using nuclear staining dye, Acridine Orange (AO), and Ethidium Bromide (EtBr) (Figure 11.12a-12i). Cells were pretreated with FA-Fe_2O_3 had an intact nucleus with strong green AO fluorescence and weak red EtBr fluorescence (11.12b and 11.12c). The scenario was reversed in the presence of light as shown in Figure 11.12c and 11.12h, demonstrating clear nuclear fragmentation, which is also observed from the intensity curves (Figure 11.12e and 11.12j).

The estimation of fractional DNA content (Sub G0-G1) in the cell cycle is widely used as a marker to determine apoptosis. Thus, to investigate the PDT effect of FA-Fe_2O_3 on HCT 116 cells underlying the role of apoptosis, flow cytometric assessment of the percentage of DNA content in the sub G0-G1 phase of the cell cycle was analyzed (Figure 11.13a). After treatment cells show a percentage of DNA content of 3.35% without any blue light exposure. After blue light exposure with different time duration (0-15 min.), there was a significant enhancement in the percentage of DNA content (6.62, 9.03, and 13.52% in 5, 10, and 15 min., respectively) of sub G0-G1 phase. The results demonstrate the role of fragmented DNA regulating the apoptotic machinery in light-induced FA-Fe_2O_3 mediated PDT. Nuclear DNA damage upon the blue light exposure on FA-Fe_2O_3 treated cells was further confirmed by comet assay, which is a single cell gel electrophoresis assay for the rapid and sensitive of DNA damage. In the case of a treated cell without blue light exposure migration of DNA from the origin was not significant, with increasing light exposure time tail length of damaged DNA increases, taking the shape of a comet (Figure 11.13 (b-e)). The head diameter in (2.70, 4.90, and 6.87 fold in 5, 10, and 15 min., respectively), % DNA in the tail (5.88, 19.51, and 20.62 fold in 5, 10, and 15 min., respectively) and tail length (2.72, 5.82, and 8.67 in 5, 10, and 15 min., respectively) were significantly ($p < 0.05$) increased with the gradual increase of blue light exposure time on FA-Fe_2O_3 treated cells. However, without light exposure on FA-Fe_2O_3 treatment did not show any upliftment of DNA damage indices (head diameter, % DNA in tail and

tail length) as compared with light-exposed treated cells (Figure 8.2.2.6 (f-h)). Light-induced enhanced ROS generation damages nuclear DNA in HCT 116 cells.

Numerous studies have revealed that ROS act as an upstream signal transducer for the p53 activation and as a downstream mediator of apoptosis [72]. To understand the involvement of p53 phosphorylation in photosensitized apoptosis machinery, flow cytometric assessment was conducted in FA-Fe_2O_3-

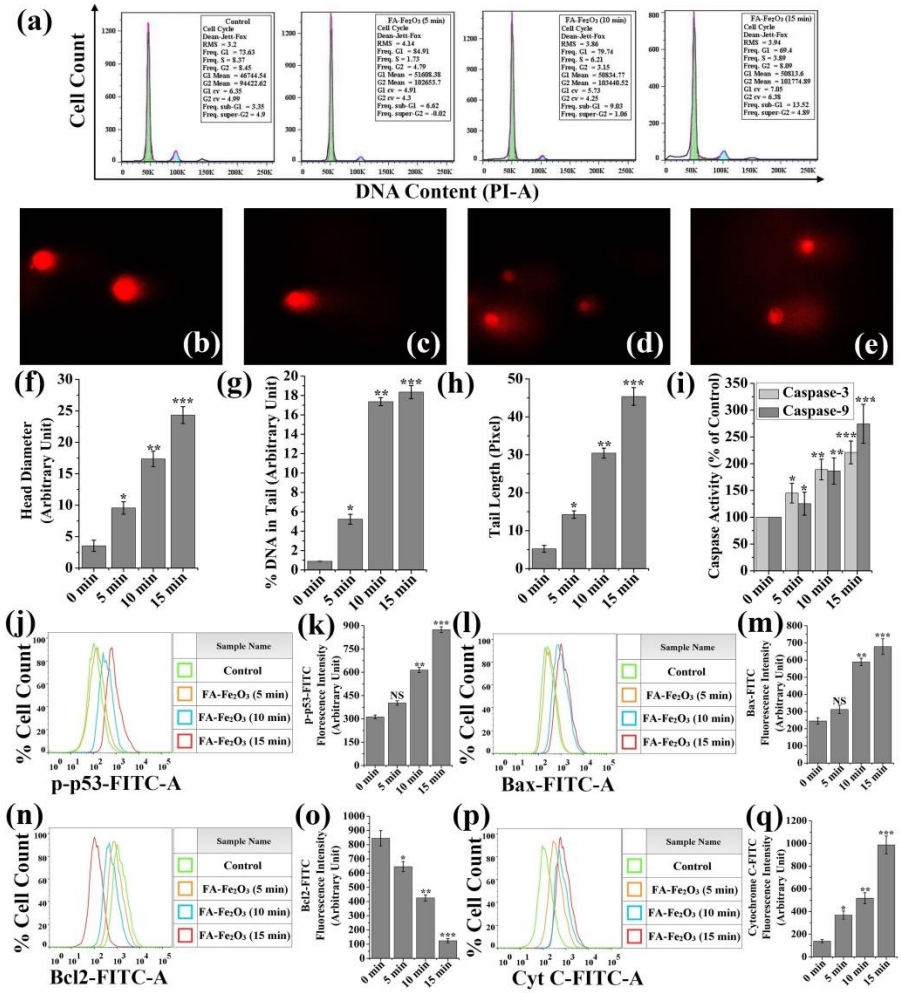

Figure 11.13: *HCT 116 cells were treated with a requisite amount of FA-Fe_2O_3 for 24 hr. followed by time dependent blue light exposure before various experiments a) DNA content in sub G0-G1 phase of the cell cycle. Representative microscopic image of Comet assay b) Control, c) 5 min., d) 10 min., e)15 min. blue light exposure. Comet Score analyzed data of microscopic image obtained from the Comet assay experiment f) head diameter g) % of DNA in tail h) tail length. i) Caspase 3 and Caspase 9 activity. Analysis of j) $p53^{Ser46}$, l) Bax, n) Bcl2, and p) Cytochrome c protein expression, respectively. Flow Jo analyzed data of k) $p53^{Ser46}$, m) Bax, o) Bcl2, and q) Cytochrome c protein expression, respectively.*

treated cells in the presence of blue light. Phosphorylation of p53 expression was significantly augmented with an increase in the light dose of 5-15 min. (Figure 11.13j). As found in the flow cytometry analysis, the fluorescence intensity of p-p53-FITC was gradually ($p < 0.05$) increased (1.29, 1.97, and 2.79 fold in 5, 10, and 15 min. respectively) with respect to the FA-Fe_2O_3 treated control cell without any blue light exposure, indicating the correlation of ROS mediated p53 phosphorylation at Ser 46 in PDT (Figure 11.13k).

An altered level of pro/anti-apoptotic proteins, Bax, Bcl2 have been shown to regulate the mitochondrial-dependent apoptosis process through the modulation of phosphorylated p53 (Ser 46). Loss of function in anti-apoptotic Bcl2 triggers the release of cyt c to the cytosol in initiating the apoptotic cascade. To evaluate the detailed mechanism of FA-Fe_2O_3 induced apoptosis in presence of blue light, flow cytometric assessment of mitochondrial-dependent apoptosis regulating protein Bax, Bcl2, and cytochrome c was carried out (Figure 11.13l, 11.13n, and 11.13p). As shown in the flow cytometric histogram, the relative FITC fluorescence intensities of Bax (1.27, 2.40, and 2.76 fold in 5, 10, and 15 min., respectively) and cyt c (2.66, 3.74, and 7.13 fold in 5, 10, and 15 min., respectively) were gradually increased with increase in the duration of light treatment (Figure 11.13l, 11.13m, 11.13p, and 11.13q). On the other hand, the expression of anti-apoptotic Bcl2 was significantly ($p < 0.05$) suppressed (0.76, 0.50, and 0.15 fold in 5, 10, and 15 min., respectively) with an increase in the light duration of light treatment compared to without any light treatment (Figure 11.13n & 11.13o). Therefore FA-Fe_2O_3 mediated PDT in HCT 116 cells initiate mitochondrial-dependent apoptosis through p53 phosphorylation and associated with ROS mediated pathway.

Caspase, a family of proteases, is responsible for triggering apoptosis by cleaving the specific enzymes. Up-regulation of Bax/cytochrome c can induce caspase activation which is responsible for the initialization of apoptosis.

Correlating with the data, a gradual augmentation of caspase 3/9 activity (1.45, 1.89, and 2.21 in 5, 10, and 15 min., respectively for caspase 3 activity and 1.25, 1.86, and 2.74 fold in 5, 10, and 15 min., respectively for caspase 9 activity) were found when the FA-Fe_2O_3 pretreated cells were exposed to blue light for the different time duration (5, 10, and 15 min., Figure 11.13i). Along with p53, Bax and Bcl2 protein expression caspase 3 and caspase 9 activity confirm that FA-Fe_2O_3 mediated PDT in HCT 116 cells induces cell death via an apoptotic pathway.

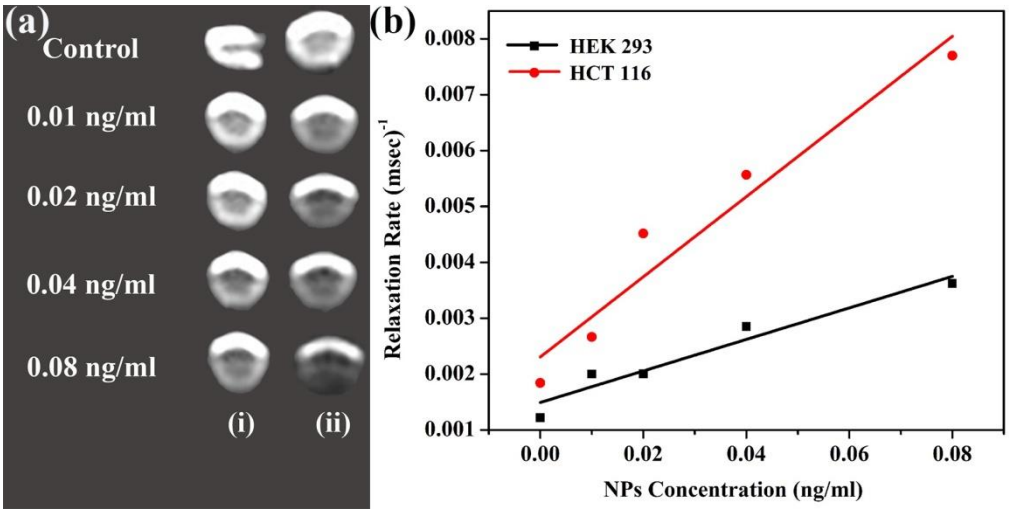

Figure 11.14: *a) Transverse relaxation time (T2) weighted MRI phantom images of (i) HEK 293 and (ii) HCT 116 cells treated with different concentrations of FA-Fe_2O_3. b) Relaxivity study of FA-Fe_2O_3 incubated in HEK 293 and HCT 116 cell lines.*

The NH (FA-Fe_2O_3) possesses selectively blue light sensitized enhanced ROS activity without any perturbation. At an optimum concentration of 0.1 µg/ml, the NH possesses optimum dark toxicity and considerable light toxicity for the implementation of PDT. Upon blue light irradiation both in extracellular and intracellular conditions, FA-Fe_2O_3 rapidly generates ROS, which is found to be hydroxyl radical from the HPF staining experiment (Figure 11.11g and 11.11h). Light-induced intracellular ROS generation causes nuclear DNA damage, which leads to an increase in p53 protein expression inside the cell followed by the up-regulation of mitochondrial Bax protein and a decrease in Bcl2 protein level. Mitochondrial started releasing cyt c leads to activation of pro caspase 9 and Pro

caspase 3 to caspase 9 and caspase 3 respectively, ultimately cell death occurs via the apoptotic pathway.

To test the potential applicability of FA-Fe_2O_3 as a diagnosis tool for cancer *in vitro* MRI study has been performed on HCT 116 cells along with HEK 293 cells as control. Figure 11.14a represents T2 weighted phantom images of FA-Fe_2O_3 treated HEK 293 and HCT 116 cells. Signal intensity changes (from bright to dark) with an increase in the concentration of FA-Fe_2O_3 (from 0.01-0.08 ng/ml) NH was observed in the case of HCT 116 compare to HEK 293 cells indicating targeted delivery of FA-Fe_2O_3 in FR overexpressed cells. The Relaxivity plot (Figure 11.14b) indicates a linear relation of relaxation rate (R_2 = 1/T2) with the NH concentration. With increasing concentration of FA-Fe_2O_3, the transverse relaxation time (T2) of the protons of water decreases, and relaxation rate (R_2) increases leading to the darkening of the specific region of interest. This indicates FA-Fe_2O_3 being a potential T2 contrast agent.

Along with therapeutic property FA-Fe_2O_3, it has also potential MRI contrasting ability in HCT 116 cells. Shaoo *et al.* developed FA conjugated silica-coated manganese ferrite (FA-MSN) NH for targeted delivery and MR imaging [73]. FA-MSN shows MRI contrasting at 0.05 mg/ml concentration, whereas in the case of FA-Fe_2O_3, we found excellent contrasting in cancer cell at 0.08 ng/ml, which is ~1000 times lower concentration with respect to the optimum dose found for the PDT. Compare to the FR deficient cells pronounced contrasting in FR+ cancer cells at very low concentration reveals its efficiency as an MRI contrast agent. FA mediated targeted delivery, light sensitized enhanced ROS activity, and MRI contrasting competence of FA-Fe_2O_3 leads to a potential biomaterial for dual application for diagnosis and therapy colorectal cancer.

11.3. Conclusion:

In summary, a simple, efficient, and field-deployable method has been proposed to decontaminate the toxic mercury from the Hg-Curcumin complex.

We propose a simple transmetalation process which can exchange up to ~70% of the toxic mercury ion from Curcumin with copper. The shift in the absorption spectra undoubtedly indicates the exchange of metal ions at the attachment site. First principles density functional theory calculation reveals that, in the presence of Cu environment near to Hg-Curcumin, upon ground state energy optimization, mercury metal is replaced by copper. The SPR band of Ag NP is employed to detect uncoupled Hg^{2+} ions. In the case of Hg-Curcumin, there was no alteration in the SPR band of Ag NP. However, Cu-treated Hg-Curcumin decouples the Hg ion from the Curcumin, which can be detected by the suppression of the SPR band of Ag NP. This simple transmetalation technique holds great potential to evolve a new approach to decouple toxic metal from essential food elements.

Besides, we have developed a facile and cost-effective synthesis methodology of a novel NH (FA-Fe_2O_3), which demonstrates blue light sensitized target specific anti-cancer activity in human colorectal carcinoma cell line along with MRI contrasting abilities. Attachment of FA with Fe_2O_3 at the molecular level was confirmed from picosecond resolved fluorescence study. Enhanced ROS activity was confirmed from extracellular and intracellular DCFH oxidation assay with different light exposure time. Cytotoxicity study in HCT 116 cells with different light exposure time reveals photoinduced enhanced cytotoxicity. Analysis of DNA content in sub G0-G1 phase of cell cycle and comet assay reveals ROS mediated nuclear DNA damage in HCT 116 cells. ROS mediated cell death via the apoptotic pathway is evident from p53, Bax, Bcl2, and cytochrome c protein expression. Apoptosis mediated cell death was further confirmed from caspase 9 and caspase 3 activity. For diagnosis purposes *in vitro* MRI study reveals excellent contrasting in FR overexpressed cancer cell (HCT 116) than FR deficient normal cell (HEK 293). Finally, this work stimulates a new approach towards the synthesis of effective, low-cost NH for diagnosis and therapy of colorectal carcinoma.

References

[1] G. H. Lee, C. H. Lee, A.M.v.d. Zande, M. Han, X. Cui, G. Arefe, C. Nuckolls, T.F. Heinz, J. Hone, P. Kim, Heterostructures based on inorganic and organic van der Waals systems, *APL Mater.* 2 (2014) 092511.

[2] N. Zhao, L. Yan, X. Zhao, X. Chen, A. Li, D. Zheng, X. Zhou, X. Dai, F. J. Xu, Versatile types of organic/inorganic nanohybrids: From strategic design to biomedical applications, *Chem. Rev.* 119 (2019) 1666.

[3] Y. Otsuka, Y. Okamoto, H. Y. Akiyama, K. Umekita, Y. Tachibana, S. Kuwabata, Photoinduced formation of polythiophene/TiO_2 nanohybrid heterojunction films for solar cell applications, *J. Phys. Chem. C* 112 (2008) 4767.

[4] H. Zhang, D. Pan, K. Zou, J. He, X. Duan, A novel core-shell structured magnetic organic-inorganic nanohybrid involving drug-intercalated layered double hydroxides coated on a magnesium ferrite core for magnetically controlled drug release, *J. Mater. Chem.* 19 (2009) 3069.

[5] Z. Lin, Organic–inorganic nanohybrids through the direct tailoring of semiconductor nanocrystals with conjugated polymers, *Chem. Eur. J.* 14 (2008) 6294.

[6] M. Safari, M. Ghiaci, M. Jafari-Asl, A.A. Ensafi, Nanohybrid organic–inorganic chitosan/dopamine/TiO_2 composites with controlled drug-delivery properties, *Appl. Surf. Sci.* 342 (2015) 26.

[7] D. Bagchi, S. Chaudhuri, S. Sardar, S. Choudhury, N. Polley, P. Lemmens, S.K. Pal, Modulation of stability and functionality of a phyto-antioxidant by weakly interacting metal ions: Curcumin in aqueous solution, *RSC Adv.* 5 (2015) 102516.

[8] B. Raut, M. Chougule, S. Nalage, D. Dalavi, S. Mali, P. Patil, V. Patil, CSA doped polyaniline/CdS organic–inorganic nanohybrid: Physical and gas sensing properties, *Ceram. Int.* 38 (2012) 5501.

[9] A. Mohammadi, F.S. Zabihi, N. Chaibakhsh, Chemical sensor using metal-organic complex: Preparation, characterization and application for highly selective

detection of cyanide ions in mixed aqueous-organic media, *J. Photochem. Photobiol. A: Chem.* 367 (2018) 384.

[10] P. Zhang, P. J. Sadler, Advances in the design of organometallic anticancer complexes, *J. Organomet. Chem.* 839 (2017) 5.

[11] H. Xu, R. Chen, Q. Sun, W. Lai, Q. Su, W. Huang, X. Liu, Recent progress in metal–organic complexes for optoelectronic applications, *Chem. Soc. Rev.* 43 (2014) 3259.

[12] M. W. Johnson, S. W. Bagley, N. P. Mankad, R. G. Bergman, V. Mascitti, F. D. Toste, Application of fundamental organometallic chemistry to the development of a gold-catalyzed synthesis of sulfinate derivatives, *Angew. Chem.* 53 (2014) 4404.

[13] C. Sanchez, B. Julián, P. Belleville, M. Popall, Applications of hybrid organic–inorganic nanocomposites, *J. Mater. Chem.* 15 (2005) 3559.

[14] K. S. Egorova, V. P. Ananikov, Toxicity of metal compounds: Knowledge and myths, *Organometallics* 36 (2017) 4071.

[15] E. Merian, M. Anke, M. Ihnat, M. Stoeppler, Elements and their compounds in the environment: Occurrence, analysis and biological relevance, *Wiley-VCH Verlag GmbH & Co. KGaA*, Weinheim, 2004

[16] P. Deria, J. E. Mondloch, O. Karagiaridi, W. Bury, J. T. Hupp, O. K. Farha, Beyond post-synthesis modification: Evolution of metal–organic frameworks via building block replacement, *Chem. Soc. Rev.* 43 (2014) 5896.

[17] M. Lalonde, W. Bury, O. Karagiaridi, Z. Brown, J. T. Hupp, O. K. Farha, Transmetalation: Routes to metal exchange within metal–organic frameworks, *J. Mater. Chem. A* 1 (2013) 5453.

[18] T. W. Clarkson, Mercury: Major issues in environmental health, *Environ. Health Perspect.* 100 (1993) 31.

[19] K. Farhadi, M. Forough, R. Molaei, S. Hajizadeh, A. Rafipour, Highly selective Hg^{2+} colorimetric sensor using green synthesized and unmodified silver nanoparticles, *Sens. Actuator B-Chem.* 161 (2012) 880.

[20] B. Wei, L. Yang, A review of heavy metal contaminations in urban soils, urban road dusts and agricultural soils from China, *Microchem. J.* 94 (2010) 99.

[21] K. Bairwa, J. Grover, M. Kania, S. M. Jachak, Recent developments in chemistry and biology of curcumin analogues, *RSC Adv.* 4 (2014) 13946.

[22] K. I. Priyadarsini, The chemistry of curcumin: From extraction to therapeutic agent, *Molecules* 19 (2014) 20091.

[23] S. Borowska, M. M. Brzóska, Metals in cosmetics: Implications for human health, *J. Appl. Toxicol.* 35 (2015) 551.

[24] Z. Hubicki, D. Kołodyńska, Selective removal of heavy metal ions from waters and waste waters using ion exchange methods, *Ion Exchange Technol.* (2012) 193.

[25] R. A. Bernhoft, Mercury toxicity and treatment: A review of the literature, *J. Environ. Public Health* 2012 (2012) 460508.

[26] L. M. Gaetke, H. S. Chow-Johnson, C. K. Chow, Copper: Toxicological relevance and mechanisms, *Arch. Toxicol.* 88 (2014) 1929.

[27] J. Wang, X. Tan, X. Pang, L. Liu, F. Tan, N. Li, MoS_2 quantum dot@ polyaniline inorganic–organic nanohybrids for *in vivo* dual-modal imaging guided synergistic photothermal/radiation therapy, *ACS Appl. Mater. Interfaces* 8 (2016) 24331.

[28] J. H. Yang, H. Jung, S. Y. Kim, C. H. Yo, J. H. Choy, Heterostructured layered aluminosilicate-itraconazole nanohybrid for drug delivery system, *J. Nanosci. Nanotechnol.* 13 (2013) 7331.

[29] Z. Hu, J. Li, C. Li, S. Zhao, N. Li, Y. Wang, F. Wei, L. Chen, Y. Huang, Folic acid-conjugated graphene–ZnO nanohybrid for targeting photodynamic therapy under visible light irradiation, *J. Mater. Chem. B* 1 (2013) 5003.

[30] A. C. Antony, The biological chemistry of folate receptors, *Blood* 79 (1992) 2807.

[31] Y. K. Lee, Preparation and characterization of folic acid linked poly (L-glutamate) nanoparticles for cancer targeting, *Macromol. Res.* 14 (2006) 387.

[32] P. Garin-Chesa, I. Campbell, P. Saigo, J. Lewis Jr, L. Old, W. Rettig, Trophoblast and ovarian cancer antigen LK26. Sensitivity and specificity in immunopathology and molecular identification as a folate-binding protein, *Am. J. Pathol.* 142 (1993) 557.

[33] A. R. Hilgenbrink, P. S. Low, Folate receptor-mediated drug targeting: From therapeutics to diagnostics, *J. Pharm. Sci.* 94 (2005) 2135.

[34] F. Sonvico, S. Mornet, S. Vasseur, C. Dubernet, D. Jaillard, J. Degrouard, J. Hoebeke, E. Duguet, P. Colombo, P. Couvreur, Folate-conjugated iron oxide nanoparticles for solid tumor targeting as potential specific magnetic hyperthermia mediators: Synthesis, physicochemical characterization, and in vitro experiments, *Bioconjug. Chem.* 16 (2005) 1181.

[35] C. H. Wang, C. W. Chang, C. A. Peng, Gold nanorod stabilized by thiolated chitosan as photothermal absorber for cancer cell treatment, *J. Nanopart. Res.* 13 (2011) 2749.

[36] H. Meng, J. Y. Chen, L. Mi, P. N. Wang, M. Y. Ge, Y. Yue, N. Dai, Conjugates of folic acids with BSA-coated quantum dots for cancer cell targeting and imaging by single-photon and two-photon excitation, *J. Biol. Inorg. Chem.* 16 (2011) 117.

[37] P. Suriamoorthy, X. Zhang, G. Hao, A. G. Joly, S. Singh, M. Hossu, X. Sun, W. Chen, Folic acid-CdTe quantum dot conjugates and their applications for cancer cell targeting, *Cancer Nanotechnol.* 1 (2010) 19.

[38] M. E. Mathew, J. C. Mohan, K. Manzoor, S. Nair, H. Tamura, R. Jayakumar, Folate conjugated carboxymethyl chitosan–manganese doped zinc sulphide nanoparticles for targeted drug delivery and imaging of cancer cells, *Carbohydr. Polym.* 80 (2010) 442.

[39] Y. Zhao, S. Liu, Y. Li, W. Jiang, Y. Chang, S. Pan, X. Fang, Y. A. Wang, J. Wang, Synthesis and grafting of folate–PEG–PAMAM conjugates onto quantum dots for selective targeting of folate-receptor-positive tumor cells, *J. Colloid Interface Sci.* 350 (2010) 44.

[40] J. J. Lin, J. S. Chen, S. J. Huang, J. H. Ko, Y. M. Wang, T. L. Chen, L. F. Wang, Folic acid–pluronic F127 magnetic nanoparticle clusters for combined targeting, diagnosis, and therapy applications, *Biomaterials* 30 (2009) 5114.

[41] T. K. Maji, D. Bagchi, N. Pan, A. Sayqal, M. Morad, S. A. Ahmed, D. Karmakar, S. K. Pal, A combined spectroscopic and ab initio study of the transmetalation of a polyphenol as a potential purification strategy for food additives, *RSC Adv.* 10 (2020) 5636.

[42] S. Wanninger, V. Lorenz, A. Subhan, F. T. Edelmann, Metal complexes of curcumin–synthetic strategies, structures and medicinal applications, *Chem. Soc. Rev.* 44 (2015) 4986.

[43] M. H. Leung, D. T. Pham, S. F. Lincoln, T. W. Kee, Femtosecond transient absorption spectroscopy of copper (II)–curcumin complexes, *Phys. Chem. Chem. Phys.* 14 (2012) 13580.

[44] T. J. Meyer, Photochemistry of metal coordination complexes: Metal to ligand charge transfer excited states, *Pure Appl. Chem.* 58 (1986) 1193.

[45] M. Subhan, K. Alam, M. Rahaman, M. Rahman, R. Awal, Synthesis and characterization of metal complexes containing curcumin ($C_{21}H_{20}O_6$) and study of their anti-microbial activities and DNA-binding properties, *J. Sci. Res.* 6 (2014) 97.

[46] W. F. Kieffer, The activity series of the metals, *J. Chem. Educ.* 27 (1950) 659.

[47] J. H. Van Vleck, Theory of the variations in paramagnetic anisotropy among different salts of the iron group, *Phys. Rev.* 41 (1932) 208.

[48] H. Maier, U. Scherz, Vibronic spectra and the dynamic Jahn-Teller effect of cubic ZnS: Cu^{2+}, *Phys. Status Solidi B* 62 (1974) 153.

[49] W. B. Jensen, The Lewis acid-base definitions: A status report, *Chem. Rev.* 78 (1978) 1.

[50] M. A. Addicoat, G. F. Metha, T. W. Kee, Density functional theory investigation of Cu (I)- and Cu (II)-curcumin complexes, *J. Comput. Chem.* 32 (2011) 429.

[51] E. Rodríguez-León, R. Iñiguez-Palomares, R. E. Navarro, R. Herrera-Urbina, J. Tánori, C. Iñiguez-Palomares, A. Maldonado, Synthesis of silver nanoparticles using reducing agents obtained from natural sources (Rumex hymenosepalus extracts), *Nanoscale Res. Lett.* 8 (2013) 318.

[52] S. Saravanan, R. Kato, M. Balamurugan, S. Kaushik, T. Soga, Efficiency improvement in dye sensitized solar cells by the plasmonic effect of green synthesized silver nanoparticles, *J. Sci. Adv. Mater. Dev.* 2 (2017) 418.

[53] M. Forough, K. Fahadi, Biological and green synthesis of silver nanoparticles, *Turkish J. Eng. Env. Sci.* 34 (2011) 281.

[54] D. Paramelle, A. Sadovoy, S. Gorelik, P. Free, J. Hobley, D. G. Fernig, A rapid method to estimate the concentration of citrate capped silver nanoparticles from UV-visible light spectra, *Analyst* 139 (2014) 4855.

[55] A. Nain, S. R. Barman, S. Jain, A. Mukherjee, J. Satija, Dual mechanism-based sensing of mercury using unmodified, heteroepitaxially synthesized silver nanoparticles, *Appl. Nanosci.* 7 (2017) 299.

[56] P. K. Sarkar, A. Halder, N. Polley, S. K. Pal, Development of highly selective and efficient prototype sensor for potential application in environmental mercury pollution monitoring, *Water Air Soil Pollut.* 228 (2017) 314.

[57] L. Rastogi, R. B. Sashidhar, D. Karunasagar, J. Arunachalam, Gum kondagogu reduced/stabilized silver nanoparticles as direct colorimetric sensor for the sensitive detection of Hg^{2+} in aqueous system, *Talanta* 118 (2014) 111.

[58] P. Kar, T. K. Maji, P. K. Sarkar, P. Lemmens, S. K. Pal, Development of a photo-catalytic converter for potential use in the detoxification of Cr (VI) metal in water from natural resources, *J. Mater. Chem. A* 6 (2018) 3674.

[59] S. Chakrabarty, T. Jana, K. De, S. Das, K. Dey, K. Chatterjee, Morphology dependent magnetic properties of α-Fe_2O_3 nanostructures, *Mater. Res. Express.* 1 (2014) 046104.

[60] Y. Wang, A. Muramatsu, T. Sugimoto, FTIR analysis of well-defined α-Fe_2O_3 particles, *Colloids Surf. A* 134 (1998) 281.

[61] S. Dutta, B. N. Ganguly, Characterization of ZnO nanoparticles grown in presence of folic acid template, *J. Nanobiotechnology* 10 (2012) 1.

[62] A. L. M. Raouf, K. K. Hammud, J. M. Mohammed, E. M. K. A. Dulimyi, Qualitative and quantitative determination of folic acid in tablets by FTIR spectroscopy, *Int. J. Adv. Pharm. Biol. Chem.* 3, (2014) 773.

[63] M. Massey, U. Baier, R. Merlin, W. Weber, Effects of pressure and isotopic substitution on the Raman spectrum of α-Fe_2O_3: Identification of two-magnon scattering, *Phys. Rev. B* 41 (1990) 7822.

[64] S. Onari, T. Arai, K. Kudo, Infrared lattice vibrations and dielectric dispersion in α−Fe_2O_3, *Phys. Rev. B* 16 (1977) 1717.

[65] Y. Teow, S. Valiyaveettil, Active targeting of cancer cells using folic acid-conjugated platinum nanoparticles, *Nanoscale* 2 (2010) 2607.

[66] D. M. Sherman, T. D. Waite, Electronic spectra of Fe^{3+} oxides and oxide hydroxides in the near IR to near UV, *Am. Min.* 70 (1985) 1262.

[67] S. Mitra, S. Das, K. Mandal, S. Chaudhuri, Synthesis of a α-Fe_2O_3 nanocrystal in its different morphological attributes: Growth mechanism, optical and magnetic properties, *Nanotechnology* 18 (2007) 275608.

[68] S. Chakrabarty, K. Chatterjee, Oriented growth of α-Fe_2O_3 nanocrystals with different morphology and their optical behavior, *J. Cryst. Growth* 381 (2013) 107.

[69] S. Chaudhuri, S. Sardar, D. Bagchi, S. Dutta, S. Debnath, P. Saha, P. Lemmens, S. K. Pal, Photoinduced dynamics and toxicity of a cancer drug in proximity of inorganic nanoparticles under visible light, *ChemPhysChem* 17 (2016) 270.

[70] M. Price, J. J. Reiners, A. M. Santiago, D. Kessel, Monitoring singlet oxygen and hydroxyl radical formation with fluorescent probes during photodynamic therapy, *Photochem. Photobiol.* 85 (2009) 1177.

[71] I. Vermes, C. Haanen, H. Steffens-Nakken, C. Reutellingsperger, A novel assay for apoptosis flow cytometric detection of phosphatidylserine expression on early apoptotic cells using fluorescein labelled annexin V, *J. Immunol. Methods* 184 (1995) 39.

[72] Z. Gu, H. Wang, L. Li, Y. Liu, X. Deng, S. Huo, F. Yuan, Z. Liu, H. Tong, L. Su, Heat stress induces apoptosis through transcription-independent p53-mediated mitochondrial pathways in human umbilical vein endothelial cell, *Sci. Rep.* 4 (2014) 4469.

[73] B. Sahoo, K. S. P. Devi, S. Dutta, T. K. Maiti, P. Pramanik, D. Dhara, Biocompatible mesoporous silica-coated superparamagnetic manganese ferrite nanoparticles for targeted drug delivery and MR imaging applications, *J. Colloid. Interface Sci.* 431 (2014) 31.

List of Publications

(Peer-reviewed Journals)

[1] **T. K. Maji**, D. Bagchi, P. Kar, D. Karmakar and S. K. Pal

"Enhanced charge separation through modulation of defect-state in wide band-gap semiconductor for potential photocatalysis application: Ultrafast spectroscopy and computational studies"

J. Photochem. Photobiol. A: Chem. 332 (2017) 391.

[2] **T. K. Maji**, J. R. Aswin, S. Mukherjee, R. Alexander, A. Mondal, S. Das, R. K. Sharma, N. K. Chakraborty, K. Dasgupta, R. Sharma, R. Hawalder, M. Pandey, A. Naik, K. Majumdar, S. K. Pal, K. V. Adarsh, S. K. Ray and D. Karmakar

"Combinatorial large-area MoS_2/anatase-TiO_2 interface: A pathway to emergent optical and opto-electronic functionalities"

ACS Appl. Mater. Interfaces 12 (2020) 44345.

[3] **T. K. Maji**, K. Vaibhav, R. Hawaldar, K. Adarsh, S. K. Pal and D. Karmakar

"Intriguing electronic and optical prospects of FCC bimetallic two-dimensional heterostructures: Epsilon near-zero behavior in UV-Vis range"

Phys. Chem. Chem. Phys. 22 (2020) 16314.

[4] **T. K. Maji**, K. Vaibhav, S. K. Pal, K. Majumdar, K. V. Adarsh and D. Karmakar

"Intricate modulation of interlayer coupling at the graphene oxide/$MoSe_2$ interface: Application in time-dependent optics and device transport"

Phys. Rev. B 99 (2019) 115309.

[5] **T. K. Maji**, P. K. Sarkar, P. Kar, B. Liu, P. Lemmens, D. Karmakar and S. K. Pal

"A combined experimental and computational study on a nanohybrid material for potential application in NIR photocatalysis"

Appl. Catal. A: Gen. 583 (2019) 117124.

[6] **T. K. Maji**, M. N. Hasan, S. Ghosh, D. Wulferding, C. Bhattacharya, P. Lemmens, D. Karmakar and S. K. Pal

"Development of a magnetic nanohybrid for multifunctional application: From immobile photocatalysis to efficient photoelectrochemical water splitting: A combined experimental and computational study"

J. Photochem. Photobiol. A: Chem. 397 (2020) 112575.

[7] **T. K. Maji**, K. Vaibhav, S.K. Pal and D. Karmakar

"Broken inversion symmetry and interface-induced spin-polarization for metal-Weyl semimetal stacked interfaces"

Sci. Rep. 10 (2020) 14438.

[8] **T. K. Maji**, D. Bagchi, N. Pan, A. Sayqal, M. Morad, S. A. Ahmed, D. Karmakar and S. K. Pal

"A combined spectroscopic and ab initio study of the transmetalation of a polyphenol as a potential purification strategy for food additives"

RSC Adv. 10 (2020) 5636.

[9] **T. K. Maji**, P. Kar, H. Mandal, C. Bhattacharya, D. Karmakar and S. K. Pal

"Halide-modulated functionality of wide band gap zinc oxide semiconductor nanoparticle"

ChemistrySelect 3 (2018) 6382.

[10] P. Kar, **T. K. Maji**, P. K. Sarkar, P. Lemmens and S. K. Pal

"Development of a photo-catalytic converter for potential use in the detoxification of Cr (VI) metal in water from natural resources"

J. Mater. Chem. A 6 (2018) 3674.

[11] R. Nandi, S. Mishra, **T. K. Maji**, K. Manna, P. Kar, S. Banerjee, S. Dutta, S. Sharma, P. Lemmens, K. D. Saha and S. K. Pal

"A novel nanohybrid for cancer theranostics: Folate sensitized Fe_2O_3 nanoparticles for colorectal cancer diagnosis and photodynamic therapy"

J. Mater. Chem. B 5 (2017) 3927.

[12] **T. K. Maji**, S. K. Pal and D. Karmakar

"Hole-doping and contact induced spin-polarization in Weyl semimetal TaAs"

AIP Conf. Proc. 1942 (2018) 130053.

[13] **T. K. Maji**, S. K. Pal and D. Karmakar
"Doping induced carrier and band-gap modulation in bulk versus nano for topological insulators: A test case of Stibnite"
AIP Conf. Proc. 1942 (2018) 090029.
[14] **T. K. Maji**, K. K. Tiwary and D. Karmakar
"Achieving tunable doping of $MoSe_2$ based devices using GO@$MoSe_2$ heterostructure" *AIP Conf. Proc.* 1832 (2017) 120019.
[15]* P. Kar, **T. K. Maji**, R. Nandi, P. Lemmens and S. K. Pal
"In-Situ hydrothermal synthesis of Bi–$Bi_2O_2CO_3$ heterojunction photocatalyst with enhanced visible light photocatalytic activity"
Nano-Micro Lett. 9 (2017) 18.
[16]* D. Bagchi, **T. K. Maji**, S. Sardar, P. Lemmens, C. Bhattacharya, D. Karmakar and S. K. Pal
"Sensitized ZnO nanorod assemblies to detect heavy metal contaminated phytomedicines: Spectroscopic and simulation studies"
Phys. Chem. Chem. Phys. 19 (2017) 2503.
[17]* P. Kar, **T. K. Maji**, J. Patwari and S. K. Pal
"Can a light harvesting material be always common in photocatalytic and photovoltaic applications?" *Mater. Chem. Phys.* 200 (2017) 70.
[18]* M. N. Hasan, **T. K. Maji**, U. Pal, A. Bera, D. Bagchi, A. Halder, S. A. Ahmed, J. H. Al-Fahemi, T. M. Bawazeer, T. Saha-Dasgupta and S. K. Pal
"Wide bandgap semiconductor-based novel nanohybrid for potential antibacterial activity: Ultrafast spectroscopy and computational studies"
RSC Adv. 10 (2020) 38890.
[19]* P. Kar, **T. K. Maji**, P.K. Sarkar, S. Sardar and S. K. Pal
"Direct observation of electronic transition–plasmon coupling for enhanced electron injection in dye-sensitized solar cells"
RSC Adv. 6 (2016) 98753.

[20]* R. K. Yadav, J. Aneesh, R. Sharma, P. Abhiramnath, **T. K. Maji**, G. J. Omar, A. K. Mishra, D. Karmakar and K. V. Adarsh

"Designing hybrids of graphene oxide and gold nanoparticles for nonlinear optical response"

Phys. Rev. A 9 (2018) 044043.

[21]* R. Sharma, J. Aneesh, R. K. Yadav, S. Sanda, A. R. Barik, A. K. Mishra, **T. K. Maji**, D. Karmakar and K. V. Adarsh

"Strong interlayer coupling mediated giant two-photon absorption in $MoSe_2$/graphene oxide heterostructure: Quenching of exciton bands"

Phys. Rev. B 93 (2016) 155433.

[22]* U. Ghanta, M. Ray, S. Biswas, S. Sardar, **T. K. Maji**, S. K. Pal, N. R. Bandyopadhyay, B. Liu and S. M. Hossain

"Effect of phonon confinement on photoluminescence from colloidal silicon nanostructures"

J. Lumin. 201 (2018) 338.

[23]* R. K. Yadav, J. Aneesh, R. Sharma, S. K. Bera, **T. K. Maji**, D. Karmakar, K. P. Loh and K. V. Adarsh

"Ultrafast direct charge transfers mediated modification of third order nonlinear optical response in Sb_2Se_3–Au core shell nanorods"

Appl. Phys. Lett. 117 (2020) 032104.

[24]* R. K. Yadav, J. Aneesh, R. Sharma, **T. K. Maji**, D. Karmakar and K. V. Adarsh

"Anisotropic nonlinear optical response in graphene oxide-gold nanohybrid"

Opt. Lett. 45 (2020) 6655.

[25]* P. Paul, **T. K. Maji**, K. K. Tiwari, B. Mandal, A. Rajarajan, R. Bhatt, D. Karmakar and T. Rao

"Theoretical and experimental study of multiferroic $BiFeO_3$"

AIP Conf. Proc. 1832 (2017) 130058.

* Not included in the thesis.

List of International/National Conferences Attended

	Name of the Conference	Place	Date	Contribution
1	*DAE-BRNS Ultrafast Science (UFS-2015)*	S.N. Bose National Centre for Basic Sciences, Kolkata	19-21 Nov 2015	Participation
2	*DAE – Solid State Physics Symposium (DAE SSPS 2016)*	KIIT University Bhubaneswar, Odisha	26-30 Dec 2016	Poster
3	*International Conference on Advances in Nanotechnology (iCAN 2017)*	Assam Don Bosco University	9-13 Jan 2017	Oral
4	*DAE – Solid State Physics Symposium (DAE SSPS 2017)*	Bhabha Atomic Research Centre (BARC), Mumbai	26-30 Dec 2017	Poster *(Two Contribution)*
5	*International Conference on Nanoscience & Technology (ICONSAT 2018)*	Indian Institute of Science, Bangalore	21-23 Mar 2018	Poster
6	*International Conference on Complex and Functional Material (ICCFM 2018)*	S.N. Bose National Centre for Basic Sciences, Kolkata	13-16 Dec 2018	Poster
7	*Recent Development in Chemistry (RDC 2018)*	National Institute of Technology, Durgapur	17-19 Dec 2018	Oral
8	*Conference in Quantum Condensed Matter (Q-Mat 2019)*	Indian Institute of Science, Bangalore	8-10 July 2019	Poster *(Two Contribution)*
9	*International Conference on Current Trends in Materials Science and Engineering (CTMS 2019)*	S.N. Bose National Centre for Basic Sciences, Kolkata	18-20 July 2019	Oral
10	*International Congress on Graphene, 2D Materials and Applications (2D Materials 2019)*	Sochi Olympic Park, Sochi, Russia	3 Sept- 4 Oct 2019	Oral and Poster *(Two Contribution)*
11	*International Symposium on Clusters and Nanomaterials (ISCAN VCU 2019)*	Richmond Virginia, USA	3-7 Nov 2019	Oral *(Selected for Hot Topic Oral Presentation)* Poster *(Two Contribution)*

	Name of the Conference	Place	Date	Contribution
12	***2019AIChE Annual Meeting***	Hyatt Regency Orlando, USA	10-15 Nov 2019	Oral ***(Short-listed for Grad Student Award)*** Poster ***(Two Contribution)***
13	***International Winter School 2019***	JNCASR, Bangalore	2-6 Dec 2019	Oral
14	***XXth International Workshop on Physics of Semiconductor Devices: (IWPSD 2019)***	S.N. Bose National Centre for Basic Sciences, Kolkata	17-20 Dec 2019	Poster ***(Best Poster Award)***
15	***International Conference on Smart Materials for Sustainable Technologies (SMST 2020)***	IIT BHU and IIT Goa (at Bogmallo Beach Resort Goa)	22-25 Feb 2020	Poster ***(Best Poster Award)***
16	***International Conference on Nanoscience & Technology (ICONSAT 2018)***	S.N. Bose National Centre for Basic Sciences, Kolkata	5-7 Mar 2020	Poster
17	***Advances in Functional Materials (AFM 2020)***	KIIT University Bhubaneswar, Odisha	27-28 Aug 2020	Participation
18	***Conference in Quantum Condensed Matter (Q-Mat 2019)***	S.N. Bose National Centre for Basic Sciences, Kolkata	7-11 Sept 2020	Oral